

**UCLA**

**UCLA Electronic Theses and Dissertations**

**Title**

Preparation of positron emission tomography (PET) tracers on advanced microvolume platforms

**Permalink**

<https://escholarship.org/uc/item/1fp031cf>

**Author**

Lu, Yingqing

**Publication Date**

2023

Peer reviewed|Thesis/dissertation

UNIVERSITY OF CALIFORNIA

Los Angeles

Preparation of positron emission tomography (PET)  
tracers on advanced microvolume platforms

A dissertation submitted in partial satisfaction of the  
requirements for the degree Doctor of Philosophy in  
Physics and Biology in Medicine

by

Yingqing Lu

2023

© Copyright by

Yingqing Lu

2023

## ABSTRACT OF THE DISSERTATION

Preparation of positron emission tomography (PET) tracers on advanced microvolume platforms

by

Yingqing Lu

Doctor of Philosophy in Physics and Biology in Medicine

University of California Los Angeles, 2023

Professor R. Michael van Dam, Chair

Positron emission tomography (PET) is a widely-used nuclear medicine imaging technique for assessing biodistribution of drugs, diagnosing diseases, and monitoring therapy response. The rapid development of new PET tracers in both research and clinical applications (to image new targets) demands new advances in radiolabeling techniques to facilitate the frequent production of diverse tracers. Recent developments in droplet-based radiochemistry have shrunk reaction volumes 100x (i.e. to  $<10 \mu\text{L}$ ), offering advantages like minimal reagent use, rapid synthesis, high yields, and increased molar activity; they also enable high-throughput optimization and scalable production, with great potential to revolutionize radiopharmaceutical production.

While our group has successfully utilized microdroplet reactors (a small Teflon-coated silicon chip containing hydrophilic reaction sites) for multiple different radiopharmaceuticals, exploration into metal-mediated radiosynthesis remains limited, primarily due to concerns about the sensitivity of metal reagents to environmental moisture in droplet-based reactors. As a proof-of-concept, I conducted the first microscale copper (Cu)-mediated synthesis of [ $^{18}\text{F}$ ]FDOPA (a clinical PET probe used for imaging dopaminergic function). Substantial enhancement in yield and time was achieved while utilizing only nanomole quantities of precursors and other reagents.

Later, I explored the versatility of this method in optimizing additional tracers employing similar Cu-mediated  $^{18}\text{F}$ -radiolabeling routes on a high-throughput microdroplet reactor. For example, across 5 days, I conducted 117 reactions, exploring 36 conditions with <15 mg of precursor, and achieved 12x yield improvement for a novel monoacylglycerol lipase (MAGL) probe ( $^{18}\text{F}$ YH149). Leveraging an automated robotic platform for high-throughput studies, we optimized the production of  $^{18}\text{F}$ FBnTP, a potentiometric radiopharmaceutical, with 64 simultaneous droplet reactions in one morning. In addition, on the technology side, many researchers have wondered whether the droplet-based optimized conditions can guide reaction conditions in conventional vial-based reactors, and I demonstrated for the first time that this indeed can be done. This suggests a rapid and economical approach for novel tracer development, i.e., optimizing radiochemistry on a high-throughput microdroplet platform (rapidly, with minimal reagents) and then performing straightforward translation to vial-based systems to enable wider applicability to the existing install base of radiosynthesis technology.

Furthermore, to assess the adaptability of droplet-based radiochemistry in handling exceptionally complex syntheses, I undertook the investigation of a highly intricate three-step radiosynthesis of  $^{18}\text{F}$ FMAU (imaging cell proliferation), encompassing radiofluorination, coupling, and deprotection reactions all within a microdroplet reactor. Compared the lengthy (~150 min) and low-yielding conventional production, the microdroplet-based radiosynthesis of  $^{18}\text{F}$ FMAU provided significant improvement, completing the production in <60 min and achieving >2x higher radiochemical yield and >3x activity yield, while consuming 34-200x less reagents.

Moreover, to establish the clinical relevance of droplet-based radiochemistry, we developed various droplet-based scale-up approaches including (i) iteratively loading and evaporating  $^{18}\text{F}$ fluoride aliquots in a single droplet reaction, (ii) pre-concentrating  $^{18}\text{F}$ fluoride in a miniature cartridge compatible with a single reaction site, and (iii) pooling multiple droplet reactions for on-demand dose. These methods, validated for reliability and versatility, successfully

delivered clinically-relevant doses of [ $^{18}\text{F}$ ]FET (an amino acid tracer), [ $^{18}\text{F}$ ]Florbetaben (an amyloid imaging agent), [ $^{18}\text{F}$ ]FBnTP, isotopic exchange fluorinated compounds, and aluminum- $^{18}\text{F}$ fluoride probes.

Apart from droplet-based radiosynthesis techniques, I also pursued other novel radiochemistry systems. I helped to develop a platform for microvolume reactions, featuring a pipettor on an XYZ motion gantry and a disposable cassette with integrated micro-vial. The versatile setup performs operations like trapping/releasing [ $^{18}\text{F}$ ]fluoride, liquid transfers, and lid installation/removal for reactor. Comprehensive experiments have been conducted to characterize the system and demonstrate the radiosynthesis feasibility, using [ $^{18}\text{F}$ ]Fallypride as an example. I also helped develop a novel electrochemical radiofluorination (ECRF) technique using a split bipolar electrode (s-BPE) for electron-rich compounds such as thioether derivatives. Unlike traditional ECRF which requires high salt concentration, this s-BPE system, with its dual conductive materials, facilitates anodic and cathodic reactions at lower salt concentrations. We achieved a 5x increase in molar activity for [ $^{18}\text{F}$ ]fluoromethyl (methylthio)acetate compared to conventional ECRF approaches, mainly attributed to reduced [ $^{19}\text{F}$ ]F $^{-}$  contamination from less salt.

Radiochemistry in droplets and electrochemistry for [ $^{18}\text{F}$ ]fluoride labeling showcased an innovative optimization approach and scalable method for clinically-relevant production, surpassing conventional methods. The methodologies outlined in this dissertation provide a comprehensive pathway to speed up the transition of both established and novel PET tracers from the laboratory to clinical application swiftly and cost-effectively.

The dissertation of Yingqing Lu is approved.

Arion-Xenofon Hadjioannou

Peter M. Clark

Jennifer M. Murphy

R. Michael van Dam, Chair

University of California, Los Angeles

2023

*Dedicated to my loving and supporting parents*



## TABLE OF CONTENTS

LIST OF FIGURES .....	xvii
LIST OF TABLES.....	xxii
ACKNOWLEDGEMENTS .....	xxvi
VITA.....	xxxii
Chapter 1 : Introduction.....	1
1.1 Positron emission tomography.....	1
1.2 PET radiopharmaceuticals.....	2
1.3 Conventional synthesizers for radiopharmaceuticals.....	4
1.4 Recent developments in microfluidic-based PET tracer manufacturing.....	5
1.5 High-throughput radiochemistry system.....	14
1.6 Production scale-up on microdroplet platforms.....	17
1.7 Microscale-to-macroscale radiosynthesis translation.....	18
1.8 Summary of the dissertation.....	19
Chapter 2 : Copper-mediated radiosynthesis of 6-[ <sup>18</sup> F]fluoro-L-DOPA ([ <sup>18</sup> F]FDOPA) in a microreactor.....	25
2.1 Introduction.....	25
2.2 Methods.....	27
2.2.1 Materials.....	27
2.2.2 Analytical equipment and methods.....	29
2.2.3 Microdroplet synthesis and optimization.....	30
2.3 Results and discussion.....	32
2.3.1 Fluorination optimization.....	32
2.3.1.1 Preliminary conditions.....	32
2.3.1.2 Initial screening of fluorination conditions.....	34
2.3.1.3 Optimization of PTC amount.....	35
2.3.1.4 Optimization of Cu reagent amount.....	36
2.3.1.5 Optimization of fluorination temperature.....	36
2.3.1.6 Optimization of fluorination time.....	37
2.3.1.7 Optimization of precursor amount.....	37
2.3.2 Deprotection optimization.....	38
2.3.2.1 Influence of deprotection time.....	38
2.3.2.2 Influence of deprotectant concentration.....	39
2.3.3 Full droplet-based radiosynthesis of [ <sup>18</sup> F]FDOPA.....	39
2.3.3.1 Automated synthesis.....	39
2.3.3.2 Additional tests.....	40

2.3.3.3 Comparison of [ <sup>18</sup> F]FDOPA synthesis in μL- and mL-scale.....	41
2.3.4 HPLC purification optimization .....	44
2.4 Conclusions .....	45
2.5 Appendix.....	46
2.5.1 Optimization of fluorination reaction .....	46
2.5.1.1 Study of activity loss in “blank” experiments .....	46
2.5.1.2 Initial screening of fluorination conditions.....	46
2.5.1.3 Optimization of phase transfer catalyst (PTC) amount .....	47
2.5.1.4 Optimization of copper reagent amount .....	47
2.5.1.5 Optimization of fluorination temperature .....	47
2.5.1.6 Optimization of fluorination time.....	48
2.5.1.7 Optimization of precursor amount .....	48
2.5.2 Optimization of deprotection reaction .....	48
2.5.2.1 Influence of deprotection time .....	48
2.5.2.2 Influence of deprotectant concentration .....	48
2.5.3 Automation of the droplet radiosynthesis.....	50
2.5.4 Optimization of radio-HPLC purification method .....	50
2.5.5 Calibration curve to determine molar activity .....	52
Chapter 3 : Proof-of-concept [ <sup>18</sup> F]AIF labeling in droplet reactions .....	53
3.1 Introduction.....	53
3.2 Methods.....	57
3.2.1 Materials .....	57
3.2.2 General microdroplet radiosynthesis .....	58
3.2.3 Analytical methods .....	60
3.3 Results and discussion .....	61
3.3.1 Model substrate: [ <sup>18</sup> F]AIF-NODA-Tz .....	61
3.3.2 Application to [ <sup>18</sup> F]AIF-FAPI-74 .....	63
3.4 Conclusions .....	68
3.5 Appendix.....	69
3.5.1 Optimization of [ <sup>18</sup> F]AIF-NODA-Tz synthesis in a droplet reactor .....	69
3.5.2 [ <sup>18</sup> F]AIF-NODA-Tz purification and radio-HPLC analysis .....	70
3.5.2.1 [ <sup>18</sup> F]AIF-NODA-Tz purification on an HLB cartridge .....	70
3.5.2.2 Example radio-HPLC analysis of [ <sup>18</sup> F]AIF-NODA-Tz .....	70
3.5.3 Optimization of [ <sup>18</sup> F]AIF-FAPI-74 synthesis in a droplet reactor .....	72
3.5.3.1 Influence of precursor amount .....	72
3.5.3.2 Influence of fluorination temperature.....	72

3.5.4 [ <sup>18</sup> F]AIF-FAPI-74 purification.....	73
3.5.4.1 [ <sup>18</sup> F]AIF-FAPI-74 purification on HLB cartridge.....	73
3.5.5 Preliminary experiment to mimic automated radiosynthesis process.....	73
Chapter 4 : Acceleration of radiochemistry through droplet reactions: 6x speedup of [ <sup>18</sup> F]FMAU preparation.....	74
4.1 Introduction.....	74
4.2 Methods.....	77
4.2.1 Materials .....	77
4.2.2 Microdroplet radiosynthesis of [ <sup>18</sup> F]FMAU .....	78
4.2.3 Analytical methods .....	79
4.3 Results and discussion .....	81
4.3.1 Initial conditions .....	81
4.3.2 Fluorination optimization .....	81
4.3.2.1 Preliminary optimization of solvent type and temperature .....	81
4.3.2.2 Preliminary optimization of type of phase transfer catalyst / base .....	82
4.3.2.3 Preliminary optimization of fluorination temperature and time .....	82
4.3.2.4 Preliminary optimization of precursor amount .....	83
4.3.2.5 Re-optimization of solvent type.....	83
4.3.2.6 Re-optimization of temperature.....	85
4.3.2.7 Re-optimization of precursor amount .....	86
4.3.3 Coupling reaction optimization .....	86
4.3.3.1 Influence of coupling temperature.....	86
4.3.3.2 Influence of amount of protected thymine .....	87
4.3.3.3 Influence of ratio of TMSOTf to HMDS (v/v).....	87
4.3.3.4 Influence of coupling temperature.....	88
4.3.3.5 Influence of coupling time .....	89
4.3.4 Deprotection optimization.....	90
4.3.5 HPLC purification optimization .....	91
4.3.6 Preliminary study of automated radiosynthesis .....	93
4.4 Conclusions .....	94
4.5 Appendix.....	95
4.5.1 Initial condition of [ <sup>18</sup> F]FMAU synthesis on droplet reactors.....	95
4.5.2 Optimization of fluorination reaction .....	96
4.5.2.1 Preliminary optimization of solvent type and temperature .....	96
4.5.2.2 Influence of type of phase transfer catalyst (PTC)/base.....	96
4.5.2.3 Preliminary optimization of fluorination temperature and time .....	97
4.5.2.4 Preliminary optimization of precursor amount .....	97

4.5.2.5 Re-optimization of solvent type .....	98
4.5.2.6 Re-optimization of temperature .....	98
4.5.2.7 Re-optimization of precursor amount .....	99
4.5.3 Optimization of coupling reaction .....	99
4.5.3.1 Influence of amount of protected thymine .....	99
4.5.3.2 Influence of ratio of TMSOTf to HMDS (v/v) .....	99
4.5.3.3 Influence of coupling temperature .....	100
4.5.3.4 Influence of coupling time .....	101
4.5.4 Optimization of deprotection reaction .....	101
4.5.4.1 Influence of deprotection time .....	101
4.5.5 Optimization of radio-HPLC purification method .....	102
4.5.6 Preliminary tests of automation .....	104
4.5.7 Example HPLC chromatograms .....	105
Chapter 5 : Robotic platform for high-throughput radiosynthesis and optimization .....	107
5.1 Introduction .....	107
5.2 Methods .....	110
5.2.1 Robotic System .....	110
5.2.2 Work Area .....	111
5.2.3 Fluidics head .....	112
5.2.4 XYZ Gantry .....	113
5.2.5 Control system and software .....	113
5.2.6 System Calibrations .....	116
5.2.7 Reagents .....	116
5.2.8 Analytical methods .....	117
5.2.9 Robotic system characterization .....	118
5.2.10 Optimization of [ <sup>18</sup> F]Fallypride synthesis .....	118
5.2.11 Optimization of [ <sup>18</sup> F]FBnTP synthesis .....	120
5.3 Results .....	121
5.3.1 System characterization .....	121
5.3.2 Optimization of [ <sup>18</sup> F]Fallypride synthesis .....	122
5.3.3 Optimization of [ <sup>18</sup> F]FBnTP synthesis .....	123
5.4 Discussion .....	125
5.5 Conclusions .....	129
5.6 Appendix .....	130
5.6.1 System components .....	130
5.6.1.1 Pipette tip remover .....	130

5.6.1.2 Fluidics head .....	131
5.6.1.3 Liquid priming system .....	132
5.6.2 Calibration of system positions .....	133
5.6.2.1 Coordinate system and system extents .....	133
5.6.2.2 Determining index locations .....	134
5.6.2.3 Pipette cone contact sensor .....	137
5.6.3 Configuration files .....	139
5.6.3.1 Master configuration .....	139
5.6.3.2 Array configuration .....	139
5.6.3.3 Liquid definitions .....	140
5.6.3.4 Experiment configuration .....	140
5.6.3.5 Using the configuration files .....	140
5.6.4 Method files .....	140
5.6.4.1 Set definitions .....	141
5.6.4.2 Dispenser specification .....	144
5.6.4.3 Commands .....	145
5.6.5 Motion acceleration algorithm .....	152
5.6.6 Subsystem calibration and characterization .....	154
5.6.6.1 Dispenser calibration .....	154
5.6.6.2 Heater Calibration .....	156
5.6.6.3 Pipette Characterization .....	156
5.6.6.4 Pressure regulator calibration .....	157
5.6.6.5 TLC spotting process .....	158
5.6.7 Characterization experiments .....	158
5.6.7.1 Uniformity of [ <sup>18</sup> F]fluoride dispensing and drying .....	158
5.6.7.2 Uniformity of replicate radiosyntheses of [ <sup>18</sup> F]Fallypride .....	161
5.6.7.3 Uniformity of replicate TLC analysis .....	163
5.6.7.4 Cross-contamination during [ <sup>18</sup> F]fluoride drying .....	164
5.6.7.5 Optimization of [ <sup>18</sup> F]Fallypride synthesis .....	165
5.6.7.6 Optimization of [ <sup>18</sup> F]FBnTP synthesis .....	167
5.6.7.7 Scale-up of [ <sup>18</sup> F]FBnTP synthesis .....	169
5.6.7.8 System speed characterization .....	170
Chapter 6 : Economical droplet-based microfluidic production of [ <sup>18</sup> F]FET and [ <sup>18</sup> F]Florbetaben suitable for human use .....	172
6.1 Introduction .....	172
6.2 Methods .....	179
6.2.1 Materials .....	179

6.2.2 Automated droplet synthesizer .....	180
6.2.3 [ <sup>18</sup> F]FET synthesis.....	182
6.2.4 [ <sup>18</sup> F]FBB synthesis .....	183
6.2.5 Analytical methods .....	184
6.2.6 Quality control testing.....	184
6.3 Results.....	186
6.3.1 [ <sup>18</sup> F]FET production and testing.....	186
6.3.2 [ <sup>18</sup> F]FBB production and testing .....	187
6.4 Discussion .....	189
6.4.1 Comparison to conventional synthesis .....	189
6.4.2 Activity scaling in droplet micro-radiosynthesizer.....	190
6.4.3 Impact of starting activity on synthesis performance .....	191
6.4.4 Quality control testing.....	192
6.5 Conclusions .....	193
6.6 Appendix.....	194
6.6.1 Droplet synthesizer setup.....	194
6.6.2 Analytical methods (radio-TLC, radio-HPLC).....	194
6.6.3 Quality control testing methods (conventional instruments).....	195
6.6.3.1 Molar activity.....	195
6.6.3.2 Residual content of TBAHCO <sub>3</sub> .....	195
6.6.3.3 Residual content of K <sub>222</sub> .....	196
6.6.3.4 Residual solvent analysis.....	196
6.6.3.5 Residual solvent analysis of [ <sup>18</sup> F]FET samples .....	196
6.6.3.6 Residual solvent analysis of [ <sup>18</sup> F]FBB samples .....	197
6.6.4 QC testing with Tracer-QC .....	198
6.6.4.1 Color.....	198
6.6.4.2 Clarity .....	198
6.6.4.3 pH.....	199
6.6.4.4 Bacterial endotoxin .....	199
6.6.4.5 Radioactivity concentration .....	199
6.6.4.6 Radionuclidic identity (half-life) .....	199
6.6.4.7 Chemical identity, chemical purity, and/or chemical content via HPLC.....	199
6.6.5 [ <sup>18</sup> F]FET synthesis (low activity) .....	201
6.6.6 [ <sup>18</sup> F]FET quality control results .....	202
6.6.7 [ <sup>18</sup> F]FBB synthesis (low activity) .....	202
6.6.8 [ <sup>18</sup> F]FBB quality control results (conventional) .....	203

6.6.9 [ <sup>18</sup> F]FBB quality control results (Tracer-QC) .....	204
Chapter 7 : Scalable droplet-based radiosynthesis of [ <sup>18</sup> F]fluorobenzyltri-phenylphosphonium cation ([ <sup>18</sup> F]FBnTP) via a numbering up approach .....	205
7.1 Introduction .....	205
7.2 Methods .....	209
7.2.1 Materials .....	209
7.2.2 Droplet-based [ <sup>18</sup> F]FBnTP synthesis .....	210
7.2.3 Analytical methods .....	211
7.3 Results and discussion .....	212
7.3.1 Preliminary development of droplet-based synthesis conditions .....	212
7.3.2 Influence of precursor amount .....	213
7.3.3 Influence of volume (and activity) of [ <sup>18</sup> F]fluoride .....	214
7.3.4 Synthesis scale-up .....	216
7.3.5 Comparison of droplet and conventional methods .....	219
7.4 Conclusions .....	220
7.5 Appendix .....	221
7.5.1 Microdroplet reaction chips .....	221
7.5.2 Preliminary experiments .....	221
7.5.3 Influence of reaction site diameter .....	222
7.5.4 Influence of amount of precursor .....	223
7.5.5 Influence of starting activity and volume of [ <sup>18</sup> F]fluoride .....	223
7.5.6 Representative HPLC chromatograms .....	224
7.5.6.1 The synthesis by pooling two droplet reactions .....	224
7.5.6.2 The synthesis by pooling four droplet reactions .....	226
7.5.7 Molar activity determination .....	228
Chapter 8 : Copper-mediated <sup>18</sup> F-radiosynthesis optimization of a novel MAGL PET tracer on a high-throughput microdroplet platform and its immediate macroscale translation .....	229
8.1 Introduction .....	229
8.2 Methods .....	232
8.2.1 Materials .....	232
8.2.2 Droplet-based radiosynthesis of [ <sup>18</sup> F]YH149 .....	233
8.2.3 Macroscale production of [ <sup>18</sup> F]YH149 .....	234
8.2.4 Analytical equipment and methods .....	236
8.3 Results and discussion .....	237
8.3.1 Optimization of [ <sup>18</sup> F]YH149 radiosynthesis using droplet reactions .....	237
8.3.1.1 Initial conditions .....	237
8.3.1.2 Influence of reaction solvent .....	237

8.3.1.3 Influence of PTC/base .....	238
8.3.1.4 Effect of temperature and base type .....	239
8.3.1.5 Effect of reaction time .....	240
8.3.1.6 Effect of base amount.....	240
8.3.1.7 Influence of precursor amount .....	241
8.3.1.8 Additional tests .....	241
8.3.1.9 Overall synthesis including purification .....	242
8.3.2 Translation of microscale conditions to vial-based reaction .....	246
8.4 Conclusions .....	251
8.5 Appendix.....	251
8.5.1 Optimization of [ <sup>18</sup> F]YH149 synthesis on droplet reactors.....	251
8.5.1.1 Initial conditions .....	251
8.5.1.2 Influence of solvent type .....	253
8.5.1.3 Influence of type of phase transfer catalyst (PTC)/base.....	253
8.5.1.4 Impact of fluorination temperature and base type .....	254
8.5.1.5 Impact of reaction time .....	255
8.5.1.6 Influence of amount of base.....	256
8.5.1.7 Influence of amount of precursor .....	257
8.5.2 Macroscale synthesis performance .....	258
8.5.3 Calibration curve to determine molar activity .....	259
8.5.4 Example HPLC chromatograms from translated synthesis.....	260
Chapter 9 : A rapid and systematic approach for the optimization of radio-TLC resolutions ....	262
9.1 Introduction.....	262
9.2 Experimental.....	263
9.2.1 Materials .....	263
9.2.2 Preparation of radiopharmaceuticals and standard mixtures .....	265
9.2.3 TLC spotting, developing, and readout.....	265
9.2.4 Radio-HPLC analysis of [ <sup>18</sup> F]Fallypride .....	266
9.3 Theory .....	266
9.3.1 Analysis of TLC plates.....	266
9.3.2 Analysis of TLC plates.....	267
9.4 Results and Discussion.....	269
9.4.1 Optimization of separation of [ <sup>18</sup> F]Fallypride samples.....	272
9.4.2 Comparison of optimized radio-TLC to radio-HPLC.....	272
9.4.3 Comparison of literature mobile phases to PRISMA-optimized mobile phase.....	274
9.4.4 Optimization of separation of [ <sup>18</sup> F]PBR-06 samples.....	277



9.4.5 Optimization of separation of [ <sup>18</sup> F]FEPPA samples .....	277
9.4.6 Optimization of separation of [ <sup>18</sup> F]FDOPA samples .....	278
9.4.7 Optimization of separation of [ <sup>18</sup> F]FPEB samples .....	278
9.4.8 Optimization of [ <sup>18</sup> F]FPEB radiosynthesis with high-resolution TLC analysis .....	279
9.4.9 Additional readout channels via staining .....	280
9.5 Conclusions .....	281
9.6 Appendix.....	283
9.6.1 PRISMA “Prism” Construction .....	284
Chapter 10 : PHENYX – A flexible pipetting-based platform for automated microvolume radiochemistry.....	295
10.1 Introduction.....	295
10.2 Materials and methods.....	298
10.2.1 System design .....	298
10.2.1.1 Robotic system and cassette stage .....	298
10.2.1.2 Disposable cassette.....	300
10.2.1.3 Pipettor attachments.....	302
10.2.1.4 Control system.....	304
10.2.2 Characterization of subsystems .....	304
10.2.3 [ <sup>18</sup> F]Fallypride synthesis .....	305
10.2.3.1 Materials.....	305
10.2.3.2 Synthesizer setup .....	305
10.2.3.3 Analytical equipment and methods .....	306
10.2.3.4 Radiosynthesis of [ <sup>18</sup> F]Fallypride .....	307
10.3 Results and discussion .....	309
10.3.1 System characterization .....	309
10.3.1.1 Pressure-lid function .....	309
10.3.1.2 Heater calibration and performance .....	309
10.3.1.3 Reactor sealing by the Lid-heater .....	309
10.3.1.4 Pipettor calibration .....	310
10.3.2 Microvolume radiosynthesis of [ <sup>18</sup> F]Fallypride .....	310
10.3.2.1 [ <sup>18</sup> F]fluoride concentration.....	310
10.3.2.2 [ <sup>18</sup> F]fallypride synthesis.....	312
10.3.2.3 [ <sup>18</sup> F]Fallypride synthesis on simplified (reactor-only) cassette .....	313
10.3.2.4 Higher-activity [ <sup>18</sup> F]Fallypride synthesis .....	314
10.3.3 Comparison to other approaches .....	317
10.4 Conclusions .....	321
10.5 Appendix.....	322

10.5.1 PHENYX system design and characterization .....	322
10.5.1.1 Pressure-lid characterization .....	322
10.5.1.2 Heater calibration and characterization .....	323
10.5.1.3 Simplified cassette with a single reactor .....	325
10.5.1.4 Characterization of reactor sealing .....	325
10.5.1.5 Pipettor calibration .....	327
10.5.1.6 Optimization of QMA Outlet reservoir design .....	329
10.5.2 Cassette cleaning .....	332
10.5.3 QMA trapping and release performance .....	332
10.5.4 Timing of synthesis steps .....	333
10.5.5 HPLC purification of [ <sup>18</sup> F]fallypride .....	333
10.5.6 Calibration curve to determine molar activity .....	335
Chapter 11 : Electrochemical Radiofluorination of Methyl (Methylthio)acetate Using a Split-Bipolar Electrode .....	336
11.1 Introduction .....	336
11.2 Result and discussion .....	338
11.3 Conclusions .....	345
11.4 Appendix .....	345
11.4.1 Materials .....	345
11.4.2 General .....	346
11.4.3 Preparation of BPE cell .....	346
11.4.4 Synthesis and purification of [ <sup>19</sup> F]F-MMTA .....	347
11.4.5 Electrochemical radiofluorination (ECF) of MMTA using a s-BPE .....	349
11.4.6 Molar activity ( <i>A<sub>m</sub></i> ) calculation .....	352
11.4.7 Effects of solvents on both elution efficiencies of [ <sup>18</sup> F]F <sup>-</sup> and RCC in ECF .....	352
Chapter 12 : Outlook .....	354
References .....	358

## LIST OF FIGURES

Figure 1-1 Mechanism of PET imaging. ....	2
Figure 1-2 Production flow for fluorine-18-labeled tracers. ....	3
Figure 1-3 PDMS-based chamber microreactor system. ....	7
Figure 1-4 Schematic procedure for one-pot microscale radiosynthesis using microvial-based system. ....	8
Figure 1-5 iMiDEV™ microfluidic radiochemistry platform. ....	9
Figure 1-6 Structure and operation of EWOD microfluidic chips. ....	10
Figure 1-7 Schematic of the two-layer EWOD radiosynthesis chip. ....	10
Figure 1-8 Schematic of the open-style EWOD chip with a dimple structure. ....	12
Figure 1-9 Microdroplet radiochemistry platforms. ....	13
Figure 1-10 High-throughput droplet radiochemistry platforms. ....	16
Figure 2-1 Microscale metal-catalyzed synthesis of [ <sup>18</sup> F]FDOPA on a microdroplet system. ....	26
Figure 2-2 Optimization of on-chip [ <sup>18</sup> F]FDOPA fluorination step. ....	36
Figure 2-3 Influence of different deprotection reaction parameters. ....	38
Figure 2-4 Example radio-HPLC chromatograms from droplet-based radiosynthesis. ....	43
Figure 2-5 Examples of radio-HPLC chromatograms for deprotection optimization. ....	49
Figure 2-6 Automated microdroplet radiosynthesizer set up for [ <sup>18</sup> F]FDOPA synthesis. ....	50
Figure 2-7 Examples of radio-HPLC chromatograms of crude [ <sup>18</sup> F]FDOPA using different HPLC methods. ....	51
Figure 2-8 Calibration curve of FDOPA reference standard (282 nm wavelength). ....	52
Figure 3-1 Schematic of [ <sup>18</sup> F]AIF radiolabelling process flow in a droplet reactor. ....	58
Figure 3-2 Radiosynthesis optimization of [ <sup>18</sup> F]AIF-NODA-Tz in a droplet reactor. ....	62
Figure 3-3 Radiosynthesis optimization of [ <sup>18</sup> F]AIF-FAPI-74 in a droplet reactor. ....	65
Figure 3-4 Representative radio-HPLC chromatograms via droplet-based [ <sup>18</sup> F]AIF radiolabelling. ....	66
Figure 3-5 Example radio-HPLC analysis of crude [ <sup>18</sup> F]AIF-NODA-Tz sample (upper: UV-254 nm and bottom: γ-ray) from a microdroplet reaction. ....	71
Figure 3-6 Example radio-HPLC analysis of purified [ <sup>18</sup> F]AIF-NODA-Tz (upper: UV-254 nm and bottom: γ-ray). ....	71
Figure 4-1 (A) [ <sup>18</sup> F]FMAU synthesis scheme and (B) process flow for radiosynthesis using a microdroplet reactor. ....	76
Figure 4-2 Influence of solvent on (A) fluorination reaction and (B) subsequent coupling reaction. ....	84
Figure 4-3 Influence of (A) temperature and (B) precursor amount on fluorination reaction. ....	85
Figure 4-4 Influence of coupling parameters on the performance (collection efficiency after deprotection and isolated RCY) of the microdroplet radiosynthesis. ....	87
Figure 4-5 Influence of coupling temperature (A,B) and coupling time (C,D) on the synthesis performance. ....	89
Figure 4-6 Influence of deprotection time on the synthesis performance. ....	90
Figure 4-7 Radio-HPLC chromatogram of crude [ <sup>18</sup> F]FMAU (upper: UV-254 nm and bottom: γ-ray) from microdroplet radiosynthesis by using varying purification methods. ....	103
Figure 4-8 Automated microdroplet radiosynthesizer setup for [ <sup>18</sup> F]FMAU synthesis. ....	104
Figure 4-9 Example of radio-HPLC chromatogram of crude [ <sup>18</sup> F]FMAU (upper: UV-254 nm and bottom: γ-ray) from microdroplet radiosynthesis obtained during purification. ....	105
Figure 4-10 Example radio-HPLC analysis of purified [ <sup>18</sup> F]FMAU produced in a droplet reaction. The analytical mobile was 95% DI water and 5% MeCN (v/v) with 0.1% TFA. Under this condition, the retention time of [ <sup>18</sup> F]FMAU (β-anomer) was 5.0 min. ....	106

Figure 4-11 Example radio-HPLC analysis of co-injection of purified [ <sup>18</sup> F]FMAU produced in a droplet reaction and reference standard. The analytical mobile phase was 95% DI water and 5% MeCN (v/v) with 0.1% TFA.	106
Figure 5-1 Overall system design.	110
Figure 5-2 Work area of robotic microdroplet radiosynthesizer platform.	111
Figure 5-3 Control system.	114
Figure 5-4 Map of reaction conditions for optimization experiments.	118
Figure 5-5 Reagent dispensing uniformity and reaction uniformity.	122
Figure 5-6 Results of the 64-reaction [ <sup>18</sup> F]Fallypride study.	123
Figure 5-7 Effect of temperature and reaction solvent on the performance of the synthesis of [ <sup>18</sup> F]FBnTP.	124
Figure 5-8 Structure and operation of the pipette tip remover.	130
Figure 5-9 Detailed design of the fluidics head and reagent dispensing system.	131
Figure 5-10 Exploded view of the fluidics head.	131
Figure 5-11 Priming sensor based on an optical liquid sensor for dispensers.	132
Figure 5-12 Parameters used to characterize each type of microwell plate.	134
Figure 5-13 The TLC plate holder.	135
Figure 5-14 Pipette cone contact sensor.	137
Figure 5-15 Time sequence of the pipette tip attachment routine.	138
Figure 5-16 Numbering of the plate nests and chip nests within the work area.	142
Figure 5-17 An exploded view of the chip heating platform at the center of the work area.	143
Figure 5-18 (A) Numbering of wells in microwell plates and the pipette tip rack. (B) Numbering of reaction sites on multi-reaction chips. (C) Number of TLC spotting locations across multiple TLC plates installed in the TLC plate holder.	144
Figure 5-19 (A) 3D CAD model of the fluidics head. (B) Top view schematic of the fluidics head showing the numbering scheme for dispensers.	145
Figure 5-20 Example calibration curves for 4 dispensers.	155
Figure 5-21 Custom chip holder.	159
Figure 5-22 Cerenkov luminescence image of chips after dispensing and drying [ <sup>18</sup> F]fluoride solution.	160
Figure 5-23 Uniformity of replicate radiosyntheses of [ <sup>18</sup> F]Fallypride.	161
Figure 5-24 Cerenkov images of the replicate [ <sup>18</sup> F]Fallypride radiosynthesis study.	162
Figure 5-25 Cerenkov luminescence image of chip used for cross-contamination experiment. ROIs for the analysis are shown in grey.	164
Figure 5-26 Cerenkov luminescence images of chips during [ <sup>18</sup> F]Fallypride synthesis.	165
Figure 5-27 Effect of the amount of TBAHCO <sub>3</sub> on the radiosynthesis of [ <sup>18</sup> F]Fallypride.	166
Figure 5-28 Effect of the amount of precursor on the radiosynthesis of [ <sup>18</sup> F]Fallypride.	167
Figure 5-29 measurements of chip radioactivity and CLI of chips.	167
Figure 5-30 Cerenkov images of the developed TLC plates for the [ <sup>18</sup> F]FBnTP study.	168
Figure 5-31 Example HPLC chromatogram of injection of [ <sup>18</sup> F]FBnTP crude product, purified product and coin-injection of [ <sup>18</sup> F]FBnTP and standard.	170
Figure 6-1 Automated microdroplet synthesis.	181
Figure 6-2 Tracer preparation scheme. PTC = phase transfer catalyst. SPE = Solid-phase extraction.	182
Figure 6-3 Synthesis routes for (A) [ <sup>18</sup> F]FET and (B) [ <sup>18</sup> F]FBB.	182
Figure 6-4 Components of the Tracer-QC platform.	185
Figure 6-5 Performance of crude [ <sup>18</sup> F]FET droplet-based radiosynthesis as a function of starting activity.	187
Figure 6-6 Example HPLC chromatograms for [ <sup>18</sup> F]FET.	187
Figure 6-7 Performance of crude [ <sup>18</sup> F]FBB droplet-based radiosynthesis as a function of starting activity.	188

Figure 6-8 Example HPLC chromatograms for [ <sup>18</sup> F]FBB. ....	189
Figure 6-9 Tracer-QC HPLC measurement protocol. ....	200
Figure 7-1 Approaches for scale-up of radiopharmaceutical product amount in droplet-based radiosynthesis. ....	208
Figure 7-2 Influence of precursor amount on the performance of the droplet radiosynthesis of [ <sup>18</sup> F]FBnTP. Each experiment was repeated n = 3 times. ....	213
Figure 7-3 Droplet synthesis performance of [ <sup>18</sup> F]FBnTP as a function of [ <sup>18</sup> F]fluoride volume (μL) loaded. ....	214
Figure 7-4 2x2 and 3x3 multi-reaction chips for high-throughput synthesis optimization and for increasing synthesis scale by pooling the crude products of parallel reactions (“numbering up”). ....	221
Figure 7-5 Radio-HPLC chromatogram, during purification on an analytical column, of crude [ <sup>18</sup> F]FBnTP by pooling two droplet reactions. The apparent split in the product peak is an artifact due to saturation of the radiation detector. ....	224
Figure 7-6 Blank injection of formulation buffer, i.e., saline and EtOH (9:1, v/v). ....	225
Figure 7-7 Radio-HPLC chromatogram of formulated [ <sup>18</sup> F]FBnTP (from pooling two droplet reactions). ....	225
Figure 7-8 Radio-HPLC chromatogram of co-injection of formulated [ <sup>18</sup> F]FBnTP (from pooling two droplet reactions) and FBnTP reference standard. ....	226
Figure 7-9 Radio-HPLC chromatogram, during purification on a semi-prep column, of crude [ <sup>18</sup> F]FBnTP by pooling four droplet reactions. ....	226
Figure 7-10 Radio-HPLC chromatogram of formulated [ <sup>18</sup> F]FBnTP (from pooling four droplet reactions). ....	227
Figure 7-11 Radio-HPLC chromatogram of coinjection of formulated [ <sup>18</sup> F]FBnTP (from pooling four droplet reactions) and FBnTP reference standard. ....	227
Figure 7-12 Calibration curve of FBnTP reference standard. UV absorbance was measured at 254 nm. ....	228
Figure 8-1 Microdroplet-based radiosynthesis of [ <sup>18</sup> F]YH149. ....	232
Figure 8-2 Influence of reaction parameters on the performance of the microdroplet radiosynthesis. ....	238
Figure 8-3 Influence of reaction parameters on the performance of the microdroplet radiosynthesis. ....	239
Figure 8-4 Example of high-throughput analysis of crude fluorination products (from study of precursor amount) using multi-lane TLC with Cerenkov luminescence imaging (CLI) readout. ....	241
Figure 8-5 Example radio-HPLC chromatograms via droplet-based radiosynthesis. ....	244
Figure 8-6 Analysis of crude fluorination products from initial experiments using multi-lane TLC with Cerenkov luminescence imaging (CLI) readout. ....	252
Figure 8-7 High-throughput analysis of crude fluorination products (from study of solvent) using multi-lane TLC with CLI readout. ....	253
Figure 8-8 High-throughput analysis of crude fluorination products (from study of PTC/base type) using multi-lane TLC with CLI readout. ....	254
Figure 8-9 High-throughput analysis of crude fluorination products (from study of reaction temperature with TEAOTf/Cs <sub>2</sub> CO <sub>3</sub> ) using multi-lane TLC with CLI readout. ....	255
Figure 8-10 High-throughput analysis of crude fluorination products (from study of reaction temperature with TEAOTf/K <sub>2</sub> CO <sub>3</sub> ) using multi-lane TLC with CLI readout. ....	255
Figure 8-11 High-throughput analysis of crude fluorination products (from study of reaction time) using multi-lane TLC with CLI readout. ....	256
Figure 8-12 High-throughput analysis of crude fluorination products (from study of base amount with K <sub>2</sub> CO <sub>3</sub> ) using multi-lane TLC with CLI readout. ....	257
Figure 8-13 High-throughput analysis of crude fluorination products (from additional tested conditions) using multi-lane TLC with CLI readout. ....	257

Figure 8-14 Implementation of radiosynthesis in a vial-based (macroscale) reaction. ....	258
Figure 8-15 Impact on fluorination efficiency of different reaction times (n = 4) in the macroscale synthesis.....	258
Figure 8-16 Calibration curve of YH149 reference standard (254 nm wavelength).....	260
Figure 8-17 Example radio-HPLC chromatogram of crude [ <sup>18</sup> F]YH149 from macroscale radiosynthesis.....	260
Figure 8-18 Example radio-HPLC chromatogram of purified [ <sup>18</sup> F]YH149 from macroscale radiosynthesis.....	261
Figure 8-19 Example radio-HPLC chromatogram of co-injection of purified [ <sup>18</sup> F]YH149 (from macroscale radiosynthesis) and reference standard.....	261
Figure 9-1. PRISMA optimization of [ <sup>18</sup> F]Fallypride.....	271
Figure 9-2. Chromatographic resolution comparison of optimized TLC against conventional isocratic HPLC.....	273
Figure 9-3. Mobile phases comparisons for the analysis of crude [ <sup>18</sup> F]Fallypride conversion.....	275
Figure 9-4. Optimization of the synthesis of [ <sup>18</sup> F]FPEB (n = 2), leveraging high-throughput analyses enabled by multi-lane radio-TLC using the PRISMA-optimized mobile phase. Reaction volume is 10 µL and reaction time is 5 min in all cases.....	282
Figure 9-5. The graphical user interface of software used for analyzing TLC images.....	283
Figure 9-6. Procedure for the 3D visualization of resolution as a function of mobile phase composition.....	286
Figure 9-7. CLI images of TLC plates spotted with 1 µL crude [ <sup>18</sup> F]TBAF (30-50 MBq [ <sup>18</sup> F]fluoride, 800 nmol TBAHCO <sub>3</sub> , diluted to 60 µL) developed with different [ <sup>18</sup> F]Fallypride mobile phases from literature (first 5 entries) and the PRISMA-derived mobile phase (last entry).....	287
Figure 9-8. UV images of TLC plates spotted with Fallypride reference standard and developed with different mobile phases from literature (first 5 entries) and the PRISMA-derived mobile phase (last entry).....	288
Figure 9-9. Isocratic HPLC compared to the PRISMA optimized mobile phase of a crude [ <sup>18</sup> F]Fallypride sample.....	289
Figure 9-10. PRISMA optimization of [ <sup>18</sup> F]PBR-06.....	290
Figure 9-11. PRISMA optimization of [ <sup>18</sup> F]FEPPA.....	291
Figure 9-12. PRISMA optimization of [ <sup>18</sup> F]FDOPA.....	292
Figure 9-13. PRISMA optimization of [ <sup>18</sup> F]FPEB.....	293
Figure 9-14. Examples of Hanessian staining possible with TLC readout.....	294
Figure 9-15. Examples of Ninhydrin staining possible with TLC readout.....	294
Figure 10-1 The PHENYX system.....	299
Figure 10-2 The stage of PHENYX.....	300
Figure 10-3 PHENYX cassette.....	301
Figure 10-4 Pressure-lid.....	303
Figure 10-5 Reactor rim designs tested for sealing.....	310
Figure 10-6 Residual radioactivity in the cassette.....	313
Figure 10-7 A. Pressure-lid testing setup. B. Pressure monitoring after isolating pressure-lid from the pressure source.....	322
Figure 10-8 Temperature calibrations.....	324
Figure 10-9 Dynamic heater temperature characterization.....	325
Figure 10-10 A. Full cassette. B. Simplified cassette with only a reactor.....	325
Figure 10-11 Parameters tested included the Reactor designs (flat-rim, double-rim, beveled-rim) and the durometer of the silicone elastomer gasket (50A, 60A, 70A) on the bottom of the Lid-heater.....	327
Figure 10-12 Volume calibration curves for ADP dispensing of reagents.....	329
Figure 10-13 Example QMA Outlet reservoir prototypes.....	331

Figure 10-14 Final QMA Outlet Reservoir design. ....	331
Figure 10-15 Radio-HPLC chromatogram of crude [ <sup>18</sup> F]Fallypride (upper: UV-254 nm and bottom: γ-ray).....	334
Figure 10-16 Radio-HPLC chromatogram of purified [ <sup>18</sup> F]Fallypride (upper: UV-254 nm and bottom: γ-ray). Radiochemical purity was >99%.....	334
Figure 10-17 Radio-HPLC chromatogram of purified [ <sup>18</sup> F]Fallypride co-injected with fallypride reference standard for identity verification. (upper: UV-254 nm and bottom: γ-ray). ....	335
Figure 10-18 Calibration curve of fallypride reference standard (254 nm wavelength).....	335
Figure 11-1 Electrochemical (radio)fluorination of MMTA following a Pummerer-type mechanism via generation of the fluorosulfonium intermediate. ....	339
Figure 11-2 (a) Scheme of ECF of MMTA under different temperature (T [°C] = 10, 40, 60). (b) The trace of RCY (non-decay corrected) of the reaction mixture collected at different reaction times. RCY was determined by radio-TLC of the reaction mixture (n = 3). ....	340
Figure 11-3 Influence of driving electrode potential and reaction time on RCY. RCY was determined by radio-TLC of the crude samples (n = 3 or 15 (37.5 V at 30 min)).....	341
Figure 11-4 Influence of different anions (X <sup>-</sup> of TBAX) on the elution efficiencies (n = 3) and RCC at 30 (blue bar) and 60 min (red bar). ....	343
Figure 11-5 (a) A photograph of the top view of a U-shaped cell. (b–d) Detail designs of the U-shaped cell, including (b) top view, (c) front view, and (d) side view. ....	347
Figure 11-6 Electrochemical synthesis of [ <sup>19</sup> F]F-MMTA condition.....	347
Figure 11-7 (a) Schematic representation of an E-cell setup with three electrodes, including two platinum electrodes, a silver reference electrode and a stirring bar. (b) Photograph of an E-cell used for the preparation of [ <sup>19</sup> F]F-MMTA. ....	348
Figure 11-8 Electrochemical radiofluorination (ECF) of MMTA using a s-BPE .....	349
Figure 11-9 Photographs of (a) a Pt electrode, (b) the U-shaped cell equipped with the driving electrode (D.E.) and a s-BPE, and (c) electrolysis setup for ECF. ....	350
Figure 11-10 Enlarged radio-HPLC chromatogram of crude [ <sup>18</sup> F]F-MMTA (upper: UV-241 nm and bottom: γ-ray). ....	351
Figure 11-11 Calibration curve of [ <sup>19</sup> F]F-MMTA reference standard (241 nm wavelength). ....	352

## LIST OF TABLES

Table 2-1. Overview of performance during initial screening of fluorination conditions. ....	33
Table 2-2 Comparison of copper-mediated [ <sup>18</sup> F]FDOPA synthesis in microscale and macroscale. ....	42
Table 2-3 Summary of activity distribution after blank experiments (no precursor). ....	46
Table 2-4 Summary of performance during initial screening fluorination conditions. ....	46
Table 2-5 Influence of varying PTC amount in the fluorination step. ....	47
Table 2-6 Impact of copper reagent amount in the fluorination step. ....	47
Table 2-7 Influence of varying reaction temperature in the fluorination step. ....	47
Table 2-8 Influence of reaction time in the fluorination step. ....	48
Table 2-9 Influence of precursor amount in the fluorination step. ....	48
Table 2-10 Influence of reaction time in the deprotection step. ....	48
Table 2-11 Influence of HCl concentration in the deprotection step. ....	49
Table 2-12 Summary of results of radio-HPLC purification optimization on an analytical Synergi™ Hydro-RP column. ....	50
Table 3-1 Examples of [ <sup>18</sup> F]AIF radiopharmaceuticals. ....	54
Table 3-2 automation example of [ <sup>18</sup> F]AIF-labeled tracers. ....	56
Table 3-3 Comparison of [ <sup>18</sup> F]AIF-FAPI-74 production performance using conventional (macroscale) methods and optimized droplet-based synthesis. ....	67
Table 3-4 Influence of varying AlCl <sub>3</sub> -to-precursor ratio (APR) with fixed precursor amount for preparing [ <sup>18</sup> F]AIF-NODA-Tz in a droplet reactor. ....	69
Table 3-5 Influence of varying precursor amount with fixed AlCl <sub>3</sub> -to-precursor ratio (APR=0.8) for preparing [ <sup>18</sup> F]AIF-NODA-Tz in a droplet reactor. ....	69
Table 3-6 Influence of varying AlCl <sub>3</sub> -to-precursor ratio (APR) and different reaction time in the presence of MeCN for preparing [ <sup>18</sup> F]AIF-NODA-Tz in a droplet reactor. ....	70
Table 3-7 Summary of [ <sup>18</sup> F]AIF-NODA-Tz purification on an HLB cartridge. Activity measurements are expressed as fraction of starting activity of purification (corrected for decay, n = 1). ....	70
Table 3-8 Influence of precursor amount with fixed APR=0.8 for preparing [ <sup>18</sup> F]AIF-FAPI-74 in a droplet reactor. ....	72
Table 3-9 Influence of fluorination temperature for preparing [ <sup>18</sup> F]AIF-FAPI-74 in a droplet reactor. ....	72
Table 3-10 Summary of [ <sup>18</sup> F]AIF-FAPI-74 purification on HLB cartridge. Activity measurements are expressed as fraction of starting activity of purification (corrected for decay, n = 1). ....	73
Table 3-11 Summary of [ <sup>18</sup> F]AIF-FAPI-74 synthesis performance via different reagent loading protocols. Activity measurements are expressed as fraction of starting activity (corrected for decay, n = 1). ....	73
Table 4-1 Comparison of performance of microscale synthesis and the previously reported macroscale method. ....	91
Table 4-2 Preliminary droplet radiosynthesis conditions for [ <sup>18</sup> F]FMAU. ....	95
Table 4-3 Impact of solvent and temperature on the fluorination performance in a microdroplet reactor. ....	96
Table 4-4 Impact of PTC/base on the fluorination performance in a microdroplet reactor. ....	96
Table 4-5 Impact of temperature and time on the fluorination performance in a microdroplet reactor. ....	97
Table 4-6 Impact of precursor amount on the fluorination performance in a microdroplet reactor. ....	97
Table 4-7 Impact of fluorination solvent on the fluorination and coupling performance in a microdroplet reactor. ....	98



Table 4-8 Impact of fluorination temperature on the fluorination performance in a microdroplet reactor. ....	98
Table 4-9 Impact of precursor amount on the fluorination performance in a microdroplet reactor. ....	99
Table 4-10 Impact of amount of protected thymine on the performance of the droplet radiosynthesis of [ <sup>18</sup> F]FMAU. ....	99
Table 4-11. Impact of ratio of TMSOTf to HMDS (v/v) on the performance of the droplet radiosynthesis of [ <sup>18</sup> F]FMAU. ....	100
Table 4-12 Impact of coupling temperature on the performance of the droplet radiosynthesis of [ <sup>18</sup> F]FMAU. ....	100
Table 4-13 Impact of coupling time on the performance of the droplet radiosynthesis of [ <sup>18</sup> F]FMAU. ....	101
Table 4-14 Impact of deprotection time on the performance of the droplet radiosynthesis of [ <sup>18</sup> F]FMAU. ....	101
Table 4-15 Summary of results of radio-HPLC purification optimization. ....	102
Table 4-16 Summary of results of automated tests of the droplet radiosynthesis. ....	104
Table 5-1 Examples of parameters that can be optimized in an <sup>18</sup> F-radiosynthesis. ....	127
Table 5-2 List of available unit operations in “method” files. ....	145
Table 5-3 Low-level steps to implement each command (unit operation) and some helper commands ....	148
Table 5-4 Impact of syringe pump flow rate on pipetting accuracy and duration of crude product collection. Measurements were performed once (n = 1). ....	157
Table 5-5 Fraction of radioactivity (%) contained within each reaction site for the four chips in the evaluation of [ <sup>18</sup> F]fluoride dispensing and drying uniformity. Ideal uniformity would give 1/16 = 6.25%. ....	160
Table 5-6 Detailed results of the [ <sup>18</sup> F]fallypride synthesis uniformity study. ....	162
Table 5-7 Fluorination conversion for a set of 16 replicate radiosyntheses of [ <sup>18</sup> F]Fallypride, each sample assessed via 4 replicate TLC assays. ....	163
Table 5-8 Fraction (%) of total chip radioactivity in each reaction site of the cross-contamination experiment as determined by ROI analysis of Cerenkov luminescence image. Reaction sites with [ <sup>18</sup> F]fluoride are highlighted in green. ....	165
Table 5-9 Detailed results of [ <sup>18</sup> F]Fallypride optimization study. ....	166
Table 5-10 Summary of optimization experiment exploring the impact of solvent and reaction temperature on the performance of [ <sup>18</sup> F]FBnTP synthesis. ....	168
Table 5-11 Reaction performance parameters for three replicate [ <sup>18</sup> F]FBnTP syntheses at higher activity scale ....	169
Table 5-12 Duration of commonly needed individual actions and groups of actions. ....	171
Table 6-1 Literature reports of microfluidic production of <sup>18</sup> F-labeled radiopharmaceuticals with sufficient quantities for human PET. N.R. = not reported. ....	176
Table 6-2 Comparison of conventional and automated methods of [ <sup>18</sup> F]FBB quality control testing. ....	185
Table 6-3 Reagent setup in automated droplet synthesizer for syntheses of [ <sup>18</sup> F]FET and [ <sup>18</sup> F]FBB. ....	194
Table 6-4 Performance of droplet-based [ <sup>18</sup> F]FET synthesis on several platforms. ....	201
Table 6-5 Conventional (manual) quality control testing results for 3 consecutive batches of [ <sup>18</sup> F]FET. ....	202
Table 6-6 A comparison of droplet-based [ <sup>18</sup> F]FBB synthesis performance when performed manually versus automated, and at 2 different precursor solution volumes. ....	203
Table 6-7 Conventional (manual) quality control testing results for 3 consecutive batches of [ <sup>18</sup> F]FBB. N.D. = not detected. Limit of detection for MeCN is 20 ppm. ....	203

Table 6-8 Tracer-QC (automated) quality control testing results for 3 consecutive batches of [ <sup>18</sup> F]FBB. ....	204
Table 7-1 Comparison of [ <sup>18</sup> F]FBnTP synthesis performance under microscale and macroscale conditions. Where applicable, values are given as averages ± standard deviations for the indicated number of replicates. ....	218
Table 7-2 Preliminary attempts at droplet radiosynthesis of [ <sup>18</sup> F]FBnTP via the Cu-mediated route by adapting literature protocols. ....	222
Table 7-3 Comparison of the reaction performance on chips with 4 mm reaction sites (this work) vs 3 mm reaction sites. ....	222
Table 7-4 Summary of data acquired when exploring the impact of precursor amount for preparing [ <sup>18</sup> F]FBnTP. Each condition was repeated n = 3 times. ....	223
Table 7-5 Summary of data acquired when exploring the impact of [ <sup>18</sup> F]fluoride volume or starting activity when preparing [ <sup>18</sup> F]FBnTP. Precursor amount for these studies was 0.45 μmol. All experiments were performed at relatively low activity (11.7-69.6 MBq). ....	223
Table 7-6 Summary of data acquired when exploring the impact of precursor amount in conjunction with higher volume of [ <sup>18</sup> F]fluoride (40 μL) when preparing [ <sup>18</sup> F]FBnTP. All experiments were performed at relatively low activity (58.2-69.6 MBq). Each condition was repeated n = 2 times. ....	223
Table 7-7 Summary of data acquired when exploring the impact of [ <sup>18</sup> F]fluoride volume or starting activity when preparing [ <sup>18</sup> F]FBnTP. Precursor amount for these studies was 0.60 μmol. Experiments were performed over a wider activity range (25.3-1510 MBq). ....	224
Table 8-1 Summary of optimization experiments and findings. At each stage, the best performing condition was selected and held constant in later experiments. ....	242
Table 8-2 Comparison of performance prior macroscale synthesis method, optimized droplet-based synthesis, and translated vial-based (macroscale) preparation. ....	246
Table 8-3 Results of initial experiments. ....	252
Table 8-4 Impact of fluorination solvent on the performance of the droplet radiosynthesis of [ <sup>18</sup> F]YH149. ....	253
Table 8-5 Impact of type of PTC/base on the performance of the droplet radiosynthesis of [ <sup>18</sup> F]YH149. ....	253
Table 8-6 Impact of fluorination temperature (when using TEAOTf/Cs <sub>2</sub> CO <sub>3</sub> ) on the performance of the droplet radiosynthesis of [ <sup>18</sup> F]YH149. ....	254
Table 8-7 Impact of fluorination temperature (when using TEAOTf/K <sub>2</sub> CO <sub>3</sub> ) on the performance of the droplet radiosynthesis of [ <sup>18</sup> F]YH149. ....	255
Table 8-8 Impact of reaction time on the performance of the droplet radiosynthesis of [ <sup>18</sup> F]YH149. ....	256
Table 8-9 Impact of amount of base on the performance of the droplet radiosynthesis of [ <sup>18</sup> F]YH149. ....	256
Table 8-10 Influence of amount of precursor on the performance of the droplet radiosynthesis of [ <sup>18</sup> F]YH149. ....	257
Table 8-11 Performance of translated (droplet to vial) radiosynthesis of [ <sup>18</sup> F]YH149. Activity measurements are expressed as fractions of starting activity (corrected for decay). ....	259
Table 9-1. Selected radiopharmaceuticals and their calculated properties. ....	270
Table 9-2. Comparison of the radiochemical composition of a crude [ <sup>18</sup> F]Fallypride sample as determined by radio-TLC and Radio-HPLC. ....	274
Table 9-3. Integration of analytes detected by radio-TLC in the analysis of [ <sup>18</sup> F]Fallypride. ....	276
Table 9-4. Solvents in Snyder selectivity groups that are miscible with n-hexanes and used for the PRISMA optimizations performed in this work. ....	283
Table 10-1 Performance of [ <sup>18</sup> F]fluoride trap and release on the integrated QMA cartridge. The starting activity was 3-10 MBq [0.08-0.3 mCi]. All percentages are decay-corrected. ....	312

Table 10-2 [ <sup>18</sup> F]Fallypride synthesis performance. All activity percentages are made relative to the starting activity (and corrected for decay) unless otherwise indicated.....	316
Table 10-3 Comparison of automated [ <sup>18</sup> F]fallypride synthesis performance on PHENYX (at higher activity level tested) with other methods. All activity percentages are made relative to the starting activity (and corrected for decay) unless otherwise indicated. ....	318
Table 10-4 QMA trapping and release performance.....	332
Table 10-5 Duration of steps involved in [ <sup>18</sup> F]fallypride synthesis.....	333
Table 11-1 Effects of the concentration of MMTA on RCC.....	344
Table 11-2 Effects of solvents on elution efficiencies and RCC.....	353

## ACKNOWLEDGEMENTS

To start with, I wanted to thank the funding sources that supported my doctoral work: the National Institutes of Health (S10 OD026942), the National Institute of Biomedical Imaging and Bioengineering (T32 EB002101, R01 EB032264), and the National Cancer Institute (R33 CA240201), and the UCLA Dissertation Year Fellowship.

I would like to take this chance to express my gratitude to all my fellow lab members in the van Dam lab, both past and present. Dr. Jia Wang, for her invaluable assistance in mastering microdroplet chip fabrication and significant contribution to the PHENYX project described in this work. Dr. Philip Chao, for his guidance in learning micro-cartridge fabrication and concentration processes. Dr. Ksenia Lisova, for engaging discussions on scalable microfluidic radiochemistry and the radiosynthesis of isotopic exchange compounds. Dr. Jason Jones, for his help in machining materials and LabView programming for various projects. Dr. Alejandra Rios, for her help in learning the electrochemical radiofluorination in 96 well cells, microdroplet chip fabrication, and all microdroplet-based radiochemistry operations. Dr. Travis S. Laferriere-Holloway, for his help in learning various analytical methods of radiolabeling compounds and his valuable insights into the radiochemistry projects described in this work. Dr. Ryan McGuan, for his help in learning the robust fabrication method of microfluidic chips and his guidance in navigating through chip fabrication issues. Jeffrey Collins, for his valuable input in the scalable radiosynthesis project described in this work and his support for providing [ $^{18}\text{F}$ ]fluoride for the radiochemistry studies. Alex Leal-Doblado, for his help in learning the computer-aided design software and using it to design new mask for microfluidic chips. Finally, I am extremely grateful to Dr. R. Michael van Dam for his guidance and mentorship throughout my years of Ph.D. I thank Dr. van Dam for giving me numerous opportunities to design and perform experiments, present and publish my work, establish collaborations, attend scientific conferences, and connect with researchers worldwide. I really appreciate that, as a mentor, he gave me lots of freedom to explore my research interests

and encouraged me to test any idea I came up with. He is always willing to assist with any problems and consistently patient in answering all my questions. Even with a mistake, he would ask questions to slowly pinpoint the area where the mistake occurred or a problem may exist, encouraging improvement without ever conveying disappointment or a sense of failure. His emphasis on the fundamental scientific principles of each project has played a crucial role in shaping me into a better scientist and critical thinker. Dr. van Dam is an incredible professor who is not only profoundly dedicated to his work but also spends lots of time with his students, listening to their thoughts about future careers and providing valuable guidance. Thank you so much for being such a patient and understanding mentor throughout my PhD years.

I want to thank all of my close collaborators: Drs. Yingfang He, Roger Schibli and Linjing Mu for the fantastic collaboration on the monoacylglycerol lipase (MAGL) project and the joint publication; Drs. Philip Miller and Gitanjali Sharma for the wonderful and productive collaboration on [ $^{18}\text{F}$ ]AIF project; Dr. Alex Hsiao for his assistance in troubleshooting experiments on PHENYX platform and finalizing the manuscript in the PHENYX project; Dr. Kuo-Shyan Lin, for providing precursor for the [ $^{18}\text{F}$ ]FBnTP studies; Dr. Kai Chen, for providing precursor and sharing valuable advices for [ $^{18}\text{F}$ ]FMAU project; Drs. Saman Sadeghi and Tomoyuki Kurioka, for providing helpful insights in electrochemical radiofluorination studies; Dr. Emmanuel Gras, for providing precursor for studying isotopic exchange  $^{18}\text{F}$ -labeled compounds; Drs. Gaoyuan Ma and Maruthi Narayanam, for helpful suggestions on radiochemistry and analytical chemistry. I also want to thank the CNSI cleanroom staff Lorna Tokunaga, Brian Matthews, Krissy Do and Tony Wright for their help and advice related to equipment questions. I want to thank Emily Fitch for her help with the documents and providing detailed answers to any related questions. Moreover, I appreciate the help received from everyone at the Crump Preclinical Imaging Technology Center.

I also want to thank the mentors and administration of the Physics and Biology in Medicine program who made me feel welcome from the start of my Ph.D. career at UCLA. I want to thank Dr. Michael McNitt-Gray for his mentorship and support while navigating throughout my PhD, for

always being there for his students, and providing resources and contacts to help students grow. I thank Reth Im and Alondra Correa Bautista for organizing PBM social events, handling all the administrative paperwork, being so supportive to answer any of my questions and provide help when I was in trouble. I also thank my fellow PBM graduate students for fun accompany, especially those in my starting year, Hengjie Liu, Zhengyang Ming, Jiayi Du, Morgan Daly, Rachel Petragallo, Daili Shang and Elena Schink.

I would like to also thank my family and friends for unwavering supporting throughout my PhD journey. I want to thank my mother, Libing Pan, who is watching me from the heaven, for her unconditional love and support in both my studies and life. I also want to thank my father, Weiyuan Lu, for his consistent encouragement and unwavering supportive. To my brothers, Shiping Lu and Yanping Lu, thank you for always lending a listening ear and providing valuable suggestions and comfort. To my aunt Miaofang Lu and cousin Shanyu Liang, thank you for all the delicious food and comfort whenever I am home. I want to thank my partner, Ziqi Pi, for always being such understanding, encouraging, caring, and kind to me. I would not have finished the program without their support. I also want to give a special thanks to my friends, Zijun Cen and Jianmei Liang, for keeping in touch for over the past 15 years, regardless of where I am in the world. I also want to thank all the friends I met at the UCHA and UCLA, for their incredible help in both dormitory life and school matters when I first arrived in the US.

Lastly, I would like to thank my doctoral committee for advising me with my research, study, and helping me to be better in all aspects. Thank you to Dr. Arion F. Chatziioannou for his invaluable insights into Cerenkov luminescence imaging and for generously sharing his wealth of experience and advice on the future academic career. Thank you to Dr. Jennifer M. Murphy for all of her helpful advice and suggestions on the copper-mediated radiofluorination project. Thank you to Dr. Peter M. Clark for always keeping his door open, providing assistance whenever I had questions related to biochemical questions or imaging equipment. Thank you to Dr. R. Michael van Dam, once again for all his help and support throughout my PhD journey.

**Chapter 2: Copper-mediated radiosynthesis of 6-[<sup>18</sup>F]Fluoro-L-DOPA ([<sup>18</sup>F]FDOPA) in a microreactor** is a modified version of a manuscript in preparation:

Lu, Y., van Dam, R.M., Copper-mediated radiosynthesis of 6-[<sup>18</sup>F]Fluoro-L-DOPA ([<sup>18</sup>F]FDOPA) in a microreactor.

**Chapter 3: Proof-of-concept [<sup>18</sup>F]AIF labeling in droplet reactions** is a modified version of a manuscript in preparation:

Lu, Y.†, Sharma, G.†, Pieve, C. D., Kramer-Marek, G., Miller, P., van Dam, R.M. Proof-of-concept [<sup>18</sup>F]AIF labeling in droplet reactions. († indicates co-first authors)

**Chapter 4: Acceleration of radiochemistry through droplet reactions: 6x speedup of [<sup>18</sup>F]FMAU preparation** is a modified version of a manuscript in preparation:

Lu, Y., Chen, K., van Dam, R.M. Acceleration of radiochemistry through droplet reactions: 6x speedup of [<sup>18</sup>F]FMAU preparation.

**Chapter 5: Robotic platform for high-throughput radiosynthesis and optimization** is a modified version of:

Jones, J., Do, V., Lu, Y., van Dam, R. M. (2023). Accelerating radiochemistry development: Automated robotic platform for performing up to 64 droplet radiochemical reactions in a morning. *Chemical Engineering Journal*, 468, 143524.

**Chapter 6: Economical droplet-based microfluidic production of [<sup>18</sup>F]FET and [<sup>18</sup>F]Florbetaben suitable for human use** is a modified version of:

Lisova, K., Wang, J., Hajagos, T. J., Lu, Y., Hsiao, A., Elizarov, A., van Dam, R. M. (2021). Economical droplet-based microfluidic production of [<sup>18</sup>F] FET and [<sup>18</sup>F] Florbetaben suitable for human use. *Scientific Reports*, 11(1), 20636.

**Chapter 7: Scalable droplet-based radiosynthesis of [<sup>18</sup>F]fluorobenzyltriphenylphosphonium cation ([<sup>18</sup>F]FBnTP) via a numbering up approach** is a modified version of a manuscript in preparation:

Lu, Y., Collins, J., Lin, K., van Dam, R. M. Scalable droplet-based radiosynthesis of [<sup>18</sup>F]fluorobenzyltriphenylphosphonium cation ([<sup>18</sup>F]FBnTP) via a numbering up approach.

**Chapter 8: Copper-mediated <sup>18</sup>F-radiosynthesis optimization of a novel MAGL PET tracer on a high-throughput microdroplet platform and its immediate macroscale translation** is a modified version of:

Lu, Y., He, Y., Schibli, R., Mu, L., van Dam, R. M. (2023). Proof-of-concept optimization of a copper-mediated <sup>18</sup>F-radiosynthesis of a novel MAGL PET tracer on a high-throughput microdroplet platform and its macroscale translation. *Lab on a Chip*, 23, 4652.

**Chapter 9: A rapid and systematic approach for the optimization of radio-TLC resolution** is a modified version of:

Laferriere-Holloway, T. S., Rios, A., Lu, Y., Okoro, C. C., van Dam, R. M. (2023). A rapid and systematic approach for the optimization of radio thin-layer chromatography resolution. *Journal of Chromatography A*, 1687, 463656.

**Chapter 10: PHENYX – A flexible pipetting-based platform for automated microvolume radiochemistry** is a modified version of:

Lu, Y., Wang, J., van Dam, R. M., Hsiao, A. (2022). PHENYX—A flexible pipetting-based platform for automated microvolume radiochemistry. *Chemical Engineering Journal*, 435, 134983.

**Chapter 11: Electrochemical radiofluorination with a split-bipolar electrode** is a modified version of a manuscript in preparation:

Kurioka, T., Lu, Y., Jones, J., Wang, X., Genady, A., van Dam, R.M., Inagi, S., Sadeghi, S. Electrochemical radiofluorination with a split-bipolar electrode.



## VITA

### EDUCATION

---

9/14-2/17 M.S. in Biomedical Radiation Science      **Seoul National University (SNU)**  
9/10-7/14 B.S. in Materials Chemistry              **South China Normal University (SCNU)**

### SELECTED JOURNAL PUBLICATIONS

---

1. **Lu, Y.\***, He, Y., Schibli, R., Mu, L., van Dam, R. M.\* (2023). Proof-of-concept optimization of a copper-mediated  $^{18}\text{F}$ -radiosynthesis of a novel MAGL PET tracer on a high-throughput microdroplet platform and its macroscale translation. *Lab on a Chip*, 23, 4652. (\*indicates corresponding author)
2. Jones, J., Do, V., **Lu, Y.**, van Dam, R. M. (2023). Accelerating radiochemistry development: Automated robotic platform for performing up to 64 droplet radiochemical reactions in a morning. *Chemical Engineering Journal*, 468, 143524.
3. Laferriere-Holloway, T. S., Rios, A., **Lu, Y.**, Okoro, C. C., van Dam, R. M. (2023). A rapid and systematic approach for the optimization of radio thin-layer chromatography resolution. *Journal of Chromatography A*, 1687, 463656.
4. **Lu, Y.**, Wang, J., van Dam, R. M., Hsiao, A. (2022). PHENYX—A flexible pipetting-based platform for automated microvolume radiochemistry. *Chemical Engineering Journal*, 435, 134983.
5. Lisova, K., Wang, J., Hajagos, T. J., **Lu, Y.**, Hsiao, A., Elizarov, A., van Dam, R. M. (2021). Economical droplet-based microfluidic production of [ $^{18}\text{F}$ ] FET and [ $^{18}\text{F}$ ] Florbetaben suitable for human use. *Scientific Reports*, 11(1), 20636.
6. **Lu, Y.**, Collins, J., Lin, K., van Dam, R. M. Scalable droplet-based radiosynthesis of [ $^{18}\text{F}$ ]fluorobenzyltri-phenylphosphonium cation ([ $^{18}\text{F}$ ]FBnTP) via a numbering up approach. *In Preparation*.
7. **Lu, Y.**, van Dam, R.M., Copper-mediated radiosynthesis of 6-[ $^{18}\text{F}$ ]Fluoro-L-DOPA ([ $^{18}\text{F}$ ]FDOPA) in a microreactor. *In Preparation*.
8. **Lu, Y.**, Chen, K., van Dam, R.M. Acceleration of radiochemistry through droplet reactions: 6x speedup of [ $^{18}\text{F}$ ]FMAU preparation. *In Preparation*.
9. **Lu, Y.†**, Sharma, G.†, Pieve, C. D., Kramer-Marek, G., Miller, P., van Dam, R.M. Proof-of-concept [ $^{18}\text{F}$ ]AIF labeling in droplet reactions. *In Preparation*. († indicates co-first authors)
10. Kurioka, T., **Lu, Y.**, Jones, J., Wang, X., Genady, A., van Dam, R.M., Inagi, S., Sadeghi, S. Electrochemical radiofluorination with a split-bipolar electrode. *In Preparation*.
11. **Lu, Y.†**, Choi, J. Y.†, Kim, S. E., Lee, B. C. (2019). HPLC-free in situ  $^{18}\text{F}$ -fluoromethylation of bioactive molecules by azidation and MTBD scavenging. *Chemical Communications*, 55(78), 11798-11801. († indicates co-first authors)
12. **Lu, Y.**, Jung, J. H., Lee, H. J., Moon, B. S., Lee, B. C., Kim, S. E. (2016). Synthesis and in vivo evaluation of a kit-type  $^{99\text{m}}\text{Tc}$ -labeled N-(2-Aminoethyl)-3-(4-(2-hydroxy-3-(isopropylaminopropoxy)phenyl) propanamide as a selective  $\beta$ 1-adrenoceptor-binding SPECT radiotracer. *Bulletin of the Korean Chemical Society*, 37(12), 2029-2035.
13. **Lu, Y.**, Lee, B. C., Kim, S. E. (2016). Recent advances in carbon-11 chemistry. *Journal of Radiopharmaceuticals and Molecular Probes*, 2 (1), 9.

### CONFERENCE PRESENTATIONS

---

1. **Lu, Y.**, He, Y., Schibli, R., Mu, L., van Dam, R. M. Rapid copper-mediated radiosynthesis optimization for a novel monoacylglycerol lipase PET tracer on a high-throughput microdroplet radiochemistry platform. The 25<sup>th</sup> iSRS. Honolulu, Hawaii, USA, May 22-26. 2023. **Poster presentation.**
2. **Lu, Y.†**, Sharma, G.†, Pieve, C. D., Kramer-Marek, G., Miller, P., van Dam, R.M. Proof of principle: [<sup>18</sup>F]AIF radiolabelling using a droplet microreactor. The 25<sup>th</sup> iSRS. Honolulu, Hawaii, USA, May 22-26. 2023. **Poster presentation.** († indicates co-first authors)
3. Jones, J., **Lu, Y.**, van Dam, R. M. Proof-of-concept optimization of copper-mediated radiosynthesis of [<sup>18</sup>F]FBnTP using a novel automated robotic high-throughput droplet radiochemistry system. The 25<sup>th</sup> iSRS. Honolulu, Hawaii, USA, May 22-26. 2023. **Oral presentation.**
4. **Lu, Y.**, van Dam, R. M. First microvolume metal-mediated synthesis of [<sup>18</sup>F] FDOPA in a microreactor (with latest data). Pacificchem. Virtual, December 16-21. 2021. **Oral presentation.**
5. **Lu, Y.**, Wang, J., van Dam, R. M., Hsiao, A. A novel flexible pipetting-based platform for automated microvolume radiochemistry (with latest data). Pacificchem. Virtual, December 16-21. 2021. **Oral presentation.**
6. **Lu, Y.**, van Dam, R. M. First microvolume metal-mediated synthesis of [<sup>18</sup>F] FDOPA in a microreactor. Nuclear Medicine and Biology, 96, S15-S16. Virtual. The 24<sup>th</sup> iSRS. May 17-19, 2021. **Short oral presentation.**
7. **Lu, Y.**, Wang, J., van Dam, R. M., Hsiao, A. A novel flexible pipetting-based platform for automated microvolume radiochemistry. Nuclear Medicine and Biology, 96, S58-S59. Virtual. The 24<sup>th</sup> iSRS. May 17-19, 2021. **Short presentation.**
8. **Lu, Y.**, Jung, J. H., Park, D. D., Lee, B. C., Kim, S. E. Evaluation of the TSPO radioligand [<sup>18</sup>F]CB251 in a rat model of autoimmune myocarditis. The Korean Association for Laboratory Animal Science (KALAS) International Symposium. Gyeongju, South Korea, August 24-26, 2016. **Oral presentation.**
9. **Lu, Y.**, Choi, J. Y., Lee, B. C., Kim, S. E. Synthesis of <sup>99m</sup>Tc-labeled 2-methyl-5-nitroimidazole analogs to identify tumor hypoxia SPECT imaging. The Korean Society of Radiopharmaceuticals and Molecular Probes Symposium. Seoul, South Korea, April 4, 2017. **Poster presentation.**
10. **Lu, Y.**, Choi, J. Y., Moon, B. S., Lee, B. C., Kim, S. E. Synthesis of <sup>99m</sup>Tc-labeled 2-Methyl-5-nitroimidazole analogs via pre-labeling method as tumor imaging agents. The Korean Society of Nuclear Medicine Meeting. Seoul, South Korea, October 27-29, 2016. **Poster presentation.**

## Patents

---

1. Lee, B. C., **Lu, Y.**, Jo, B. M. Method for preparing fluorine-18-labeled fluoromethyl-substituted radiopharmaceuticals using selective azide substitution reaction and precursor scavenging. U.S. Patent Application US20210205482 A1.

## Book Chapters

---

1. **Lu, Y.**, van Dam, R. M. Rapid radiosynthesis via open-droplet reactions. *In Preparation.*
2. **Lu, Y.**, van Dam, R. M. *et al.* High-throughput technique in radiochemistry. *In Preparation.*

# Chapter 1: Introduction

## 1.1 Positron emission tomography

Positron emission tomography (PET) is a potent nuclear imaging modality, providing invaluable insights into both preclinical and clinical domains. It enables the elucidation of in vivo biochemical processes (1,2), plays a crucial role in disease diagnosis (3–5), and facilitates the prediction or monitoring of therapeutic responses (6–8). The process involves administering a trace quantity of a biomolecule chemically linked to a positron-emitting radionuclide, referred to as a radiotracer. Upon injection into the body, the radiotracer molecules circulate and interact with the body, accumulating in specific cells or tissues. Upon decay of the associated radionuclide, positrons (i.e., particles carrying an electric charge of  $+1e$ ) are emitted. Subsequent interactions between these emitted positrons and nearby electrons result in annihilation events, generating two gamma rays (511 keV) moving in nearly opposite directions. Detection of these gamma rays is achieved using a ring of scintillator crystals (9), which emit a burst of light in response to gamma rays that is subsequently detected by photomultiplier tubes. Coincidence detection is used to pair together gamma rays from the same decay event, pinpointing the decay to a line between the two activated detectors. Recent time-of-flight (TOF) techniques allow partial localization of the annihilation event along the line (10). Through computerized analysis, the reconstruction of images of decay events becomes possible, offering a comprehensive view of radioactivity biodistribution within the body (11) (**Figure 1-1**). To provide an anatomical reference for the remarkably sensitive PET signal, PET is often integrated with computed tomography (i.e., PET/CT) (12,13) or magnetic resonance imaging (i.e., PET/MRI) (14–17). The exceptional sensitivity of PET allows for the acquisition of detailed images with minimal amounts of the administered radiotracer, ranging from picomoles to nanomoles, thereby minimizing the potential for any biological effects caused by the tracer (18).

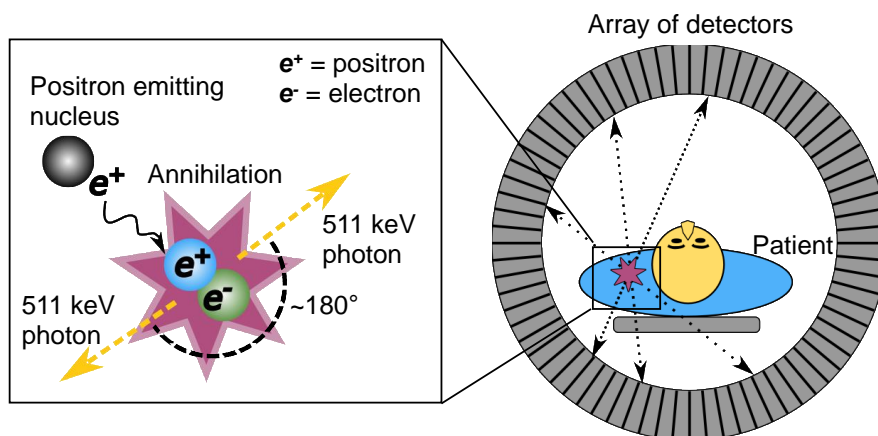


**Figure 1-1 Mechanism of PET imaging.**

PET image is formed based on detection of sets of coincident 511 keV photons emitted upon annihilation events after positron decays. Image courtesy of National Cancer Institute.

## 1.2 PET radiopharmaceuticals

PET radiopharmaceuticals represent approved radiotracers that meet the stringent standards set by the Food and Drug Administration (FDA). For diagnostic purposes, these radiopharmaceuticals are typically labeled with short-lived radioisotopes emitting low-energy positrons, such as nonmetal elements: carbon-11 ( $t_{1/2} = 20.4$  min), nitrogen-13 ( $t_{1/2} = 10.0$  min), oxygen-15 ( $t_{1/2} = 2.0$  min), fluorine-18 ( $t_{1/2} = 109.8$  min); or radiometals: gallium-68 ( $t_{1/2} = 67.7$  min), zirconium-89 ( $t_{1/2} = 78.4$  h), or rubidium-82 ( $t_{1/2} = 1.3$  min). Fluorine-18, in particular, stands out as the most utilized PET radionuclide due to its high positron decay ratio (97%), short half-life (109.8 min) that provides adequate time for radiotracer preparation yet ensures a low radiation dose to the patient, low positron energy (635 keV), and widespread availability (19–21).

Considering the short half-lives of these radioisotopes, the late-stage radiolabeling concept was introduced for PET radiopharmaceutical manufacturing, i.e., introducing the radioisotope into a well-design non-radioactive compound (i.e., precursor) at the latest possible stage of the radiopharmaceutical synthesis (22–24). This strategy offers several advantages, including minimizing the number of reaction steps involving radioisotopes (ideally limited to 1 or 2), reducing activity decay losses within the apparatus, and minimizing radiation exposure,

allowing maximizing the quantity of the final product, catering to both preclinical and clinical study supply needs (24).

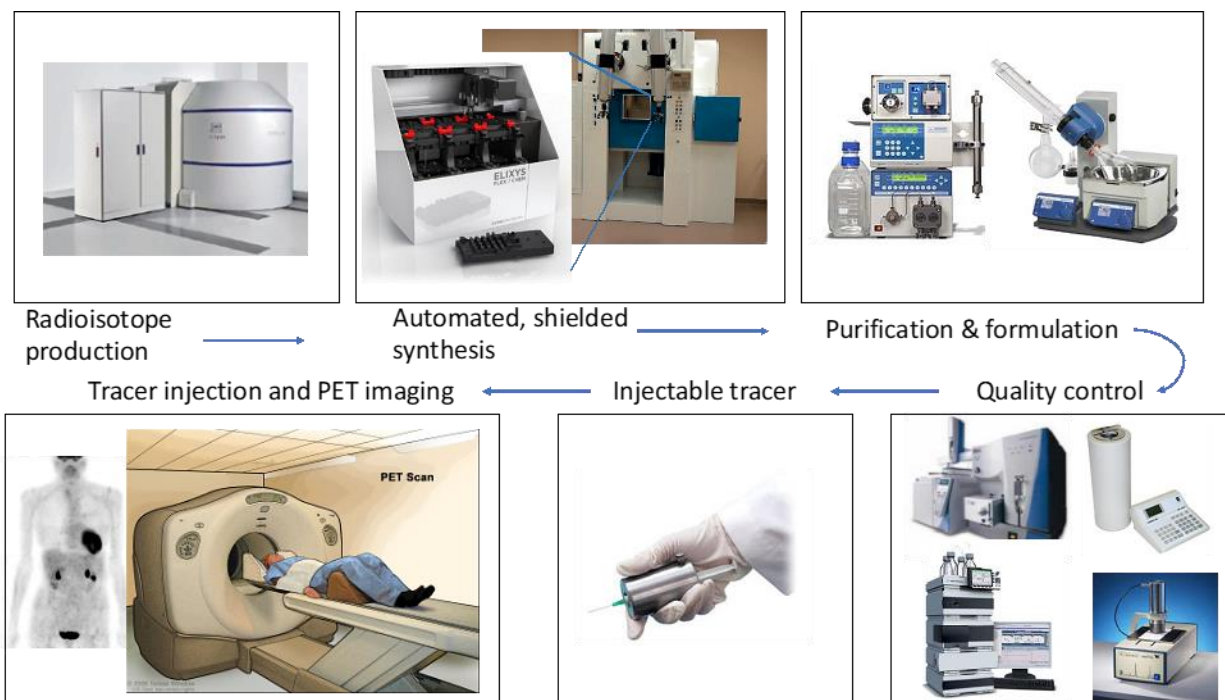


**Figure 1-2 Production flow for fluorine-18-labeled tracers.**

In the production of an  $^{18}\text{F}$ -labeled PET tracer, two main methods are employed: electrophilic substitution with  $[^{18}\text{F}]\text{F}_2$  or nucleophilic substitution with  $[^{18}\text{F}]\text{fluoride}$  ( $[^{18}\text{F}]\text{F}^-$ ). The crucial distinction lies in their resulting molar activity, as determined by the ratio between radioactive molecules and non-radioactive molecules (25). In modern radiochemistry, the electrophilic form of  $[^{18}\text{F}]\text{fluorine}$  ( $[^{18}\text{F}]\text{F}_2$ ) sees less use due to its lower molar activity ( $<0.02$  Ci/ $\mu\text{mol}$  [ $<0.6$  GBq/ $\mu\text{mol}$ ]) compared to the nucleophilic method (typically 2.7 Ci/ $\mu\text{mol}$  [100 GBq/ $\mu\text{mol}$ ]) (20,26). In **Figure 1-2**, the radiofluorination process typically begins by obtaining nucleophilic ( $[^{18}\text{F}]\text{F}^-$ ) in  $[^{18}\text{O}]\text{H}_2\text{O}$  through bombarding oxygen-18 enriched water with 2-15 MeV protons ( $^1\text{H}$ ) via the nuclear reaction  $[^{18}\text{O}(\text{p},\text{n})^{18}\text{F}]$  in a cyclotron. When in the presence of  $[^{18}\text{O}]\text{H}_2\text{O}$ , the potent nucleophile  $[^{18}\text{F}]\text{F}^-$  tends to establish hydrogen bonds with surrounding water, rendering it unreactive towards fluorination with other substrates. To eliminate water,  $[^{18}\text{F}]\text{F}^-$  is

typically trapped on an anion-exchange cartridge, then eluted with a base/phase-transfer catalyst (PTC) solution in a mixture of water and organic solvent, followed by multiple cycles of azeotropic evaporative drying. The incorporation of a PTC, such as Kryptofix 222 ( $K_{222}$ ) or tetrabutylammonium cation, enhances the solubility of  $[^{18}\text{F}]\text{F}^-$  in less aqueous conditions. After evaporation, the activated nucleophilic  $[^{18}\text{F}]\text{F}^-$  is introduced into the precursor molecule through aliphatic or aromatic nucleophilic reactions by reaction typically at elevated temperature in an organic solvent. The resulting crude product undergoes semi-preparative high-performance liquid chromatography (HPLC) or solid-phase extraction (SPE) for purification before being formulated into an injectable solution. Stringent quality control checks are carried out prior to administration in preclinical or clinical settings.

### **1.3 Conventional synthesizers for radiopharmaceuticals**

The short half-life of F-18 requires fresh batches to be made nearly daily at many different locations throughout the world. To ensure the safe and dependable production of routinely used PET tracers, we utilize automated modules housed within shielded fume hoods, commonly referred to as hot-cells, and often operate them remotely with preprogrammed synthesis sequences. Typically, these modules are designed to deliver reagents to a reactor, apply heating and gas flow as needed, recover the crude synthesis product, and transfer it for subsequent purification and formulation with minimal user intervention. Current commercial radiosynthesizers can be roughly classified into cassette-based modules (e.g. GE FASTlab (27), Siemens Explora (28), IBA Synthera (29)), fixed-tubing modules (e.g. GE TRACERlab FX series (30), GmbH Synthra (31) or Eckert & Ziegler Modular-Labs (32)), and hybrid modules (e.g. ELIXYS FLEX/CHEM (33,34)). Primarily designed for relatively large batches of clinical-grade PET radiopharmaceuticals, these systems aim to provide sufficient radiotracers for imaging multiple patients and are typically operated once per day (35). The centralized production of large batches

helps distribute the high production cost among numerous patient doses. However, this approach renders current radiosynthesizers inefficient when smaller batches are required.

Furthermore, in commercial systems with milliliter-scale reaction volumes, achieving reasonable reaction rates demands the use of substantial quantities of radioisotopes, along with excess amount of precursors and other components, to reach high enough concentrations that reactions proceed quickly. This holds true even for small batches required for in vitro studies, preclinical scans, or single clinical scans, leading in such cases to the disposal of a significant portion of the total radiopharmaceutical batch. Consequently, this practice results in substantial waste and introduces challenges in downstream purification to remove excess precursors and side products. These inefficiencies, combined with the high costs of radiochemistry equipment and facilities, contribute to the overall expense and complexity of integrating radiopharmaceuticals into research. In addition, these systems are less conducive to synthesis optimization due to the substantial time and effort and material requirements for each data point. Consequently, this limitation severely hampers further multi-center collaborative studies and larger cohort investigations, particularly for tracers with suboptimal production processes.

To enhance accessibility to a variety of PET tracers and streamline the production of novel tracers for early-stage studies, there is a pressing need for advancements in radiosynthesis technology. These advancements should enable the affordable production of smaller batches of radiopharmaceuticals on demand, potentially eliminating the requirement for specialized facilities and costly instrumentation.

#### **1.4 Recent developments in microfluidic-based PET tracer manufacturing**

Microfluidic devices have emerged as efficient, compact, and cost-effective platforms with substantial potential for diverse radiotracer production. This progress has fueled the development of various microfluidic tools in radiochemistry over the past 15 years (36–40). These systems can be broadly categorized into two types: flow chemistry systems and microscale batch systems.

Flow-based reactors facilitate synthesis by directing reagent streams through a mixer and a thermally controlled capillary or channel. Reactions in this high surface-to-volume regime have been observed to be rapid (41–43). Both custom and commercially available flow systems have been employed with a diverse range of PET radionuclides, including carbon-11, nitrogen-13, fluorine-18, copper-64, gallium-68, zirconium-89, and lutetium-177 (44–48). Despite their versatility, these systems often face challenges as they tend to be bulky and expensive, requiring additional external macroscale systems for both upstream (e.g., radioisotope concentration) and downstream (e.g., semi-pre HPLC purification) processes relative to the flow reactor (49,50). This resemblance to conventional radiosynthesizers in terms of size, shielding requirements, and operating volumes has limited the practical utility of flow-based systems in establishing a cost-effective pathway for on-demand PET radiopharmaceutical production.

Recent advancements in batch-based systems mark significant progress in the production of clinical quantities of radiopharmaceuticals, showcasing improvements in volume reduction, system size, and integration with upstream and downstream processes (51–53). These systems, ranging from microvial reactors (54–56) to channel-based devices with integrated isotope processing and purification (57,58) and droplet-reaction systems (39), exhibit substantial potential for cost reduction in on-demand PET radiopharmaceutical production. Operating at the microliter scale, these batch approaches can achieve a remarkable 2-3 orders of magnitude reduction in reagent costs compared to conventional milliliter-scale radiosynthesizer technologies and microfluidic flow chemistry approaches. Miniaturizing the synthesizer also contributes to a significant decrease in the cost of specialized radiation-shielded facilities and equipment, such as hot cells or minicells. The small volume scale minimizes contamination risks, particularly fluorine-19 derived from reagents (51), benefiting  $^{18}\text{F}$ -labeled tracers with high molar activities. High molar activity is crucial for neuroreceptor imaging, and also in early-stage tracer development in preclinical research, enabling sufficient activity injection for high signal-to-noise ratio images without inducing pharmacologic effects. Generally, small animals are injected with much higher



concentrations of the tracer than humans to achieve sufficient signal for small animal scanners with small voxel sizes (59,60). Due to the greatly reduced quantities of reagents and the small volume (10 microliters) of crude product, microvolume radiosynthesis facilitates simple purification of crude products using radio-HPLC on an analytical scale rather than a semi-preparative scale. Analytical-scale chromatography provides a more rapid purification process (shorter retention times), and a smaller volume of the pure product is collected, simplifying the formulation of the tracer into an injectable solution downstream.

Over the past five years, numerous batch-based systems have been developed and integrated into preclinical imaging studies, and even clinical production, especially in applications involving radiofluorination (39,40,61).

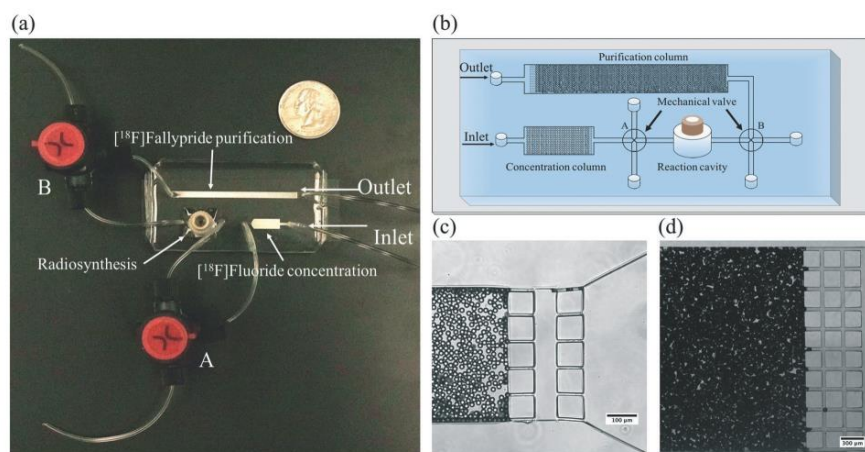


**Figure 1-3 PDMS-based chamber microreactor system.**

(A) Photograph of the microfluidic chip with a US quarter for size comparison. (B) Schematic illustration of the microfluidic chip employed for [<sup>18</sup>F]fallypride production, including a [<sup>18</sup>F]fluoride concentration column, fluorination reaction cavity and [<sup>18</sup>F]fallypride purification column. (C) Photograph of anion exchange beads trapped inside a microchannel by PDMS pillars with 10 μm gap. (D) Photograph of reverse phase C18 microparticles trapped inside a microchannel by PDMS pillars with 40 μm gap. The figure was adapted from reference (57).

Zhang et al. introduced a novel polydimethylsiloxane (PDMS)-based chamber microreactor (**Figure 1-3**) (57). This microreactor comprises two built-in columns (for [<sup>18</sup>F]fluoride concentration and product purification), along with an external valve system to control reagent transfer. The system successfully produced [<sup>18</sup>F]fallypride, yielding up to 5 mCi with high integration in about 60 min. However, PDMS is not chemically resistant to most organic solvents

frequently used in radiosyntheses, thus limiting the range of radiochemical reactions feasible in this chip. Moreover, the synthesis suffered significant radioactivity loss, likely attributed to a suspected reaction between PDMS and  $[^{18}\text{F}]$ fluoride under certain conditions.

Iwata et al. aimed to simplify microscale synthesis using easily accessible materials and developed a microvial-based system for reactions as low as  $\sim 5 \mu\text{L}$  (**Figure 1-4**) (62,63). This system, resembling conventional setups, applied  $[^{18}\text{F}]$ FET and  $[^{18}\text{F}]$ fallypride as examples. While achieving similar yields to macroscale methods (64,65), this setup required higher temperatures or longer reaction times due to reduced heat transfer efficiency with these microvials. Despite its simplicity and use of readily available devices, no automation has been reported for this microscale approach as of yet.

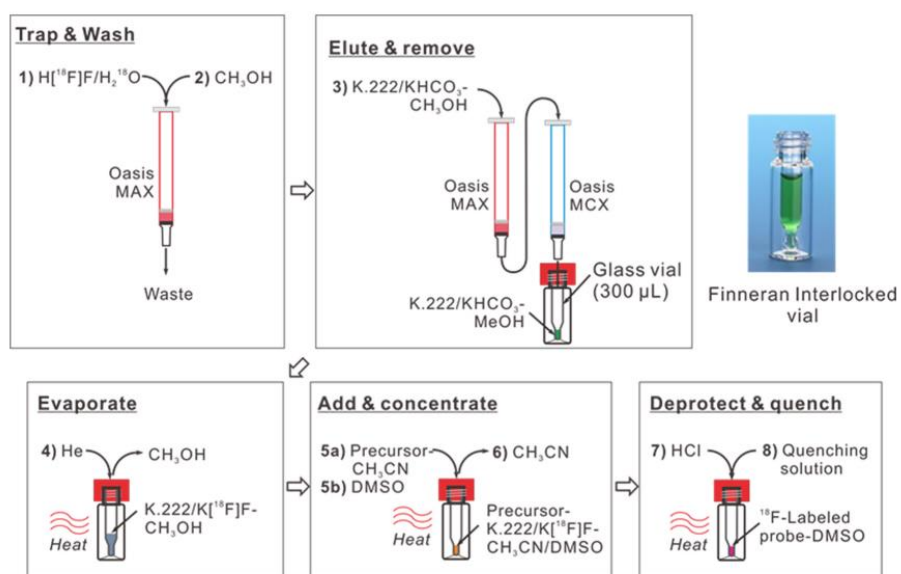


**Figure 1-4 Schematic procedure for one-pot microscale radiosynthesis using microvial-based system.**

The figure was adapted from reference (55).

Ovdiichuk et al. introduced iMiDEV, a novel platform designed for small-scale radiopharmaceutical production, aiming for fully automated microscale synthesis using  $[^{18}\text{F}]\text{NaF}$  as an example (66). Later, Mallapura et al. and Ovdiichuk et al. further tested its viability, extending its application to  $[^{11}\text{C}]$ carbon labelled Flumazenil and L-Deprenyl (67), and  $[^{68}\text{Ga}]\text{Ga-PSMA-11}$

(68), respectively. This commercially available system includes a disposable cassette-based synthesizer, a "Docking station" supplying compressed gases, and an HPLC system for product purification and analysis, accommodating synthesis in both liquid and gas phases (see **Figure 1-5**). The user-friendly interface provides operators with all necessary information for manual or fully automated synthesis control. However, the platform involves numerous fluidic tubes, valves, reagent vials, and pressure sources complicate the system and introduce risks of failures, making it relatively expensive. Additionally, the system allows only one synthesis at a time, resulting in low throughput and hindering efforts for synthesis optimization. Further work is needed to demonstrate its versatility in accommodating diverse and more intricate radiosynthesis practices.

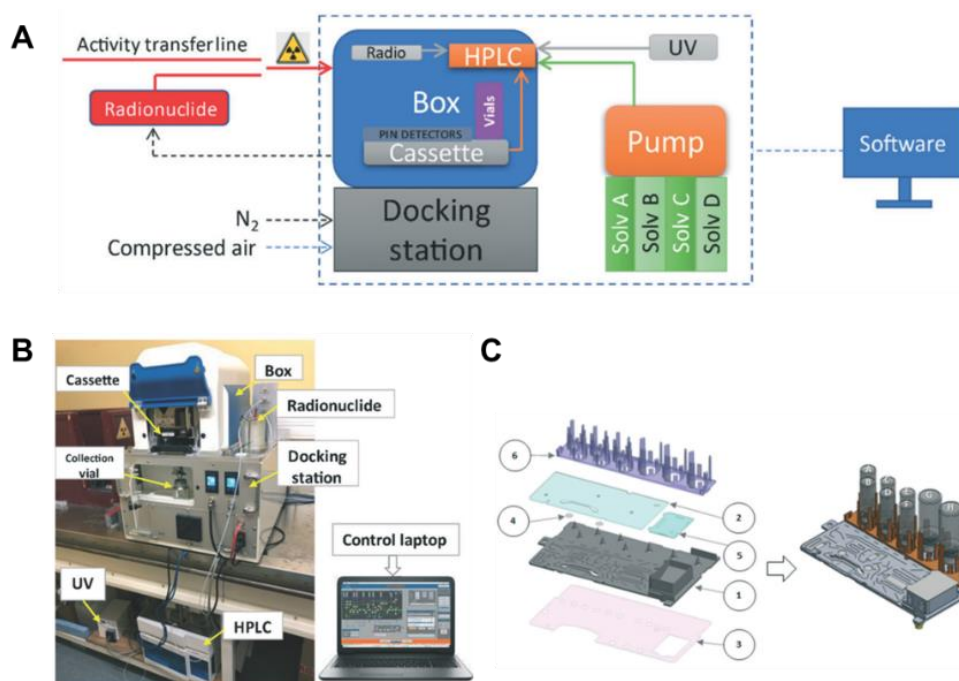


**Figure 1-5 iMiDEV™ microfluidic radiochemistry platform.**

(A) Schematic of iMiDEV™ system components; box (synthesizer) outer dimensions: 320 mm × 400 mm × 300 mm. (B) iMiDEV™ microfluidic platform including the box, docking station, HPLC. (C) iMiDEV 3D cassette representation: 1 – middle COP layer with valves, chambers and spikes for vials; 2 – top COP layer; 3– bottom COC-E-140 membrane; 4 – hydrophobic filters; 5 – formulation chamber cover; 6 – vial holder. The figures were adapted from reference (66).

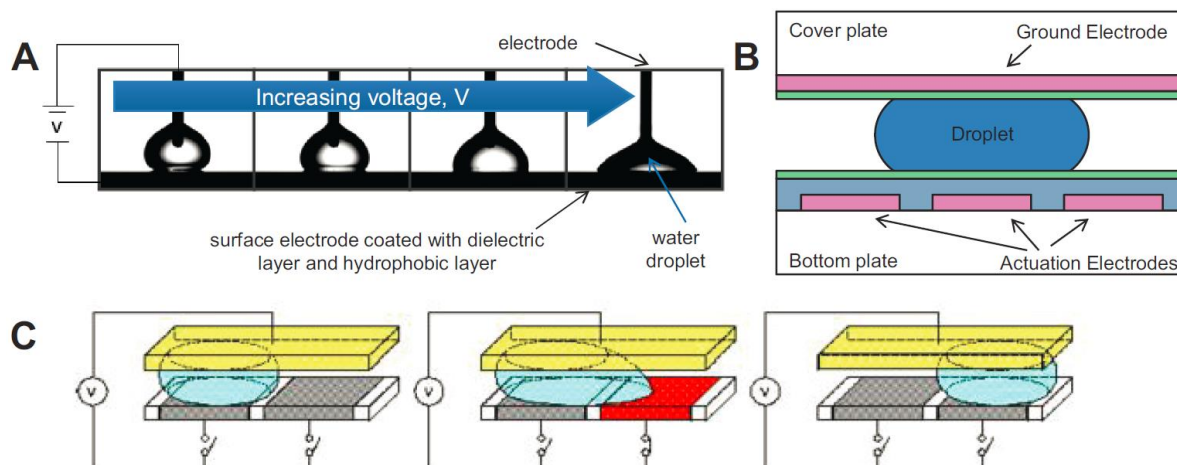


**Figure 1-6 Structure and operation of EWOD microfluidic chips.**

(A) Electronic control of the droplet interaction with the surface due to electrowetting effect. (B) In a typical EWOD device, the droplet is sandwiched between two plates with the electrode configuration as shown. The blue layer is an insulating dielectric layer and the green layer is a hydrophobic coating. (C) By applying a voltage to one end of a droplet with an actuation electrode, a force is generated, pulling the droplet toward the activated electrode, allowing linear transport, splitting, and other manipulations of droplets. The figure was adapted from reference (53).

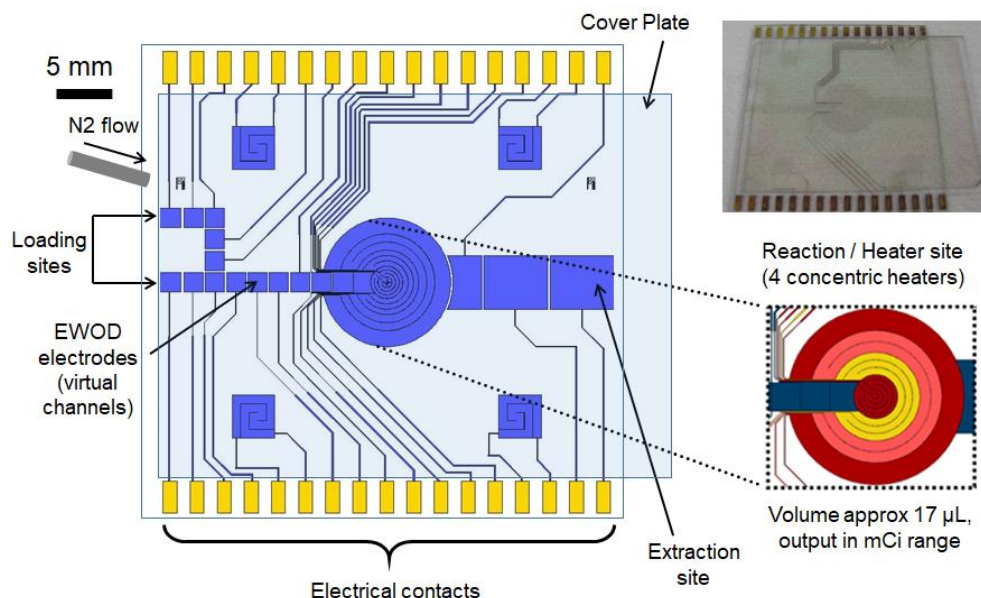


**Figure 1-7 Schematic of the two-layer EWOD radiosynthesis chip.**

The schematic shows electrode pattern of the central reaction size (with concentric resistive heaters) and reagent pathways. A photograph of the actual device is shown at the top right of the figure. The figure was adapted from reference (53).

To create a more compact and disposable microfluidic system for PET radiopharmaceutical production, our lab utilized droplet-based electrowetting-on-dielectric

(EWOD) technology (69–72). The EWOD chip, illustrated in **Figure 1-6**, has a bottom plate with individual electrodes controlling droplet movement through the electro-wetting phenomenon. A cover plate with a ground electrode completes the setup. Both plates are coated to facilitate droplet movement and ensure compatibility with various solvents and reagents. In EWOD microfluidic chips, sequential electrode activation transports reagent droplets from fixed loading sites to a central, temperature-controlled zone. This zone facilitates evaporation and reaction processes, enabling multi-step radiosynthesis (see **Figure 1-7**). The EWOD system has successfully synthesized various tracers for preclinical imaging, including [ $^{18}\text{F}$ ]fallypride (71), [ $^{18}\text{F}$ ]FDG (73), 3'-fluoro-3'-[ $^{18}\text{F}$ ]fluorodthymidine ([ $^{18}\text{F}$ ]FLT) (74), and N-succinimidyl-4-[ $^{18}\text{F}$ ]fluorobenzoate ([ $^{18}\text{F}$ ]SFB) (70). In another innovative approach, Mogi et al. developed an open-style EWOD device with a dimple structure to mitigate erroneous movements caused by experimental conditions (e.g., substrate tilt and distortion) (75). Illustrated in **Figure 1-8**, the EWOD substrate comprised a 300  $\mu\text{m}$  thick paper and a 10  $\mu\text{m}$  thick insulating membrane. An electrode pattern, consisting of 10 jagged tiles and conductive paths, was printed on the paper using an inkjet printer. The dimple structure on each tile was formed by embossing the paper substrate laminated with an insulating membrane. Using technetium-99m diethylenetriamine pentaacetate ([ $^{99\text{m}}\text{Tc}$ ]Tc-DTPA) as an example, the experiment achieved high chelation efficiency, producing a sufficient quantity for mouse imaging. More recently, Ahmadi et al. integrated a machine learning approach to systematically screen diverse experimental conditions on a novel two-layer EWOD device (76). This chip facilitated both the synthesis and purification of [ $^{18}\text{F}$ ]FDG, featuring reservoir electrodes for each reagent stock solution and a novel PDMS-based purifier disc with Alumina beads for purification. However, the intricate and expensive fabrication workflow of EWOD devices, coupled with high device failure rates under harsh chemical conditions, limits their disposability, posing a challenge for cost-effective PET radiopharmaceutical production.

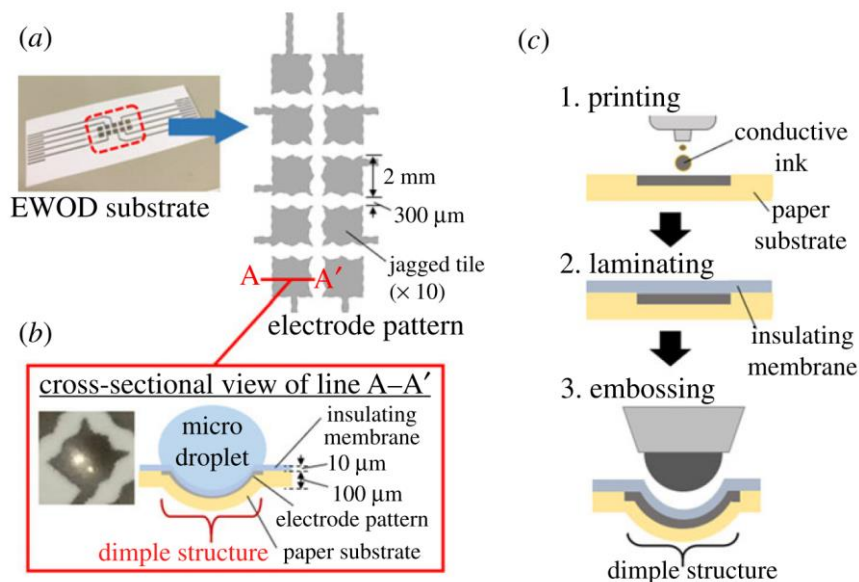


**Figure 1-8 Schematic of the open-style EWOD chip with a dimple structure.**

(A) Outline and electrode pattern of the substrate; 2 mm square jagged tiles are aligned with 300 μm spacing. (B) Cross-sectional view of line A – A'. The thin-film substrate is composed of an insulating membrane and the paper on which the electrodes are printed. A dimple structure with a spherical-cap shape is formed on each tile. (C) The fabrication process of a dimple structure on the EWOD substrate. The figures were adapted from reference (77).

More recently, our lab has embraced a simplified approach using Teflon-coated silicon (or glass) as a cost-effective alternative to EWOD chips. This eliminates the need for the electrode and dielectric layers, streamlining the fabrication process. The materials in contact with the reaction mixture and thermal properties remain consistent with EWOD substrates (51,78–80) (Figure 1-9).

The initial simplified version was a square-shaped Teflon-coated glass chip, created by coating a plain glass (25.0 x 25 mm) with Teflon. Similar to the EWOD "sandwich" configuration, the droplet on the bottom substrate was covered with a second substrate placed atop (see Figure 1-9A). This simple setup demonstrated practical use for synthesizing tracers (e.g., [<sup>18</sup>F]fallypride and [<sup>18</sup>F]AMBF<sub>3</sub>-TATE) for pre-clinical imaging (51,79). However, the glass chip was prone to Teflon layer damage from physical contact, harsh chemicals, and potential radiation. It also

required significant manual intervention, such as the placement and removal of the cover plate, making automation challenging.

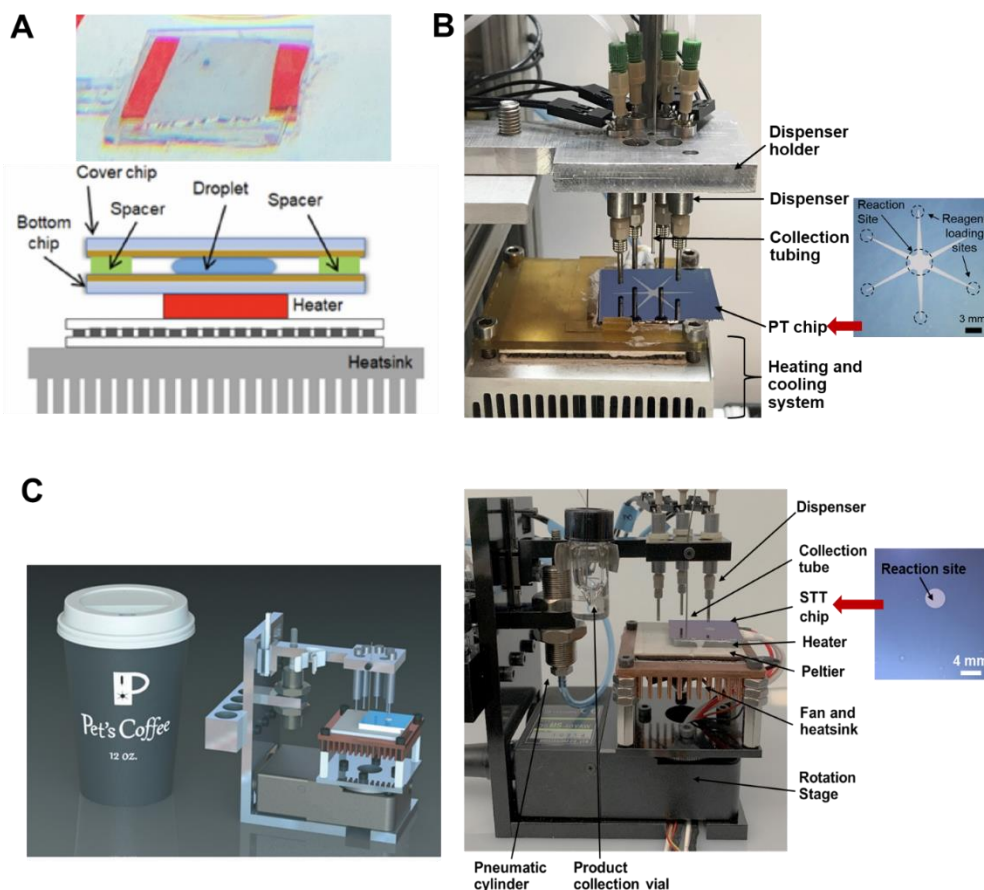


**Figure 1-9 Microdroplet radiochemistry platforms.**

(A) Closed reactor consisting of 2 Teflon-coated glass substrates with spacer strips on the sides to control the height of a sandwiched droplet. (B) Automated radiosynthesizer with a passive transport (PT) chip. (C) Ultra-compact automated radiosynthesizer with a surface tension trap (STT) chip. The figures were adapted from references (78–80).

Our lab later introduced an automated platform with a passive transport (PT) silicon chip (25.0 x 27.5 mm) (**Figure 1-9B**). This chip employs a hydrophilic tapered pattern on a hydrophobic surface, allowing droplets to move spontaneously along radially-oriented channels without the need for actuation electrodes. When a small droplet is dispensed at one of the narrow ends of the delivery channels (0.17 mm), it spontaneously moves towards the wider end due to the strong net force (hemiwicking and Laplace pressure) between the two ends (81). The radiosynthesizer

system includes a heating and cooling system, with a PT chip atop a ceramic heater. Dispensers/collection tubing above the chip automate reagent delivery using piezoelectric dispensers connected to pressurized reagent vials. Reactions occur on the chip's open surface, and the final product is automatically recovered via retractable collection tubing into a designated vial via vacuum (78,82,83). Automated synthesis using the PT chip was demonstrated for [<sup>18</sup>F]fallypride, [<sup>18</sup>F]FET and [<sup>18</sup>F]FDG. However, the PT mechanism proved sensitive to solvent, temperature, and volumes, causing volume spreading issues out of the reaction site and migration backward along the tapered channels. These challenges, leading to potential decreases in reaction yields and inconsistencies, necessitate cumbersome optimization for each combination of volume, solvent and temperature, complicating the adoption of this platform for versatile everyday use (80,84).

To address challenges with the PT mechanism, our lab's most recent approach involves the direct dispensing of reagents into the reaction site within an automated prototype system (80). Instead of a star-shaped hydrophilic pattern, a circular reaction site (4 mm diameter) was removed from the Teflon coating by reactive ion etching, creating a hydrophilic region of exposed silicon acting as a surface tension trap (STT) for the reaction. While Teflon-coated glass and EWOD substrates struggled to confine reaction volume, the STT chip effectively prevented reagent or product spreading within the pattern boundaries. To streamline reagent delivery and enable the use of multiple dispensers, the chip and heater were mounted on a rotating platform, aligning the reaction site below a selected dispenser (all dispensers were arranged in a circle in a fixture above the chip) (see **Figure 1-9C**). This simple platform facilitated the efficient radiosynthesis of various tracers, including [<sup>18</sup>F]FET, [<sup>18</sup>F]FBB, [<sup>18</sup>F]fallypride and [<sup>18</sup>F]FDOPA (80,80,84–86).

## 1.5 High-throughput radiochemistry system

Conventional radiosynthesizers are tailored for generating sizable clinical batches of radiopharmaceuticals, typically once per day, making them unsuitable for reaction optimization or



the development of novel radiopharmaceuticals. Each data point in these systems involves substantial reagent consumption, and contamination necessitates waiting for each radioactive decay before subsequent use. Low-volume microfluidic synthesizers, by reducing reagent costs per synthesis, enhance the feasibility of conducting detailed optimization studies. Additionally, these microfluidic systems offer the advantage of performing multiple experiments from a single batch of radioisotope in a single day.

Microfluidic flow-based radiosynthesizers, such as the Advion NanoTek microfluidic system in 'discovery mode,' can sequentially conduct dozens of reactions, each utilizing only tens of microliters of reaction volume (87). Various groups have demonstrated the sequential performance of numerous small-scale radiochemical reactions using flow-chemistry capillary reactor platforms, with crude products collected and analyzed offline (50,88,89). However, certain reaction parameters, like the choice of reaction solvent or the conditions for azeotropic drying of [<sup>18</sup>F]fluoride, which are conducted outside the flow system, cannot be investigated in a high-throughput manner. In a similar approach, our lab has previously experimented with polydimethylsiloxane (PDMS) microfluidic chips for generating mixtures of reagents (approximately 120 nL each) with programmable composition and pH to optimize the labeling of antibody fragments with the prosthetic group ([<sup>18</sup>F]SFB) (90). However, these devices and studies were limited to room temperature aqueous conditions.

Laube et al. employed multi-vial heating blocks to conduct approximately 50 radiofluorinations per day, involving the drying of a small aliquot of [<sup>18</sup>F]fluoride eluted from a QMA cartridge, followed by reactions at the 25-50  $\mu$ L scale (91). While showcasing parallelism and low reagent consumption, this technique required significant manual handling of vials, including the installation and removal of vial caps. More recently, Verhoog et al. reported a similar optimization strategy for copper-mediated synthesis of 12 arylboronate esters through parallel reactions in a 24- or 96-well format, utilizing a special "lid" that could close all glass vials at once (92). However,

external [ $^{18}\text{F}$ ]fluoride processing with a QMA cartridge, azeotropic drying, and dissolving in an anhydrous solvent was needed before aliquoting to each reaction vial, and the common heating element used for all reactions limits explorations to a single temperature per batch of experiments.

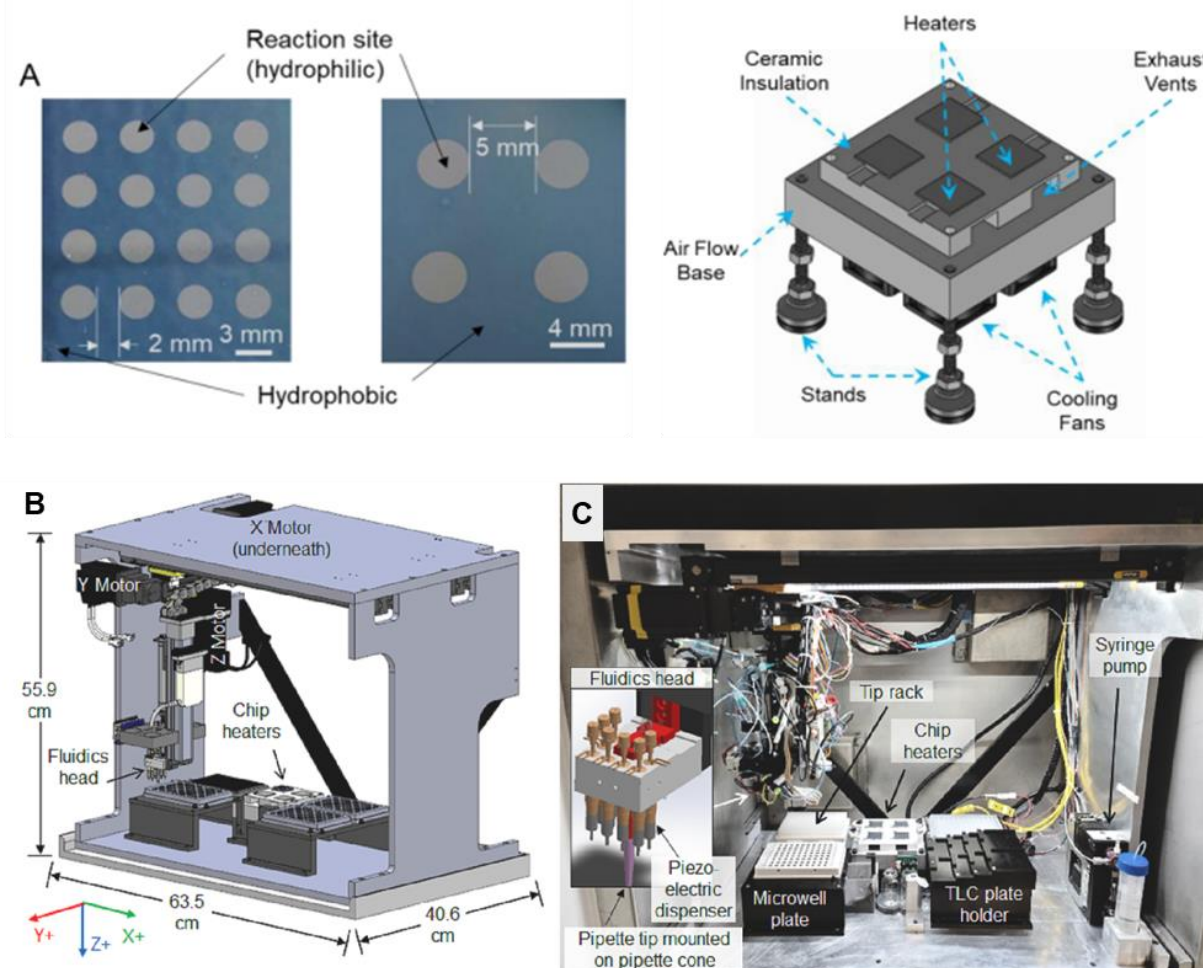


**Figure 1-10 High-throughput droplet radiochemistry platforms.**

(A) Droplet platforms using surface tension traps on 4-heater platform for high-throughput optimization manually. (B) 3D rendering of the automated robotic optimization platform showing the geometry and major components. (C) Photograph of the system inside a minicell. The fluidics head is shown in the inset to illustrate the piezoelectric reagent dispensers and pipette system. The figures were adapted from references (93,94).

To enhance reaction throughput, our lab recently designed a high-throughput chip with multiple hydrophilic traps, allowing for up to 16 simultaneous reactions. We also developed a platform that accommodates four chips, enabling temperature and reaction variations in parallel (**Figure 1-10A**) (93,95). This high-throughput platform facilitated 64 simultaneous reactions in a

day, and the disposable chips eliminate the need for decontamination procedures, allowing for even more reactions. Although the high-throughput droplet radiochemistry technique has been successful for hundreds of experiments weekly (93), it involves a significant amount of manual pipetting for reagent addition and crude product collection and analysis. These manual operations make experiments tedious and prone to human error. To address these challenges and minimize radiation exposure, we developed a fully-automated robotic platform (94) (**Figure 1-10B,C**), which is described in **Chapter 5** of this dissertation. This platform handles all liquid transfer operations and system control, including delivering isotopes and reagents to reaction sites, performing evaporations or reactions, collecting products into individual reservoirs, and spotting crude samples onto thin-layer chromatography (TLC) plates, allowing for rapid multi-lane radio-TLC analysis (96).

## 1.6 Production scale-up on microdroplet platforms

Given the utilization of a relatively low initial activity during the optimization study, there arises the need for a scale-up synthesis to generate an adequate quantity of product suitable for preclinical and clinical research purposes. Within a typical optimization study, 5-10  $\mu\text{L}$  of [ $^{18}\text{F}$ ]fluoride (directly obtained from the cyclotron) is mixed with PTC/base and then dried on the chip in one step, followed by the fluorination process. During the transition to a scaled-up synthesis, where an increased volume of [ $^{18}\text{F}$ ]fluoride is needed to increase the activity level, a modified process is needed to accommodate the large activity volume.

Previously, we presented two distinct strategies for scaling up droplet reactions: (1) accumulating [ $^{18}\text{F}$ ]fluoride at a reaction site by depositing small aliquots of the [ $^{18}\text{F}$ ]fluoride solution, evaporating the liquid, and repeating the process (78,97), and (2) pre-concentrating the [ $^{18}\text{F}$ ]fluoride using a trap-elute process on a miniature cartridge, allowing a larger amount of activity to be loaded onto a reaction site (98). While the first approach is straightforward and suitable for moderate scale-up, handling very large activity amounts and volumes becomes

impractical due to extended evaporation times at a single reaction site. Conversely, the second approach effectively works with much larger radioisotope volumes and avoids the build-up of impurities but requires a more complex setup.

To overcome these challenges, we developed an alternative scale-up method based on the concept of “numbering up,” wherein multiple droplet reactions are conducted in parallel and pooled together to increase the product quantity. This novel approach, outlined and compared to the other approaches in **Chapter 7** of this dissertation, proves faster than other methods by eliminating the need to process [ $^{18}\text{F}$ ]fluoride ahead of the reactions. It has the additional advantage that the replicated reactions are performed under identical conditions and activity scales, eliminating the possibility that the performance of individual reactions will deviate from the results observed during optimization studies. Conducting each individual reaction at a smaller scale also mitigates issues related to radiolysis or impurities in the radioisotope source. Numbering up offers a swift path to scale-up, minimizing the effort and cost needed to transition from optimizing droplet-based reactions at low activity scales to larger-scale production.

## **1.7 Microscale-to-macroscale radiosynthesis translation**

While we have demonstrated the feasibility of performing relatively large-scale individual droplet reactions (83,99), in some cases sufficient for many patient doses, the limited availability of droplet reactor systems hinders widespread adoption of the improved synthesis processes we have developed. Therefore, we explored the potential of directly scaling the optimized droplet conditions to a vial-based (macroscale) reaction, using the copper-mediated synthesis of a novel monoacylglycerol lipase (MAGL) PET tracer ([ $^{18}\text{F}$ ]YH149) as a proof-of-concept example. As described in more detail in **Chapter 8**, we successfully translated the optimized microscale conditions to a vial-based method, achieving a comparable yield of [ $^{18}\text{F}$ ]YH149 compared to microscale method. The significance lies in providing a pathway for using droplet radiochemistry as a development tool, allowing for rapid and economical synthesis optimization, and then

enabling immediate, widespread benefits of this optimization study for the majority of researchers currently heavily invested in vial-based radiosynthesizers for radiopharmaceutical production.

## 1.8 Summary of the dissertation

In recent years, the development of increasing numbers of PET tracers for both preclinical and clinical applications has highlighted the demand for frequent manufacturing of various tracers. Microfluidic technologies, known for their cost-effectiveness and sophisticated liquid handling capabilities, offer efficient and on-demand tracer production in clinical, preclinical, and research settings. This dissertation illustrates the practicality, efficiency, and economic viability of microfluidic syntheses for a range of novel and established tracers. Utilizing simple and affordable microfluidic devices, we successfully synthesized fluorine-18-labeled radiotracers, producing high-quality tracers suitable for PET imaging. Across different chapters, I showcase the application of microfluidics in new tracer development, small-scale on-demand production for preclinical studies, and the generation of clinically-suitable batches of radiopharmaceuticals. Overall, the microfluidic methods demonstrated a significant reduction in precursor consumption compared to conventional methods, and achieved very high molar activities with minimal radioisotope quantities, and the use of multiple example chemistries highlights the versatility of microfluidic techniques in diverse tracer syntheses. Moreover, through collaboration with other radiochemistry labs, we extended the application of microfluidic synthesizers beyond our own research. While further efforts are needed to optimize and validate microfluidic systems for routine clinical PET diagnostics, this work establishes their immediate and valuable utility in preclinical research, providing a diverse array of PET tracers to researchers.

In **Chapter 2**, I describe the development of the first copper-mediated radiosynthesis of the widely-used clinical PET radiopharmaceutical for imaging dopaminergic function, 6- $[^{18}\text{F}]$ Fluoro-L-DOPA ( $[^{18}\text{F}]$ FDOPA), conducted on a microreactor. This endeavor aimed to explore the feasibility of metal-synthesis in a droplet format, taking into account the sensitivity of metal

reagents to contaminants or to environmental moisture in open reactors. Additionally, the synthesis optimization of [<sup>18</sup>F]FDOPA using a microreactor sought to significantly reduce reagent consumption and preparation times. Under the optimal droplet-based radiosynthesis conditions, I successfully produced [<sup>18</sup>F]FDOPA with a markedly improved activity yield ( $41 \pm 4\%$ ,  $n = 5$ ), ~7-fold higher than the conventional method (5-6%,  $n = 26$ ), while reducing the total preparation time to 25 min (compared to 110 min for the conventional method).

**Chapter 3** presents a collaborative effort with Drs. Philip Miller and Gitanjali Sharma at Imperial College London in the UK. Their project involved the development of radiolabeled imaging agents including small molecules and proteins using aluminum fluoride ([<sup>18</sup>F]AlF) radiochemistry and solid-phase extraction (SPE) cartridge purification. We performed a microscale droplet labeling of a tetrazine analogue (NODA-Tz) as a model substrate and [<sup>18</sup>F]AlF-FAPI-74 (a promising PET agent targeting fibroblast activation protein which is currently undergoing clinical trials) as an example application. The droplet synthesis demonstrated approximately a two-fold increase in both radiochemical yield (RCY) (88%,  $n = 1$ ) and activity yield (77.3%,  $n = 1$ ) compared to the prior macroscale approach (RCY:  $45.0 \pm 5.2\%$ ; activity yield:  $37.0 \pm 4.3\%$ ;  $n = 10$ ), all achieved in about half the preparation time (17 min for the microscale reaction vs. 31 min for the macroscale method).

In **Chapter 4**, we expand our microdroplet platform to synthesize 2'-deoxy-2'-[<sup>18</sup>F]fluoro-β-D-arabinofuranosyluracil ([<sup>18</sup>F]FMAU), a promising PET tracer under clinical trial for directly visualizing cellular proliferation but suffering from a highly challenging multi-step radiosynthesis process involving corrosive reagents. This collaboration with Dr. Kai Chen at the University of Southern California (USA) addressed challenges like highly corrosive reagents and a complex three-step synthesis in one pot. The microdroplet approach, under optimal conditions, achieved [<sup>18</sup>F]FMAU synthesis with over 33x less sugar precursor and 154x less protected thymine than conventional methods. This droplet format allowed a rapid, simple, and efficient preparation of [<sup>18</sup>F]FMAU with high radiochemical and activity yields in just 28 min (compared to ~150 min in

conventional radiosynthesis). The Teflon-coated microfluidic chip reactors demonstrated excellent tolerance to corrosive reagents, and the microliter scale significantly reduced the use of hazardous chemicals like trimethylsilyl trifluoromethanesulfonate (TMSOTf), improving safety and environmental friendliness.

In **Chapter 5**, we introduce a robotic radiochemistry device to automate droplet radiochemistry, reducing manual pipetting and exposure. This system demonstrated high-speed, accurate liquid handling, and uniform drying. A 64-reaction study on the synthesis of [ $^{18}\text{F}$ ]Fallypride revealed comparable performance to manual experiments, assessing the impact of TBAHCO<sub>3</sub> and precursor. As a proof-of-concept for novel radiosynthesis optimization, we collaborated with Dr. Kuo-Shyan Lin at the University of British Columbia in Canada, investigating the effects of reaction temperature and solvent on the copper-mediated radiosynthesis of [ $^{18}\text{F}$ ]fluorobenzyltriphenylphosphonium cation ([ $^{18}\text{F}$ ]FBnTP) (100). The study identified high-performing conditions, demonstrating a high RCY ( $66 \pm 6\%$ ,  $n = 3$ ) in 42 min when combined with purification and formulation.

In **Chapter 6**, we advance our previous microscale studies on [ $^{18}\text{F}$ ]FET and [ $^{18}\text{F}$ ]FBB by developing automated protocols for higher activity syntheses, suitable for 1-2 human doses. Consecutively produced batches successfully passed all required quality controls. Radioactivity scaling, often challenging for microscale synthesis, was addressed by employing a direct evaporative approach on chip, scaling the starting radioactivity to up to  $\sim 100$  mCi [ $\sim 4$  GBq]. This simplified the macro-to-micro interface challenge without external devices, reducing room for error and potential system complexity. The use of simple, inexpensive disposable chips and a compact, low-cost device makes this approach particularly attractive for radiochemistry, addressing the cost concerns associated with introducing microfluidic devices in radiopharmaceutical production. Quality control testing ensured the suitability of the product for human injections. Additionally, for [ $^{18}\text{F}$ ]FBB, we collaborated with Trace-Ability Inc. to perform a more convenient, automated, and faster set of quality control (QC) tests using the Tracer-QC platform.

While the sequential drying steps of [ $^{18}\text{F}$ ]fluoride directly on the chip successfully provided a clinically-relevant tracer dose, we encountered some drop in yield with higher activity. To address this challenge, in **Chapter 7**, I develop an alternative scale-up method based on the concept of 'numbering up'. Multiple droplet reactions were conducted in parallel and pooled together to increase the product quantity. This novel approach is faster than others, eliminating the need to process [ $^{18}\text{F}$ ]fluoride ahead of reactions. Each individual reaction at a smaller scale minimizes issues due to radiolysis or impurities in the radioisotope source, resulting in a rapid and high-yield production of [ $^{18}\text{F}$ ]FBnTP at clinically-relevant levels.

In **Chapter 8**, I describe a collaborative project with Drs. Roger Schibli, Linjing Mu, and Yingfang He at ETH Zurich in Switzerland, addressing two remaining questions in the microdroplet-based radiosynthesis. (1) How useful is the droplet method for optimizing radiotracer synthesis through Cu-mediated radiofluorination at an early stage of radiochemical and preclinical development? (2) Can the microscale optimized conditions be translated to macroscale radiosynthesis protocols compatible with existing vial-based radiosynthesis modules? In 5 days, I conducted a total of 117 experiments, studying 36 distinct conditions, utilizing only <15 mg total organoboron precursor. Compared to the original report with an RCY of  $4.4 \pm 0.5\%$  ( $n = 5$ ), the optimized droplet condition showed a substantial improvement in RCY ( $52 \pm 8\%$ ,  $n = 4$ ), with excellent radiochemical purity (100%) and molar activity (77-854 GBq/ $\mu\text{mol}$ ). Furthermore, we showed for the first time a translation of the optimized microscale conditions to a vial-based method. With similar starting activity, the translated synthesis exhibited a comparable RCY of  $50 \pm 10\%$  ( $n = 4$ ), maintaining excellent radiochemical purity (100%) and acceptable molar activity (20-46 GBq/ $\mu\text{mol}$ ). While macroscale studies were limited by precursor availability, this work establishes a connection between microscale and macroscale reactions, suggesting a rapid and economical approach for novel tracer development—optimizing radiochemistry on a high-throughput microdroplet platform and then straightforwardly translating to vial-based systems for



wider applicability to the current radiosynthesis technology (vial-based systems) in the majority of research labs.

In **Chapter 9**, we introduce the PRISMA approach, a systematic method for developing thin-layer chromatography (TLC) mobile phase conditions to achieve high chromatographic resolution in a set of radiopharmaceuticals with diverse chemical properties. Without prior knowledge of impurities, the PRISMA method relies on observing the separation resolution between a radiopharmaceutical and its nearest radioactive or non-radioactive impurities via UV imaging for different mobile phases. This approach enabled the development of high-resolution separation conditions for a wide range of  $^{18}\text{F}$ -radiopharmaceuticals ( $[^{18}\text{F}]\text{PBR-06}$ ,  $[^{18}\text{F}]\text{FEPPA}$ ,  $[^{18}\text{F}]\text{Fallypride}$ ,  $[^{18}\text{F}]\text{FPEB}$ , and  $[^{18}\text{F}]\text{FDOPA}$ ). Each optimization only took a few hours and required only a single batch of crude radiopharmaceutical. Moreover, the optimized TLC method demonstrated greater accuracy (compared to other published TLC methods) in determining the product abundance of one radiopharmaceutical studied in more depth ( $[^{18}\text{F}]\text{Fallypride}$ ) and was capable of resolving a comparable number of species, with similar resolution, as isocratic radio-HPLC.

In **Chapter 10**, I describe a novel cassette-based automated system (“PHENYX”) (56) that has been developed in parallel with the droplet approaches. This system performs reactions down to  $\sim 5\ \mu\text{L}$  volume in a plastic conical reactor. It features a removable heated lid to seal reactors for microvolume radiosyntheses suffering from unwanted evaporation due to open formats (e.g.  $[^{18}\text{F}]\text{AMBF}_3\text{-TATE}$  (79) and  $[^{18}\text{F}]\text{flumazenil}$  (93)). The system includes a pipettor mounted on an XYZ motion gantry for accessing a pipette tip rack, specialized pipette attachments, and a disposable cassette. All synthesis operations, such as trapping and releasing  $[^{18}\text{F}]\text{fluoride}$  from the QMA cartridge, liquid transfers among reservoirs and the reactor, and installation or removal of the heated lid, are performed by the pipette. This design enables the implementation of a wide range of radiosynthesis protocols. As a proof-of-concept, we synthesized  $[^{18}\text{F}]\text{Fallypride}$  on the platform. Concentrating up to 2 mL of aqueous  $[^{18}\text{F}]\text{fluoride}$  (2-540 MBq) to  $\sim 34\ \mu\text{L}$  was achieved

by trapping on a preconditioned micro-QMA cartridge (3 mg resin) and eluting with TBAHCO<sub>3</sub> (0.35 μmol). The concentrated radioisotope underwent evaporation in the reactor, followed by the addition of 8 μL of precursor solution (0.62 μmol) and heating at 110 °C for 7 min. After collection and analytical-scale HPLC purification, the RCY was 71 ± 6% (n = 3), and the product exhibited high radiochemical purity (>99%) and a molar activity of 290-670 GBq/μmol.

In **Chapter 11**, I describe the application of electrochemistry for introducing nucleophilic [<sup>18</sup>F]fluoride to electron-rich molecules, such as thioethers. Collaborating with Dr. Tomoyuki Kurioka (Tokyo Institute of Technology, Japan) and Dr. Saman Sadeghi (McMaster University, Canada), we developed a novel electrochemical radiofluorination (ECRF) technique using a split bipolar electrode (s-BPE) for an electron-rich compound as an example. Unlike traditional ECRF, which requires high salt concentration, this s-BPE system, with its dual conductive materials, facilitates anodic and cathodic reactions at lower salt concentrations. We achieved a 5x increase in molar activity for [<sup>18</sup>F]fluoromethyl (methylthio)acetate compared to conventional ECRF approaches, mainly attributed to reduced [<sup>19</sup>F]F<sup>-</sup> contamination from less salt.

This dissertation concludes with **Chapter 12**, exploring the potential outlook of microvolume reactors and utilizing the findings for the development of a truly microscale radiosynthesizer, enabling cost-effective on-demand production of radiopharmaceuticals.

## Chapter 2: Copper-mediated radiosynthesis of 6-[<sup>18</sup>F]fluoro-L-DOPA ([<sup>18</sup>F]FDOPA) in a microreactor

### 2.1 Introduction

6-[<sup>18</sup>F]fluoro-L-DOPA ([<sup>18</sup>F]FDOPA) is a powerful positron emission tomography (PET) tracer used in imaging Parkinson's disease (101,102), brain tumors (103–105), focal congenital hyperinsulinism of infancy (CHI) (106,107), medullary thyroid carcinoma (MTC) (108–110), and many other neuroendocrine related diseases (111,112), by monitoring dopaminergic dysfunction or abnormal amino acid transport (113,114).

Despite its increasing application in preclinical and clinical studies, production of [<sup>18</sup>F]FDOPA remains challenging. Due to the strong electron donating hydroxyl and amino acid groups on its aromatic core, the routine labeling pathway of [<sup>18</sup>F]FDOPA has traditionally been carried out through an electrophilic strategy by employing [<sup>18</sup>F]F<sub>2</sub> (115,116) or [<sup>18</sup>F]acetyl hypofluorite (117). However, the production of [<sup>18</sup>F]F<sub>2</sub> involves the introduction of non-radioactive [<sup>19</sup>F]fluoride and thus prepared [<sup>18</sup>F]FDOPA has very limited molar activity which increases the risk of pharmacologic effects. Moreover, [<sup>18</sup>F]F<sub>2</sub>-based production is not commonly accessible in many radiochemistry labs due to the challenges associated with handling gas-type radioactive sources (118–121).

This issue can be overcome by instead using a nucleophilic fluorination strategy employing [<sup>18</sup>F]fluoride. In the past decade, radiochemists have developed several new nucleophilic precursors of [<sup>18</sup>F]FDOPA, including organoboron (122), diaryliodonium salt (123) and nickel complexes (124). Among them, copper-mediated organoboron fluorination has received much attention due to its relatively simple synthesis process and high radiochemical yield (RCY). Using such an approach, Zischler and his co-workers managed to achieve [<sup>18</sup>F]FDOPA in high RCY up to 40% in the presence of alcohol solvent (125), but the large amount of organoboron

precursor (30 mg) and copper reagent (36 mg) used in this process required a complicated purification process by using a precolumn HPLC system leading to long separation time. More recently, Mossine et al. has succeeded to obtain [ $^{18}\text{F}$ ]FDOPA using lower amounts of reagents (3 mg precursor, 14 mg copper catalyst) by employing the same precursor in an anhydrous DMF solvent system (119,126). However, the cost of reagents remains high, the yield was relatively low (activity yield of 5 - 6%), and this protocol faces similar problems as other reactions implemented on conventional automated synthesizers, including a long preparation time (110 min), large and expensive apparatus, and requirement for specialized infrastructure (hot cell), requiring major investment to establish a new production facility.

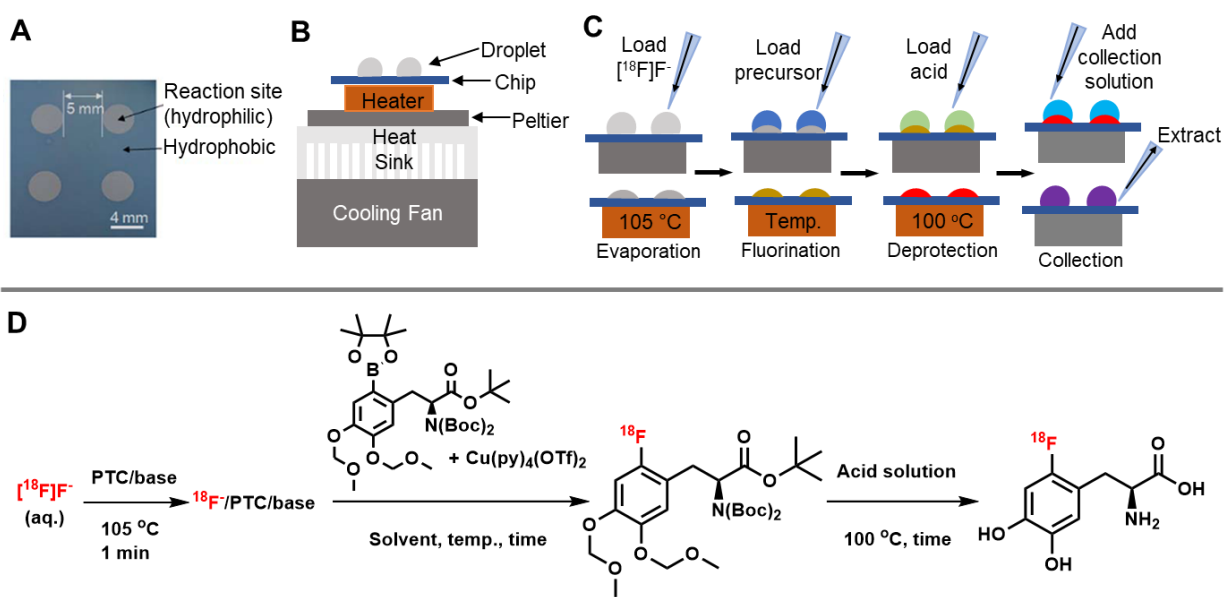


**Figure 2-1 Microscale metal-catalyzed synthesis of [ $^{18}\text{F}$ ]FDOPA on a microdroplet system.** (A) Photograph of the 2 × 2 multi-reaction chip. The diameter of each reaction site is 4 mm and the pitch is 9 mm. (B) Side view of the temperature control platform for the microdroplet reaction chip. (C-D) [ $^{18}\text{F}$ ]FDOPA synthesis scheme and process flow for droplet-based synthesis.

To overcome the current limitations, in this work, we developed the first microscale metal-catalyzed synthesis of [ $^{18}\text{F}$ ]FDOPA on a microdroplet system (**Figure 2-1**). Research in radiosynthesizers has led to a variety of microscale approaches to perform radiochemistry (44,53,61,127,128), including droplet-based reaction systems that are able to minimize the reaction

volume (78,95). Over the past several years, our group has succeeded to employ microdroplet reactors to prepare diverse radiotracers such as [<sup>18</sup>F]FDG (70,78,129,130), [<sup>18</sup>F]FET (131), [<sup>18</sup>F]SFB (70,132), [<sup>18</sup>F]fallypride (70,70,78,93,95,133,134), [<sup>18</sup>F]florbetaben (85,99), [<sup>18</sup>F]FNB (134), [<sup>18</sup>F]AMBF3-TATE (79), [<sup>18</sup>F]FLT (70,72) and [<sup>18</sup>F]FDOPA (iodononium salt method) (86), [<sup>18</sup>F]Flumazenil (93), [<sup>18</sup>F]PBR06 (93), [<sup>18</sup>F]FEPPA (93,135), [<sup>18</sup>F]FPEB (135), [<sup>18</sup>F]FBnTP (94) and [<sup>18</sup>F]YH149 (136). Microdroplet reactors enable both one-step and multi-step radiochemical reactions to be readily performed in microliter-scale volumes, with advantages of minimal reagent cost, repeatable conditions, fast heating and evaporation times, and high molar activity (134). In fact, the required precursor amount can be reduced 100x compared to conventional (macroscale) methods, while continuing to offer comparable or even higher RCY when starting with equivalent activity. Furthermore, the tiny amounts of reagents remarkably decreases the quantity of side products and impurities, and facilitates purification with analytical-scale radio-HPLC that significantly shortens the total separation and formulation time of the final product.

Herein, we leverage this extensive past experience to explore the feasibility of conducting the first copper-mediated organoboron-precursor-based synthesis of [<sup>18</sup>F]FDOPA on a microdroplet reactor. We optimized the fluorination and deprotection conditions on microfluidic chips *via* an extensive set of experiments exploring the impact of diverse phase transfer catalysts (PTCs), bases, solvents, additives, reaction temperatures and acids (deprotection reagents). In addition, different amounts of precursor and copper reagents were investigated in detail. Using the optimized conditions, we then automated the synthesis using a previously developed ultra-compact automated microdroplet reactor (133).

## 2.2 Methods

### 2.2.1 Materials

Anhydrous *N,N*-dimethylformamide (DMF, 99.8%), *N,N*-dimethylacetamide (DMA, 99.8%), dimethyl sulfoxide (DMSO, 99.9%), *n*-butanol (*n*BuOH, 99.5%), pyridine (Py, 99.8%),

methanol (MeOH, 99.9%), Ethanol (EtOH, >99.5), 4-dimethylaminopyridine (DMAP, 99%), tetraethylammonium bicarbonate (TEAHCO<sub>3</sub>, 95%), tetraethylammonium trifluoroethanesulfonate (TEAOTf, 98%), tetrabutylammonium trifluoromethanesulfonate (TBAOTf, 99%), tetrakis(pyridine)copper(II) triflate (Cu(OTf)<sub>2</sub>(py)<sub>4</sub>, 95%), potassium carbonate (K<sub>2</sub>CO<sub>3</sub>, 99.99%), cesium carbonate (Cs<sub>2</sub>CO<sub>3</sub>, 99.99%), hydrochloric acid (HCl, 37%, i.e., 12N), glacial acetic acid (AcOH, 99.7%), phosphoric acid (H<sub>3</sub>PO<sub>4</sub>, >85% wt.% in H<sub>2</sub>O), sodium phosphate monobasic (NaH<sub>2</sub>PO<sub>4</sub>, >99%), sodium phosphate dibasic (Na<sub>2</sub>HPO<sub>4</sub>, >99%), L-ascorbic acid (99%) and ethylenediaminetetraacetic acid (EDTA, 99%) were purchased from Sigma-Aldrich (St. Louis, MO, USA) and used without further purification unless otherwise specified. O-MOM-N-(Boc)<sub>2</sub>-protected Bpin precursor (>95%) was purchased from WuXi AppTech (Hong Kong, China), and reference standards of 6-fluoro-L-DOPA hydrochloride (>95%), 6-fluoro-(D,L)-DOPA hydrochloride (>95%), 6-hydroxide-(D,L)-DOPA (>95%) and 6-H-(D,L)-DOPA (95%) were purchased from ABX Advanced Biochemical Compounds (Radeberg, Germany). HPLC-grade acetonitrile was purchased from Fisher Scientific (Pittsburgh, PA, USA). Deionized (DI) water was obtained from a Milli-Q water purification system (EMD Millipore Corporation, Berlin, Germany). Reagent and collection vials (forensic DNA grade) were purchased from Eppendorf (Hamburg, Germany). PBS buffer was prepared at a 0.1 M concentration with a pH of 5 using Na<sub>2</sub>HPO<sub>4</sub> and NaH<sub>2</sub>PO<sub>4</sub> on the same day as the experiment. The polyether ether ketone tubing (PEEK, 1/16" OD x 0.010" ID, 1531L; 360 OD x 100 μm ID, 1571) used for reagent dispensing was purchased from IDEX Health and Sciences (Northbrook, IL, USA). [<sup>18</sup>F]fluoride in [<sup>18</sup>O]H<sub>2</sub>O was obtained from the UCLA Crump Cyclotron and Radiochemistry Center. The activity was used directly as provided by cyclotron without further purification for both droplet-based microscale radiosynthesis.

Stock solutions were freshly prepared before each set of experiments. Stock solutions of phase transfer catalysts (PTCs, including TEAHCO<sub>3</sub>, TBAOTf and TEAOTf) and bases (including Cs<sub>2</sub>CO<sub>3</sub> or K<sub>2</sub>CO<sub>3</sub>) were prepared depending on the conditions being explored, and consisted of

720  $\mu\text{mol}$  PTC and 11.4  $\mu\text{mol}$  base dissolved in 1 mL DI water. When TBAOTf was used as the PTC, the mixture was instead dissolved in 1 mL of a mixture of EtOH and DI water (50:50, v/v). Bpin precursor (2.0 mg, 3.0  $\mu\text{mol}$ ) was completely dissolved in 100  $\mu\text{L}$  of anhydrous DMF. DMF/pyridine stock solution was prepared by adding 40.4  $\mu\text{L}$  of pyridine into 500  $\mu\text{L}$  of anhydrous DMF and mixing them completely.  $\text{Cu}(\text{py})_4(\text{OTf})_2$  (12.0 mg, 16.9  $\mu\text{mol}$ ) was completely dissolved in 125  $\mu\text{L}$  of DMF/pyridine stock solution. Right before reaction,  $\text{Cu}(\text{py})_4(\text{OTf})_2$  stock solution was mixed with Bpin precursor stock solution in 1:1 (v/v) ratio to provide the reaction with 0.1 mg (0.15  $\mu\text{mol}$ ) of Bpin precursor and 0.48 mg (0.72  $\mu\text{mol}$ ) of  $\text{Cu}(\text{py})_4(\text{OTf})_2$ . For experiments that explored different solvent types, and amounts of precursor,  $\text{Cu}(\text{py})_4(\text{OTf})_2$ , PTC and base, the recipes for the respective stock solutions were adjusted accordingly. To collect the crude product from chips, a collection solution (2 mL) was prepared with a 4:1 (v/v) mixture of MeOH and DI water.

## 2.2.2 Analytical equipment and methods

Radioactivity measurements (activity deposited or residual activity on chips, and activity of collected product) were performed with a calibrated dose calibrator (CRC-25R, Capintec, Florham Park, NJ, USA). Crude reaction products (intermediate or final product) collected from chips were analyzed via radio-TLC and HPLC.

In radio-TLC measurements, a 0.5  $\mu\text{L}$  sample was spotted onto a TLC plate (silica gel 60 F<sub>254</sub> TLC plastic plate, Merck KGaA, Darmstadt, Germany). The spotted TLC plate was developed with a mixture of MeCN and DI water (95:5 v/v). After drying, the TLC plate was measured by miniGITA radio-TLC scanner (Elysia-Raytest GmbH, Straubenhardt, Germany) for 5 min. The fluorination conversion was computed using GINA-STAR software (Elysia-Raytest) by computing areas under the peaks corresponding to the radio-fluorinated intermediate ( $R_f = 1.0$ ) and unreacted [<sup>18</sup>F]fluoride ( $R_f = 0.0$ ), and dividing the fluorinated intermediate peak area by the sum of all peak areas.

The initial purification protocol was adapted from the reference (119,126), using mobile phase of MeCN/10 mM  $\text{NH}_4\text{HCO}_2$  (75:25, v/v, pH = 6) with flow rate of 1.5 mL/min under

wavelength of 282 nm, on an analytical column (Luna NH<sub>2</sub> column, 5 μm, 250 × 4.6 mm, Phenomenex, Torrance, CA, USA). Retention times of <sup>18</sup>F-fluorinated intermediate and [<sup>18</sup>F]FDOPA were 1.6 and 10.1 min, respectively, while [<sup>18</sup>F]fluoride was not eluted out with the above condition (**Figure 2-5**). For further HPLC purification optimization, we also used a reversed-phase (RP) analytical column (Synergi™ Hydro-RP C18, RP, 4 μm, 4.6 × 250 mm). The radio-HPLC system comprised a Smartline HPLC system (Knauer, Berlin, Germany) equipped with a degasser (Model 5050), pump (Model 1000), UV detector (254 nm; Eckert & Ziegler, Berlin, Germany), gamma-radiation detector (BFC-4100, Bioscan, Inc., Poway, CA, USA), and counter (BFC-1000; Bioscan, Inc., Poway, CA, USA). To determine radiochemical purity (RCP), and to confirm product identity via co-injection of reference standard, the purified [<sup>18</sup>F]FDOPA was analyzed on the same radio-HPLC system using the NH<sub>2</sub> column method described above. The same analytical scale radio-HPLC system (as for analysis of the purified sample) was employed to determine the molar activity of the purified [<sup>18</sup>F]FDOPA, by injecting a portion of purified [<sup>18</sup>F]FDOPA and computing mass based on a linear calibration curve of FDOPA reference standard. The enantiomeric purity was verified by co-injection of the purified product and the mixture of D and L type reference standard and analyzed on a chiral column (Crownpack CR(+), 5 μm, 150 × 4 mm, Chiral Technologies, West Chester, PA, USA) using a mobile phase of HClO<sub>4</sub> solution (pH = 2) at a flow rate of 1 mL/min. Retention times of D-FDOPA and L-FDOPA were 8.5 min and 11.0 min, respectively.

### 2.2.3 Microdroplet synthesis and optimization

For [<sup>18</sup>F]FDOPA preparation, there are two major steps, including fluorinating the organoboron precursor and deprotecting the intermediate to obtain the final product, and we sequentially optimized them.

To develop and optimize a microscale synthesis of [<sup>18</sup>F]FDOPA, we initially performed some experiments to give baseline measurements of the amount of radioactivity loss at different



steps with and without the presence of certain reagents. Next, numerous experiments were conducted to optimize the fluorination and deprotection conditions using multi-reaction microfluidic chips. The microdroplet chips used in these experiments contains 2x2 arrays of circular hydrophilic (silicon) reaction sites (4 mm diameter) surrounded by a hydrophobic (Teflon AF) coating (**Figure 2-1A**), prepared as previously described (78,95). The disposable microfluidic chip was operated on top of a temperature control platform (78,133) (**Figure 2-1B**). In initial experiments, reagents were loaded and crude products were collected using a micropipette. The protocol was also implemented on our automated droplet-based radiosynthesizer (86).

For each condition, the reaction was performed as shown in **Figure 2-1C**. A droplet (5  $\mu\text{L}$ ) of [ $^{18}\text{F}$ ]F-/[ $^{18}\text{O}$ ]H $_2\text{O}$  (19-152 MBq) was first delivered onto each reaction site on a microfluidic chip, with an activity measurement after each spot was loaded to determine the starting activity for each reaction. The PTC (TBAOTf, TEAOTf or TEAHCO $_3$ ) and the base (Cs $_2$ CO $_3$  or K $_2$ CO $_3$ ) in 5  $\mu\text{L}$  of stock solution were added and the total 10  $\mu\text{L}$  of solution was dried at 105  $^\circ\text{C}$  for 1 min. Due to the minimal amount of water, we found this 1 min drying time to be sufficient (without any need for azeotropic distillation) before the fluorination step. Fluorination was performed by adding precursor and Cu(OTf) $_2$ (py) $_4$  in 10  $\mu\text{L}$  of desired solvent and heated at the desired temperature for the desired reaction time. In order to maintain an average reaction volume of  $\sim$ 10  $\mu\text{L}$ , the reaction was replenished with 8  $\mu\text{L}$  of solvent every 30 s (for solvents DMF/Py, DMA/Py, DMA/*n*BuOH, or pyridine), or 8  $\mu\text{L}$  of solvent every 60 s (for DMSO/Py). The crude fluorinated product was collected from chips by adding a 20  $\mu\text{L}$  droplet of a mixture of MeOH and DI water (4:1 v/v) and then transferred to a 0.5 mL vial, which was repeated a total of 4 times to minimize residual activity left on the chip. Fluorination conversion was determined via radio-TLC analysis of the collected crude fluorination product. Collection efficiency (%) was computed as the collected activity from chips divided by the initially loaded activity (decay-corrected), and crude fluorination yield (decay-corrected) was calculated by multiplying fluorination conversion and

collection efficiency (%). Moreover, residual activity on chip (%) was computed as the total residual activity on chip for all spots divided by the total activity loaded on chip, and residual activity on pipette tips (%) was calculated via the residual activity on pipette tips after each collection divided by the initial activity loaded on a corresponding spot, respectively. The volatile loss (%) was calculated by subtracting the sum of recovered activity, residual activity on chip and residual activity on pipette tips from the total loaded activity (100%). When optimizing the deprotection, we collected the final crude product using the same collection protocol. Deprotection yield was computed by radio-HPLC analysis, i.e. dividing the area under the [<sup>18</sup>F]FDOPA peak by the area under all peaks in the radio-chromatogram. In some experiments, we performed purification after collecting the crude [<sup>18</sup>F]FDOPA product. The sample was injected into radio-HPLC and the purified [<sup>18</sup>F]FDOPA was collected into a 5 mL vial for further analysis.

## 2.3 Results and discussion

### 2.3.1 Fluorination optimization

#### 2.3.1.1 Preliminary conditions

To implement the fluorination step in droplet format, we first adapted the reaction conditions of Zischler *et al.* (125) by scaling down the fluorination reaction volumes and reagent amounts by 120x, i.e., reducing from 1200  $\mu$ L to 10  $\mu$ L, while maintaining the same reagent concentrations and ratios. Due to low solubility of precursor and copper reagent in DMA and *n*BuOH (2:1, v/v), we reduced even further the amounts of precursor (15 mM used vs 50 mM calculated) and Cu(Py)<sub>4</sub>(OTf)<sub>2</sub> (15 mM used vs 44 mM calculated). The reaction was conducted with TEAHCO<sub>3</sub> (0.12  $\mu$ mol) as PTC and Cu(py)<sub>4</sub>(OTf)<sub>2</sub> (0.15  $\mu$ mol) as copper reagent with 0.1 mg (0.15  $\mu$ mol) of organoboron precursor at 110 °C for 5 min in 10  $\mu$ L of DMA and *n*BuOH (2:1, v/v). However, no intermediate was formed and the reaction showed a significant loss of activity (36%, n = 4, decay-corrected) after fluorination (**Table 2-1, entry 1**). Even though many attempts (not

shown in **Table 2-1**) were made using different amounts of PTC and copper reagent, different solvents (DMA, DMF, and mixtures of DMA and *n*BuOH), temperatures, and reaction times, we failed to achieve a detectable fluorination yield.

**Table 2-1. Overview of performance during initial screening of fluorination conditions.**

Entry <sup>a</sup>	PTC	Base	Fluorination Solvent <sup>b</sup>	Fluorination conversion (%)	Collection efficiency (%)	Crude fluorination yield (%)
1 <sup>c</sup>	TEAHCO <sub>3</sub>	None	2:1 DMA/ <i>n</i> BuOH <sup>c</sup>	Trace	47 ± 1	Trace
2	TBAOTf	K <sub>2</sub> CO <sub>3</sub>	96:4 DMF/Py	29 ± 2	59 ± 2	16 ± 1
3	TBAOTf	None	96:4 DMF/Py	26 ± 2	8 ± 0	2 ± 0
4	TBAOTf	K <sub>2</sub> CO <sub>3</sub>	96: 4DMSO/Py	1 ± 0	71 ± 3	1 ± 0
5	TBAOTf	K <sub>2</sub> CO <sub>3</sub>	Py	12 ± 0	60 ± 4	7 ± 0
6	TBAOTf	Cs <sub>2</sub> CO <sub>3</sub>	96:4 DMA/Py	37 ± 4	66 ± 6	25 ± 5
7	TEAOTf	Cs <sub>2</sub> CO <sub>3</sub>	96:4 DMA/Py	60 ± 4	71 ± 2	43 ± 2
8	TEAOTf	Cs <sub>2</sub> CO <sub>3</sub>	96:4 DMF/Py	70 ± 2	65 ± 2	45 ± 2
9	TEAOTf	Cs <sub>2</sub> CO <sub>3</sub>	DMF	18 ± 3	48 ± 3	8 ± 1
10	TEAOTf	Cs <sub>2</sub> CO <sub>3</sub>	DMF/DMAP <sup>d</sup>	9 ± 0	85 ± 1	8 ± 0

<sup>a</sup>Each radiosynthesis was carried out by first loading [<sup>18</sup>F]fluoride mixed with PTC (720 nmol) and base (10 nmol), and drying at 105 °C for 1 min. Radiofluorination was performed by adding 0.1 mg (150 nmol) precursor and 750 nmol of Cu(py)<sub>4</sub>(OTf)<sub>2</sub> in 10 μL of solvent heated at 110 °C for 5 min. Each condition was repeated n=4 times. <sup>b</sup>All solvent mixtures are v/v. <sup>c</sup>Reaction was conducted with less PTC (0.12 μmol) and Cu(py)<sub>4</sub>(OTf)<sub>2</sub> (0.15 μmol) in 10 μL of DMA/*n*BuOH (2:1, v/v). <sup>d</sup>4.8 μmol of DMAP was added in 10 μL of solvent.

To our delight, adapting the conditions of Mossine *et al.* (119,126) to the microscale by implementing in 10 μL and using 27x reduced reagent amounts, i.e., 0.72 μmol of TBAOTf (PTC), 0.01 μmol of K<sub>2</sub>CO<sub>3</sub> (base) and 0.75 μmol of Cu(py)<sub>4</sub>(OTf)<sub>2</sub> and 0.1 mg (0.15 μmol) of precursor in DMF/Py (96:4, v/v), we succeeded to obtain the desired intermediate with fluorination conversion of 29 ± 2% (n = 4) and collection efficiency of 59 ± 2% (n = 4), resulting in crude fluorination yield of 16 ± 1% (n = 4) (**Table 2-1, entry 2**). Notably, during fluorination, to align with the precursor amount used in the prior experiment (**Table 2-1, entry 1**) for further comparison, the precursor concentration in a droplet was higher (15 mM vs. 4 mM) than that in Mossine's condition. This adjustment was made despite a 27x reduction in all reagents, maintaining a 100x reduction in reaction volume. We then proceeded to further modify these conditions.

### 2.3.1.2 Initial screening of fluorination conditions

Firstly, to understand the significant loss of activity from the reaction mixture, “blank” experiments were carried out without precursor or copper reagent (**Table 2-3, entries 1-3**). Working with the same amount of base ( $\text{Cs}_2\text{CO}_3$ ; 0.01  $\mu\text{mol}$ ) and different PTCs (TBAOTf, TEAOTf and TEAHCO<sub>3</sub>; 0.72  $\mu\text{mol}$ ), the activity after drying at 105 °C for 1 min was at least 99% (n = 12, decay-corrected) of the initial activity, which was consistent with non-blank experiments. When the blank fluorination reaction was subsequently performed, the collection efficiency was quite high (82-87%), with only 10-12% loss (as volatile species). We suspect that this volatile loss was probably induced from the formation of volatile [<sup>18</sup>F]HF during heating process under the low base condition, and assume that a comparable amount of loss occurs during the non-blank reactions. Interestingly, in **entry 4 (Table 2-3)**, when copper reagent was added into the blank experiment (but still no precursor), the collection efficiency notably dropped down to 30 ± 3% (n = 4). This suggests that the copper reagent might facilitate the separation of [<sup>18</sup>F]fluoride from [<sup>18</sup>F]TEAF complex, increasing its reactivity with the precursor but also facilitating formation of [<sup>18</sup>F]HF that leads to high amount of volatile loss.

We then considered the importance of the amount of base, and attempted the synthesis with no base (**Table 2-3, entry 3**). Though reaction conditions were otherwise identical to **Table 2-3, entry 2**, the absence of base resulted in similar fluorination conversion (26 ± 2% for **entry 3** vs. 29 ± 2% for **entry 2**; n = 4) but very low collection efficiency (8 ± 0% for **entry 3** vs. 59 ± 2% for **entry 2**; n = 4). This is consistent with the idea that base is needed to prevent the formation of [<sup>18</sup>F]HF and loss of activity during the fluorination step.

Next, we investigated the radiofluorination performance by varying the solvent and PTC types. Full details, including additional measurements for each condition, are reported in **Table 2-4**. Comparing **Table 2-1, entries 2, 4, and 5**, in which reaction solvent was varied but PTC type and base were fixed (TBAOTf and K<sub>2</sub>CO<sub>3</sub>), DMF/Py (96:4, v/v) (**entry 2**) provided the highest

fluorination conversion of  $29 \pm 2\%$  ( $n = 4$ ), collection efficiency of  $59 \pm 2\%$ ,  $n = 4$ , and crude yield of  $16 \pm 1\%$  ( $n = 4$ ). The use of DMSO/Py (96:4, v/v) (**entry 4**) gave extremely poor fluorination conversion ( $1 \pm 0\%$ ,  $n = 4$ ) and crude fluorination yield ( $1 \pm 0\%$ ,  $n = 4$ ), but had slightly higher radioactivity recovery ( $71 \pm 3\%$ ,  $n = 4$ ). With only Py as solvent (**entry 5**), the collection efficiency ( $60 \pm 4\%$ ,  $n = 4$ ) was similar to that with DMF/Py (96:4, v/v), but the fluorination conversion was significantly lower ( $12 \pm 0\%$ ,  $n = 4$ ), leading to reduced crude fluorination yield ( $7 \pm 0\%$ ,  $n = 4$ ). In parallel, exploration of the influence of different PTCs showed that TEAOTf pairing with  $\text{Cs}_2\text{CO}_3$  (base) (**Table 2-1, entry 7**) offered a much higher fluorination conversion ( $60 \pm 4\%$ ,  $n = 4$ ) and crude fluorination yield ( $43 \pm 2\%$ ,  $n = 4$ ), and slightly better collection efficiency ( $71 \pm 2\%$ ,  $n = 4$ ) compared to the use of TBAOTf/ $\text{Cs}_2\text{CO}_3$  (**Table 2-1, entry 6**). While both these entries used DMA/Py (96:4, v/v) as a reaction solvent, switching to DMF/Py (96:4, v/v) as solvent (**Table 2-1, entry 8**) improved the fluorination conversion up to  $70 \pm 2\%$  ( $n = 4$ ), resulting in slightly higher crude fluorination yield of  $45 \pm 2\%$  ( $n = 4$ ).

We also considered the role of the additives in the reaction solvent, either with Py (**Table 2-1, entry 8**), without Py (**Table 2-1, entry 9**), or with DMAP (**Table 2-1, entry 10**). The use of Py offered the highest fluorination conversion ( $70 \pm 2\%$ ,  $n = 4$ ) and the corresponding crude fluorination yield ( $45 \pm 2\%$ ,  $n = 4$ ), while the reaction in the absence of Py or in the presence of DMAP all resulted in inferior fluorination performance with  $\sim 6\text{x}$  lower crude fluorination yield.

In summary, the initial screening identified TEAOTf as PTC,  $\text{Cs}_2\text{CO}_3$  as base and DMF/Py (96:4, v/v) as reaction solvent for subsequent optimization studies.

### 2.3.1.3 Optimization of PTC amount

We next explored the influence of PTC amount (**Figure 2-2A**). Details of measurements and calculations can be found in **Table 2-5**. For low PTC amounts (75, 150 nmol), the crude fluorination yield was  $\sim 40\%$  (range 39-41%), while for PTC amounts from 300-900 nmol, the crude fluorination yield was slightly higher (43-49%). Increasing TEAOTf to 1050 nmol resulted in a

significant drop in crude fluorination yield ( $31 \pm 3\%$ ,  $n = 4$ ). We selected an amount of 300 nmol, with crude fluorination yield of  $49 \pm 2\%$  ( $n = 4$ ) for further studies.

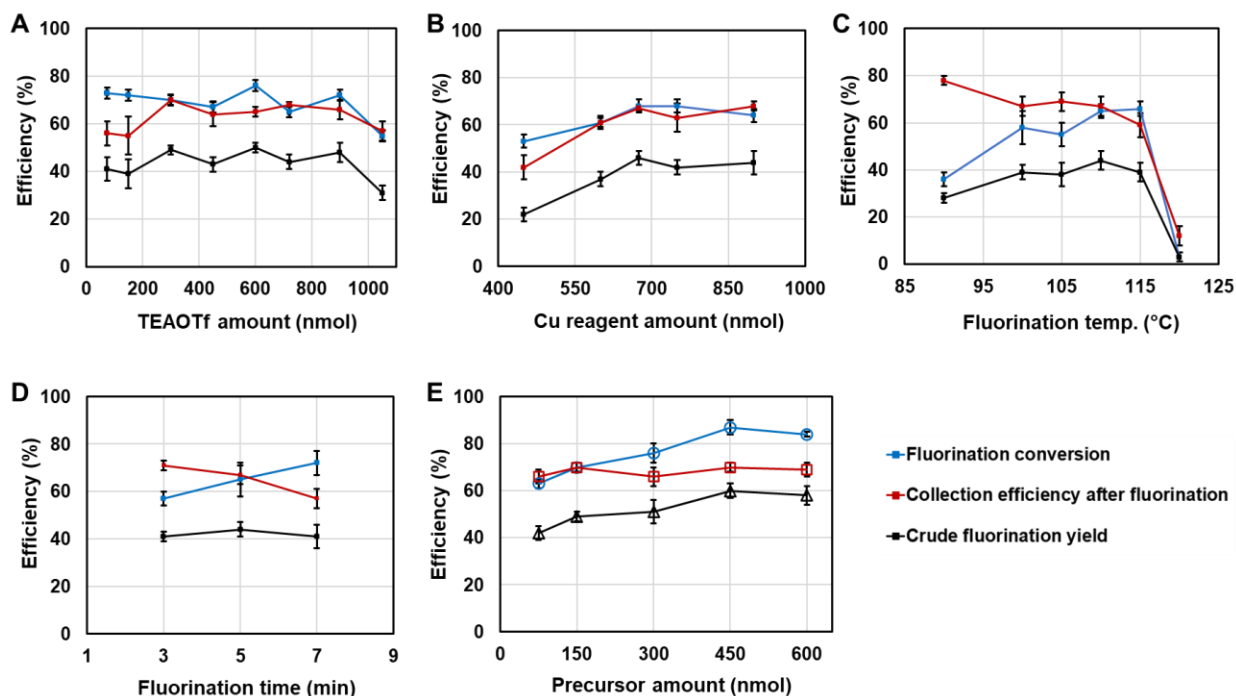


**Figure 2-2 Optimization of on-chip  $[^{18}\text{F}]$ FDOPA fluorination step.**

Effect on reaction performance of (A) phase transfer catalyst (TEAOTf) amount, (B) Cu reagent ( $\text{Cu}(\text{py})_4(\text{OTf})_2$ ) amount, (C) fluorination temperature, (D) fluorination time, and (E) precursor amount.

### 2.3.1.4 Optimization of Cu reagent amount

Next, we investigated the impact of Cu reagent amount (**Figure 2-2B**). Details of measurements and calculations can be found in **Table 2-6**. The fluorination conversion exhibited a notable increase with rising quantity of  $\text{Cu}(\text{Py})_4(\text{OTf})_2$ , reaching a maximum of  $68 \pm 4\%$  with 680 nmol of  $\text{Cu}(\text{Py})_4(\text{OTf})_2$ . The collection efficiency also presented enhanced performance with the increasing amount of  $\text{Cu}(\text{Py})_4(\text{OTf})_2$ . Overall, the peak crude fluorination yield of  $46 \pm 3\%$  ( $n = 4$ ) was achieved using 680 nmol of  $\text{Cu}(\text{Py})_4(\text{OTf})_2$ .

### 2.3.1.5 Optimization of fluorination temperature

We further explored the impact of fluorination temperatures (**Figure 2-2C**). Comprehensive measurements and calculations are detailed in **Table 2-7**. The fluorination conversion exhibited a substantial increase with temperature, peaking at  $66 \pm 3\%$  ( $n = 4$ ) at 115 °C, followed by a notable decrease at 120 °C. Additionally, higher temperatures were observed to result in increased volatile losses, leading to a decline in collection efficiency. The overall crude fluorination yield exhibited a sharp increase with temperature, rising from  $28 \pm 2\%$  ( $n = 4$ ) at 90 °C to  $44 \pm 4\%$  ( $n = 4$ ) at 110 °C, and then slightly decreasing to  $39 \pm 4\%$  ( $n = 4$ ) 115 °C. However, a significant drop was observed at 120 °C, with almost no yield ( $0.4 \pm 0.1\%$ ,  $n = 4$ ). This marked decline may be attributed to the degradation of the precursor, as indicated by the color change of the reaction mixture turning black immediately after heating at 120 °C. We suspect it is the precursor that degrades since no degradation of PTC or  $\text{Cu(Py)}_4(\text{OTf})_2$  was observed in prior studies of other Cu-mediated radiosyntheses even at much higher temperatures like 140 °C (94,136). The maximum crude RCY of  $44 \pm 4\%$  ( $n = 4$ ) was achieved at 110 °C, accompanied by a fluorination conversion of  $65 \pm 3\%$  ( $n = 4$ ) and a collection efficiency of  $67 \pm 4\%$  ( $n = 4$ ).

#### 2.3.1.6 Optimization of fluorination time

Based on the optimal fluorination temperature, a brief study of different reaction times was conducted (**Figure 2-2D**). Details of measurements and calculations can be found in **Table 2-8**. We observed an increase in fluorination conversion over time, accompanied by a decrease in collection efficiency due to increased volatile loss. The maximum crude fluorination yield ( $44 \pm 4\%$ ,  $n = 4$ ) was attained at 5 min, with fluorination conversion of  $65 \pm 3\%$  ( $n = 4$ ) and collection efficiency of  $67 \pm 4\%$  ( $n = 4$ ).

#### 2.3.1.7 Optimization of precursor amount

We further explored the influence of precursor amount (**Figure 2-2E**). Details of measurements and calculations can be found in **Table 2-9**. Notably, fluorination conversion exhibited a significant increase with the precursor amount, peaking at  $87 \pm 3\%$  ( $n = 4$ ) with 450

nmol of precursor, and then reaching a plateau beyond this quantity. In contrast to fluorination conversion, the precursor amount did not exhibit an obvious impact on collection efficiency. Utilizing 450 nmol of precursor resulted in the highest crude fluorination yield ( $60 \pm 3\%$ ,  $n = 4$ ), with fluorination conversion of  $87 \pm 3\%$  ( $n = 4$ ) and collection efficiency of  $70 \pm 2\%$  ( $n = 4$ ).

In summary, with starting activity ranging from 19-152 MBq, the optimal evaporation process involved drying [ $^{18}\text{F}$ ]fluoride with TEAOTf (300  $\mu\text{mol}$ ) and  $\text{Cs}_2\text{CO}_3$  (10 nmol) at 105 °C for 1 min. No azeotropic drying steps were necessary. Subsequently, the fluorination reaction was carried out at 110 °C for 5 min using 450 nmol of precursor and 680 nmol of  $\text{Cu}(\text{OTf})_2(\text{Py})_4$  in a 10  $\mu\text{L}$  solvent mixture of DMF/Py (96:4, v/v).

### 2.3.2 Deprotection optimization

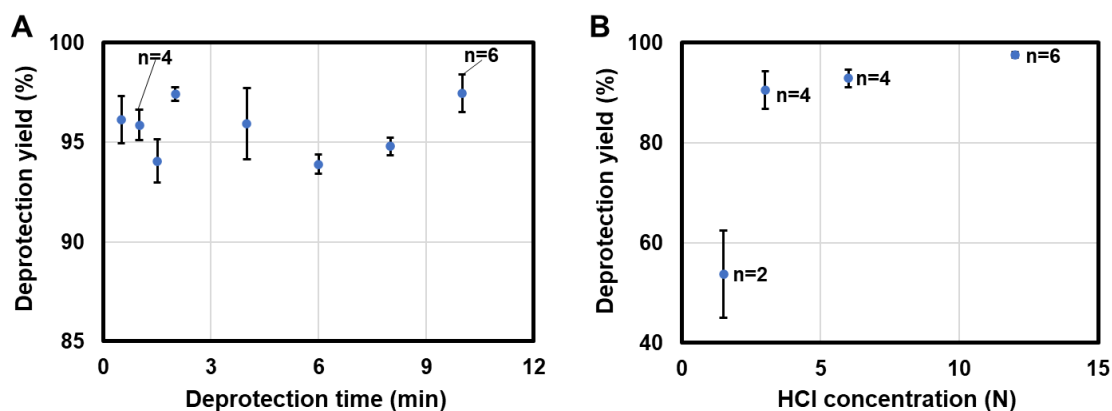


**Figure 2-3 Influence of different deprotection reaction parameters.**

(A) Influence of deprotection time on deprotection yield of crude [ $^{18}\text{F}$ ]FDOPA intermediate. Reaction was performed at 100 °C using 15  $\mu\text{L}$  of mixture of 0.25 M ascorbic acid and 12 N HCl (1:3, v/v). (B) Influence of HCl concentration. All data points were performed with  $n = 2$  repeats unless otherwise indicated.

#### 2.3.2.1 Influence of deprotection time

We then proceeded to study the deprotection step. While maintaining the same deprotection solution and temperature as Mossine *et al.* (119), we first considered the deprotection time (Figure 2-3A and Table 2-10). The deprotection reaction was performed at 100 °C after adding a 15  $\mu\text{L}$  mixture of 0.25 M ascorbic acid and 12 N HCl (1:3, v/v). As the reaction time



increased, only minor impact on the deprotection yield was observed. We chose 2 min, where the deprotection yield reached 97% (n=2; determined by radio-HPLC), as the deprotection time for further experiments.

### 2.3.2.2 Influence of deprotectant concentration

We further explored the influence of deprotectant concentration (i.e., HCl) (**Figure 2-3B**). Details of measurements can be found in **Table 2-11**, and examples of radio-HPLC analysis can be found in **Figure 2-5**. The deprotection yield exhibited a notable increase with higher HCl concentration, reaching a peak value of  $98 \pm 1\%$  (n = 6) when using 12N HCl.

## 2.3.3 Full droplet-based radiosynthesis of [<sup>18</sup>F]FDOPA

### 2.3.3.1 Automated synthesis

The radiosynthesis was then combined with radio-HPLC purification to provide purified [<sup>18</sup>F]FDOPA. In manual preparation under the above optimal condition with similar starting activity (0.06-0.15 GBq), high isolated RCY of  $30 \pm 4\%$  (n = 7) was achieved, accompanied with excellent RCP (>99%) and enantiomeric purity (100%). Before purification, the crude RCY was  $38 \pm 1\%$  (n = 7), arising from a fluorination conversion of  $87 \pm 3\%$ , deprotection yield of  $98 \pm 1\%$  and collection efficiency after deprotection of  $44 \pm 6\%$ . The discrepancy between the crude and isolated RCY is presumably due to losses during HPLC purification. The overall preparation time was ~25 min (including ~10 min for on-chip reactions and ~15 min for purification), contributing to high activity yield ( $26 \pm 3\%$ , n = 7).

For automation, [<sup>18</sup>F]FDOPA synthesis was conducted on an automated microdroplet synthesizer (133) with starting activities of 0.14-0.22 GBq. Given the potential for contamination from metal components in piezoelectric dispensers for the Cu reagent, and the corrosive nature of the deprotectant (12N HCl) which could corrode the dispensers, we explored the use of tubing (PEEK, 1/16" OD x 0.010" ID) mounted in place of dispensers for remote delivery of the precursor/Cu(OTf)<sub>2</sub>(py)<sub>4</sub> stock solution and deprotection solution to the chip (**Figure 2-6**).

Specifically, we loaded a pre-measured reagent bolus into a small v-vial (0.3 mL) connected to the tubing, and applied nitrogen pressure to push the bolus through the tubing onto the chip when needed. For the precursor/ $\text{Cu}(\text{OTf})_2(\text{py})_4$  stock solution, 13.5  $\mu\text{L}$  (slightly higher than the optimal volume of 10  $\mu\text{L}$  after accounting for minor residual losses in the fluid path) was added to vial, and the loading process used 5 psi to transfer the liquid onto the chip. To maintain an average reaction volume of  $\sim 10$   $\mu\text{L}$ , the reaction was replenished with 8  $\mu\text{L}$  of DMF/Py (96:4, v/v) every 30 s using a piezoelectric dispenser. After fluorination, 0.1  $\mu\text{L}$  of sample (1-2% of activity) was taken and diluted in 20  $\mu\text{L}$  of MeCN for further radio-TLC analysis. For deprotection, 20  $\mu\text{L}$  of deprotection solution (slightly higher than the optimal volume of 15  $\mu\text{L}$  after accounting for minor residual losses in the fluid path) was pre-loaded into the deprotectant vial and delivered to the chip with nitrogen (5 psi). To transfer the final crude product from the chip to the collection vial, a PEEK tubing (360  $\mu\text{m}$  OD x 100  $\mu\text{m}$  ID) was mounted in the dispenser fixture, with the end approximately 0.5 mm above the chip surface. Following synthesis, 20  $\mu\text{L}$  of the collection solution was loaded into the reaction site by a piezoelectric dispenser, and the crude product was transferred to the collection vial under vacuum ( $\sim 2$  psi). These steps were repeated a total of 4x to minimize activity residue on the chip. The overall fluorination conversion was  $80 \pm 6\%$  ( $n = 2$ ), with isolated RCY of  $26 \pm 2\%$  ( $n = 2$ ) and activity yield of  $22 \pm 2\%$  ( $n = 2$ ), and molar activity  $>198$  GBq/ $\mu\text{mol}$ . The RCP was  $>99\%$  and enantiomeric purity was 100%. The total preparation time was similar to that of manual synthesis,  $\sim 25$  min. The slightly lower yield of the automated synthesis may be due to losses in tubing or due to small differences in the performance of the heating systems for the manual and automated setups.

### 2.3.3.2 Additional tests

Later, inspired by a separate study that demonstrated significantly improved production of the radiotracer  $^{18}\text{F}$ FBnTP using DMI as a solvent instead of DMF (94), we conducted additional tests for  $^{18}\text{F}$ FDOPA synthesis. Due to DMI's higher boiling point (224-226  $^\circ\text{C}$ ) compared to DMF

(153 °C), there was no need for additional solvent replenishment during the fluorination reaction, simplifying the radiosynthesis process. In a manual synthesis comparison, we replaced DMF with DMI under fixed conditions derived from previous optimization (**Table 2**). Following synthesis, the results displayed a lower fluorination conversion ( $60 \pm 1\%$ ,  $n = 5$  with DMI vs  $87 \pm 3\%$ ,  $n = 7$  for DMF). However, the collection efficiency after deprotection was significantly higher ( $70 \pm 4\%$ ,  $n = 5$  with DMI vs  $44 \pm 6\%$ ,  $n = 7$  with DMF). This suggests that the high-boiling solvent may assist in maintaining activity on the chip during the deprotection reaction. Consequently, the resulting isolated RCY improved to  $50 \pm 3\%$  ( $n = 5$ ), and the activity yield reached  $41 \pm 4\%$  ( $n = 5$ ), while maintaining high RCP (>99%) and enantiomeric purity (100%).

### 2.3.3.3 Comparison of [ $^{18}\text{F}$ ]FDOPA synthesis in $\mu\text{L}$ - and $\text{mL}$ -scale

The overall microscale synthesis performance is summarized in **Table 2-2** and compared to the results of macroscale synthesis (119,125,126), highlighting significant improvements in synthesis time and RCY.

Compared to the originally-reported macroscale synthesis by Mossine *et al.* (119,126), the microdroplet synthesis was conducted with higher concentration of precursor ( $\sim 11\text{x}$ ) and copper reagent ( $\sim 3\text{x}$ ). Despite this, there was a remarkable  $\sim 9\text{x}$  reduction in precursor consumption and  $\sim 29\text{x}$  reduction in copper reagent consumption, achieved by utilizing a significantly smaller reaction volume (10 vs. 1000  $\mu\text{L}$ ). This increased concentration likely improved the reaction rate, allowing for a shortened fluorination time of only 5 min at the microscale, a 4x reduction compared to macroscale synthesis. Leveraging the advantages of microscale radiosynthesis, the collected crude product volume ( $\sim 80 \mu\text{L}$ ) and reagent mass were sufficiently low to allow purification using an analytical radio-HPLC system under isocratic conditions. Purified product collection took only  $\sim 12$  min (**Figure 2-4**) (vs.  $\sim 23$  min on a semi-pre column (119,126)). Overall, the droplet synthesis exhibited a  $\sim 4$ -fold increase in RCY ( $50 \pm 3\%$ ,  $n = 5$ ) and a  $\sim 7\text{x}$ -fold increase in activity yield ( $41 \pm 4\%$ ,  $n = 5$ ) compared to the macroscale approach (RCY: 10-12%; activity yield: 5-6%;  $n = 26$ ).

The comparable fluorination conversion at macroscale ( $55 \pm 13\%$ ,  $n = 26$ ) and microscale ( $60 \pm 1\%$ ,  $n = 5$ ) suggests that the much lower RCY for the macroscale synthesis could be attributed to significant activity loss in the radiosynthesis system and/or HPLC purification platform. Interestingly, a similar phenomenon was observed at the microscale with the same solvent system (96:4 DMF/Py (v/v)) under suboptimal conditions (i.e. high activity loss / low collection efficiency after the deprotection step), suggesting that replacing DMF with DMI might also benefit the macroscale synthesis. The preparation time after purification was shortened to only 25 min, excluding the formulation process. Even considering 5-10 min additional time for formulation, the total estimated preparation time (30-35 min) was significantly shorter than the macroscale method (110 min).

**Table 2-2 Comparison of copper-mediated [ $^{18}\text{F}$ ]FDOPA synthesis in microscale and macroscale.**

	$\mu\text{L}$ -scale (this work)			mL-scale	
	Manual	Automated	Manual	Mossine et al. (Automated)	Zischler et al. (Manual)
Number of repeats (n)	7	2	5	26	3
Starting activity (GBq)	0.06-0.15	0.14-0.22	0.05-0.06	35-63	1-2
Precursor amount ( $\mu\text{mol}$ ) (concentration, mM)	0.45 (45)	0.45 (45)	0.45 (45)	4 (4)	60 (50)
$\text{Cu}(\text{OTf})_2(\text{py})_4$ amount ( $\mu\text{mol}$ ) (concentration, mM)	0.68 (68)	0.68 (68)	0.68 (68)	20 (20)	53 (44)
Solvent (reaction volume, $\mu\text{L}$ ) <sup>a</sup>	96:4 DMF/Py (10)	96:4 DMF/Py (10)	96:4 DMI/Py (10)	96:4 DMF/Py (1000)	1:2 DMA/nBuOH (1200)
Fluorination temperature ( $^{\circ}\text{C}$ )	110	110	110	110	110
Fluorination time (min)	5	5	5	20	10
Fluorination conversion (%) <sup>b</sup>	$87 \pm 3^c$	$80 \pm 6^d$	$60 \pm 1^c$	$55 \pm 13$	$68 \pm 3$
Deprotection efficiency (%) <sup>e</sup>	>97	>97	>97	>99 <sup>b</sup>	NR
Collection efficiency after deprotection (%)	$44 \pm 6$	$44 \pm 5$	$70 \pm 4$	NR	NR
RCY (%; decay-corrected) <sup>e</sup>	$30 \pm 4$	$26 \pm 2$	$50 \pm 3$	10-12 <sup>f</sup>	$40 \pm 4$
RCP (%) <sup>e</sup>	>99	>99	>99	>98	NR
Enantiomeric excess (ee, %) <sup>e</sup>	100	100	100	100	100
Activity yield (%; non-decay corrected)	$26 \pm 3$	$22 \pm 2$	$41 \pm 4$	5-6	NR
Molar activity (GBq/ $\mu\text{mol}$ ) <sup>g</sup>	NA	>198	NA	46-106	37
Total preparation time (min)	$\sim 25^h$	$\sim 25^h$	$\sim 25^h$	110	NR

<sup>a</sup>Mixtures are presented as v/v. <sup>b</sup>Fluorination conversion (%) was analyzed by radio-TLC. <sup>c</sup>The value was obtained from separate fluorination optimization study, with  $n = 4$  repeats for DMF/Py system and  $n = 3$  repeats for DMI/Py system. <sup>d</sup>0.1  $\mu\text{L}$  of sample was taken right after fluorination for radio-TLC analysis. <sup>e</sup>Deprotection efficiency, RCYs, RCP and ee

were determined by radio-HPLC. <sup>a</sup>The valve was calculated based on other information in the literature report. <sup>g</sup>Determined at end of synthesis (EOS). <sup>h</sup>Final product formulation is not included. NA = Not assessed. NR = Not reported.

Comparing our droplet-based synthesis results with the previously reported macroscale conditions of Zischler et al. (125), interesting findings emerge. Despite a slightly higher precursor concentration (45 mM vs. 50 mM), Zischler et al.'s approach provided a slight increase in fluorination conversion ( $68 \pm 3\%$ ,  $n = 3$  vs.  $60 \pm 1\%$ ,  $n = 5$  for DMI/Py), but their RCY was 10% lower than that with the microscale method ( $40 \pm 4\%$ ,  $n = 3$  vs.  $50 \pm 3\%$ ,  $n = 5$  for DMI/Py), suggesting potential activity loss in the radiosynthesis and/or HPLC purification system.

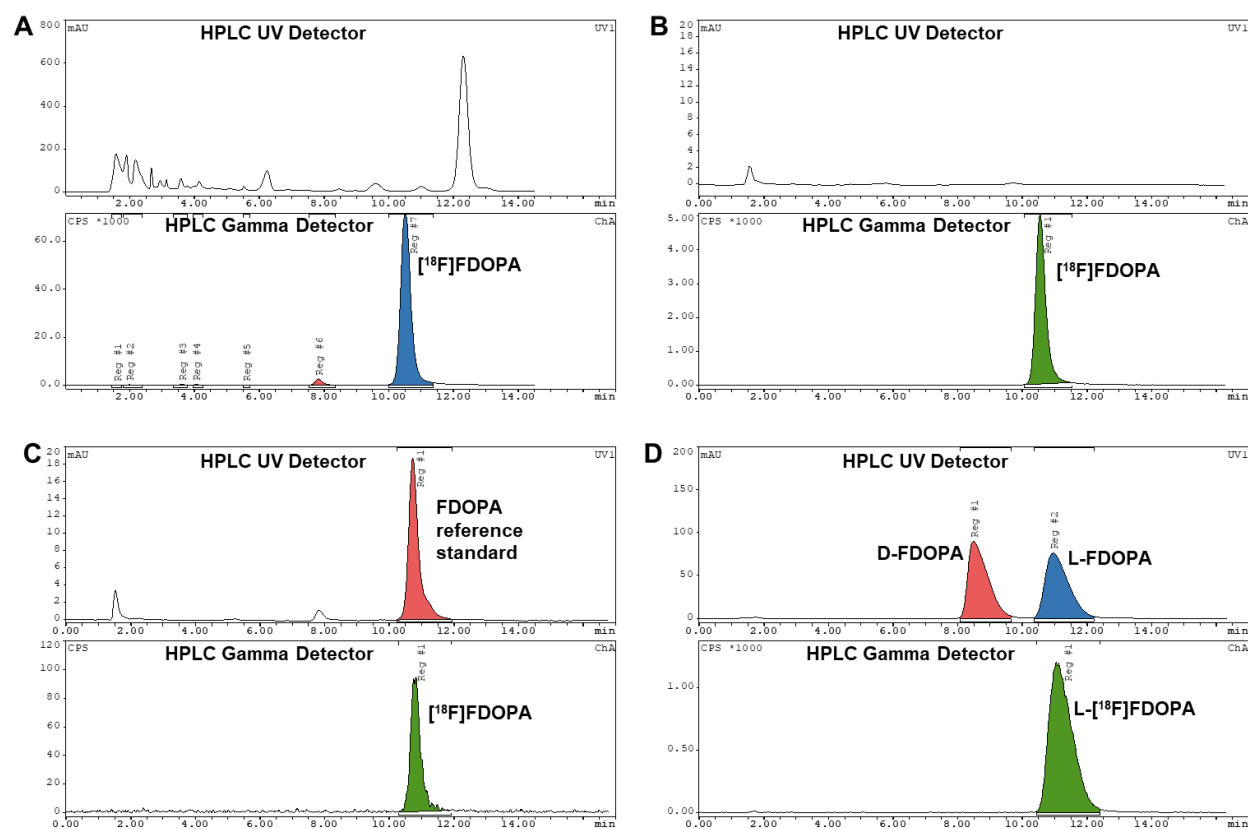


**Figure 2-4 Example radio-HPLC chromatograms from droplet-based radiosynthesis.** (A) crude [<sup>18</sup>F]FDOPA, (B) purified [<sup>18</sup>F]FDOPA, (C) co-injection of purified [<sup>18</sup>F]FDOPA and FDOPA reference standard, and (D) co-injection of purified [<sup>18</sup>F]FDOPA and FDOPA reference standard (mixture of D- and L-FDOPA). A-C were analyzed on a NH<sub>2</sub> column, and D was analyzed on an a chiral column.

### 2.3.4 HPLC purification optimization

The initial adapted HPLC purification method from reference (119,126), employing an analytical normal phase (NP) column (Luna HN<sub>2</sub>, 5 μm, 4.6 × 250 mm) showed excellent separation performance, providing purified [<sup>18</sup>F]FDOPA with high (radio)chemical purity (>99%). Representative radio-HPLC chromatograms using the mentioned column are illustrated in **Figure 2-4 (A-C)**. Given the relatively low-polarity mobile phase required, like MeCN/10 mM NH<sub>4</sub>HCO<sub>2</sub> (75:25, v/v, pH = 6), compared to the stationary phase (NH<sub>2</sub>-coated resin) for NP HPLC column chromatography, post-purification formulation was necessary.

Inspired by the purification method outlined in Zischler et al. and Hoffmann et al.'s works (125,137), which utilized an injectable aqueous solution as the mobile phase on a reverse-phase (RP) column, we pursued further optimization on a similar analytical column (Synergi™ Hydro-RP, 4 μm, 4.6 × 250 mm). Comprehensive details, including mobile phases, retention times of [<sup>18</sup>F]FDOPA, volumes of collected product from radio-HPLC, and individual radio-HPLC chromatograms of crude [<sup>18</sup>F]FDOPA, are provided in **Table 2-12** and **Figure 2-7**.

Initially, two slightly different isocratic mobile phases were tested, both using a flow rate of 1 mL/min on the analytical RP column (**Test 1**: 100% H<sub>3</sub>PO<sub>4</sub> water (0.1%, v/v) with pH = 2; **Test 2**: 1% EtOH (v/v) in H<sub>3</sub>PO<sub>4</sub> water (0.1%, v/v) with pH = 2) (137). Unfortunately, both **Test 1** and **Test 2** showed an impurity (visible in the UV chromatograph) co-eluting with [<sup>18</sup>F]FDOPA.

In **Test 3**, we adopted a different buffer from another reference (86) (i.e., 1mM EDTA, 50mM AcOH, 0.57mM ascorbic acid, 1% EtOH (v/v)) instead of H<sub>3</sub>PO<sub>4</sub> water (0.1%, v/v) to enhance the separation between the UV impurity and [<sup>18</sup>F]FDOPA. However, the UV baseline was not flat due to the sensitive absorbance of ascorbic acid under this wavelength (282 nm), adversely impacting the determination of timing for product collection.

Subsequently, in **Test 4**, we replaced the mobile phase with PBS buffer (100 mM) with 0.1% EtOH (v/v) under pH = 5. Encouragingly, no UV impurity overlapped with [<sup>18</sup>F]FDOPA, but

a radioactive impurity was eluted close to [<sup>18</sup>F]FDOPA. Attempting to ensure complete separation, we removed EtOH from the mobile phase in **Test 5**. However, the retention-time difference exhibited only a slight increase from 0.4 min to 0.5 min, not enough to observe if there was any overlap of two peaks.

Given that the acid solution resulted in better separation of [<sup>18</sup>F]FDOPA and the radioactive impurity in previous **Tests 1-3** (with more substantial retention-time differences), we slightly decreased the pH of PBS buffer to ~4 by adding 0.04% AcOH (v/v) in **Test 6**. To our delight, a complete separation of [<sup>18</sup>F]FDOPA and the radioactive impurity was achieved, with the retention-time difference increasing to 1.2 min. As a result, the radio-HPLC conditions from **Test 6** were selected as the optimal purification method for [<sup>18</sup>F]FDOPA synthesis, eliminating the need for the formulation step following HPLC purification.

## 2.4 Conclusions

In this work, we employed a novel droplet-based high-throughput technique to perform a comprehensive optimization of the Cu-mediated radiosynthesis for the well-known clinical PET tracer [<sup>18</sup>F]FDOPA by systematically varying parameters such as PTC type and amount, base type, solvent type, additive type, amount of precursor, amount of copper reagent, concentration of deprotection solution, and reaction temperatures and times. The optimized synthesis achieved a remarkable RCY of up to  $50 \pm 3\%$  ( $n = 5$ ) within a rapid 25 min process, demonstrating a substantial improvement over the initially reported macroscale synthesis condition (with RCY of 10-12%,  $n = 26$ ) that required 110 min. Moreover, the optimized method exhibited excellent radiochemical purity (>99%) and enantiomeric purity (100%). Furthermore, this rapid and efficient preparation approach significantly enhanced the activity yield to  $41 \pm 4\%$  ( $n = 5$ ), ~7x higher compared to the conventional method. To assess the feasibility of implementing this microscale method in clinical practice, ongoing investigations involve scaling up production and then establishing performing synthesis validation in a cGMP environment. These studies were carried

out using a custom automated miniature synthesis system, showing promising potential to deliver [<sup>18</sup>F]FDOPA for patients on demand in short time and low cost.

## 2.5 Appendix

### 2.5.1 Optimization of fluorination reaction

#### 2.5.1.1 Study of activity loss in “blank” experiments

**Table 2-3 Summary of activity distribution after blank experiments (no precursor).**

Entry <sup>a</sup>	PTC	Collection efficiency (%)	Residual activity on chip (%)	Residual activity on pipette tip (%)	Volatile loss (%)
1	TEAHCO <sub>3</sub>	87 ± 3	1	2 ± 1	10
2	TBAOTf	82 ± 2	4	3 ± 1	11
3	TEAOTf	85 ± 2	1	2 ± 1	12
4 <sup>b</sup>	TEAOTf	30 ± 3	11	2 ± 0	57

<sup>a</sup>Blank reactions were conducted with only PTC (720 nmol) and base (Cs<sub>2</sub>CO<sub>3</sub>, 10 nmol) in 10 μL of DMF and Py (96:4, v/v), i.e., no Cu(Py)<sub>4</sub>(OTf)<sub>2</sub> or precursor. <sup>b</sup>This reaction also included Cu(Py)<sub>4</sub>(OTf)<sub>2</sub> (750 nmol).

#### 2.5.1.2 Initial screening of fluorination conditions

**Table 2-4** was the identical data as **Table 1**, except with extra data regarding to activity loss during fluorination reaction.

**Table 2-4 Summary of performance during initial screening fluorination conditions.**

Entry <sup>a</sup>	PTC	Base	Solvent <sup>b</sup>	Fluorination conversion (%)	Collection efficiency (%)	Residual activity on chip (%)	Residual activity on pipette tip (%)	Volatile loss (%)	Crude fluorination yield (%)
1 <sup>c</sup>	TEAHCO <sub>3</sub>	None	2:1 DMA/nBuOH <sup>c</sup>	Trace	47 ± 1	13	4 ± 0	36	Trace
2	TBAOTf	K <sub>2</sub> CO <sub>3</sub>	96:4 DMF/Py	29 ± 2	59 ± 2	16	2 ± 0	23	16 ± 1
3	TBAOTf	None	96:4 DMF/Py	26 ± 2	8 ± 0	5	3 ± 0	84	2 ± 0
4	TBAOTf	K <sub>2</sub> CO <sub>3</sub>	96:4 DMSO/Py	1 ± 0	71 ± 3	12	1 ± 0	16	1 ± 0
5	TBAOTf	K <sub>2</sub> CO <sub>3</sub>	Py	12 ± 0	60 ± 4	13	3 ± 0	24	7 ± 0
6	TBAOTf	Cs <sub>2</sub> CO <sub>3</sub>	96:4 DMA/Py	37 ± 4	66 ± 6	9	2 ± 1	23	25 ± 5
7	TEAOTf	Cs <sub>2</sub> CO <sub>3</sub>	96:4 DMA/Py	60 ± 4	71 ± 2	3	2 ± 0	24	43 ± 2
8	TEAOTf	Cs <sub>2</sub> CO <sub>3</sub>	96:4 DMF/Py	70 ± 2	65 ± 2	5	3 ± 0	28	45 ± 2
9	TEAOTf	Cs <sub>2</sub> CO <sub>3</sub>	DMF	18 ± 3	48 ± 3	5	2 ± 0	45	8 ± 1
10	TEAOTf	Cs <sub>2</sub> CO <sub>3</sub>	DMF/DMAP <sup>d</sup>	9 ± 0	85 ± 1	2	2 ± 1	11	8 ± 0

<sup>a</sup>Each radiosynthesis was carried out by first loading [<sup>18</sup>F]fluoride mixed with PTC (720 nmol) and base (10 nmol), and drying at 105 °C for 1 min. Radiofluorination was performed by adding 0.1 mg (150 nmol) precursor and 750 nmol of Cu(py)<sub>4</sub>(OTf)<sub>2</sub> in 10 μL of solvent heated at 110 °C for 5 min. Each condition was repeated for 4 times. <sup>b</sup>All solvent mixtures are v/v. <sup>c</sup>Reaction was conducted with less PTC (0.12 μmol) and Cu(py)<sub>4</sub>(OTf)<sub>2</sub> (0.15 μmol) in 10 μL of DMA/nBuOH (2:1, v/v). <sup>d</sup>4.8 μmol of DMAP was added in 10 μL of solvent.



### 2.5.1.3 Optimization of phase transfer catalyst (PTC) amount

**Table 2-5 Influence of varying PTC amount in the fluorination step.**

PTC amount (nmol) <sup>a</sup>	Fluorination conversion (%)	Collection efficiency (%)	Residual activity on chip (%)	Residual activity on pipette tip (%)	Volatile loss (%)	Crude fluorination yield (%)
75	73 ± 3	56 ± 5	6	1 ± 1	37	41 ± 5
150	72 ± 1	55 ± 8	8	1 ± 1	36	39 ± 6
300	70 ± 2	70 ± 2	9	2.6 ± 0.2	19	49 ± 2
450	67 ± 1	64 ± 5	7	2.0 ± 0.1	27	43 ± 3
600	76 ± 1	65 ± 2	8	1.3 ± 0.1	26	49 ± 2
720	65 ± 4	68 ± 1	8	0.7 ± 0.1	24	44 ± 3
900	72 ± 2	66 ± 4	7	1.2 ± 0.1	26	48 ± 4
1050	55 ± 6	57 ± 4	7	1.2 ± 0.1	35	31 ± 3

<sup>a</sup>The radiosynthesis (n = 4) was carried out with TEAOTf (varied amounts), Cs<sub>2</sub>CO<sub>3</sub> (10 nmol), precursor (0.1 mg, 150 nmol) and Cu(Py)<sub>4</sub>(OTf)<sub>2</sub> (680 nmol) in 10 μL of DMF/Py (96:4, v/v), heating at 110 °C for 5 min.

### 2.5.1.4 Optimization of copper reagent amount

**Table 2-6 Impact of copper reagent amount in the fluorination step.**

Cu(Py) <sub>4</sub> (OTf) <sub>2</sub> amount (nmol) <sup>a</sup>	Fluorination conversion (%)	Collection efficiency (%)	Residual activity on chip (%)	Residual activity on pipette tip (%)	Volatile loss (%)	Crude fluorination yield (%)
450	53 ± 3	42 ± 5	5	1.9 ± 0.4	51	22 ± 3
600	61 ± 6	61 ± 2	5	1.7 ± 0.4	32	37 ± 3
680	68 ± 4	67 ± 1	5	1.7 ± 0.1	26	46 ± 3
750	68 ± 3	63 ± 6	7	2.1 ± 0.1	28	42 ± 3
900	64 ± 6	68 ± 2	5	2.7 ± 0.1	24	44 ± 5

<sup>a</sup>The radiosynthesis (n = 4) was carried out with TEAOTf (300 nmol), Cs<sub>2</sub>CO<sub>3</sub> (10 nmol), precursor (0.1 mg, 150 nmol) and Cu(Py)<sub>4</sub>(OTf)<sub>2</sub> (varied amounts) in 10 μL of DMF/Py (96:4, v/v) heating at 110 °C for 5 min.

### 2.5.1.5 Optimization of fluorination temperature

**Table 2-7 Influence of varying reaction temperature in the fluorination step.**

Fluorination temperature (°C) <sup>a</sup>	Fluorination conversion (%)	Collection efficiency (%)	Residual activity on chip (%)	Residual activity on pipette tip (%)	Volatile loss (%)	Crude fluorination yield (%)
90	36 ± 3	78 ± 2	5	2.0 ± 0.3	15	28 ± 2
100	58 ± 7	67 ± 4	5	2 ± 1	26	39 ± 3
105	55 ± 5	69 ± 4	5	2 ± 1	24	38 ± 5
110	65 ± 3	67 ± 4	5	2 ± 1	26	44 ± 4
115	66 ± 3	59 ± 5	8	2.3 ± 0.3	32	39 ± 4
120	3 ± 2	12 ± 4	5	2.1 ± 0.1	81	0.4 ± 0.1

<sup>a</sup>The radiosynthesis (n = 4) was carried out with TEAOTf (300 nmol), Cs<sub>2</sub>CO<sub>3</sub> (10 nmol), precursor (0.1 mg, 150 nmol) and Cu(Py)<sub>4</sub>(OTf)<sub>2</sub> (680 nmol) in 10 μL of DMF/Py (96:4, v/v) heating at for varied temperatures for 5 min.

### 2.5.1.6 Optimization of fluorination time

**Table 2-8 Influence of reaction time in the fluorination step.**

Fluorination time (min) <sup>a</sup>	Fluorination conversion (%)	Collection efficiency (%)	Residual activity on chip (%)	Residual activity on pipette tip (%)	Volatile loss (%)	Crude fluorination yield (%)
3	57 ± 4	71 ± 3	6	2.1 ± 0.1	21	41 ± 3
5	65 ± 3	67 ± 4	5	2 ± 1	26	44 ± 4
7	72 ± 4	57 ± 10	5	2.7 ± 0.1	35	41 ± 8

<sup>a</sup>The radiosynthesis (n = 4) was carried out with TEAOTf (300 nmol), Cs<sub>2</sub>CO<sub>3</sub> (10 nmol), precursor (0.1 mg, 150 nmol) and Cu(Py)<sub>4</sub>(OTf)<sub>2</sub> (680 nmol) in 10 μL of DMF/Py (96:4, v/v) heating at 110 °C for varied reaction times.

### 2.5.1.7 Optimization of precursor amount

**Table 2-9 Influence of precursor amount in the fluorination step.**

Precursor amount (mg) <sup>a</sup>	Precursor amount (nmol)	Fluorination conversion (%)	Collection efficiency (%)	Residual activity on chip (%)	Residual activity on pipette tip (%)	Volatile loss (%)	Crude fluorination yield (%)
0.05	75	63 ± 2	66 ± 3	6	0.7 ± 0.3	27	42 ± 3
0.1	150	70 ± 2	70 ± 2	9	2.6 ± 0.2	19	49 ± 2
0.2	300	76 ± 4	66 ± 4	7	0.9 ± 0.4	26	51 ± 5
0.3	450	87 ± 3	70 ± 2	7	1 ± 1	22	60 ± 3
0.4	600	84 ± 1	69 ± 3	7	0.8 ± 0.1	23	58 ± 4

<sup>a</sup>The radiosynthesis (n = 4) was carried out with TEAOTf (300 nmol), Cs<sub>2</sub>CO<sub>3</sub> (10 nmol), precursor (varied amounts) and Cu(Py)<sub>4</sub>(OTf)<sub>2</sub> (680 nmol) in 10 μL of DMF/Py (96:4, v/v) heating at 110 °C for 5 min.

## 2.5.2 Optimization of deprotection reaction

### 2.5.2.1 Influence of deprotection time

**Table 2-10 Influence of reaction time in the deprotection step.**

Deprotection time (min) <sup>a</sup>	Number of repeats (n)	Deprotection yield (%)
0.5	2	96 ± 1
1	2	96 ± 1
1.5	2	94 ± 1
2	2	97 ± 0
4	2	96 ± 2
6	2	94 ± 0
8	2	95 ± 0
10	6	97 ± 1

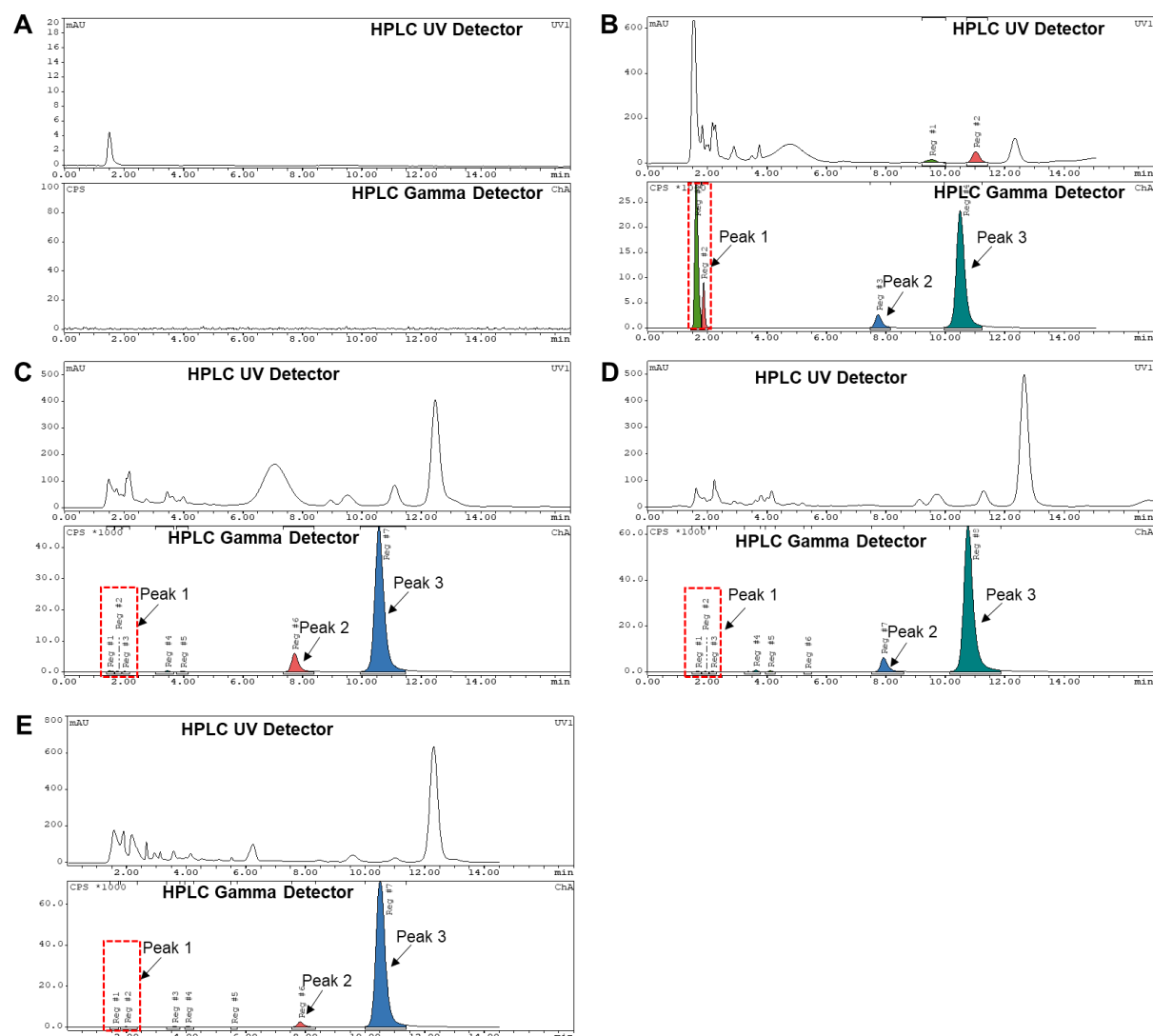
<sup>a</sup>The radiosynthesis was carried out with TEAOTf (300 nmol), Cs<sub>2</sub>CO<sub>3</sub> (10 nmol), precursor (450 nmol) and Cu(Py)<sub>4</sub>(OTf)<sub>2</sub> (680 nmol) in 10 μL of DMF/Py (96:4, v/v) heating at 110 °C for 5 min for fluorination, followed by addition of 15 μL of mixture of 0.25 M ascorbic acid and 12 N HCl (1:3, v/v) and reaction at 100 °C for varied times to perform the deprotection step.

### 2.5.2.2 Influence of deprotectant concentration

**Table 2-11 Influence of HCl concentration in the deprotection step.**

HCl concentration (N) <sup>a</sup>	Number of repeats (n)	Deprotection yield (%)
1.5	2	54 ± 9
3	4	91 ± 4
6	4	93 ± 2
12	6	98 ± 1

<sup>a</sup>The radiosynthesis was carried out with TEAOTf (300 nmol), Cs<sub>2</sub>CO<sub>3</sub> (10 nmol), precursor (450 nmol) and Cu(Py)<sub>4</sub>(OTf)<sub>2</sub> (680 nmol) in 10 μL of DMF/Py (96:4, v/v) heating at 110 °C for 5 min for fluorination, followed by addition of 15 μL of mixture of 0.25 M ascorbic acid and HCl (with varied concentration) (1:3, v/v) and reaction at 100 °C for 2 min to perform the deprotection step.

**Figure 2-5 Examples of radio-HPLC chromatograms for deprotection optimization.**

(A) 80 μCi of [<sup>18</sup>F]F<sup>-</sup> in 80 μL of mobile phase. (B-E) Crude product after deprotection with 0.25 M ascorbic acid and different concentrations of HCl (1:3, v/v) at 100 °C for 2 min. (B) 1.5N HCl; (C): 3N HCl; (D) 6N HCl; (E) 12N HCl. Peak 1 was radiofluorinated intermediate, Peak 2 was partial

deprotected [ $^{18}\text{F}$ ]FDOPA and Peak 3 was [ $^{18}\text{F}$ ]FDOPA. All samples were analyzed on a normal-phase analytical column (Luna  $\text{NH}_2$  column, 5  $\mu\text{m}$ , 250  $\times$  4.6 mm) with initial purification protocol.

### 2.5.3 Automation of the droplet radiosynthesis

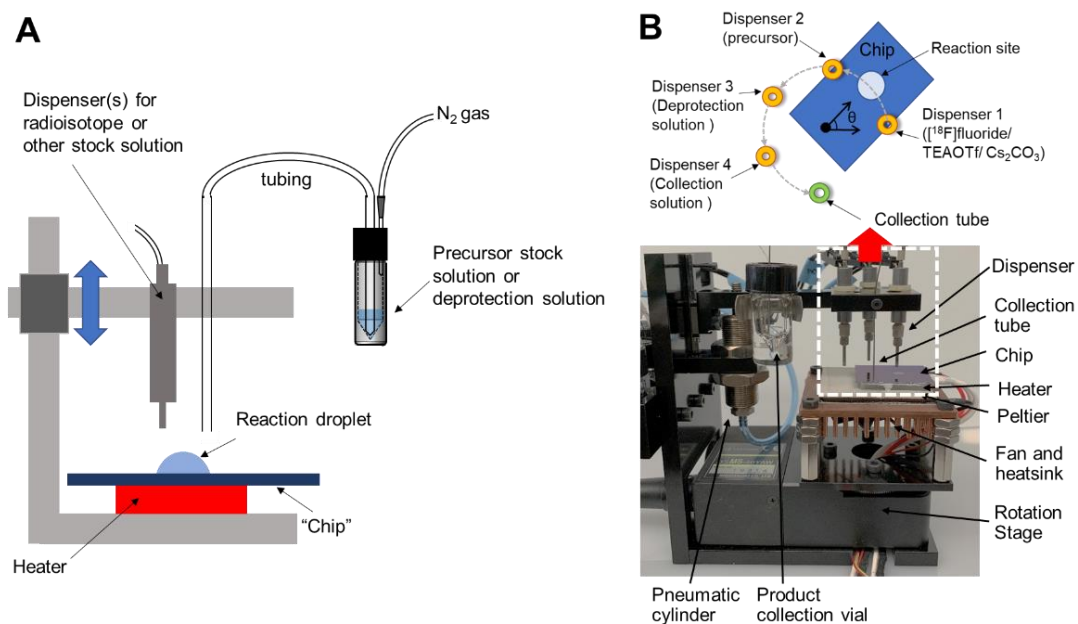


**Figure 2-6 Automated microdroplet radiosynthesizer set up for [ $^{18}\text{F}$ ]FDOPA synthesis.**

(A) Diagram of “One-shot” tubing system for remote delivery of precursor stock solution or deprotection solution, and piezoelectric dispensers for radioisotope or other stock solution. (B) Configuration of automated microdroplet system for preparing [ $^{18}\text{F}$ ]FDOPA. (Top) Top view showing positions of reagent dispensers and collection tubing above the chip. (Bottom) Photograph of the automated droplet synthesizer.

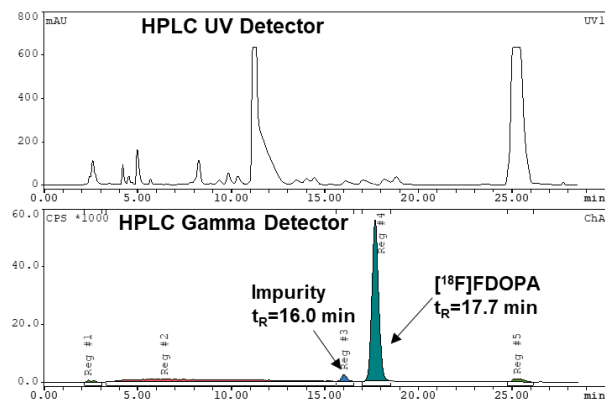
### 2.5.4 Optimization of radio-HPLC purification method

**Table 2-12 Summary of results of radio-HPLC purification optimization on an analytical Synergi™ Hydro-RP column.**

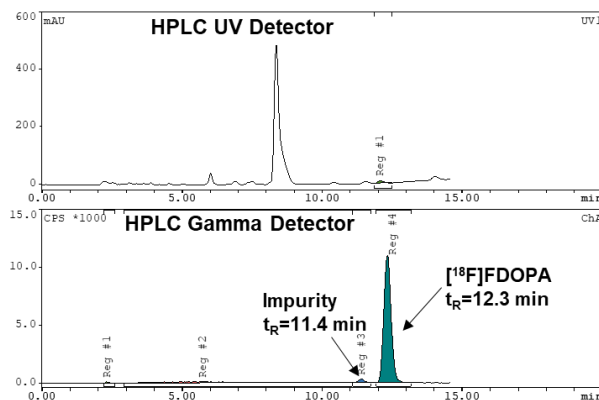
Test <sup>a</sup>	Mobile phase	Retention time of [ $^{18}\text{F}$ ]FDOPA (min)	Volume of collected product (mL)
1	100% $\text{H}_3\text{PO}_4$ water (0.1%, v/v), pH=2	17.7	1
2	1% EtOH (v/v) in $\text{H}_3\text{PO}_4$ (0.1%, v/v) water, pH=2	12.3	0.6
3	1mM EDTA, 50mM AcOH, 0.57mM ascorbic acid, 1% EtOH (v/v)	9.4	0.5
4	1% EtOH (v/v) in PBS buffer (100 mM), pH=5	6.8	0.45
5	100% PBS buffer (100 mM), pH=5	9.7	0.55
6	100% PBS buffer (100 mM), 0.04% AcOH (v/v), pH=4	11.1	0.6

<sup>a</sup>The purification was performed at the flow rate of 1 mL/min under wavelength of 282 nm

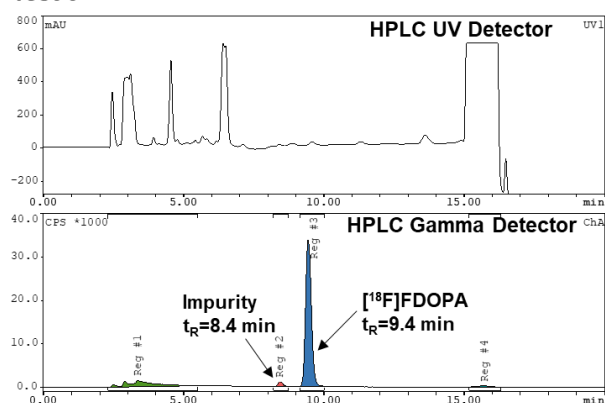
Test 1



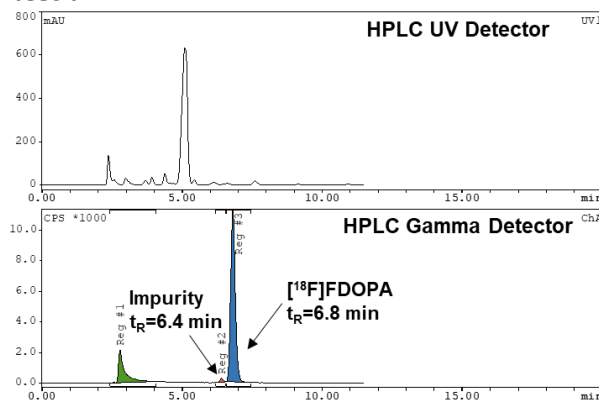
Test 2



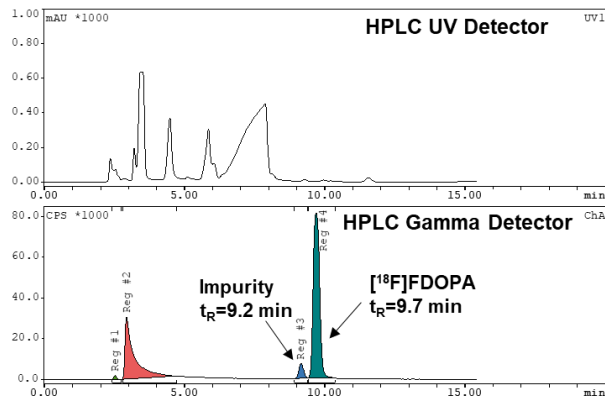
Test 3



Test 4



Test 5



Test 6

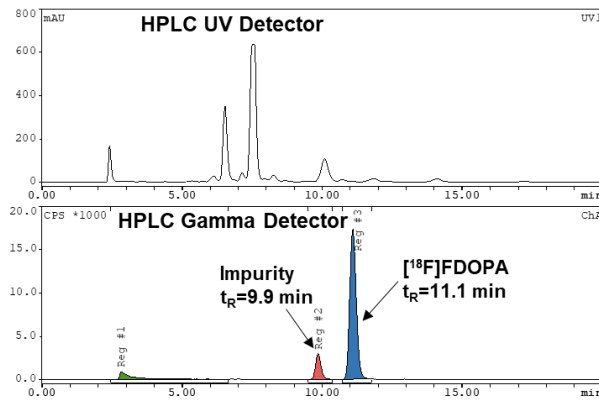


Figure 2-7 Examples of radio-HPLC chromatograms of crude [<sup>18</sup>F]FDOPA using different HPLC methods.

Descriptions of conditions (Test #X) are found in corresponding entries of Table S10.

### 2.5.5 Calibration curve to determine molar activity

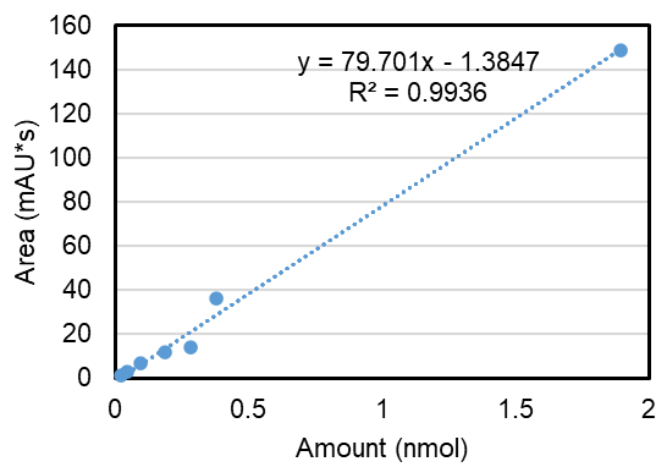


Figure 2-8 Calibration curve of FDOPA reference standard (282 nm wavelength).

## Chapter 3: Proof-of-concept [ $^{18}\text{F}$ ]AlF labeling in droplet reactions

### 3.1 Introduction

The [ $^{18}\text{F}$ ]AlF method has recently become a popular and well implemented radiolabeling procedure of labelling clinical radiopharmaceuticals and preclinical candidates (138). Being a 'pseudo-radiometal' procedure, it combines cyclotron produced F-18 with the convenience of metal chelation radiochemistry. The preparation and use of the [ $^{18}\text{F}$ ]AlF complex was first described in 2009 by *McBride et al* to radiolabel proteins (139,140). Prior to the development of this method, proteins were radiolabeled in a multi-step, time intensive process involving the labelling of a prosthetic group, (e.g., [ $^{18}\text{F}$ ]SFB) and further conjugation to the protein (141).

The method is based on the formation of a strong aluminum-fluoride bond (670 kJ/mol) and the complexation of the [ $^{18}\text{F}$ ]AlF $^{2+}$  ion by common chelators such as NOTA to form a [ $^{18}\text{F}$ ]AlF-chelate-peptide complex (139). Importantly, the formation of [ $^{18}\text{F}$ ]AlF $^{2+}$  is achieved at mild conditions (e.g. at room temperature and in aqueous solution) and does not require F-18 drying. Radiolabeling at room temperature overcomes issues of protein tertiary structures denaturing. The [ $^{18}\text{F}$ ]AlF complex is heavily pH dependent, with the optimum pH ranging between 4 and 5. The more acidic the pH (<4), the formation of [ $^{18}\text{F}$ ]HF is favored, whilst more basic conditions leads to the insoluble precipitate of aluminum hydroxide (AlOH $_3$ ) forming (142,143). Aluminum normally forms octahedral complexes, but the [ $^{18}\text{F}$ ]AlF $^{2+}$  complex requires pentadentate ligands, due to the fluoride already occupying a site in the complex. The chelator complex is stable in radiopharmaceutical formulations and at high temperatures and in physiological conditions, making it an effective radiolabeling procedure. Low doses of the aluminium-fluoride complex are compatible *in vivo*, allowing for its efficient use in molecular imaging.

Multiple examples of [ $^{18}\text{F}$ ]AlF radiopharmaceuticals, ranging from small molecules to peptides, nanobodies and affibodies are present in the literature, as shown in **Table 3-1**. The

most common chelators are the pentadentate, cyclic NOTA and NODA chelators, due to commercial availability and affordability.

**Table 3-1 Examples of [<sup>18</sup>F]AIF radiopharmaceuticals.**

Target	Agent	Use	Reference
SSTR	[ <sup>18</sup> F]AIF-NOTA-octreotide	Pre/Clinical	Tshibangu T. et al., EJNMMI 2020, 5, 1-23
Integrins receptors	[ <sup>18</sup> F]AIF-RGD <sub>2</sub>	Preclinical	Liu S. et al., EJNMMI 2011, 38, 1732
	[ <sup>18</sup> F]Alfatide I	Clinical	Wan W. et al., J. Nucl. Med., 2013, 54, 691
	[ <sup>18</sup> F]Alfatide II	Clinical	Mi B. et al., Theranostics, 2015, 5, 1115
PSMA	[ <sup>18</sup> F]AIF-PSMA-11	Preclinical	Malik N. et al., Mol. Imaging Biol, 2015, 17, 777
	[ <sup>18</sup> F]AIF-PSMA-BCH	Pre/Clinical	Liu T. et al., J. Nucl. Med., 2019, 60, 1284
Gastrin-releasing peptide receptor (GRPR)	[ <sup>18</sup> F]AIF-BBN	Preclinical	Dijkgraaf I. et al., J. Nucl. Med., 2012, 53, 947
	[ <sup>18</sup> F]AIF-NOTA-PEG2-RM26	Preclinical	Varasteh Z. et al., PLoSOne, 2013, 8, e81932
	[ <sup>18</sup> F]AIF-JNV5132	Preclinical	Chatalic K.L.S. et al., J. Nucl. Med., 2014, 55, 2050
HER2	[ <sup>18</sup> F]AIF-NOTA-Z <sub>HER2:2395</sub>	Preclinical	Heskamp S. et al., J. Nucl. Med., 2012, 53, 146
	[ <sup>18</sup> F]AIF-NOTA-Z <sub>HER2:342</sub>	Preclinical	Xu Y. et al., J. Cancer, 2017, 8, 1170
	[ <sup>18</sup> F]AIF-NOTA-sdAb2Rs15d	Preclinical	Zhou Z. et al., Bioconjug. Chem, 2018, 29, 4090
EGFR	[ <sup>18</sup> F]AIF-NOTA-Z <sub>HER2:2395</sub>	Preclinical	Su X. et al., Mol. Pharm, 2014 11, 3947
HER3	[ <sup>18</sup> F]AIF-Z <sub>HER3:8698</sub>	Preclinical	Da Pieve C. et al., Bioconjug. Chem., 2016, 27, 1839
PD-L1	[ <sup>18</sup> F]AIF-NOTA-Z <sub>PD-L1</sub>	Preclinical	Gonzalez Trotter D.E., et al., J. Nucl. Med., 2017, 58, 1852 Sharma G. et al., Cancers, 2023, 15, 3131
Apoptosis	[ <sup>18</sup> F]AIF-NOTA-MAL-Cys-Annexin V	Preclinical	Lu C. et al., Oncotarget, 2017, 8, 51086
Integrins receptors	[ <sup>18</sup> F]AIF-NODA-IA	Preclinical	Wang W. et al., Bioconjug. Chem., 2015, 26, 24
Amyloid β	[ <sup>18</sup> F]AIF-NODA-Benzothiazole	Preclinical	Song J. et al., ACS Omega, 2018, 3, 13089
Folate receptor	[ <sup>18</sup> F]AIF-NOTA-Folate	Preclinical	Sivola J.M.U. et al., Sci. Rep., 2018, 8, 9720
	[ <sup>18</sup> F]AIF-NOTA-PEG <sub>12</sub> -Folate	Preclinical	Chen Q. et al., Mol. Pharm., 2017, 14, 4353
FAP	[ <sup>18</sup> F]AIF-FAPI-74	Clinical	Giesel F.L., et al., J. Nucl. Med., 2021, 62, 201
	[ <sup>18</sup> F]AIF-FAPI-04	Clinical	Jiang X. et al., Front. Oncol., 2021, 11, 649148

The potential for [<sup>18</sup>F]AIF to replace existing Ga-68 radiometal chemistry to address limitations of short half-life and limited batch size due to generator capacity has been recently explored (144). An example includes the development of [<sup>18</sup>F]AIF-NOTA-octreotide, as an alternative to the [<sup>68</sup>Ga]Ga-DOTA-TATE/ DOTA-TOC agent imaging the somatostatin receptor type 2 (SSTR2) in patients with neuroendocrine tumors (NETs) (145). The NETTER-1 trial has also been successful in showing patient stratification using PET to receive [<sup>177</sup>Lu]Lu-DOTA-TATE



peptide receptor radionuclide therapy (PRRT) (146). Clinical comparisons of [<sup>68</sup>Ga]Ga-DOTA-TATE and [<sup>18</sup>F]AlF-NOTA-octreotide in patients with metastatic rectal NETs showed both produced similar results, with improved contrast in multiple smaller tumor lesions and no significant difference in organ uptake (147). Additionally, even with similar image quality, the F-18 analogue showed lower liver uptake with improved lesion detection, hence highlighting the potential for F-18 analogues to serve as an alternative to already successful Ga-68 agents (148). Other examples include the development of [<sup>18</sup>F]AlF-PSMA-11, as a derivative of the FDA approved [<sup>68</sup>Ga]Ga-PSMA-11 for the imaging of PSMA positive lesions in patients with prostate cancer (149). Uptake in tumor was higher for the F-18 agent, whilst the bone uptake was higher and renal uptake lower compared to Ga-68. Even with PSMA-11 bearing a HBED chelator, (with unfavorable configuration for chelating the [<sup>18</sup>F]AlF complex), the stability in the final formulated dose was confirmed up till 4 h, conforming to European Pharmacopeia guidelines (150). The lower mean effective dose of [<sup>18</sup>F]AlF-PSMA-11 (12.8 μSv/MBq) compared to [<sup>68</sup>Ga]Ga-PSMA-11 (220 μSv/MBq) and similar clinically relevant diagnostic value, shows the promise of the F-18 agent (151,152). The chelator selection is important to allow translation from Ga-68 to F-18 with use of the NOTA chelator preferred and encouraged. The theragnostic pair of Ga-68/ Lu-177 therefore has the potential to be supplemented with the versatile pair F-18/Lu-177 (153–155). The possibilities of newer [<sup>18</sup>F]AlF radiopharmaceuticals are endless with great scope for optimization and development.

The aluminum fluoride radiolabeling methodology has been implemented with manual preparation processes (156) and on automated radiosynthesis (157–159) with the aim to produce [<sup>18</sup>F]AlF radiopharmaceuticals for the GMP clinical use. Generally, overall preparation time depends on the final product purification requirements but is usually under an hour for both the manual and the automated preparation. Kit based, one-step lyophilized methods to manually provide F-18 labelled peptides have been developed with optimized pH conditions and final

formulations. The automation of various tracers has since been completed with some examples in **Table 3-2**.

**Table 3-2 automation example of [<sup>18</sup>F]AIF-labeled tracers.**

Agent	Automation method	Result
[ <sup>18</sup> F]AIF-NOTA-octreotide	GE TRACERLab™ Trasis AllInOne™	56.2 ± 4.2% RCY, A <sub>M</sub> 12.7 ± 0.14 GBq/μmol 26.1 ± 3.6% RCY, A <sub>M</sub> 160.5 ± 75.3 GBq/μmol, 40 mins EOS
[ <sup>18</sup> F]AIF-PSMA-11	GE TRACERLab™ SyntheraFCHOL™	18 ± 3% RCY, RCP > 95% 21 ± 3% RCY, RCP > 95%
[ <sup>18</sup> F]AIF-FAPI-74 [ <sup>18</sup> F]AIF-FAPI-04	CFN-MPS200 Trasis AllInOne™	37 ± 4% RCY, RCP > 97% 26.4 ± 1.5% RCY

Although automated methods are crucial and have been successful, they require facilities with large overhead costs. Not to mention the optimization and development of new [<sup>18</sup>F]AIF agents will require extensive work, which can be cumbersome to complete on large automated systems; not built for small scale, high throughput reactions. Typically, radiosynthesisers work with reaction volumes in the 1-5 mL range, and precursor amounts are in the 1-10 mg range per reaction. Since the operators must wait for the radioactivity in the hot cell to decay between consecutive syntheses (even with cassette based automated systems), only two to three preparations/ day can be carried out. Parallel radiosyntheses cannot be performed in the same hot cell with the same radiosynthesiser. The resulting running costs are acceptable for the preparation of radiopharmaceuticals (high quantity) for commercial purposes by specialized companies or centers but non-viable for development and optimization of novel precursors.

The advantages of droplet-based radiochemistry includes the ability to overcome some of these issues and simultaneously obtain high specific and molar activities. The high throughput screening of multiple compounds, rapid optimization of radiolabeling reaction conditions, and the possibility of using a benchtop platform for the manufacturing of clinical radiotracers in the future makes droplet-based microscale radiochemistry a promising approach.

The development of [ $^{18}\text{F}$ ]AIF methodology on microscale technology is novel and has never previously been successfully attempted on a droplet scale microchip before. The technology developed by van Dam et al. has been used to produce [ $^{18}\text{F}$ ]Fallypride, [ $^{18}\text{F}$ ]FET and [ $^{18}\text{F}$ ]FDOPA amongst other radiotracers (160–162). The improvement of yield, radiolabeling efficiency, molar activity, and purification processes were highlighted. This work will highlight the potential to complete the [ $^{18}\text{F}$ ]AIF methodology on a droplet scale using both a model small molecule and clinically relevant FAP targeting tracer FAPI-74.

## 3.2 Methods

### 3.2.1 Materials

Aluminum chloride hexahydrate ( $\text{AlCl}_3 \cdot 6\text{H}_2\text{O}$ , 99%), sodium acetate (NaOAc, >99%), glacial acetic acid (AcOH, >99%), sodium hydroxide solution (10 M, NaOH), sodium phosphate monobasic ( $\text{NaH}_2\text{PO}_4$ , >99%), trifluoroacetic acid (TFA, >99%), ethyl alcohol (EtOH, >99.5%), anhydrous dimethyl sulfoxide (DMSO, >99.9%), and anhydrous acetonitrile (MeCN, 99.8%) were purchased from Sigma-Aldrich (St. Louis, MO, USA). 0.9% NaCl (saline, USP) was obtained from Hospira (Lake Forest, IL, USA). The model precursor, tetrazine conjugated to 1,4,7-triazacyclononane-1,4-diacetic acid (NODA-Tz), was prepared as previously reported(157). The precursor for preparing [ $^{18}\text{F}$ ]AIF-FAPI-74 was obtained from SOFIE, Inc. (Dulles, VA, USA). Deionized (DI) water was obtained from a Milli-Q water purification system (EMD Millipore Corporation, Berlin, Germany). QMA plus light cartridges (130 mg sorbent) and Oasis HLB plus light cartridges (30 mg sorbent) were purchased from Waters Corporation (Milford, MA, USA). Eppendorf tubes (0.5 or 2.5 mL) were purchased from Eppendorf (Hamburg, Germany). 50 mL polypropylene centrifuge tubes were purchased from Corning Inc. (430304, Corning, NY, USA). The following stock solutions were prepared before each experiment: (i) 0.5M NaOAc (pH = 4), (ii) 10 mM  $\text{AlCl}_3$  in 0.5M NaOAc, (iii) 2 mM  $\text{AlCl}_3$  in 0.5M NaOAc, and (iv) collection solution comprising MeCN and DI water (7:3, v/v) with 0.1% TFA (v/v). [ $^{18}\text{F}$ ]fluoride in [ $^{18}\text{O}$ ]H $_2$ O was

obtained from the UCLA Crump Cyclotron and Radiochemistry Center. Prior to each set of experiments,  $[^{18}\text{F}]\text{F}^-$  was processed with a light QMA cartridge (preconditioned with 3 mL EtOH and 10 mL of DI water) and eluted with 0.6 mL of DI water and saline (5:2, v/v), or was used directly from the cyclotron and mixed with saline (5:2, v/v) to simulate the QMA process.

### 3.2.2 General microdroplet radiosynthesis

Optimization of droplet-based reactions was performed on Teflon-coated silicon chips featuring 3x3 arrays of hydrophilic reaction sites (**Figure 3-1**), each with a diameter of 4 mm. The chips were operated on a temperature-controlled heating platform, as previously described (160).

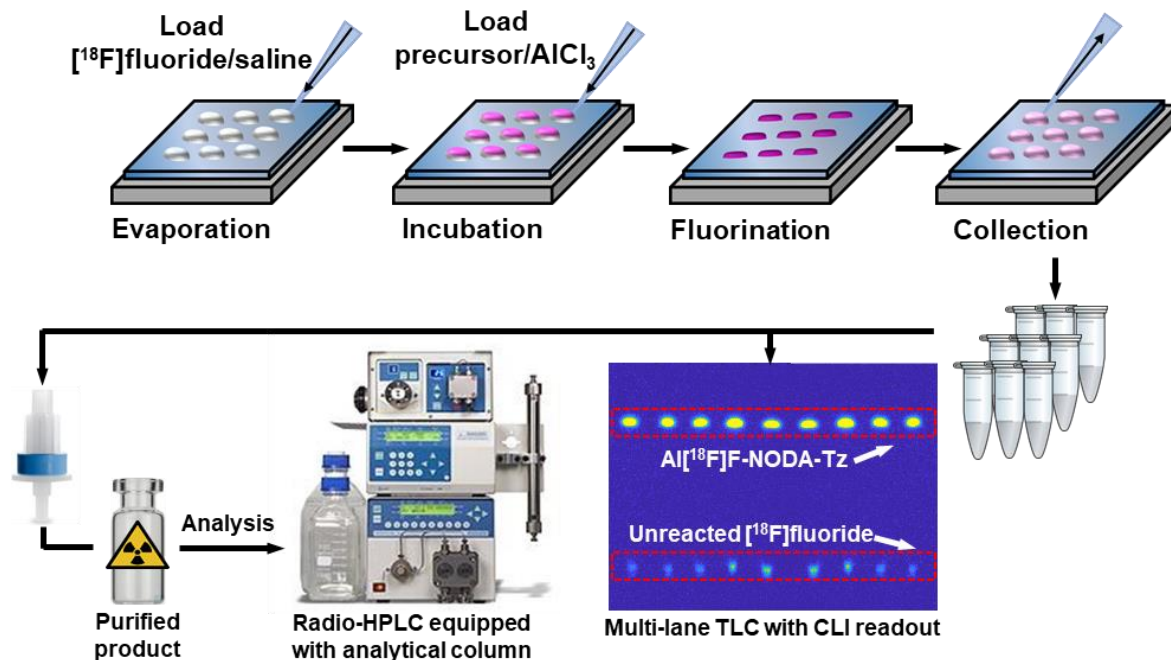


**Figure 3-1** Schematic of  $[^{18}\text{F}]\text{AlF}$  radiolabelling process flow in a droplet reactor.

The general droplet reaction procedure is shown in **Figure 3-1**, though several variations were explored in this work. Since  $[^{18}\text{F}]\text{AlF}$  labeling protocols often include a step where  $[^{18}\text{F}]\text{F}^-$  and  $\text{AlCl}_3$  are first incubated at room temperature (RT) prior to adding the precursor and heating, we compared the influence of (i) adding  $\text{AlCl}_3$  to the  $[^{18}\text{F}]\text{F}^-/\text{saline}$  solution first and incubating for 1

min before adding the precursor, and (ii) adding both  $\text{AlCl}_3$  and precursor to the  $[^{18}\text{F}]\text{F}^-/\text{saline}$  solution, and incubating for 1 min at RT before reaction. The results of these tests showed no difference, and thus we opted for the simpler (latter) approach. In General protocol 1, the reagents were mixed off-chip and only the reaction was performed on chip. Specifically,  $[^{18}\text{F}]\text{F}^-/\text{saline}$  solution was premixed with  $\text{AlCl}_3$  and precursor, incubated at RT for 1 min, then added to the droplet reactor, where it was reacted at 95 °C for 5 min. In General protocol 2, designed to facilitate automation,  $[^{18}\text{F}]\text{F}^-/\text{saline}$  solution was first added to the droplet reactor, dried at 105 °C for ~1 min, and then  $\text{AlCl}_3$  and precursor were added in subsequent step. The resulting mixture was incubated at RT for 1 min and then heated at 95 °C for 5 min. For both protocols, following synthesis, the crude product was extracted from the reaction site by adding a collection solution (20  $\mu\text{L}$ ) and transferring it via micropipette to a 0.5 mL Eppendorf tube for further analysis. The collection step was repeated a total of 4 times to minimize activity residue on the chip.

For the synthesis of  $[^{18}\text{F}]\text{AIF-NODA-Tz}$ ,  $[^{18}\text{F}]\text{F}^-/\text{saline}$  solution (5:2, v/v; 5  $\mu\text{L}$ ; containing 39-73 MBq) was mixed with 10  $\mu\text{L}$  of a 2.8:7.2 v/v mixture of DMSO and 0.5 M NaOAc containing different amounts of  $\text{Al}_2\text{Cl}_3$  and precursor. The DMSO was needed for to ensure good solubility of the precursor. In some studies, DMSO was replaced by other solvents, while the volume ratio of solvent and buffer solution remained the same.

For the synthesis of  $[^{18}\text{F}]\text{AIF-FAPI-74}$ ,  $[^{18}\text{F}]\text{F}^-/\text{saline}$  solution (5:2, v/v; 5.5  $\mu\text{L}$ , containing 14-29 MBq) was mixed with 10  $\mu\text{L}$  of 7.5:2 v/v mixture of DMSO and 0.5 M NaOAc containing different amounts of  $\text{Al}_2\text{Cl}_3$  and precursor. In the study of DMSO impact, the ratio of DMSO and 0.5M NaOAc in the 10  $\mu\text{L}$  portion was varied. In the scale-up synthesis (Protocol 2), the dried  $[^{18}\text{F}]\text{F}^-/\text{saline}$  (280 MBq) was mixed with a 15  $\mu\text{L}$  droplet comprised of 5  $\mu\text{L}$  of DI water combined plus 10  $\mu\text{L}$  of the optimal ratio of DMSO: 0.5 M NaOAc and containing optimal amounts of  $\text{Al}_2\text{Cl}_3$  and precursor.

### 3.2.3 Analytical methods

Radioactivity measurements were conducted with a calibrated dose calibrator (CRC-25R, Capintec, Florham Park, NJ, USA). Fluorination conversion was assessed via multi-lane radio-thin layer chromatography (radio-TLC) methods (96). Briefly, samples (0.5  $\mu\text{L}$ ) were spotted on TLC plates (6 cm x 5 cm pieces cut from 20 cm x 5 cm sheets, silica gel 60 F<sub>254</sub>, Merck KGaA, Darmstadt, Germany). Plates were developed for a 4 cm distance using a mobile phase of MeCN and DI water (1:1, v/v) with 0.1% TFA (v/v), dried, and then covered with a glass microscope slide (75x50x1 mm<sup>3</sup>, Fisher Scientific, Hampton, NH, USA) and read out by Cerenkov luminescence imaging (CLI) with 5 min exposure time. Fluorination conversion of each sample (lane) was determined via ROI analysis as previously described (96). Collection efficiency was determined by dividing the activity of product mixture collected from the droplet reactor by the starting activity (corrected for decay). Crude radiochemical yield (RCY) was computed as the fluorination conversion multiplied by the collection efficiency. The isolated RCY was determined by performing purification on an HLB cartridge (preconditioned with 3 mL of EtOH and 10 mL of DI water) and eluting the product with 1 mL of EtOH. The activity yield was computed as the amount of purified product by the starting activity (not corrected for decay). The [<sup>18</sup>F]AIF-NODA-Tz reaction mixture and the purified [<sup>18</sup>F]AIF-NODA-Tz were analyzed on an analytical column (ZORBAX RP Eclipse Plus C18, 100 x 4.6 mm, 3.5  $\mu\text{m}$ , Agilent Technologies, Santa Clara, CA, USA), using an isocratic mobile phase of DI water and MeCN (70:30, v/v) with 0.1% TFA (v/v) at a flow rate of 1 mL/min under UV of 254 nm. The radio-HPLC system comprised a Smartline HPLC system (Knauer, Berlin, Germany) equipped with a degasser (Model 5050), pump (Model 1000), UV detector (Eckert & Ziegler, Berlin, Germany), gamma-radiation detector (BFC-4100, Bioscan, Inc., Poway, CA, USA), and counter (BFC-1000; Bioscan, Inc., Poway, CA, USA). Similarly, the [<sup>18</sup>F]AIF-FAPI-74 reaction mixture and the purified [<sup>18</sup>F]AIF-FAPI-74 were analyzed on the same radio-HPLC system, but a different mobile phase of 10 mM NaH<sub>2</sub>PO<sub>4</sub> (pH = 4.5-5) and MeCN (84:16, v/v) was used with a flow rate of 1 mL/min under UV of 240 nm. Co-injection of the purified [<sup>18</sup>F]AIF-FAPI-

74 and FAPI-74 (precursor) was performed to confirm product identity. The same analytical scale radio-HPLC system was employed to determine the molar activity of the purified [ $^{18}\text{F}$ ]AIF-FAPI-74, utilizing a linear calibration curve of FAPI-74.

### 3.3 Results and discussion

#### 3.3.1 Model substrate: [ $^{18}\text{F}$ ]AIF-NODA-Tz

As a proof-of-concept to implement the aluminium fluoride ( $^{18}\text{F}$ ]AIF) labeling in a droplet format, we utilized NODA-Tz as a model substrate and assessed its radiosynthesis performance under diverse reaction conditions. In the initial macroscale radiosynthesis of [ $^{18}\text{F}$ ]AIF-NODA-Tz conducted by Allott et al. (157), NODA-Tz (30-60 nmol) and  $\text{AlCl}_3$  (26-54 nmol) were reacted with non-purified [ $^{18}\text{F}$ ]fluoride (300-380  $\mu\text{L}$ ,  $\sim 1000$  MBq) in the presence of NaOAc buffer and MeCN at 105  $^\circ\text{C}$  for 15 min. To scale down the reaction in a droplet format, we started with a smaller precursor amount of 7.5 nmol and a corresponding reduced quantity of  $\text{AlCl}_3$  within a 15  $\mu\text{L}$  volume (2.8  $\mu\text{L}$  of DMSO, 7.2  $\mu\text{L}$  of 0.5 M NaOAc and 5  $\mu\text{L}$  of [ $^{18}\text{F}$ ]fluoride/saline) at a lower temperature (95  $^\circ\text{C}$ ) for 5 min, referencing our previous microscale adoption in a similar reagent scale (79,163). To simplify purification and QC, we replaced the toxic co-solvent MeCN with DMSO.

One of our initial investigations focused on the  $\text{AlCl}_3$ -to-precursor ratio (APR). Details of measurements and calculations can be found in **Figure 3-2B** and **Table 3-4**. In one set of experiments, we maintained a constant precursor amount (7.5 nmol), and varied APR from 0.4 to 4.0 by utilizing varying  $\text{AlCl}_3$  amount (ranging from 3 to 30 nmol). We observed a steep decrease in fluorination conversion from  $89 \pm 0\%$  ( $n = 2$ , for APR = 0.4) to  $20 \pm 0\%$  ( $n = 2$ , for APR = 4.0) with an increase in APR. Combined with a consistently high collection efficiency, this led to a steep reduction in crude RCY as APR was increased. The peak crude RCY ( $84 \pm 2\%$ ,  $n=2$ ) was achieved at APR = 0.8, using 6 nmol of  $\text{AlCl}_3$  and 7.5 nmol of precursor.

We then performed a study with fixed APR of 0.8, and varied the amount of precursor (and  $\text{AlCl}_3$ ). Detailed measurements and calculations can be found in **Figure 3-2C** and **Table 3-5**. Interestingly, the amount of precursor had only a slight impact on the various performance metrics of the reaction, with 30 nmol of precursor (and 24 nmol of  $\text{AlCl}_3$ ) yielding the highest overall crude RCY of  $89 \pm 2\%$  ( $n = 2$ ).

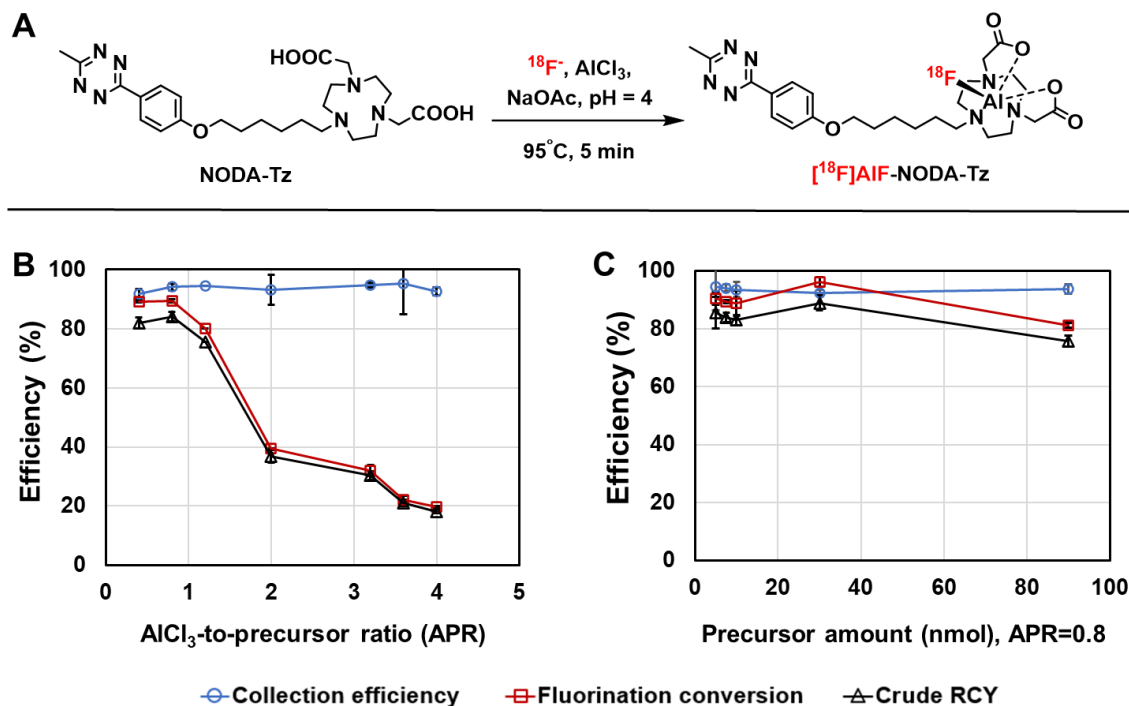


**Figure 3-2 Radiosynthesis optimization of  $[\text{18F}]\text{AIF-NODA-Tz}$  in a droplet reactor.**

(A)  $[\text{18F}]\text{AIF-NODA-Tz}$  synthesis scheme.  $[\text{18F}]\text{AIF-NODA-Tz}$  synthesis results showing impact ( $n = 2$  replicates each condition) of using varying  $\text{AlCl}_3$ -to-precursor ratio (APR) with fixed precursor amount (7.5 nmol) (B), or constant APR (fixed at 0.8) with varying precursor amount (C). Reactions were performed at  $95^\circ\text{C}$  for 5 min.

We then investigated the influence of reaction solvent and time. Detailed measurements and calculations can be found in **Table 3-6**. With the optimal APR of 0.8 and precursor amount of 30 nmol, we also compared whether the reaction worked with the originally reported solvent (MeCN) (139,157). The resulting performance exhibited a significant decrease in fluorination conversion (14%,  $n = 1$ ) and a poor crude RCY (13%,  $n = 1$ ), highlighting the substantial impact of the solvent on the reaction. Interestingly, the synthesis results closely align with Allott et al.'s



prior macroscale study using an identical precursor amount (30 nmol) and a similar APR (0.87) (fluorination conversion:  $14.8 \pm 1.6\%$ ,  $n = 3$ ; isolated RCY:  $12.7 \pm 1.3\%$ ,  $n = 3$ ). Notably, in contrast to the synthesis in DMSO, a slight increase in APR from 0.8 to 1 contributed to a 2.5x higher fluorination conversion (36%,  $n = 1$ ), resulting in a higher crude RCY of 34% ( $n = 1$ ). This suggests that APR may require re-optimization in a different solvent system. In a brief reaction time study, with APR of 0.8 in MeCN, only 5% ( $n = 1$ ) of fluorination conversion was achieved in 3 min, notably lower than that in a 5 min-reaction with 14% ( $n = 1$ ). This suggests that a longer reaction time is necessary for optimal performance.

In summary, the optimal radiosynthesis of [ $^{18}\text{F}$ ]AIF-NODA-Tz involved using 5  $\mu\text{L}$  of [ $^{18}\text{F}$ ]fluoride/saline (5:2, v/v) in combination with 30 nmol of NODA-Tz and 24 nmol of  $\text{AlCl}_3$  (i.e., APR = 0.8), in the presence of 2.8  $\mu\text{L}$  of DMSO and 7.2  $\mu\text{L}$  of 0.5 M NaOAc at 95 °C for 5 min. This achieved high fluorination conversion ( $96 \pm 2\%$ ,  $n = 2$ ) and collection efficiency ( $92 \pm 1\%$ ,  $n = 2$ ) at the end of the reaction, resulting in a crude RCY of  $89 \pm 2\%$  ( $n = 2$ ). For purification (see **Table 3-7**), the collected reaction mixture was further diluted with 1 mL of DI water and loaded onto an HLB cartridge (preconditioned with 3 mL of EtOH and 6 mL of DI water), followed by washing with an additional 10 mL of DI water to remove unreacted [ $^{18}\text{F}$ ]fluoride. Of the collected crude reaction mixture, 79% ( $n = 1$ ) of the activity was trapped on the cartridge and the waste contained 14% ( $n=1$ ). Most of the activity was eluted out with 1 mL of EtOH, recovering 78% ( $n = 1$ ) of the collected crude product activity with minimal residual activity on the cartridge (1%,  $n = 1$ ). According to radio-HPLC (), the purified [ $^{18}\text{F}$ ]AIF-NODA-Tz exhibited a radiochemical purity (RCP) of 100%, compared to 91.8% before cartridge purification. The overall preparation time was ~17 min, including ~7 min for the reaction in the microreactor and ~10 min for purification and formulation.

### 3.3.2 Application to [ $^{18}\text{F}$ ]AIF-FAPI-74

To assess the versatility of this developed microdroplet-based [ $^{18}\text{F}$ ]AIF radiolabeling method, we extended our investigation to a clinically-relevant PET probe, [ $^{18}\text{F}$ ]AIF-FAPI-74,

targeting fibroblast activation protein (FAP) which is overexpressed in the stroma of various cancer types currently undergoing clinical trials (**Figure 3-3**).

Encouraged by the excellent radiosynthesis performance of [<sup>18</sup>F]AIF-NODA-Tz even with small precursor amount down to 5 nmol (crude RCY of 86 ± 5%, n = 2), with the optimal APR (0.8) determined from the previous model study, we firstly explored the influence of varying the precursor amount of FAPI-74, ranging from 0.1 to 10 nmol (**Figure 3-3B** and **Table 3-8**). The fluorination conversion exhibited a substantial increase with the precursor, reaching a peak of 90% (n = 1) with 5 nmol of precursor. Meanwhile, the collection efficiency remained consistently high (>91%) with no significant change, resulting in an excellent crude RCY of 92% (n = 1) by using 5 nmol of precursor. However, using precursor beyond 5 nmol had a negative impact on the synthesis performance, leading to both inferior fluorination conversion and crude RCY.

We then aimed to reduce the amount of precursor by increasing the reaction temperature. Results of a study using 0.5 nmol of FAPI-74 precursor are summarized in **Figure 3-3C** and **Table 3-9**. Increasing temperature from 95 to 125 °C led to a reduction in crude RCY from 40% (n = 1) to 28% (n = 1).

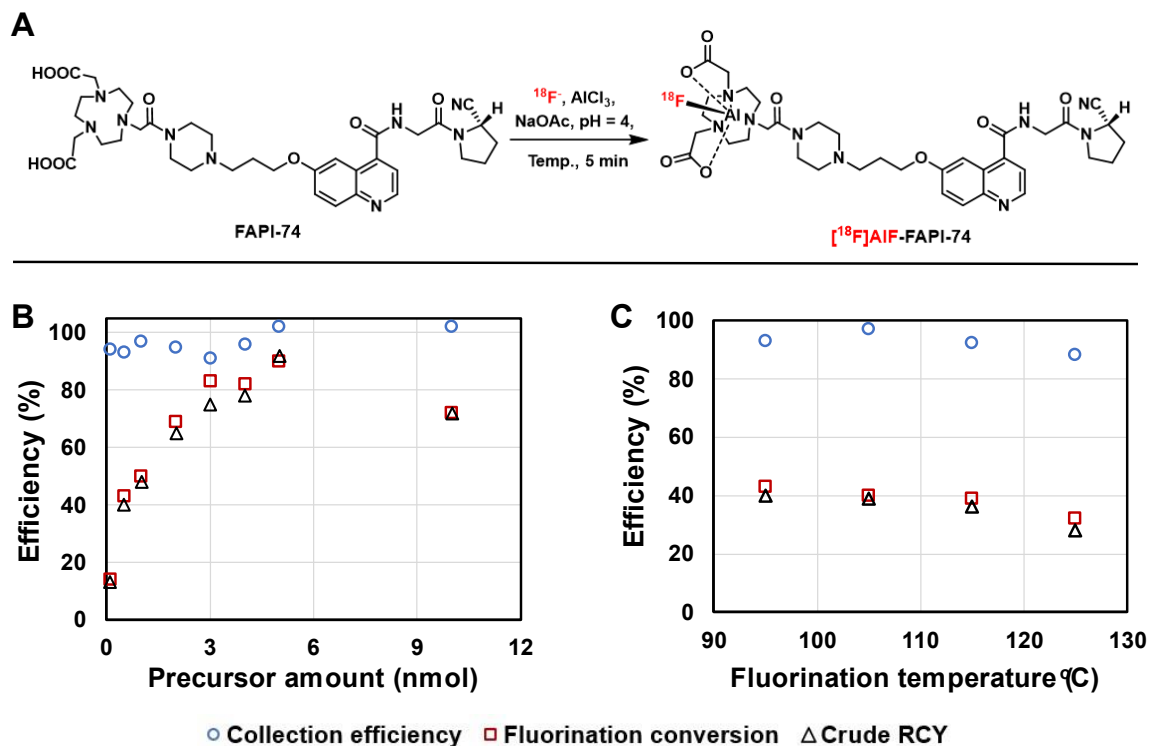


**Figure 3-3 Radiosynthesis optimization of [<sup>18</sup>F]AIF-FAPI-74 in a droplet reactor.**

(A) [<sup>18</sup>F]AIF-FAPI-74 synthesis scheme. [<sup>18</sup>F]AIF-FAPI-74 synthesis results (n = 1 for each condition) showing impact of (B) precursor amount (with AlCl<sub>3</sub> to precursor ratio (APR = 0.8), temperature = 95 °C, time = 5 min) or (C) fluorination temperature (with precursor = 0.5 nmol and APR = 0.8).

Overall, the optimal radiosynthesis of [<sup>18</sup>F]AIF-FAPI-74 involved employing aqueous 5.5 μL of [<sup>18</sup>F]fluoride/saline (5:2, v/v) with 5 nmol of FAPI-74 and 4 nmol of AlCl<sub>3</sub> (i.e., APR = 0.8), in the presence of 7.5 μL of DMSO and 2 μL of 0.5 M NaOAc at 95 °C for 5 min, achieving high fluorination conversion (90%, n = 1) and collection efficiency (102%, n = 1) at the end of the reaction, resulting in a crude RCY of 92% (n = 1). The reaction mixture was further purified on an HLB cartridge using the same protocol as [<sup>18</sup>F]AIF-NODA-Tz purification (**Table 3-10**). 93% (n = 1) of the crude collected product was trapped on the cartridge, and the waste activity resulting from the trapping and washing procedure was only 4% (n = 1) of crude collected product. The majority of the activity was eluted out with 1 mL of EtOH, recovering 92% (n = 1) of crude collected product with minimal residual activity on the cartridge (1%, n = 1). According to the radio-HPLC

measurement (**Figure 3-4**), the purified [ $^{18}\text{F}$ ]AIF-FAPI-74 exhibited a radiochemical purity (RCP) of 100%. The co-injection of [ $^{18}\text{F}$ ]AIF-FAPI-74 and FAPI-74 confirmed the chemical identity of the product. The overall preparation time was the same as for [ $^{18}\text{F}$ ]AIF-NODA-Tz, ~17 min.

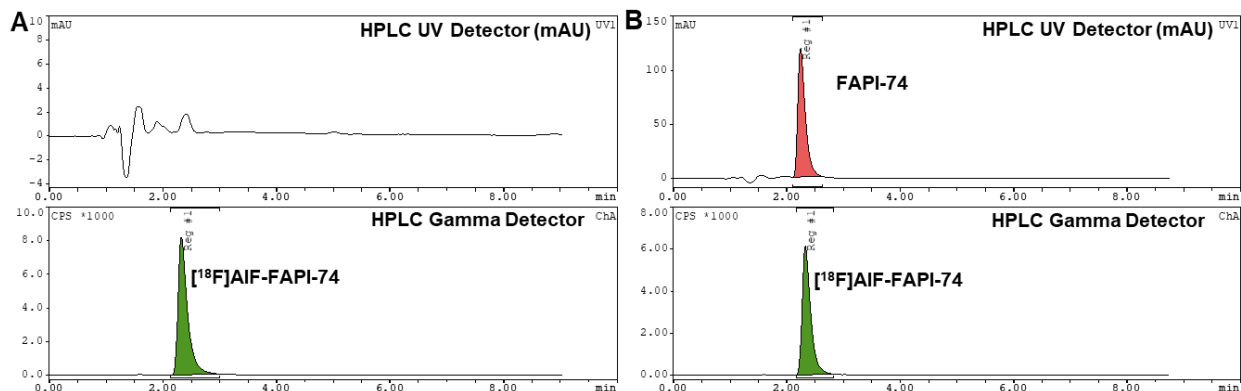


**Figure 3-4 Representative radio-HPLC chromatograms via droplet-based [ $^{18}\text{F}$ ]AIF radiolabelling.**

(A) purified [ $^{18}\text{F}$ ]AIF-FAPI-74, and (B) co-injection of purified [ $^{18}\text{F}$ ]AIF-FAPI-74 and AIF-FAPI-74 reference standard.

The performance of microdroplet-based synthesis of [ $^{18}\text{F}$ ]AIF-FAPI-74 is summarized in **Table 3-3** and compared to the results of the conventional (macroscale) synthesis (164), highlighting notable improvements in synthesis time and yield. One possible factor contributing to the enhanced RCY at the microscale could be the increased precursor concentration (0.33 mM vs 0.13 mM). Despite this increased concentration, we achieved an overall 16x reduction in precursor consumption by employing a considerably smaller reaction volume (15 vs. 630  $\mu\text{L}$ ). The droplet synthesis exhibited a ~2-fold increase in RCY (88%,  $n = 1$ ) and activity yield (77.3%,  $n = 1$ ) compared to the prior macroscale approach (RCY:  $45.0 \pm 5.2\%$ ; activity yield:  $37.0 \pm 4.3\%$ ;  $n = 10$ ), all while requiring only about half the preparation time (17 min for microscale reaction vs. 31 min for macroscale method).

**Table 3-3 Comparison of [<sup>18</sup>F]AIF-FAPI-74 production performance using conventional (macroscale) methods and optimized droplet-based synthesis.**

	Macroscale synthesis	Microdroplet synthesis
	Automated	Manual
	Naka et al.	This work
Number of repeats (n)	10	1
Starting activity (GBq)	32-40	0.05
Amount of precursor (nmol)	80	5
Precursor concentration (mM)	0.13	0.33
Reaction volume (μL)	630	15
Incubation time (min)	5	1
Fluorination temperature and time	95°C, 15 min	95°C, 5 min
Radiochemical yield (RCY, %) <sup>a</sup> , decay corrected	45.0 ± 5.2 <sup>b</sup>	88
Activity yield (%), non-decay-corrected	37.0 ± 4.3	77.3
Activity yield (GBq)	11.3 ± 1.1	0.04
Radiochemical purity (RCP, %) <sup>c</sup>	≥97	100
Molar activity (GBq/μmol) at EOS	220 ± 45	Not measured
Total preparation time (min)	31	~17

<sup>a</sup>RCY was obtained by cartridge purification. <sup>b</sup>The value was calculated based on the synthesis time and activity yield in the reference. <sup>c</sup>RCP was determined by radio-HPLC.

To produce clinically-relevant levels (i.e. multiple patient doses) of [<sup>18</sup>F]AIF-FAPI-74, scaled-up production is currently undergoing on an automated microdroplet radiosynthesizer. We conducted preliminary experiments to ensure that [<sup>18</sup>F]fluoride and the reagents could be added separately to the reaction site and did not need to be premixed (**Table 3-11**). We first performed the synthesis by using general protocol 1 with low activity volume of 5.5 μL [<sup>18</sup>F]fluoride/saline (5:2, v/v) solution at 46 MBq. The resulting performance was excellent, with fluorination conversion of 98% (n = 1), collection efficiency of 95%, and crude RCY of 94% (n = 1). To further mimic the scale-up synthesis, we increased the volume of [<sup>18</sup>F]fluoride of 25 μL. Using protocol 2, the [<sup>18</sup>F]fluoride was first dried with 1.5 μL of saline at 105 °C for ~1.5 min in the droplet reactor, and then the mixed solution of FAPI-74 precursor (2 μL in 0.5 M NaOAc), AlCl<sub>3</sub> (7.5 μL in DMSO) and 5.5 μL of DI water (added to maintain the reaction volume as in prior optimal condition) was loaded and incubated at RT for 1 min before heating to 95 °C for 5 min to perform fluorination.

After synthesis, comparable fluorination conversion was achieved (97%, n = 1). However, the collection efficiency exhibited a lower performance compared to the synthesis with a lower F-18 volume, resulting in a decreased crude RCY of 83% (n = 1). The activity loss occurred mainly during the drying process (5% of starting activity loss) and activity residue on the chip after product collection (4% of starting activity loss), as the total volatile and chip residual loss were <5% for the previous reaction with lower F-18 volume. Further optimization might require an increased amount of saline along with [<sup>18</sup>F]fluoride evaporation, and a more optimal collection solution to extract all activity from the chip.

### 3.4 Conclusions

In this work we have demonstrated the efficacy of droplet reactions within the framework of the [<sup>18</sup>F]AIF radiolabeling technique. Starting with [<sup>18</sup>F]AIF-NODA-Tz as the model substrate, we systematically explored key synthesis factors, such as the AlCl<sub>3</sub>-to-precursor ratio (APR), precursor amount, and the impact of reaction solvent and time. By optimizing droplet reactions on a small scale with high-throughput methods, we achieved [<sup>18</sup>F]AIF-NODA-Tz with high fluorination conversion rate of 96 ± 2% (n = 2) and collection efficiency of 92 ± 1% (n = 2), resulting in a crude radiochemical yield (RCY) of 89 ± 2% (n = 2). Utilizing the optimal APR of 0.8 and DMSO as the reaction co-solvent, we extended our investigation to the synthesis of [<sup>18</sup>F]AIF-FAPI-74 in a droplet reactor, starting with an initial activity of 0.05 GBq. We successfully achieved an isolated RCY of 88% (n = 1) after solid-phase extraction (SPE) purification and formulation in just 17 min, using a minimal 5 nmol of precursor—a significant 16-fold reduction compared to conventional methods. This streamlined approach yielded an excellent activity yield of 77.3% (n = 1) along with excellent radiochemical purity of 100%. The simplicity and speed of this synthesis method, along with improved yield and reduced precursor amount, promise to expedite further evaluations of [<sup>18</sup>F]AIF-FAPI-74 as a diagnostic modality for various tumors. After microscale copper-mediated radiosynthesis, this work highlights another successful application of metal-based radiochemistry

in a droplet microreactor. The ongoing efforts to scale up the synthesis and implement automation hold great promise for supporting preclinical and clinical studies. Additionally, the robust microdroplet-based [<sup>18</sup>F]AIF synthesis approach may have potential applications in labeling other biomolecules in the future.

## 3.5 Appendix

### 3.5.1 Optimization of [<sup>18</sup>F]AIF-NODA-Tz synthesis in a droplet reactor

**Table 3-4 Influence of varying AlCl<sub>3</sub>-to-precursor ratio (APR) with fixed precursor amount for preparing [<sup>18</sup>F]AIF-NODA-Tz in a droplet reactor.**

AlCl <sub>3</sub> -to-precursor ratio (APR) <sup>a</sup>	Fluorination conversion (%)	Collection efficiency (%)	Crude RCY (%)
0.4	89 ± 0	92 ± 2	82 ± 2
0.8	89 ± 1	94 ± 1	84 ± 2
1.2	80 ± 0	95 ± 0	76 ± 0
2.0	80 ± 0	95 ± 0	76 ± 0
3.2	32 ± 2	95 ± 1	30 ± 1
3.6	22 ± 1	95 ± 10	21 ± 1
4.0	20 ± 0	93 ± 1	18 ± 1

<sup>a</sup>All reactions were performed with 46-70 MBq of [<sup>18</sup>F]F<sup>-</sup>, 7.5 nmol of NODA-Tz and specific amount of AlCl<sub>3</sub> in 15 μL of mix solution (including 7.5 μL of DMSO) at 95 °C for 5 min (n = 2 replicates each condition).

**Table 3-5 Influence of varying precursor amount with fixed AlCl<sub>3</sub>-to-precursor ratio (APR=0.8) for preparing [<sup>18</sup>F]AIF-NODA-Tz in a droplet reactor.**

Amount of precursor (nmol) <sup>a</sup>	Fluorination conversion (%)	Collection efficiency (%)	Crude RCY (%)
5	90 ± 2	95 ± 8	86 ± 5
7.5	89 ± 1	94 ± 1	84 ± 2
10	89 ± 4	94 ± 3	83 ± 2
30	96 ± 2	92 ± 1	89 ± 2
90	81 ± 1	94 ± 2	76 ± 2

<sup>a</sup>All reactions were performed with 40-56 MBq of [<sup>18</sup>F]F<sup>-</sup> and fixed AlCl<sub>3</sub>-to-precursor ratio (APR = 0.8) in 15 μL of mix solution (including 7.5 μL of DMSO) at 95 °C for 5 min (n = 2 replicates each condition).

**Table 3-6 Influence of varying AlCl<sub>3</sub>-to-precursor ratio (APR) and different reaction time in the presence of MeCN for preparing [<sup>18</sup>F]AIF-NODA-Tz in a droplet reactor.**

AlCl <sub>3</sub> -to-precursor ratio (APR) <sup>a</sup>	Reaction time (min)	Fluorination conversion (%)	Collection efficiency (%)	Crude RCY (%)
0.8	5	14	94	13
1	5	36	94	34
0.8	3	5	93	5

<sup>a</sup>All reactions were performed with 67-73 MBq of [<sup>18</sup>F]F<sup>-</sup>, 30 nmol of precursor and specific amount of AlCl<sub>3</sub> in 15 μL of mix solution (including 7.5 μL of DMSO) at 95 °C for 5 min (n = 1 replicates each condition).

### 3.5.2 [<sup>18</sup>F]AIF-NODA-Tz purification and radio-HPLC analysis

#### 3.5.2.1 [<sup>18</sup>F]AIF-NODA-Tz purification on an HLB cartridge

**Table 3-7 Summary of [<sup>18</sup>F]AIF-NODA-Tz purification on an HLB cartridge. Activity measurements are expressed as fraction of starting activity of purification (corrected for decay, n = 1).**

Process	Results (%)
Activity of diluted crude product in vial before loading on cartridge	100
Activity residue in vial after loading	8
Activity trapped on cartridge	79
Waste from loading process	13
Waste from rinsing cartridge	1
Activity trapped on cartridge after rinse	78
Activity eluted out with 1 mL EtOH and diluted in saline (i.e., purification efficiency)	78
Activity residue on cartridge	1

#### 3.5.2.2 Example radio-HPLC analysis of [<sup>18</sup>F]AIF-NODA-Tz



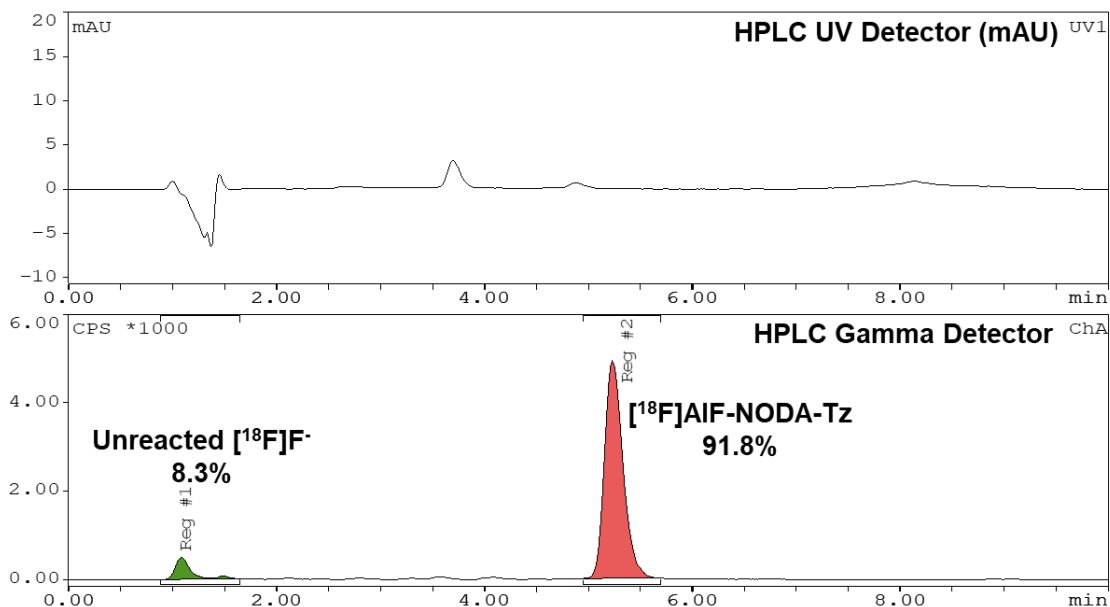


**Figure 3-5 Example radio-HPLC analysis of crude  $^{18}\text{F}$ AIF-NODA-Tz sample (upper: UV-254 nm and bottom:  $\gamma$ -ray) from a microdroplet reaction.**

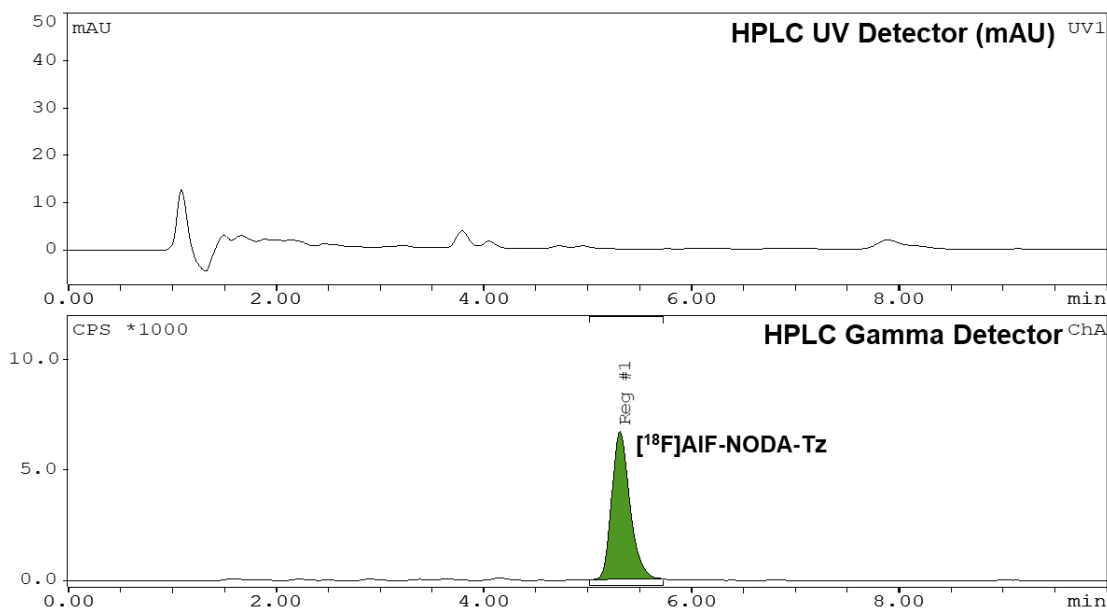


**Figure 3-6 Example radio-HPLC analysis of purified  $^{18}\text{F}$ AIF-NODA-Tz (upper: UV-254 nm and bottom:  $\gamma$ -ray).**

### 3.5.3 Optimization of [<sup>18</sup>F]AIF-FAPI-74 synthesis in a droplet reactor

#### 3.5.3.1 Influence of precursor amount

**Table 3-8 Influence of precursor amount with fixed APR=0.8 for preparing [<sup>18</sup>F]AIF-FAPI-74 in a droplet reactor.**

Amount of precursor (nmol) <sup>a</sup>	Fluorination conversion (%)	Collection efficiency (%)	Crude RCY (%)
0.1	14	94	13
0.5	43	93	40
1	50	97	48
2	69	95	65
3	83	91	75
4	82	96	78
5	90	102	92
10	72	102	72

<sup>a</sup>All reactions were performed with 14-29 MBq of [<sup>18</sup>F]F<sup>-</sup>, specific amount of FAPI-74 and AlCl<sub>3</sub> in 15 μL of mix solution (including 7.5 μL of DMSO) at 95 °C for 5 min (n = 1 replicates each condition).

#### 3.5.3.2 Influence of fluorination temperature

**Table 3-9 Influence of fluorination temperature for preparing [<sup>18</sup>F]AIF-FAPI-74 in a droplet reactor.**

Fluorination temperature (°C) <sup>a</sup>	Fluorination conversion (%)	Collection efficiency (%)	Crude RCY (%)
95	43	93	40
105	40	97	39
115	39	92	36
125	32	88	28

<sup>a</sup>All reactions were performed with 14-29 MBq of [<sup>18</sup>F]F<sup>-</sup>, 0.5 nmol of FAPI-74 and 0.4 nmol of AlCl<sub>3</sub> in 15 μL of mix solution (including 7.5 μL of DMSO) at specific temperature for 5 min (n = 1 replicates each condition).

### 3.5.4 [<sup>18</sup>F]AIF-FAPI-74 purification

#### 3.5.4.1 [<sup>18</sup>F]AIF-FAPI-74 purification on HLB cartridge

**Table 3-10 Summary of [<sup>18</sup>F]AIF-FAPI-74 purification on HLB cartridge. Activity measurements are expressed as fraction of starting activity of purification (corrected for decay, n = 1).**

Process	Results (%)
Activity of diluted crude product in vial before loading on cartridge	100
Activity residue in vial after loading	2
Activity trapped on cartridge	93
Waste from loading process	3
Waste from rinsing cartridge	1
Activity trapped on light HLB after rinse	92
Activity eluted out with 1 mL EtOH and diluted in saline (i.e., purification efficiency)	92
Activity residue on cartridge	1

### 3.5.5 Preliminary experiment to mimic automated radiosynthesis process

**Table 3-11 Summary of [<sup>18</sup>F]AIF-FAPI-74 synthesis performance via different reagent loading protocols. Activity measurements are expressed as fraction of starting activity (corrected for decay, n = 1).**

Protocol <sup>a</sup>	1	2
Starting activity (MBq)	46	281
[ <sup>18</sup> F]F <sup>-</sup> volume (μL)	4	24
Activity on chip after drying (%)	Not measured	95
Collection of crude product from chip (%)	95	85
Activity residue on Tip after product collection (%)	2	0.1
Activity residue on chip after product collection (%)	0	4
Fluorination conversion (%)	98	97
Crude RCY (%)	94	83

<sup>a</sup>All reactions were performed with 1.5 μL of saline, 5 nmol of FAPI-74 and 4 nmol of AlCl<sub>3</sub> (in 2 μL of 0.5 M NaOAc) in total 15 μL of mix solution (including 7.5 μL of DMSO) at 95 °C for 5 min.

## Chapter 4: Acceleration of radiochemistry through droplet reactions: 6x speedup of [<sup>18</sup>F]FMAU preparation

### 4.1 Introduction

Over the past several decades, a greater understanding of tumor biology has yielded better clinical care and improved survival for many patients with cancer (165–168). Advances in morphological and molecular imaging techniques have improved the detection and staging of tumors, as well as the measurement of therapy response (169–174). In particular, the advancement of positron emission tomography (PET) technology provides the opportunity to noninvasively image tumor biochemistry and metabolism (18,175), providing an extra layer of information beyond the anatomical details from a computed tomography (CT) or magnetic resonance imaging (MRI) scan.

As a prominent hallmark in cancer, uncontrolled cell division is responsible for tumor growth, serving as a key factor in distinguishing malignant tumors from normal tissue and assessing the effectiveness of therapy (176–178). PET imaging with the glucose analog [<sup>18</sup>F]FDG has well-established clinical utility in diagnosing, grading, and staging, as well as monitoring tumor progression (170). However, it is important to note that [<sup>18</sup>F]FDG uptake primarily reflects the density of viable cells and their glucose metabolism, and measures processes only indirectly related to cell division and DNA synthesis. Due to the high metabolism present in the brain and heart, there is an increased background of [<sup>18</sup>F]FDG in these areas, and a similar issue in the cases of infection and inflammation, potentially leading improper diagnoses. Furthermore, in many preclinical and clinical scenarios, the [<sup>18</sup>F]FDG signal contradicts the ongoing cell proliferation, often indicating a negative or relatively weak association with tumor and cell proliferation (177,179–183). Therefore, a clinically applicable PET tracer for visualizing a more direct measure of cell division is required.

Many additional tracers are being developed that provide improved contrast, sensitivity, and accuracy compared to [ $^{18}\text{F}$ ]FDG (184,185). A particularly interesting one is the nucleoside analog [ $^{18}\text{F}$ ]FMAU, which is directly incorporated into DNA when cells divide and thus directly measures cell proliferation (177). Promising clinical data of [ $^{11}\text{C}$ ]FMAU (chemically identical to [ $^{18}\text{F}$ ]FMAU) and preclinical data of [ $^{18}\text{F}$ ]FMAU have led to initial clinical studies of [ $^{18}\text{F}$ ]FMAU in 14 cancer patients with active tumors in the breast, brain lung or prostate (186–191) for one-time imaging, and there is high interest to pursue clinical studies of [ $^{18}\text{F}$ ]FMAU PET as a means to assess treatment response in diverse cancer types (191–194).

However, the production of [ $^{18}\text{F}$ ]FMAU remains a major challenge. Achieving direct, stereospecific (arabino) fluorination through  $\text{S}_{\text{N}}2$  substitution at the 2'-position of the furanosyl moiety in a pyrimidine nucleoside has not yet been realized (195,196) and thus multi-step synthesis is necessary. Manger et al. and Alauddin et al. reported the initial radiolabeling of [ $^{18}\text{F}$ ]FMAU and its thymidine analogs through fluorination of a ribose precursor, followed by bromination and coupling steps to install the base, and a final deprotection step (197,198). However, this laborious method involves multiple reaction vessels and intermediate purification steps, resulting in low yields. Li et al. later developed a synthetic approach using Friedel–Crafts catalysts to simplify the coupling process to a single step, and were able to demonstrate that the modified 3-step radiosynthesis could be implemented as a one-pot process with significantly reduced synthesis time (199–201). They recently enhanced the one-pot process by replacing the toxic reaction solvent 1,2-dichloroethane with 1,4-dioxane (202). [ $^{18}\text{F}$ ]FMAU was obtained in  $12 \pm 3\%$  decay-corrected radiochemical yield ( $\sim 5\%$  activity yield) with  $>99\%$  radiochemical purity. However, this synthesis still takes  $\sim 150$  min and poses challenges for automation using commercially-available synthesis modules (e.g. extremely corrosive reagents) hindering routine clinical production.

To address the long synthesis time, we explored microscale radiosynthesis approaches based on droplet radiochemistry, which use 10-20  $\mu\text{L}$  reaction volumes instead of the 0.5-2 mL volumes typical of conventional vial-based apparatus. Compared to conventional synthesis, the small volume droplet-based methods use 20-150x less precursor, and require 2-3x shorter time, yet have comparable or better yields (39). Droplet radiochemistry has been applied to a variety of radiotracers with 1-step (radiofluorination) (78,79,93,98,136) and 2-step (radiofluorination plus deprotection) (78,82,162,203–205) synthesis protocols. Because of the small volume and low precursor mass, purification can be performed with an analytical-scale HPLC column (39) instead of semi-prep, enabling improved separation resolution, shorter purification time, and accelerated formulation (via micro-SPE (203)) due to the low volume of purified fraction. A further advantage of droplet reactions is that they can be used as a platform for high-throughput studies to speed the synthesis development process (206–208).

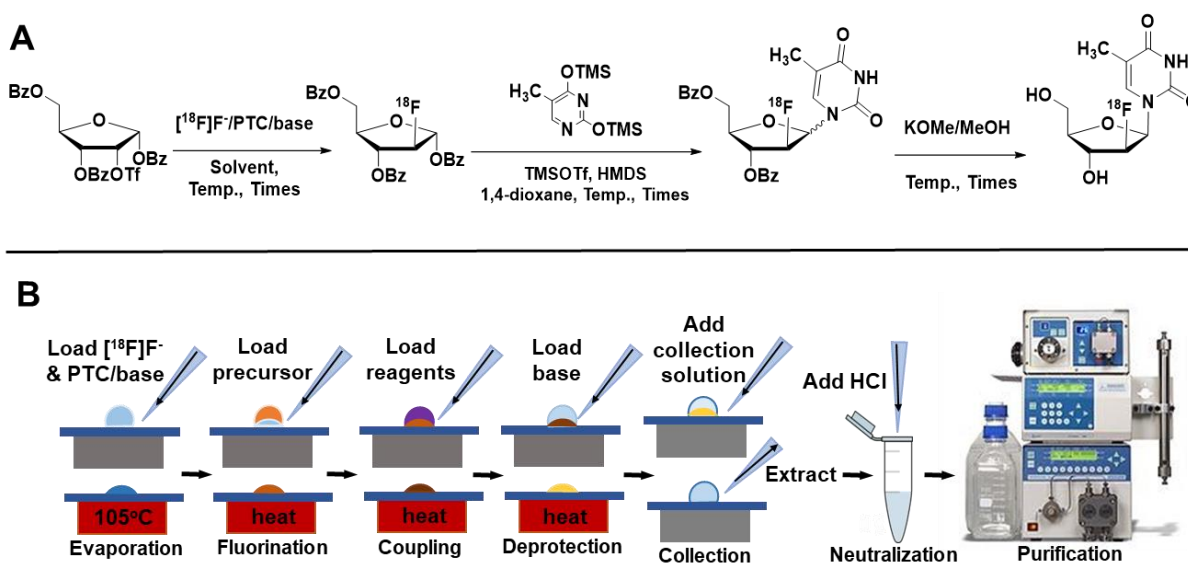


**Figure 4-1 (A)  $[^{18}\text{F}]$ FMAU synthesis scheme and (B) process flow for radiosynthesis using a microdroplet reactor.**

Herein, we leverage this extensive past experience to explore the feasibility of conducting the one-pot three-step radiosynthesis of  $[^{18}\text{F}]$ FMAU on a microdroplet reactor (**Figure 4-1**). We optimized the fluorination, coupling and deprotection conditions on microfluidic chips via an

extensive set of experiments on a novel high-throughput radiochemistry platform, exploring the impact of diverse phase transfer catalysts (PTCs)/bases, solvents, reaction temperatures and times. In addition, different amounts of precursor and coupling reagents were investigated in detail. Moreover, taking advantage with the microscale reaction, optimization of the purification process was able to be explored on an analytical radio-HPLC system. This work represents the most complex radiosynthesis to date performed in droplet-based reactions.

## 4.2 Methods

### 4.2.1 Materials

Tetrabutylammonium hydrogen carbonate (TBAHCO<sub>3</sub>, 75 mM in ethanol) was purchased from ABX Advanced Biochemical Compounds (Radeberg, Germany). Tetrabutylammonium trifluoromethane-sulfonate (TBAOTf, >99%), Kryptofix® 222 (K<sub>222</sub>, >99%), potassium carbonate (K<sub>2</sub>CO<sub>3</sub>, >99%), tetraethylammonium bicarbonate (TEAHCO<sub>3</sub>, >95%), tetrabutylammonium perchlorate (TBAClO<sub>4</sub>, >95%), sodium phosphate monobasic (NaH<sub>2</sub>PO<sub>4</sub>, >99%), sodium phosphate dibasic (Na<sub>2</sub>HPO<sub>4</sub>, >99%), (*N,N*-dimethylformamide (DMF, 99.8%), anhydrous dimethyl sulfoxide (DMSO, >99.9%), anhydrous acetonitrile (MeCN, 99.8%), anhydrous ethyl alcohol (EtOH, >99.5%), 2,3-dimethyl-2-butanol (hexyl alcohol, 98%), anhydrous 1,4-dioxane (99.8%), trifluoroacetic acid (TFA, 99%) acetic acid (>99.7%), hexane (>99%), ethyl acetate (99.8%), and potassium methoxide solution (25 wt.% of KOMe in MeOH) were purchased from Sigma-Aldrich (St. Louis, MO, USA). Tetraethylammonium trifluoromethanesulfonate (TEAOTf, >99%) and *N*-Methyl-2-pyrrolidone (NMP, >99%) was purchased from TCI America (Portland, Oregon, USA). 2-O-(trifluoromethanesulfonyl)-1,3,5-tri-O-benzoyl- $\alpha$ -D-ribofuranose (i.e., precursor) and reference standard were prepared as previously reported (201) or obtained from ABX Advanced Biochemical Compounds (Radeberg, Germany). Coupling reagents, O,O'-bis-(trimethylsilyl)thymine (i.e., protected thymine, 97%), hexamethyldisilane (HMDS, >99%), and trimethylsilyl trifluoromethanesulfonate (TMSOTf, 99%) were purchased from Sigma-Aldrich (St.

Louis, MO, USA). Deionized (DI) water was obtained from a Milli-Q water purification system (EMD Millipore Corporation, Berlin, Germany). Reagent and collection vials were purchased from Eppendorf (Hamburg, Germany). PBS buffer was prepared at a 0.1 M concentration with a pH of 6 using  $\text{Na}_2\text{HPO}_4$  and  $\text{NaH}_2\text{PO}_4$  on the same day as the experiment. The high purity perfluoroalkoxy (PFA) tubing (HPFA, 1/16" OD x 0.030", 1912L) used for loading reagent solutions in automation tests was purchased from IDEX Health and Sciences (Northbrook, IL, USA). V-vials (0.3 mL) were purchased from Chrom Tech, Inc. (Apple Valley, MN, USA).  $^{18}\text{F}$ fluoride in  $^{18}\text{O}$  $\text{H}_2\text{O}$  was obtained from the UCLA Crump Cyclotron and Radiochemistry Center. The activity was used directly as provided by cyclotron without further purification for both droplet-based microscale radiosynthesis

#### 4.2.2 Microdroplet radiosynthesis of $^{18}\text{F}$ FMAU

Droplet-based reactions were conducted on Teflon-coated silicon chips featuring 2x2 or 4x4 arrays of hydrophilic reaction site, operated on a temperature-controlled heating platform, as previously described (206).

The general synthesis process involved the following steps (**Figure 4-1B**) Initially these were performed manually with a micropipette and later were automated with a droplet radiosynthesizer. First, 10  $\mu\text{L}$  of a  $^{18}\text{F}$ fluoride stock solution (containing 15-1240 MBq of activity mixed with a desired amount of PTC and base) was loaded onto a reaction site of the chip and dried at 105 °C for 1 min. Next, 10  $\mu\text{L}$  of precursor stock solution was added and heated for fluorination. After that, a specific volume of coupling stock solution was added and heated for coupling conjugation. For deprotection, 15  $\mu\text{L}$  of deprotection solution was added and heated followed by replenishing another 15  $\mu\text{L}$  of deprotection solution after 1.5 min. The crude product was extracted from the reaction site using a collection solution (20  $\mu\text{L}$ ) and transferring the diluted crude product to a 0.5 mL eppendorf tube via for further analysis, repeating this process 4x to minimize activity residue on the chip.



Several stock solutions were prepared just before each batch of experiments. Stock solutions of PTC and base were prepared in DI water, with each 5  $\mu\text{L}$  aliquot containing the desired amount of PTC and base for a single droplet reaction. The optimized amounts were determined as part of this study. [ $^{18}\text{F}$ ]fluoride stock solution was prepared by mixing [ $^{18}\text{F}$ ]fluoride/[ $^{18}\text{O}$ ]H $_2\text{O}$  with the desired PTC / base stock solution in 1:1 (v/v) ratio, resulting in 10  $\mu\text{L}$  portion containing 15-1240 MBq of activity, along with the desired amount of PTC and base for a single reaction. Stock solution of precursor (21 mM for the initial condition and 16.8 mM for other experiments) was prepared in the desired reaction solvent, with each 8 or 10  $\mu\text{L}$  portion containing 0.168  $\mu\text{mol}$  of precursor. In the study of precursor amount, varied concentration of the precursor stock solution was prepared with each 10  $\mu\text{L}$  portion containing the desired amount of precursor. For the coupling reaction, varying concentration of stock solution of protected thymine was prepared in 1,4-dioxane, with a 5 or 9  $\mu\text{L}$  (explored during optimization) portion containing the desired amount. HMDS and TMSOTf were added into the stock solution of protected thymine just prior to synthesis. Deprotection solution was prepared by mixing 25% KOMe in MeOH with EtOH in 2:1 (v/v). Collection solution was prepared by mixing MeCN and H $_2\text{O}$  (95:5, v/v) or hexane and ethyl acetate (1:1, v/v).

### 4.2.3 Analytical methods

Radioactivity measurements were performed using a calibrated dose calibrator (CRC-25R, Capintec, Florham Park, NJ, USA). Fluorination conversion and coupling percentage were evaluated through multi-lane radio-thin layer chromatography (radio-TLC) methods (96). Briefly, 0.5  $\mu\text{L}$  samples were spotted on TLC plates (6 cm x 5 cm pieces cut from 20 cm x 5 cm sheets, silica gel 60 F $_{254}$ , Merck KGaA, Darmstadt, Germany). Plates were developed for a 4 cm distance using a mobile phase of hexane and ethyl acetate (1:1, v/v), dried, and then covered with a glass microscope slide (75x50x1 mm $^3$ , Fisher Scientific, Hampton, NH, USA) and read out via Cerenkov luminescence imaging (CLI) with 5 min exposure time.

Fluorination conversion or coupling percentage of each sample (lane) was determined via ROI analysis as previously described (96). Collection efficiency after fluorination, after coupling or after deprotection was obtained by dividing the activity of the collected mixture (after the corresponding reaction) by the starting activity and corrected for decay. Crude fluorination yield was computed as fluorination conversion multiplied by the collection efficiency after fluorination. Crude coupling product was computed as coupling percentage multiplied by the collection efficiency after coupling. The isolated RCY and the ratio of  $\beta$ - to  $\alpha$ -anomer were determined by performing radio-HPLC purification on an analytical column (Luna C18 (2), RP, 5  $\mu$ m, 250  $\times$  4.6 mm, Phenomenex, Torrance, CA, USA; ZORBAX RP Eclipse Plus C18, 100  $\times$  4.6 mm, 3.5  $\mu$ m, Agilent Technologies, Santa Clara, CA, USA; Symmetry C18 Column, 3.5  $\mu$ m, 150  $\times$  4.6 mm, Waters Corporation, Milford, MA, USA) using an isocratic mobile phase which was optimized as part of this study. The radio-HPLC system comprised a Smartline HPLC system (Knauer, Berlin, Germany) equipped with a degasser (Model 5050), pump (Model 1000), UV detector (254 nm; Eckert & Ziegler, Berlin, Germany), gamma-radiation detector (BFC-4100, Bioscan, Inc., Poway, CA, USA), and counter (BFC-1000; Bioscan, Inc., Poway, CA, USA). The purified [ $^{18}$ F]FMAU was analyzed on the same radio-HPLC system equipped with ZORBAX RP Eclipse Plus C18 (100  $\times$  4.6 mm, 3.5  $\mu$ m) to confirm radiochemical purity (RCP) using a mobile phase of DI water and MeCN (95:5, v/v) with 0.1% TFA (v/v) at the flow rate of 1.2 mL/min. Under this condition, the retention of [ $^{18}$ F]FMAU was 5.0 min. The ratio of  $\beta$ - to  $\alpha$ -anomer was calculated from the areas under the peaks corresponding to those species (in the radiation signal chromatogram). Co-injection of the purified [ $^{18}$ F]FMAU and reference standard was performed to confirm product identity.

## 4.3 Results and discussion

### 4.3.1 Initial conditions

To begin to adapt the macroscale synthesis to a microdroplet format, we first followed closely the conditions reported by Li et al. (202), reducing the volumes and reagent amounts by 100x, i.e. reducing the fluorination reaction volume from 800  $\mu\text{L}$  to 8  $\mu\text{L}$  and reducing the coupling reaction volume from 650  $\mu\text{L}$  to 6.5  $\mu\text{L}$ , while maintaining all the same reagent concentrations and ratios. We employed the same fluorination and coupling temperatures as in the original report (both at 85 °C) but shortened their reaction times (4 min for fluorination and 5 min for coupling conjugation) due to the higher heat transfer efficiency of droplet-based reaction. Details of the preliminary experiment's conditions and performance are provided in **Table 4-2**. While achieving moderate fluorination conversion (61%,  $n = 1$ ), the coupling percentage was low (20%,  $n = 1$ ), and there was poor collection efficiency after coupling (13%,  $n = 1$ ), leading to low crude coupling product at only 2.6% ( $n = 1$ ). Using this as a starting point, we systematically optimized the [ $^{18}\text{F}$ ]FMAU radiosynthesis, addressing fluorination, coupling and deprotection reactions in a step by step fashion.

### 4.3.2 Fluorination optimization

#### 4.3.2.1 Preliminary optimization of solvent type and temperature

Drawing on our extensive experience in droplet-based optimization (136,205,207,208), we anticipated that an elevated fluorination temperature would positively impact the conversion efficiency. For example, in previous droplet-based synthesis of [ $^{18}\text{F}$ ]flumazenil, enhanced performance was observed by transitioning to solvents with higher boiling points and increased temperatures (207). Therefore assessed the impact of elevated temperature in various solvents that have performed well for other droplet reactions by performing a rapid screening of: MeCN (85 °C; initial condition), NMP (150 °C), DMF (150 °C), thexyl alcohol/DMSO (4:1, v/v) (100 °C), and thexyl alcohol/NMP (4:1, v/v) (100 °C). Details of measurements and calculations are

tabulated in **Table 4-3**. Moreover, in line with a precedent set by a report on [<sup>18</sup>F]FDG synthesis with the same leaving group and a similar fluorination mechanism (73), in section 3.2.1 to 3.2.3, we also reduced the base amount from the initial condition of 0.54 μmol to 0.176 μmol, with the presence of 0.17 μmol of precursor, while maintaining a fixed precursor-to-base ratio of 1:1.1. Among these tests, use of the solvent mixture hexyl alcohol/NMP (4:1, v/v) exhibited the highest fluorination conversion (80 ± 3%, n = 4) and collection efficiency after fluorination (41 ± 1%, n=4), resulting in the highest crude fluorination yield (33 ± 1%, n = 4), and thus this mixture was used for further optimization.

#### **4.3.2.2 Preliminary optimization of type of phase transfer catalyst / base**

The subsequent exploration involved different types of phase transfer catalysts (PTCs) and bases, with comprehensive measurements and calculations available in **Table 4-4**. For certain choices of PTC/base, namely TBAClO<sub>4</sub> and TBAOTf, significant loss of radioactivity was observed during the [<sup>18</sup>F]F<sup>-</sup> drying step, indicate they were not suitable under the reaction conditions, and we did not perform the subsequent fluorination. For another PTC, TEAOTf, no volatile loss was observed during the initial drying, but no fluorinated product was formed after the fluorination reaction. With TBAHCO<sub>3</sub>, the fluorination conversion (86 ± 8%, n=2) and collection efficiency after fluorination (46 ± 1%, n=2) provided a crude fluorination yield (39 ± 3%, n = 2) that was slightly better than using the initially attempted PTC/base combination of K<sub>222</sub> and K<sub>2</sub>CO<sub>3</sub>, which gave a crude fluorination yield of 33 ± 1% (n=2). In the synthesis using TEAHCO<sub>3</sub>, we observed inferior performance in both fluorination conversion and collection efficiency after fluorination, leading to a lower crude fluorination yield (29 ± 2%, n=2) compared that with TBAHCO<sub>3</sub>. Hence, TBAHCO<sub>3</sub> was selected as the optimal PTC for subsequent studies.

#### **4.3.2.3 Preliminary optimization of fluorination temperature and time**

Next, we conducted additional investigation into the fluorination temperatures and times. A comprehensive listing of measurements and calculations can be found in **Table 4-5**. Maintaining

a constant reaction time of 3 min, the fluorination conversion exhibited a notable increase with reaction temperature, peaking at  $92 \pm 1\%$  ( $n = 2$ ) at  $100\text{ }^{\circ}\text{C}$ . At the same time, increasing temperature led to increase in volatile radioactivity losses and thus reduced collection efficiency after fluorination, dropping from  $43 \pm 0\%$  ( $n = 2$ ) at  $80\text{ }^{\circ}\text{C}$  to  $28 \pm 1\%$  ( $n = 3$ ) at  $100\text{ }^{\circ}\text{C}$  ( $n = 2$ ). Overall the reaction at  $80\text{ }^{\circ}\text{C}$  gave the best result with a fluorination conversion of  $87 \pm 1\%$  ( $n = 2$ ), collection efficiency after fluorination of  $50 \pm 1\%$  ( $n = 2$ ), and corresponding crude fluorination yield of  $43 \pm 0\%$  ( $n = 2$ ). Extending the fluorination from 3 min to 5 min did not yield improvements in either fluorination conversion or collection efficiency after fluorination, and in fact resulted in a lower crude fluorination efficiency at both  $75\text{ }^{\circ}\text{C}$  and  $80\text{ }^{\circ}\text{C}$ .

#### 4.3.2.4 Preliminary optimization of precursor amount

We further explored the influence of precursor amount. Detailed measurements and calculations can be found in **Table 4-6**. Increasing the precursor amount resulted in higher fluorination conversion and collection efficiency after fluorination in both experiments, whether with a fixed base amount (i.e.,  $0.176\text{ }\mu\text{mol}$  of  $\text{TBAHCO}_3$ ) or a fixed precursor-to-base ratio (1:1.1), resulting in an improved crude fluorination yield. The most favourable outcome was achieved with  $0.5\text{ }\mu\text{mol}$  of precursor using the fixed amount of  $\text{TBAHCO}_3$  ( $0.176\text{ }\mu\text{mol}$ ), where the fluorination efficiency reached  $90 \pm 4\%$  ( $n = 2$ ), collection efficiency after fluorination was  $64 \pm 4\%$  ( $n = 2$ ), and the crude fluorination yield was  $57 \pm 6\%$  ( $n = 2$ ). Notably, we observed no significant difference in fluorination performance between experiments a fixed base amount (i.e.,  $0.176\text{ }\mu\text{mol}$  of  $\text{TBAHCO}_3$ ) and those with a fixed precursor-to-base ratio (1:1.1). As a result, we continued to use the fixed amount of  $\text{TBAHCO}_3$  ( $0.176\text{ }\mu\text{mol}$ ) for further optimization exploration.

#### 4.3.2.5 Re-optimization of solvent type

Upon performing coupling reaction (in 1,4-dioxane) after the optimized fluorination, we found the reaction failed to form the desired coupling product (**Figure 4-2** and **Table 4-7**). We believe this outcome could be attributed to the residual effects of the fluorination solvent (i.e.,

hexyl alcohol / NMP) adversely influencing the coupling conjugation with protected thymine. Notably, Li et al. also reported poor [<sup>18</sup>F]FMAU radiosynthesis performance when employing polar aprotic solvents such as DMF, DMSO, or co-solvent with only 10% DMSO (v/v) or DMF (v/v) as coupling solvents in a previously published paper (199).

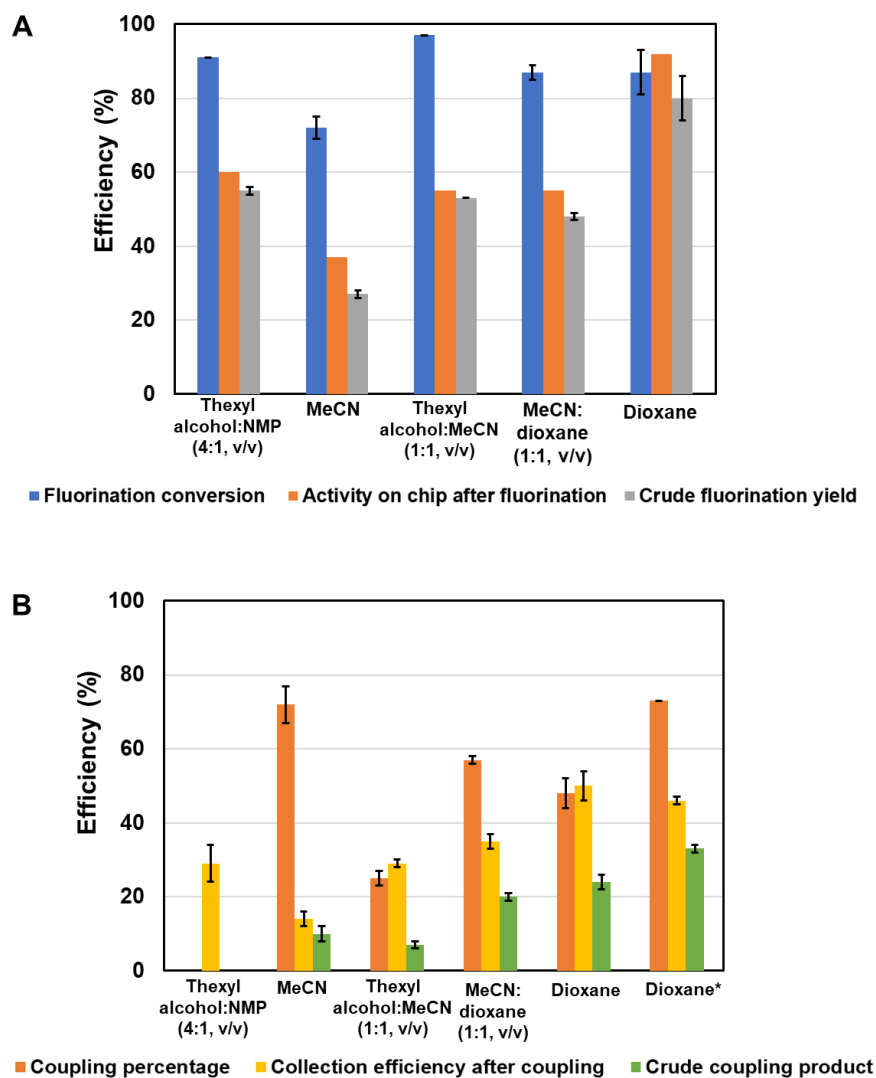


**Figure 4-2 Influence of solvent on (A) fluorination reaction and (B) subsequent coupling reaction.**

All fluorination reactions were performed at 80°C for 3 min. All coupling reactions were conducted at 85°C for 5 min, except the one indicated by an asterisk “\*” which was performed at 100°C for 5 min. Each condition was repeated n = 2 times.

To further this potential residual solvent effect, we tested various fluorination solvent systems, including (i) MeCN (a polar aprotic solvent, widely used for nucleophilic substitution), (ii)

thexyl alcohol (a polar protic solvent) / MeCN (1:1, v/v), (iii) MeCN / 1,4-dioxane (a nonpolar solvent), and (iv) 1,4-dioxane. The fluorination reaction was conducted at 80 °C for 3 min, followed by a subsequent coupling conjugation at 85 °C for 5 min ( $n = 2$ ). To our delight, the desired intermediate coupling product was formed in all cases. Interestingly, using 1,4-dioxane as the fluorination solvent yielded a higher fluorination performance than previously tested solvents, with crude fluorination yield of  $80 \pm 6\%$  ( $n = 2$ ), affirming its compatibility for nucleophilic substitution. Although the mixed solvent systems, namely thexyl alcohol / MeCN (1:1, v/v) and MeCN / 1,4-dioxane (1:1, v/v), presented similar or even higher fluorination conversion, these reactions exhibited significant activity losses, resulting in lower crude fluorination yields of  $53 \pm 0\%$  ( $n = 2$ ) and  $48 \pm 1\%$  ( $n = 2$ ), respectively. Among the various solvents used in the fluorination reaction, the use of 1,4-dioxane also led to the highest yield in the subsequent coupling reaction with a crude coupling yield of  $33 \pm 1\%$  ( $n=2$ ).

#### 4.3.2.6 Re-optimization of temperature

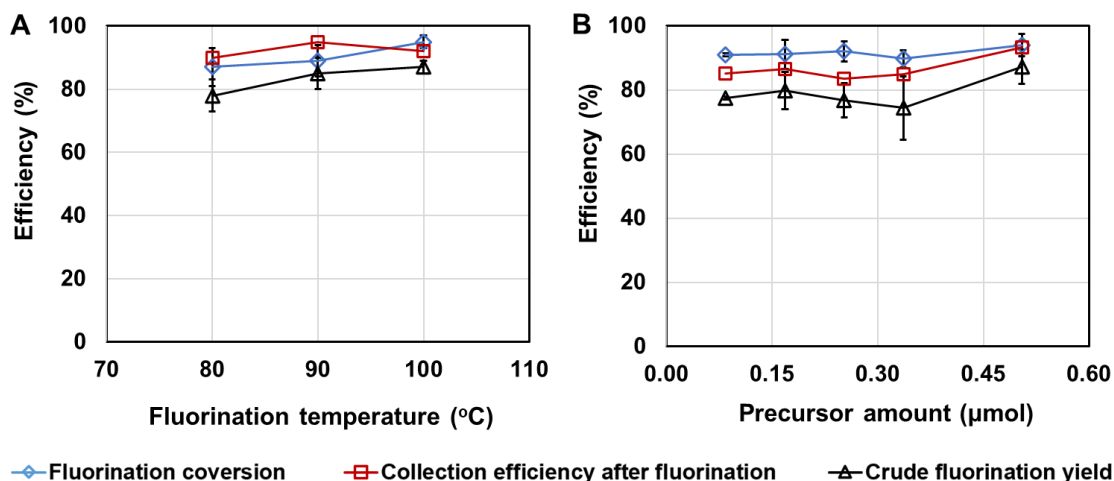


**Figure 4-3 Influence of (A) temperature and (B) precursor amount on fluorination reaction.**

Maintaining 1,4-dioxane as the fluorination solvent, we re-investigated the influence of fluorination temperature. Details of measurements and calculations can be found in **Figure 4-3A** and **Table 4-8**. Increasing the fluorination temperature from 80 °C to 100 °C improved the

performance, and nearly quantitative fluorination conversion was achieved at 100 °C ( $95 \pm 2\%$ ,  $n = 2$ ) as well as high collection efficiency (92%), resulting in high crude fluorination yield ( $87 \pm 2\%$ ,  $n = 2$ ).

#### 4.3.2.7 Re-optimization of precursor amount

Based on the optimal fluorination solvent and temperature, we re-explored the influence of precursor amount. Details of measurements and calculations can be found in **Figure 4-3B** and **Table 4-9**. We found that decreasing the precursor amount reduced performance, but the magnitude of the impact was lower than in the preliminary precursor study. The highest performance was obtained using 0.5  $\mu\text{mol}$ , which provided fluorination conversion of  $94 \pm 4\%$  ( $n = 4$ ) and collection efficiency (93%), resulting in enhanced crude fluorination yield of  $87 \pm 5\%$  ( $n = 4$ ). This amount was then established as the fixed parameter for subsequent optimization studies.

### 4.3.3 Coupling reaction optimization

In some of the preceding experiments we performed both fluorination and coupling and discovered an interaction of the fluorination solvent on the coupling reaction, corrected this and performed further optimization of the fluorination step. Owing to the good performance using 1,4-dioxane as the coupling solvent in those tests, we kept the coupling solvent fixed and optimized other coupling reaction parameters.

#### 4.3.3.1 Influence of coupling temperature

In the presence of 1,4-dioxane, Li et al. explored two different temperatures for the coupling reaction (85 °C and 100 °C) and determined that the lower coupling temperature (85 °C) yielded better synthesis performance (202). In microdroplet-based synthesis, we also examined coupling reactions at 85 °C and 100 °C (**Figure 4-2** and **Table 4-7**). Interestingly, a higher coupling percentage ( $73 \pm 0\%$ ,  $n = 2$ ) was observed at 100 °C. Consequently, we adopted this as a starting point for further exploration in coupling reactions.



#### 4.3.3.2 Influence of amount of protected thymine

We further explored the influence of amount of protected thymine. Detailed measurements and calculations can be found in **Figure 4-4A** and **Table 4-10**, respectively. In the coupling reaction, protected thymine conjugates with the fluorinated intermediate, producing both  $\beta$ - and  $\alpha$ -anomers. To better monitor and maximize the yield of the desired product ( $\beta$ -anomer) in the coupling optimization study, coupling was followed by deprotection, so that radio-HPLC analysis could be used to quantify the isolated RCY of [ $^{18}\text{F}$ ]FMAU ( $\beta$ -anomer). Despite some small variation in collection efficiency (after deprotection) with different amounts of protected thymine (ranging from 0.2 to 0.6  $\mu\text{mol}$ ), no significant impact was observed on the isolated RCY.

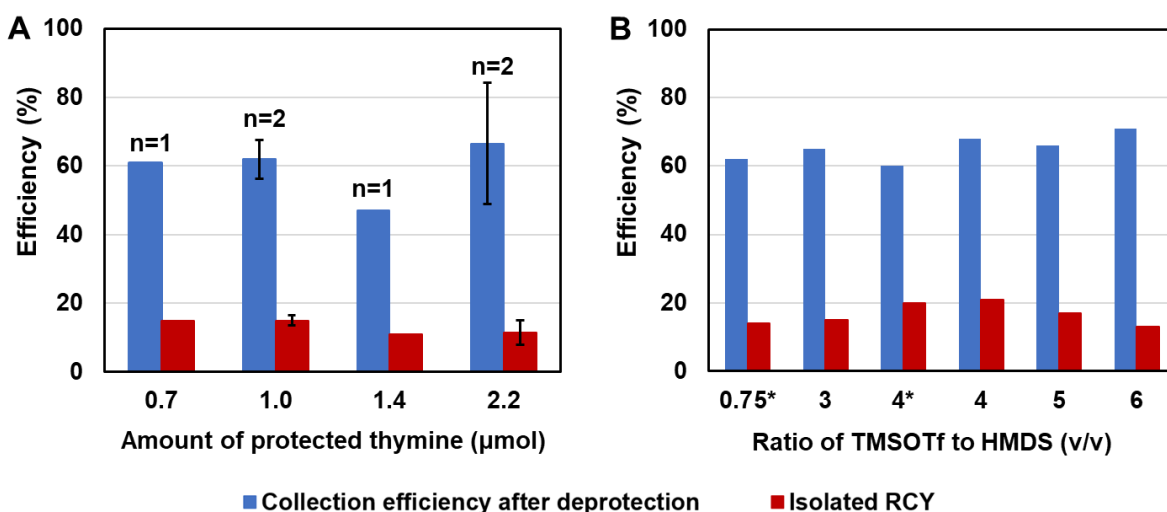


**Figure 4-4 Influence of coupling parameters on the performance (collection efficiency after deprotection and isolated RCY) of the microdroplet radiosynthesis.**

(A) Impact of amount of protected thymine. (B) Impact of ratio of TMSOTf to HMDS (v/v). All coupling reactions in A were performed with fixed ratio of TMSOTf to HMDS of 0.75, i.e., TMSOTf (4.5  $\mu\text{L}$ ) and HMDS (6  $\mu\text{L}$ ). All coupling reactions in B were conducted with 0.5  $\mu\text{mol}$  of protected thymine, except the ones indicated by an asterisk "\*" which were performed with 1  $\mu\text{mol}$  of protected thymine. n=1 for all conditions.

#### 4.3.3.3 Influence of ratio of TMSOTf to HMDS (v/v)

Next, we conducted additional investigation into the ratio of TMSOTf to HMDS (v/v). Detailed measurements and calculations can be found in **Figure 4-4B** and **Table 4-11**, respectively. Both collection efficiency (after deprotection) and isolated RCY exhibited gradual

increase as the ratio of TMSOTf to HMDS was elevated from 0.75 to 4. Beyond a ratio of 4, a slight decrease was observed in isolated RCY, although the collection efficiency (after deprotection) remained high. The optimal isolated RCY (21%, n = 1) was achieved when the ratio of TMSOTf to HMDS was 4. (In these studies, the amount of protected thymine was fixed at 0.5  $\mu\text{mol}$ .)

#### 4.3.3.4 Influence of coupling temperature

Next, we investigated the impact of coupling temperature (**Figure 4-5 (A-B)**). Detailed measurements and calculations can be found in **Table 4-12**. As the temperature increased from 85 °C to 130 °C, a sharp rise was observed in both collection efficiency (after deprotection) and isolated RCY. However, further temperature increases to 140°C and 150°C resulted in reduced performance. Simultaneously, the ratio of  $\beta$ - to  $\alpha$ -anomer exhibited a steep increase with rising coupling temperatures (ranging from 85 °C to 150°C), suggesting that the  $\alpha$ -anomer (i.e., side product) might be less stable than the  $\beta$ -anomer (i.e., [ $^{18}\text{F}$ ]FMAU) under elevated coupling temperatures.

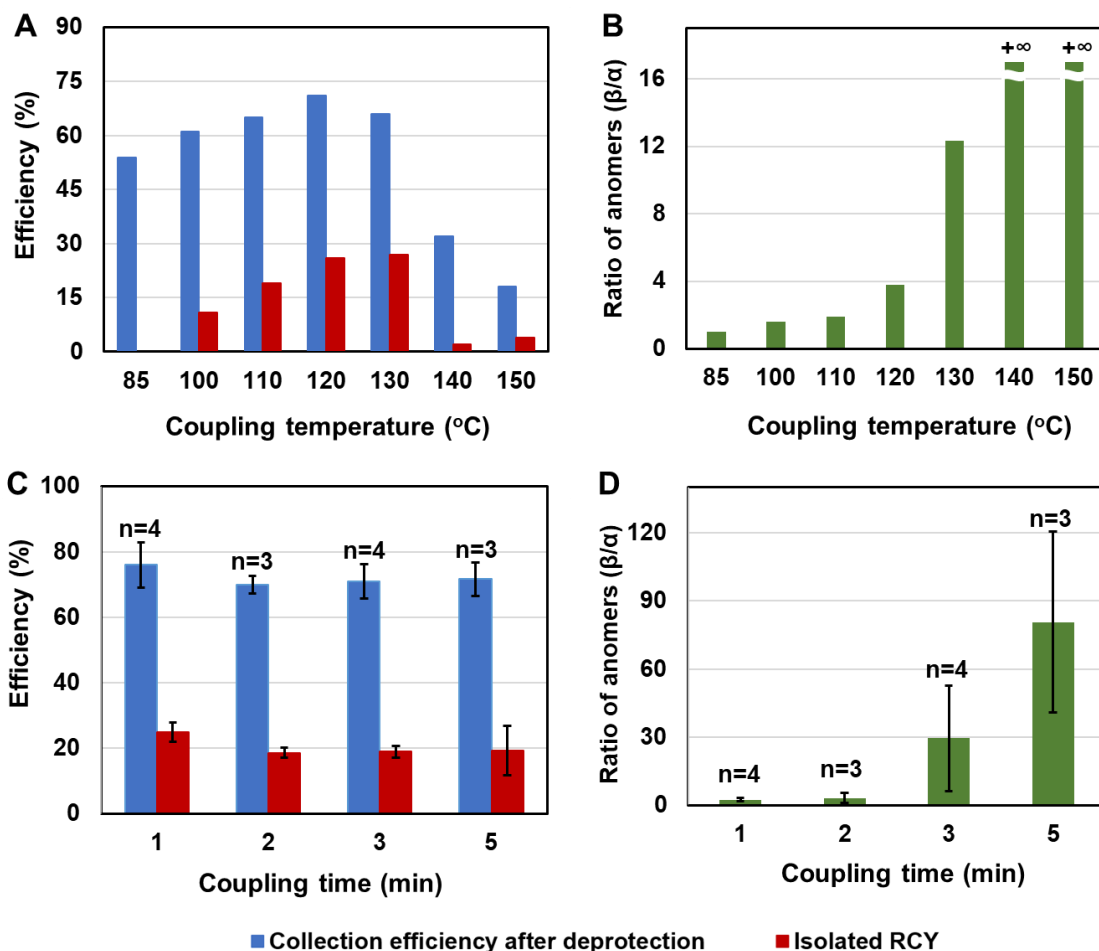


**Figure 4-5 Influence of coupling temperature (A,B) and coupling time (C,D) on the synthesis performance.**

The performance includes collection efficiency of crude product from the chip, isolated RCY, and ratio of  $\beta$ -anomer ( $[^{18}\text{F}]\text{FMAU}$ ) to  $\alpha$ -anomer (side product).

#### 4.3.3.5 Influence of coupling time

Based on the optimal coupling temperature (130 °C), a study of different coupling time was conducted (**Figure 4-5 (C-D)**). Detailed measurements and calculations can be found in **Table 4-13**. The synthesis results demonstrated that a 1 min coupling reaction sufficed for optimal results. Prolonged coupling processes have a detrimental impact on both collection efficiency (after deprotection) and isolated RCY, although the ratio of  $\beta$ - to  $\alpha$ -anomer improved significantly, presumably to degradation of both species (but much faster for the  $\alpha$ -anomer).

#### 4.3.4 Deprotection optimization

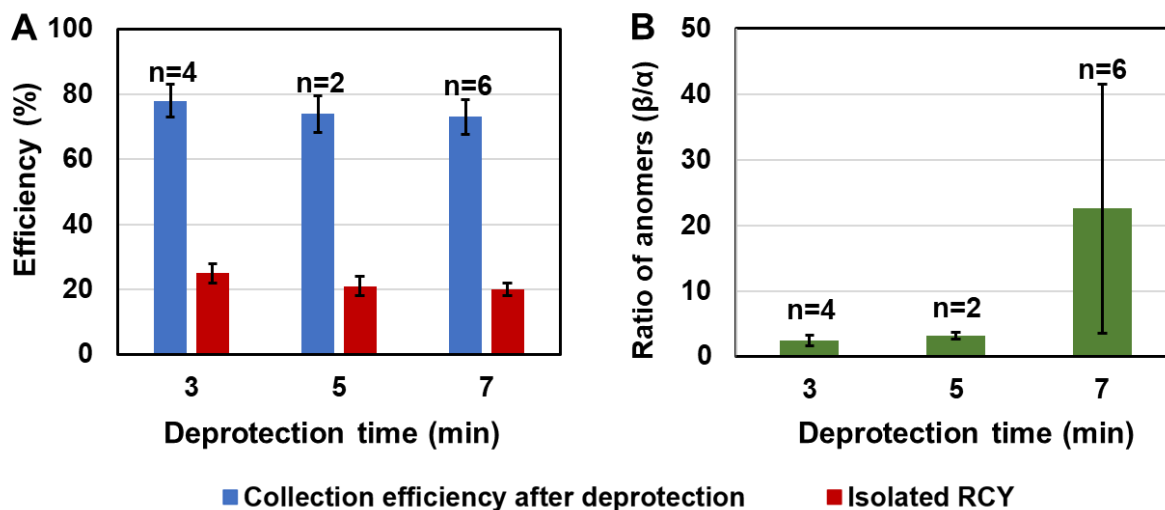


**Figure 4-6 Influence of deprotection time on the synthesis performance.**

It was measured by (A) collection efficiency of crude product and isolated RCY, and (B) the ratio of  $\beta$ -anomer ( $[^{18}\text{F}]\text{FMAU}$ ) to  $\alpha$ -anomer (side product).

Finally, we optimized the deprotection reaction. Begin with the initial conditions adapted from Li et al. (202), i.e. using 800  $\mu\text{L}$  of 25% KOMe in MeOH (wt.) and MeOH (v/v, 1:1) at 85  $^{\circ}\text{C}$  for 5 min, we further explored the influence of deprotection time, ranging from 3 to 7 min at 85  $^{\circ}\text{C}$  (Figure 4-6). Additionally, we opted for EtOH instead of MeOH as the co-solvent for the deprotectant solution due to its higher boiling point (EtOH: 78  $^{\circ}\text{C}$ ; MeOH: 65  $^{\circ}\text{C}$ ). Detailed measurements and calculations can be found in Table 4-14. The results indicated that 3 min was sufficient for the deprotection reaction, yielding the highest collection efficiency (78  $\pm$  5%, n = 4) and isolated RCY (25  $\pm$  3%, n = 4) (Table 4-1). Longer deprotection times led to inferior synthesis performance, although they provided a higher ratio of  $\beta$ - to  $\alpha$ -anomer, likely explainable by degradation as above.

**Table 4-1 Comparison of performance of microscale synthesis and the previously reported macroscale method.**

	Microscale synthesis	Macroscale synthesis
	This work (manual, n=4)	Li et al. (automated, n=4)
Starting activity (GBq)	0.22-1.22	7.4-11.1
Precursor used for fluorination ( $\mu\text{mol}$ )	0.5	16.8
Protected thymine used for coupling ( $\mu\text{mol}$ )	0.48	74.0
TMSOTf / HMDS used for coupling ( $\mu\text{L}$ )	4 / 1	150 / 200
Radiochemical yield (RCY, %), decay-corrected	$25 \pm 3$	$12 \pm 3$
Activity yield (%), non-decay-corrected	$19 \pm 2$	$\sim 5^a$
Radiochemical purity (RCP, %)	>99	>99
Ratio of anomers ( $\beta/\alpha$ )	$2.4 \pm 0.8$	1.5
Total production time (min)	$28 \pm 1$	$\sim 150$

<sup>a</sup>The value was calculated based on information in the literature.

#### 4.3.5 HPLC purification optimization

The preparation of [<sup>18</sup>F]FMAU involves multiple-step reactions with various reagents, resulting in increasing amounts of UV impurity, radioactive side products, and residual reagents as the synthesis progresses. To completely separate the product from these interferences, a lengthy radio-HPLC purification time (25-35 min) using a semi-prep column is required in macroscale production (201,202). In this study, we also explored the efficiency of three different analytical columns for purification, along with variations in the mobile phase, to achieve the final purified product ([<sup>18</sup>F]FMAU) within the shortest possible time. A detailed listing of column types, mobile phases, flow rates, retention times of [<sup>18</sup>F]FMAU, volumes of collected product from radio-HPLC, and individual radio-HPLC chromatograms of crude [<sup>18</sup>F]FMAU can be found in **Table 4-15** and **Figure 4-7**.

Initially, we performed purification on an analytical column, using the analytical condition (i.e., Luna C18, RP, 100 Å, 5  $\mu\text{m}$ , 250  $\times$  4.6 mm; mobile phase: 92% H<sub>2</sub>O, 8% MeCN, 0.1% TFA

(v/v); flow rate: 1 mL/min) as reference (202). Unfortunately, in **Test 1** (Table 4-15 and Figure 4-7), an impurity (visible in UV chromatograph) co-eluted with [<sup>18</sup>F]FMAU. In **Test 2**, we addressed this challenge by reducing the percentage of MeCN, replacing TFA with acetic acid (eliminating the risk of TFA residue for future product formulation), and employing a slightly higher flow rate (1.2 mL/min vs. 1 mL/min). Encouragingly, [<sup>18</sup>F]FMAU was successfully separated from the UV impurity, albeit with a 7.1 min longer retention time (18.1 min for **Test 2** vs. 11.0 min for **Test 1**). However, the volume of collected product increased from ~2 to ~5 mL compared to that in **Test 1**, requiring a much higher dilution volume in order to perform the SPE-formulation process (or requiring an extended time for an evaporation-based formulation process). In **Test 3**, utilizing PBS buffer (0.1 M concentration with pH = 6) instead of water and acetic acid yielded a slightly sharper product peak. However, the retention time remained long (19.1 min), and the collected volume was ~4 mL.

Given the late retention time of [<sup>18</sup>F]FMAU and the large volume of the purified product fraction when using a 250 mm long column, we investigated the use of a shorter one, a 100 mm long analytical column (Agilent Zorbax Eclipse Plus C18, 95 Å, 3.5 µm, 100 × 4.6 mm). With the same mobile phase as **Test 3**, the retention time of [<sup>18</sup>F]FMAU was significantly reduced to 5.9 min using the shorter column (**Test 4**) and the product peak became much sharper and required less volume (~1.2 mL) of collected fraction. In **Test 5**, to explore an injectable mobile phase for imaging studies and eliminate the need for an additional reformulation step, we replaced MeCN with EtOH. To our delight, a similar retention time of [<sup>18</sup>F]FMAU (6.0 min) was achieved, maintaining excellent separation efficiency. To ensure complete separation of the [<sup>18</sup>F]FMAU peak from the UV impurity, we slightly decreased the EtOH percentage from 5% to 4% in **Test 6**, optimizing the retention time to 8.6 minutes. Another column option with a length of 150 mm (Symmetry C18 Column, 100 Å, 3.5 µm, 150 × 4.6 mm) was considered as well (**Test 7**). Employing the same mobile phase as the optimal combination in **Test 6**, the retention time of [<sup>18</sup>F]FMAU was 3.5 min longer, along with a slightly higher volume of collected product (~1.8 mL).

Finally, we selected the radio-HPLC condition from **Test 6** as the optimal purification method for [<sup>18</sup>F]FMAU synthesis.

#### 4.3.6 Preliminary study of automated radiosynthesis

Considering that the coupling reagent TMSOTf used in the radiosynthesis process is highly corrosive to the majority of materials, it is incompatible with the internal wetted materials of the reagent dispensers (and their nozzles) integrated in our droplet-based synthesis module (78,133). Instead of using the piezoelectric dispensers for this reagent, we explored the use of tubing (HPFA, 0.03"), mounted in place of a dispenser, for remote delivery of the coupling stock solution to the droplet synthesizer and its subsequent coupling reaction (**Figure 4-8**). In particular, we loaded a pre-measured bolus of the reagent into a small v-vial (0.3 mL) connected to the tubing, and applied nitrogen pressure to push the bolus through the tubing and onto the chip when needed. When studying automated implementation of certain reactions, we typically added the reagents for prior steps manually, to minimize introducing too many new variables all at once.

In the initial attempt (**Test 1 in Table 4-16**), a volume of 12  $\mu$ L (slightly higher than the optimal volume 10  $\mu$ L to account for minor residual losses in the fluid path) of coupling stock solution was added into the transfer glass vial, and the loading process was initiated by applying 5 psi until all liquid was dispensed onto the chip. However, less than 4  $\mu$ L of the solution (roughly measured by a micropipette) reached the chip, and no coupling product was observed after the reaction. This could be attributed to the viscosity of HMDS and TMSOTf, leading to significant adherence on the tubing as a thin film before reaching the chip. Thus we tried diluted coupling reagents with MeCN in **Test 2 (Table 4-16)**, i.e., adding an additional 10  $\mu$ L of MeCN to the 12  $\mu$ L of coupling stock solution. We believed that the addition of MeCN could mitigate the residual losses of coupling reagents during dispensing, and a larger volume would ensure a more reliable delivery. The total 22  $\mu$ L of the combined solution was manually loaded onto the chip by a micropipette. We achieved good coupling performance with a high coupling percentage (71%, n = 1) and collection efficiency after coupling (81%, n = 1), resulting in crude coupling product of

58% (n = 1). When we attempted it automatically (i.e., loading 22  $\mu$ L of diluted coupling solution by applying 5 psi) in **Test 3 (Table 4-16)**, we observed similar performance. Although the crude coupling product (51% vs. 58% for the manual method) was a slightly lower than the manual method, along with a reduced coupling percentage (64% vs. 71% for the manual method) and collection efficiency after coupling (79% vs. 81% for the manual method), further optimization efforts in the automated approach could be focused on a more precise loading volume control.

This approach for loading TMSOTf, using vials of pre-measured reagents and tubing, could be used in general for loading other corrosive reagents or potentially all reagents. In the future, we will optimize the tubing material/geometry, loading protocol etc. for each reagent, and potentially this approach form the basis for a disposable reagent loading system and full automation of droplet radiochemistry.

#### **4.4 Conclusions**

In this work, we employed a novel droplet-based high-throughput technique to perform a comprehensive optimization study of a three-step, one-spot radiosynthesis for the nucleoside analog PET tracer [ $^{18}$ F]FMAU.

Under optimal conditions (**Table 4-1**), the microdroplet-based radiosynthesis of [ $^{18}$ F]FMAU requires >33x less sugar precursor and 154x less protected thymine (used for coupling reaction) compared to conventional methods. The droplet format facilitates an exceptionally rapid, simple, and efficient preparation of [ $^{18}$ F]FMAU with high radiochemical yield and activity yield in just 28 min (compared to ~150 min needed for conventional radiosynthesis approach). The Teflon-coated microfluidic chip reactors exhibited excellent tolerance to highly corrosive reagents, and the microliter scale substantially minimizes the use of hazardous chemicals (e.g. TMSOTf), enhancing safety and environmental friendliness.

Continued efforts are focused on automating the current microdroplet-based synthesis of [ $^{18}$ F]FMAU, with the aim of scaling up to accommodate multiple patient doses.



## 4.5 Appendix

### 4.5.1 Initial condition of [<sup>18</sup>F]FMAU synthesis on droplet reactors

**Table 4-2 Preliminary droplet radiosynthesis conditions for [<sup>18</sup>F]FMAU.**

The microscale conditions were adapted from Li et al.'s macroscale conditions (202), in which the fluorination reaction was performed with: K<sub>222</sub> (39.8 μmol), K<sub>2</sub>CO<sub>3</sub> (54.3 μmol), and 2-O-(trifluoromethanesulfonyl)-1,3,5-tri-O-benzoyl-α-D-ribofuranose (precursor, 16.0 μmol) in 800 μL of MeCN at 85 °C for 20 min, the coupling reaction was performed with: O,O'-bis-(trimethylsilyl)thymine (protected thymine, 74.0 μmol), 200 μL of HMDS, and 150 μL of TMSOTf mixed with 300 μL of 1,4-dioxane at 85 °C for 60 min, and the deprotection reaction was performed at 85 °C for 5 min. Microscale conditions used the same reagent ratios as the macroscale conditions. The fluorination reaction was reduced from 800 μL to 8 μL, and coupling reaction was reduced from 650 μL to 6.5 μL, and all reagent amounts were reduced by 100x.

	<b>Adapted microscale condition (n = 1)</b>
PTC and base composition (μmol)	K <sub>222</sub> (0.40), K <sub>2</sub> CO <sub>3</sub> (0.54)
Precursor 1 (μmol)	0.16
Fluorination solvent (8 μL)	MeCN
Fluorination temperature and time	85°C, 4 min
Protected thymine (μmol)	0.74
Coupling reagent (μL)	HMDS (2), TMSOTf (1.5)
Coupling solvent (μL)	1,4-dioxane (3)
Coupling temperature and time	85°C, 5 min
<b>Performance</b>	
Starting activity (MBq)	14.5
Fluorination conversion (%)	61
Coupling percentage (%)	20
Collection efficiency after coupling (%)	13
Crude coupling product (%)	2.6

## 4.5.2 Optimization of fluorination reaction

### 4.5.2.1 Preliminary optimization of solvent type and temperature

**Table 4-3 Impact of solvent and temperature on the fluorination performance in a microdroplet reactor.**

Solvent <sup>a</sup>	Fluorination temperature (°C)	Fluorination conversion (%)	Collection efficiency after fluorination (%)	Crude fluorination yield (%)
MeCN	85	30 ± 1	40 ± 3	12 ± 0
NMP	150	77 ± 2	39 ± 1	30 ± 2
DMF	150	50 ± 13	29 ± 3	14 ± 4
thexyl alcohol/DMSO (4:1, v/v)	100	82 ± 3	30 ± 0	24 ± 1
thexyl alcohol/NMP (4:1, v/v)	100	80 ± 3	41 ± 0	33 ± 1

<sup>a</sup>All reactions were performed with K<sub>2</sub>CO<sub>3</sub> (0.176 μmol) and K<sub>222</sub> (0.312 μmol), and 0.168 μmol of precursor in 10 μL of solvent at specific temperature for 3 min (n = 4 replicates each condition). Chip collection solvent: 4 x 20 μL of MeCN and H<sub>2</sub>O (95:5, v/v). The radio-TLC was developed in hexane and ethyl acetate (1:1, v/v).

### 4.5.2.2 Influence of type of phase transfer catalyst (PTC)/base

**Table 4-4 Impact of PTC/base on the fluorination performance in a microdroplet reactor.**

Type of PTC/base <sup>a</sup>	Fluorination conversion (%)	Collection efficiency after fluorination (%)	Crude fluorination yield (%)
TEAOTf	0	26 ± 3	0
TEAHCO <sub>3</sub>	80 ± 0	36 ± 3	29 ± 2
TBACIO <sub>4</sub> <sup>b</sup>	N.M.	N.M.	N.M.
TBAOTf <sup>b</sup>	N.M.	N.M.	N.M.
K <sub>222</sub> /K <sub>2</sub> CO <sub>3</sub>	80 ± 3	41 ± 0	33 ± 1
TBAHCO <sub>3</sub>	86 ± 8	46 ± 1	39 ± 3

<sup>a</sup>All reactions were performed with 0.176 μmol of PTC or K<sub>222</sub> (0.312 μmol)/K<sub>2</sub>CO<sub>3</sub> (0.176 μmol) for the [<sup>18</sup>F]fluoride drying step, and 0.16 μmol of precursor in 10 μL of thexyl alcohol/NMP (4:1, v/v) at 100 °C for 3 min (n = 2 replicates each condition). Chip collection solvent: 4 x 20 μL of hexane and ethyl acetate (1:1, v/v). The radio-TLC was developed in the same solvent system. <sup>b</sup>After drying with the PTC, only ~27% of activity remained on the microdroplet reactor, so subsequent radiofluorination was not performed. N.M. = Not measured.

#### 4.5.2.3 Preliminary optimization of fluorination temperature and time

**Table 4-5 Impact of temperature and time on the fluorination performance in a microdroplet reactor.**

Temperature (°C) <sup>a</sup>	Fluorination conversion (%)	Collection efficiency after fluorination (%)	Crude fluorination yield (%)
70	71 ± 4	59 ± 0	42 ± 3
75 <sup>b</sup>	57 ± 18	58 ± 4	33 ± 9
80	87 ± 1	50 ± 1	43 ± 0
80 <sup>b</sup>	81 ± 3	49 ± 0	81 ± 3
90	88 ± 1	44 ± 1	38 ± 1
100	92 ± 1	30 ± 1	28 ± 1

<sup>a</sup>All reactions were performed with 0.176 μmol of TBAHCO<sub>3</sub> and 0.16 μmol of precursor in 10 μL of hexyl alcohol/NMP (4:1, v/v) at specific temperature for 3 min (n = 4 replicates each condition). Chip collection solvent: 4 x 20 μL of hexane and ethyl acetate (1:1, v/v). The radio-TLC was developed in the same solvent system. <sup>b</sup>The reaction time was 5 min.

#### 4.5.2.4 Preliminary optimization of precursor amount

**Table 4-6 Impact of precursor amount on the fluorination performance in a microdroplet reactor.**

Precursor amount (μmol) <sup>a</sup>	Fluorination conversion (%)	Collection efficiency after fluorination (%)	Crude fluorination yield (%)
0.16	79 ± 1	51 ± 0	40 ± 1
0.16 <sup>b</sup>	72 ± 3	51 ± 2	37 ± 0
0.25	84 ± 1	60 ± 1	50 ± 0
0.25 <sup>b</sup>	87 ± 1	57 ± 1	49 ± 0
0.34	90 ± 1	61 ± 2	55 ± 1
0.34 <sup>b</sup>	88 ± 1	57 ± 1	50 ± 0
0.50	90 ± 4	64 ± 4	57 ± 6
0.50 <sup>b</sup>	90 ± 0	65 ± 1	59 ± 1

<sup>a</sup>All reactions were performed with desired amount of precursor and 0.176 μmol of TBAHCO<sub>3</sub> in 10 μL of hexyl alcohol/NMP (4:1, v/v) at 80 °C for 3 min (n=2 replicates each condition) unless other claim. Chip collection solvent: 4 x 20 μL of hexane and ethyl acetate (1:1, v/v). The radio-TLC was developed in the same solvent system. <sup>b</sup>The ratio of precursor to base was 1:1.1, i.e., the amount of TBAHCO<sub>3</sub> was matched with the amount of precursor based on the fixed ratio.

#### 4.5.2.5 Re-optimization of solvent type

**Table 4-7 Impact of fluorination solvent on the fluorination and coupling performance in a microdroplet reactor.**

Solvent <sup>a</sup>	Fluorination conversion (%)	Activity on chip after fluorination (%)	Crude fluorination yield (%)	Coupling percentage (%)	Collection efficiency after coupling (%)	Crude coupling product (%)
Thexyl alcohol/NMP (4:1, v/v)	91 ± 0	60	55 ± 1	0	29 ± 5	0
MeCN	72 ± 3	37	27 ± 1	72 ± 5	14 ± 2	10 ± 2
Thexyl alcohol/MeCN (1:1, v/v)	97 ± 0	55	53 ± 0	25 ± 2	29 ± 1	7 ± 1
MeCN: 1,4-dioxane (1:1, v/v)	87 ± 2	55	48 ± 1	57 ± 1	35 ± 2	20 ± 1
1,4-dioxane	87 ± 6	92	80 ± 6	48 ± 4	50 ± 4	24 ± 2
1,4-dioxane <sup>b</sup>	87 ± 6	92	80 ± 6	73 ± 0	46 ± 1	33 ± 1

<sup>a</sup>All fluorination reactions were performed with 0.176 μmol of TBAHCO<sub>3</sub> and 0.5 μmol of precursor in 10 μL of solvent at 80 °C for 3 min (n = 2 replicates each condition). After fluorination, the remaining activity on microdroplet chips were measured by dose calibrator. To measure the fluorination conversion, 0.1 μL of fluorinated intermediate sample was taken after adding 5 μL of 1,4-dioxane and mixing it well with the mixture in reaction sites. Coupling reaction was performed with protected thymine (0.6 mg, 2.2 μmol), HMDS (6 μL, 28.6 μmol), TMSOTf (4.5 μL, 24.8 μmol) and 1,4-dioxane (9 μL) at 85 °C, 5 min. Chip collection solvent: 4 x 20 μL of hexane and ethyl acetate (1:1, v/v). The radio-TLC was developed in the same solvent system. <sup>b</sup>The coupling reaction was performed at 100 °C instead of 85°C for 5 min.

#### 4.5.2.6 Re-optimization of temperature

**Table 4-8 Impact of fluorination temperature on the fluorination performance in a microdroplet reactor.**

Fluorination temperature (°C) <sup>a</sup>	Fluorination conversion (%)	Activity on chip after fluorination (%)	Crude fluorination yield (%)
80	87 ± 6	90	78 ± 5
90	89 ± 5	95	85 ± 5
100	95 ± 2	92	87 ± 2

<sup>a</sup>All fluorination reactions were performed with 0.176 μmol of TBAHCO<sub>3</sub> and 0.5 μmol of precursor in 10 μL of 1,4-dioxane at specific temperature for 3 min (n = 2 replicates each condition). Chip collection solvent: 4 x 20 μL of hexane and ethyl acetate (1:1, v/v). The radio-TLC was developed in the same solvent system.

#### 4.5.2.7 Re-optimization of precursor amount

Table 4-9 Impact of precursor amount on the fluorination performance in a microdroplet reactor.

Amount of precursor ( $\mu\text{mol}$ ) <sup>a</sup>	Fluorination conversion (%)	Activity on chip after fluorination (%)	Crude fluorination yield (%)
0.08	91 $\pm$ 1	85	77 $\pm$ 0
0.17	91 $\pm$ 4	86	80 $\pm$ 6
0.25	92 $\pm$ 3	83	77 $\pm$ 5
0.34	90 $\pm$ 3	85	74 $\pm$ 10
0.50	94 $\pm$ 4	93	87 $\pm$ 5

<sup>a</sup>All fluorination reactions were performed with 0.176  $\mu\text{mol}$  of TBAHCO<sub>3</sub> and precursor in 10  $\mu\text{L}$  of 1,4-dioxane at 100 °C for 3 min (n=4 replicates each condition). Chip collection solvent: 4 x 20  $\mu\text{L}$  of hexane and ethyl acetate (1:1, v/v). The radio-TLC was developed in the same solvent system.

#### 4.5.3 Optimization of coupling reaction

##### 4.5.3.1 Influence of amount of protected thymine

Table 4-10 Impact of amount of protected thymine on the performance of the droplet radiosynthesis of [<sup>18</sup>F]FMAU.

Amount of protected thymine ( $\mu\text{mol}$ ) <sup>a</sup>	Number of repeats (n)	Collection efficiency after deprotection (%)	Isolated RCY of [ <sup>18</sup> F]FMAU (%) <sup>b</sup>
0.7	1	61	15
1.0	2	62 $\pm$ 6	15 $\pm$ 1
1.4	1	47	11
2.2	2	67 $\pm$ 18	12 $\pm$ 4

<sup>a</sup>All fluorination reactions were performed with 0.176  $\mu\text{mol}$  of TBAHCO<sub>3</sub> and 0.5  $\mu\text{mol}$  of precursor in 10  $\mu\text{L}$  of 1,4-dioxane at 100 °C for 3 min. Coupling reaction was performed with protected thymine, HMDS (6  $\mu\text{L}$ , 28.6  $\mu\text{mol}$ ), TMSOTf (4.5  $\mu\text{L}$ , 24.8  $\mu\text{mol}$ ) and 1,4-dioxane (9  $\mu\text{L}$ ) at 100 °C, 5 min. Deprotection reaction was performed with 20  $\mu\text{L}$  of 25% KOMe in MeOH at room temperature for 5 min. The crude product was collected with 20  $\mu\text{L}$  x 4 of HPLC purification mobile. <sup>b</sup>Isolated RCY was obtained by radio-HPLC isolation and is calculated by dividing activity of collected pure product by initial activity and correcting for decay.

##### 4.5.3.2 Influence of ratio of TMSOTf to HMDS (v/v)

**Table 4-11. Impact of ratio of TMSOTf to HMDS (v/v) on the performance of the droplet radiosynthesis of [<sup>18</sup>F]FMAU.**

Ratio of TMSOTf to HMDS (v/v) <sup>a</sup>	TMSOTf (μL)	HMDS (μL)	Collection efficiency after deprotection (%)	Isolated RCY of [ <sup>18</sup> F]FMAU (%) <sup>c</sup>
0.75 <sup>b</sup>	4.5	6	62	14
3	3	1	65	15
4 <sup>b</sup>	8	2	60	20
4	4	1	68	21
5	5	1	66	17
6	6	1	71	13

<sup>a</sup>All fluorination reactions were performed with 0.176 μmol of TBAHCO<sub>3</sub> and 0.5 μmol of precursor in 10 μL of 1,4-dioxane at 100 °C for 3 min. Coupling reaction was performed with 0.5 μmol of protected thymine, HMDS, TMSOTf, and 1,4-dioxane (5 uL) at 100 °C for 5 min. Deprotection reaction was performed with 30 uL of 25% KOMe in MeOH and EtOH (v/v, 2:1), 85 °C for 3 min. The crude product was collected with 20 μL x 4 of HPLC purification mobile (n=1 replicates each condition). <sup>b</sup>1 μmol of protected thymine was used for coupling reaction. <sup>c</sup>Isolated RCY was obtained by radio-HPLC isolation and is calculated by dividing activity of collected pure product by initial activity and correcting for decay.

#### 4.5.3.3 Influence of coupling temperature

**Table 4-12 Impact of coupling temperature on the performance of the droplet radiosynthesis of [<sup>18</sup>F]FMAU.**

Coupling temperature (°C) <sup>a</sup>	Collection efficiency after deprotection (%)	Isolated RCY of [ <sup>18</sup> F]FMAU (%) <sup>b</sup>	Ratio of anomers (β/α)
85	54	0	1.0
100	61	11	1.6
110	65	19	1.9
120	71	26	3.8
130	66	27	12.3
140	32	2	Very high <sup>c</sup>
150	18	4	+∞-Very high <sup>c</sup>

<sup>a</sup>All fluorination reactions were performed with 0.176 μmol of TBAHCO<sub>3</sub> and 0.5 μmol of precursor in 10 μL of 1,4-dioxane at 100 °C for 3 min. Coupling reaction was performed with 0.5 μmol of protected thymine, HMDS (1 μL), TMSOTf (4 μL), and 1,4-dioxane (5 uL) at specific temperature for 5 min. Deprotection reaction was performed with 30 uL of 25% KOMe in MeOH and EtOH (v/v, 2:1), 85 °C for 3 min. The crude product was collected with 20 μL x 4 of HPLC purification mobile. <sup>b</sup>Isolated RCY was obtained by radio-HPLC isolation and is calculated by dividing activity of collected pure product by initial activity and correcting for decay. <sup>c</sup>α-Anomer was zero, therefore the ratio of β- to α-anomer could not be calculated.

#### 4.5.3.4 Influence of coupling time

**Table 4-13 Impact of coupling time on the performance of the droplet radiosynthesis of [<sup>18</sup>F]FMAU.**

Coupling time (min) <sup>a</sup>	Repeat number (n)	Collection efficiency after deprotection (%)	Isolated RCY of [ <sup>18</sup> F]FMAU (%) <sup>b</sup>	Ratio of anomers (β/α)
1	4	78 ± 5	25 ± 3	2.4 ± 0.8
2	3	70 ± 3	19 ± 2	3.2 ± 2.3
3	4	71 ± 5	19 ± 2	29.5 ± 23.3
5	3	72 ± 5	19 ± 8	80.7 ± 39.8

<sup>a</sup>All fluorination reactions were performed with 0.176 μmol of TBAHCO<sub>3</sub> and 0.5 μmol of precursor in 10 μL of 1,4-dioxane at 100 °C for 3 min. Coupling reaction was performed with 0.5 μmol of protected thymine, HMDS (1 μL), TMSOTf (4 μL), and 1,4-dioxane (5 uL) at 130°C. Deprotection reaction was performed with 30 uL of 25% KOMe in MeOH and EtOH (v/v, 2:1), 85 °C for 3 min. The crude product was collected with 20 μL x 4 of HPLC purification mobile.

<sup>b</sup>Isolated RCY was obtained by radio-HPLC isolation and is calculated by dividing activity of collected pure product by initial activity and correcting for decay.

#### 4.5.4 Optimization of deprotection reaction

##### 4.5.4.1 Influence of deprotection time

**Table 4-14 Impact of deprotection time on the performance of the droplet radiosynthesis of [<sup>18</sup>F]FMAU.**

Deprotection time (min) <sup>a</sup>	Repeat number (n)	Collection efficiency after deprotection (%)	Isolated RCY of [ <sup>18</sup> F]FMAU (%) <sup>b</sup>	Ratio of anomers (β/α)
3	4	78 ± 5	25 ± 3	2.4 ± 0.8
5	2	74 ± 6	21 ± 3	3.2 ± 0.5
7	6	73 ± 5	20 ± 2	22.5 ± 19.0

<sup>a</sup>All fluorination reactions were performed with 0.176 μmol of TBAHCO<sub>3</sub> and 0.5 μmol of precursor in 10 μL of 1,4-dioxane at 100 °C for 3 min. Coupling reaction was performed with 0.5 μmol of protected thymine, HMDS (1 μL), TMSOTf (4 μL), and 1,4-dioxane (5 uL) at 130 °C for 1 min. Deprotection reaction was performed with 30 uL of 25% KOMe in MeOH and EtOH (v/v, 2:1) at 85 °C. The crude product was collected with 20 μL x 4 of HPLC purification mobile. <sup>b</sup>Isolated RCY was obtained by radio-HPLC isolation and is calculated by dividing activity of collected pure product by initial activity and correcting for decay.

#### 4.5.5 Optimization of radio-HPLC purification method

**Table 4-15 Summary of results of radio-HPLC purification optimization.**

Test	Column type	Mobile phase <sup>a</sup>	Flow rate (mL/min)	Retention time of [ <sup>18</sup> F]FMAU	Volume of collected product (mL)
1	Phenomenex Luna C18 (2), RP, 100 Å, 5 µm, 250x4.6 mm	92% H <sub>2</sub> O, 8% MeCN, 0.1% TFA (v/v)	1.0	11.0	~2
2		Gradient: • 0-20 min: 95% H <sub>2</sub> O, 5% MeCN, 0.1% acetic acid • 20-21 min: changed to 100% MeCN • 21-30 min: 100% MeCN	1.2	18.1	~5
3		Gradient: • 0-20 min: 95% PBS buffer, 5% MeCN • 20-21 min: changed to 30% PBS buffer and 70% MeCN • 21-30 min: PBS 30% buffer and 70% MeCN	1.2	19.1	~4
4	Agilent ZORBAX Eclipse Plus C18, 95 Å, 3.5 µm, 100x4.6 mm	Gradient: • 0-13 min: 95% PBS buffer, 5% MeCN • 13-14 min: changed to 30% PBS buffer and 70% MeCN • 14-20 min: PBS 30% buffer and 70% MeCN	1.2	5.9	~1.2
5		Gradient: • 0-13 min: 95% PBS buffer, 5% EtOH • 13-14 min: changed to 30% PBS buffer and 70% MeCN • 14-20 min: PBS 30% buffer and 70% MeCN	1.2	6.0	~1.2
6		Gradient: • 0-13 min: 96% PBS buffer, 4% EtOH • 13-14 min: changed to 15% PBS buffer and 85% MeCN • 14-20 min: PBS 15% buffer and 85% MeCN	1.2	8.6	~1.2
7	Waters Symmetry C18 Column, 100 Å, 3.5 µm, 150x4.6 mm	Gradient: • 0-13 min: 96% PBS buffer, 4% EtOH • 13-14 min: changed to 15% PBS buffer and 85% MeCN • 14-20 min: PBS 15% buffer and 85% MeCN	1.2	12.1	~1.8

<sup>a</sup>The PBS buffer was prepared at 0.1 M concentration with pH = 6.



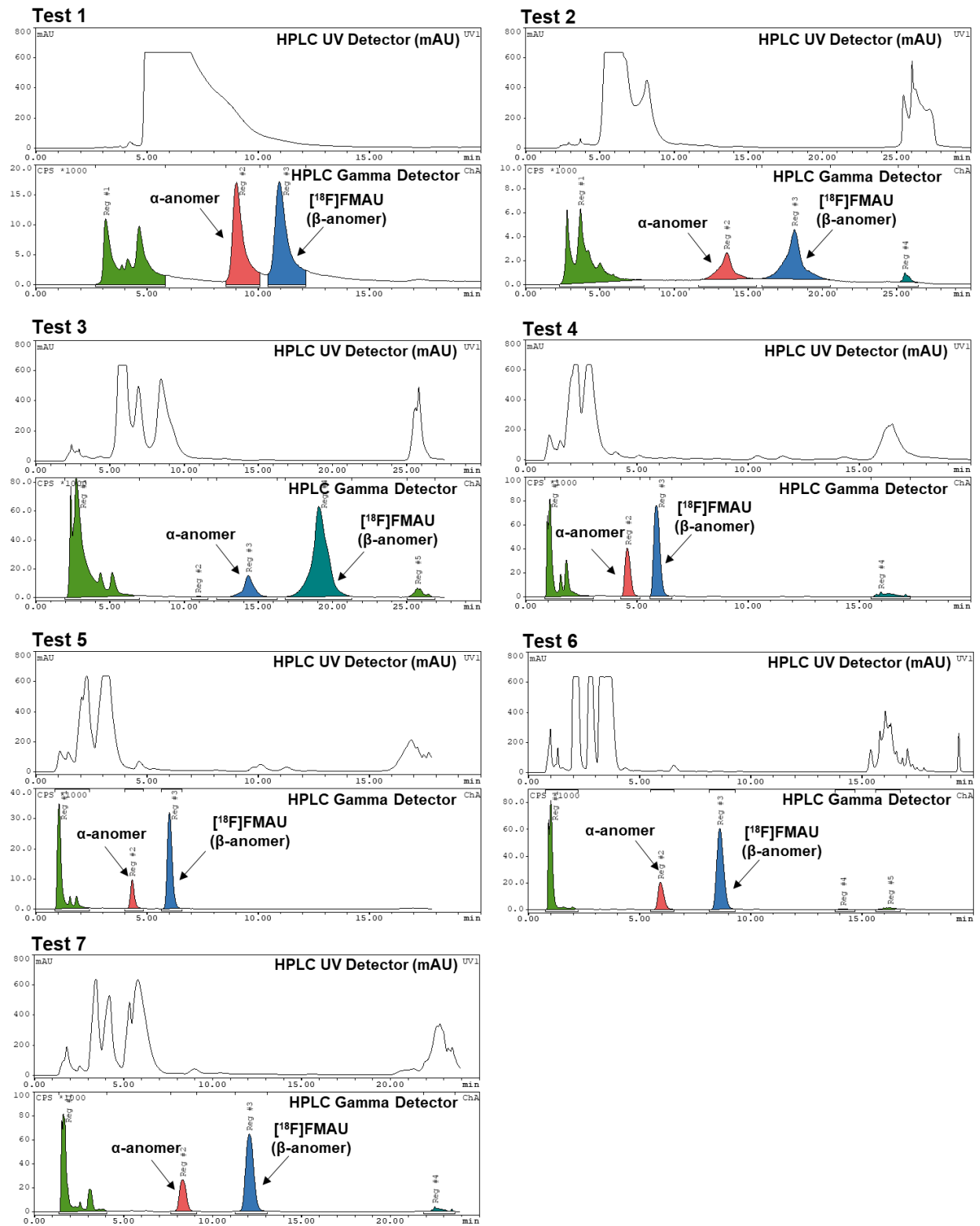


Figure 4-7 Radio-HPLC chromatogram of crude  $[^{18}\text{F}]$ FMAU (upper: UV-254 nm and bottom:  $\gamma$ -ray) from microdroplet radiosynthesis by using varying purification methods.

## 4.5.6 Preliminary tests of automation

**Table 4-16 Summary of results of automated tests of the droplet radiosynthesis.**

Synthesis parameter	Test <sup>a</sup>		
	1	2	3
Starting activity (MBq)	96	93	93
Loading approach	Automated	Manual	Automated
Loading protocol for coupling reagent	12 $\mu$ L of stock	12 $\mu$ L of stock + 10 $\mu$ L of MeCN	
Collection efficiency after coupling (%)	9	81	79
Activity residue on tip after collection (%)	0	1	0
Activity residue on Chip after collection (%)	2	1	1
Coupling percentage (%)	-	71	64
Crude coupling product (%)	-	58	51

<sup>a</sup>Fluorination solution was loaded manually by pipetting on chip and all fluorination was performed with 0.176  $\mu$ mol of TBAHCO<sub>3</sub> and 0.5  $\mu$ mol of precursor in 10  $\mu$ L of 1,4-dioxane at 100 °C for 3 min. Coupling stock solution were loaded manually by pipetting or automatically by dispenser, and each 10  $\mu$ L of coupling stock solution included 0.5  $\mu$ mol of protected thymine, HMDS (1  $\mu$ L), TMSOTf (4  $\mu$ L), and 1,4-dioxane (5  $\mu$ L). To ensure the sufficient volume of coupling stock solution was loaded on chip, 12  $\mu$ L of stock solution was used for dispensing. All coupling reaction was at 130 °C for 1 min. Chip collection solvent: 4 x 20  $\mu$ L of hexane and ethyl acetate (1:1, v/v). The radio-TLC was developed in the same solvent system.

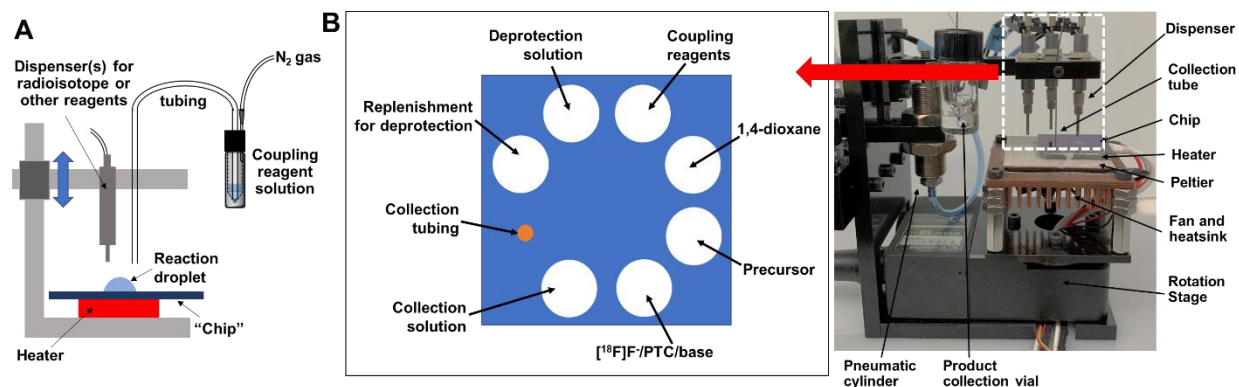


**Figure 4-8 Automated microdroplet radiosynthesizer setup for [<sup>18</sup>F]FMAU synthesis.**

(A) Diagram of “One-shot” tubing system for remote delivery of the coupling reagents and piezoelectric dispensers for radioisotope or other reagents. (B) Configuration of automated microdroplet system for preparing [<sup>18</sup>F]FMAU. (Left) Top view showing positions of reagent dispensers and collection tubing above the chip. (Right) Photograph of the droplet synthesizer.

#### 4.5.7 Example HPLC chromatograms

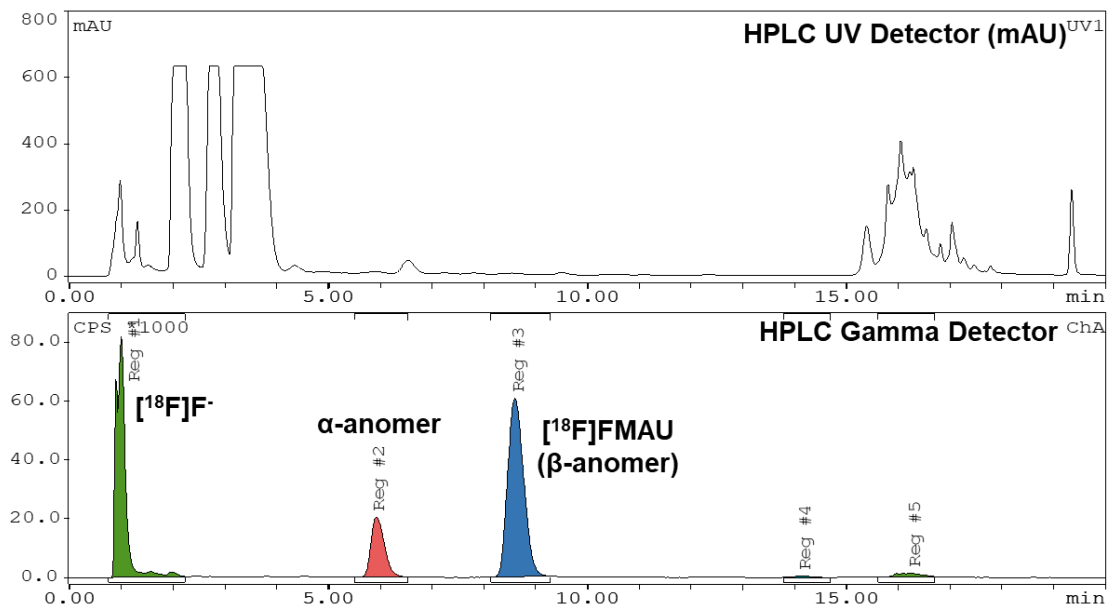


**Figure 4-9 Example of radio-HPLC chromatogram of crude [<sup>18</sup>F]FMAU (upper: UV-254 nm and bottom: γ-ray) from microdroplet radiosynthesis obtained during purification.**

The purification mobile phase was 96% PBS buffer and 4% EtOH (v/v) for the first 13 min, then it was changed to 15% PBS buffer and 85% MeCN (v/v) in 1 min followed by another 6 min under the same mobile phase. Under this condition, the retention time of [<sup>18</sup>F]FMAU (β-anomer) was 8.6 min and a α-anomer was 5.9 min.

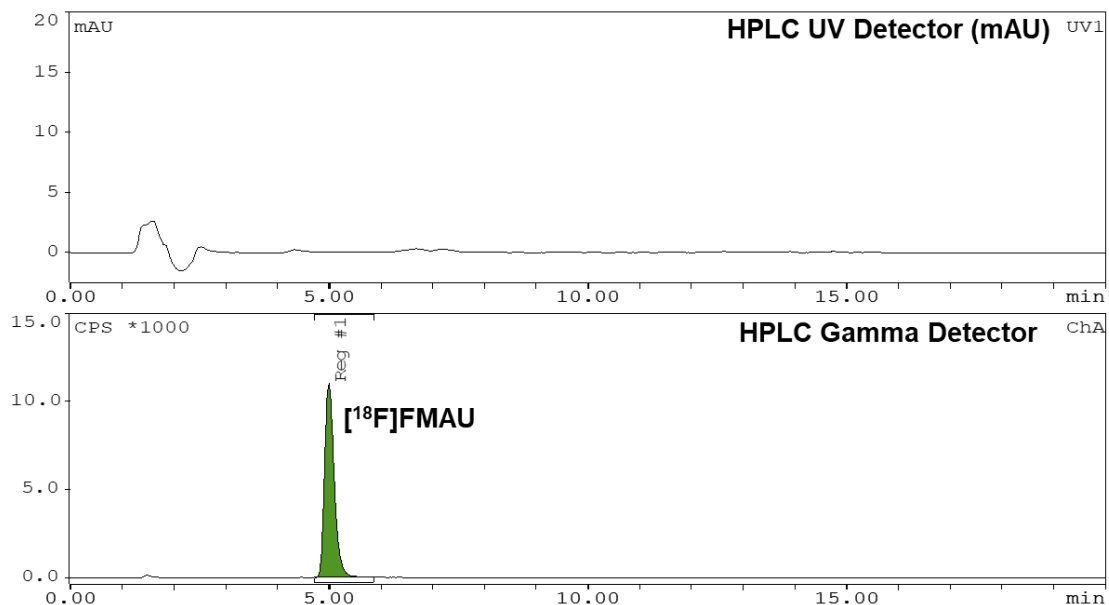


**Figure 4-10 Example radio-HPLC analysis of purified [<sup>18</sup>F]FMAU produced in a droplet reaction. The analytical mobile phase was 95% DI water and 5% MeCN (v/v) with 0.1% TFA. Under this condition, the retention time of [<sup>18</sup>F]FMAU (β-anomer) was 5.0 min.**

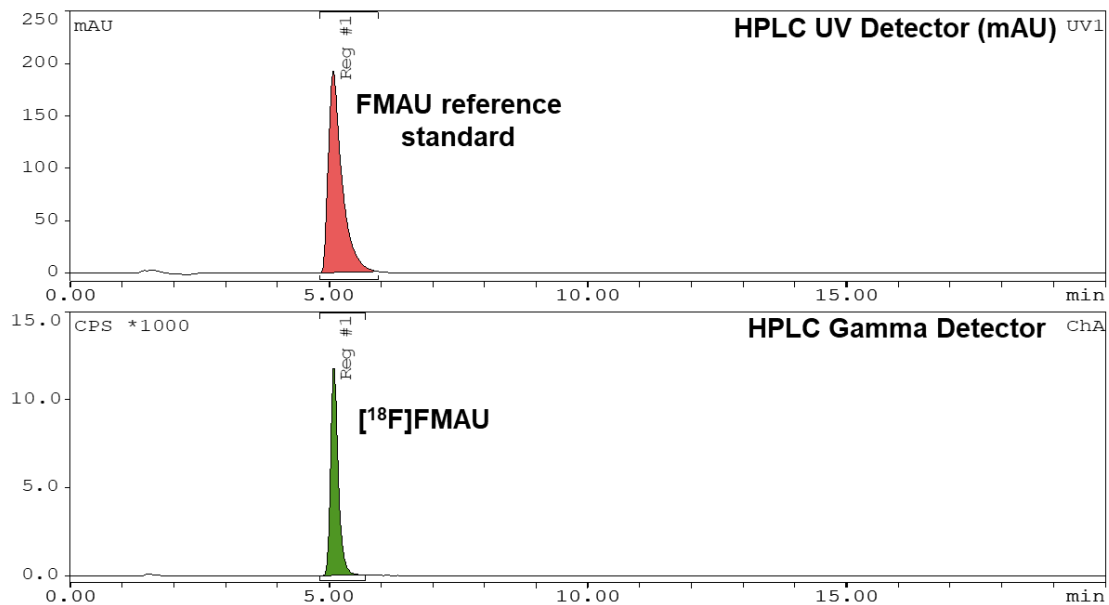


**Figure 4-11 Example radio-HPLC analysis of co-injection of purified [<sup>18</sup>F]FMAU produced in a droplet reaction and reference standard. The analytical mobile phase was 95% DI water and 5% MeCN (v/v) with 0.1% TFA.**

# Chapter 5: Robotic platform for high-throughput radiosynthesis and optimization

## 5.1 Introduction

Positron emission tomography (PET) is a non-invasive imaging modality that uses trace amounts of radiolabeled compounds to image specific biochemical processes within living subjects with high sensitivity and specificity(209, 18). To investigate different biological processes, thousands of different radiotracers have been developed(210,211), and as new biological targets are discovered, there is ongoing need to develop tracers to image these targets. Currently, it can take many years between new target discovery and the development of a useful imaging tracer, and even longer for translation into the clinic. Though there are several factors in this timeline, the difficulty in synthesizing novel radiolabeled compounds with sufficient reliability and yield at each stage of development is a significant bottleneck.

The majority of available radiosynthesizers are designed to safely and automatically perform routine large-scale batch production of radiotracers(212,213). Several characteristics of these systems are poorly suited to early stage radiotracer development and synthesis optimization. For example, the need to wait for decay of residual radioactivity within the system between experiments (e.g. overnight for F-18) severely limits experimental throughput. Each experiment may provide a limited amount of data, unless manual interventions are performed to make measurements of radioactivity or radiochemical composition at multiple stages throughout the synthesis process. Additionally, the typical reactor size requires relatively large quantities of expensive precursors (e.g., 1-10 mg for 1 mL reaction volume) per experiment. Finally the high value of these systems in service of clinical production often limits their availability for research purposes.

A variety of approaches are being developed to overcome these limitations. One strategy is to try to reduce the number of experiments needed to achieve the desired optimization goals.

Using a design of experiments (DoE) approach, which helps to identify the most critical reaction parameters (factors), Bowden *et al.* showed more than 2x improvement in experimental efficiency for optimization of copper-mediated radiofluorination of arylstannanes(214). Machine learning approaches are also being developed to enable synthesis optimization through reduced numbers of experiments(215,216).

Another strategy is to modify radiochemistry hardware or experimental approaches in order to increase throughput and decrease experimental costs. For example, Zhang *et al.* leveraged the high sensitivity of LC-MS/MS to detect ultra-low amounts of product when performing reactions in conventional radiosynthesizers using nanomolar concentrations of non-radioactive isotopes (e.g. [<sup>19</sup>F]fluoride instead of [<sup>18</sup>F]fluoride)(217). The low concentrations simulate the typical concentrations encountered in <sup>18</sup>F-radiochemistry, and the authors observed a good correlation between the synthesis performance of MDL100907 when using F-19 or F-18, enabling increased throughput by avoiding the waiting time for radioactive decay, and finding conditions that could be directly translated to a conventional synthesizer. However, each data point still consumes a full batch quantity of precursor and other reagents.

In another approach, Laube *et al.* reported performing >50 vial-based reactions per day (25-50  $\mu$ L scale) from a single batch of [<sup>18</sup>F]fluoride by using multi-vial heating blocks to carry out groups of simultaneous reactions to investigate the syntheses of [<sup>18</sup>F]FDG and a celecoxib analog(91). This approach both increases throughput and decreases reagent usage, but required extensive manual handling, and there is a chance that some degree of re-optimization would be needed when translating the optimal conditions to a larger sized vial in a conventional radiosynthesizer(218).

Flow-chemistry methods, where the precursor and radioactive material are mixed and flowed through a heated reactor in a continuous fashion, have been used to perform reagent-efficient optimization (generally 10-40  $\mu$ L range) but in a more automated fashion. Using the Advion Nanotek capillary-based synthesizer, investigators have shown the possibility to

sequentially perform dozens of optimization reactions per day from a single batch of radioisotope to conveniently explore the influence of temperature or flow rate (which affects reagent ratios, residence time, or concentration)(87). Scale-up of optimal conditions is then achieved by scaling up the volumes (i.e. running the flow system for a longer time). However, some reaction parameters (e.g. reaction solvent, or the conditions for azeotropic drying of [<sup>18</sup>F]fluoride, which are done outside of the flow system) cannot be investigated in a high-throughput manner. In a similar approach, our lab has previously experimented with polydimethylsiloxane (PDMS) microfluidic chips for generating mixtures of reagents (~120 nL each) with programmable composition and pH for optimization of labeling of antibody fragments with the prosthetic group N-succinimidyl-4-[<sup>18</sup>F]fluorobenzoate ([<sup>18</sup>F]SFB)(90,219), but these devices and studies were limited to room temperature aqueous conditions.

We have recently reported an approach for reagent-efficient high-throughput reaction optimization in which up to 64 reactions could be performed simultaneously in the form of ~10 μL droplets trapped on arrays of hydrophilic sites patterned on Teflon-coated silicon “chips”(93,95). Because all steps are performed at each reaction site, any conditions of the overall synthesis process (drying conditions, base, precursor, and other reagents amounts, reaction volume, solvent, temperature, and duration) can be studied in a high-throughput manner. Once the optimal conditions are found, the conditions can be directly transferred to production via the use of an automated droplet radiosynthesizer(80). Droplet-based radiochemistry systems have successfully been used to synthesize a wide range of <sup>18</sup>F-labeled tracers including [<sup>18</sup>F]FDG(78), [<sup>18</sup>F]Fallypride(93,95), [<sup>18</sup>F]FET(99), [<sup>18</sup>F]FDOPA(86), [<sup>18</sup>F]FBB(99), [<sup>18</sup>F]Flumazenil(93), [<sup>18</sup>F]PBR06(93), [<sup>18</sup>F]FEPPA(93), [<sup>18</sup>F]FPEB(220), and [<sup>18</sup>F]AMBF<sub>3</sub>-TATE(79), with several demonstrated at the scale of one or more clinical doses(83,99).

While the high-throughput droplet radiochemistry technique has been used to perform hundreds of experiments per week(93), it requires a large amount of manual pipetting operations to add reagents and collect and analyze crude reaction products. Experiments are thus very

tedious and prone to human error. To address these factors, and to minimize radiation exposure, we developed a fully-automated robotic platform for optimization. It automatically performs all of the liquid transfer operations and system control, including delivering isotope and reagents to reaction sites, performing evaporations or reactions, collecting products into individual reservoirs, and spotting crude samples onto thin-layer chromatography (TLC) plates (e.g. for rapid multi-lane radio-TLC analysis(96)). This new platform has the potential to increase the accessibility and throughput of high-throughput radiochemistry. In this paper, we describe the design, characterization, and proof-of-concept demonstrations of the robotic platform.

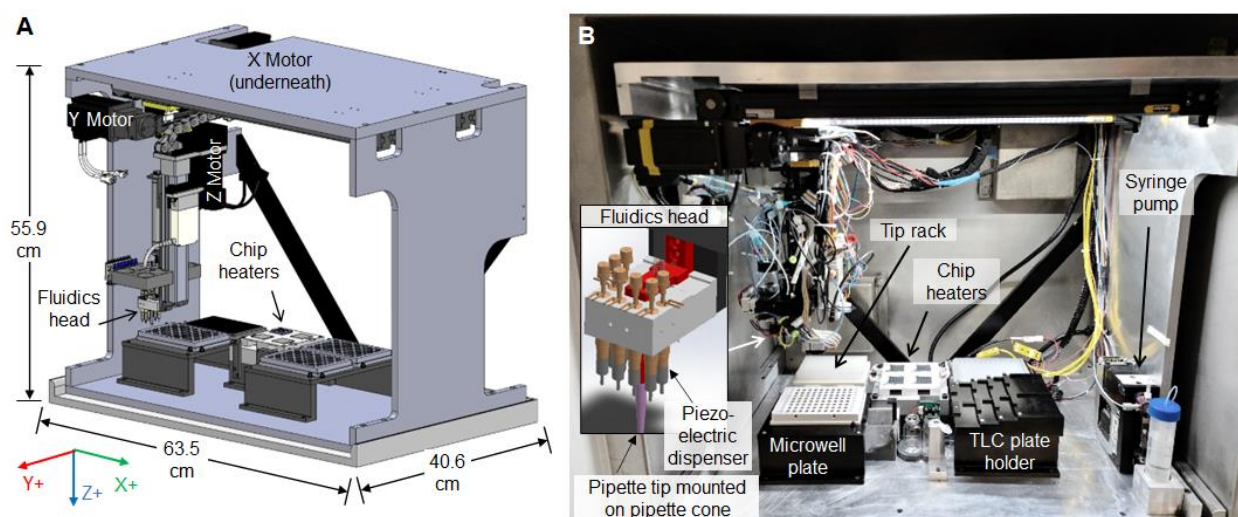


**Figure 5-1 Overall system design.**

(A) 3D rendering of the optimization platform showing the geometry and major components. (B) Photograph of the system inside a minicell. The fluidics head is shown in the inset to illustrate the piezoelectric reagent dispensers and pipette system.

## 5.2 Methods

### 5.2.1 Robotic System

The overall system design is shown in **Figure 5-1**. With a size of 63.5 x 40.6 x 55.9 cm<sup>3</sup> (W x H x D), it can fit within a small mini-cell (68 x 50 x 61 cm<sup>3</sup> interior; Von Gahlen, Zevenaar, Netherlands). The system consists of three main elements: a work area (where microfluidic multi-reaction chips are operated, where reagents and collected products are stored, and where TLC



plates are spotted), a fluidics head with multiple piezoelectric dispensers for reagent dispensing and a pipetting system for liquid transfers, and an XYZ motion gantry to move the fluidics head around the work area.

### 5.2.2 Work Area

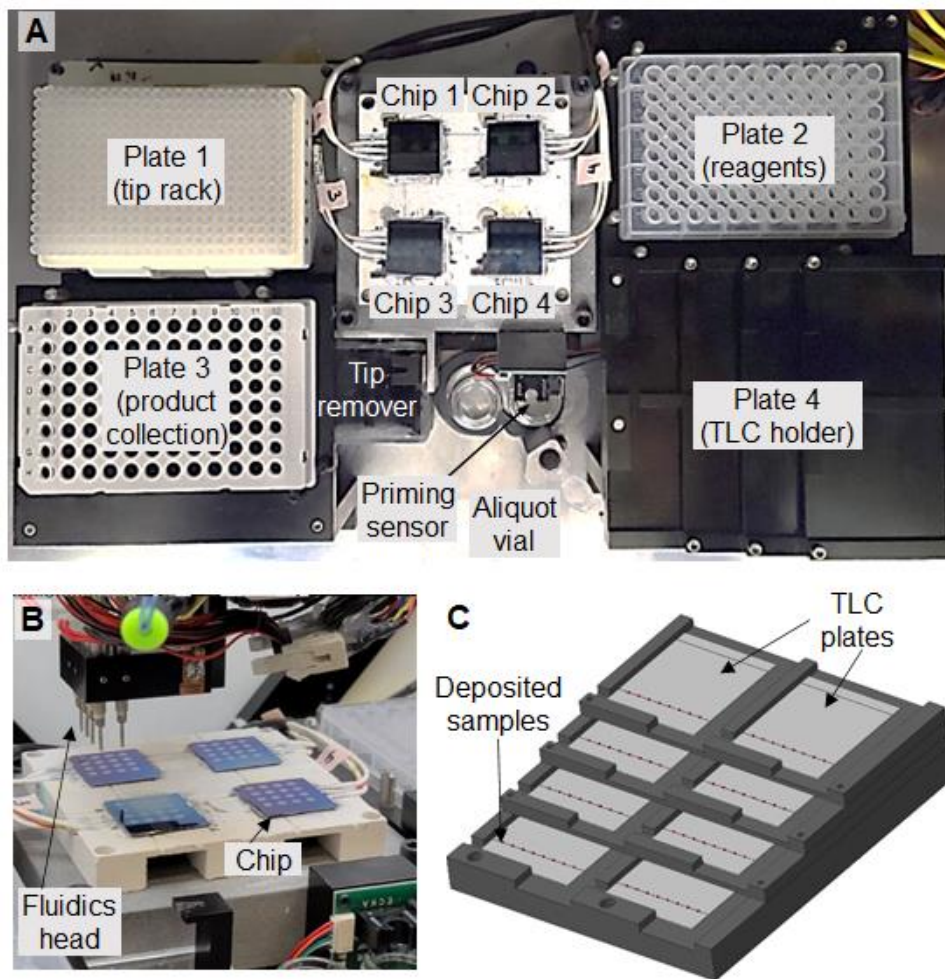


**Figure 5-2 Work area of robotic microdroplet radiosynthesizer platform.**

(A) Overview of the system work area showing major components of the system. (B) Close-up photograph of the heaters with chips installed for 64 parallel reactions. In this photograph the pipette system is retracted so that the piezoelectric dispensers can be used to deliver reagents to the chip. (C) Detail of “stacked” structure of the TLC plate holder that allows up to 64 samples to be spotted on multi-lane TLC plates.

The work area (**Figure 5-2A**) consists of a multi-heater platform for operating four multi-reaction chips simultaneously with independent temperature control<sup>(93,95)</sup> (**Figure 5-2B**), four plate nests that hold standard microwell plates, a pipette tip remover, and a priming sensor. Chips

were aligned to the heaters with the aid of Delrin walls on two sides of each heater. Typical plate nest configuration was: (i) 384-position pipette tip rack (epT.I.P.S. 384, Eppendorf, Hamburg, Germany), (ii) a 96-well plate (Costar 3363, Corning Inc. Corning, NY, USA) containing reagents (e.g. precursors, dilution series), (iii) a 96-position strip-well plate (TRC9601 plate, TLS0801 stripwells, Bio-Rad Laboratories, Inc. Hercules, CA, USA) for collection of crude products, and (iv) a custom TLC plate holder with a laddered design to accommodate eight 50 mm wide TLC plates for parallel separation of 8 samples (0.5  $\mu$ L spotted at 4.5 mm pitch)(96) (**Figure 5-2C**). The infrared (IR) liquid priming sensor (OCB350L250Z, Optek-Danulat GmbH, Essen, Germany) was used to ensure the piezoelectric dispensers and pipetting system (and associated tubing) are fully filled with reagent or water, respectively. Pipette tips were removed with a forked tool and collected in a waste container (**Appendix 5.6.1.1**).

### **5.2.3 Fluidics head**

The fluidics head (**Appendix 5.6.1.2**) comprises set of seven non-contact piezoelectric dispensers (INKX0514300A and INKX0514100A, The Lee Company, Westbrook CT, USA) and a custom pipette cone, designed to mate with the disposable tips for aspirating and dispensing liquids. The piezoelectric dispensers were used for the dispensing of reagents shared across many reaction sites, such as collection solutions and [ $^{18}\text{F}$ ]fluoride solutions. Dispensers were each connected via 0.03" ID or 0.01" ID PTFE tubing dip tubes to septum capped reagent vials, comprising either 20 mL scintillation vials (03-340-25Q, Thermo Fischer Scientific, Waltham, MA, USA), 5 mL V-vials (NextGen V Vial, Wheaton Industries, New Jersey, USA), or 1.5mL V-vials ( $\mu$ Vial 09-1400, Microliter Analytical Supplies Inc., Suwanee, Georgia, USA) based on the total volume needed of the corresponding reagent. Each vial was connected to the output of a pneumatic valve (S070B-5DG, SMC Corporation, Tokyo, Japan) allowing the vial to be either pressurized (inert nitrogen) or vented. The pipetting system was used for delivery of varied reagents (e.g. precursor prepared in different concentrations or solvents for optimization) and for collecting crude products from reaction sites. The pipette cone was mounted on vertical slide

(8381K2, McMaster-Carr) with its position (extended or retracted) controlled using a dual-acting pneumatic actuator (6498K003, McMaster-Carr, Elhurst IL, USA). When retracted, attached pipette tips would be out of the way of the dispensers, allowing reagent dispensing without removing the tip. To attach a tip, the pipette cone was extended and pressed into the tip with a pressure of 20 psig (~13N force). The pipette cone was also fitted with an electrical microswitch that could be used to precisely determine the Z-axis position of the top of the multi-reaction chips. The pipette cone was connected to a syringe pump (Microlab PSD/4, Hamilton Company, Reno NV, USA) equipped with 250  $\mu$ L syringe (with ~100 nL volume accuracy) mounted at the side of the workspace, via 0.03" ID PTFE tubing (~1 m long). The syringe pump could switch between the pipette cone and a DI water reservoir, allowing filling of the tubing with DI water to improve responsiveness and accuracy compared to air. Details of priming of the fluidics systems is described in the **Appendix 5.6.1.3**.

#### **5.2.4 XYZ Gantry**

Fast motion actuators were selected to minimize radioactive decay during movement operations. The X and Y axes consist of belt-driven slides (LCR30, Parker Hannifin Corporation, Irwin PA, USA), arranged in an H-formation, providing 40 cm travel in the X-direction and 21 cm in Y, with a maximum speed of 57 cm/s and positioning repeatability of  $\pm 100\mu\text{m}$ . For the Z-axis, a 12 mm/rev pitch lead-screw slide (MLC028, PBC Linear, Roscoe IL, USA) was used, with a repeatability of  $\pm 20\mu\text{m}$  and maximum speed of 12 cm/s. All three axes were powered by stepper motors (eCLM-S233F, Parker Hannifin) using hall-effect sensors to define a home position in the top back-left-most position. A full explanation of the coordinate system and component positioning is provided in the **Appendix 5.6.2**.

#### **5.2.5 Control system and software**

Front-end control was implemented using a LabView program (National Instruments, Riverside, CA, USA) which controlled communications with external devices (microcontroller, data

acquisition modules (DAQs), syringe pump), initialize all equipment, load configuration files and populate global variables, read method file, and perform all listed method steps. The system configuration and calibration information are described in XML files (**Appendix 5.6.3**) while the method file, written by the user in a custom scripting language (**Appendix 5.6.4**), is used to define the optimization study. The system was operated with a Windows computer, but any computer / operating system that can run LabView can be used.

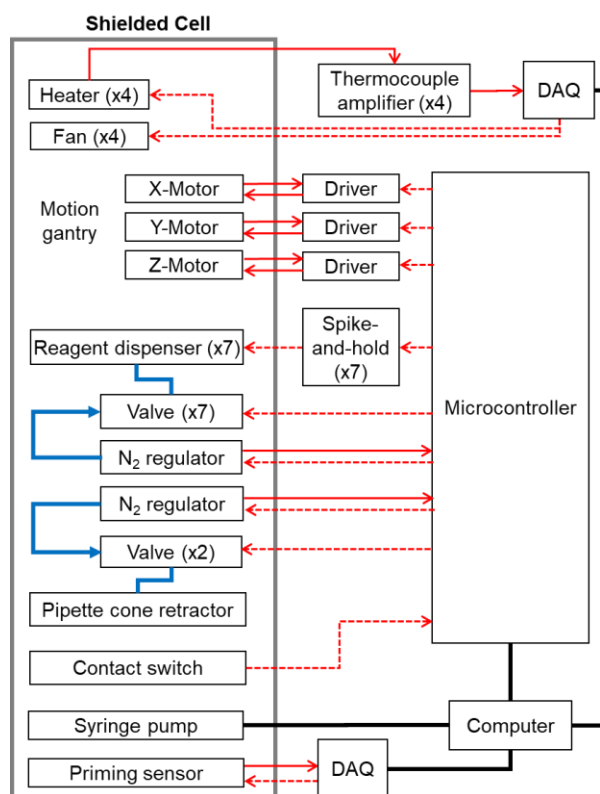


**Figure 5-3 Control system.**

Block diagram of the control system. Blue lines represent gas pathways, solid red represents analog signals, dashed red represents digital signals, and black represents serial communication.

The control system (**Figure 5-3**) comprises multiple subsystems driven by the front-end computer. The temperature control system for the heater platform has been previously described(93). Briefly, signals from integrated heater thermocouples were amplified (MAX31856, Adafruit Industries, New York New York, USA) and measured via a DAQ (USB-202, Measurement Computing Corporation, Norton MA, USA) which also digitally controlled a dedicated relay and

fan per heater, allowing closed-loop on-off software temperature control. The syringe pump was controlled via RS485 serial commands from LabView via a USB to RS485 adapter (USB-485B, Sima S. Enterprises, Los Angeles, CA, USA). A separate DAQ (USB-201, Measurement Computing Corporation) monitored the analog output of the priming sensor to detect liquid and controlled the reset signal for priming sensor recalibration.

All other systems were interfaced to a microcontroller (Arduino Mega, Arduino AG, Sommerville MA, USA) in communication with the front-end computer via USB. Custom firmware was written in C++ and compiled using the GNU C++ compiler. The stepper motors (and built-in encoders) were connected to closed-loop stepper drivers (CL57T, OMC Corporation, Nanjing City, China) which were in turn controlled via step and direction signals from the microcontroller for each axis. A stepping algorithm was implemented in the microcontroller to allow smooth acceleration and deceleration (**Appendix 5.6.5**). The pneumatic system contained two electronic pressure regulators (ITV0050-3UMS, SMC Corporation) – one for the reagent driving pressure for the dispensers, and one for the pipette cone pneumatic actuator. Pressure setpoints were controlled by converting digital outputs from the microcontroller to analog signal signals via digital potentiometer voltage dividers (10 k $\Omega$ , AD5220, Analog Devices, Norwood, MA, USA) in conjunction with op-amp follower circuits (1x amplification, AD8012, Analog Devices), and analog signals from the regulators representing current pressure were monitored via the microcontroller. The valves controlling pressure to each dispenser reagent reservoir, and the two valves to actuate the pneumatic cylinder for the pipette cone, were interfaced via a Darlington transistor array (ULN2803A, Texas Instruments Inc., Dallas, Texas, USA) to digital outputs of the microcontroller. The reagent dispensers were powered by dedicated spike-and-hold drivers (IECX0501350A, Lee Company) triggered by the microcontroller to cause the desired open duration.

### 5.2.6 System Calibrations

System positions were determined as described in **Appendix 5.6.2**, while heater temperatures, pressure regulators, automated TLC spotting protocol, and piezoelectric dispensers were calibrated as described in the **Appendix 5.6.6**.

### 5.2.7 Reagents

[<sup>18</sup>F]fluoride in [<sup>18</sup>O]H<sub>2</sub>O was obtained from the UCLA Crump Cyclotron and Radiochemistry Center. Anhydrous methanol (MeOH, 99.8%), anhydrous acetonitrile (MeCN, 99.8%), acetone (99.9%), ammonium formate (NH<sub>4</sub>HCO<sub>2</sub>, 97%), dichloromethane (DCM, ≥99.8%), 2-3-dimethyl-2-butanol (hexyl alcohol, 98%), tetrahydrofuran (THF, ≥99.9%), hexanes (HPLC grade), pyridine (99.8%), triethylamine (TEA, 99%), trifluoroacetic acid (TFA, 99%), ethanol (EtOH, >99.5%) N,N-dimethylacetamide (DMA, 99.8%), 1,3-dimethyl-2-imidazolidinone (DMI, ≥99%), and N,N-dimethylformamide (DMF, 99.8%) were purchased from Sigma-Aldrich (St. Louis, MO, USA). Tetrabutylammonium bicarbonate (TBAHCO<sub>3</sub>, 75mM in ethanol), tetrakis(pyridine)copper(II) triflate (Cu(py)<sub>4</sub>OTf<sub>2</sub>, 95%), cesium carbonate (Cs<sub>2</sub>CO<sub>3</sub>, >99%), and 3-[3,4-dimethoxy-5-[[[(2S)-1-prop-2-enylpyrrolidin-2-yl]methylcarbamoyl]phenyl]propyl-4-methylbenzenesulfonate (precursor for [<sup>18</sup>F]fallypride, >95%) were purchased from ABX Advanced Biochemical Compounds (Radeberg, Germany). Deionized (DI) water was obtained from a Milli-Q water purification system (IQ 7000, EMD Millipore Corporation, Berlin, Germany). N-methyl-2-pyrrolidone (NMP, >99%) and tetraethylammonium trifluoromethanesulfonate (TEAOTf, >99%) were purchased from Tokyo Chemical Industry (Tokyo, Japan). FBnTP precursor ((4-methylphenylboronic acid pinacol ester)triphenylphosphonium triflate) and reference standard (4-fluorobenzyl-triphenylphosphonium) were generously provided by Dr. Kuo-shyan Lin (University of British Columbia, Canada).

Teflon-coated silicon chips (containing 4x4 arrays of 3 mm diameter surface tension traps) for performing parallel reactions were fabricated as described previously(95).

### 5.2.8 Analytical methods

Measurements of radioactivity were made in a calibrated dose calibrator (CRC-25PET, Capintec Inc., Florham Park, NJ, USA) or a gamma counter (Wizard 3" 1480, PerkinElmer, Waltham, MA, USA). To ensure repeatable dose calibrator measurements, a custom acrylic holder was machined to hold Eppendorf tubes, strip wells, and chips in consistent positions within the dose calibrator chamber. Gamma counting of samples was performed for 45 s, and an empty well was measured every 8 samples for background subtraction.

Fluorination efficiency was determined via multi-lane radio-TLC methods(96). TLC plates (silica gel 60 F<sub>254</sub>, 200 mm x 50 mm, Merck KgaA, Darmstadt, Germany) were cut into 50 mm x 50 mm pieces before use. Samples (0.5  $\mu$ L) were spotted 10 mm from the bottom edge of the TLC plates. Up to 8 samples were spotted per plate at 4.5 mm spacing between "lanes". Development distance was 35 mm. TLC plates containing crude [<sup>18</sup>F]Fallypride samples were developed in a mobile phase of 30.0% TEA, 14.7% acetone, 18.8% THF, and 36.5% hexanes (v/v)(220). For samples of crude [<sup>18</sup>F]FBnTP, the mobile phase was 9:2 DCM:MeOH (v/v)(221). Readout of plates was performed by covering with a glass microscope slide (75 x 50 x 1 mm<sup>3</sup>, Fisher Scientific, Hampton, NH, USA) using Cerenkov luminescence imaging with 5 min exposure time as previously described(96), and fluorination efficiency for each sample (lane) was computed from the resulting images using (manual) region of interest analysis as previously described(96). Collection efficiency for a reaction was computed by dividing the activity of the collected crude product by the initial activity, correcting for decay. The initial activity was estimated via measurement of an Eppendorf tube ("aliquot vial") loaded with the same volume as dispensed to all reaction sites. The crude RCY was determined by multiplying the fluorination efficiency by the collection efficiency. To determine the activity of a single reaction site on a chip (e.g. residual activity after collecting the crude product), the total chip activity was first measured in a dose calibrator, then multiplied by the fraction of the total activity corresponding to that reaction site.

This fraction was determined by obtaining a CLI image of the chip (covered with 1 mm glass microscope slide, 5 min exposure time unless otherwise noted) and then dividing the integrated pixel intensity within the desired reaction site by the total integrated pixel intensity of all reaction sites.

### 5.2.9 Robotic system characterization

Characterization of the performance of the ceramic heater system and pipetting system, the piezoelectric reagent dispenser repeatability, assessment of cross-contamination during synthesis operations, and repeatability of parallel synthesis, are described in detail in the **Appendix 5.6.7**.

### 5.2.10 Optimization of [<sup>18</sup>F]Fallypride synthesis

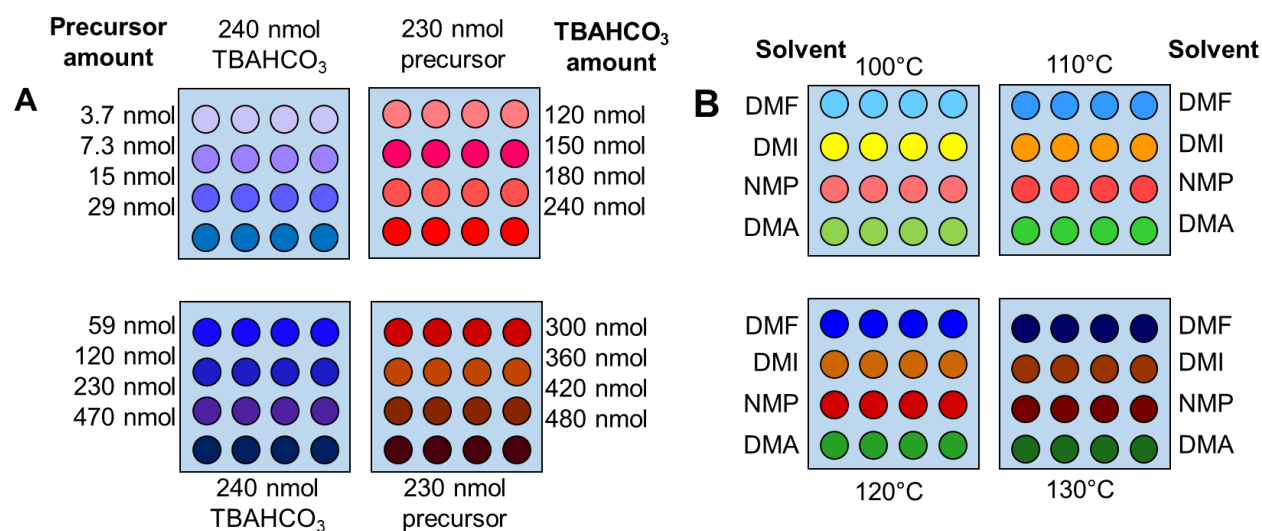


**Figure 5-4 Map of reaction conditions for optimization experiments.**

(A) Map of reaction conditions for [<sup>18</sup>F]Fallypride optimization experiments with varied amount of TBAHCO<sub>3</sub> and precursor. Reactions were all performed in 1:1 v/v thexyl alcohol:MeCN at 110°C for 7 min. (B) Map of conditions for [<sup>18</sup>F]FBnTP optimization experiments. All reactions were performed for 5 min with 10 nmol Cs<sub>2</sub>CO<sub>3</sub>, 300 nmol TEAOTf, 450 nmol precursor, and 680 nmol Cu(py)<sub>4</sub>OTf<sub>2</sub>.

To validate the overall system, we performed a study of the synthesis of [<sup>18</sup>F]Fallypride, including conditions for which we have previously reported the performance using manually-



performed droplet reactions(93,95). **Figure 5-4A** shows the experimental layout. One set of 32 reactions was performed with constant amount of precursor (230 nmol) but different amounts of TBAHCO<sub>3</sub> (8 values, 120-480 nmol, n=4 replicates each). Another set of 32 reactions was performed with a fixed amount of TBAHCO<sub>3</sub> (240 nmol) but different amounts of the precursor (8 values, 3.65 – 468 nmol, n=4 replicates each).

To prepare the experiment, a stock precursor solution (154 mM) in 1:1 v/v hexyl alcohol:MeCN was prepared and additional concentrations (77 – 0.6 mM) were prepared by dilution with the same solvent mixture. 250 µL of each stock precursor concentration were loaded into wells of a 96 well plate (Costar 3363, Corning Inc., Glendale, AZ, USA) for the reactions with varied precursor amount, and an additional 250 µL of 38.5 mM solution was loaded into another well for the remaining reactions. A stock collection solution was prepared by mixing 20 mL 9:1 MeOH:DI water and connecting to a reagent dispensers. A 1.5 mL activity stock solution was prepared from [<sup>18</sup>F]fluoride, DI water, and TBAHCO<sub>3</sub> (final concentrations ~740 MBq/mL, 24 mM TBAHCO<sub>3</sub>) and then loaded into a second dispenser, and a 1.5 mL stock solution of 30 mM TBAHCO<sub>3</sub> in DI water was loaded into a third dispenser.

Synthesis of [<sup>18</sup>F]Fallypride at each reaction site was similar to our previous report(95). First, 5 µL of the [<sup>18</sup>F]fluoride/TBAHCO<sub>3</sub> stock solution was dispensed to each reaction site. Additional amounts of TBAHCO<sub>3</sub> solution (0-7 µL) were then dispensed to achieve the desired total amount of TBAHCO<sub>3</sub> for each reaction. The droplets were then dried by heating all chips at 92°C for 30s, 98°C for 30 s, and 105°C for 60s. Next, 6 µL of precursor solution was loaded to each reaction site, with concentration chosen to achieve the desired precursor amount for each reaction site. The fluorination reaction was performed by heating all chips at 110°C for 7 min. Individual reactions were collected using 4 collection cycles (i.e. adding 10 µL of collection solution to the reaction site, mixing via pipette, and transferring via pipette to a dedicated location in a strip-well plate). A 0.5 µL sample of each crude product was spotted to a location on a TLC plate. At the end of the experiment, activity of the collected products and aliquot vial was

measured, and TLC plates were developed and imaged. Additional activity measurements and CLI imaging of chips were performed after [ $^{18}\text{F}$ ]fluoride drying, fluorination, and collection steps.

### 5.2.11 Optimization of [ $^{18}\text{F}$ ]FBnTP synthesis

Next we performed an optimization study of a synthesis for which we had not previously studied, namely the copper-mediated synthesis of [ $^{18}\text{F}$ ]FBnTP(222). Based on previous study of the droplet-based synthesis of [ $^{18}\text{F}$ ]FDOPA via a similar copper-mediated route, we found significant impact of reaction solvent and temperature, and thus implemented the experimental layout in **Figure 5-4B** to explore the influence of solvent (DMF, DMI, NMP, and DMA, each with 3.8% v/v pyridine) and temperature (100, 110, 120, and 130°C) in the synthesis of [ $^{18}\text{F}$ ]FBnTP.

To prepare the experiment, stock solutions of the FBnTP precursor (90 mM) were prepared in each of the 4 solvent mixtures, and, similarly, stock solutions of  $\text{Cu}(\text{py})_4\text{OTf}_2$  (136 mM) were prepared in each solvent mixture. 20 mL of collection stock solution was prepared by mixing 2:3 v/v MeCN:DI water and loading into a reagent dispenser. A 1.5 mL stock solution of [ $^{18}\text{F}$ ]fluoride was prepared by mixing aqueous [ $^{18}\text{F}$ ]fluoride with DI water and adding  $\text{Cs}_2\text{CO}_3$  and TEAOTf (~740 MBq/mL, 1 mM  $\text{Cs}_2\text{CO}_3$ , 30 mM TEAOTf), corresponding to 10 nmol of  $\text{Cs}_2\text{CO}_3$ , 300 nmol TEAOTf, and ~7.4 MBq per reaction site.

To perform the droplet reactions, 10  $\mu\text{L}$  of the [ $^{18}\text{F}$ ]fluoride stock solution was first dispensed to each reaction site. Droplets were dried by heating all chips to 92°C for 15 s, 98°C for 15 s, and 105°C for 60 s. Immediately before fluorination, for each solvent mixture, 125  $\mu\text{L}$  of the corresponding precursor and  $\text{Cu}(\text{py})_4\text{OTf}_2$  stock solutions were mixed together to create 4 new precursor stock solutions (each containing 45 mM FBnTP precursor and 68 mM  $\text{Cu}(\text{py})_4\text{OTf}_2$ ). The system then deposited 10  $\mu\text{L}$  to each reaction site according to the experimental plan, and fluorination was performed by heating chips for 5 min to the temperatures in the experimental plan. Crude products and measurements were collected in the same manner as for [ $^{18}\text{F}$ ]Fallypride.

Some batches of [ $^{18}\text{F}$ ]FBnTP were purified via radio-HPLC using an analytical column (ZORBAX RR Eclipse Plus C18, 4.6 x 100 mm, 3.5  $\mu\text{m}$  particle size, Agilent, Santa Clara, CA, USA) using a mobile phase of DI water and MeCN (66:34 v/v) with 0.1%TFA (v/v) and flow rate of 1.2 mL/min. The radio-HPLC system setup comprised a Smartline HPLC system (Knauer, Berlin, Germany) equipped with a degasser (Model 5050), pump (Model 1000), UV detector (254 nm; Eckert & Ziegler, Berlin, Germany), gamma-radiation detector (BFC-4100, Bioscan, Inc., Poway, CA, USA), and counter (BFC-1000; Bioscan, Inc., Poway, CA, USA). The purified product was then formulated via solid-phase extraction using a C18 cartridge (Sep-Pak Plus Short, WAT020515, Waters Corporation, Milford, MA, USA) pre-conditioned before use with 3 mL of EtOH followed by 20 mL of DI water. The purified product was diluted with 20 mL of DI water and then slowly loaded onto the cartridge followed by rinsing with 20 mL of DI water. The final product was eluted with 1 mL of EtOH and diluted with DI water to 10 mL. This final diluted product was analyzed on the same HPLC system to confirm radiochemical purity using mobile phase of water and MeCN (60:40 v/v) with 0.1%TFA (v/v) and flow rate of 1.2 mL/min. Co-injection of the final diluted [ $^{18}\text{F}$ ]FBnTP and reference standard was performed to confirm product identity.

## 5.3 Results

### 5.3.1 System characterization

Several experiments were performed to establish the ability of the system to accurately assess reaction performance. First, one of the piezoelectric reagent dispensers was loaded with 1.5 mL [ $^{18}\text{F}$ ]fluoride/TBAHCO<sub>3</sub> stock solution (~3.7 MBq/mL, 25 mM) and 10  $\mu\text{L}$  was dispensed sequentially into each of 96 strip-wells. Gamma counting (with decay correction) of the individual separated (and capped) strip wells revealed high repeatability of dispensed amount, with a standard deviation of 1.9% (n=96) (**Figure 5-5A**). Based on this excellent repeatability, we were able to estimate the initial activity on each reaction site during a high-throughput experiment by

dispensing an equal portion into an “aliquot vial” that could be measured via dose calibrator or gamma counter.

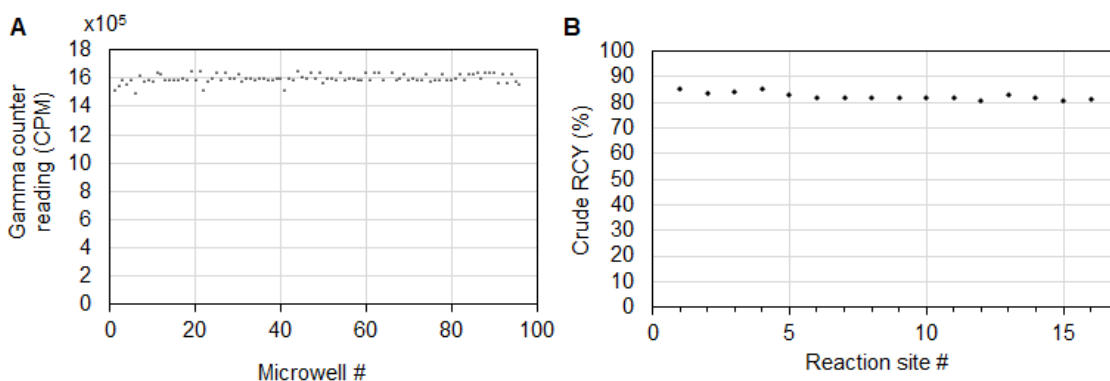


**Figure 5-5 Reagent dispensing uniformity and reaction uniformity.**

(A) Reagent dispensing uniformity. Graph shows gamma counter measurements (decay-corrected) for 96 individual dispenses of [<sup>18</sup>F]fluoride into wells of a strip-well plate. (B) Reaction uniformity. Crude RCY of [<sup>18</sup>F]Fallypride synthesized under identical conditions at 16 reaction sites. (Conditions: TBAHCO<sub>3</sub> amount: 240 nmol, precursor amount: 230 nmol, reaction temperature: 110°C, reaction time: 5 min).

We also assessed uniformity of [<sup>18</sup>F]fluoride dispensing and drying on chip reaction sites (n=64) and found excellent site-to-site uniformity and chip-to-chip uniformity (see **Appendix 5.6.7.1**). We further assessed uniformity by performing replicate [<sup>18</sup>F]Fallypride syntheses under identical conditions (n=16). Performance was highly consistent across reactions with fluorination efficiency of 90.4 ± 0.7 % (n=16), collection efficiency of 91 ± 2 % (n=16) and crude RCY of 83 ± 1 % (n=16) (**Figure 5-5B**). Full details can be found in **Appendix 5.6.7.2** and **5.6.7.3**. A cross-contamination test was performed by dispensing a [<sup>18</sup>F]fluoride/TBAHCO<sub>3</sub> solution to alternate reaction sites on a chip and then performing a drying step (see **Appendix 5.6.7.4**), and the unused reaction sites contained negligible radioactivity.

### 5.3.2 Optimization of [<sup>18</sup>F]Fallypride synthesis

Results of the 64-reaction [<sup>18</sup>F]Fallypride study (exploring the influence of precursor amount and TBAHCO<sub>3</sub> amount) are summarized in **Figure 5-6**, with more details available in the

**Appendix 5.6.7.5.** Excellent agreement was observed between the reaction performance in this automated study and results of a previous manual study(95). The current study found the optimal condition (180 nmol TBAHCO<sub>3</sub>, 230 nmol precursor) had a crude RCY of 92.5 ± 0.5 % (n=4), while in the prior study, the optimum condition (240 nmol TBAHCO<sub>3</sub>, 230 nmol precursor) had a crude RCY of 92 ± 1% (n=2)(95). While in the current study, the crude RCY for 240 nmol TBAHCO<sub>3</sub> (89 ± 5%, n=8) was not significantly different from the prior study, and the inclusion of intermediate base amounts allowed us to find the more optimal 180 nmol value, which also provides more robustness (lower sensitivity to deviations in amount of TBAHCO<sub>3</sub>).

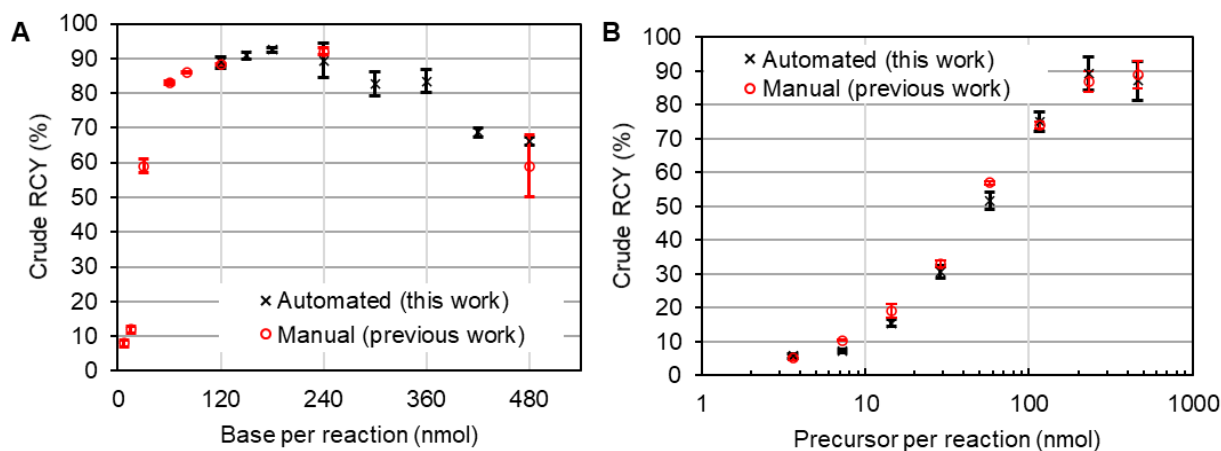


**Figure 5-6 Results of the 64-reaction [18F]Fallypride study.**

(A) Crude RCY for the droplet synthesis of [18F]Fallypride as a function of the amount of TBAHCO<sub>3</sub> with constant precursor amount of 230 nmol. (B) Crude RCY as a function of the amount of precursor with amount of TBAHCO<sub>3</sub> fixed at 240 nmol. Other conditions were fixed: reaction temperature: 110°C, reaction time: 5min. Results of the current study (black symbols) are compared to results of manually-performed experiments previously reported(95) (red symbols).

**5.3.3 Optimization of [18F]FBnTP synthesis**

During initial [18F]FBnTP experiments, we discovered that there can be significant evaporation of the collection solution from the microwells during the 1.34 h collection process. For the collection solution used in this case (3:2 v/v MeCN:H<sub>2</sub>O), this evaporation could change the composition, and we suspect that this affected the solubility of the product in the collection solution, resulting in sampling error when the TLC spotting occurred. This is consistent with our

observations of unexpectedly low product signal (and low overall signal) when developing and imaging the TLC plates. To overcome this issue, we modified the control software to immediately transfer a sample of the crude product to TLC right after the collection step, rather than first collecting all reaction droplets into microwells, and then subsequently transferring samples of all microwells onto TLC plates. This change appeared to eliminate the sampling error, and we confirmed that samples spotted onto TLC plates were stable, with no difference in the resulting TLC separation regardless of the time the sample was on the plate before the developing step.

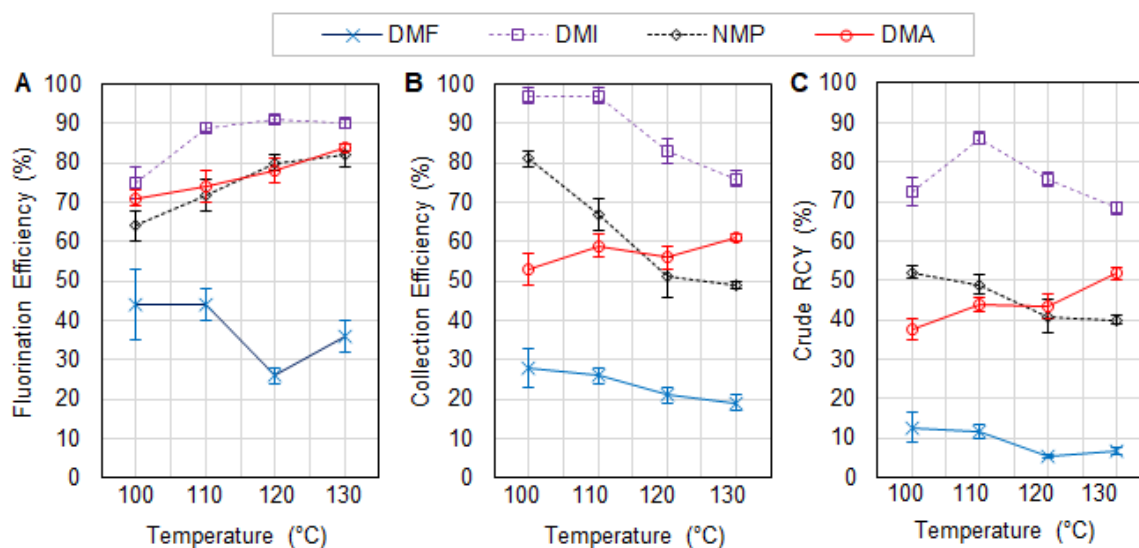


**Figure 5-7 Effect of temperature and reaction solvent on the performance of the synthesis of  $[^{18}\text{F}]\text{FBnTP}$ .**

(A) Fluorination efficiency, (B) collection efficiency, and (C) crude RCY. Each of the indicated solvents contains 3.8% v/v pyridine. Fixed conditions: 5 min reaction time, 10 nmol  $\text{Cs}_2\text{CO}_3$ , 300 nmol TEAOTf, 450 nmol precursor, 680 nmol  $\text{Cu}(\text{py})_4\text{OTf}_2$ .

Results of the improved [ $^{18}\text{F}$ ]FBnTP study (exploring impact of reaction solvent and temperature) are summarized in **Figure 5-7**, with additional details in **Appendix 5.6.7.6**. The solvent had a particularly large impact on reaction performance, and the optimal condition was found to be 110°C in DMI (with 3.8% v/v pyridine), providing a fluorination efficiency of 89±1% (n=4), collection efficiency of 97±2% (n=4) and overall crude RCY of 86±2% (n=4). These results compare favorably to the reported macroscale reaction with a fluorination conversion of ~60% (isolated RCY not reported)(222). The full set of 64 reactions was automatically performed in 180 min, with an additional ~60 min needed to perform manual radioactivity measurements and TLC analysis. Of the 180 min, the majority of the time (120 min) was spent collecting crude reaction products from the reaction sites into the microwell plate. A detailed analysis of the timing for high-throughput experiments is given in the **Appendix 5.6.7.8**.

Using the optimal condition, the droplet radiosynthesis of [ $^{18}\text{F}$ ]FBnTP was slightly scaled up, by using higher initial [ $^{18}\text{F}$ ]fluoride activity, to an amount sufficient for preclinical imaging studies (~120 MBq). After purification via radio-HPLC and cartridge formulation, the RCY was 66 ± 6% (n=3), with excellent radiochemical purity of 100% (n=3). The overall preparation time including on-chip fluorination, HPLC purification and cartridge formulation was only 42 ± 1 min (n=3). Taking advantage of this rapid and efficient production format, the activity yield was 49 ± 3% (n=3).

## 5.4 Discussion

We previously showed that arrays of droplet reactions provide an efficient means to perform optimization studies by enabling 64 simultaneous reactions while consuming a total amount of precursor equivalent to a single conventional synthesis(93). After optimization, the synthesis can then be automated via a miniature droplet radiosynthesizer(80), and, if needed, scaled to higher activity levels by increasing the starting activity(83,99). In the present work we

have developed and demonstrated a novel platform to implement this technique in a highly automated fashion to increase throughput as well as safety for the radiochemist. The high uniformity of operations of the automated platform (exemplified by the consistent performance of n=16 replicate syntheses of [<sup>18</sup>F]Fallypride), combined with the observation of negligible crosstalk, confirms that the automated platform can be relied upon to perform large sets of independent reactions with high reliability. The close agreement of the results of our 64-reaction exploration of the synthesis of [<sup>18</sup>F]Fallypride with prior manually-performed experiments(95) further validates the current platform as an optimization tool. Due to the wide compatibility of droplet reactions with a variety of different <sup>18</sup>F-labeled tracers and labeling methods(84), and the successful optimization of a reaction not previously studied in droplet format (i.e. copper-mediated radiofluorination route to produce [<sup>18</sup>F]FBnTP), we expect this platform to have wide applicability to other <sup>18</sup>F-radiotracers and likely other isotopes.

The robotic system software provides a high degree of customizability without a steep learning curve. Experiments are programmed by stringing together a series of parameterizable unit operations using a flexible scripting language. In practice, a new optimization experiment can often be defined by editing a previously-created program in <15 min by a user familiar with the scripting language. Beyond the reaction parameters studied here (base amount, precursor amount, solvent, reaction temperature), the platform can also be used to explore a variety of different parameters for every stage of the synthesis (see **Table 5-1**).

Compared to previously reported manual optimization studies(93,95), the automated platform presented here provides enormous practical and safety advantages by eliminating tedious manual pipetting steps and minimizing radiation exposure. For example, in the [<sup>18</sup>F]Fallypride experiment described here, there were a total of 768 pipetting operations (including all reagent loading and liquid transfer steps, but not counting complex manipulations such as “mixing”) and 138 pipette tip changes. It is not difficult to imagine that when performing such an experiment manually, there is a high likelihood of human error, such as forgetting a pipetting step,



pipetting the wrong reagent, or dispensing or aspirating to/from the wrong reaction site(93); these errors are eliminated with the automated system. Although, in principle, manual operation could be simplified using multi-channel pipettes, the increased complexity of reagent preparation and the need to continually adjust tip spacing to match either a microwell plate (4.5 mm or 9 mm spacing) or chips (5 mm spacing), makes this impractical in the current chip and heater design.

**Table 5-1 Examples of parameters that can be optimized in an  $^{18}\text{F}$ -radiosynthesis.**

Stage of radiosynthesis process	Parameter(s)
$^{18}\text{F}$ fluoride loading and activation	<ul style="list-style-type: none"> <li>• Amount(s) and type(s) of base / phase transfer catalyst</li> <li>• Drying conditions (temperature, time)</li> <li>• Azeotropic drying conditions (with additional MeCN)</li> <li>• Activity scale</li> </ul>
Reactions ( <i>fluorination, deprotection, etc.</i> )	<ul style="list-style-type: none"> <li>• Amount of reagent(s) (e.g. precursor, deprotectant)</li> <li>• Reaction solvent(s)</li> <li>• Amount(s)/type(s) of additives (e.g. catalyst)</li> <li>• Temperature</li> <li>• Time</li> </ul>
Collection	<ul style="list-style-type: none"> <li>• Collection solution composition</li> <li>• Volume of collection solution (each step)</li> <li>• Incubation conditions (temperature, time)</li> <li>• Number of collection steps</li> </ul>

From choice of actuators to relative positioning of components within the work area, the hardware system was designed for rapid operation and high throughput. The described experiments each took ~3 h of automated system operation, plus an additional ~1 h of manual effort to perform radioactivity measurements and Cerenkov imaging of chips (i.e. at intermediate steps and after the collection step), measure radioactivity of collected crude products, and to develop and image the TLC plates. Further system developments are underway to enable these radioactivity measurements to be performed *in situ*, which will increase safety and reduce overall experiment time. Even including the manual interventions, the effective time per data point (i.e., 3 h / 64 reactions = 2.8 min/reaction) is extremely short when compared with conventional radiochemistry apparatus, in which experiments (each taking up to several hours) are performed sequentially. Leveraging this throughput allows a study that would normally require many months of experiments to be completed in just days. We contemplate that the current throughput can

potentially be even further enhanced by operating the system multiple times per day, increasing the number of parallel reaction sites, or parallelizing the pipetting operations. Additionally, in principle, the robotic system could assist with reagent preparation (e.g. prepare dilution series) to further reduce the experimental setup time.

Performing high-throughput radiochemistry studies requires a high-throughput method to analyze the radiochemical composition of crude reaction products. While typical analysis is performed via radio-HPLC, the high time requirement per sample (>15-40 min for cleaning, equilibration, injection and separation) makes this infeasible for 64 sequential samples before they decay to unusable levels. In this work we used multi-lane TLC techniques(96), which are particularly convenient due to the capability for simultaneous multi-lane separation and high-resolution Cerenkov luminescence imaging-based readout of 8 samples per plate. We recently reported a systematic approach for determining the optimal mobile phase for TLC separation that, for analysis of [ $^{18}\text{F}$ ]Fallypride enabled comparable resolution to HPLC, and that will enable extension of high-resolution TLC methods to additional radiopharmaceutical compounds(220). We are also investigating the use of other high-throughput analysis techniques such as ultra-performance liquid chromatography (UPLC), which can be optimized to reduce the time per sample to the order of ~1 min(223).

There are a few cases in which the open nature of the droplet reactions in our platform could introduce some limitations. (i) Currently the platform would not be able to handle reactions where the radioisotope, intermediate species, or product is volatile. (ii) Atmospheric exposure could be an issue for certain reactions involving reagents sensitive to oxygen or moisture (e.g. copper-mediated radiofluorination). However, in this work, the observed yield of the open-droplet copper-mediated radiosynthesis of [ $^{18}\text{F}$ ]FBnTP exceeded that reported for (closed) vial-based reactions, and thus atmospheric exposure does not appear to have a significant adverse impact. (iii) Special measures must be taken for reactions involving volatile solvents as the solvent can rapidly evaporate at elevated temperature, which can limit the duration of reactions. We have

found that the issue can be addressed by replenishing the solvent at regular intervals, using short reaction times (e.g. 30 s), or by switching to higher boiling point solvents(93).

In addition to rapid synthesis optimization, the platform described here could potentially also assist with labeling of libraries of radiopharmaceutical compounds to screen *in vitro* or *in vivo* properties(224), or to generate training data for novel machine learning approaches in radiochemistry(215).

## 5.5 Conclusions

We developed a robotic, high-throughput radiochemistry platform that fits inside most commercially-available mini-cells and hot cells and can perform a set of 64 droplet-based reactions on patterned Teflon-coated silicon chips nearly simultaneously. The process is highly automated, only requiring manual intervention for intermediate radioactivity measurements and analysis of final products. The system automates all aspects of the synthesis including isotope dispensing, isotope drying by evaporation, reagent loading, heating to activate the radiolabeling reaction, cooling, collecting crude product into microwell plates or tubes, and transferring crude samples to TLC plates for analysis. In characterization experiments, performance of replicate reactions was highly repeatable and negligible crosstalk among different reaction sites was observed. We performed a 64-reaction study to explore the effects of amount of TBAHCO<sub>3</sub> and precursor in the synthesis of [<sup>18</sup>F]Fallypride and found performance closely matched a similar prior study in which experiments were conducted manually. As a proof-of-concept of novel radiosynthesis optimization, we investigated the impact of reaction temperature and solvent on the copper-mediated radiosynthesis of [<sup>18</sup>F]FBnTP(222). As a result of the 64-reaction study, we found high-performing conditions for the synthesis and demonstrated that the conditions could be combined with purification and formulation to achieve a high RCY (66%) in a 42 min synthesis time. The platform will enable routinely performing droplet-array-based radiochemistry studies(93)

without the tedious pipetting, chance of human error, and radiation exposure of manual techniques.

## 5.6 Appendix

### 5.6.1 System components

#### 5.6.1.1 Pipette tip remover

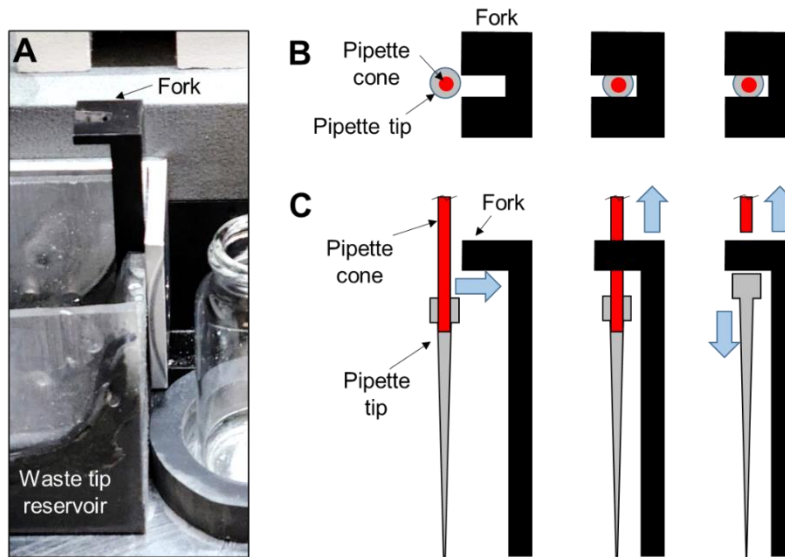


**Figure 5-8 Structure and operation of the pipette tip remover.**

(A) Photograph of forked tool for removing pipette tips. It is positioned at the edge of a plastic container which captures the waste tips. (B-C) Top view and side view schematics of step-by-step movements of the fluidics head for removing a pipette tip. First the tip is moved horizontally under the fork. Then the fluidics head is lifted up. When the attachment point of the pipette tip hits the fork, the tip will be dislodged while the fluidics head continues to be lifted.

### 5.6.1.2 Fluidics head

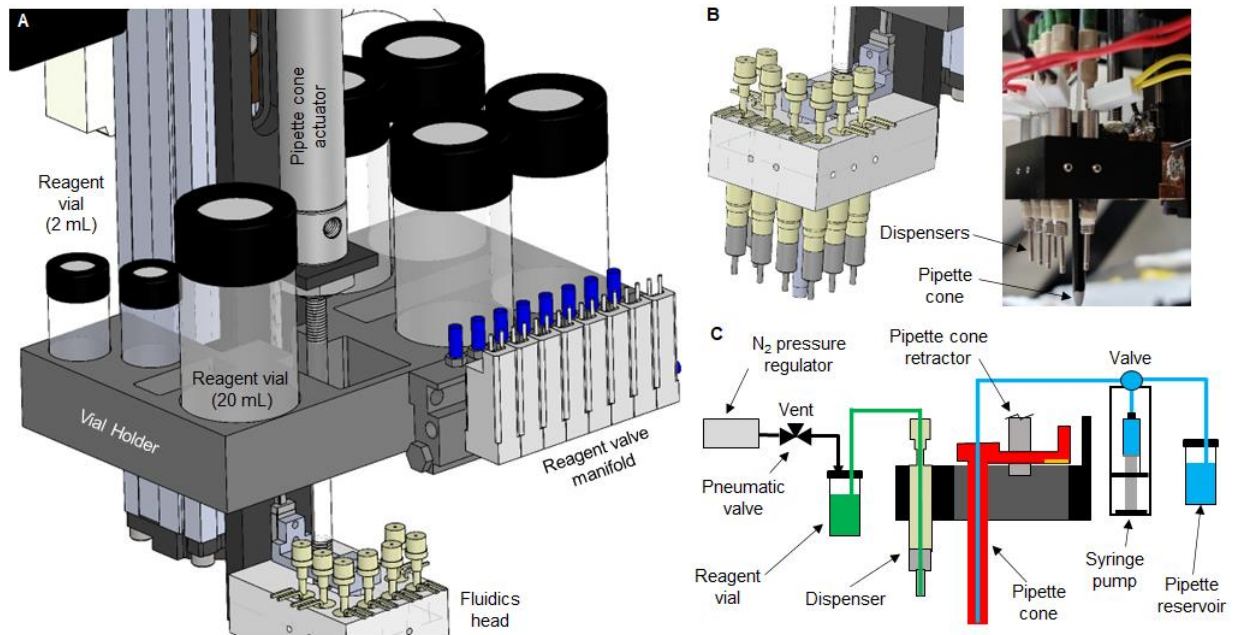


**Figure 5-9 Detailed design of the fluidics head and reagent dispensing system.**

(A) 3D CAD design of a portion of the Z-axis showing the attachment of the fluidics head, location of reagent vials, and the pipette cone actuator for retracting the pipette cone. (B) CAD model and photograph of the fluidics head. (C) Fluidic diagram of how reagents are connected to reagent dispensers, and how the syringe pump is connect to the pipette cone.

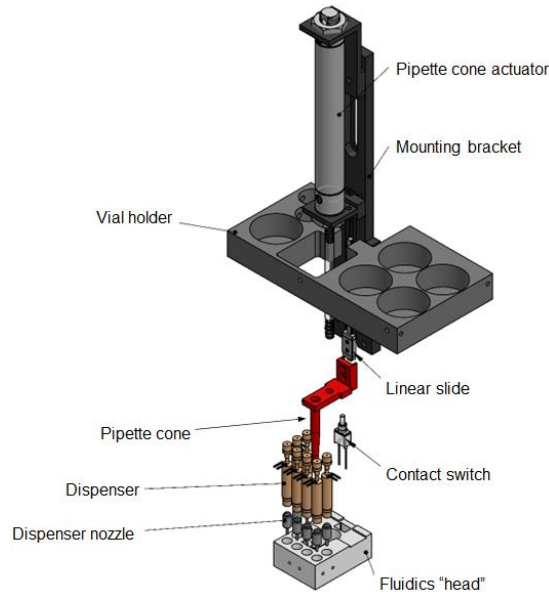


**Figure 5-10 Exploded view of the fluidics head.**

All components are rigidly connected to a mounting bracket (which is affixed to the Z-axis actuator), but the pipette cone can be independently extended and retracted through a hole in the fluidics head.

### 5.6.1.3 Liquid priming system

Each of the dispensers and the pipette cone are primed before use in an experiment using a priming sensor based on an optical liquid sensor (**Figure 5-11**). To prime either a reagent dispenser or the pipette cone, the system will first move it above the priming sensor (applying the predefined position offsets), and then dispense liquid in repeated volume increments while monitoring the liquid sensor to determine if liquid was dispensed.

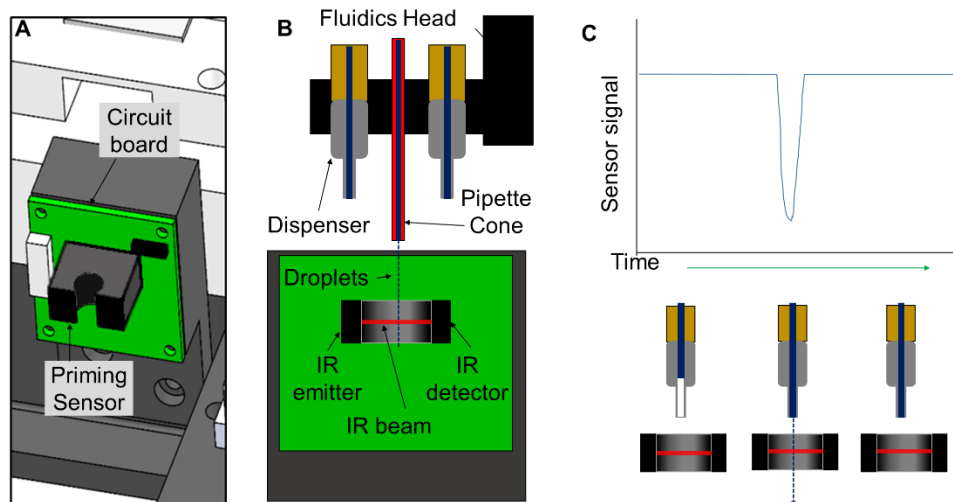


**Figure 5-11 Priming sensor based on an optical liquid sensor for dispensers.**

(A) 3D CAD model of the priming sensor. (B) Front view of priming sensor showing the fluidics head in position to prime the pipette cone. The signal at the IR detector is altered when liquid passes through the IR beam. (C) Schematic time series of the priming process of a dispenser. (Left) Liquid has not yet reached the nozzle tip. (Center) Once the nozzle is filled, the next volume increment leads to actual dispensing of liquid and detection by the priming sensor. (Right) The dispenser is now primed.

For priming reagent dispensers, the pipette cone must be in the retracted position. Prior to the first time a dispenser is primed, the line is first purged by dispensing a large initial volume (equal to twice the volume of tubing between the reservoir and dispenser nozzle) to flush any residual cleaning solvents or air pockets from the fluid path and ensure the tubing is filled with the reservoir liquid. The volume increment for priming is defined in the calibration settings. Typically 0.5  $\mu\text{L}$  was used, as it minimizes reagent waste while ensure reliable detection by the sensor. To

avoid false positive detections where small air pockets could be present in the tubing, liquid was only considered “detected” if 3 consecutive droplets were observed by the sensor.

When priming the pipette system, the pipette cone is in the extended position. During system initialization, the pipette system is first purged. To do so, the cone is moved above a nearby waste vial. The syringe pump then performs an aspirate step to collect any liquid within the pipette cone or the tubing between the pipette cone and syringe pump. This volume is then dispensed to the DI water reservoir by switching the syringe valve. Subsequently, the syringe performs another aspirate step, filling with water from the DI water reservoir, and then the syringe valve is switched and the water dispensed to fill the tubing and pipette cone. (10% extra volume is dispensed to ensure the path is completely filled with liquid.) To prime the pipette cone, the syringe pump dispenses 10  $\mu\text{L}$  at a time until a single droplet forms on the tip of the cone and falls past the optical sensor.

## **5.6.2 Calibration of system positions**

### **5.6.2.1 Coordinate system and system extents**

The origin for the system coordinate system (shown in **VA** of the main paper) was chosen as the bottom-center of the extended pipette cone, when the fluidic head is in the back-most, left-most, upward-most location of the XYZ gantry (i.e. the home position of all motors). Looking from the front of the system, the positive X direction is toward the right, positive Y direction is toward the front, and positive Z direction is downwards.

Extents of movement in each axis were software-limited to 348.3 mm in X, 210.4 mm in Y, and 90.0 mm in Z. While the X-axis can physically move further, the limitation was imposed to avoid collisions with certain components, including the syringe pump and the Z-axis motor. The clearance height of the system (“*Clearance\_Z\_Global*”), i.e. lowest Z-position for which the fluidics head could be moved to any (X,Y) position without collision, was set to ensure a minimum 5 mm gap ( $Z = +45$  mm).

### 5.6.2.2 Determining index locations

The reference position of each plate nest is defined by its left rear corner. To find this position, an aluminum block (127.7 mm x 85.5 mm x 30.0 mm) was locked into the plate nest and the XY coordinates of the left-most, back-most corner of the block was determined by manually jogging the center of the pipette cone tip as close as possible to the desired corner and then using an automated contact-finding routine (**Appendix 5.6.2.3**) to fine-tune the Z-coordinate. To the final position, the thickness of the aluminum block was added to the Z-coordinate to reflect the height of the top of the plate nest.

To access wells in a microwell plate, a set of offsets (relative to the plate nest location) must be measured for each type of microwell plate used (**Figure 5-12**), including the XY distance from the index corner of the plate nest to the left-most, rear-most microwell position (i.e. A1 or (1,1)), the pitch in each of X and Y (distance between centers of adjacent wells), the total number of wells in each direction (e.g. 12x8 for a 96-well plate), the height of the plate, and the depth of the wells from the top of the plate.

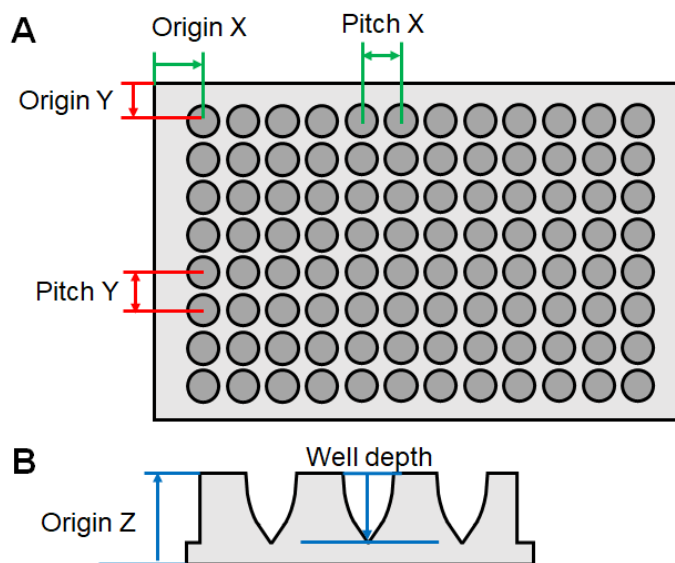


**Figure 5-12** Parameters used to characterize each type of microwell plate.



The TLC plate holder (**Figure 5-13**) was designed to hold up to eight TLC plates arranged in two rows of four. The geometry was handled similarly to other well plates to identify the locations where individual samples should be spotted but some differences were needed to account for the division of spotting locations among multiple independent plates. In particular, the Size\_Y value was recorded on a per-plate basis (e.g. 8) but was internally doubled to account for the total number of spotting positions per X coordinate. In addition, an additional variable, Plate\_Pitch\_Y, was added to the geometry definition, to enable determination of the correct spotting position for Y coordinates larger than Size\_Y. Due to the stacked arrangement of plates, an additional new parameter (Z pitch) was needed to define the increase in vertical position of the plates as the X coordinate was increased from 1 to 4.

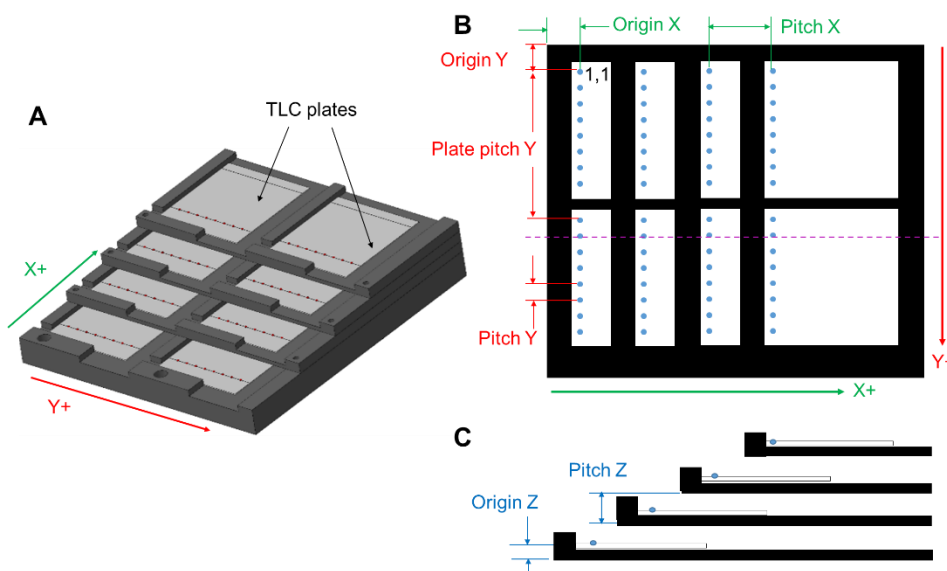


**Figure 5-13 The TLC plate holder.**

(A) 3D CAD model of the TLC plate holder with TLC plates installed. (B) Top-view schematic of the TLC plate holder. (C) Side-view schematic of the TLC plate holder along the dashed purple line in B.

The 4 chip heaters acted as “chip nests”, with a set of parameters (Origin X, Origin Y, Origin Z, Pitch X, Pitch Y) to define the positions of the individual reaction sites. Similar to microwell plates, the reference position for each heater was defined as the top, back, left corner.

The position of the priming sensor was determined by moving the pipette cone (in fully-extended state) to an XY position visually above the approximate center of the sensor opening, and Z position 2.0 cm above the center of the IR beam. (This Z position was chosen to ensure there were no collisions with the reagent dispensers while priming the pipette cone.) With the cone in position, a droplet of water (50  $\mu\text{L}$ , the minimum volume necessary to generate a droplet) was dispensed from the pipette cone and the signal from the IR sensor was monitored to determine if the beam was interrupted by the droplet. The X and Y offsets were refined until a position was found where the droplet interrupted the beam and did not make contact with any side of the sensor opening.

The positions of the tips of the reagent dispensers were defined as offsets relative to the pipette cone center to enable the system to position the desired dispenser at the optimal height above a desired reaction site on a chip or well in a microwell plate. The Z offset (a single value for all dispensers) was set to a value that caused the tip of the nozzle to be 1.0 cm above the surface when the fully-extended pipette cone contacted that same surface. The X and Y offset positions were initially set to values determined from the CAD model, but were individually refined. Beginning with the initial position of a dispenser over a chip reaction site, the X and Y offsets were fine-tuned to ensure that 1  $\mu\text{L}$  droplets of DI water were dispensed to the center of the reaction site. Fine-tuning was repeated until a position was found where 20 successive droplets could be dispensed without any splashing. For accessing the priming sensor, a set of additional position offsets (applied in additive manner to the other offsets) was defined for each reagent dispenser. This was needed both because the dispensers do not dispense liquid in a perfectly vertical direction and because the priming sensor uses a 2.0 cm gap between the nozzle tip and the IR beam of the sensor (compared to the 1.0 cm gap used when dispensing to other locations). Starting in the initial offset position, the X and Y offsets were refined until a position was found where a 1  $\mu\text{L}$  droplet of DI water caused a significant change in the IR sensor signal (>50 mV change from baseline).

### 5.6.2.3 Pipette cone contact sensor

To provide a capability for accurate vertical positioning, a “contact sensor” was integrated into the pipette cone. Small pieces of copper tape (CTF-1/4, Bertech-Kelex Inc. Torrance, CA, USA) were affixed in two distinct locations: the underside of the pipette cone mount and on the top surface of the fluidic head main body (**Figure 5-14**). Wires were soldered to each of two separate pieces of tape on the lower portion, such that when the pipette cone was fully extended, the upper tape would make contact and bridge the electrical circuit. One wire was held at +5 V, while the other was connected to a digital input port on the microcontroller with a pull-down resistor. When the pipette cone was fully extended and contact was made, the circuit is completed and a +5 V signal is detected by the microcontroller. When used as a contact sensor, the Z position is lowered until the extended pipette cone touches a surface, and because the pipette cone is mounted via a pneumatic cylinder (essentially a spring), the cone can move upwards slightly and break the circuit, causing the microcontroller to read a 0 V signal.

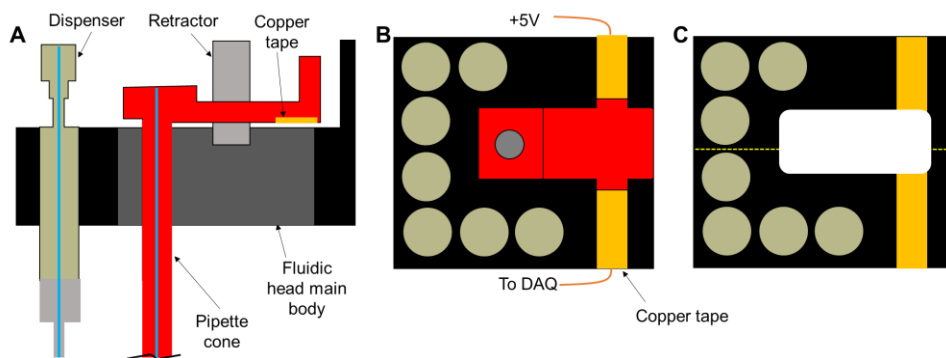


**Figure 5-14 Pipette cone contact sensor.**

(A) Section view of the fluidics head and pipette cone to show the detailed design of the contact sensor. (B) Top view schematic showing the tape arrangement for bridging the circuit when contact is made. (C) Top view but the pipette tip is removed, and the two separate copper tape lines are shown. The dotted yellow line indicates the location of the section plane for (A).

To determine a surface location, the fluidics head would be moved above the location of interest and the pipette cone fully extended. The cone actuator pressure was set to “low” (5 psig), and the fluidics head was then lowered very slowly until the microcontroller detects that contact

is made. As a “debouncing” algorithm, contact was confirmed if the contact signal remained at +5V for an additional number of downward movement steps (150  $\mu\text{m}$ ) of the fluidics head. The height value was set to be the Z position at which contact was first detected.

The contact sensor is also used during optimization experiments for accurate determination of the position of the top surface of installed multi-reaction chips. The height can vary slightly due to the use of thermal paste between the heaters and chips, and compensation is needed during the crude product collection process to ensure efficient transfer of liquid off of the reaction site.

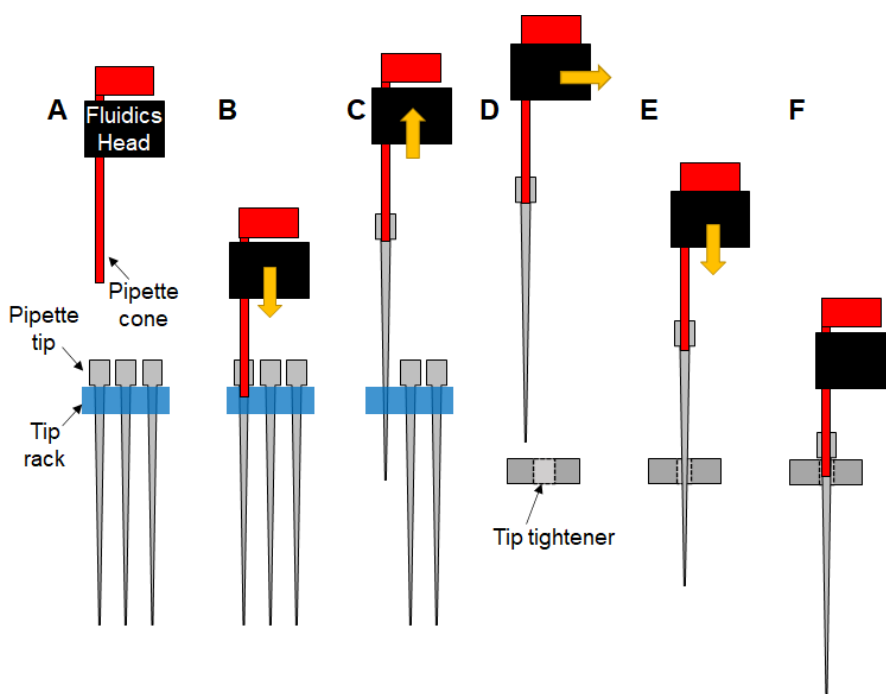


**Figure 5-15 Time sequence of the pipette tip attachment routine.**

(A) Pipette cone moved above next pipette tip. (B) Fluidics head lowered until contact sensor is triggered. (C) Pipette tip lefted out of rack. (D) Pipette and cone moved above tip tightener. (E) Pipette tip aligned with center of hole and lowered. (F) Lowering is continued to a fixed Z position to ensure a tight fit of pipette tip to the cone.

Automated contact sensing is also used during pipette tip installation to ensure reliable attachment of tips to the pipette cone. We discovered that the pipette tip rack is not very rigid and flexes when the pipette cone is lowered to install the next new pipette tip, giving rise to variability in how far the cone is inserted into each tip. We developed an algorithm (**Figure 5-15**) making

use of the contact sensor to reduce this variation. First, the pipette cone is moved above the location of the next available pipette tip (tracked by the program), and the pipette cone is extended with pressure set to the “tip attach” setting (10 psig). The fluidics head is then moved downwards until the contact sensor is triggered, ensuring the tip is reliably picked up. (Error checking and correction systems are implemented in case of a missing pipette tip, or in case the cone initially hits the edge of the pipette tip.) Next, the cone and tip are retracted and moved over to a nearby tip tightener to ensure a leak-free tip installation. The tip tightener is rigid with a hole that is large enough for the tapered tip to pass through, but smaller than the tip attachment point. With the pipette cone actuator set at the maximum setting (30 psig), the fluidic head is then lowered to ensure a snug fit of the cone into the tip.

### **5.6.3 Configuration files**

Configuration and calibrations are stored in a set of four XML-like files – the master configuration, array definitions, liquid definitions, and experiment configuration.

#### **5.6.3.1 Master configuration**

This file contains information about the XYZ actuator’s physical settings (*e.g.* step-to-mm conversion rate), the locations of specific components that never change (*e.g.* tip removal, priming sensor), the communication settings for the control system, physical offsets (in X, Y, and Z) for the 7 dispensers with respect to the pipette cone (plus additional offsets needed for priming), excess volume used in TLC spotting pipette actions, tubing volumes for each dispenser, syringe pump settings (*e.g.* pump speed, tubing volume), heater temperature calibrations, maximum temperature, and the index positions of the “nests” for the four plate and four chip locations.

#### **5.6.3.2 Array configuration**

This file contains the definitions and parameters for all of the plate types and chip designs that have been set up for use in the system. New types can be added by modifying this file. For each ‘array’ definition, configuration information includes a descriptive name, type of array (chip,

plate, TLC plate holder, or tip rack) and physical dimensions such as origin X and Y values (i.e. location of center of (1,1) position with respect to the plate nest reference), Z-axis offsets for specific positions and clearances above this object, number of positions in X and Y, pitch (i.e. center to center distance) in X and Y directions, and maximum volume (tip, well, or reaction site). The pipette tip rack and TLC plate holder definitions also include parameters specific to their type (e.g. tip racks include the length of the pipette tips).

### **5.6.3.3 Liquid definitions**

This file contains the calibrations for all of the reagent dispensers. For each dispenser, configuration information includes the dispenser number, descriptive name of calibration data, date/time of last calibration, solvent name, reagent dispensing pressure, calibration curve slope and intercept (i.e. of volume dispensed versus valve-open-duration), the volume to be dispensed per priming “droplet”, and repriming interval (i.e. if elapsed time since last dispense exceeds this value, the dispenser will be re-primed before further use).

### **5.6.3.4 Experiment configuration**

This file specifies which types of pipette tips, well plates, chip designs, and TLC plates are installed in each of the plate or chip nests for the experiment.

### **5.6.3.5 Using the configuration files**

At the beginning of an experiment the configuration files are loaded in the following order: (i) master configuration, (ii) array definitions, (iii) liquid definitions, (iv) experiment configuration, (v) method file (defined below). The LabView program decodes the files and loads the configuration information into an in-memory global variable for use during runtime.

## **5.6.4 Method files**

Each optimization experiment is specified via a “method” file, which contains definitions and a list of commands to perform. The underlying scripting language was inspired by the software design of the ELIXYS FLEX/CHEM radiosynthesizer (SOFIE, Inc.), where a synthesis protocol is

defined not by a time series of individual hardware state changes, but by a short sequence of intuitive “unit operations” (e.g. ‘add reagent’, ‘evaporate’, ‘react’, etc.)(225). The LabView program parses this file and creates an array of states that the main program traverses to carry out the automated experiment. For more complicated experiments, a “method writer wizard” was developed to assist with script generation via a graphical user interface.

#### 5.6.4.1 Set definitions

Most experiments require repeated operations involving the same group of reaction sites, e.g. a subset of all chips, a single full chip, or a subset of reaction sites representing replicates of a specific condition. To simplify programming, a simple variable declaration syntax allows users to define a “set” of locations on plates or chips that will instruct the system to repeat an operation with all locations within the set. This reduces program length and debugging time. The syntax of set definitions is as follows:

$$\$SetName = [C \text{ or } P]( (N_1, X_1, Y_1), (N_2, X_2, Y_2), \dots (N_n, X_n, Y_n) )$$

[C or P] denotes the type of set ([C]hip or [P]late), and each grouping of (N, X, Y) is a specific reaction site or microwell, with N denoting the chip or plate number, and X and Y denoting the array indices of the particular reaction site or microwell within the chip or plate.

The plates and chips are numbered as shown in **Figure 5-16**. An exploded view of the heating platform is shown in **Figure 5-17**.

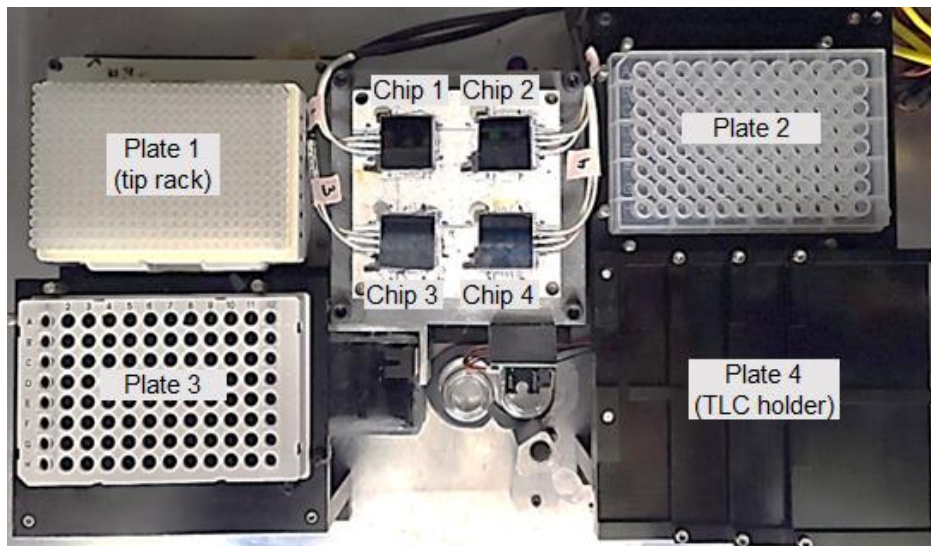


**Figure 5-16** Numbering of the plate nests and chip nests within the work area.



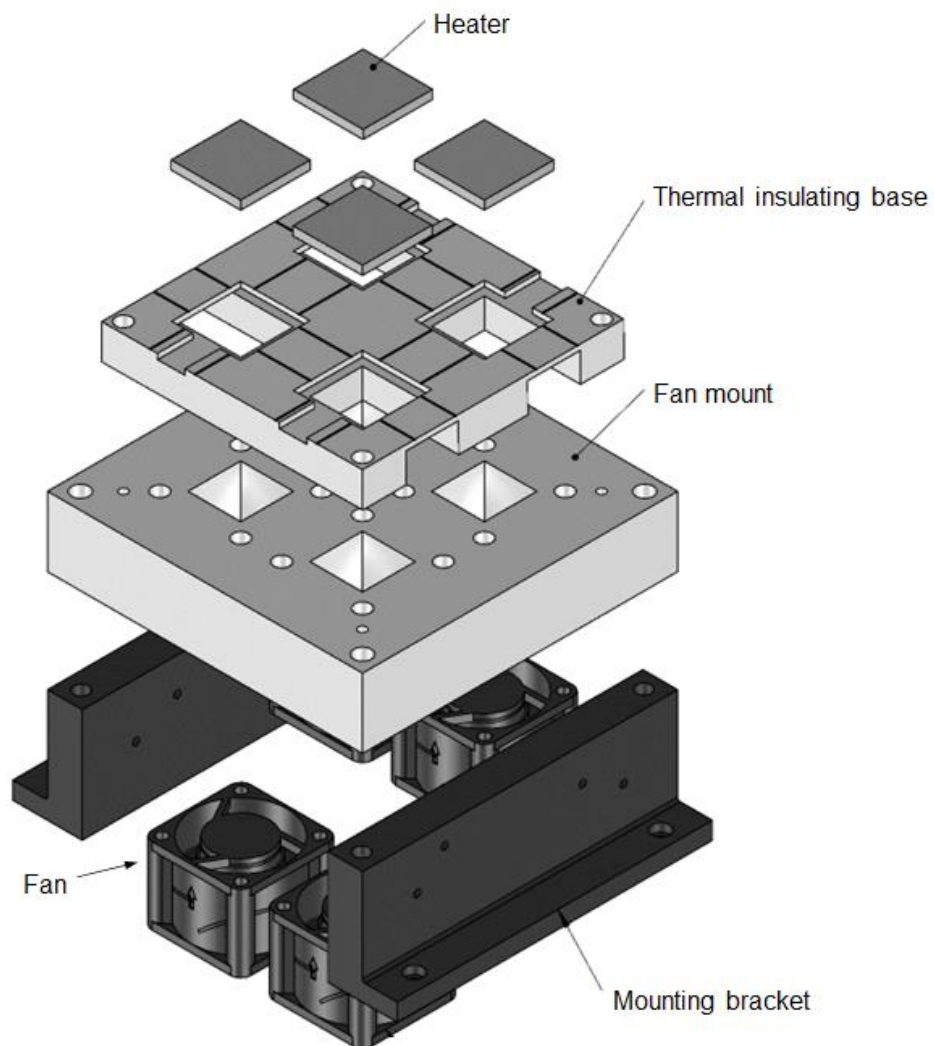


**Figure 5-17** An exploded view of the chip heating platform at the center of the work area.

As shown in **Figure 5-18A,B**, individual microwells or reaction sites are numbered with X,Y coordinates beginning with 1,1 in the left, rear corner (reference position). In the case of TLC plates, there are up to 8 TLC plates installed, but there is a single set of spotting positions numbered as shown in **Figure 5-18C**.

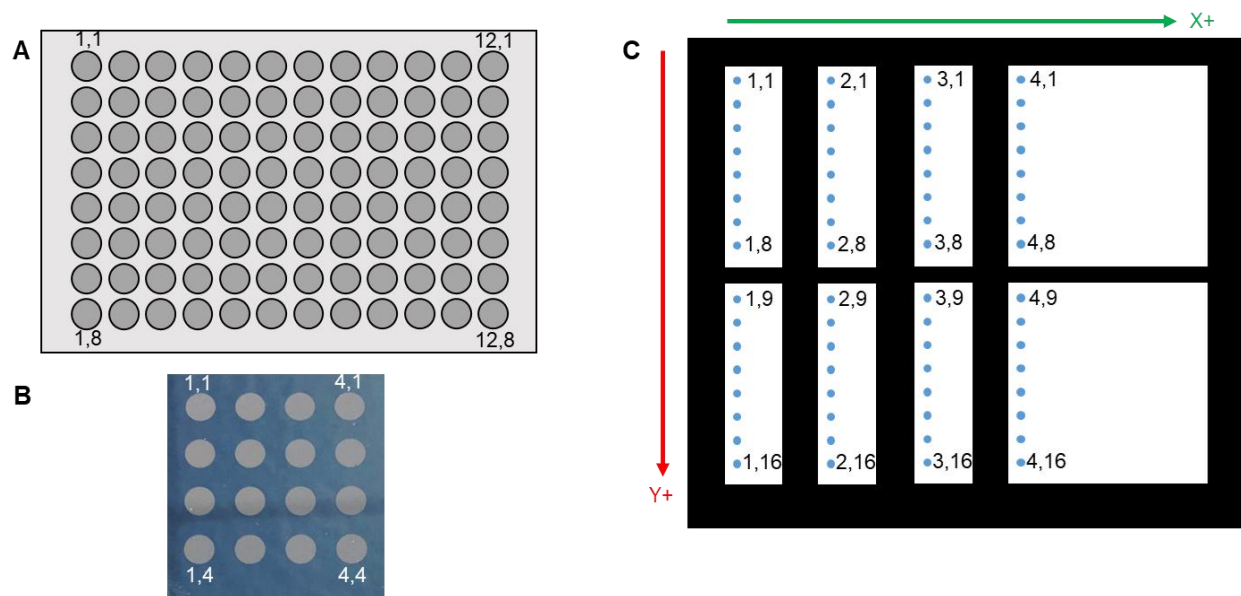


**Figure 5-18 (A) Numbering of wells in microwell plates and the pipette tip rack. (B) Numbering of reaction sites on multi-reaction chips. (C) Number of TLC spotting locations across multiple TLC plates installed in the TLC plate holder.**

#### 5.6.4.2 Dispenser specification

Additional notation was created for defining the dispensers to be used in the experiment.

*#DispenserName = (dispenserNumber, CalibrationName)*

Here *dispenserNumber* is the physical dispenser within the system (**Figure 5-19**) to be used and can range from 1 to 7, and *CalibrationName* references a specific calibration in the liquid definitions configuration file corresponding to the desired solvent at the desired reagent driving pressure for that dispenser. All dispensers defined in this manner are considered to be “active” during the synthesis, meaning that they will be pressurized.

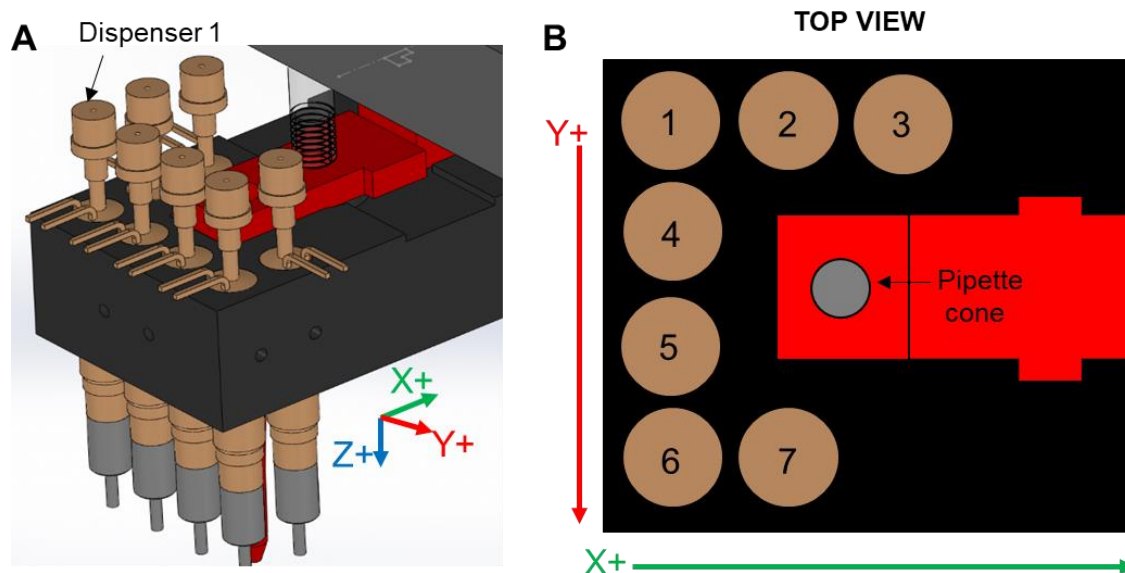


**Figure 5-19 (A) 3D CAD model of the fluidics head. (B) Top view schematic of the fluidics head showing the numbering scheme for dispensers.**

#### 5.6.4.3 Commands

The full set of available unit operations (and associated parameters) is listed in **Table 5-2**. Note that there are a few restrictions implicit in these definitions. For operations with multiple parameters that are “sets”, the sets must match in size. For example, if performing `Transfer_NN_Plate_Chip`, the sets designated by `FROM_Plate` and `TO_Chip` must have the same length, and each of the designated wells in `FROM_Plate` will be transferred to the corresponding reaction site in `TO_Chip`. Volume parameters can either be an array of values (with the same size as any sets used in the operation), or it can be a single value. Note that the ordering of sets and arrays is critical – the elements will be matched up in the order they are listed.

Note that the system automatically keeps track of the Z-position of the fluidics head, and will raise it to the clearance height as needed before any XY movements between plates, chips, or other parts of the system.

**Table 5-2 List of available unit operations in “method” files.**

Operation, Description, and Syntax	Parameters	
<p><b>Pause</b></p> <p>Tells the system to wait, with motors disabled, until the user presses the continue button on the main software front panel.</p> <p>Pause( Location [optional], "Note")</p>	<p><i>Location</i></p> <p>A single word which tells the system what to do before and after the pause step. Any number of these words can be added, separated by commas before the Note</p> <p><i>Home:</i> The system will move to the home position (0,0,0) before pausing.</p> <p><i>Chip:</i> The system will perform a chip height measurement after the pause step for all installed chips.</p> <p><i>Access:</i> The system will move to a specific location that allows the user to easily install or remove dispense reservoirs or tubing.</p>	
	<i>Note</i>	A string, in quotation marks, which displays during the pause step on the front panel. Allows a user to remind themselves on which steps are taking place and to perform imaging if desires.
<p><b>Transfer_1N_Plate-Chip</b></p> <p>Transfer a specified volume from 1 plate well to N different reaction sites on installed chips</p> <p>Transfer_1N_Plate-Chip( FROM_Plate, TO_Chip, VolumeEach)</p>	<i>FROM_Plate</i>	Set describing well location(s) to transfer FROM
	<i>TO_Chip</i>	Set describing reaction sites to transfer TO
	<i>VolumeEach</i>	Array of volume(s) ( $\mu\text{L}$ ) to be dispensed to each chip site OR a single volume used across all transfers
<p><b>Transfer_NN_Plate-Chip</b></p> <p>Transfer a specified volume from N different plate wells to N different reaction sites on installed chips</p> <p>Transfer_NN_Plate-Chip( FROM_Plate, TO_Chip, VolumeEach, Mix)</p>	<i>FROM_Plate</i>	Set describing well locations to transfer FROM
	<i>TO_Chip</i>	Set describing reaction sites to transfer TO
	<i>VolumeEach</i>	Array of volume(s) ( $\mu\text{L}$ ) to be dispensed to each chip site OR a single volume used across all transfers
	<i>Mix</i>	Boolean to define if mixing should occur after each transfer
<p><b>Transfer_NN_Chip-Plate</b></p> <p>Transfer a specified volume from N different reaction sites on installed chips to N different wells</p> <p>Transfer_NN_Chip-Plate( FROM_Chip, TO_Plate, VolumeEach, Mix)</p>	<i>FROM_Chip</i>	Set describing reaction sites to transfer FROM
	<i>TO_Plate</i>	Set describing well locations to transfer TO
	<i>VolumeEach</i>	Array of volume(s) ( $\mu\text{L}$ ) to be dispensed to each well location OR a single volume used across all transfers or
	<i>Mix</i>	Boolean to define if mixing should occur after each transfer
<p><b>Dispense_Chip</b></p> <p>Dispense a volume of reagent from desired dispenser to reaction sites</p> <p>Dispense_Chip( #Dispenser, TO_Chip, Volume, Dump[optional])</p>	<i>#Dispenser</i>	Dispenser ID for this action, defined beforehand in method
	<i>TO_Chip</i>	Set describing reactions sites to dispense reagent TO
	<i>Volume</i>	Array of volume(s) ( $\mu\text{L}$ ) to be dispensed to each chip site OR a single volume used for all dispenses
	<i>Dump</i>	Single character ("D"), if included, tells the system to empty the reservoir of this dispenser into the priming waste after this action.
<p><b>Dispense_Plate</b></p>	<i>#Dispenser</i>	Dispenser ID for this dispense, defined beforehand in method

Dispense a volume of reagent from desired dispenser to plate wells  Dispense_Plate( <i>#Dispenser,</i> <i>TO_Plate,</i> <i>Volume</i> )	<i>TO_Plate</i>	Set describing the plate wells to dispense reagent TO
	<i>Volume</i>	Array of volume(s) (µL) to be dispensed to each well location OR a single volume used for all dispenses
<b>Heat</b>  Sets the array of heaters to the specified temperatures for the specified durations  Heat( <i>[(Temperature,Duration),...],</i> <i>NoCooldown</i> )	<b>Special Array Syntax</b>	( (Temperature1, Duration1), (Temperature2, Duration2), (Temperature3, Duration3), (Temperature4, Duration4) )
	<i>--Temperature<sub>N</sub></i>	Temperature set point for heater N (°C); if set to 0, heater N is inactive during operation
	<i>--Duration<sub>N</sub></i>	Time that heater N should stay at the specified set point (seconds); if set to 0, heater N is inactive during operation
	<i>NoCooldown</i>	Single character ("N"), if included, tells the system to bypass the cooling time after this heating step. Used in ramping heating procedures.
<b>Heat_Replenish</b>  Sets the array of heaters to the specified temperatures for the specified durations, and also dispenses a specific volume to all reaction sites at a set interval (except heaters for which the heating duration has expired)  Heat_Replenish( <i>[(Temperature, Time)],</i> <i>#Dispenser,</i> <i>ReplenishTime,</i> <i>SET_Replenish,</i> <i>Volume</i> )	<b>Special Array Syntax</b>	( (Temperature1, Duration1), (Temperature2, Duration2)... )
	<i>--Temperature<sub>N</sub></i>	Temperature set point for heater N (°C); if set to 0, heater N is inactive during operation
	<i>--Duration<sub>N</sub></i>	Time that heater N should stay at the specified set point (seconds); if set to 0, heater N is inactive during operation
	<i>#Dispenser</i>	Dispenser ID for this operation, defined beforehand in method
	<i>ReplenishTime</i>	Interval that must pass between each dispensing to the active chips (seconds)
	<i>SET_Replenish</i>	Set describing the reaction sites to be replenished  Note: Once a heater has finished its Duration, all reaction sites for that heater are ignored for replenishment
	<i>Volume</i>	Array of volume(s) (µL) to be dispensed to each chip site OR a single volume used across all transfers
<b>Plate-TLC</b>  Transfers a small volume from N plate wells to TLC plates. TLC plate sets are described in the next section.  Plate-TLC( <i>FROM_Plate,</i> <i>SET_TLC,</i> <i>Volume</i> )	<i>FROM_Plate</i>	Set describing well locations to transfer FROM
	<i>SET_TLC</i>	Set describing TLC plate locations to spot TO
	<i>Volume</i>	Array of volume(s) (µL) to be dispensed to each chip site OR a single volume used across all transfers
<b>Collect_Chip</b>  Dispenses collection solvent to reaction sites and then transfers that volume to plate wells in series, with multiple repeats of dispense/transfer per site  Collect_Chip( <i>FROM_Chip,</i> <i>TO_Plate,</i> <i>#Dispenser,</i> <i>Volume_dispen</i> <i>se,</i> <i>Volume_initial,</i> <i>N_repeats</i> )	<i>FROM_Chip</i>	Set describing reaction sites to transfer FROM
	<i>TO_Plate</i>	Set describing plate wells to transfer TO
	<i>#Dispenser</i>	Dispenser ID for this dispense, defined beforehand in method
	<i>Volume_dispen</i> <i>se</i>	Volume (µL) to dispense each collection cycle
	<i>Volume_initial</i>	Estimated volume (µL) expected to be at the reaction sites at the beginning of this operation
	<i>N_repeats</i>	Number of times to repeat the dispense and transfer cycle per collection site
<b>Collect_TLC</b>	<i>FROM_Chip</i>	Set describing reaction sites to transfer FROM

Dispenses collection solvent to reaction sites and then transfers that volume to plate wells in series, with multiple repeats of dispense/transfer per site. This step also immediately spots to the specified TLC location after collection.  Collect_Chip( FROM_Chip, TO_Plate, #Dispenser, Volume_dispense, Volume_initial, N_repeats, SET_TLC, TLC_volume)	TO_Plate	Set describing plate wells to transfer TO
	#Dispenser	Dispenser ID for this dispense, defined beforehand in method
	Volume_dispense	Volume (μL) to dispense each time a transfer happens
	Volume_initial	Estimated volume (μL) expected to be at the reaction sites at the beginning of this action
	N_repeats	Number of times to repeat the dispense and transfer routine per collection site
	SET_TLC	Set describing which TLC sites to spot each collection TO
	TLC_Volume	Volume (μL) to spot to each TLC plate after collection

**Table 5-3** summarizes the low-level steps that are performed internally to implement each operation. The table is written with pseudocode and uses terminology from **Table 5-2**. Note that the software automatically finds certain needed parameters from the configuration files. For example, Z\_Pipette\_Aspirate is the value for the specific type of plate being used in the method file. Additionally, the appropriate dispenser offsets in X, Y or Z are automatically applied depending on which dispenser is specified by the unit operation parameters.

**Table 5-3 Low-level steps to implement each command (unit operation) and some helper commands**

Unit operation	Steps (psuedocode)
<b>Pause</b>  Tells the system to wait, with motors disabled, until the user presses the continue button on the main software front panel.  Pause( Location [optional], "Note")	Display Note IF Location INCLUDES "Home" Home() IF Location INCLUDES "Access" MoveXY to Access_Coordinatnes MoveZ to Access_Z Disable Motors Wait until Continue_Button=True IF Location INCLUDES "Chips" Chip_Surface_Routine()
<b>Chip_Surface_Routine</b>  Measures the chip height of all installed chips and calculates the chip height profile for accurate Z movement.  Chip_Surface_Routine()	Loop (j = 1 to N=size(Installed_Chips)) Loop over 4 corners MoveXY to Corner(Chip j) - EdgeOffset MoveZ to Clearance_Z_Local Extend Pipette Cone Set Cone Pressure to Low Debounce=0 While Debounce < Debounce_Limit MoveZ down 1 IF Contact_Sensor = HIGH Debounce+1 ELSE Debounce=0

Unit operation	Steps (psuedocode)
	<pre> Set Corner Height MoveZ to Clearance_Z_Local Origin_Z(j) = Top Left Height DZ/DX(j) = (Top Right + Bottom Right) - (Top Left + Bottom Left) / 2 * Distance DZ/DY(j) = (Bottom Left + Bottom Right) - (Top Left + Top Right) / 2 * Distance </pre>
<p><b>Pipette_Mix</b></p> <p>Mix current contents in pipette tip via repeated aspirate and dispense steps.</p> <p>Pipette_Mix( Volume)</p>	<pre> Loop (j = 1 to Num_Mix_Cycles) Aspirate Volume (pipette) IF (j = Num_Mix_Cycles) Dispense Volume + TipMaxVolume/4 (pipette) ELSE Dispense Volume (pipette) </pre>
<p><b>Pipette_Mix_Microwell</b></p> <p>Mix contents of a microwell at the current XYZ position via repeated aspirate and dispense steps.</p> <p>Pipette_Mix_Microwell ( Volume, Z_Aspirate, Z_Dispense)</p>	<pre> Pipette_Mix(Volume) Loop j = 1 to Num_Mix_Cycles Aspirate Volume (pipette) IF (j = Num_Mix_Cycles) Dispense Volume + TipMaxVolume/4 (pipette) ELSE Dispense Volume (pipette) Move Z to Z_Dispense Aspirate TipMaxVolume/4 (pipette) Move Z to Z_Aspirate </pre>
<p><b>Transfer_1N_Plate-Chip</b></p> <p>Transfer a specified volume from 1 plate well to N different reaction sites on installed chips</p> <p>Transfer_1N_Plate-Chip( FROM_Plate, TO_Chip, VolumeEach)</p>	<pre> Get next tip Loop (i=1 to N=Size(TO_Chip)) IF (Volume_In_Tip = 0) Move XY to position FROM_Plate IF (i = 1) Pipette_Mix_Microwell (Tip_Max_Volume, Z_Pipette_Aspirate for FROM_Plate[i], Z_Pipette_Dispense for FROM_PLATE[i]) While (Volume_In_Tip+VolumeEach &lt;= TipMaxVolume) Aspirate VolumeEach (pipette) Move XY to position TO_Chip[i] Move Z to Z_Pipette_Dispense for TO_Chip[i] Dispense VolumeEach Remove tip Dispense Volume_In_Tip </pre>
<p><b>Transfer_NN_Plate-Chip</b></p> <p>Transfer a specified volume from N different plate wells to N different reaction sites on installed chips</p> <p>Transfer_NN_Plate-Chip( FROM_Plate, TO_Chip, VolumeEach, Mix)</p>	<pre> Loop (i=1 to N=Size(TO_Chip)) Get next tip Move XY to position FROM_Plate[i] Move Z to Z_Pipette_Aspirate for FROM_Plate[i] Pipette_Mix_Microwell (Tip_Max_Volume, Z_Pipette_Aspirate for FROM_Plate[i], Z_Pipette_Dispense for FROM_PLATE[i]) Aspirate VolumeEach Move XY to position TO_Chip[i] Move Z to Z_Pipette_Dispense for TO_Chip[i] Dispense volume IF (Mix) Pipette_Mix(VolumeEach) Remove tip </pre>
<p><b>Transfer_NN_Chip-Plate</b></p> <p>Transfer a specified volume from N different reaction sites on installed chips to N different wells</p>	<pre> Loop (i=1 to N=Size(TO_Plate)) Get next tip Move XY to position FROM_Chip[i] Move Z to Z_Pipette_Aspirate for FROM_Chip[i] Aspirate VolumeEach Move to position TO_Plate[i] </pre>

Unit operation	Steps (psuedocode)
Transfer_NN_Chip-Plate( <i>FROM_Chip,</i> <i>TO_Plate,</i> <i>VolumeEach,</i> <i>Mix</i> )	<pre> Move Z to Z_Pipette_Dispende for TO_Plate[i]   IF (Mix)     Pipette_Mix(VolumeEach) Dispense VolumeEach + Volume_In_Tip/4 (pipette) Remove tip Aspirate Volume_In_Tip/4 (pipette) </pre>
<b>Dispense_Chip</b>  Dispense a volume of reagent from desired dispenser to reaction sites  Dispense_Chip( <i>#Dispenser,</i> <i>TO_Chip,</i> <i>Volume</i> )	<pre> IF(time since last use &gt; repriming time for dispenser)   Prime Dispenser Loop (i=1 to N=Size(TO_Chip))   Move XY to position TO_Chip[i]   Move Z to Z_Dispenser_Dispende for TO_Chip[i]   Dispense Volume[i] (dispenser) </pre>
<b>Dispense_Plate</b>  Dispense a volume of reagent from desired dispenser to plate wells  Dispense_Plate( <i>#Dispenser,</i> <i>TO_Plate,</i> <i>Volume</i> )	<pre> IF(time since last use &gt; repriming time for dispenser)   Prime Dispenser Loop (i=1 to N=Size(TO_Plate))   Move XY to position TO_Plate[i]   Move Z to Z_Dispenser_Dispende for TO_Plate[i]   Dispense Volume[i] (dispenser) </pre>
<b>Heat</b>  Sets the array of heaters to the specified temperatures for the specified durations  Heat( <i>[(Temperature,Duration),...]</i> )	<pre> Set temperature = Setpoint Wait Duration Set Heater_Temp = Cool_Temperature Wait (60s OR until Heater_Temp ≤ Cool_Temperature) </pre>
<b>Heat_Replenish</b>  Sets the array of heaters to the specified temperatures for the specified durations, and also dispenses a specific volume to all reaction sites at a set interval (except heaters for which the heating duration has expired)  Heat_Replenish( <i>[(Temperature, Time)],</i> <i>#Dispenser,</i> <i>ReplenishTime,</i> <i>SET_Replenish,</i> <i>Volume</i> )	<pre> Prime Dispenser Set Heater_Temp = Setpoint While(time elapsed &lt; Duration)   IF(time since last replenish &gt; Replenish_Time)     Loop (i=1 to N=Size(SET_Replenish))       Move XY to position SET_Replenish[i]       Move Z to Z_Dispenser_Dispende       Dispense Volume[i] (dispenser)     ELSE       Do nothing   Set Heater_Temp = Cool_Temperature   Wait (60s OR until Heater_Temp ≤ Cool_Temperature) </pre>
<b>Plate_TLC</b>  Transfers a small volume from N plate wells to TLC plates. TLC plate sets are described in the next section.	<pre> Loop (i=1 to N=Size(SET_TLC))   Get next tip   Move XY to position FROM_Plate[i]   Move Z to Z_Pipette_Aspirate for FROM_Plate[i]   Loop (j=1 to 5)     Aspirate Volume * 2 (pipette)     Dispense Volume * 2 (pipette) </pre>



Unit operation	Steps (psuedocode)
Plate-TLC( <i>FROM_Plate,</i> <i>SET_TLC,</i> <i>Volume)</i>	Aspirate Volume + AdditionalVolume Move XY to position SET_TLC[i] Move Z to Z_Pipette_Dispende for SET_TLC[i] Wait Dwell_Time Dispense Volume + Volume_In_Tip/4 (pipette) Remove tip Aspirate Volume_In_Tip/4 - AdditionalVolume (pipette)
<b>Collect_Chip</b>  Dispenses collection solvent to reaction sites and then transfers that volume to plate wells in series, with multiple repeats of dispense/transfer per site  Collect_Chip( <i>FROM_Chip,</i> <i>TO_Plate,</i> <i>#Dispenser,</i> <i>Volume_dispense,</i> <i>Volume_initial,</i> <i>N_repeats)</i>	Home Prime Dispenser Loop(i=1 to Size(FROM_Chip)) Get next tip Loop(j=1 to Collection_Cycles) Retract Tip Move XY to dispenser position FROM_Chip[i] Move Z to Z_Dispenser_Dispende for FROM_Chip[i] IF(j=1) Dispense Volume[i] - starting Volume[i] (dispenser) ELSE Dispense Volume[i] (dispenser) Move XY to pipette position FROM_Chip[i] Extend Tip Move Z to Z_Pipette_Aspirate for FROM_Chip[i] Loop(k=1 to Mixes) Aspirate Volume[i] (pipette) Dispense Volume[i] (pipette) Aspirate Volume[i] Move XY to pipette position TO_Plate[i] Move Z to Z_Pipette_Dispende for TO_Plate[i] Dispense Volume[i]+ Volume_In_Tip/4 (pipette) Move Z to Z_Pipette_Dispende - 1 cm Aspirate Volume_In_Tip/4 µL (pipette) Move Z to Z_Pipette_Aspirate Loop(j=1 to Mixes) Aspirate Pipette Tip_Volume - Volume_In_Tip/4 (pipette) Dispense Pipette Tip_Volume - Volume_In_Tip/4 (pipette) Move Z to Z_Local_Clearance Wait 500 ms Dispense Volume_In_Tip/4 (pipette) Remove Tip Aspirate Volume_In_Tip/4 (pipette) Remove Tip and Aspirate Volume_In_Tip/4 (pipette)
<b>Collect_TLC</b>  Dispenses collection solvent to reaction sites and then transfers that volume to plate wells in series, with multiple repeats of dispense/transfer per site. This step also immediately spots to the specified TLC location after collection.  Collect_Chip(	Home Prime Dispenser Loop(i=1 to Size(SET_TLC)) Get next tip Loop(j=1 to Collection_Cycles) Retract Tip Move XY to dispenser position FROM_Chip[i] Move Z to Z_Dispenser_Dispende for FROM_Chip[i] IF(j=1) Dispense Volume[i] - starting Volume[i] (dispenser) ELSE

Unit operation	Steps (psuedocode)
<p><i>FROM_Chip,</i>  <i>TO_Plate,</i>  <i>#Dispenser,</i>  <i>Volume_dispense,</i>  <i>Volume_initial,</i>  <i>N_repeats,</i>  <i>SET_TLC,</i>  <i>TLC_volume</i></p>	<pre> Dispense Volume[i] (dispenser) Move XY to pipette position FROM_Chip[i] Extend Tip Move Z to Z_Pipette_Aspirate for FROM_Chip[i] Loop(k=1 to Mixes)     Aspirate Volume[i] (pipette)     Dispense Volume[i] (pipette)     Aspirate Volume[i] (pipette) Move XY to pipette position TO_Plate[i] Move Z to Z_Pipette_Dispense for TO_Plate[i] Dispense Volume[i]+ Volume_In_Tip/4 (pipette) Move Z to Z_Pipette_Dispense - 1 cm Aspirate Volume_In_Tip/4 μL (pipette) Move Z to Z_Pipette_Aspirate Loop(j=1 to Mixes)     Aspirate Pipette Tip_Max_Volume - Volume_In_Tip/4 (pipette)     Dispense Pipette Tip_Max_Volume - Volume_In_Tip/4 (pipette) Aspirate TLC_volume + AdditionalVolume Move to SET_TLC[i] Move Z to Z_Pipette_Dispense Dispense TLC_volume + Volume_In_Tip/4 Remove Tip Aspirate Volume_In_Tip/4 μL - AdditionalVolume (pipette) </pre>

### 5.6.5 Motion acceleration algorithm

To maximize movement accuracy and precision, motors are operated at a setting of 4000 microsteps/revolution. Because high motion speed is also critical (to minimize radioactive decay), motors were driven at the highest practical speeds. Under these circumstances, we found that the LabView program could not reliably supply the stepper drivers with the needed pulse rates, and thus instead used a microcontroller to generate pulses and direction signals to the stepper motor drivers.

Since our system has a large momentum arm (Z-axis actuator plus fluidics head), we found it necessary to implement smooth acceleration and deceleration, requiring varying delays (intervals) between subsequent pulses. For computational efficiency, we pre-computed and stored these delays in a look-up table in the microcontroller memory. The same lookup table was used for all 3 motion axes. Calculations were based on an S-curve motion profile, following the

concepts and discretized kinematic equations described by Zeng *et al.*(226) and Nguyen *et al.*(227).

$$J(t_n) = \begin{cases} J_0 & V(t_n) \leq V_{t_0} + (V_{MAX} - V_{t_0})/2 \\ -J_0 & V(t_n) > V_{t_0} + (V_{MAX} - V_{t_0})/2 \end{cases} \quad (1)$$

$$A(t_n) = A(t_{n-1}) + J(t_n) \quad (2)$$

$$V(t_n) = \begin{cases} V_{t_0} & t = 0 \\ V(t_{n-1}) + A(t_n) & otherwise \end{cases} \quad (3)$$

$$D(t_n) = 1/V(t_n) \quad (4)$$

For these equations,  $J$  is the jerk (pulses/s<sup>2</sup>/μs),  $A$  is the acceleration (pulses/s/μs),  $V$  is the velocity (pulses/s),  $D$  is the delay (μs between pulses), and  $t_n$  is the time which increments by 1 μs for each increment of  $n$ .  $V_{MAX}$  is the maximum velocity specified in the master configuration file (40000 pulses/s).  $A_0$  is the initial acceleration (assumed to be 0).  $V_0$  is the startup velocity (a slow velocity used as the initial speed for motion operations).  $J_0$  is the magnitude of the jerk value.

To generate the lookup table, we iterate through  $n$  (starting at 0) to calculate the motion, and store selected values of  $D(t_n)$  into an array  $D_m$  indexed by  $m$  (starting at 0), according to the following algorithm:

Set initial time  $t_0 = 0$

Calculate initial motion values,  $J(t_0)$ ,  $A(t_0)$ ,  $V(t_0)$ ,  $D(t_0)$  from the equations

Save  $D_0 = D(t_0)$  into the lookup table (index  $m = 0$ )

Define  $T_m$  as the time value of the most recent lookup table entry. Set  $T_0 = t_0$  (index  $m = 0$ )

Loop while  $V(t_n) < V_{MAX}$ :

Increment  $n$

Compute  $t_n = t_{n-1} + 1$

Compute  $J(t_n)$ ,  $A(t_n)$ ,  $V(t_n)$ ,  $D(t_n)$  from the equations

If  $D(t_n) \leq (t_n - T_m)$  (i.e. a new pulse is needed):

Increment  $m$

Save  $D_m = D(t_n)$  into the lookup table

Set  $T_m = t_n$

Note that for our microcontroller, the lookup table could only fit 2500 entries, i.e. the time intervals between the first 2500 pulses. To maximize the smoothness of acceleration (and deceleration), the jerk value listed above was empirically chosen so the acceleration profile from  $V_0$  to  $V_{MAX}$  would require exactly 2500 pulses. Additionally, any necessary unit conversions have been excluded from the algorithm as written above for readability.

The completed lookup table was then used whenever a motion needed to be executed in this system. When beginning the motion step (acceleration phase), the lookup table values were read in order to determine the delay time between each of the initial 2500 pulses. For the next part of the motion (maximum velocity phase), the interval between pulses was taken as the final value in the lookup table. When the motion reached a position 2500 steps before the end point (deceleration phase), the lookup table values were read in reverse order to determine the interval between pulses for the final 2500 pulses. In circumstances where the total movement distance was less than 5000 steps (a full acceleration and deceleration), half of that number of values were read from the beginning of the table forward and then the same values in reverse order without a maximum speed section.

## **5.6.6 Subsystem calibration and characterization**

### **5.6.6.1 Dispenser calibration**

To calibrate a dispenser, a reservoir of the same size as the typical reservoir that would be used with the solvent (e.g. a 1.5 mL vial for [ $^{18}\text{F}$ ]fluoride mixture or precursors solutions, 5 mL vial for reaction solvents or deprotectants, and 20 mL vial for a collection solution) is filled at least 75% full and attached to the dispenser. The vial is then pressurized with the intended dispensing pressure (typically 5 psig) and the dispenser is primed. Next, sets of 10 sequential dispenses are performed with 200 ms delay between droplets, with the liquid from the full set of 10 dispenses

captured in an Eppendorf tube and the amount of collected liquid determined gravimetrically. This process is repeated for multiple sets of 10, each set having a different dispensing durations (i.e. 10 ms, 50 ms, 150 ms, 400 ms). The data is then used to construct a linear calibration curve of volume dispensed versus dispensing time. The calibration data are recorded in the “liquid definition” configuration file, indexed by a unique name and dispenser number, with details of solvent type, operating pressure, date of calibration, and fit parameters (slope, intercept).

We found that dispenser operation remains relatively consistent over time provided we performed regular cleaning and avoided corrosive solutions. To minimize drift in performance, recalibration was performed occasionally: ~monthly for solvents, and ~biweekly for solute-containing solutions. Note, however, that we found significant differences among different individual dispensers (see **Figure 5-20**), and thus it was critical that separate calibrations are performed for each individual dispenser in the system. All dispensers were all calibrated for DI water and MeCN, and additional calibrations were performed for additional solvents frequently used in conjunction with particular dispensers.

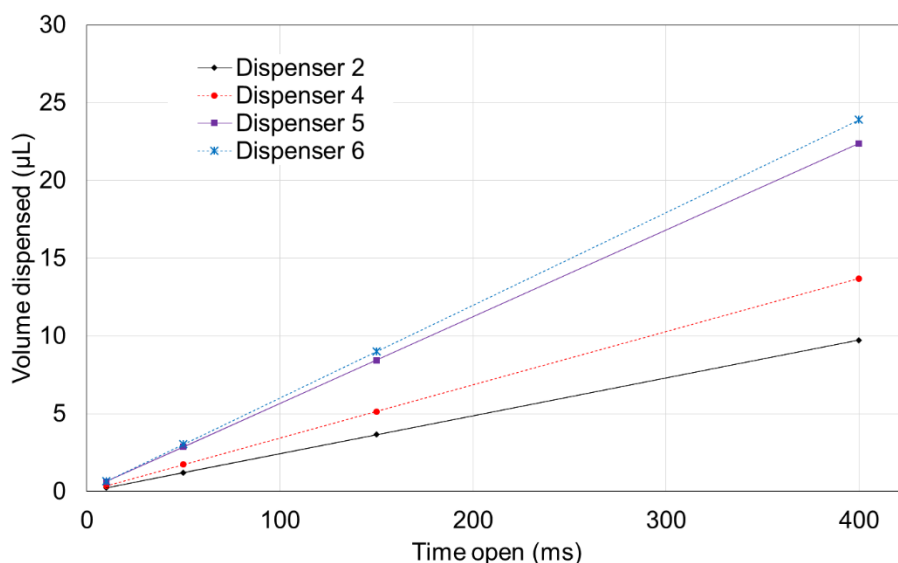


**Figure 5-20 Example calibration curves for 4 dispensers.**

In all cases, the solvent was filtered DI water, driving pressure was 5 psig, and reservoir size was 1.5 mL.

### **5.6.6.2 Heater Calibration**

Calibration of the heaters was performed by painting the top surface of each with a special high-emissivity paint (NEXTEL-Suede Coating 3101, Mankiewicz Gebr. & Co., Hamburg, Germany) and the temperature measured with an infrared (IR) camera (T621xx, FLIR Systems, Wilsonville OR, USA). Camera settings were changed to match the emissivity value of the paint (0.96) before imaging. Using an initial basic calibration based on output of the amplifier (AD8495, Adafruit Industries LLC, New York New York, USA) connected to the heater's built-in thermocouple, each heater was set to multiple temperatures between 20 and 125°C, and the surface temperature measured via an IR image (calculated as average of a region of interest that covers the heater surface). The IR-derived temperature was plotted as a function of thermocouple amplifier reading, and a linear fit was calculated to enable conversion of thermocouple amplifier signal to temperature. The slope and intercept for each heater were added to the "master configuration" file. (Note that preferably the calibration should include setpoints that match or exceed the highest temperatures expected during reactions, but the maximum operating temperature of the high-emissivity paint was 125°C.). Characterization of the performance of these heaters and on-off control algorithm has been reported in prior work(93).

### **5.6.6.3 Pipette Characterization**

To account for all aspects of pipetting, optimization of pipetting parameters and performance characterization were performed in the context of performing droplet collection operations. Collection was performed on an empty reaction site of a multi-reaction chip. A 3-cycle process was performed, in which 10  $\mu$ L of 9:1 MeOH:DI water was dispensed to the chip, and then transferred to a well in a strip-well plate. (No "mixing" operation, i.e. repeated aspirate and dispense steps, was used in these experiments.) Gravimetric measurements of the amount of liquid transferred to the strip-well, and measurements of the duration of the collection process,

were made as a function of syringe pump flow rates (**Table 5-4**). The pipette flow rate setting had relatively low impact on the duration of the collection process, but did have a significant impact on reliability. With a flow rate of 20  $\mu\text{L/s}$  or higher, the liquid in the pipette tip could “split” upon aspiration or dispensing leading to splashing or bubbling. Thus, we selected to use a rate of 10  $\mu\text{L/s}$  for further experiments.

**Table 5-4 Impact of syringe pump flow rate on pipetting accuracy and duration of crude product collection. Measurements were performed once (n = 1).**

Pipette flow rate setting ( $\mu\text{L/s}$ )	Volume collected ( $\mu\text{L}$ )	Duration of collection step (s)	Splashing / splitting / bubbling observed?
5	29.7	39.9	Never
10	28.7	35.9	Never
10	29.2	35.9	Never
20	29.0	33.3	Occasionally
30	28.8	33.5	Always
40	28.5	33.5	Always
50	28.3	33.5	Always
60	28.4	33.4	Always

#### 5.6.6.4 Pressure regulator calibration

To calibrate each pressure regulator, the regulator was supplied with  $\text{N}_2$  gas via a manual pressure regulator (ARX20-N01, SMC Corporation) set to  $\sim 62$  psig, and a digital pressure monitor (ISE30A-N01-C, SMC Corporation, Chiyoda City, Tokyo, Japan) was attached to the pneumatic output. To generate an analog electrical signal for the pressure setpoint, digital signals from the microcontroller were used to drive a digital potentiometer voltage divider. The microcontroller was used to generate various setpoint voltages in the range 0 – 3 V, and for each value we recorded the digital setting by the microcontroller, the resulting analog voltage divider output, the resulting stabilized pressure, and the analog electrical output of the pressure regulator (present value signal). From this data, we generated two linear calibrations: (i) actual pressure as a function of the digital setting for the potentiometer, and (ii) actual pressure as a function of the analog electrical pressure signal from the regulator. The slope and intercepts were stored within the microcontroller firmware. The calibration was repeated every few months.

The first calibration was used to enable the microcontroller to send appropriate signals to achieve a desired regulator pressure. The second calibration was used to enable the microcontroller to read the present pressure value. After setting a new pressure value, if the desired pressure is not reached (to ~0.1 psig tolerance) within 500 ms, the microcontroller will try nearby setpoints. If the desired pressure is not reached with 5 s, a timeout occurs.

#### **5.6.6.5 TLC spotting process**

We performed limited investigation of how to reliably to transfer samples via pipette to spotting locations on the TLC plate, based on the use of 0.5  $\mu\text{L}$  sample volume. (This volume was previously reported to be suitable for use on multi-lane TLC plates with similar pitch between lanes(96).) Several parameters were examined in the pursuit of a reliable method including: volume of sample initially aspirated, dwell time of the tip in contact with the TLC plate, and the volume of a dispense operation after the dwell time has elapsed. The most reliable protocol was to (i) aspirate 0.75  $\mu\text{L}$  of sample, place in contact with the TLC plate for 1 s, and then dispense a volume of 6.0  $\mu\text{L}$ . After extensive usage, this final protocol has resulted in zero failed TLC spotting attempts, no observed splashing, and qualitative consistency among sample deposition positions and volumes.

We did not more thoroughly characterize the accuracy of spotting volume, as TLC analysis only relies on the relative comparison between bands within a single lane, and small differences in volume or activity level of adjacent lanes does not affect the analysis.

### **5.6.7 Characterization experiments**

#### **5.6.7.1 Uniformity of [ $^{18}\text{F}$ ]fluoride dispensing and drying**

A dispenser reservoir was filled with 1.5 mL of an aqueous solution containing [ $^{18}\text{F}$ ]fluoride (370 MBq/mL) and  $\text{TBAHCO}_3$  (24 mM). 10  $\mu\text{L}$  portions were dispensed to all 64 reaction sites on 4 multi-reaction chips, and then the droplets were dried by heating to 95°C for 30 s and 110°C for 60s. The total radioactivity of each chip was assayed via dose calibrator, and the 4 chips were placed in a custom holder for simultaneous Cerenkov imaging (using a 60s exposure time). The



holder (**Figure 5-21**) was machined from black Delrin and contained 4 recesses (800  $\mu\text{m}$  deep) into which chips were inserted. An extra 2 mm deep pocket was machined in each recess to enable chips to be picked up more easily with tweezers after imaging. The chips were oriented as shown in the figure to fit them into the field of view of the camera.

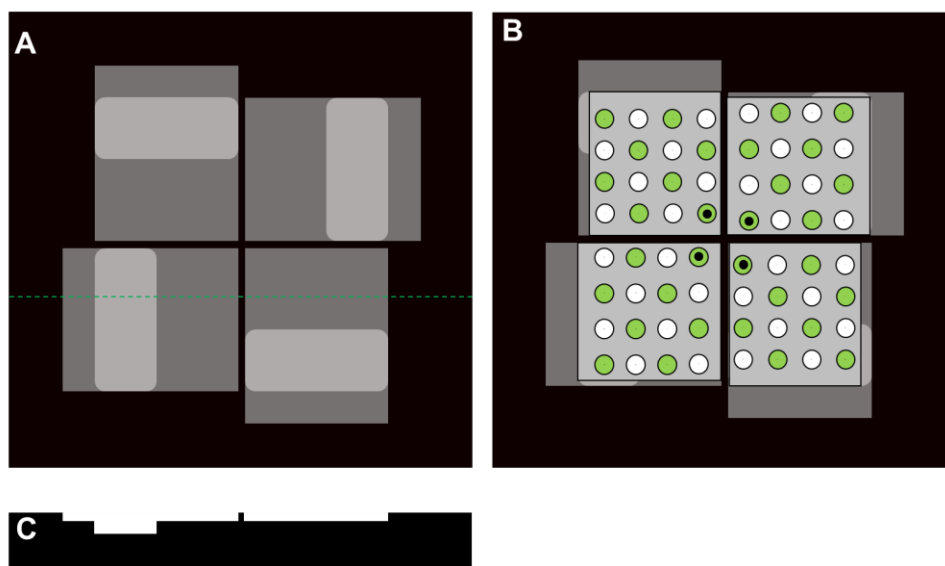


**Figure 5-21 Custom chip holder.**

(A) Top view schematic of the custom chip holder. (B) Schematic showing the placement of chips. In each case the 1,1 reagent site (designated by a black dot on each chip) is positioned at the center of the holder. (C) Side view of the holder along the dashed green line in A.

To quantitatively assess the uniformity of dispensing and drying within a single chip, we computed the fraction of the total chip radioactivity that is at each reaction site (via Cerenkov imaging analysis). For each chip, Circular ROIs (**Figure 5-22**) were drawn around each reaction site, and integrated pixel intensity was computed within each ROIs. Each of these values was then divided by the sum of all the ROI integrated pixel intensities. The results tabulated in **Table 5-5** show excellent dispensing uniformity. Ideal uniformity would result in  $1/16 = 6.25\%$  of the activity in each reaction site. The average activity fraction for chip 1 was  $6.25 \pm 0.26\%$  ( $n=16$ ), and for chips 2, 3, and 4 was  $6.25 \pm 0.13\%$  ( $n=16$ ),  $6.25 \pm 0.19\%$  ( $n=16$ ) and  $6.25 \pm 0.22\%$  ( $n=16$ ), respectively. Importantly, there was no evidence of radioactivity outside of the reaction sites, indicating there was no splashing during the dispensing or drying processes.

The individual radioactivity measurements for each chip were 30.8, 30.4, 31.1, and 30.6 MBq (decay-corrected to first measurement) which suggests there is also high chip-to-chip uniformity.

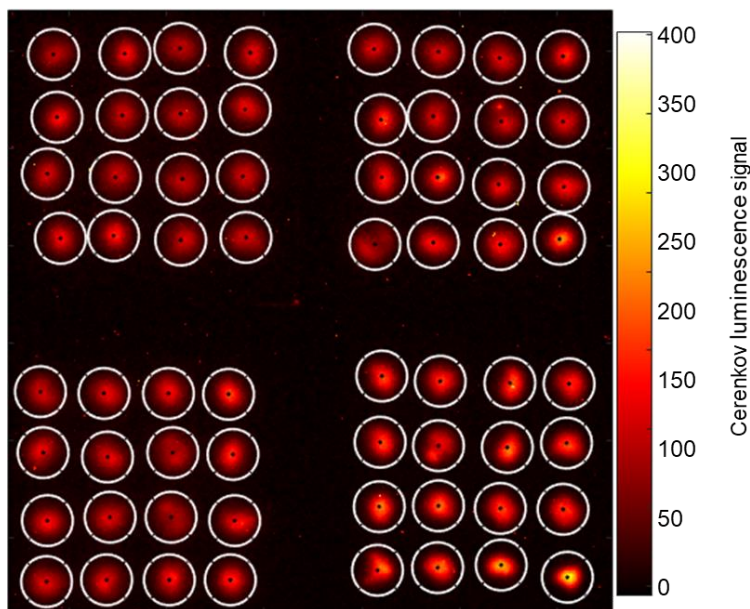


**Figure 5-22 Cerenkov luminescence image of chips after dispensing and drying [<sup>18</sup>F]fluoride solution.**

The white lines indicate the ROIs used for the analysis of each reaction site, and the central black dots were used for positioning the ROIs. Chips are in the orientations described in **Figure 5-21B**.

**Table 5-5 Fraction of radioactivity (%) contained within each reaction site for the four chips in the evaluation of [<sup>18</sup>F]fluoride dispensing and drying uniformity. Ideal uniformity would give 1/16 = 6.25%.**

Chip 1 reaction sites					Chip 2 reaction sites				
Row	Column				Row	Column			
	1	2	3	4		1	2	3	4
1	6.03%	6.63%	6.60%	6.40%	1	6.10%	6.23%	6.47%	6.33%
2	6.29%	6.59%	5.67%	6.54%	2	6.13%	6.13%	6.38%	6.48%
3	6.21%	6.29%	6.26%	6.11%	3	6.18%	6.29%	6.39%	6.27%
4	6.03%	6.22%	6.11%	6.02%	4	6.08%	6.23%	6.16%	6.16%
Chip 3 reaction sites					Chip 4 reaction sites				
Row	Column				Row	Column			
	1	2	3	4		1	2	3	4
1	6.51%	6.37%	6.15%	5.91%	1	6.38%	6.40%	6.33%	6.22%
2	6.51%	6.24%	6.29%	6.21%	2	6.31%	6.38%	6.14%	5.97%
3	6.50%	6.18%	5.88%	6.33%	3	6.63%	6.30%	6.29%	6.37%
4	6.36%	6.30%	6.05%	6.21%	4	6.30%	6.00%	6.29%	5.68%

### 5.6.7.2 Uniformity of replicate radiosyntheses of [ $^{18}\text{F}$ ]Fallypride

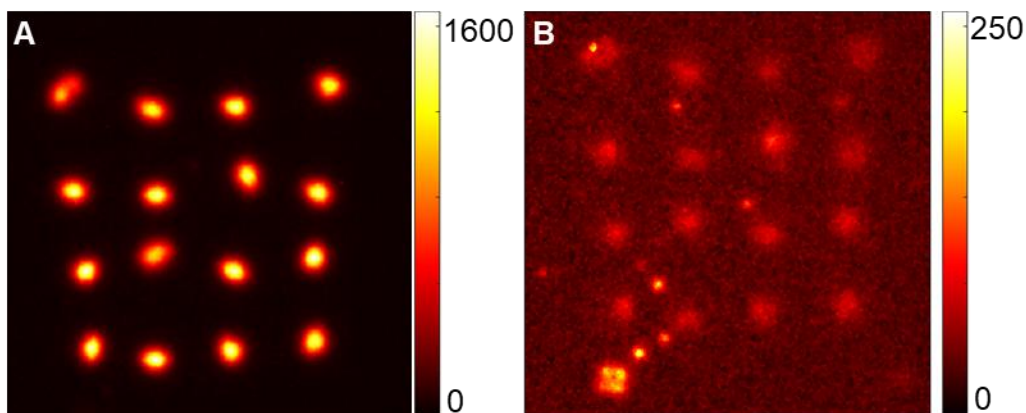


**Figure 5-23 Uniformity of replicate radiosyntheses of [ $^{18}\text{F}$ ]Fallypride.**

(A) Cerenkov luminescence image (60 s exposure) of chip after drying [ $^{18}\text{F}$ ]fluoride at 16 reaction sites. (B) Cerenkov image (5 min exposure) of residual activity on chip after performing parallel [ $^{18}\text{F}$ ]Fallypride syntheses at all sites followed by collection of crude products. Both images show the chip in the same orientation.

16 replicate syntheses of [ $^{18}\text{F}$ ]Fallypride were performed on a single multi-reaction chip. First, a 10  $\mu\text{L}$  droplet of [ $^{18}\text{F}$ ]fluoride solution (containing  $\sim 16$  MBq activity, 240 nmol  $\text{TBAHCO}_3$ ) was dispensed to each reaction site. (An additional 10  $\mu\text{L}$  was dispensed into an empty “aliquot vial”, which was assayed to estimate the starting activity for each reaction site.) The array of droplets was dried by heating the chip at 100 $^\circ\text{C}$  for 15 s and 105 $^\circ\text{C}$  for 45 s. Next, 6  $\mu\text{L}$  of precursor solution (containing 230 nmol precursor) was dispensed to each site, and fluorination reactions were performed by heating the chip at 110  $^\circ\text{C}$  for 7 min. Crude reaction products were collected into individual wells of a strip-well plate as described in the main paper. For each of the strip-wells, the collected product was “mixed” via repeated aspiration and dispense operations of the pipette, and then a 0.5  $\mu\text{L}$  sample was transferred to a TLC plate. After the [ $^{18}\text{F}$ ]fluoride drying and collection steps, the chip was assayed via dose calibrator and Cerenkov luminescence imaging was performed (**Figure 5-23**) to analyze the reaction performance (**Table 5-6**). Cerenkov luminescence images of the TLC plates are shown in **Figure 5-24**.

**Table 5-6 Detailed results of the [<sup>18</sup>F]fallypride synthesis uniformity study.**

Fluorination efficiency and crude RCY are based on n=4 replicate TLC results. Reaction conditions: 240 nmol TBAHCO<sub>3</sub>, 230 nmol precursor, 7 min reaction time, 110 °C reaction temperature.

Reaction site	Reaction site coordinates	Fluorination efficiency (% , n=4)	Collection efficiency (%)	Crude RCY (% , n=4)
1	1,1	91 ± 1	89.8	82 ± 1
2	1,2	91.2 ± 0.6	89.3	81.5 ± 0.5
3	1,3	91.5 ± 0.9	91.8	84.0 ± 0.8
4	1,4	90.4 ± 0.3	91.9	83.0 ± 0.3
5	2,1	91 ± 1	91.4	83 ± 1
6	2,2	89 ± 2	94.5	84 ± 2
7	2,3	90.6 ± 0.9	92.1	83.4 ± 0.8
8	2,4	90.1 ± 0.9	91.6	82.4 ± 0.8
9	3,1	89.6 ± 0.9	91.6	82.1 ± 0.8
10	3,2	91 ± 2	92.7	84 ± 2
11	3,3	90 ± 2	93.2	84 ± 2
12	3,4	90 ± 1	92.8	84 ± 1
13	4,1	90 ± 1	87.2	78 ± 1
14	4,2	90 ± 1	92.9	83 ± 1
15	4,3	90 ± 1	90.9	82 ± 1
16	4,4	92 ± 1	90.4	83 ± 1

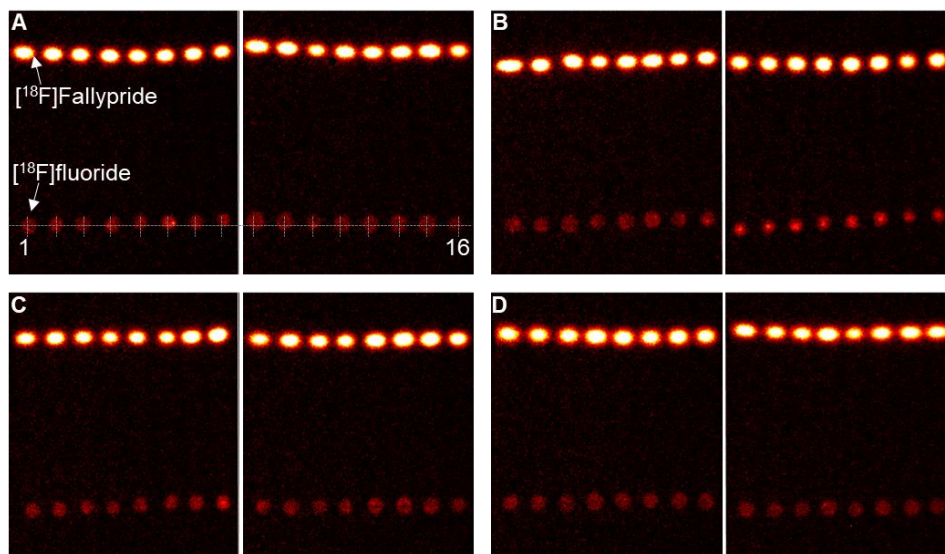


**Figure 5-24 Cerenkov images of the replicate [<sup>18</sup>F]fallypride radiosynthesis study.**

(A) Cerenkov images of developed TLC plates spotted with samples of all 16 reactions from the replicate [<sup>18</sup>F]fallypride radiosynthesis study. Origin lines and spotting locations are shown. (B-D) The same crude samples were spotted onto additional sets of TLC plates to assess the repeatability of TLC spotting.

### 5.6.7.3 Uniformity of replicate TLC analysis

While performing the 16 replicate radiosyntheses of [<sup>18</sup>F]Fallypride, each crude product was spotted onto 4 different TLC plates. Cerenkov images of the developed TLC plates (**Figure 5-24**) exhibit excellent qualitative consistency. The calculated fluorination efficiency values are tabulated in **Table 5-7**. For each reaction site, the fluorination efficiency determined from replicate analyses (replicate spotting, TLC development, Cerenkov imaging and ROI analysis) shows very good repeatability.

**Table 5-7 Fluorination conversion for a set of 16 replicate radiosyntheses of [<sup>18</sup>F]Fallypride, each sample assessed via 4 replicate TLC assays.**

Reaction site coordinate (X,Y)	Fluorination efficiency (%)				
	TLC set 1	TLC set 2	TLC set 3	TLC set 4	Average
1,1	92	92	90	92	91 ± 1
2,1	91	92	91	91	91 ± 1
3,1	92	91	90	92	91 ± 1
4,1	90	91	91	90	90.4 ± 0.3
2,1	91	89	90	92	91 ± 1
2,2	86	90	88	91	89 ± 2
3,2	91	90	90	92	91 ± 1
4,2	90	90	89	91	90 ± 1
3,1	90	88	90	90	90 ± 1
3,2	91	88	91	92	91 ± 2
3,3	91	87	92	91	90 ± 2
4,3	91	89	91	91	90 ± 1
4,1	90	88	90	91	90 ± 1
4,3	90	88	90	90	90 ± 1
4,3	91	89	91	91	90 ± 1
4,4	92	90	92	93	92 ± 1

#### 5.6.7.4 Cross-contamination during [<sup>18</sup>F]fluoride drying

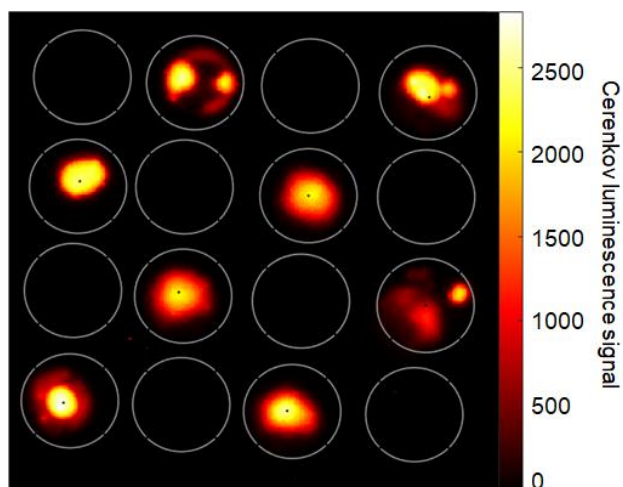


**Figure 5-25** Cerenkov luminescence image of chip used for cross-contamination experiment. ROIs for the analysis are shown in grey.

Cross-contamination was previously investigated by drying [<sup>18</sup>F]fluoride in a checkerboard pattern in chips with the same design and was found to be negligible for manual liquid addition(95). Here we assessed the cross-contamination during automated operation. An aqueous [<sup>18</sup>F]fluoride solution (370 MBq/mL) containing TBAHCO<sub>3</sub> (24 mM) was prepared and 10  $\mu$ L droplets were dispensed in a checkerboard pattern on a 4x4 multi-reaction chip. The droplets were then dried at 95°C for 15s, 98°C for 15 s and 105°C for 60 s, and the chip was then visualized with Cerenkov luminescence imaging (60 s exposure time). The resulting image (**Figure 5-25**) was analyzed by drawing ROIs around all reaction sites. The average integrated pixel intensity for reaction sites containing [<sup>18</sup>F]fluoride was  $14 \pm 2 \times 10^6$  and the average for the empty reaction sites was  $1000 \pm 1200$ . We can thus estimate the cross contamination of activity into adjacent reaction sites is  $< 0.01\%$ .

**Table 5-8 Fraction (%) of total chip radioactivity in each reaction site of the cross-contamination experiment as determined by ROI analysis of Cerenkov luminescence image. Reaction sites with [<sup>18</sup>F]fluoride are highlighted in green.**

Row	Column			
	1	2	3	4
1	0.0	12.6	0.0	12.9
2	12.7	0.0	13.2	0.0
3	0.0	13.2	0.0	13.4
4	12.9	0.0	9.1	0.0

#### 5.6.7.5 Optimization of [<sup>18</sup>F]Fallypride synthesis

During the study, measurements of chip radioactivity and Cerenkov luminescence imaging of chips was performed after [<sup>18</sup>F]fluoride drying, after fluorination, and after collection (**Figure 5-26**). The somewhat irregular pattern of activity after [<sup>18</sup>F]fluoride drying is commonly seen when using TBAHCO<sub>3</sub> as the phase transfer catalyst, as it tends to form small residue globules as it dries. Other phase transfer catalysts tend to spread out as a thin film over the entire reaction site.

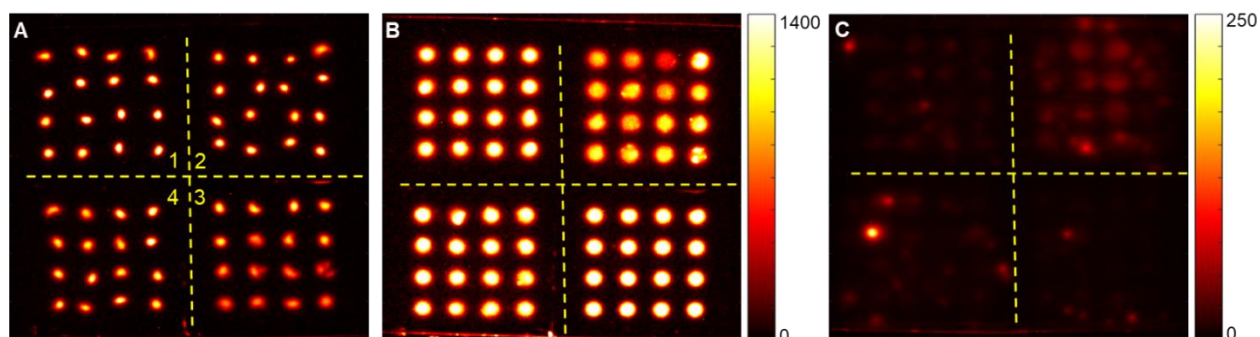


**Figure 5-26 Cerenkov luminescence images of chips during [<sup>18</sup>F]Fallypride synthesis.** Cerenkov luminescence images of the four chips after (A) [<sup>18</sup>F]fluoride drying (60 s exposure), (B) fluorination (60 s exposure), and (C) collection (5 min exposure). A and B use the same intensity scale (shown in B). Chips are numbered as shown in A.

The results of performance calculations are summarized in **Table 5-9**. Fluorination efficiency was evaluated via TLC. For each condition, replicate reactions show excellent consistency. Graphs of the fluorination efficiency, collection efficiency, and crude RCY for both the base study and precursor study are shown in **Figure 5-27** and **Figure 5-28**, respectively.

**Table 5-9 Detailed results of [<sup>18</sup>F]Fallypride optimization study.**

Note that a mis-positioning error when reinstalling chips into the system after Cerenkov imaging, led to an issue when collecting from two of the reaction sites; the affected reactions were excluded from the analysis.

Amount of TBAHCO <sub>3</sub> (nmol)	Amount of precursor (nmol)	Number of replicates (n)	Fluorination efficiency (%)	Collection efficiency (%)	Crude RCY (%)	Residual Radioactivity on Chip (%)
240	3.7	4	6.3 ± 0.8	93 ± 3	5.9 ± 0.7	3.1 ± 0.7
240	7.3	4	8 ± 1	91 ± 8	7.3 ± 0.5	2.3 ± 0.2
240	15	3	19 ± 4	82 ± 18	15 ± 1	2.5 ± 0.3
240	29	3	32 ± 3	99 ± 15	32 ± 2	1.9 ± 0.7
240	59	4	56 ± 3	93 ± 4	52 ± 2	1.9 ± 0.3
240	120	4	78 ± 3	96 ± 2	75 ± 3	2.4 ± 0.6
240	470	4	93 ± 2	96 ± 5	89 ± 5	1.8 ± 0.5
120	230	4	92 ± 1	95 ± 5	87 ± 6	1.4 ± 0.2
150	230	4	90.7 ± 0.4	98 ± 1	89 ± 2	1.6 ± 0.4
180	230	4	91.6 ± 0.6	99 ± 1	91 ± 1	1.6 ± 1.1
240	230	8	93.1 ± 0.6	99 ± 1	92 ± 1	1.2 ± 0.4
300	230	4	85 ± 3	98 ± 2	83 ± 4	1.8 ± 0.1
360	230	4	84 ± 2	99 ± 1	83 ± 3	1.5 ± 0.3
420	230	4	70 ± 1	98 ± 2	69 ± 1	2.2 ± 0.7
480	230	4	68 ± 1	98 ± 1	66 ± 1	3.5 ± 3.6

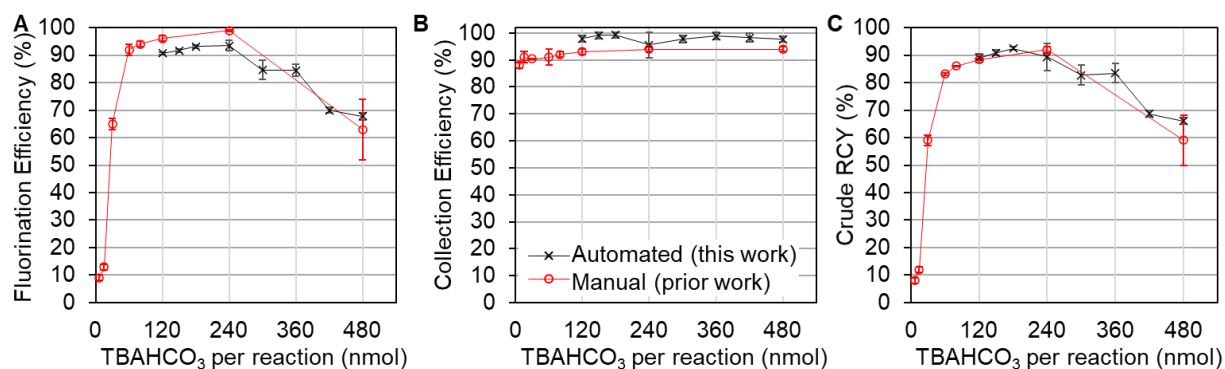


**Figure 5-27 Effect of the amount of TBAHCO<sub>3</sub> on the radiosynthesis of [<sup>18</sup>F]Fallypride.**

A) fluorination efficiency, (B) collection efficiency, and (C) crude RCY. Fixed conditions: precursor amount: 230 nmol, 7 min reaction time, 110 °C reaction temperature.



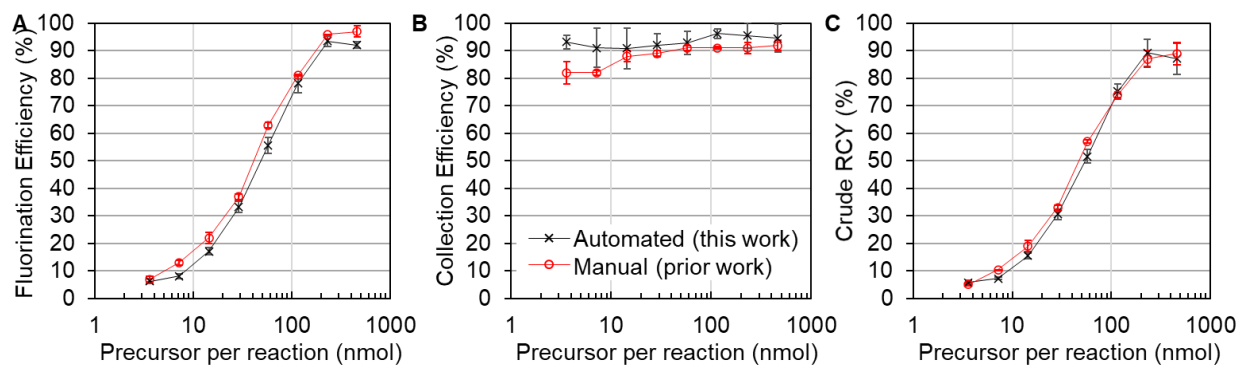


**Figure 5-28 Effect of the amount of precursor on the radiosynthesis of [ $^{18}\text{F}$ ]Fallypride.** (A) fluorination efficiency, (B) collection efficiency, and (C) crude RCY. Fixed conditions: 240 nmol TBAHCO<sub>3</sub>, 7 min reaction time, 110 °C reaction temperature.

### 5.6.7.6 Optimization of [ $^{18}\text{F}$ ]FBnTP synthesis

During the study, measurements of chip radioactivity and Cerenkov luminescence imaging of chips was performed after [ $^{18}\text{F}$ ]fluoride drying and after collection (**Figure 5-29**). Cerenkov images of developed TLC plates are shown in **Figure 5-30**. Reaction performance is tabulated in **Table 5-10**.

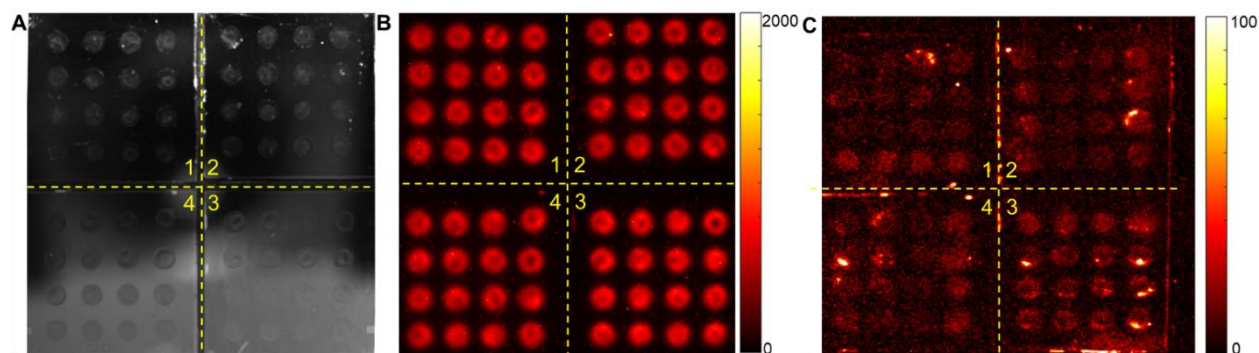


**Figure 5-29 measurements of chip radioactivity and CLI of chips.** (A) Brightfield and (B) Cerenkov images (60 s exposure time) of the four chips after [ $^{18}\text{F}$ ]fluoride drying during the optimization of [ $^{18}\text{F}$ ]FBnTP. (C) Cerenkov image (5 min exposure time) of the

same set of chips after the collection step. Numbers correspond to the chip positions on the heater platform.

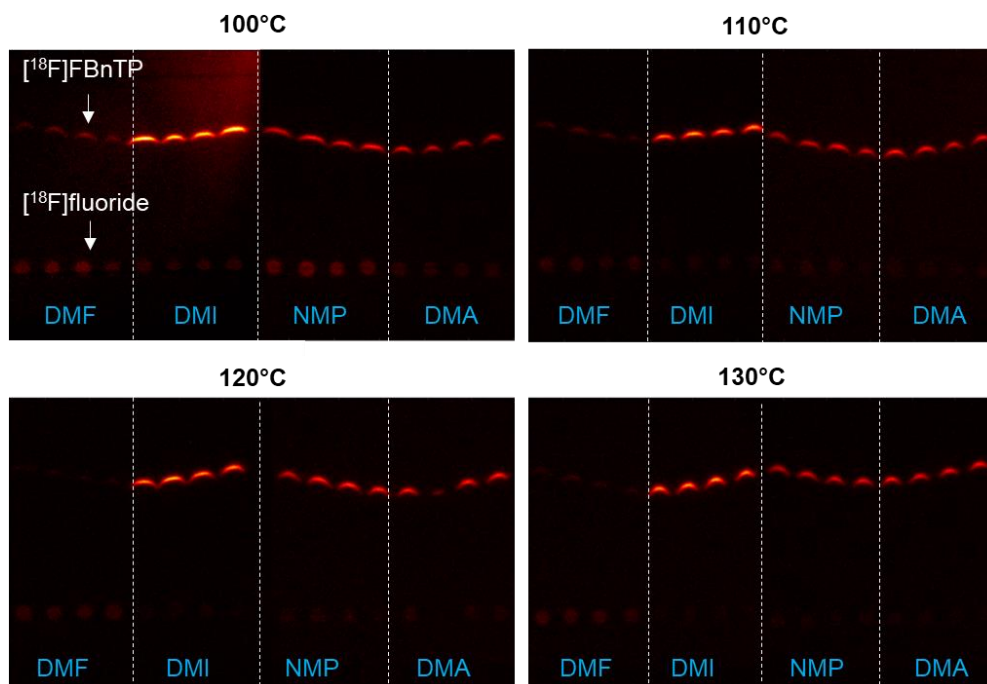


**Figure 5-30 Cerenkov images of the developed TLC plates for the  $[^{18}\text{F}]$ FBnTP study.**

Samples on TLC plates are grouped by condition (n=4 replicates) for each combination of temperature and solvent. Each solvent contains 3.8% v/v pyridine. Signal is low in reactions performed with DMF due to the high volatile activity loss.

**Table 5-10 Summary of optimization experiment exploring the impact of solvent and reaction temperature on the performance of  $[^{18}\text{F}]$ FBnTP synthesis.**

For each condition, n=4 replicates were performed. Each solvent contains 3.8% v/v pyridine.

Solvent	Performance measure	Temperature ( $^{\circ}\text{C}$ )			
		100	110	120	130
DMF	Fluorination (%)	44 $\pm$ 9	44 $\pm$ 4	26 $\pm$ 2	36 $\pm$ 4
	Collection (%)	28 $\pm$ 5	26 $\pm$ 2	21 $\pm$ 2	19 $\pm$ 2
	Crude RCY (%)	13 $\pm$ 4	12 $\pm$ 2	5.4 $\pm$ 0.5	6.7 $\pm$ 0.9
DMI	Fluorination (%)	75 $\pm$ 4	89 $\pm$ 1	91 $\pm$ 1	90 $\pm$ 1
	Collection (%)	97 $\pm$ 2	97 $\pm$ 2	83 $\pm$ 3	76 $\pm$ 2
	Crude RCY (%)	72 $\pm$ 4	86 $\pm$ 2	76 $\pm$ 2	68 $\pm$ 2
NMP	Fluorination (%)	64 $\pm$ 4	72 $\pm$ 4	80 $\pm$ 2	82 $\pm$ 3
	Collection (%)	81 $\pm$ 2	67 $\pm$ 4	51 $\pm$ 5	49 $\pm$ 1
	Crude RCY (%)	52 $\pm$ 2	49 $\pm$ 2	41 $\pm$ 4	40.0 $\pm$ 0.9
DMA	Fluorination (%)	71 $\pm$ 2	74 $\pm$ 4	78 $\pm$ 3	84 $\pm$ 1
	Collection (%)	53 $\pm$ 4	59 $\pm$ 3	56 $\pm$ 3	61 $\pm$ 1
	Crude RCY (%)	37 $\pm$ 3	44 $\pm$ 2	43 $\pm$ 3	52 $\pm$ 2

### 5.6.7.7 Scale-up of [<sup>18</sup>F]FBnTP synthesis

Using the optimal synthesis conditions, we performed three replicate syntheses at a higher activity scale, sufficient for preclinical imaging of small animals. Steps were performed manually, and the crude product was purified via analytical-scale HPLC and formulated via solid-phase extraction. Measurements for each of the replicates are tabulated in **Table 5-11** and example chromatograms shown in **Figure 5-31**.

**Table 5-11 Reaction performance parameters for three replicate [<sup>18</sup>F]FBnTP syntheses at higher activity scale**

Reaction Step	Trial 1	Trial 2	Trial 3	Average ± Std dev
Starting activity (MBq)	122	122	122	122 ± 0
Collection efficiency (%)	88	90	87	88 ± 2
HPLC fluorination efficiency (%)	94	94	93	94 ± 1
Purification efficiency (%)	89	79	79	82 ± 6
Isolated yield (%)	74	67	64	66 ± 6
Activity yield (MBq)	63	61	56	60 ± 4
Activity yield (%)	52	50	46	49 ± 3

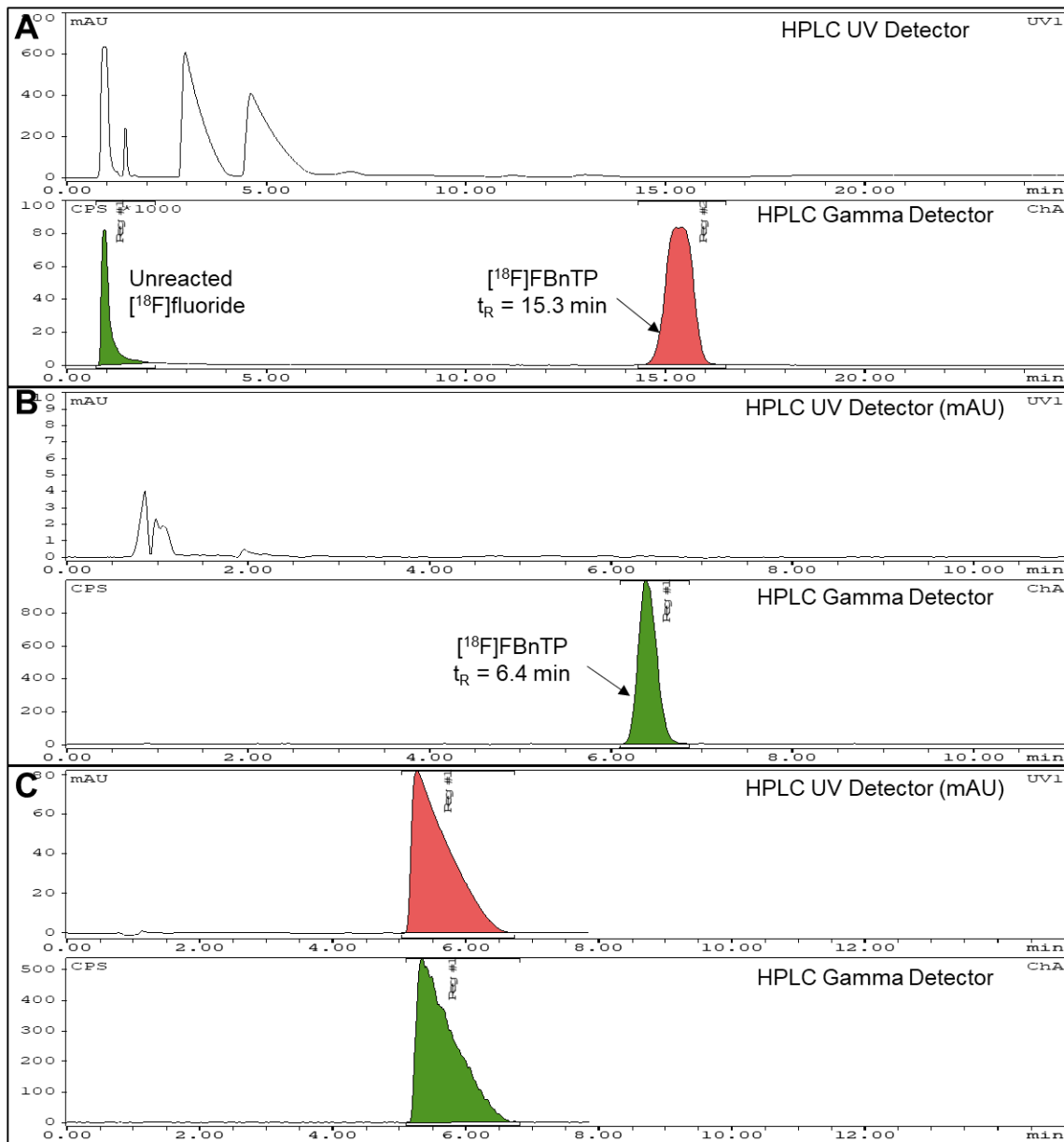


**Figure 5-31 Example HPLC chromatogram of injection of  $[^{18}\text{F}]\text{FBnTP}$  crude product, purified product and coin-injection of  $[^{18}\text{F}]\text{FBnTP}$  and standard.**

(A) Example HPLC chromatogram obtained during purification of crude  $[^{18}\text{F}]\text{FBnTP}$  prepared via the optimized droplet synthesis conditions. (B) Radiochemical and chemical purity analysis of the purified and formulated product. (C) Confirmation of radiochemical identity via co-injection of reference standard. Note that purification was performed using a different mobile phase than analytical tests.

#### 5.6.7.8 System speed characterization

We initially set some aggressive goals for the operating speed of the system, in particular ensuring the motion actuators were fast enough to move the fluidics head across the entire workspace within < 1.0 s. To get a better sense of the operating speed of the system and the duration of actions within an optimization study, we performed a timing analysis summarized in

**Table 5-12.**

**Table 5-12 Duration of commonly needed individual actions and groups of actions.**

Average and standard deviation are computed from n=3 replicate timing measurements. Any action involving attaching pipette tips used a new tip for each of the three replicates.

Step(s) performed	Duration (s)
<i>Initialization Actions</i>	
Homing (maximum travel distance)	50.3 ± 0.2
Chip height measurement (4 chips)	244 ± 2
<i>Simple Actions</i>	
Dispense 10 µL to 64 sites	35.1 ± 0.1
Attach tip (starting from chip 1 position 1,1)	6.5 ± 0.4
Remove tip (starting from chip 1 position 1,1)	2.5 ± 0.1
Heater heat from 21°C to 100°C	3.8 ± 0.4
Heater cool from 100°C to 30°C (w/ fan)	93 ± 3
<i>Compound Actions</i>	
Transfer 10 µL (via pipette) from 1 microwell to 16 reaction sites	66 ± 2
Transfer 10 µL (via pipette) from 64 wells to 64 sites	660 ± 10
Collection of 1 site (10 µL, 4 cycles, include mixing)	74 ± 1
Collection of 64 sites (10 µL, 4 cycles, include mixing)	4840 ± 50
Spot from 1 microwell to TLC plate	7.6 ± 0.3
Spot from 64 microwells to 64 TLC plate locations	490 ± 10

# Chapter 6: Economical droplet-based microfluidic production of [<sup>18</sup>F]FET and [<sup>18</sup>F]Florbetaben suitable for human use

## 6.1 Introduction

Diagnostic radiopharmaceuticals (tracers) used in positron-emission tomography (PET) imaging enable a wide range of research and clinical applications including cancer diagnostics and tumor severity grading (228–230), evaluation of response to cancer therapy (231,232), diagnostics of neurodegenerative disease (233–235), cardiac function assessment (236,237), drug development (238–240) and development of novel gene- and cell-based therapies (241–243). Of thousands of developed tracers to probe different biological targets and processes (210,211), only very few are routinely available. The complexity and high cost of manufacturing short-lived PET tracers has led to a centralized production model, where large batches of the tracers are produced in radiopharmacies, and then batches (and costs) are split to be distributed to multiple PET centers. Since a significant demand is needed to justify the high costs of establishing and performing the syntheses using conventional instrumentation and facilities, availability of specialized tracers is limited.

Recent advancements in PET radiochemistry directed at development of batch-on-demand systems are creating new possibilities to expand availability of diverse diagnostic radiopharmaceuticals at low cost. Microfluidics offers a promising approach to enable economic production of one to a few patient doses due to advantages such as reduced (10-100x) reagent consumption, faster reaction kinetics, improved product yields, and reduced equipment footprint and shielding size (44,53,61,84,244,245). Numerous reports have established the feasibility of synthesizing various radiopharmaceuticals using microfluidic synthesizers. However, due to the disparity between the volume of radioisotope solutions (~1 mL) and reaction volumes of microscale systems (as low as 1-10s of  $\mu\text{L}$ ), relatively small amounts of product activity have been acquired, suitable only for preclinical imaging (61,84,246). Nevertheless, clinically-relevant

quantities of various diagnostic radiopharmaceuticals has been produced with such microscale systems: [<sup>13</sup>N]NH<sub>3</sub> (247), [<sup>68</sup>Ga]Ga-PSMA-11 (58(p11)), [<sup>89</sup>Zr]Zr-DFO-Trastuzumab (46), [<sup>18</sup>F]FDG (248,249), [<sup>18</sup>F]FET (55), [<sup>18</sup>F]fallypride (83,250), [<sup>18</sup>F]FT807 (251), [<sup>18</sup>F]FPEB (252), [<sup>18</sup>F]FLT (253) and [<sup>18</sup>F]FMISO (253,254). A summary of reports of the <sup>18</sup>F-labeled ones is included in **Table 6-1**.

Microfluidic reactors can be classified in two categories: continuous-flow synthesizers, where the reaction volume is flowed through a microchannel or capillary, and batch-mode synthesizers, that contain a fixed reaction volume confined within a miniature reaction chamber (57) or within an isolated droplet (53,84). In the continuous-flow systems, radioisotope and precursor solution streams are mixed prior to entering the heated reaction zone. Scaling of the product activity can be easily achieved by increasing radioisotope volume and also a corresponding increase of precursor solution volume, or by concentrating the isotope prior to synthesis. The first PET tracer suitable for human use produced in a microfluidic continuous-flow reactor was demonstrated using the commercial NanoTek radiosynthesizer (Advion, Inc., Ithaca, NY): Liang *et al.* reported starting activities of up to 170 GBq, and the synthesis of 1.7 GBq of [<sup>18</sup>F]FPEB (252). In a separate report, Liang *et al.* also reported the synthesis of 4.4 GBq batches of [<sup>18</sup>F]T807 (each with 16 GBq starting activity), for the first time administering the tracer produced by continuous-flow reactor to a human subject (251(p807)). Using the same system, Zheng *et al.* reported the synthesis of up to 1.9 GBq of [<sup>18</sup>F]FMISO (with 5.6 GBq starting activity) for use in clinical research, and Akula *et al.* reported the sequential production of 2 tracers [<sup>18</sup>F]FLT and [<sup>18</sup>F]FMISO in ~2 GBq quantities, each from 13 GBq of starting radioactivity (253). Despite impressive scalability, continuous-flow reactors use relatively large total reaction volumes (100s of μL), with 100s of μg of precursor to prepare these clinical-scale batches, and require an extended time for the initial [<sup>18</sup>F]fluoride preparation step (84).

Batch reactors offer a drastic reduction in precursor consumption (<100 μg) which is independent of the amount of loaded radioisotope. However, to produce clinically-relevant

quantities of the radiopharmaceutical in these tiny reaction volumes, pre-concentration of [ $^{18}\text{F}$ ]fluoride is necessary. By adapting conventional azeotropic drying to the ISAR platform (GE Global Research Europe), Frank *et al.* reported the synthesis of >100 GBq of [ $^{18}\text{F}$ ]FDG using starting activity up to 170 GBq (248). Using the BG75 system (ABT Molecular Imaging, Knoxville, TN) system, which integrates into a small cyclotron, Awasthi *et al.* reported synthesis of [ $^{18}\text{F}$ ]FDG from 1.9 GBq of starting activity, concentrated via azeotropic drying in the reaction vessel, to produce single, injectable human doses (0.4-0.6 GBq) (249). Iwata *et al.* developed a trap-and-release process using a combination of commercially-available cation- and anion-exchange cartridges to trap 1 mL of cyclotron-produced [ $^{18}\text{F}$ ]fluoride (up to 6 GBq) and release it in a 0.2 mL methanolic solution that could be rapidly evaporated in a small vial designed for 5-20  $\mu\text{L}$  subsequent reaction to produce [ $^{18}\text{F}$ ]FET (55). The first human images obtain using a microfluidically-produced PET tracer were synthesized in a 50  $\mu\text{L}$  batch reactor platform, in this work Lebedev *et al.* performed an upstream trap-and-release process on a miniature QMA cartridge to concentrate a full cyclotron-target volume of [ $^{18}\text{F}$ ]fluoride (e.g. ~100 GBq in 2 mL) into <45  $\mu\text{L}$ . This could be loaded into the reactor and evaporatively dried, enabling the synthesis of up to 38 GBq of [ $^{18}\text{F}$ ]fallypride (250). Chao *et al.* designed a standalone radioisotope concentrator system based on a similar mini-QMA approach, capable of concentrating milliliter-scale [ $^{18}\text{F}$ ]fluoride batches into ~12  $\mu\text{L}$  volume (255). The device was subsequently integrated with an automated droplet radiosynthesizer, to concentrate starting activities of up to 41 GBq. Production of quantities of formulated [ $^{18}\text{F}$ ]fallypride up to 7.2 GBq were demonstrated (83).

While these methods are all effective, integration with any type of concentrator increases system complexity and synthesis time, and, except for the Iwata *et al.* method (55), requires optimization of base quantities used during the [ $^{18}\text{F}$ ]fluoride elution process to avoid adversely affecting the downstream synthesis. Instead, a simpler sequential drying approach can be used with droplet reactors, in which the initial radioisotope solution is subdivided into smaller portions each added and then rapidly evaporated (due to the high surface to volume ratio of small



volumes), to build up the amount of activity in the reaction site. For example, Chen *et al.* heated a 200  $\mu\text{L}$  droplet of [ $^{18}\text{F}$ ]fluoride solution on an open surface until it shrunk to 5  $\mu\text{L}$  and then transported this concentrated droplet into an electrowetting-on-dielectric (EWOD) radiosynthesis chip for completion of the drying step (70). We later demonstrated the possibility for rapid concentration by evaporation by sequentially loading to 2  $\mu\text{L}$  portions to a pre-heated chip (78). Since each drying iteration takes time, there is a practical limit on the volume/amount of radioactivity that can be concentrated, but evaporation is quite quick for modest batches. Drying of volumes in a range of a few hundred microliters is feasible, and can provide enough starting radioactivity for synthesis of clinically-relevant batches (84). In this work, we leverage the larger volume of the reaction site of the surface-tension trap (STT) design chip (80) compared to the passive transport (PT) design chip (78), and concentrate [ $^{18}\text{F}$ ]fluoride by loading and drying it in 30  $\mu\text{L}$  increments. The goal of the present work is to demonstrate that tracers other than [ $^{18}\text{F}$ ]fallypride can be produced at clinically-relevant scales using this simple approach for [ $^{18}\text{F}$ ]fluoride concentration and thus with a simple overall apparatus.

Previously, we reported the production of the amino acid PET tracer O-(2-[ $^{18}\text{F}$ ]fluoroethyl)-L-tyrosine ([ $^{18}\text{F}$ ]FET) (82) and the stilbene derivative 4-[(E)-2-(4-{2-[2-(2-[ $^{18}\text{F}$ ]fluoroethoxy)ethoxy] ethoxy}phenyl)vinyl]-N-methylaniline ([ $^{18}\text{F}$ ]florbetaben, [ $^{18}\text{F}$ ]FBB, Neuraceq<sup>TM</sup>, BAY-949172) in a droplet reactor, observing, for each, significant advantages compared to conventional synthesis methods. [ $^{18}\text{F}$ ]FET PET assesses amino acid transport and is used for glioma differentiation from non-neoplastic lesions and glioma grading (256), while [ $^{18}\text{F}$ ]FBB PET visualizes amyloid plaques and aids in diagnosis of Alzheimer's disease (235). Using the simplified [ $^{18}\text{F}$ ]fluoride concentration method described above, we adapted the previous synthesis methods to scale up the production of [ $^{18}\text{F}$ ]FET and [ $^{18}\text{F}$ ]FBB to amounts sufficient for clinical use (i.e. one to a few human doses). Furthermore, quality control (QC) testing was performed to ensure the tracer batches meet the necessary specifications for clinical use. Some of the QC tests were performed using the Tracer-QC automated testing platform (Trace-Ability,

Inc., Van Nuys, CA, USA), showing the successful integration of a novel compact microfluidic radiosynthesis platform and a modern benchtop QC testing platform, and demonstrating the possibility for clinically-relevant radiotracer production with an overall compact, user-friendly system.

**Table 6-1 Literature reports of microfluidic production of <sup>18</sup>F-labeled radiopharmaceuticals with sufficient quantities for human PET. N.R. = not reported**

Reference	This work		Wang et al. 2020 (83)	Lebedev et al. 2013 (250)	Frank et al. 2018 (248)	Liang et al. 2014 (251)
Microfluidic synthesis platform	Droplet-based radiosynthesizer		Droplet-based radiosynthesizer	PEEK/pDPCD chip with syringe-type microvalves	GE ISAR	Advion NanoTek
Synthesis format	Batch		Batch	Batch	Batch	Flow
Tracer(s) produced	[ <sup>18</sup> F]FET	[ <sup>18</sup> F]FBB	[ <sup>18</sup> F]Fallypride	[ <sup>18</sup> F]Fallypride	[ <sup>18</sup> F]FDG	[ <sup>18</sup> F]T807
Starting activity (GBq)	2.7 ± 0.4 (n=3)	3.2 ± 0.8 (n=6)	Up to 41	Up to 111	Up to 170	16.1 ± 4.4 (n=3)
Product activity (GBq)	0.6 ± 0.2 (n=3)	0.5 ± 0.2 (n=6)	Up to 7.2	N.R.	>100	4.4 ± 0.1 (n=3)
Molar activity (GBq/μmol)	420 ± 50 (n=3)	480 ± 160 (n=5)	Up to 270	N.R.	N.R.	220 ± 50 (n=3)
Synthesis time (min)	60	60	50	45	<25	<100
Precursor consumed (nmol)	60	80	616	1940	N.R.	1560
Reaction volume (μL)	10	10	8	50	650 <sup>a</sup>	400
QC testing reported?	Yes	Yes	Yes	Yes	No	Yes
Used in patients?	No	No	No	Yes	No	Yes

Reference	Liang et al. 2014 (252)	Zheng et al. 2014 (254)	Akula et al. 2019 (253)		Awasthi 2014 (249)	Iwata et al. 2020 (55)
Microfluidic synthesis platform	Advion NanoTek	Advion NanoTek	Advion NanoTek		ABT BG75	Disposable glass vials with a fused 300-μL insert
Synthesis format	Flow	Flow	Flow		Batch	Batch
Tracer(s) produced	[ <sup>18</sup> F]FPEB	[ <sup>18</sup> F]FMISO	[ <sup>18</sup> F]FLT	[ <sup>18</sup> F]FMISO	[ <sup>18</sup> F]FDG	[ <sup>18</sup> F]FET
Starting activity (GBq)	80.9	~5.6	13 <sup>b</sup>	13 <sup>b</sup>	~1.9	Up to 6
Product activity (GBq)	1.7 ± 0.4 (n=3)	1.5-1.9	2.2	2.1	0.4-0.6	Up to 4 <sup>c</sup>
Molar activity (GBq/μmol)	160 ± 10 (n=3)	120 ± 30 (n=4)	>74	>74	N.R.	480 ± 130 (n=7)
Synthesis time (min)	75	106 ± 11 (n=15)	77	53	40-60	50
Precursor consumed (nmol)	21500	940	24100	11800	N.R.	177
Reaction volume (μL)	1000	200	2000	2000	N.R.	60

QC testing reported?	Yes	Yes	No	No	Yes	No
Used in patients?	No	Yes	No	No	No	No

<sup>a</sup>Precise reaction volume was not reported, but the total reactor size was 650  $\mu\text{L}$ . <sup>b</sup>Total activity used for [ $^{18}\text{F}$ ]FLT and [ $^{18}\text{F}$ ]FMISO sequential syntheses combined is reported, approximately half used in each synthesis. <sup>c</sup>Estimated from reported crude yield value for 6 GBq starting activity and assuming 50 min synthesis time

Batch reactors offer a drastic reduction in precursor consumption (<100  $\mu\text{g}$ ) which is independent of the amount of loaded radioisotope. However, to produce clinically-relevant quantities of the radiopharmaceutical in these tiny reaction volumes, pre-concentration of [ $^{18}\text{F}$ ]fluoride is necessary. By adapting conventional azeotropic drying to the ISAR platform (GE Global Research Europe), Frank *et al.* reported the synthesis of >100 GBq of [ $^{18}\text{F}$ ]FDG using starting activity up to 170 GBq (248). Using the BG75 system (ABT Molecular Imaging, Knoxville, TN) system, which integrates into a small cyclotron, Awasthi *et al.* reported synthesis of [ $^{18}\text{F}$ ]FDG from 1.9 GBq of starting activity, concentrated via azeotropic drying in the reaction vessel, to produce single, injectable human doses (0.4-0.6 GBq) (249). Iwata *et al.* developed a trap-and-release process using a combination of commercially-available cation- and anion-exchange cartridges to trap 1 mL of cyclotron-produced [ $^{18}\text{F}$ ]fluoride (up to 6 GBq) and release it in a 0.2 mL methanolic solution that could be rapidly evaporated in a small vial designed for 5-20  $\mu\text{L}$  subsequent reaction to produce [ $^{18}\text{F}$ ]FET (55). The first human images obtain using a microfluidically-produced PET tracer were synthesized in a 50  $\mu\text{L}$  batch reactor platform, in this work Lebedev *et al.* performed an upstream trap-and-release process on a miniature QMA cartridge to concentrate a full cyclotron-target volume of [ $^{18}\text{F}$ ]fluoride (e.g. ~100 GBq in 2 mL) into <45  $\mu\text{L}$ . This could be loaded into the reactor and evaporatively dried, enabling the synthesis of up to 38 GBq of [ $^{18}\text{F}$ ]fallypride (250). Chao *et al.* designed a standalone radioisotope concentrator system based on a similar mini-QMA approach, capable of concentrating milliliter-scale [ $^{18}\text{F}$ ]fluoride batches into ~12  $\mu\text{L}$  volume (255). The device was subsequently integrated with an automated droplet radiosynthesizer, to concentrate starting activities of up to 41 GBq. Production of quantities of formulated [ $^{18}\text{F}$ ]fallypride up to 7.2 GBq were demonstrated (83).

While these methods are all effective, integration with any type of concentrator increases system complexity and synthesis time, and, except for the Iwata *et al.* method (55), requires optimization of base quantities used during the [<sup>18</sup>F]fluoride elution process to avoid adversely affecting the downstream synthesis. Instead, a simpler sequential drying approach can be used with droplet reactors, in which the initial radioisotope solution is subdivided into smaller portions each added and then rapidly evaporated (due to the high surface to volume ratio of small volumes), to build up the amount of activity in the reaction site. For example, Chen *et al.* heated a 200 μL droplet of [<sup>18</sup>F]fluoride solution on an open surface until it shrunk to 5 μL and then transported this concentrated droplet into an electrowetting-on-dielectric (EWOD) radiosynthesis chip for completion of the drying step (70). We later demonstrated the possibility for rapid concentration by evaporation by sequentially loading to 2 μL portions to a pre-heated chip (78). Since each drying iteration takes time, there is a practical limit on the volume/amount of radioactivity that can be concentrated, but evaporation is quite quick for modest batches. Drying of volumes in a range of a few hundred microliters is feasible, and can provide enough starting radioactivity for synthesis of clinically-relevant batches (84). In this work, we leverage the larger volume of the reaction site of the surface-tension trap (STT) design chip (80) compared to the passive transport (PT) design chip (78), and concentrate [<sup>18</sup>F]fluoride by loading and drying it in 30 μL increments. The goal of the present work is to demonstrate that tracers other than [<sup>18</sup>F]fallypride can be produced at clinically-relevant scales using this simple approach for [<sup>18</sup>F]fluoride concentration and thus with a simple overall apparatus.

Previously, we reported the production of the amino acid PET tracer O-(2-[<sup>18</sup>F]fluoroethyl)-L-tyrosine ([<sup>18</sup>F]FET) (82) and the stilbene derivative 4-[(E)-2-(4-{2-[2-(2-[<sup>18</sup>F]fluoroethoxy)ethoxy] ethoxy}phenyl)vinyl]-N-methylaniline ([<sup>18</sup>F]florbetaben, [<sup>18</sup>F]FBB, Neuraceq™, BAY-949172) in a droplet reactor, observing, for each, significant advantages compared to conventional synthesis methods. [<sup>18</sup>F]FET PET assesses amino acid transport and is used for glioma differentiation from non-neoplastic lesions and glioma grading (256), while

[<sup>18</sup>F]FBB PET visualizes amyloid plaques and aids in diagnosis of Alzheimer's disease (235). Using the simplified [<sup>18</sup>F]fluoride concentration method described above, we adapted the previous synthesis methods to scale up the production of [<sup>18</sup>F]FET and [<sup>18</sup>F]FBB to amounts sufficient for clinical use (i.e. one to a few human doses). Furthermore, quality control (QC) testing was performed to ensure the tracer batches meet the necessary specifications for clinical use. Some of the QC tests were performed using the Tracer-QC automated testing platform (Trace-Ability, Inc., Van Nuys, CA, USA), showing the successful integration of a novel compact microfluidic radiosynthesis platform and a modern benchtop QC testing platform, and demonstrating the possibility for clinically-relevant radiotracer production with an overall compact, user-friendly system.

## 6.2 Methods

### 6.2.1 Materials

No-carrier-added [<sup>18</sup>F]fluoride was produced by the <sup>18</sup>O(p, n)<sup>18</sup>F reaction from [<sup>18</sup>O]H<sub>2</sub>O (84% isotopic purity, Zevacor Pharma, Noblesville, IN, USA) in an RDS-112 cyclotron (Siemens; Knoxville, TN, USA) at 11 MeV using a 1 mL tantalum target with havar foil. Acetonitrile (MeCN; anhydrous, 99.8%), methanol (MeOH; anhydrous, 99.8%), 2,3-dimethyl-2-butanol (hexyl alcohol (TA); 98%), ethanol (EtOH; 200 proof, >99.5%), hydrochloric acid (HCl; 1M), dimethylsulfoxide (DMSO; 98%), deionized (DI) water, and polyethylene glycol 400 (PEG 400), Kryptofix 222 (K<sub>222</sub>) and potassium carbonate (K<sub>2</sub>CO<sub>3</sub>) were purchased from Millipore Sigma (St. Louis, MO, USA). Sodium phosphate dibasic (Na<sub>2</sub>HPO<sub>4</sub>·7H<sub>2</sub>O) and sodium phosphate monobasic (NaH<sub>2</sub>PO<sub>4</sub>·H<sub>2</sub>O) were purchased from Fisher Scientific (Thermo Fisher Scientific, Waltham, MA). Saline (0.9% sodium chloride injection, USP) was obtained from Hospira Inc. (Lake Forest, IL, USA). Tetrabutylammonium bicarbonate 0.075M (TBAHCO<sub>3</sub>, >99%), (2S)-O-(2'-tosyloxyethyl)-N-trityl-tyrosine-tert-butyl ester (TET; >95%) (FET precursor), O-2-fluoroethyl-L-tyrosine (FET-HCl; >95%) (FET reference standard) were purchased from ABX GmbH (Radeberg, Germany).

([Methanesulfonic acid 2-{2-[2-(4-{2-[4-(tert-butoxycarbonyl-methyl-amino)-phenyl]-vinyl)-phenoxy]-ethoxy]-ethoxy}-ethyl ester) (FBB precursor) and (4-[(E)-2-(4-{2-[2-(2-[<sup>18</sup>F]fluoroethoxy)ethoxy] ethoxy} phenyl) vinyl]-N-methylaniline) (FBB reference standard) were generously provided by Life Molecular Imaging GmbH as a part of [<sup>18</sup>F]Florbetaben synthesis kits (Life Molecular Imaging GmbH, Berlin, Germany). Dry scavenger (to prevent radiolysis), consisting of sodium ascorbate with L-ascorbic acid (87:13 w/w), was also obtained from the same [<sup>18</sup>F]Florbetaben kits. All reagents were used as received without further purification. Ultrapure 18 MΩ H<sub>2</sub>O was obtained from a Milli-Q Integral 3 purification system (Millipore Sigma, St. Louis, MO, USA).

Stock K<sub>222</sub>/K<sub>2</sub>CO<sub>3</sub> solution (for [<sup>18</sup>F]FBB synthesis) was prepared by first making an aqueous 61 mM K<sub>2</sub>CO<sub>3</sub> mixture and adding K<sub>222</sub> to reach 85 mM concentration. Stock solutions were prepared for FET precursor (6 mM in MeCN:TA 1:1 (v/v)), FBB precursor (8 mM in DMSO), and for [<sup>18</sup>F]FET collection solution (1:1 MeOH:H<sub>2</sub>O (v/v)) and [<sup>18</sup>F]FBB collection solution (1:1 MeCN: H<sub>2</sub>O (v/v)). Acid mixture used for deprotection in both syntheses was made by mixing MeCN and HCl 1:1 (v/v). Scavenger solution for [<sup>18</sup>F]FBB was prepared either at 33 mg/mL or 10 mg/mL in H<sub>2</sub>O. Formulation dilution solution for [<sup>18</sup>F]FBB contained 39 mg/mL of dry scavenger in a 4:13 (v/v) mixture of PEG 400 and H<sub>2</sub>O.

### 6.2.2 Automated droplet synthesizer

Radiosyntheses were performed in a droplet format on the surface of disposable silicon-Teflon chips (surface-tension trap (STT) chips) and using an automated radiosynthesizer system to dispense reagents and recover syntheses products (**Figure 6-1A**) (80). Each 25.0 x 27.5 mm<sup>2</sup> chip was coated with hydrophobic Teflon layer with an etched hydrophilic circular reaction site (4 mm diameter), which acted as a surface-tension trap to confine reagents during the multi-step radiosynthesis. The details of the STT chip fabrication were previously reported (80). The chip was placed atop a heater that can rotate, and reagents were delivered by piezoelectric dispensers

arranged in a circular pattern above the chip. Dispensers were calibrated and primed before use as described previously (78). The operation of this synthesizer is illustrated in **Figure 6-1B**.

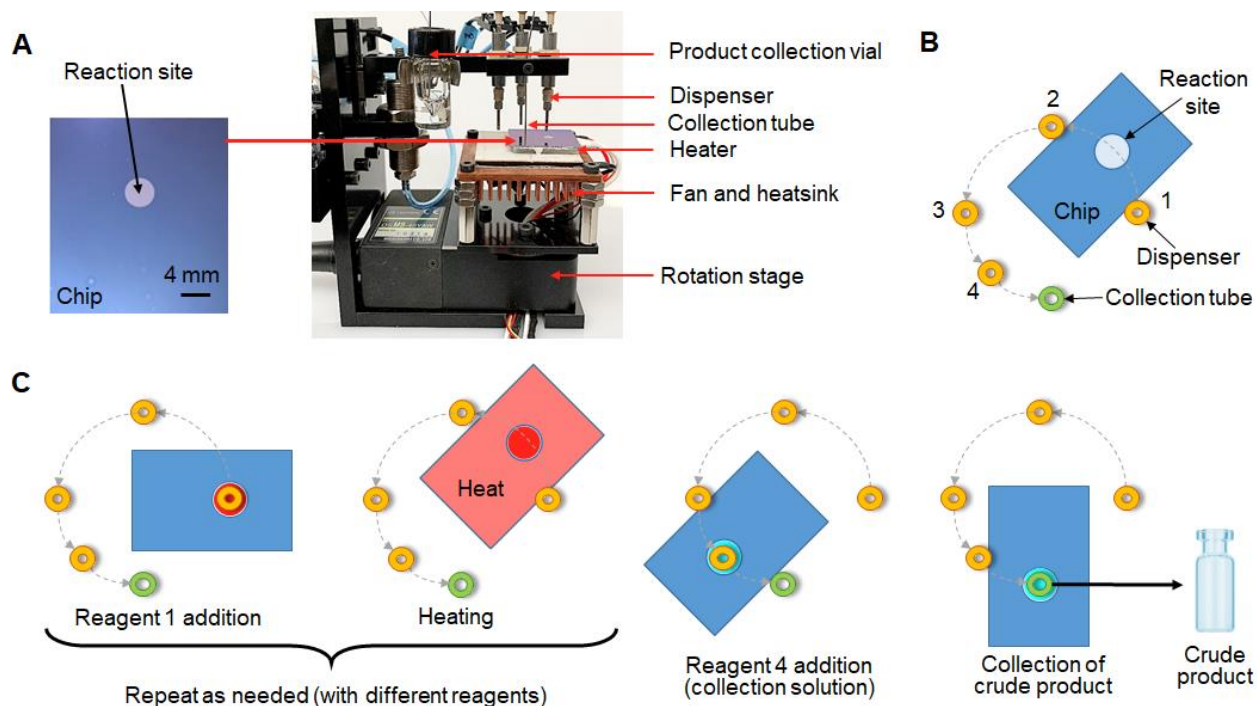


**Figure 6-1 Automated microdroplet synthesis.**

(A) Photographs of a disposable reaction chip (left) and automated droplet synthesizer (right). (B) Top view schematic of dispenser arrangement for a multi-step droplet synthesis. (C) Simplified schematic showing position of rotating platform during various steps of a typical radiosynthesis (reagent addition, heating, and collection of crude product).

For synthesis with high (up to multi-GBq) starting activities, the desired quantity of [ $^{18}\text{F}$ ]fluoride was pre-mixed with either  $\text{TBAHCO}_3$  (113 nmol) for synthesis of [ $^{18}\text{F}$ ]FET or  $\text{K}_{222}/\text{K}_2\text{CO}_3$  (383/275 nmol) for synthesis of [ $^{18}\text{F}$ ]FBB, then dispensed and dried on chip in portions of up to 30  $\mu\text{L}$  at a time (the maximum capacity of the reaction site). Up to 4 droplets were used to load activities in the range 0.02 – 4 GBq.

Following crude synthesis of the tracers, purification was achieved using analytical-scale HPLC with a tracer-specific method reported previously (82,85). Then the tracers were reformulated either by evaporation and resuspension ([ $^{18}\text{F}$ ]FET)(82), or automated solid-phase extraction (SPE) ([ $^{18}\text{F}$ ]FBB) (85) (**Figure 6-2**) followed by sterile filtration.

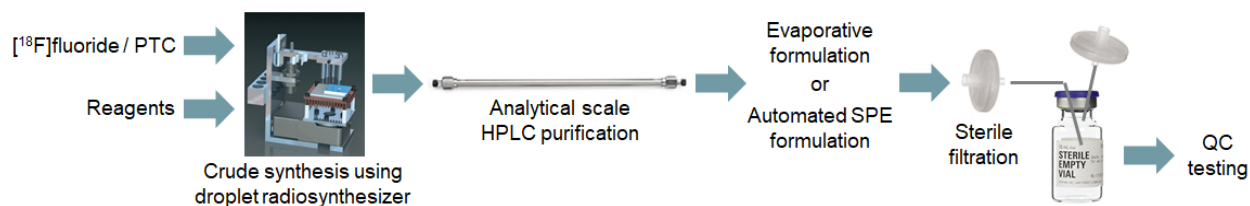


**Figure 6-2 Tracer preparation scheme. PTC = phase transfer catalyst. SPE = Solid-phase extraction.**

### 6.2.3 [<sup>18</sup>F]FET synthesis

The production of [<sup>18</sup>F]FET was performed using identical reaction conditions as previously reported for manual droplet-based synthesis (82) adapted from a conventional 2-step synthesis route (65,257).

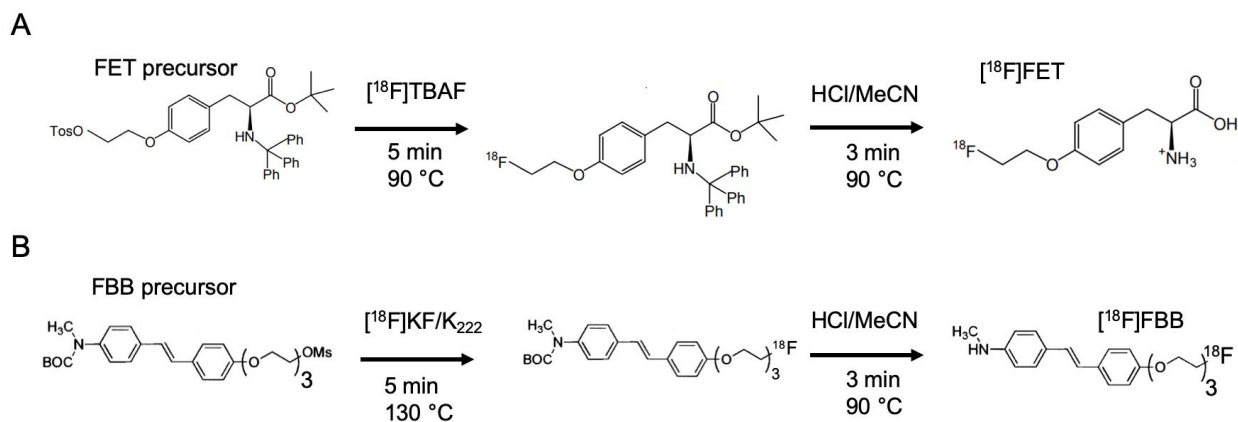


**Figure 6-3 Synthesis routes for (A) [<sup>18</sup>F]FET and (B) [<sup>18</sup>F]FBB.**

The synthesizer was set up by loading stock solutions into reagent dispensers as indicated in **Table 6-3**. As the last setup step, the desired activity of [<sup>18</sup>F]fluoride was mixed with 1.5 μL of 0.075M TBAHCO<sub>3</sub> and loaded in the corresponding dispenser. The 2-step (fluorination and deprotection) crude synthesis was carried out as shown in **Figure 6-3A**. The [<sup>18</sup>F]fluoride / TBAHCO<sub>3</sub> solution was loaded 30 μL at a time, each droplet dried at 100 °C for 1.5 min. To the dried residue, precursor solution (10 μL) was added and the radiofluorination step was performed (5 min, 90°C). Acid mixture was then added to perform deprotection (3 min, 90°C). 20 μL was



added at the beginning, and another 20  $\mu\text{L}$  was added after 1.5 min. The crude product was recovered with FET collection solution (4x20  $\mu\text{L}$ ). To obtain purified [ $^{18}\text{F}$ ]FET, the crude collection mixture was diluted with 100  $\mu\text{L}$  water (to lower MeCN concentration, improve separation quality and reduce losses during sample transfer) and injected into analytical radio-HPLC for purification (conditions described below). The [ $^{18}\text{F}$ ]FET peak was collected in a pyrex vial (WHEATON® V vial 5 mL, Millville, NJ, USA), evaporated to dryness in an oil bath at 120 °C and resuspended in 5 mL of sterile saline. The formulated product was sterile filtered (13 mm diameter, 0.22 mm pore size, PVDF membrane; Fisherbrand™, Waltham, MA, USA) into a sterile product vial (2 mL, ALK, Denmark) and samples taken under aseptic conditions for QC testing. Clinical-scale batches were prepared with at least 2 GBq of starting activity.

#### 6.2.4 [ $^{18}\text{F}$ ]FBB synthesis

Automated production of [ $^{18}\text{F}$ ]FBB in droplet format, adapted from a 2-step conventional synthesis route **Figure 6-3B** using a Boc-protected precursor (258), was previously reported (85). In this work the volume of precursor solution was increased from 10 to 15  $\mu\text{L}$  to reduce sensitivity of the reaction performance (85) in case of dispensing errors associated with the viscous DMSO-based precursor solution.

The configuration of dispensers is described in **Table 6-3**. The desired activity of [ $^{18}\text{F}$ ]fluoride was mixed with 4.5  $\mu\text{L}$  of  $\text{K}_{222}/\text{K}_2\text{CO}_3$  stock solution and dispensed 30  $\mu\text{L}$  at a time, with each droplet dried at 100 °C for 1.5 min. To the dried residue, precursor solution (10 or 15  $\mu\text{L}$ ) was added, and then the chip was heated for 5 min at 130 °C to perform radiofluorination of the precursor. Then, the acid solution was added (20  $\mu\text{L}$  at  $t=0$ , and another 20  $\mu\text{L}$  at  $t=1.5$  min) to remove protecting groups (5 min, 90°C). The crude product was recovered with FBB collection solution (4x20 $\mu\text{L}$ ) into a vial pre-filled with 64  $\mu\text{L}$  of 33 mg/mL scavenger solution, diluted with 50  $\mu\text{L}$   $\text{H}_2\text{O}$ , and purified via analytical HPLC. The purified product was formulated via SPE using an automated system (85), from where it was eluted in ethanol and diluted with formulation dilution solution to achieve 15% EtOH concentration in a final volume of 5 mL, and sterile filtered

(Whatman®, Anotop® 10 mm diameter, 0.02 µm pore size; Cytiva, Marlborough, MA, USA). Samples were taken for QC testing. Batches intended for QC testing used at least 2 GBq starting activity. In case of samples analyzed with the Tracer-QC system, the elution step during formulation was performed with 150 µL EtOH, and the final formulated volume was 1 mL.

### 6.2.5 Analytical methods

A calibrated ion chamber (CRC 25-PET, Capintec, Florham Park, NJ, USA) was used to perform radioactivity measurements. Radioactivity recovery was determined by dividing radioactivity of collected crude product by the amount of starting activity (correcting for decay). Fluorination efficiency was determined from radio-TLC as a percentage of desired product in the crude product. Crude radiochemical yield (crude RCY) was calculated by multiplying radioactivity recovery and fluorination efficiency. Overall RCY is a ratio of final formulated product activity to the starting activity. Molar activity was quantified based on isolated product radioactivity collected after HPLC purification and area under the corresponding UV peak of the purification chromatogram converted to molar quantity using a calibration curve.

Fluorination efficiency was determined via radio-thin-layer chromatography (radio-TLC). Radio-HPLC analysis and purification were performed on an analytical-scale HPLC system. These methods were reported previously, and are summarized in the **Appendix 6.6.2**.

### 6.2.6 Quality control testing

Quality control tests were performed on 3 consecutive batches of [<sup>18</sup>F]FET and 3 consecutive batches of [<sup>18</sup>F]FBB. Details of conventional quality control testing are described in the **Appendix 6.6.3**. An additional 3 batches of [<sup>18</sup>F]FBB were prepared and transported to Trace-Ability, Inc. (Van Nuys, CA, USA), and tested using an automated QC testing system (Tracer-QC, Trace-Ability, Inc.).

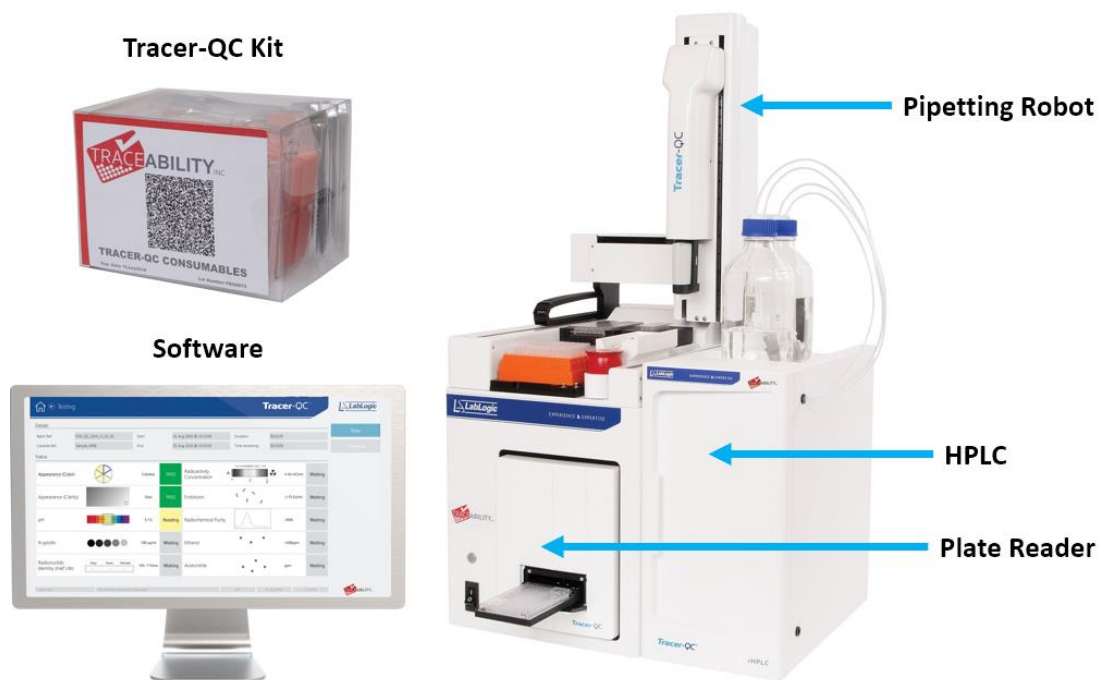


**Figure 6-4 Components of the Tracer-QC platform.**

**Table 6-2 Comparison of conventional and automated methods of [<sup>18</sup>F]FBB quality control testing**

QC test	Conventional method	Tracer-QC method
Color	Visual assessment	Absorbance measurement (with disposable indicators)
Clarity	Visual assessment	
pH	Indicator + visual assessment	
Residual Kryptofix	Spot test + visual assessment	
Endotoxin concentration	Portable test system (PTS) reader	Emission measurement (with disposable scintillators)
Residual solvents	Gas chromatograph	
Radionuclidic identity (half-life)	Dose calibrator + clock	
Radioactivity concentration	Dose calibrator + syringe	Radio-HPLC integrated in Tracer-QC supported by a disposable kit
Radiochemical identity/purity	Stand-alone radio-HPLC	
Chemical identity/purity		
Molar activity		

This platform enables complete automation of PET tracer QC and comprises a plate reader, liquid handler and HPLC integrated into a single system that operates with disposable test kits (**Figure 6-4**) (259). To operate the system, the user installs the kit, initiates the program, delivers the sample, triggers the analysis and collects the report. After the process is complete

and the used kit is removed, the system is ready for the next analysis without any further preparation. **Table 6-2** summarizes the tests developed for FBB with comparison to conventional test methods. These tests have been developed and validated individually and then merged into an integrated protocol for automated execution. They have been subsequently verified or re-validated as suitable for QC testing of [<sup>18</sup>F]FBB produced on the miniaturized platform. The effects of the unique composition of [<sup>18</sup>F]FBB resulting from such syntheses were studied and reflected in the method development and validation. Details of the tests are summarized in the **Appendix 6.6.4**.

## 6.3 Results

### 6.3.1 [<sup>18</sup>F]FET production and testing

In initial synthesis runs with <20 MBq starting activity, the automated droplet synthesis exhibited very good  $70 \pm 9\%$  (n=9) crude RCY. Notably, this was higher than the previously reported manual droplet-based synthesis ( $59 \pm 7\%$ , n=4) (82) or automated results using the passive-transport droplet-based synthesizer ( $54 \pm 6\%$ , n=5) (82). Additionally, the system had an improved synthesis time of 18 min compared to 24 min or 19 min for manual or passive transport automated system, respectively. Detailed comparison of various parameters is shown in **Table 6-4**. Previous work with [<sup>18</sup>F]fallypride showed similar improvements when transitioning from the passive-transport (PT) chip to the STT chip (80).

The impact of increased starting activity on the performance of the crude synthesis was also explored (**Figure 6-5**). Crude RCY decreased from ~70% to ~40% as activity was increased in the range 0.2 to 4 GBq. The crude RCY is a product of radioactivity recovery and fluorination efficiency and both these parameters show a slight decrease with increased starting activity. A similar result was previously observed with [<sup>18</sup>F]fallypride synthesis (83).

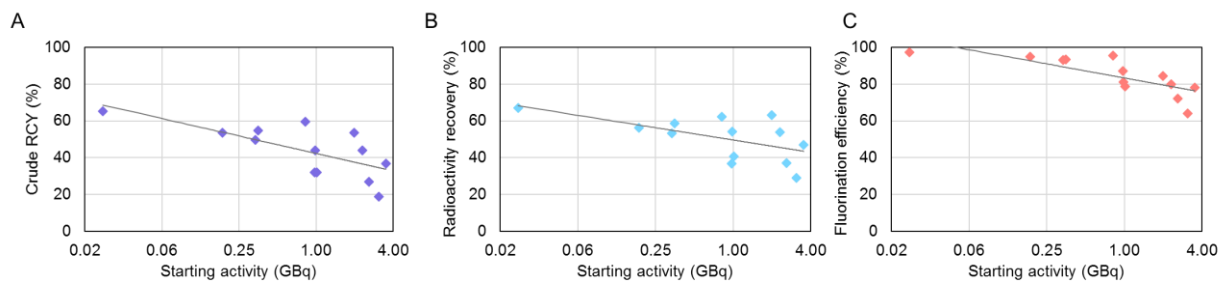


**Figure 6-5 Performance of crude [<sup>18</sup>F]FET droplet-based radiosynthesis as a function of starting activity.**

(A) Crude RCY. (B) Radioactivity recovery. (C) Fluorination efficiency. Note that the x-axis is plotted on a logarithmic scale, and a logarithmic trendline is generated for all graphs.

The overall synthesis time, including purification and formulation, was 60 min. For clinical-scale batches, the synthesis exhibited  $28 \pm 14\%$  ( $n=3$ ) overall activity yield,  $>99\%$  radiochemical purity, and high molar activity ( $418 \pm 52$  GBq/ $\mu\text{mol}$ ,  $n=3$ ; EOS). Three consecutive batches of formulated [<sup>18</sup>F]FET passed QC tests (**Table 6-5**), with most impurities being below detectable limits or extremely low. Example chromatograms during [<sup>18</sup>F]FET purification and assessment of radiochemical purity and identity are shown in **Figure 6-6**.

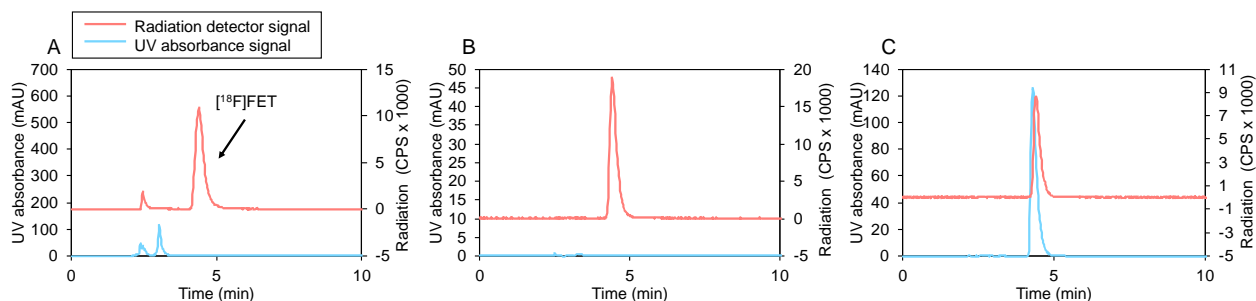


**Figure 6-6 Example HPLC chromatograms for [<sup>18</sup>F]FET.**

(A) Crude product. (B) Formulated product. (C) Formulated product co-injected with reference standard.

### 6.3.2 [<sup>18</sup>F]FBB production and testing

The initial runs using low ( $<20$  MBq) starting activities were performed for syntheses with 2 different precursor volumes (10  $\mu\text{L}$  and 15  $\mu\text{L}$ ). The crude RCY was similar in both cases ( $54 \pm 9\%$ ,  $n=5$  for 15  $\mu\text{L}$  and  $58 \pm 7\%$ ,  $n=6$  for 10  $\mu\text{L}$ ) as were other parameters (**Table 6-6**). Using a

larger precursor volume helped to increase tolerance to any dispensing errors that may occur due to the high viscosity of the precursor solution.

The impact of starting activity on the synthesis performance was also investigated (**Figure 6-7**). Across the range of 0.02 to 4.0 GBq, the crude RCY exhibited a slight decrease, though the impact was negligible up to ~1 GBq of starting activity. Both the component measurements radioactivity recovery and fluorination efficiency exhibited a similar trend.

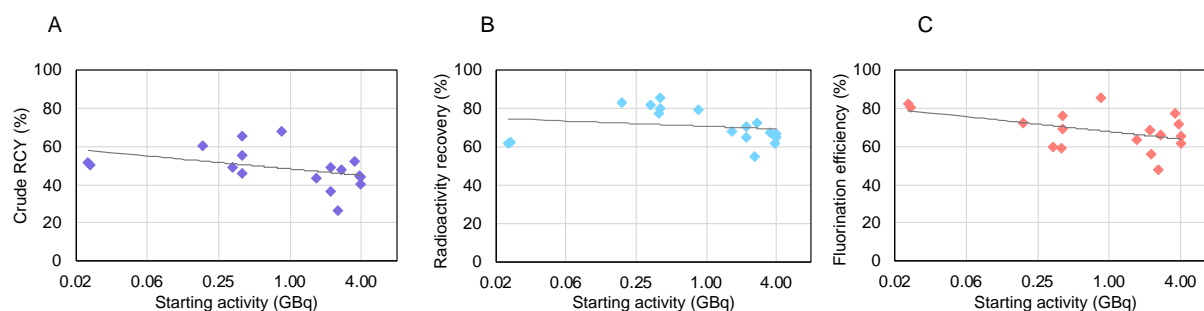


**Figure 6-7 Performance of crude [<sup>18</sup>F]FBB droplet-based radiosynthesis as a function of starting activity.**

(A) Crude RCY. (B) Radioactivity recovery. (C) Fluorination efficiency. Note that the x-axis is plotted on a logarithmic scale, and a logarithmic trendline is generated for all graphs.

Complete tracer production – microdroplet synthesis followed by analytical HPLC purification and automated SPE formulation – took ~60 min and resulted in a radiochemically pure (>95%) product. Three consecutive batches exhibited  $15 \pm 4\%$  ( $n=3$ ) overall activity yield, and high molar activity  $480 \pm 190$  GBq/ $\mu\text{mol}$  ( $n=3$ ; EOS). All batches passed necessary QC tests (**Table 6-7**). Example chromatograms during [<sup>18</sup>F]FBB purification and assessment of radiochemical purity and identity are shown in **Figure 6-8**.

Another three consecutive batches were prepared for QC analysis with the Tracer-QC system. This set of runs exhibited overall activity yield of  $16 \pm 4\%$  ( $n=3$ ) and molar activities of  $490 \pm 130$  GBq/ $\mu\text{mol}$  ( $n=2$ ; EOS). Automated testing of each batch was followed by automated analysis producing a summary page along with a detailed 26-page report. All samples passed all acceptance criteria for release of the doses, with many impurities below detection limits. The acceptance criteria for [<sup>18</sup>F]FBB QC, along with measured results for each batch are summarized

in **Table 6-8**. The demonstration with 3 consecutive samples confirms consistency of both the synthesis and QC testing.

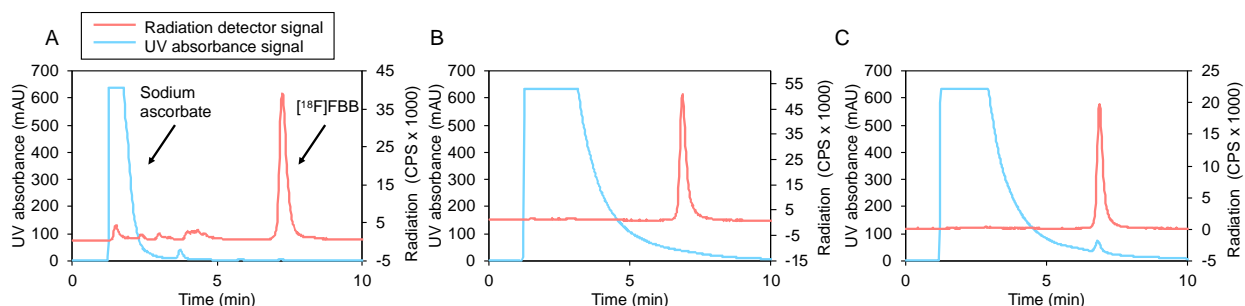


**Figure 6-8 Example HPLC chromatograms for [<sup>18</sup>F]FBB.**

(A) Crude product. (B) Formulated product. (C) Formulated product co-injected with reference standard.

## 6.4 Discussion

### 6.4.1 Comparison to conventional synthesis

We previously showed, for the syntheses of [<sup>18</sup>F]FET (82) and [<sup>18</sup>F]FBB (85), that miniaturization of radiopharmaceutical production leads to many benefits compared to conventional synthesis, including reduced reagent consumption, shorter reaction time, high molar activity, and high reaction yields, on top of the very small physical footprint of the microfluidic system. In this work the synthesis activity scale is increased up to 4 GBq with minimal modifications to the synthesis parameters. The precursor consumption remained low, consuming 100-150x less than macroscale methods. With higher starting activities the synthesis time is slightly longer, due to the need to dry a larger volume of the radioisotope solution, but still remains <60 min (conventional reported synthesis times vary between 45-90 min). The yields are comparable to the range reported for conventional methods. Here, [<sup>18</sup>F]FET was produced with  $36 \pm 7\%$  ( $n=3$ ) overall yield and generally, for conventional syntheses the reported yields vary between 20-40% (65,257,260). Microdroplet [<sup>18</sup>F]FBB synthesis resulted in  $23 \pm 3\%$  ( $n=6$ ) overall yield comparable to 10-30% yield range of most reported methods (258,261,262,263(p94),264).

As expected, the molar activity of the microscale synthesis remained high (>400 GBq/ $\mu\text{mol}$ ) at the increased activity scale.

#### **6.4.2 Activity scaling in droplet micro-radiosynthesizer**

In previous work by our group, droplet-based synthesis of [ $^{18}\text{F}$ ]fallypride was demonstrated with starting activities ranging up to 41 GBq (83), highlighting the scalability of the droplet radiosynthesis techniques. Up to 7.2 GBq of injectable [ $^{18}\text{F}$ ]fallypride was produced, which would be sufficient for multiple clinical doses. This work further demonstrates that product amounts of additional clinically-relevant radiotracers ([ $^{18}\text{F}$ ]FET and [ $^{18}\text{F}$ ]FBB) can be scaled up to amounts sufficient for clinical PET scans.

For [ $^{18}\text{F}$ ]fallypride, the concentration of aqueous fluoride-18 was performed using a custom micro-cartridge-based radioisotope concentrator that could reduce the volume from several mL to less than 30  $\mu\text{L}$  in under 8 min (255). However, this and other cartridge-based concentration approaches add complexity to the overall synthesizer setup. In this work, the starting [ $^{18}\text{F}$ ]fluoride activity was scaled (up to 4 GBq) by directly loading and drying multiple 30  $\mu\text{L}$  droplets of the [ $^{18}\text{F}$ ]fluoride solution (without using a cartridge or additional valves). Another significant advantage of this concentration method is that it can be used with any amount of base (in contrast to cartridge concentration methods, in which the type and amount of base is linked to the elution efficiency). The independence of the approach here is that one can ensure that the total amount of base added with the [ $^{18}\text{F}$ ]fluoride matches the optimal amount of base in the reaction as determined from low-activity optimization studies. While it is possible to load even higher activities than reported here (i.e., >4 GBq) with this method, drying a large volume (e.g. 1 mL) would require many (33) droplets to be sequentially loaded and dried. With each evaporation cycle run for 1.5 min, drying of 1 mL would take approximately 50 min. We expect ~300-600  $\mu\text{L}$  to be an upper practical limit, which could be concentrated in 15-30 min, though for many applications, smaller volumes and activity levels would be sufficient. For example, the concentration of 100  $\mu\text{L}$  could be completed in <6 min, which can contain 4 GBq or more of activity, depending on target volume



and bombardment parameters. In this work ~100  $\mu\text{L}$  of [ $^{18}\text{F}$ ]fluoride (~2-4 GBq) afforded 0.4-0.7 GBq of injectable tracer, which is sufficient for a typical clinical PET scan (~0.37 GBq per injection). Overall, sequential drying results in a significantly simpler procedure and more compact synthesis system compared to cartridge-based methods (83).

At the same time as we are attempting to increase the activity scale of the synthesis, improvements in scanner technology are requiring less activity for clinical PET scans. In particular, recent developments with total-body PET allowed good human [ $^{18}\text{F}$ ]FDG scans to be obtained with only 25 MBq of administered activity (265), about ~10x lower than what is typically injected. Such advancements mean that in the future the modest sized batches produced here may each be suitable for many patients, or batches for one or a few patients could be produced with lower starting activity levels.

### 6.4.3 Impact of starting activity on synthesis performance

Increasing starting radioactivity in radiopharmaceutical syntheses can directly affect the stoichiometry of a reaction and amplify radiolysis effects. We observed that the reaction performance was relatively unaffected up to ~1 GBq starting activity, and then started to show some reduction for both [ $^{18}\text{F}$ ]FET and [ $^{18}\text{F}$ ]FBB. Both the fluorination efficiency and radioactivity recovery exhibited some decline, suggesting reduced fluoride-18 incorporation and resulting in moderately lower crude RCY. In previous work with [ $^{18}\text{F}$ ]fallypride, the decrease in crude RCY only became significant around 20 GBq (83), indicating that this effect may vary between different syntheses. Interestingly, for a microvial-based synthesis of [ $^{18}\text{F}$ ]FET in 10  $\mu\text{L}$  volume by Iwata *et al.*, the reaction yield was reported constant when starting activity was varied between 0.1 and 6 GBq (55). However, upon addition of fluoride-19 carrier (simulating a further increase in activity), the RCY was reduced significantly (55). Looking at the work by Iwata *et al.* and the current reported results of [ $^{18}\text{F}$ ]FET syntheses, a higher activity may have been better tolerated in the first case due to the higher amount of precursor used (180 nmol, compared to 60 nmol in our work), or differences in purity of the [ $^{18}\text{F}$ ]fluoride source (i.e. the [ $^{18}\text{F}$ ]fluoride undergoes cartridge trap

and release process while in our case it is used directly from a cyclotron). Overall, impurities in the fluoride-18 solution, reduced excess of precursor, and radiolysis are all potential culprits for the observed reduction in the reaction yields with higher starting activities. Further studies are needed to fully understand these effects and improve reaction scalability in the future.

#### **6.4.4 Quality control testing**

After synthesis, purification, and formulation, quality control (QC) testing of the radiopharmaceuticals is a crucial step necessary to ensure safety prior to use in patients (266–271). In this work we performed QC testing both using conventional procedures as well as a new automated QC testing platform (Tracer-QC). In general, likely due to the small total amounts of solvents and reagents, the amounts of impurities were extremely low, suggesting that microvolume methods may offer some inherent safety advantages for radiopharmaceutical production. Conventional QC tests require an array of expensive analytical instrumentation, all of which requires space, maintenance, training, calibration, and documentation, making such testing a time-consuming, expensive procedure (259,272). Furthermore, some of the tests require manual handling of the radioactive batches resulting in high radiation exposure to the operator (273) and higher margin for human error or subjective interpretation. Moreover, pairing a compact microfluidic reactor system with a large analytical laboratory facility undermines the economic and practical advantages offered by microfluidic technology. In contrast, the compact and automated Tracer-QC system with integrated HPLC (259) offers key advantages which allow to overcome these challenges. (1) Ease and safety of use. Unlike conventional test methods that require expertise in operation and maintenance of many different analytical instruments, the integrated platform requires only a simple setup and operating procedure with minimal need for training. It also avoids the need for subjective assessments of test results, reducing variability and preventing human error. Safety is significantly improved because there is never a direct line of sight between the user and unshielded sample, and minimal user interaction with the system is needed. The instrument is also very easy to maintain due of its simplicity, absence of cleaning and the large

number of automated internal diagnostics. (2) Efficiency. Because Tracer-QC runs completely unattended, personnel are freed up to perform other tasks after setup and initiation of tests. All necessary QC tests for [ $^{18}\text{F}$ ]FBB batches were carried out completely unattended, and the software automatically generated a detailed report with “pass/fail” results for all QC tests. The automated suitability checks and calibrations further reduce the operator effort. Additional efficiencies arise due to the compact size of the system, minimizing the laboratory space dedicated to QC testing. The kit-based design minimizes effort to maintain the consumables inventory and supports the production of multiple different radiopharmaceuticals daily by a single Tracer-QC system.

## 6.5 Conclusions

In this work we demonstrate the use of a compact automated microdroplet synthesizer to rapidly produce batches of formulated [ $^{18}\text{F}$ ]FET and [ $^{18}\text{F}$ ]FBB with high yield and high molar activity. In contrast to previously reported production of [ $^{18}\text{F}$ ]fallypride on a microdroplet chip which was coupled to a separated radionuclide concentrator to increase the synthesis scale (83), the radioisotope was concentrated in this work using a simpler and faster approach still capable of clinically-relevant synthesis scale. Though a modest reduction in RCY was observed when scaling up, it is nonetheless clear that droplet-based radiochemistry systems have sufficient scaling capacity to produce batches for one or multiple clinical doses (that pass clinical quality control tests), while offering advantages such as compact size, reduced reagent usage, high molar activity and fast synthesis time (84). Because employing conventional approaches to perform QC testing seriously undermines the potential of miniaturized synthesizers, in this work we demonstrate an alternative approach. Pairing of the droplet synthesizer with an automated benchtop QC testing system (Tracer-QC) has the potential to establish a robust, rapid, compact and economical method for batch-on-demand production of PET radiopharmaceuticals, without requiring large radiochemistry and analytical chemistry facilities.

## 6.6 Appendix

### 6.6.1 Droplet synthesizer setup

During setup of the automated microvolume synthesis system, reagents were loaded into the dispensers as shown in **Table 6-3**. Dispensers were primed before use.

**Table 6-3 Reagent setup in automated droplet synthesizer for syntheses of [<sup>18</sup>F]FET and [<sup>18</sup>F]FBB.**

	[ <sup>18</sup> F]FET	[ <sup>18</sup> F]FBB
<b>Dispenser 1</b>	[ <sup>18</sup> F]fluoride / TBAHCO <sub>3</sub>	[ <sup>18</sup> F]fluoride / K <sub>222</sub> / K <sub>2</sub> CO <sub>3</sub>
<b>Dispenser 2</b>	FET precursor solution	FBB precursor solution
<b>Dispenser 3</b>	FET deprotection solution	FBB deprotection solution
<b>Dispenser 4</b>	FET collection solution	FBB collection solution

### 6.6.2 Analytical methods (radio-TLC, radio-HPLC)

Fluorination efficiency was determined via radio-thin-layer chromatography (radio-TLC). For [<sup>18</sup>F]FET, silica gel 60 F254 plates (Merck KGaA, Darmstadt, Germany) were cut into 15 x 60 mm pieces (with 40 mm developing distance), spotted with 0.5 μL of the sample and developed in 80% (v/v) MeCN in H<sub>2</sub>O. TLC plates were analyzed with a Cherenkov luminescence imaging system as previously described (95). Retention factors of the observed radioactive species were: 0 ([<sup>18</sup>F]fluoride), 0.3 ([<sup>18</sup>F]FET), and 0.8 (fluorinated intermediate). For [<sup>18</sup>F]FBB, reverse phase TLC plates (RP-18 silica gel 60 F254 sheets; aluminum backing; Millipore Sigma, St. Louis, MO, USA) were prepared and used in a similar fashion, but developed in 90% (v/v) MeCN in H<sub>2</sub>O. Retention factors of the observed radioactive species were: 0.0 ([<sup>18</sup>F]fluoride), 0.4 ([<sup>18</sup>F]FBB), and 0.8 (fluorinated intermediate).

Radio-HPLC analysis and purification were performed on an analytical-scale Smartline HPLC system (Knauer, Berlin, Germany) with 200 μL injection loop, a pump (Model 1000), degasser (Model 5050), UV detector (Model 2500) and a radiometric detector (Bioscan B-FC-4000, Bioscan Inc., Washington DC, USA). Samples were separated using a C18 column (Luna, 5 μm particles, 100Å pores, 250 x 4.6 mm, Phenomenex, Torrance, CA, USA) with guard column

(SecurityGuard C18, Phenomenex). For [ $^{18}\text{F}$ ]FET, separation was performed isocratically using 10% (v/v) EtOH in  $\text{H}_2\text{O}$  at a flow rate of 1 mL/min, and UV absorbance was measured at 269 nm. The retention time of [ $^{18}\text{F}$ ]fluoride was ~2-3 min, and ~5 min for [ $^{18}\text{F}$ ]FET. The fluorinated intermediate and other impurities were eluted off the column by switching the mobile phase to 95:5 (v/v) MeCN: $\text{H}_2\text{O}$ . For [ $^{18}\text{F}$ ]FBB, the mobile phase was 60:40 (v/v) MeCN : 25 mM phosphate buffer at a flow rate of 1.5 mL/min, and UV absorbance was measured at 254 nm. The observed retention times were ~2-3 min for [ $^{18}\text{F}$ ]fluoride, 6 min for [ $^{18}\text{F}$ ]FBB, and 14 min for the fluorinated intermediate.

### **6.6.3 Quality control testing methods (conventional instruments)**

Quality control tests for appearance, pH, radionuclide purity and identity, bacterial endotoxins, sterility, radiochemical and chemical purity were determined as previously described (83).

#### **6.6.3.1 Molar activity**

Molar activity was estimated by quantifying amount of the tracer in purification chromatogram using ultraviolet (UV) peak and cold standard calibration curve, then dividing by radioactivity of the isolated product after purification.

#### **6.6.3.2 Residual content of $\text{TBAHCO}_3$**

Residual  $\text{TBAHCO}_3$ , which has acceptable limit of 2.6 mg/V, in the purified sample was determined using a thin-layer chromatography (TLC) spot test method reported by Kuntzsch et al (274). For 5 mL formulation volume the calculated limit would be 520 mg/L, however the expected quantity of  $\text{TBAHCO}_3$  would be much less. Thus a low concentration standard solution of  $\text{TBAHCO}_3$  (45 mg/L) was created and spotted alongside the formulated [ $^{18}\text{F}$ ]FET (2  $\mu\text{L}$ ) onto a silica TLC plate (JT4449-2, J.T. Baker, Center Valley, PA, USA), and air dried. 10  $\mu\text{L}$  of a developing solution (0.72M  $\text{NH}_4\text{OH}$  in 90% MeOH) was added on top of each spot, dried, and then the TLC strip was developed in a chamber containing iodine crystals for 1 min. The color

intensity of the spot of the purified sample was compared to that of the standard solution to confirm the residual amount was below the injectable limit.

#### **6.6.3.3 Residual content of K<sub>222</sub>**

Residual kryptofix content was determined using a TLC spot test as reported by Halvorsen et al (275). Iodoplatinated TLC strips were prepared according to the reported procedure. The standard solutions containing 50 µg/mL (injectable limit) and 12.5 µg/mL of kryptofix in a formulation matrix identical to [<sup>18</sup>F]FBB formulation matrix were prepared. 2 µL of [<sup>18</sup>F]FBB sample was spotted alongside the standards onto a iodoplatinated TLC strip, the spots were air dried followed by addition of 1% H<sub>2</sub>O<sub>2</sub> (2.5 µL). After 1 min of drying the sample spots were analyzed for K<sub>222</sub> content.

#### **6.6.3.4 Residual solvent analysis**

The concentration of residual solvents (i.e. methanol, acetonitrile, hexyl alcohol, ethanol and DMSO) was determined using gas chromatography mass spectrometry (GCMS).

#### **6.6.3.5 Residual solvent analysis of [<sup>18</sup>F]FET samples**

Gas chromatography mass spectrometry (GC-MS) measurements were carried out on a GC system (6890N, Agilent) equipped with mass spectrometry detector (5975 MSD) and autosampler (7683B). The instrument was controlled by Enhanced Chemstation software version E.01. The inlet was operated in split mode at 250 °C. Ultra-high purity He (Airgas West, Culver City, CA) was used as the carrier gas with the flowrate set to 1.2 mL / min. Separation was carried out on a 30 m x 250 µm x 0.25 µm DB-Wax column (Agilent J&W). The GC oven was initially held at 70°C, heated to 140 °C at 10 °C/min, and then heated to 260 °C at 30 °C/min. The MSD was operated in the scan mode and used EI ionization.

Instrument response for known concentrations of pure analytes in butanol was measured to determine the analyte concentrations in the samples. More specifically, a 4-point calibration

curve was generated for all solvents (MeOH, MeCN, TA, EtOH). The concentration of the residual analytes was then interpolated from this calibration curve.

#### **6.6.3.6 Residual solvent analysis of [<sup>18</sup>F]FBB samples**

The concentrations of residual solvents (i.e. acetonitrile, DMSO, ethanol) were determined using headspace gas chromatography mass spectrometry (GCMS). To 100  $\mu$ L of each sample, 1  $\mu$ L of <sup>2</sup>H<sub>6</sub>-DMSO was added as an internal standard. For acetonitrile and DMSO, an aliquot (10  $\mu$ L) of each sample was transferred to 10 mL glass headspace vials fitted with magnetic caps. For measurement of ethanol concentrations, the samples were diluted 1 to 100 with water prior to the transfer. Samples were incubated for 20 min at 200 °C with gentle agitation every 10 seconds. After incubation, 1 mL of headspace vapor was withdrawn with a heated (110 °C) syringe and injected onto a GC inlet (1/10 split, 250 °C). Ultra-high purity He (Airgas West, Culver City, CA) was used as the carrier gas at constant flow (1 mL/min). Separations were carried out on a bonded-phase non-polar fused silica capillary column (60 m x 250  $\mu$ m x 0.25  $\mu$ m Zebron ZB-5plus column, Phenomenex). The GC oven was initially held at 50°C for 2 min, then was heated to 250 °C at 10 °C/min. The end of the column (GC/EI-MS transfer line at 250°C) was inserted into the EI source (200°C, 70 eV) of a high resolution Orbitrap mass spectrometer (Thermo Scientific Q Exactive GCMS, calibrated with perfluorotributylamine immediately prior to the analysis of each batch of samples), scanning from m/z 30-500 at a resolution (FWHM) of 60,000. Data were collected with instrument manufacturer-supplied software (Thermo Xcalibur v4.1). Instrument response from known concentrations of pure analytes in PEG400/water mixtures containing the same amount of internal standard was measured to determine the analyte concentrations in the samples. More specifically, a five-point calibration curve was generated for all three solvents at the following concentration levels: 0, 25.625, 51.25, 102.5, and 205 PPM for acetonitrile; 0, 312.5, 325, 1250, 2500 PPM for DMSO; and 0, 3.75, 7.5, 15, and 30% (w/v) for ethanol. Calibration curves for acetonitrile and ethanol were constructed by directly comparing absolute peak area (ordinate) and solvent concentration (abscissa). On the other hand, for the

DMSO calibration curve, ratios of DMSO/<sup>2</sup>H<sub>6</sub>-DMSO peak areas were used as the ordinate to account for potential sulfoxide oxidation.

#### **6.6.4 QC testing with Tracer-QC**

The Tracer-QC system uses optical measurements for all non-chromatographic QC tests. For color and clarity, the signal is the spectrophotometric measurement of absorbance of light passed through the sample in the plate reader. For pH, kryptofix, endotoxin and acetonitrile, the sample's interaction with an indicator (contained in the disposable kit) designated for each of the tests (and mixed with sample by the liquid handler) leads to unique changes in the absorbance spectrum. For radionuclidic identity and radioactivity concentration, the signal is a luminescence measurement detecting the emission of light from scintillating materials that interact with the radioactive sample in the kit. For the HPLC group of tests the signals are the UV and radio-chromatograms generated by traditional HPLC detectors. The Tracer-QC software processes the obtained signals in the context of pre-set parameters and measurements from reference standards (contained in the disposable kit) to determine the values of all QC parameters. Each test has automated suitability checks which confirm whether the produced measurement is valid. After values have been calculated and verified for all QC tests, the software produces a comprehensive report with these values along with acceptance criteria and pass/fail determination. These principles allow the entire QC process to be automated and objective while supporting completely traceable and tamper-free data flow from raw measurements to the report.

##### **6.6.4.1 Color**

A spectrophotometric measurement of the sample is performed together with a positive control solution containing one or more color standards with known absorbance.

##### **6.6.4.2 Clarity**

A turbidimetric analysis of the sample along with positive and negative control solutions is conducted through spectrophotometric measurements.



### **6.6.4.3 pH**

The solution to be analyzed is mixed with an indicator solution, which produces a pH-dependent change in the indicator's absorbance spectrum within the sample and indicator mixture.

### **6.6.4.4 Bacterial endotoxin**

Enzymatic activation of serine proteases from horseshoe crab amebocyte lysate by interaction with bacterial endotoxin is used to produce a chromogenic signal that can be analyzed spectrophotometrically.

### **6.6.4.5 Radioactivity concentration**

The radioactivity of an aliquot of sample solution is determined from the intensity of its radioluminescent emission.

### **6.6.4.6 Radionuclidic identity (half-life)**

The time-dependent radioactivity of an aliquot of sample solution is determined from the intensity of its radioluminescent emission.

### **6.6.4.7 Chemical identity, chemical purity, and/or chemical content via HPLC**

While chemical identity, chemical purity, and chemical content are all separate properties that each have distinct meaning and corresponding product specification, in common practice they can be derived from the same experiment simultaneously in cases where a product specification calls for the determination of more than one. In addition, these tests can be carried out concomitantly with determination of radiochemical identity, radiochemical impurity, and/or specific activity. For the Tracer-QC platform, all liquid handling required for sample preparation and injection is handled by the pipetting robot, mated to a conventional HPLC system utilized to set flow rates and/or gradients and detect elution of compounds.

#### *Radiochemical identity, radiochemical purity, and/or molar activity via Radio-HPLC*

The radiochemical identity and radiochemical purity, and molar activity tests can be carried out concomitantly with determination of chemical identity, and/or chemical purity. Molar activity is

then derived from a combination of the chemical content and radiochemical purity measurements (via HPLC) and radioactivity concentration.

The Tracer-QC HPLC method (**Figure 6-9**) is an adaptation of the validated HPLC method for analysis of Neuroceq formulation. For the blank injection, Neuroceq formulation matrix is injected directly with no dilution steps. For quantification of analyte peaks, a reference standard solution of <sup>19</sup>F-FBB (1.5 µg/mL), Stb-OMs (1.25 µg/mL), and Boc-Stb-TEG (2.5 µg/mL) in acetonitrile is also injected directly with no dilution steps. In order to minimize the volume of sample dose required for the TA-FBB-HPLC test, the sample dose is diluted in a 1:4 ratio with water before injection.

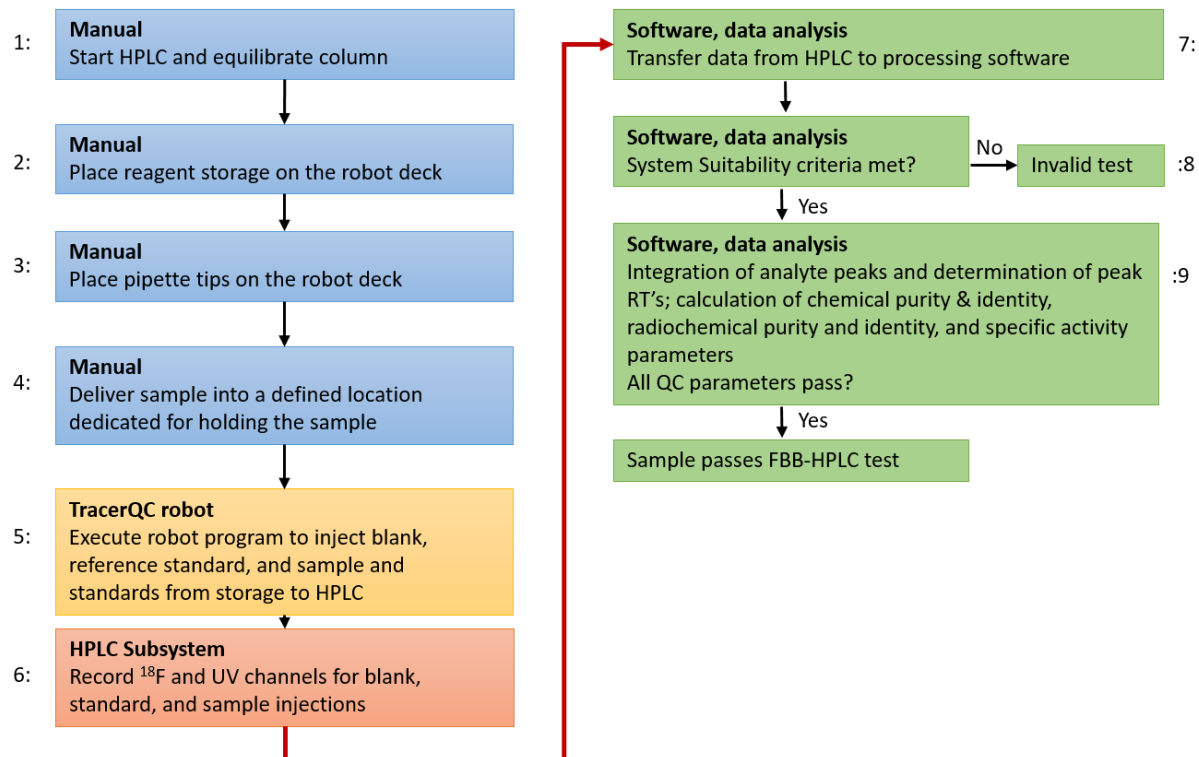


**Figure 6-9 Tracer-QC HPLC measurement protocol.**

Once the blank, standard, and sample dose injections have been completed, integration of the analyte peaks is performed, and data processing software calculates the values of all parameters required for release testing.

### 6.6.5 [<sup>18</sup>F]FET synthesis (low activity)

**Table 6-4** summarizes [<sup>18</sup>F]FET synthesis performance at low starting activity (<20 MBq) and compares the results to previous work using manual operation of a simplified droplet reaction chip (82) and automated operation of a passive-transport reaction chip (82). For manual operation, this chip was mounted on a similar heater, but reagents were delivered with a micropipette and product was collected with a micropipette.

**Table 6-4 Performance of droplet-based [<sup>18</sup>F]FET synthesis on several platforms.**

	Surface-tension trap chip (this work)	Surface-tension trap chip	Passive-transport chip
<b>Synthesis operation</b>	Automated	Manual	Automated
<b>Number of replicates (n)</b>	9	4	5
<b>Radioactivity recovery (%)</b>	80 ± 6	64 ± 5	59 ± 10
<b>[<sup>18</sup>F]FET conversion (%)</b>	88 ± 7	92 ± 4	93 ± 6
<b>Synthesis time (min)</b>	18	24	19
<b>Crude RCY (%)</b>	70 ± 9	59 ± 7	54 ± 6
<b>Residual activity on chip (%)</b>	0.7 ± 0.6	1.3 ± 0.5	3.2 ± 1.5

### 6.6.6 [<sup>18</sup>F]FET quality control results

**Table 6-5 Conventional (manual) quality control testing results for 3 consecutive batches of [<sup>18</sup>F]FET.**

Test	Testing Criteria	Batch 1	Batch 2	Batch 3
Appearance	Clear, colorless, particle free	Pass	Pass	Pass
Radioactivity concentration	7.4-74 MBq/mL [0.2-2 mCi/mL]	47 MBq/mL [1.3 mCi/mL]	56 MBq/mL [1.5 mCi/mL]	46 MBq/mL [1.3 mCi/mL]
Molar Activity	> 37 GBq/μmol [1 Ci/ μmol]	420 GBq/μmol [11.4 Ci/μmol]	697 GBq/μmol [18.8 Ci/μmol]	595 GBq/μmol [16.1 Ci/μmol]
Radiochemical identity	Retention time ratio of radio peak vs cold standard (0.9-1.1)	1.0	1.0	1.0
TBAHCO <sub>3</sub>	<520 mg/L <sup>a</sup>	< 45 mg/L	< 45 mg/L	< 45 mg/L
Residual solvents	MeCN < 410 PPM MeOH < 3000 PPM TA < 5000 PPM EtOH < 10%	N.D. N.D. N.D. N.D.	N.D. N.D. N.D. N.D.	N.D. N.D. N.D. N.D.
Radiochemical purity	> 95%	> 99%	> 99%	> 99%
Radionuclide identity	104-115 min	109	108	110
pH	4.0-7.0	5.0	5.5	5.5
Filter integrity	> 50 PSI	> 50 PSI	> 50 PSI	> 50 PSI
Shelf life	Pass appearance, pH and radiochemical purity after 240 min	Pass	Pass	Pass
Gamma ray emission energy	496-526 keV photons	Pass	Pass	Pass
Radionuclide purity	No less than 99.5%	Pass	Pass	Pass
Bacterial endotoxin	< 175 EU/total batch	Pass	Pass	Pass
Sterility	No colony growth observed for 14 days	Pass	Pass	Pass

<sup>a</sup>Acceptable limit is calculated based on < 2.6 mg/V regulation where V is a total maximum injection volume, in this case we compute for 5 mL as total formulation volume. N.D. = not detected. Limits of detection for residual solvents are: 40 ppm for MeCN, 30 ppm for MeOH, 40 ppm for TA, 50 ppm for EtOH.

### 6.6.7 [<sup>18</sup>F]FBB synthesis (low activity)

**Table 6-6** summarizes [<sup>18</sup>F]FBB synthesis performance at low starting activity (<20 MBq) on the surface tension trap chip, and compares the effect of using 10 or 15 μL of precursor stock solution.

**Table 6-6 A comparison of droplet-based [<sup>18</sup>F]FBB synthesis performance when performed manually versus automated, and at 2 different precursor solution volumes.**

	Automated	Automated	Manual
Precursor volume (μL)	15	10	10
Number of replicates (n)	5	6	4
Radioactivity recovery (%)	63 ± 6	69 ± 9	66 ± 6
[ <sup>18</sup> F]FBB conversion (%)	86 ± 9	86 ± 9	96 ± 1
Synthesis time (min)	18	18	23
Crude RCY (%)	54 ± 9	58 ± 7	63 ± 6
Residual activity on chip (%)	7 ± 6	8 ± 4	1 ± 1

### 6.6.8 [<sup>18</sup>F]FBB quality control results (conventional)

**Table 6-7 Conventional (manual) quality control testing results for 3 consecutive batches of [<sup>18</sup>F]FBB. N.D. = not detected. Limit of detection for MeCN is 20 ppm.**

Test	Testing Criteria	Batch 1	Batch 2	Batch 3
Appearance	Clear, colorless, particle free	Pass	Pass	Pass
Radioactivity concentration (MBq/mL)	45-5000	83 MBq/mL [2.2 mCi/mL]	97 MBq/mL [2.6 mCi/mL]	151 MBq/mL [4.1 mCi/mL]
Molar Activity (GBq/μmol)	> 37	593 GBq/μmol [16.0 Ci/μmol]	262 GBq/μmol [7.1 Ci/μmol]	583 GBq/μmol [15.7 Ci/μmol]
Radiochemical identity	Retention time ratio of radio peak vs cold standard (0.9-1.1)	1.0	1.0	1.0
K <sub>222</sub>	< 50 mg/L	< 13 mg/L	< 13 mg/L	< 13 mg/L
Residual solvents	MeCN < 410 PPM DMSO < 5000 PPM Ethanol < 15%	N.D.* 529 PPM 8%	N.D. 218 PPM 7%	N.D. 229 PPM 7%
Radiochemical purity	> 95%	97%	98%	98%
Radionuclide identity	105-115 min	113	112	113
pH	4.0 - 8.0	5.5	5.5	5.5
Filter integrity	> 50 PSI	> 50 PSI	> 50 PSI	> 50 PSI
Shelf life	Pass appearance, pH and radiochemical purity after 240 min	Pass	Pass	Pass
Gamma ray emission energy	496-526 keV photons	Pass	Pass	Pass
Radionuclide purity	No less than 99.5%	Pass	Pass	Pass
Bacterial endotoxin	< 175 EU/total batch	Pass	Pass	Pass
Sterility	No colony growth observed for 14 days	Pass	Pass	Pass

### 6.6.9 [<sup>18</sup>F]FBB quality control results (Tracer-QC)

The report of the QC testing performed on additional 3 consecutive batches of [<sup>18</sup>F]FBB with an automated Tracer-QC unit are shown in **Table 6-8**. Note that the indicated values for concentration and molar activity are slightly lower than would be expected in practice due to the decay that occurred during transport of samples from UCLA to Trace-Ability (~30 min) prior to starting the QC tests.

**Table 6-8 Tracer-QC (automated) quality control testing results for 3 consecutive batches of [<sup>18</sup>F]FBB.**

Test Parameter	Specification	Batch #1	Batch #2	Batch #3
Color (mAU)	< 500	98.2	43.7	91.8
Clarity (NTU)	< 10	8.0	7.3	9.9
pH	4.5 – 7.5	5.2	5.3	5.3
Endotoxin (EU/mL)	< 7.5	< 1	< 1	< 1
Acetonitrile (µg/mL)	< 410	< 100	< 100	< 100
Kryptofix (µg/mL)	< 50	< 50	< 50	< 50
Concentration (GBq/mL)	45 – 5000	285	244	400
Half-Life (min)	105 – 115	110.7	113.2	114.6
Chemical Identity (%RRT)	90 – 110	100.0	100.0	100.0
trans-FBB Content (µg/mL)	≤ 3.0	0.53	0.62	0.78
Stilbene-OMs Content (µg/mL)	≤ 3.0	0.00	0.00	0.08
BOC-Stilbene-TEG Content (µg/mL)	≤ 1.5	0.06	0.11	0.00
Unspecified Impurity Content (µg/mL)	≤ 5.0	0.00	0.00	0.00
trans-FBB Radiochemical Identity (%RRT)	90 – 110	100.0	100.0	100.0
cis-FBB Radiochemical Identity (RRT)	1.12 – 1.16	Not Detected	Not Detected	Not Detected
cis/trans-FBB Radiochemical Purity (%)	≥ 93	96.6	95.4	96.4
cis-FBB Radiochemical Content (%)	≤ 6%	0.0	0.0	0.0
Unspecified Radiochemical Impurity (%)	≤ 7%	3.4	4.6	3.6
Molar activity (GBq/µmol)	≥ 3	196.0	142.9	185.3

# Chapter 7: Scalable droplet-based radiosynthesis of [<sup>18</sup>F]fluorobenzyltri-phenylphosphonium cation ([<sup>18</sup>F]FBnTP) via a numbering up approach

## 7.1 Introduction

The recent World Health Organization report highlights ischemic heart disease as the leading cause of global mortality, causing 8.9 million deaths in 2019 (276). Early and precise detection of cardiac ischemia is crucial, enabling timely consideration of appropriate therapy and reducing the risk of disease progression. Utilizing molecular imaging modalities like positron emission tomography (PET) and single-photon emission computed tomography (SPECT), myocardial perfusion imaging (MPI) emerges as a powerful non-invasive tool for early detection and disease monitoring of cardiac ischemia (277–281).

In the United States, the Food and Drug Administration (FDA) has approved six MPI radiotracers, including four SPECT tracers ([<sup>99m</sup>Tc]Tc-teboroxime, [<sup>99m</sup>Tc]Tc-sestamibi, and [<sup>99m</sup>Tc]Tc-tetrofosmin all with half-life  $t_{1/2} = 6.04$  h, and [<sup>201</sup>Tl]thallium chloride with  $t_{1/2} = 73.1$  h) and two PET tracers ([<sup>13</sup>N]NH<sub>3</sub> ( $t_{1/2} = 10$  min) and [<sup>82</sup>Rb]Rb-chloride ( $t_{1/2} = 1.27$  min)). Despite the numerous advantages of PET over SPECT, such as high spatial resolution, attenuation correction, sensitivity, and quantitation, SPECT tracers continue to play a central role in clinical use, mainly due to the limited accessibility of MPI PET tracers (277,278,280–282). Challenges of using [<sup>82</sup>Rb]Rb-chloride include its ultrashort half-life, low first-pass extraction (~65% at rest), high positron range (2.6 mm), and the high cost of monthly generator replacement (278,279,281), and [<sup>13</sup>N]NH<sub>3</sub> is restricted by the requirement for an on-site cyclotron for production, significantly limiting its availability. PET imaging with F-18 presents an alternative that can overcome these limitations and provide several benefits, like longer half-life ( $t_{1/2} = 109.8$  min) enabling greater flexibility in study design, lower injected activity requirement due to low position energy and high

positron yield, and the feasibility of using exercise for stress imaging (in contrast to short half-life tracers that only permit pharmacological stress) (279).

The tracer 4-[<sup>18</sup>F]fluorobenzyltriphenylphosphonium cation ([<sup>18</sup>F]FBnTP) developed by the Dannals group(283) is a promising option. Previous reports have demonstrated its uniform distribution in the myocardium and favorable organ biodistribution, showing comparable accumulation to clinical tracers [<sup>99m</sup>Tc]Tc-sestamibi and [<sup>99m</sup>Tc]Tc-tetrofosmin (284–287). Further clinical trials are required to confirm its suitability for human use, but such studies are hindered by its complex and low-efficiency radiosynthesis procedure. The original method, reported by Ravert *et al.* in 2004 (283), involved a demanding 4-step manual process that required large amounts of precursor (20 μmol for fluorination) and reagents (20-7930 μmol per step), involved high corrosive reagents (HBr), and had low activity yield (6%) and long preparation time (82 min). Using microwave activation, Ravert *et al.* later showed the synthesis could be performed more quickly (52 min) and the activity yield increased to 8.3% (288); however the requirement for a custom synthesis module was limiting. Further improvements were made By Waldmann *et al.* in 2018, including automation on a commercially-available synthesis module (ELIXYS FLEX/CHEM, Sofie Inc., Dulles, VA, USA), as well as an improvement in activity yield (16%) (289), but the complex synthesis route remained a challenge for routine preclinical and clinical studies in most radiochemistry labs. Tominaga *et al.* later reduced the reaction steps from four to three, though critical information such as activity yield, molar activity, and synthesis time were not disclosed (284). More recently, Zhang *et al.* introduced a vastly-simplified one-step preparation of [<sup>18</sup>F]FBnTP through Cu-mediated radiofluorination of a pinacolyl arylboronate precursor (290). This method substantially streamlined the radiosynthesis and exhibited high fluorination conversion (62 ± 1.4%, n = 2), though the overall synthesis performance was not disclosed.

Recently, we showed that droplet-based radiochemistry approaches could be leveraged to substantially improve Cu-mediated radiosynthesis of [<sup>18</sup>F]FDOPA (291) and a novel



monoacylglycerol lipase (MAGL) ligand, [<sup>18</sup>F]YH-149 (136). Droplet radiochemistry offers advantages of minimal reagent cost, rapid synthesis time, high yield, high molar activity, and low space and infrastructure requirements. A further advantage of droplet radiochemistry is the ability to perform high-throughput optimization via arrays of droplet reactions performed in parallel (160,292). Using a newly developed robotic platform, we used this technique to develop a preliminary droplet-based radiosynthesis of [<sup>18</sup>F]FBnTP (208), resulting in substantial reduction in reagent usage and enhancement in radiosynthesis performance ( $89 \pm 1\%$ ,  $n = 4$  fluorination conversion). Following purification and formulation, [<sup>18</sup>F]FBnTP was produced with high isolated radiochemical yield (RCY,  $66 \pm 6\%$ ,  $n = 3$ ) within 42 min, corresponding to an activity yield of  $49 \pm 3\%$  ( $n = 3$ ).

In this work, we aimed to establish the clinical relevance of the previous result by scaling up the droplet-based production of [<sup>18</sup>F]FBnTP. Previously, we have shown two different approaches for scale-up of droplet reactions: (1) accumulating [<sup>18</sup>F]fluoride at a reaction site by depositing a small aliquot of the [<sup>18</sup>F]fluoride solution, evaporating the liquid, and repeating (**Figure 7-1A**) (78,97) and (2) pre-concentrating the [<sup>18</sup>F]fluoride using a trap-elute process on a miniature cartridge, enabling a greater amount of activity to be loaded to a reaction site (**Figure 1B**) (98). While the first approach is straightforward and suitable for moderate scale-up, handling very large activity amounts and volumes becomes impractical due to extended evaporation times at a single reaction site. In addition, a modest drop in RCY was observed, potentially due to the increased amount of impurities present when using large volumes of radioisotope source solution (292). Conversely, the second approach effectively worked with much larger volumes and avoids the build-up of impurities, but required a more complex setup. Furthermore, this approach requires optimization of the [<sup>18</sup>F]fluoride elution protocol for each radiotracer because the type and amount of phase transfer catalyst (PTC) and base needed for efficient elution can impact the subsequent

radiotracer synthesis. Moreover, reductions in RCY were observed at higher activity levels, potentially attributable to radiolysis and/or other factors (98).

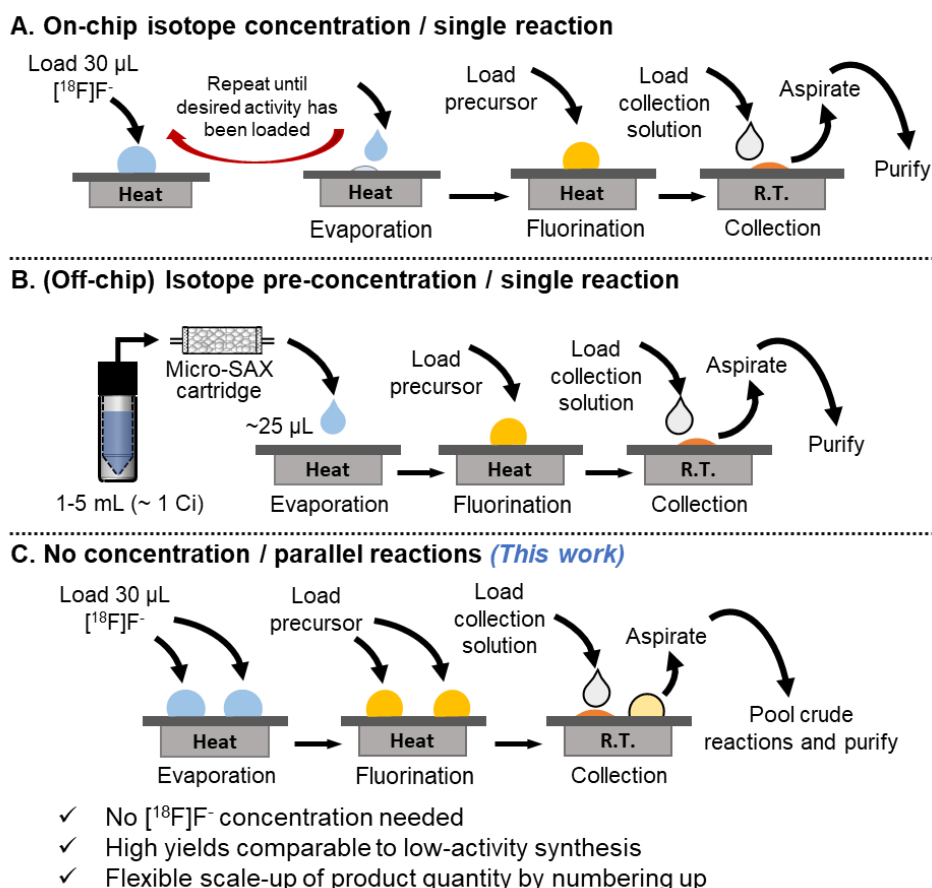


**Figure 7-1 Approaches for scale-up of radiopharmaceutical product amount in droplet-based radiosynthesis.**

(A) Starting activity for a single droplet reaction is increased by repeated loading and evaporation of  $[^{18}\text{F}]\text{fluoride}$  aliquots on the droplet reaction chip prior to the fluorination reaction. (B)  $[^{18}\text{F}]\text{fluoride}$  is pre-concentrated using a miniature cartridge into a final volume that is compatible with a single reaction site. (C) Multiple reaction sites are loaded with 20-30  $\mu\text{L}$  of (unconcentrated)  $[^{18}\text{F}]\text{fluoride}$  and multiple droplet reactions are conducted in parallel. The crude reaction products are pooled prior to purification to increase the total product activity.

To address these challenges, we developed an alternative scale-up method based on the concept of “numbering up”, in which multiple droplet reactions are conducted in parallel and pooled together to increase the product quantity (**Figure 7-1C**). This novel approach is faster than the other approaches because it eliminates the need to process the  $[^{18}\text{F}]\text{fluoride}$  ahead of the reactions, and because each individual reaction is performed at smaller scale, issues due to

radiolysis or impurities in the radioisotope source are eliminated. Numbering up provides a rapid path to scale-up, minimizing the effort and cost spend to transition from optimization of droplet-based reactions (at low activity scales) to larger scale production. We demonstrate that this approach can be used to conduct production of [<sup>18</sup>F]FBnTP at clinically-relevant levels in a rapid and high-yield manner.

## 7.2 Methods

### 7.2.1 Materials

Cesium carbonate (Cs<sub>2</sub>CO<sub>3</sub>, 99%), potassium carbonate (K<sub>2</sub>CO<sub>3</sub>, >99%), potassium trifluoromethanesulfonate (KOTf, 98%), anhydrous pyridine (Py, 99.8%), anhydrous methanol (MeOH, 99.8%), dichloromethane (DCM, >99.8%), anhydrous *N,N*-dimethylformamide (DMF, 99.8%), 1,3-dimethyl-2-imidazolidinone (DMI, >99.5%), trifluoroacetic acid (TFA, 99%), copper(II) trifluoromethanesulfonate (Cu(OTf)<sub>2</sub>, 98%), and tetrakis(pyridine)copper(II) triflate (Cu(OTf)<sub>2</sub>(Py)<sub>4</sub>, 95%) were purchased from Sigma-Aldrich (St. Louis, MO, USA). Tetraethylammonium trifluoromethanesulfonate (TEAOTf, >99%) was purchased from TCI America (Portland, Oregon, USA). Precursor and reference standard were prepared as described previously (290). Deionized (DI) water was obtained from a Milli-Q water purification system (EMD Millipore Corporation, Berlin, Germany). Reagent and collection vials (0.5 mL, PCR clean) were purchased from Eppendorf (Hamburg, Germany). Acetonitrile for high performance liquid chromatography (HPLC) was purchased from Fisher Scientific (Pittsburgh, PA, USA). C18 Plus Short cartridges (WAT020515) were purchased from Waters Corporation (Milford, MA, USA). 50 mL polypropylene centrifuge tubes were purchased from Corning Inc. (430304, Corning, NY, USA). [<sup>18</sup>F]Fluoride in [<sup>18</sup>O]H<sub>2</sub>O was obtained from the UCLA Crump Cyclotron and Radiochemistry Center.

### 7.2.2 Droplet-based [<sup>18</sup>F]FBnTP synthesis

Droplet-based reactions were conducted on Teflon-coated silicon chips, featuring 2x2 or 3x3 arrays of arrays of circular (4 mm diameter) hydrophilic reaction sites (**Figure 7-4**). These chips were operated on a temperature-controlled heating platform, as previously described (160). The general synthesis process (**Figure 7-1C**) involved the following steps: First, 10-47  $\mu\text{L}$  of a [<sup>18</sup>F]fluoride stock solution containing 25-1510 MBq of activity mixed with a desired amount of phase-transfer catalyst (PTC) and base, was added via micropipette onto a reaction site of the chip. The droplet was then dried at 105°C for 1-2 min. Next, 10  $\mu\text{L}$  of a precursor/ $\text{Cu}(\text{OTf})_2(\text{py})_4$  stock solution was added and heated at 110°C for 5 min to facilitate fluorination. After completion of the reaction, the crude product was extracted from the reaction site by adding a collection solution (20  $\mu\text{L}$ ) and transferring it to a 0.5 mL Eppendorf tube for further analysis. To ensure minimal activity residue on the chip, the collection step was repeated a total of 4 times.

Several stock solutions were prepared just prior to each set of experiments. The stock solution of PTC and base was prepared in DI water, with a 5  $\mu\text{L}$  aliquot containing 0.3  $\mu\text{mol}$  of TEAOTf and 0.01  $\mu\text{mol}$  of  $\text{Cs}_2\text{CO}_3$  for a single droplet reaction unless otherwise indicated. [<sup>18</sup>F]Fluoride stock solution was prepared by mixing a desired volume (5-42  $\mu\text{L}$ ) of [<sup>18</sup>F]fluoride/[<sup>18</sup>O]H<sub>2</sub>O (containing 25.3-1510 MBq of activity) with a 5  $\mu\text{L}$  aliquot of PTC/base stock solution. Individual stock solutions of the precursor (with varied concentration based on precursor amount studies) and  $\text{Cu}(\text{OTf})_2(\text{Py})_4$  (136 mM) were prepared in the desired reaction solvent mixture, and then these stock solutions were mixed in a 1:1 (v/v) ratio just before synthesis, such that each 10  $\mu\text{L}$  portion of the mixed solution contained the desired amount of precursor and 0.68  $\mu\text{mol}$  of  $\text{Cu}(\text{OTf})_2(\text{Py})_4$ . The collection solution was prepared by mixing MeCN and DI water (35:65, v/v) with 0.1% TFA (v/v), matching the mobile phase used for HPLC purification.

When performing scaled-up synthesis, the single droplet process was repeated at multiple reaction sites on the same chip. For these reactions, the crude product was collected with smaller

aliquots of collection solution (i.e. 10  $\mu\text{L}$  x 4 instead of 20  $\mu\text{L}$  x 4). For example, when performing two reactions in parallel, the total volume of the pooled crude products was  $\sim 80$   $\mu\text{L}$ .

### 7.2.3 Analytical methods

Radioactivity measurements were performed using a calibrated dose calibrator (CRC-25R, Capintec, Florham Park, NJ, USA). To assess fluorination conversion, we employed multi-lane radio-thin layer chromatography (radio-TLC) methods (96). Briefly, 0.5  $\mu\text{L}$  of samples were spotted on TLC plates (6 cm x 5 cm pieces cut from 20 cm x 5 cm sheets, silica gel 60 F<sub>254</sub>, Merck KGaA, Darmstadt, Germany). These plates were then developed for 4 cm using a mobile phase of DCM and MeOH (9:2, v/v), dried, and then covered with a glass microscope slide (75x50x1 mm<sup>3</sup>, Fisher Scientific, Hampton, NH, USA) for readout via Cerenkov luminescence imaging (CLI) with a 5 min exposure time. The fluorination conversion of each sample (lane) was determined via region of interest (ROI) analysis as previously described (96). The collection efficiency was obtained by dividing the activity of the product mixture collected from the microdroplet reactor by the starting activity (corrected for decay). The crude RCY was computed as fluorination conversion multiplied by the collection efficiency. To determine RCY, radio-HPLC purification was performed using an analytical column (ZORBAX RP Eclipse Plus C18, 100 x 4.6 mm, 3.5  $\mu\text{m}$ , Agilent Technologies, Santa Clara, CA, USA) using an isocratic mobile phase of DI water and MeCN (65:35, v/v) with 0.1% TFA (v/v) at a flow rate of 1.2 mL/min. For some experiments, purification was performed on a semi-prep column (C18 Gemini-NX, 250 x 10 mm, 5  $\mu\text{m}$ , Phenomenex, Torrance, CA, USA) using isocratic mobile phase of DI water and MeCN (60:40, v/v) with 0.1% TFA (v/v) at a flow rate of 5 mL/min. This was followed by formulation via a C18 plus short cartridge (preconditioned with 3 mL of EtOH and then 20 mL of DI water). The radio-HPLC system (Smartline, Knauer, Berlin, Germany) was equipped with a degasser (Model 5050), pump (Model 1000), UV detector (254 nm; Eckert & Ziegler, Berlin, Germany), and a gamma-radiation detector and counter (BFC-4100 and BFC-1000, Bioscan, Inc., Poway, CA, USA). To

confirm the radiochemical purity (RCP), we analyzed the formulated [ $^{18}\text{F}$ ]FBnTP on the same analytical radio-HPLC system using a mobile phase of DI water and MeCN (60:40, v/v) with 0.1% TFA (v/v) at a flow rate of 1.2 mL/min. Co-injection of the formulated [ $^{18}\text{F}$ ]FBnTP with reference standard was performed to validate product identity.

## 7.3 Results and discussion

### 7.3.1 Preliminary development of droplet-based synthesis conditions

To enable high-throughput exploration of reactions on 4 mm diameter reaction sites, we developed a new chip with a 3x3 array of reaction sites (**Figure 7-4**). As a starting point for the droplet-based synthesis of [ $^{18}\text{F}$ ]FBnTP, we conducted experiments using four sets of conditions. First, we scaled down the macroscale synthesis method described by Zhang et al. (290) from 850  $\mu\text{L}$  to 10  $\mu\text{L}$ , reducing reagents by  $\sim 27\times$  (**Condition 1**). Second and third, we employed our previously reported droplet-based conditions for the Cu-mediated synthesis of [ $^{18}\text{F}$ ]FDOPA (291) but substituted the [ $^{18}\text{F}$ ]FBnTP precursor (**Conditions 2, 3**). For **Condition 2**, the precursor amount (0.15  $\mu\text{mol}$ ) was set to match **Condition 1**. For **Condition 3**, the precursor amount (0.45  $\mu\text{mol}$ ) matched our prior work with [ $^{18}\text{F}$ ]FDOPA (291). Additionally, we used our previous preliminary droplet conditions for [ $^{18}\text{F}$ ]FBnTP, but performed reactions on 4 mm reaction sites instead of 3 mm sites (208) (**Condition 4**). Comprehensive details of reaction conditions and summary of performance can be found in **Table 7-2**.

Surprisingly, our attempts to produce [ $^{18}\text{F}$ ]FBnTP using **Condition 1** did not yield any product ( $n = 3$ ). This could potentially be attributed to the fast degradation of  $\text{Cu}(\text{OTf})_2$  due to exposure to atmosphere in the open droplet reaction format, or low effectiveness of  $\text{Cu}(\text{OTf})_2$  to promote the fluorination in a droplet reaction. In our previous report (136), the preparation of [ $^{18}\text{F}$ ]YH149 via a similar Cu-mediated route but using the copper reagent  $\text{Cu}(\text{Py})_4(\text{OTf})_2$  resulted in a fluorination conversion of 0% ( $n = 2$ ) in the absence of pyridine. Interestingly, in the current study, the synthesis of [ $^{18}\text{F}$ ]FBnTP using the copper reagent  $\text{Cu}(\text{OTf})_2$  even with the addition of

pyridine led to a similar outcome (no conversion). This observation might suggest that  $\text{Cu}(\text{Py})_4(\text{OTf})_2$  and pyridine could be a critical pair of reagents necessary for forming the radiofluorinated product.

After switching the PTC/base to  $\text{Cu}(\text{Py})_4(\text{OTf})_2/\text{Cs}_2\text{CO}_3$  (**Condition 2**), we observed a small amount of product formation, but with a poor crude RCY of only  $8 \pm 0\%$  ( $n = 3$ ), due to both low fluorination conversion ( $25 \pm 1\%$ ,  $n = 3$ ) and low collection efficiency ( $32 \pm 1\%$ ,  $n = 3$ ). Increasing the precursor amount from 0.15 to 0.45  $\mu\text{mol}$  (i.e. **Condition 3**) resulted in a significant improvement in fluorination conversion ( $53 \pm 8\%$ ,  $n = 3$ ), but the collection efficiency remained low ( $33 \pm 1\%$ ,  $n = 3$ ), resulting in only a moderate improvement in crude RCY ( $17 \pm 3\%$ ,  $n = 3$ ).

In contrast, when taking conditions from our previous high-throughput optimization study (**Condition 4**), but performing the reaction on a 4 mm reaction site, the performance was significantly improved, with high fluorination conversion ( $92 \pm 1\%$ ,  $n = 3$ ) and collection efficiency ( $90 \pm 1\%$ ,  $n = 3$ ), corresponding to a high crude RCY of  $83 \pm 2\%$  ( $n = 3$ ), similar to the performance observed when using 3 mm diameter reaction sizes previously (**Table 7-3**).

### 7.3.2 Influence of precursor amount

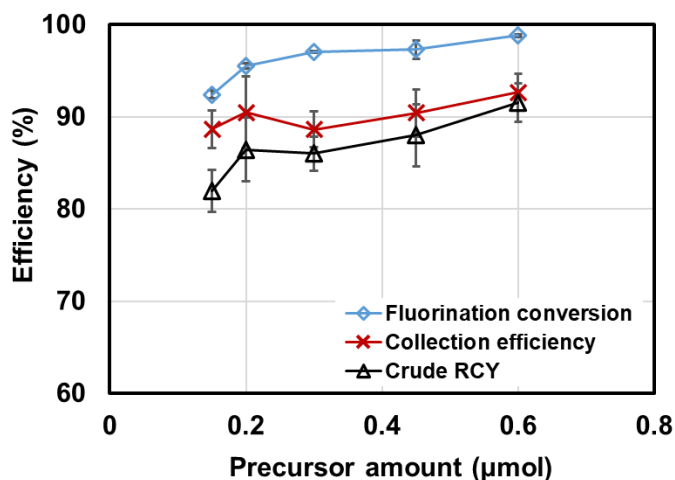
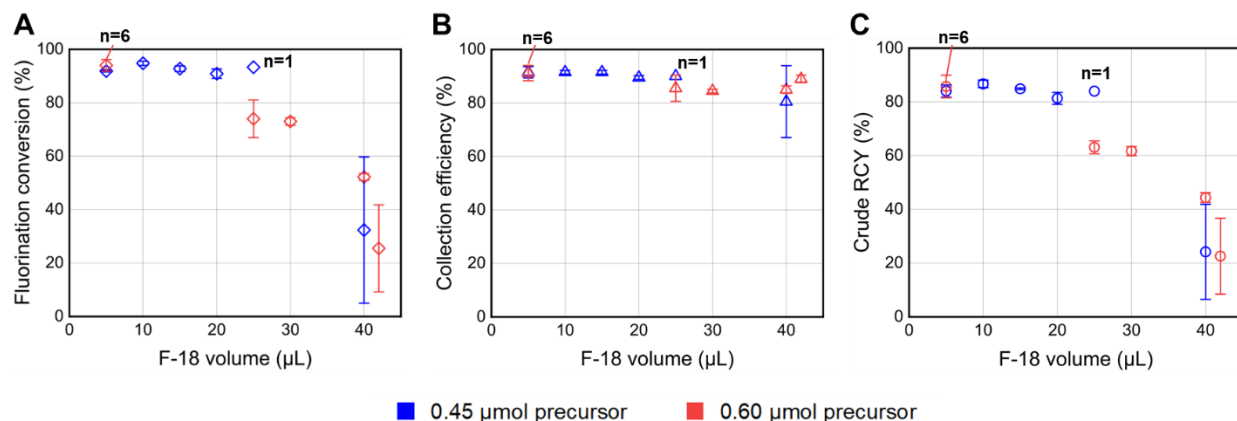


Figure 7-2 Influence of precursor amount on the performance of the droplet radiosynthesis of  $^{18}\text{F}$ FBnTP. Each experiment was repeated  $n = 3$  times.

According to the initial experiments with **Condition 2** and **3**, the precursor amount showed a significant effect on the synthesis performance of [ $^{18}\text{F}$ ]FBnTP. Therefore, we performed further optimization to investigate the influence of the precursor amount. Details of measurements and calculations can be found in **Table 7-4** and results are summarized in **Figure 7-2**. Excellent performance was achieved even with a small amount of precursor (even at the lowest amount tested, i.e., 0.15  $\mu\text{mol}$ ). We observed that an increased amount of precursor led to a slight increase in fluorination conversion and no significant change in collection efficiency, and thus a slight increase in crude RCY. The highest performance was observed for 0.45 and 0.60  $\mu\text{mol}$  of precursor, giving crude RCY of  $88 \pm 3\%$  ( $n = 3$ ) and  $92 \pm 2\%$  ( $n = 3$ ), respectively, and these amounts were used in further studies.

### 7.3.3 Influence of volume (and activity) of [ $^{18}\text{F}$ ]fluoride

In our previous report on scaling up the droplet synthesis of [ $^{18}\text{F}$ ]FET and [ $^{18}\text{F}$ ]FBB (97), we observed a reduction in the performance of droplet reactions when higher starting activity was used. The decrease was attributed to multiple potential factors, but the cause was not conclusively identified.



**Figure 7-3 Droplet synthesis performance of [ $^{18}\text{F}$ ]FBnTP as a function of [ $^{18}\text{F}$ ]fluoride volume ( $\mu\text{L}$ ) loaded.**

Impact on (A) fluorination conversion, (B) collection efficiency, and (C) crude RCY are shown. (Each conditions was repeated  $n = 2$  times unless otherwise indicated).



In the present work, we first explored the possibility of scaling up the synthesis of [<sup>18</sup>F]FBnTP by loading larger amounts of [<sup>18</sup>F]fluoride. To eliminate the potential impact of radiolysis, we first performed a study where the volume of [<sup>18</sup>F]fluoride used for a reaction was varied (5 to 40 μL), but activity level were kept low (11.7 to 69.6 MBq) where there is no impact of radiolysis. To maintain a relatively low activity level for higher volumes, the activity was allowed to decay for different amounts of time prior to use. This study was performed using 0.45 μmol of precursor. Detailed measurements and calculations are tabulated in **Table 7-5** and the performance is summarized in **Figure 7-3** (with blue markers). When using 5-25 μL of aqueous [<sup>18</sup>F]fluoride, we achieved high fluorination conversion and collection efficiency with excellent consistency, resulting in similar crude RCY among these conditions (fluorination conversion of 91-95%, collection efficiency of 90-92%, and crude RCY of 81-87 %; n = 9). However, when increasing the isotope volume to 40 μL, we observed a significant drop and lower consistency of fluorination conversion ( $32 \pm 27\%$ , n = 2), collection efficiency ( $81 \pm 13\%$ , n = 2), and corresponding crude RCY ( $24 \pm 18\%$ , n = 2). Since we can rule out radiolysis, these results suggest that increased amount of impurities from the isotope solution could be responsible for the reduced performance.

We performed a small study of precursor quantity during experiments involving a higher volume of [<sup>18</sup>F]fluoride (i.e., 40 μL) to assess whether performance could be improved using increased amounts of precursor (i.e., 0.45-1.05 μmol). Detailed measurements and calculations are tabulated in **Table 7-6**. Increasing the precursor quantity from 0.45 to 0.6 μmol did not restore the high performance, but significantly increased the crude RCY (from  $24 \pm 18\%$  (n = 2) to  $44 \pm 2\%$  (n = 2)). Subsequent increments did not exhibit significant changes in synthesis performance, and therefore we selected 0.6 μmol as the precursor amount for later scale-up synthesis.

Next, we performed additional tests where the activity level (25-1510 MBq) of the initial [<sup>18</sup>F]fluoride was varied over nearly 2 orders of magnitude. For practical reasons, it was not

possible to maintain a consistent volume of [ $^{18}\text{F}$ ]fluoride, which varied from 5-42  $\mu\text{L}$  in these studies. Detailed measurements and calculations can be found in **Table 7-7** and the performance is summarized in **Figure 7-3** (with red markers). These data exhibited a similar trend as the prior isotope volume study. Regardless of activity level, volumes up to 20  $\mu\text{L}$  exhibited high performance (crude RCY 80-90%), volumes of 25 and 30  $\mu\text{L}$  exhibited moderate performance (crude RCY 60-80%) and higher volumes gave much lower and variable crude RCY.

Since the product yield drops significantly if using >30  $\mu\text{L}$  of [ $^{18}\text{F}$ ]fluoride, we used this as a maximum volume of isotope to load in each reaction site, and to perform further scale-up we performed multiple syntheses in parallel (numbering up).

### 7.3.4 Synthesis scale-up

Assuming a [ $^{18}\text{F}$ ]fluoride concentration of  $\sim 30$  MBq/ $\mu\text{L}$ , each 30  $\mu\text{L}$  portion of fluoride contains  $\sim 900$  MBq. Thus, given an estimated crude RCY ( $\sim 60\%$ ) and estimated synthesis time of  $\sim 40$  min, we estimated that combining two droplet reactions would be sufficient to prepare a batch ( $>740$  MBq) sufficient for two or more clinical doses (estimated to be 92.5-315.5 MBq each, based on doses used for [ $^{18}\text{F}$ ]Flurpiridaz (293)), or one dose, if significant transport is required prior to use. The results are summarized in **Table 7-1**. This study, where two reactions with combined starting activity of 1.6-2.1 GBq, resulted in RCY of  $54 \pm 6\%$  ( $n = 3$ ), activity yield of  $43 \pm 5\%$  ( $n = 3$ ) and radiochemical purity (RCP) of 100% (**Figure 7-5,6,7,8**). A comparison with the results from a 30  $\mu\text{L}$  reaction in a previous optimization study within this work (i.e., crude RCY of  $62 \pm 2\%$  ( $n = 2$ )), exhibited a slightly lower RCY than in the scaled-up synthesis. This discrepancy can likely be attributed to minor activity loss during HPLC purification and the product formulation process. With this scale-up strategy, we successfully provided a clinically-relevant dose of [ $^{18}\text{F}$ ]FBnTP (0.76-0.80 GBq,  $n = 3$ ) with excellent molar activity of 665-877 GBq/ $\mu\text{mol}$  at the end of synthesis. Since all reactions ran in parallel, the preparation time remained similar to performing a single droplet reaction, the only difference being that additional time is required for the collection step (since multiple droplets need to be sequentially collected). The total synthesis time was 37

$\pm 1$  min. Note that this synthesis time is shorter than reported in our prior high-throughput optimization study ( $42 \pm 1$  min) (208), due to using a different mobile phase for radio-HPLC purification with a slightly higher proportion of MeCN which shortened the retention time (14.0 vs. 15.3 min), and reducing the amount of dilution of purified product (15 vs 20 mL) which shortened the formulation process (10 min vs 13 min).

Noting that the use of 20  $\mu$ L aliquots of [ $^{18}$ F]fluoride performed better than 30  $\mu$ L in our isotope volume study, we performed an additional set of experiments, in which we performed pooling of four droplet reactions, each starting with 20  $\mu$ L of activity (**Table 7-1**). For purification, we used a semi-prep column instead of analytical to ensure that the mass and volume of injection material did not exceed the column capacity (**Figure 7-9**). Starting with 0.9-2.7 GBq, the resulting performance exhibited slightly higher RCY ( $64 \pm 2\%$ ,  $n = 2$ ) and activity yield ( $48 \pm 2\%$ ,  $n = 2$ ) than the 30  $\mu$ L study, while maintaining high RCP ( $\sim 100\%$ ) and molar activity (339 GBq/ $\mu$ mol for the synthesis starting with 2.7 GBq of activity) (**Figure 7-10,11**). Following purification and formulation, up to 1.26 GBq of [ $^{18}$ F]FBnTP was produced. Due to the use of the semi-prep column, the HPLC purified fraction had larger volume, and required more dilution for formulation, than the two-droplet experiments, increasing the formulation time (from 10 min to 19 min), and thus extending the overall synthesis time by  $\sim 9$  min.

**Table 7-1 Comparison of [<sup>18</sup>F]FBnTP synthesis performance under microscale and macroscale conditions. Where applicable, values are given as averages ± standard deviations for the indicated number of replicates.**

Conditions	<i>This work</i> (2 droplets)	<i>This work</i> (4 droplets)	Ravert et al. 2004 (283)	Ravert et al. 2014 (288)	Tominaga et al. 2016 (294)	Zhang et al. 2016 (290) <sup>e</sup>	Waldmann et al. 2018(289)	Jones et al. 2023(208)
<b>METHOD</b>								
Radiosynt hesis platform	Droplet- based synthesizer	Droplet-based synthesizer	5 mL v-vial	5 mL v-vial in a microwave cavity	Glass vial	Glass vial	ELIXYS FLEX/CHEM	Droplet- based synthesizer
Manual or automated?	Manual	Manual	Manual	Remote control	Manual	Manual	Automated	Manual
Synthesis steps	1	1	4	4	3	1	4	1
Synthesis route	Cu-mediated fluorination	Cu-mediated fluorination	1) Fluorination 2) Reduction 3) Bromination 4) Alkylation	1) Fluorination 2) Reduction 3) Bromination 4) Alkylation	1) Fluorination 2) Reduction 3) Alkylation	Cu-mediated fluorination	1) Fluorination 2) Reduction 3) Bromination 4) Alkylation	Cu- mediated fluorination
Precursor consumed (μmol)	0.6 × 2	0.6 × 4	20	12.8	42.9	4	14.3	0.45
Major reagent(s) consumed (μmol)	Cu(Py) <sub>4</sub> (OTf) <sub>2</sub> (0.68 × 2)	Cu(Py) <sub>4</sub> (OTf) <sub>2</sub> (0.68 × 4)	1) N(Me) <sub>3</sub> Bz•OTf (20), K <sub>2</sub> CO <sub>3</sub> (20), K <sub>222</sub> (30) 2) NaBH <sub>4</sub> (7930) 3) PBr <sub>2</sub> Ph <sub>3</sub> (200) 4) PPh <sub>3</sub> (80)	1) N(Me) <sub>3</sub> Bz•OTf (12.8), K <sub>2</sub> CO <sub>3</sub> (82.6), K <sub>222</sub> (111) 2) NaBH <sub>4</sub> (31.7) 3) HBr (48% aq; 0.8 mL) 4) PPh <sub>3</sub> (11.4)	1) N(Me) <sub>3</sub> Bz•OTf (42.9), K <sub>2</sub> CO <sub>3</sub> (N.R.), K <sub>222</sub> (37) 2) NaBH <sub>4</sub> (529.) 3) PPh <sub>3</sub> •HBr (367)	Cu(OTf) <sub>2</sub> (20)	1) N(Me) <sub>3</sub> Bz•OTf (14.3), K <sub>2</sub> CO <sub>3</sub> (7), K <sub>222</sub> (27) 2) NaBH <sub>4</sub> •(Al <sub>2</sub> O <sub>3</sub> ) <sub>x</sub> (10 wt.%, 350 mg) 3) PBr <sub>2</sub> Ph <sub>3</sub> (200) 4) PPh <sub>3</sub> (11.4)	Cu(Py) <sub>4</sub> (OTf) <sub>2</sub> (0.68)
Solvent volume (μL)	10 × 2	10 × 4	200-3000	400-1400	600-6000	850	800-4100	10
<b>PERFORMANCE</b>								
Number of repeats (n)	3	2	20	27	5	2	3	3
Starting activity (GBq)	1.6-2.1	0.9-2.7	N.R.	N.R.	3.7-5.6	N.R.	9.4-12.0	0.12
Radiochemi cal yield (RCY, %) <sup>a</sup>	54 ± 6	64 ± 2	10 <sup>d</sup>	11.5 ± 3.3 <sup>d</sup>	12-14	N.R.	28.6 ± 5.1	66 ± 6
Radiochemi cal purity (RCP, %) <sup>b</sup>	100	99.5	>99	>99	>99	>97	>99	100
Activity yield (GBq)	0.76-0.80	0.38-1.26	N.R.	N.R.	N.R.	N.R.	1.4-2.2	0.056-0.063
Activity yield (%)	43 ± 5	48 ± 2	6	8.3 ± 2.4	N.R.	N.R.	14.9-18.3 <sup>d</sup>	49 ± 3
Molar activity (GBq/μmol) at EOS	665-877	339 <sup>c</sup>	16.7	534.5 ± 371.4	N.R.	N.R.	80-99	N.R.
Total synthesis time (min)	37 ± 1	47 ± 1	82	52.4±14	N.R.	N.R.	90-92	42 ± 1

<sup>a</sup>RCY includes purification and formulation. <sup>b</sup>RCP was determined by radio-HPLC. <sup>c</sup>The molar activity was calculated from the synthesis starting with 2.7 GBq of activity. <sup>d</sup>These values were calculated based on other information in the literature report. <sup>e</sup>Overall performance was not reported, but radiochemical conversion of product was 62 ± 1.4 (n = 2), determined by radio-HPLC using an aliquot of diluted crude product. N.R. = Not reported. EOS = End of synthesis. K<sub>222</sub> = 4,7,13,16,21,24-hexaoxa-1,10-diazabicyclo[8.8.8]hexa-cosane.

### 7.3.5 Comparison of droplet and conventional methods

In comparison to the previously reported macroscale conditions by Zhang *et al.* (290), this scaled-up droplet synthesis through the same Cu-mediated route offered significant advantages. The droplet format reduced the reaction volume from 850  $\mu\text{L}$  to 10  $\mu\text{L}$ , allowing for higher reagent concentration while consuming much less reagents (i.e., 2-3x less precursor and 7-14x less copper reagent, depending whether 2 or 4 droplets are pooled). Moreover, our droplet synthesis achieved superior radiochemical purity of 100% (vs. 97% in (290)). In addition, the radio-HPLC chromatogram of the crude [ $^{18}\text{F}$ ]FBnTP injection displayed excellent separation resolution on both analytical and semi-prep columns (**Figure 7-5** and **Figure 7-9**). Only two major radio-peaks, corresponding to unreacted [ $^{18}\text{F}$ ]fluoride and [ $^{18}\text{F}$ ]FBnTP, were observed in the HPLC chromatogram from the droplet reaction (**Figure 7-5** and **Figure 7-9**), whereas multiple peaks were seen in the initial macroscale reactions (290). This suggests that the microscale synthesis had fewer side reactions which may give opportunities for further optimization and shortening of the purification process. Though the numbering up method required more precursor consumption compared to the single-reaction paired with concentration method (**Figure 7-1A,B**), the quantity is still lower than that for macroscale approach (1.2-2.4  $\mu\text{mol}$  for 2-4 droplet reactions vs. 4  $\mu\text{mol}$  for the macroscale reaction).

In comparison to other macroscale conditions involving multiple reaction steps, the one-step radiosynthesis approach significantly simplifies the preparation of [ $^{18}\text{F}$ ]FBnTP, shortens the synthesis time and purification, and eliminates the need for handling corrosive reagents, making it more practical for both preclinical and clinical studies. Moreover, the droplet scale-up method dramatically reduced precursor consumption by 2-35x while providing 2-6x higher RCY (compared to reported data by Ravert *et al.* (283,288), by Tominage *et al.* (294) and Waldmann *et al.* (289)) and 3-8x higher activity yield (compared to reported values by Ravert *et al.* 2014 (288) and Waldmann *et al.* (289)). Even with 3-4x lower starting activity compared to Waldmann *et al.*'s

method (2.7 GBq in this work vs. 9.4-12.0 GBq in (289)), the droplet scale-up technique achieves comparable quantity of [<sup>18</sup>F]FBnTP (1.26 GBq from 4 droplet reactions vs. 1.4-2.2 GBq (289)), and over 4-8x higher molar activity. This enables efficient production of small tracer batches through Cu-mediated radiofluorination, especially suitable for preclinical imaging scenarios where high molar activity is needed. Additionally, the total preparation time is 5-55 min shorter than all reported macroscale approaches.

Building on the successful flexible scale-up of radiotracer product amount by parallel droplet reactions presented in this study, further investigations could explore the feasibility of combining more droplet reactions to provide multiple patient doses in an automated format.

## 7.4 Conclusions

In this work, we successfully developed a droplet-based one-step Cu-mediated fluorination synthesis for [<sup>18</sup>F]FBnTP using a pinacolyl arylboronate precursor. After performing optimization of droplet reactions at low activity scale using high-throughput techniques, a short study enabled determination of the maximum practical volume of [<sup>18</sup>F]fluoride per reaction (i.e. that did adversely impact performance). Subsequently, within this constraint, the synthesis was scaled by performing multiple reactions in parallel to achieve the desired amount of product. The resulting radiochemical yield after purification and formulation was high for both a two-reaction approach (30  $\mu$ L per reaction; RCY =  $54 \pm 6\%$ ,  $n = 3$ ) and four-reaction approaches (20  $\mu$ L per reaction; RCY =  $64 \pm 2\%$ ,  $n = 2$ ), with excellent radiochemical purity (100%) and high molar activity (339-877 GBq/ $\mu$ mol). Sufficient product for multiple clinical doses, 0.76-1.26 GBq, was efficiently achieved from 1.6 to 2.7 GBq of [<sup>18</sup>F]fluoride in a synthesis time of just 37-47 min. The simplicity and speed of this synthesis method, along with improved yield and reduced precursor amount, will greatly facilitate further preclinical and clinical evaluation of [<sup>18</sup>F]FBnTP for MPI or other applications, like lung cancer studies (295,296). Moreover, this efficient droplet-based scale-up technique can readily be applied to prepare other radiotracers on demand, enabling quick and

cost-effective production of various radiotracers for diverse applications. This work represents the first successful trial of scaling up the synthesis in a droplet microreactor by the numbering up technique. Automation of this approach is ongoing and provides a promising route to reliably supply multiple patient doses per batch using droplet radiochemistry methods.

## 7.5 Appendix

### 7.5.1 Microdroplet reaction chips

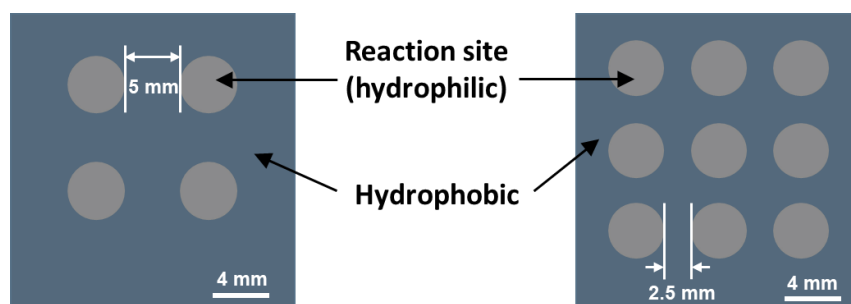


**Figure 7-4 2x2 and 3x3 multi-reaction chips for high-throughput synthesis optimization and for increasing synthesis scale by pooling the crude products of parallel reactions (“numbering up”).**

### 7.5.2 Preliminary experiments

**Table 7-2 Preliminary attempts at droplet radiosynthesis of [<sup>18</sup>F]FBnTP via the Cu-mediated route by adapting literature protocols.**

**Condition 1** was adapted from the macroscale conditions reported by Zhang *et al.* (297) (i.e. KOTf (1.33 μmol), K<sub>2</sub>CO<sub>3</sub> (1.81 nmol), Cu(OTf)<sub>2</sub> (20 μmol), precursor (4 μmol) in 850 μL of DMF at 110 °C for 20 min). The microscale reaction was performed by scaling down from 850 μL to 10 μL and keep the same reagent ratios, but with increased concentration (~3x). **Conditions 2 and 3** are based on a previously reported droplet-based radiosynthesis of [<sup>18</sup>F]FDOPA (291) (fluorination reaction) but with [<sup>18</sup>F]FBnTP precursor instead, and two different amounts of precursor. **Condition 4** is the preliminary droplet condition for [<sup>18</sup>F]FBnTP synthesis reported in our recent paper (208). All reactions were performed at 110 °C for 5 min.

Condition	1	2	3	4
Reference	(297)	(291)	(291)	(208)
PTC and base composition (nmol)	KOTf (50) K <sub>2</sub> CO <sub>3</sub> (0.0675)	TEAOTf (300) Cs <sub>2</sub> CO <sub>3</sub> (10)	TEAOTf (300) Cs <sub>2</sub> CO <sub>3</sub> (10)	TEAOTf (300) Cs <sub>2</sub> CO <sub>3</sub> (10)
Precursor (μmol)	0.15	0.15	0.45	0.45
Copper reagent (μmol)	Cu(OTf) <sub>2</sub> (0.75)	Cu(Py) <sub>4</sub> (OTf) <sub>2</sub> (0.68)	Cu(Py) <sub>4</sub> (OTf) <sub>2</sub> (0.68)	Cu(Py) <sub>4</sub> (OTf) <sub>2</sub> (0.68)
Solvent composition (10 μL reaction)	DMF/Py (96:4, v/v)	DMF/Py (96:4, v/v)	DMF/Py (96:4, v/v)	DMI/Py (96:4, v/v)
<b>Performance (n = 3)</b>				
Starting activity (MBq)	262 ± 4	262 ± 4	262 ± 4	262 ± 4
Collection efficiency (%)	80 ± 4	32 ± 1	33 ± 1	90 ± 1
Residual on pipette tip (%)	1 ± 0	1 ± 1	0.3 ± 0.2	0.4 ± 0.2
Fluorination conversion (%)	0	25 ± 1	53 ± 8	92 ± 1
Crude RCY (%)	0	8 ± 0	17 ± 3	83 ± 2

### 7.5.3 Influence of reaction site diameter

**Table 7-3 Comparison of the reaction performance on chips with 4 mm reaction sites (this work) vs 3 mm reaction sites.**

	Reaction site diameter (mm)	Number of replicates (n)	Fluorination conversion (%)	Collection efficiency (%)	Crude RCY (%)
This work <sup>a</sup>	4	3	92 ± 1	90 ± 1	83 ± 2
Previous work <sup>a</sup>	3	4	89 ± 1	97 ± 2	86 ± 2

<sup>a</sup>All reactions were performed as follows. 5 μL of [<sup>18</sup>F]F<sup>-</sup> and 5 μL of TEAOTf (0.3 μmol)/Cs<sub>2</sub>CO<sub>3</sub> (0.01 μmol) were dispensed on the reaction site and dried at 105 °C for 1 min. The precursor (0.45 μmol) and Cu(OTf)<sub>2</sub>(Py)<sub>4</sub> (0.68 μmol) in 10 μL of DMI/pyridine (96:4, v/v) were then added and reacted at 110 °C for 5 min.



### 7.5.4 Influence of amount of precursor

**Table 7-4 Summary of data acquired when exploring the impact of precursor amount for preparing [<sup>18</sup>F]FBnTP. Each condition was repeated n = 3 times.**

Precursor amount (μmol) <sup>a</sup>	Fluorination conversion (%)	Collection efficiency (%)	Crude RCY (%)
0.15	92 ± 0	89 ± 2	82 ± 2
0.20	96 ± 0	90 ± 4	86 ± 3
0.30	97 ± 0	89 ± 2	86 ± 2
0.45	97 ± 1	90 ± 3	88 ± 3
0.60	99 ± 0	93 ± 2	92 ± 2

<sup>a</sup>All reactions were performed as follows. 5 μL of [<sup>18</sup>F]F<sup>-</sup> and 5 μL of TEAOTf (0.3 μmol)/Cs<sub>2</sub>CO<sub>3</sub> (0.01 μmol) were dispensed on the reaction site and dried at 105 °C for 1 min. The precursor (amounts indicated) and Cu(OTf)<sub>2</sub>(Py)<sub>4</sub> (0.68 μmol) in 10 μL of DMI/pyridine (96:4, v/v) were then added and reacted at 110 °C for 5 min.

### 7.5.5 Influence of starting activity and volume of [<sup>18</sup>F]fluoride

**Table 7-5 Summary of data acquired when exploring the impact of [<sup>18</sup>F]fluoride volume or starting activity when preparing [<sup>18</sup>F]FBnTP. Precursor amount for these studies was 0.45 μmol. All experiments were performed at relatively low activity (11.7-69.6 MBq).**

[ <sup>18</sup> F]fluoride volume (μL)	Number of replicates (n)	Starting activity (MBq)	Fluorination conversion (%)	Collection efficiency (%)	Crude RCY (%)
5	2	11.9 ± 0.3	92 ± 0	92 ± 2	84 ± 2
10	2	23.6 ± 0.4	95 ± 1	92 ± 1	87 ± 1
15	2	34.6 ± 0.3	93 ± 1	92 ± 1	85 ± 0
20	2	45.7 ± 0.8	91 ± 2	90 ± 1	81 ± 2
25	1	56.2	93	90	84
40	2	68.0 ± 2.3	32 ± 27	81 ± 13	24 ± 18

**Table 7-6 Summary of data acquired when exploring the impact of precursor amount in conjunction with higher volume of [<sup>18</sup>F]fluoride (40 μL) when preparing [<sup>18</sup>F]FBnTP. All experiments were performed at relatively low activity (58.2-69.6 MBq). Each condition was repeated n = 2 times.**

Precursor amount (μmol)	Starting activity (MBq)	Fluorination conversion (%)	Collection efficiency (%)	Crude RCY (%)
0.45	68.0 ± 2.3	32 ± 27	81 ± 13	24 ± 18
0.60	60.5 ± 1.8	52 ± 1	85 ± 1	44 ± 2
0.75	59.2 ± 1.4	47 ± 3	88 ± 7	41 ± 6
0.90	60.3 ± 1.9	55 ± 12	84 ± 4	47 ± 13
1.05	59.8 ± 0.1	65 ± 5	89 ± 1	57 ± 4

**Table 7-7 Summary of data acquired when exploring the impact of [<sup>18</sup>F]fluoride volume or starting activity when preparing [<sup>18</sup>F]FBnTP. Precursor amount for these studies was 0.60 μmol. Experiments were performed over a wider activity range (25.3-1510 MBq).**

[ <sup>18</sup> F]fluoride volume (μL)	Number of replicates (n)	Starting activity (MBq)	Fluorination conversion (%)	Collection efficiency (%)	Crude RCY (%)
5	6	86 ± 47	94 ± 2	91 ± 3	86 ± 4
25	2	710 ± 270	74 ± 7	86 ± 5	63 ± 2
30	2	930 ± 180	73 ± 1	85 ± 1	62 ± 2
40	2	60.5 ± 1.8	52 ± 1	85 ± 1	44 ± 2
42	2	970 ± 770	26 ± 16	89 ± 1	23 ± 14

## 7.5.6 Representative HPLC chromatograms

### 7.5.6.1 The synthesis by pooling two droplet reactions

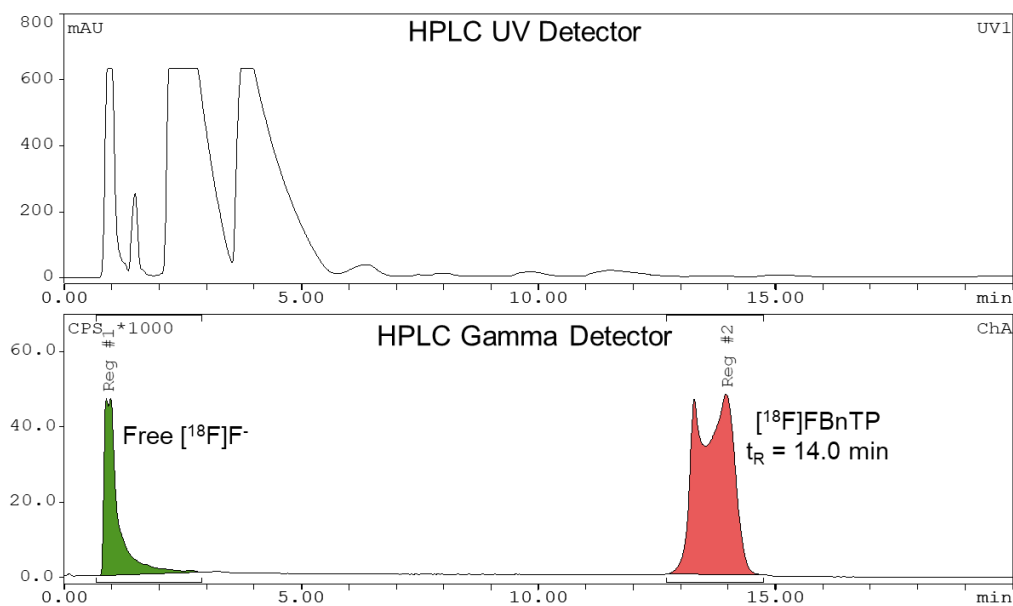


**Figure 7-5 Radio-HPLC chromatogram, during purification on an analytical column, of crude [<sup>18</sup>F]FBnTP by pooling two droplet reactions. The apparent split in the product peak is an artifact due to saturation of the radiation detector.**

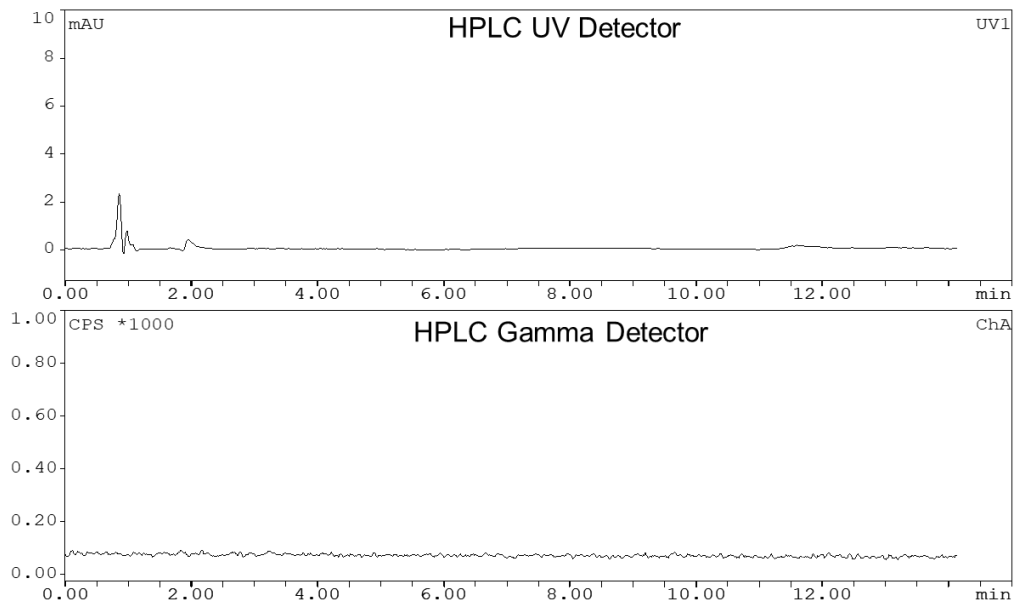


**Figure 7-6 Blank injection of formulation buffer, i.e., saline and EtOH (9:1, v/v).**

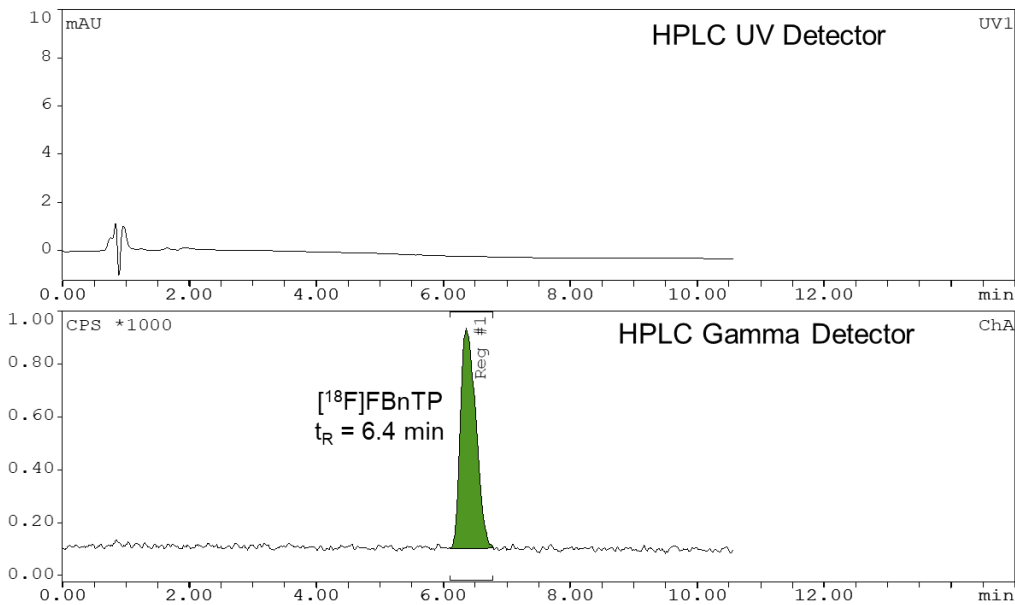


**Figure 7-7 Radio-HPLC chromatogram of formulated  $[^{18}\text{F}]\text{FBnTP}$  (from pooling two droplet reactions).**

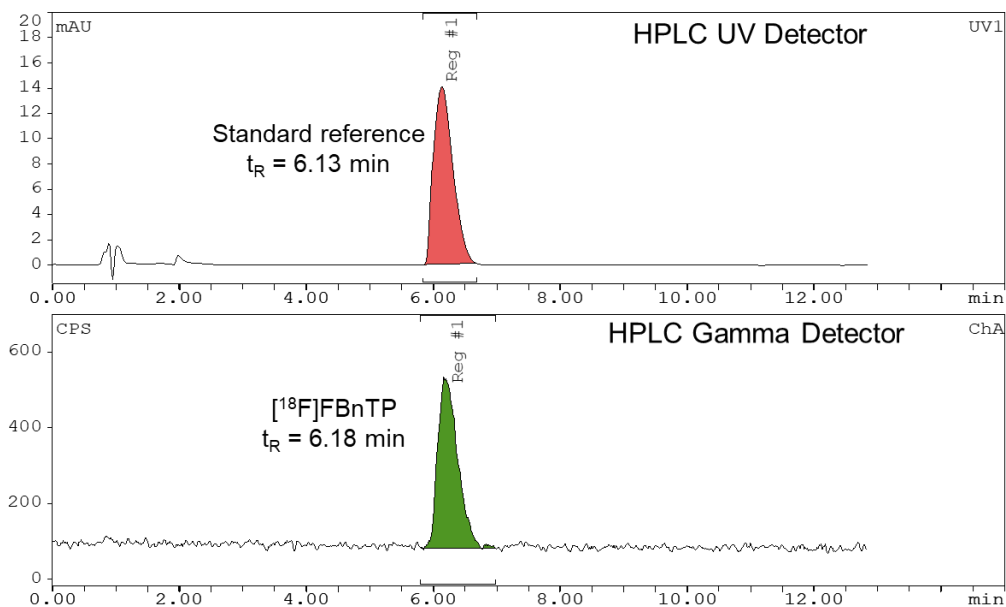


**Figure 7-8** Radio-HPLC chromatogram of co-injection of formulated  $[^{18}\text{F}]\text{FBnTP}$  (from pooling two droplet reactions) and FBnTP reference standard.

### 7.5.6.2 The synthesis by pooling four droplet reactions

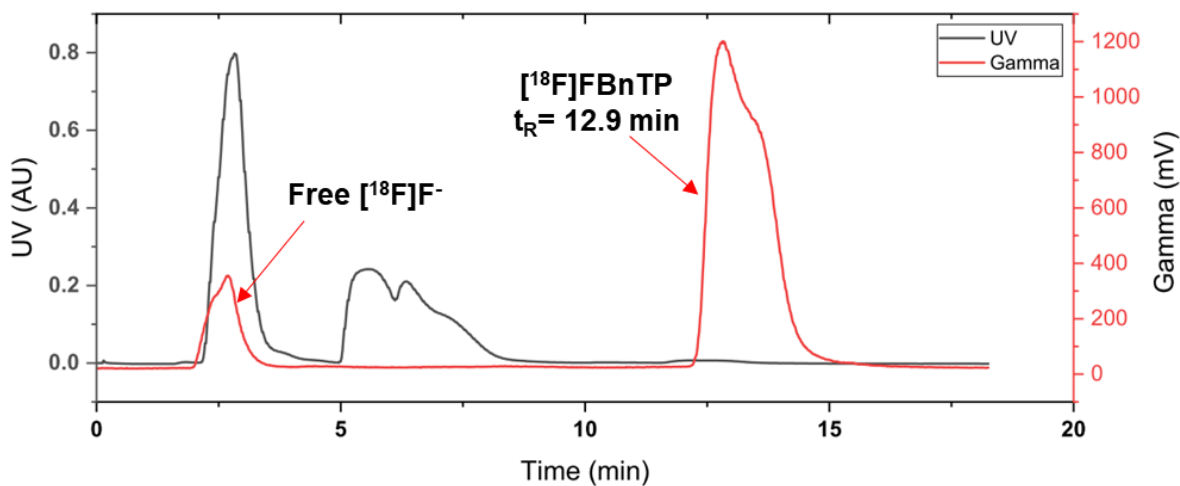


**Figure 7-9** Radio-HPLC chromatogram, during purification on a semi-prep column, of crude  $[^{18}\text{F}]\text{FBnTP}$  by pooling four droplet reactions.

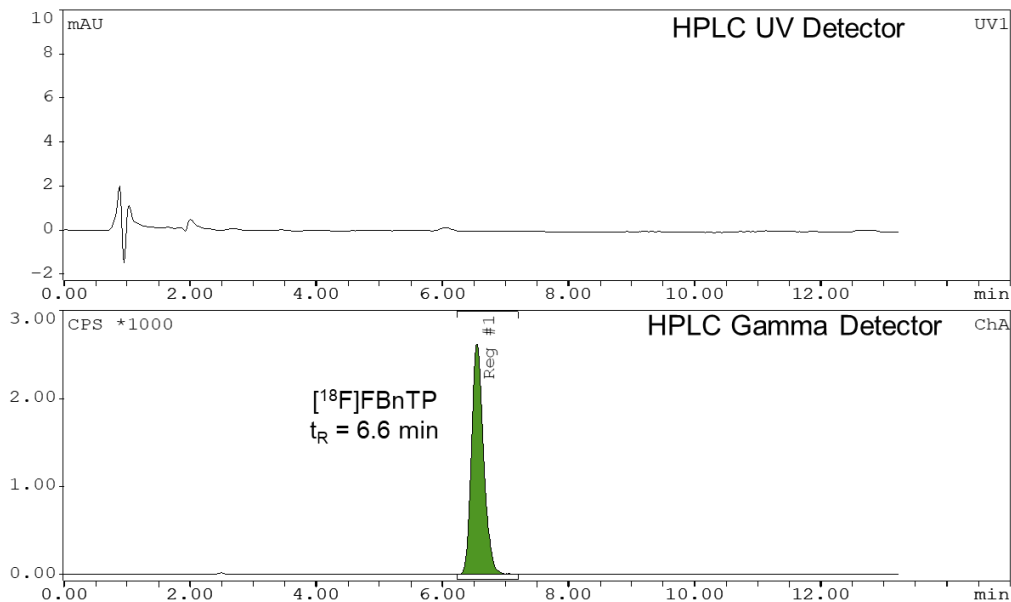


**Figure 7-10** Radio-HPLC chromatogram of formulated [<sup>18</sup>F]FBnTP (from pooling four droplet reactions).

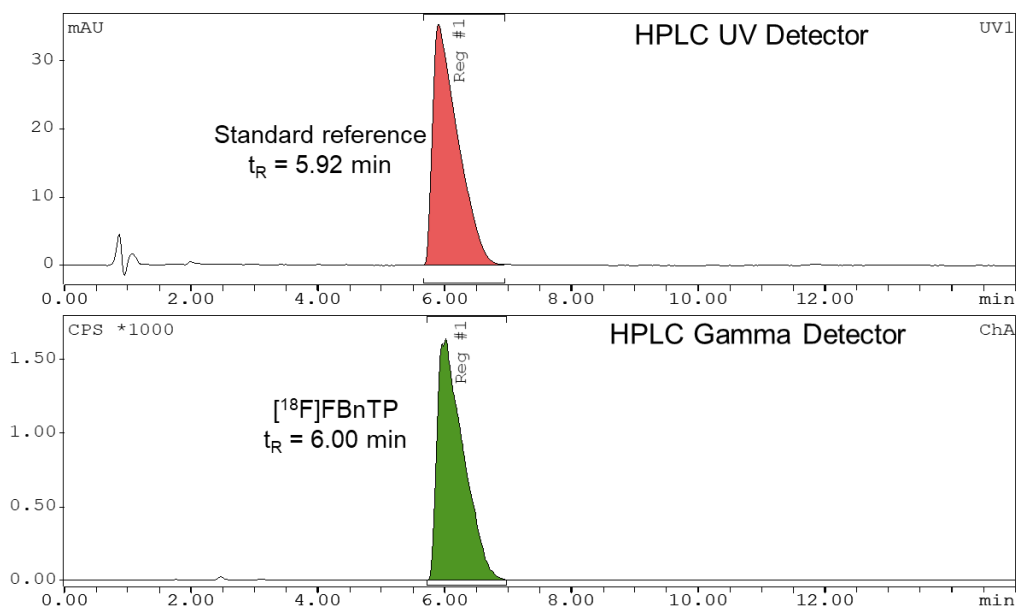


**Figure 7-11** Radio-HPLC chromatogram of conijection of formulated [<sup>18</sup>F]FBnTP (from pooling four droplet reactions) and FBnTP reference standard.

### 7.5.7 Molar activity determination

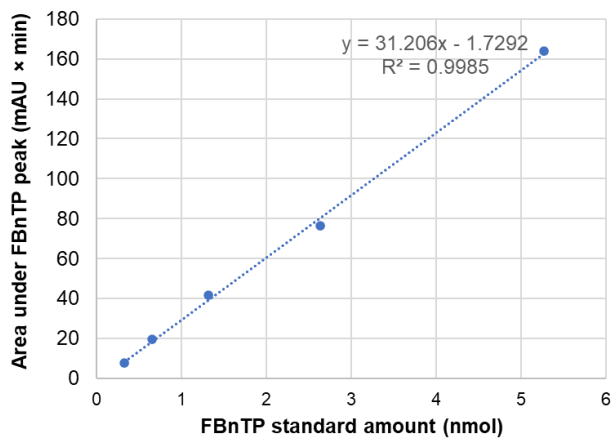


**Figure 7-12 Calibration curve of FBnTP reference standard. UV absorbance was measured at 254 nm.**

# Chapter 8: Copper-mediated $^{18}\text{F}$ -radiosynthesis optimization of a novel MAGL PET tracer on a high-throughput microdroplet platform and its immediate macroscale translation

## 8.1 Introduction

Positron emission tomography (PET) is a vital nuclear imaging technique for studying *in vivo* biodistribution, diagnosing diseases, monitoring therapy response, and developing new drugs (6). PET relies on positron-electron annihilation, generating gamma rays that are detected by PET scanners, and provides valuable insights into the binding and uptake behavior of radiolabeled compounds (i.e. radiotracers) to specific biomolecular targets (11). Fluorine-18, with its favorable nuclear and physical properties such as high positron yield, low energy, short range, and suitable half-life, is widely used to label biomolecules for PET imaging (298,299). Aromatic systems labeled with [ $^{18}\text{F}$ ]fluorine, in particular, tend to offer good *in vivo* stability, making them ideal for PET tracer development (300). Numerous approaches have been reported for  $^{18}\text{F}$ -labeling of aromatic compounds, though introducing [ $^{18}\text{F}$ ]fluoride into neutral and electron-rich aromatic rings remains challenging (299,301–303).

Currently, the Cu-mediated radiofluorination technique has emerged as a highly promising and primary method for introducing aromatic C- $^{18}\text{F}$  bonds into both novel and established PET tracers (304–314). This innovative approach successfully overcomes numerous challenges associated with conventional fluorination methods, such as the limited shelf life of precursors, difficulties in synthesizing labeling complexes, and the demanding synthesis conditions, making it a valuable and indispensable strategy for labeling aromatic systems with F-18.

Despite the wide scope of this method, achieving efficient manufacturing of specific tracers often requires extensive optimization efforts to consider the impact of various factors such as solvent system, phase transfer catalyst (PTC) or base types, precursor amount, copper mediator

type, reaction temperature, labeling time etc. (315–318). However, current commercial radiosynthesizers designed for milliliter-scale reactions, present limitations in terms of cost, hot cell operation, and limited synthesis capacity per day, largely hindering their contribution to intensive optimization endeavors. Additionally, to ensure reasonable reaction rates at the milliliter scale, significant amounts of precursors and other species are utilized, resulting in significant waste and challenges in downstream purification to remove excess reactants and by-products. Particularly, in the case of Cu-mediated radiofluorination, the presence of protoarene impurities generated from competing protodeborylation reactions complicates high-performance liquid chromatography (HPLC) purification due to their similar chemical properties to the desired product, further exacerbating the challenges (319).

Microfluidic devices have emerged as efficient, compact, and cost-effective platforms with great potential for diverse radiotracer production, leading to the development of various microfluidic tools in radiochemistry over the past 15 years (36–40). These systems can be roughly divided into two categories: flow chemistry systems and microscale batch systems. Flow-based reactors have shown great effectiveness in synthesizing various radiopharmaceuticals (44), but these setups rely on macroscale components for some synthesis steps (e.g., radioisotope concentration and product purification), making them similar to conventional radiosynthesizers in terms of size, shielding requirements, and operating volumes. Recent batch-based systems have been reported that can provide clinical amounts of numerous radiopharmaceuticals, and offer improvements due to significantly lower volumes (51), smaller system size, as well as improved integration with upstream and downstream processes. A variety of batch approaches have been pursued, including microvial reactors (54–56), channel-based devices with integrated isotope processing and purification (57,58), and droplet-reaction systems.

Within our research group, we have focused on the latter because of its simplicity, speed and versatility, and have developed several generations of semi- and fully-automated droplet-based reaction chips, including EWOD (320,321), passive transport chips (322,323), and surface-



tension trap chips (324). These devices have demonstrated comparable yields to conventional approaches but with significantly shorter overall synthesis times and 100x reduction in precursor, and provide high molar activity, regardless of whether one is producing small or large (radioactivity amount) batches (134,162,325). The enhanced speed is primarily attributed to an efficient chip surface heating and cooling system combined with the low solution volumes during reaction and evaporation steps, as well as microvolume purification (using analytical-scale HPLC) of <100  $\mu$ L crude product, eliminating the need for semi-preparative HPLC. Notably, we have recently showcased the feasibility of Cu-mediated radiosynthesis in a microdroplet reactor using [ $^{18}$ F]FDOPA as an example, achieving substantial improvements in radiofluorination (crude RCY of  $43 \pm 2\%$  ( $n = 4$ ) from fluorination conversion via TLC of  $60 \pm 4\%$  and collection efficiency of  $71 \pm 2\%$ ) with only 150 nmol of precursor (291).

In this work, we address two key remaining questions. Firstly, how useful is the droplet method for optimizing radiotracer synthesis through Cu-mediated radiofluorination at an early stage of radiochemical and preclinical development? Secondly, can the microscale optimized conditions be translated to macroscale radiosynthesis protocols to be compatible with currently available radiosynthesizer technologies, i.e., existing vial-based modules? To address these questions, we conducted a study using a novel PET tracer ([ $^{18}$ F]YH149) targeting the monoacylglycerol lipase (MAGL) as a proof-of-concept (326). Designed and synthesized via a Cu-mediated route (**Figure 8-1A**), [ $^{18}$ F]YH149 targets MAGL in the endocannabinoid system, a critical enzyme associated with inflammation, neurodegenerative disorders, and cancer. Evaluation of [ $^{18}$ F]YH149 in mice demonstrated excellent selectivity and specificity towards MAGL, along with significantly higher brain uptake in PET imaging compared to other reversible MAGL tracers (326), indicating its promising potential for clinical translation. However, the low RCY ( $4.4 \pm 0.5\%$ , decay-corrected) obtained using a macroscale synthesis platform is suboptimal for further imaging trials, severely limiting multi-center collaborative studies and larger cohort investigations. The pressing need for synthesis improvement makes [ $^{18}$ F]YH149 an ideal

candidate for a high-throughput microdroplet-based optimization study, as well as an exploration of its translation to macroscale synthesis. In the present study, we systematically screened various  $^{18}\text{F}$ -labeling parameters to develop an improved radiosynthesis for  $[^{18}\text{F}]\text{YH149}$  and subsequently explored the scaling of optimal conditions to a vial-based reaction.

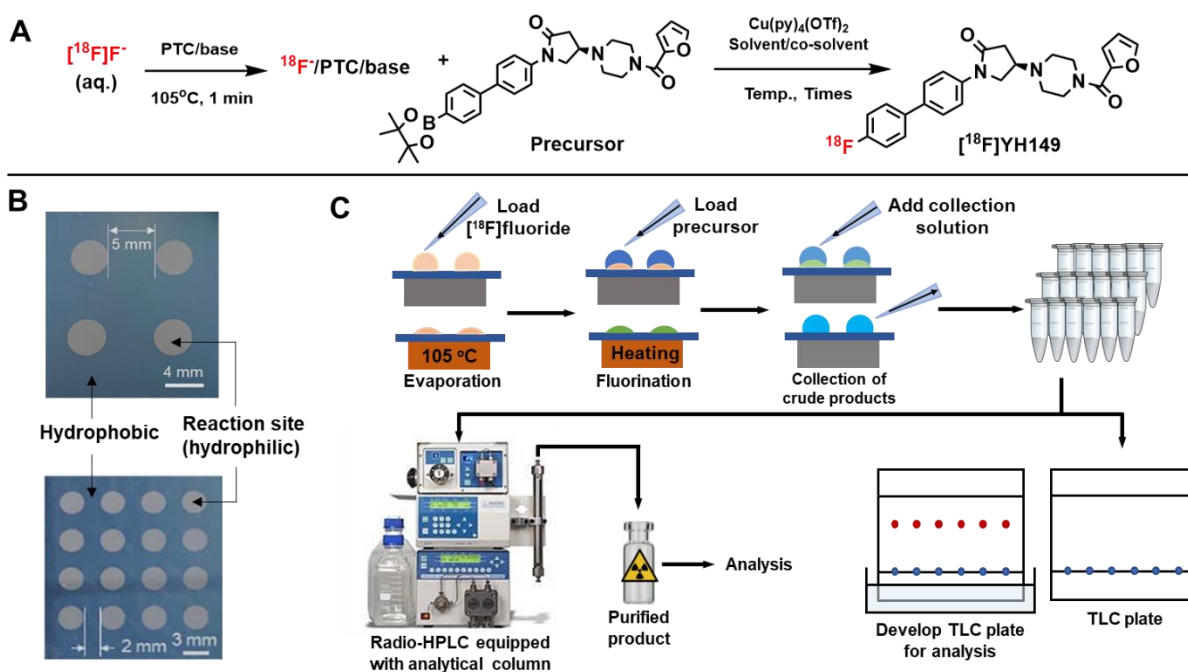


**Figure 8-1 Microdroplet-based radiosynthesis of  $[^{18}\text{F}]\text{YH149}$ .**

(A)  $[^{18}\text{F}]\text{YH149}$  synthesis scheme. (B) 2x2 and 4x4 multi-reaction chips for high-throughput synthesis optimization. (C) Process flow for (parallel) droplet-based radiosynthesis. Subsequently, the collected crude products are subject to multi-lane radio-TLC analysis (for synthesis optimization) or radio-HPLC purification (for  $[^{18}\text{F}]\text{YH149}$  production using a droplet system).

## 8.2 Methods

### 8.2.1 Materials

Tetrabutylammonium hydrogen carbonate ( $\text{TBAHCO}_3$ , 75 mM in ethanol) was purchased from ABX Advanced Biochemical Compounds (Radeberg, Germany). Tetrabutylammonium trifluoromethane-sulfonate ( $\text{TBAOTf}$ , >99%), Kryptofix® 222 ( $\text{K}_{222}$ , >99%) and potassium oxalate ( $\text{K}_2\text{C}_2\text{O}_4$ , 99%) were purchased from Sigma-Aldrich (St. Louis, MO, USA). Tetraethylammonium trifluoromethanesulfonate ( $\text{TEAOTf}$ , >99%) was purchased from TCI America (Portland, Oregon,

USA). Cesium carbonate ( $\text{Cs}_2\text{CO}_3$ , 99%), potassium carbonate ( $\text{K}_2\text{CO}_3$ , >99%), anhydrous pyridine (Py, 99.8%), anhydrous *N,N*-dimethylformamide (DMF, 99.8%), anhydrous *N,N*-dimethylacetamide (DMA, 99.8%), anhydrous dimethyl sulfoxide (DMSO, >99.9%), *n*-butanol (*n*BuOH, 99.9%), 1,3-dimethyl-2-imidazolidinone (DMI, >99.5%), anhydrous acetonitrile (MeCN, 99.8%), anhydrous ethyl alcohol (EtOH, >99.5%), phosphoric acid ( $\text{H}_3\text{PO}_4$ , >85 wt. % in  $\text{H}_2\text{O}$ ) and tetrakis(pyridine)copper(II) triflate ( $\text{Cu}(\text{OTf})_2(\text{Py})_4$ , 95%) were purchased from Sigma-Aldrich (St. Louis, MO, USA). *N*-Methyl-2-pyrrolidone (NMP, >99%) was purchased from TCI America (Portland, Oregon, USA). The precursor and reference standard were prepared as previously reported (326). Deionized (DI) water was obtained from a Milli-Q water purification system (EMD Millipore Corporation, Berlin, Germany). C18 plus light cartridges (130 mg Sorbent, WAT023501) were purchased from Waters Corporation (Milford, MA, USA). Reagent and collection vials were purchased from Eppendorf (Hamburg, Germany). Reaction vials (4 mL) for macroscale reactions were purchased from Chemglass Life Sciences (CG-4904-06, Vineland, NJ, USA). Silicone oil (CAS 63148-62-9) used in the vial heating block was purchased from Fisher chemical (Pittsburgh, PA, USA). 50 mL polypropylene centrifuge tubes were purchased from Corning Inc. (430304, Corning, NY, USA). [ $^{18}\text{F}$ ]fluoride in [ $^{18}\text{O}$ ]H $_2\text{O}$  was obtained from the UCLA Crump Cyclotron and Radiochemistry Center. The activity was used directly as provided by cyclotron without further purification for both droplet-based and vial-based macroscale radiosynthesis.

### 8.2.2 Droplet-based radiosynthesis of [ $^{18}\text{F}$ ]YH149

Droplet-based reactions were performed on Teflon-coated silicon chips patterned with 2x2 or 4x4 arrays of multiple hydrophilic reaction sites (**Figure 8-1B**), operated on a temperature-controlled heating platform, as previously described (160).

The general synthesis process (**Figure 8-1C**) was as follows: 10  $\mu\text{L}$  of a [ $^{18}\text{F}$ ]fluoride stock solution (containing 23-170 MBq of activity mixed with a desired amount of PTC and base) was delivered via micropipette onto a reaction site of the chip and dried at 105  $^\circ\text{C}$  for 1 min. Next, 10  $\mu\text{L}$  of a precursor /  $\text{Cu}(\text{OTf})_2(\text{py})_4$  stock solution was added via micropipette and heating to perform

the fluorination. After synthesis, the crude product was extracted from the reaction site by adding a collection solution (20  $\mu$ L) and transferring via micropipette to a 0.5 mL eppendorf tube for further analysis. The collection step was repeated a total of 4x to minimize activity residue on the chip. Studies were performed to optimize the reaction solvent type, PTC/base type and amount, reaction temperature, reaction time, and precursor amount.

Several stock solutions were prepared just prior to each batch of experiments. Stock solutions of PTC and base was prepared in DI water at concentrations such that a 5  $\mu$ L aliquot contained the desired amount of PTC and base for a single droplet reaction. The amounts were optimized as part of this study. [ $^{18}$ F]fluoride stock solution was prepared by mixing [ $^{18}$ F]fluoride/[ $^{18}$ O]H<sub>2</sub>O with the desired PTC / base stock solution in 1:1 (v/v) ratio, such that each 10  $\mu$ L portion contained 23-170 MBq of activity along with the desired amount of PTC and base for a single reaction. Stock solutions of precursor (37 mM) and Cu(OTf)<sub>2</sub>(Py)<sub>4</sub> (136 mM) were separately prepared in the desired reaction solvent mixture. These components were mixed in 1:1 (v/v) ratio just prior to synthesis such that each 10  $\mu$ L portion of the mixed solution contained 0.185  $\mu$ mol (0.1 mg) of precursor and 0.68  $\mu$ mol of Cu(OTf)<sub>2</sub>(Py)<sub>4</sub>. In studies of precursor amount, a similar procedure was followed except the concentration of the precursor stock solution was varied. Collection solution was prepared by mixing MeCN and DI water (6:4, v/v).

In some cases (for comparison of performance of droplet and vial-based reactions), droplet reactions were prepared at higher activity scale. In these cases, a 20  $\mu$ L of [ $^{18}$ F]fluoride (0.2-1.45 GBq with the optimal PTC/base amount) was dried on the chip for a slightly longer time (~1.5 min), followed by the optimal fluorination process. The crude product was collected as described above, but using HPLC mobile phase (composition described below), followed by analytical-scale HPLC purification.

### **8.2.3 Macroscale production of [ $^{18}$ F]YH149**

Macroscale synthesis was performed in a 4 mL GC vial. Heat was provided by placing the vial into a preheated aluminum vial block (Ohaus 30400185, Hogentogler & Co. Inc., Columbia,

MD, USA) filled with 2 mL silicone oil. The vial block was heated on a hot plate (PC-420D, Corning Inc., Corning, NY, USA) equipped with a temperature probe (6795PR, Corning Inc., Corning, NY, USA) inserted into the heating block.

The droplet-based synthesis was implemented as a vial-based reaction by scaling up reagent amounts of the optimal conditions by 10x and performing reactions in 300  $\mu\text{L}$  of reaction solvent mixture, but otherwise maintaining the same conditions as the droplet reaction. 20  $\mu\text{L}$  of aqueous [ $^{18}\text{F}$ ]fluoride (0.2-1.44 GBq), mixed with 10x the optimized amounts of PTC and base, was added to the reactor, and dried at 105  $^{\circ}\text{C}$  until all liquid evaporated. Azeotropic drying was performed three times, each time by adding MeCN (30  $\mu\text{L}$ ) and drying at the same temperature. Stock solutions of precursor and  $\text{Cu}(\text{OTf})_2(\text{Py})_4$  were each prepared in the optimized solvent system, and were mixed in 1:1 (v/v) ratio right before synthesis. 300  $\mu\text{L}$  of the resulting mixture (containing 10x the amounts of precursor and  $\text{Cu}(\text{OTf})_2(\text{Py})_4$  as the optimized droplet reaction) was added into the reaction vial and heated to the fluorination temperature via the heating block. The reaction was sampled at different time points to monitor its fluorination progress. At each time point, the reaction vial was moved from the heat block and cooled down with a water bath ( $\sim 20^{\circ}\text{C}$ ) for  $\sim 1$  min, and a 0.5  $\mu\text{L}$  sample was taken from the reaction mixture and diluted with 20  $\mu\text{L}$  of collection solution for TLC analysis. After taking the sample, the reaction vial was put back into the heat block until the next timepoint. After the 0.5  $\mu\text{L}$  sample was taken from the final reaction mixture, the reaction mixture was quenched with 1 mL of DI water, transferred to a 50 mL centrifuge tube and further diluted with 20 mL of DI water. Prior to HPLC purification, the solvent was exchanged by loading the diluted crude product on a light C18 cartridge (preconditioned with 5 mL of EtOH and then 20 mL of DI water), washing with 6 mL of DI water, and eluting with 0.5 mL of MeCN. The eluate was further concentrated to  $<0.1$  mL by heating at 60  $^{\circ}\text{C}$  in a v-vial, enabling the crude product to be purified via analytical-scale HPLC.

## 8.2.4 Analytical equipment and methods

Radioactivity measurements were conducted with a calibrated dose calibrator (CRC-25R, Capintec, Florham Park, NJ, USA). Fluorination conversion was assessed via multi-lane radio-thin layer chromatography (radio-TLC) methods (96). Briefly, samples (0.5  $\mu\text{L}$ ) were spotted on TLC plates (6 cm x 5 cm pieces cut from 20 cm x 5 cm sheets, silica gel 60 F<sub>254</sub>, Merck KGaA, Darmstadt, Germany). Plates were developed for a 4 cm distance using a mobile phase of MeCN and DI water (7:3, v/v), dried, and then covered with a glass microscope slide (75x50x1 mm<sup>3</sup>, Fisher Scientific, Hampton, NH, USA) and read out by Cerenkov luminescence imaging (CLI) with 5 min exposure time. Fluorination conversion of each sample (lane) was determined via ROI analysis as previously described (96). Collection efficiency was obtained by dividing the activity of product mixture collected from the droplet or vial reactor by the starting activity (corrected for decay). Crude RCY was computed as fluorination conversion multiplied by the collection efficiency. The isolated RCY was determined by performing radio-HPLC purification on an analytical column (ZORBAX RP Eclipse Plus C18, 100 x 4.6 mm, 3.5  $\mu\text{m}$ , Agilent Technologies, Santa Clara, CA, USA) using an isocratic mobile phase of DI water and MeCN (74:26, v/v) with 0.1% H<sub>3</sub>PO<sub>4</sub> (v/v) at a flow rate of 1.2 mL/min. The radio-HPLC system comprised a Smartline HPLC system (Knauer, Berlin, Germany) equipped with a degasser (Model 5050), pump (Model 1000), UV detector (254 nm; Eckert & Ziegler, Berlin, Germany), gamma-radiation detector (BFC-4100, Bioscan, Inc., Poway, CA, USA), and counter (BFC-1000; Bioscan, Inc., Poway, CA, USA). The purified [<sup>18</sup>F]YH149 was analyzed on the same radio-HPLC system to confirm radiochemical purity (RCP) using a mobile phase of DI water and MeCN (70:30, v/v) with 0.1% H<sub>3</sub>PO<sub>4</sub> (v/v) at a flow rate of 1.2 mL/min. Co-injection of the purified [<sup>18</sup>F]YH149 and reference standard was performed to confirm product identity. The same analytical scale radio-HPLC system was employed to determine the molar activity of the purified [<sup>18</sup>F]YH149, utilizing a linear calibration curve of YH149 reference standard. The comprehensive measurement details can be found in the **Appendix 8.5.3**.

## 8.3 Results and discussion

### 8.3.1 Optimization of [<sup>18</sup>F]YH149 radiosynthesis using droplet reactions

#### 8.3.1.1 Initial conditions

As a starting point for droplet-based synthesis of [<sup>18</sup>F]YH149 we tried two sets of conditions. First (**Condition 1**), we scaled down the macroscale synthesis method described by He et al.(326) from 300  $\mu$ L to 10  $\mu$ L with 10x reduced reagents, while preserving ingredient ratios except for Cu(OTf)<sub>2</sub>(Py)<sub>4</sub>, (we used 30x less instead of 10x less due to solubility issues). Second (**Condition 2**), we used our previously reported droplet-based conditions for the Cu-mediated synthesis of [<sup>18</sup>F]FDOPA (291) but used the [<sup>18</sup>F]YH149 precursor. The detailed conditions and performance of the reactions can be found in **Table 8-3**. Surprisingly, our attempts to produce [<sup>18</sup>F]YH149 by **Condition 1** yielded no product (n = 2) (**Figure 8-6**). To our delight, we successfully obtained [<sup>18</sup>F]YH149 by using **Condition 2**, with moderate fluorination conversion of  $44 \pm 1\%$  (n = 2), good collection efficiency of  $81 \pm 2\%$  (n = 2) and crude RCY of  $36 \pm 2\%$  (n = 2). Despite this initial attempt already exceeding the performance of the vial-based reaction conditions,(326) we proceeded with further optimization starting with **Condition 2**.

Noticing that the main differences between **Conditions 1** and **2** were reaction solvent composition and the type and amount of PTC/base, we focused initial optimization studies on these parameters, and systematically explored various parameters in the following order: 1) solvent type, 2) type of PTC and base, 3) reaction temperature, 4) fluorination time, and 5) precursor amount. At each stage of optimization, we selected the best-performing condition, which was then fixed for subsequent experiments.

#### 8.3.1.2 Influence of reaction solvent

Various solvent systems were investigated for the preparation of [<sup>18</sup>F]YH149 (**Figure 8-2A**). Details of measurements and calculations are tabulated in **Table 8-4**, the CLI readout of the multi-lane TLC is shown in **Figure 8-7**. All reactions were conducted with TEAOTf (0.3  $\mu$ mol)

/  $\text{Cs}_2\text{CO}_3$  (0.01  $\mu\text{mol}$ ) as PTC/base,  $\text{Cu}(\text{py})_4(\text{OTf})_2$  (0.68  $\mu\text{mol}$ ) as copper reagent and 0.1 mg (0.18  $\mu\text{mol}$ ) of precursor in 10  $\mu\text{L}$  solvent at 110  $^\circ\text{C}$  for 5 min. Among the different solvent systems tested, the mixed solvent DMA/nBuOH/pyridine (64:32:4, v/v) provided the best performance, with a fluorination conversion of  $49 \pm 2\%$  ( $n = 3$ ), collection efficiency of  $75 \pm 1\%$  ( $n = 3$ ) and crude RCY of  $35 \pm 0\%$  ( $n = 3$ ). Notably, the absence of pyridine (i.e., using only DMA/nBuOH (2:1, v/v)) resulted in a fluorination conversion of 0% ( $n = 2$ ), suggesting pyridine is a critical additive for the formation of the radiofluorinated product. Pyridine likely serves as a stabilizer to maintain the functionality of the copper catalyst solution under ambient conditions, and its necessity was also mentioned by Mossine et al. in previous reports (311,319).

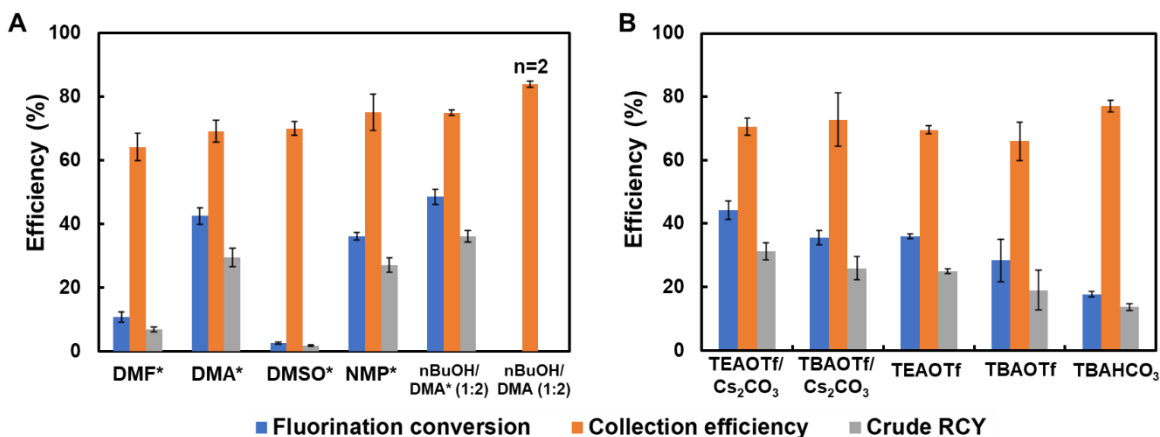


**Figure 8-2 Influence of reaction parameters on the performance of the microdroplet radiosynthesis.**

(A) Impact of fluorination solvent / co-solvent. Solvent mixtures are all v/v, and asterisks “\*” indicate that the solvent contains 4% pyridine. (B) Impact of type of phase transfer catalyst (PTC) and base used during  $^{18}\text{F}$ fluoride drying.

### 8.3.1.3 Influence of PTC/base

The next investigation involved different types of PTCs and bases (**Figure 8-2B**). The detailed measurements and calculations can be found in **Table 8-5** and multi-lane TLC data are shown in **Figure 8-8**. In the absence of base ( $\text{Cs}_2\text{CO}_3$ ), the reaction with TEAOTf exhibited the highest fluorination conversion among the three PTCs tested, achieving  $36 \pm 1\%$  ( $n = 3$ ), along



with a good collection efficiency of  $70 \pm 1\%$  ( $n = 3$ ) and resulting crude RCY of  $25 \pm 1\%$  ( $n = 3$ ). The use of TBAOTf or TBAHCO<sub>3</sub> as the PTC exhibited significantly lower fluorination conversion, resulting in substantially lower crude RCY ( $19 \pm 6\%$ ,  $n = 3$  for TBAOTf and  $14 \pm 1\%$ ,  $n = 3$  for TBAHCO<sub>3</sub>). The addition of the base Cs<sub>2</sub>CO<sub>3</sub> further improved the fluorination conversion ( $44 \pm 3\%$ ,  $n = 3$  for TEAOTf/Cs<sub>2</sub>CO<sub>3</sub> and  $36 \pm 2\%$ ,  $n = 3$  for TBAOTf/Cs<sub>2</sub>CO<sub>3</sub>), resulting in higher crude RCYs of  $31 \pm 3\%$  ( $n = 3$ ) for TEAOTf/Cs<sub>2</sub>CO<sub>3</sub> and  $26 \pm 4\%$  ( $n = 3$ ) for TBAOTf/Cs<sub>2</sub>CO<sub>3</sub>, respectively. Hence, TEAOTf was identified as the optimal PTC for preparing [<sup>18</sup>F]YH149, and the addition of base (Cs<sub>2</sub>CO<sub>3</sub>) was also important for a good manufacture.

### 8.3.1.4 Effect of temperature and base type

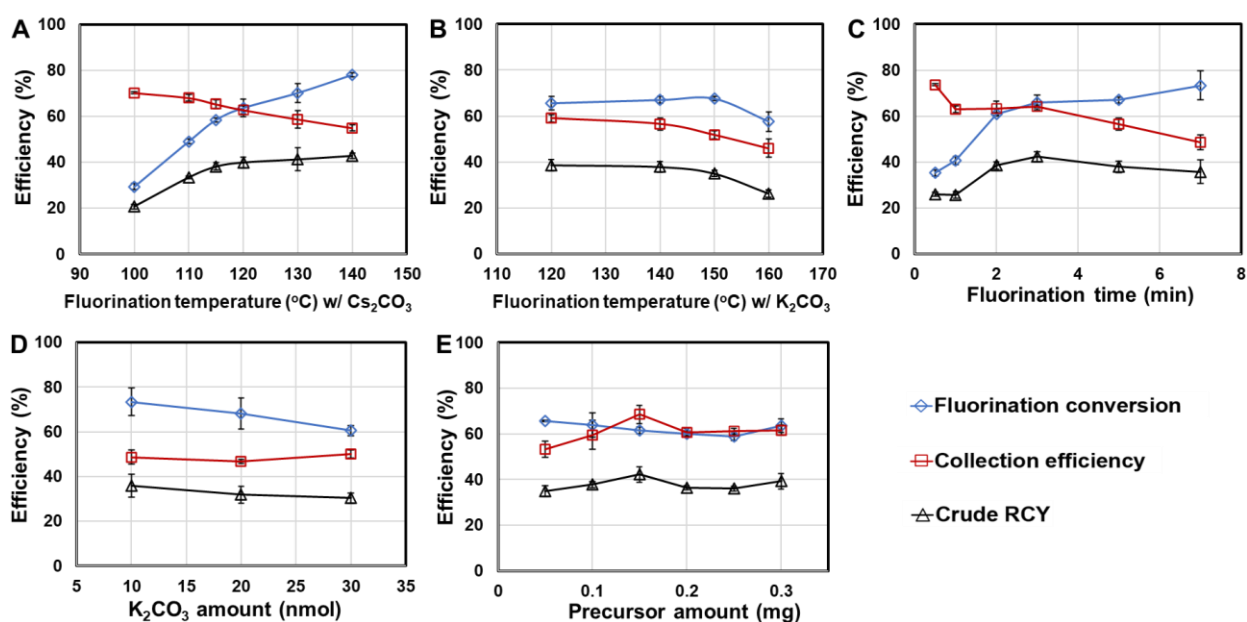


**Figure 8-3 Influence of reaction parameters on the performance of the microdroplet radiosynthesis.**

(A, B) Impact of fluorination temperature for two base types. (C) Impact of reaction time. (D) Impact of amount of base. (E) Impact of amount of precursor.

We conducted additional investigation into the fluorination temperatures (**Figure 8-3A,B**). As a mild and common base source in aprotic solvents, we also opted to explore K<sub>2</sub>CO<sub>3</sub> as an alternative to Cs<sub>2</sub>CO<sub>3</sub> in this temperature study. A comprehensive listing of measurements and

calculations, and multi-lane radio-TLC images can be found in **Table 8-6,7** and **Figure 8-9,10**, respectively. In the presence of  $\text{Cs}_2\text{CO}_3$ , the fluorination conversion exhibited a significant increase with temperature, reaching a maximum of  $78 \pm 1\%$  ( $n = 3$ ) at  $140^\circ\text{C}$ . However, it was observed that higher temperatures led to increased volatile losses, resulting in a decline in the collection efficiency. The overall crude RCY demonstrated a sharp increase with temperature, rising from  $21 \pm 1\%$  ( $n = 3$ ) at  $100^\circ\text{C}$  to  $40 \pm 2\%$  ( $n = 3$ ) at  $120^\circ\text{C}$ , and then tended to stabilize beyond  $120^\circ\text{C}$ . The maximum crude RCY of  $43 \pm 1\%$  ( $n = 3$ ) was achieved at  $140^\circ\text{C}$ , accompanied by a fluorination conversion of  $78 \pm 1\%$  ( $n = 3$ ) and a collection efficiency of  $55 \pm 1\%$  ( $n = 3$ ). When  $\text{K}_2\text{CO}_3$  was used as the base (tested over a slightly higher temperature range), the fluorination conversion showed a small rise with increasing temperature, however, the collection efficiency exhibited a gradual decrease, with a net overall result of gradually decreasing crude RCY. At  $160^\circ\text{C}$ , a more significant drop in reaction performance was observed. Nearly the best crude RCY occurred at  $140^\circ\text{C}$ , where the fluorination efficiency was  $67 \pm 1\%$  ( $n = 3$ ), collection efficiency was  $57 \pm 3\%$  ( $n = 3$ ) and crude RCY was  $38 \pm 2\%$  ( $n = 3$ ). Considering the higher volatile losses observed with  $\text{Cs}_2\text{CO}_3$  at  $140^\circ\text{C}$  (collection efficiency:  $55 \pm 1\%$ ,  $n = 3$  vs.  $57 \pm 3\%$ ,  $n = 3$  for  $\text{K}_2\text{CO}_3$ ) and its more basic property in aprotic solvents (327), we adopted  $\text{K}_2\text{CO}_3$ , the milder base, as the base for further experiments.

#### **8.3.1.5 Effect of reaction time**

Next, we investigated the impact of reaction time (**Figure 8-3C**). Detailed measurements and calculations and radio-TLC analysis can be found in **Table 8-8** and **Figure 8-11**. We observed that radiofluorination proceeded rapidly within the first 2 min, followed by gradual growth, but collection efficiency showed an inverse trend, with increasing loss of volatile activity during longer reaction times. The resulting crude RCY exhibited a peak at 3 min, with a value of  $42 \pm 2\%$  ( $n = 3$ ).

#### **8.3.1.6 Effect of base amount**

Based on the optimal reaction time, a study of different amounts of base was conducted (Figure 8-3D). Details of measurements and calculations and radio-TLC images can be found in Table 8-9 and Figure 8-12. We observed that increased amount of the base led to a gradual decrease in fluorination conversion, while the collection efficiency did not exhibit significant changes, resulting in a gradual decline in crude RCY. Based on these results, minimal use of base (10 nmol) was selected for the next optimization stage.

### 8.3.1.7 Influence of precursor amount

We further explored the influence of precursor amount (Figure 8-3E). Detailed measurements and calculations and radio-TLC images can be found in Table 8-10 and Figure 8-4, respectively. Interestingly, the amount of precursor had only a slight impact on the various measures of performance of the reaction. Using 0.15 mg of precursor gave the highest overall crude RCY ( $42 \pm 4\%$ ,  $n = 3$ ).

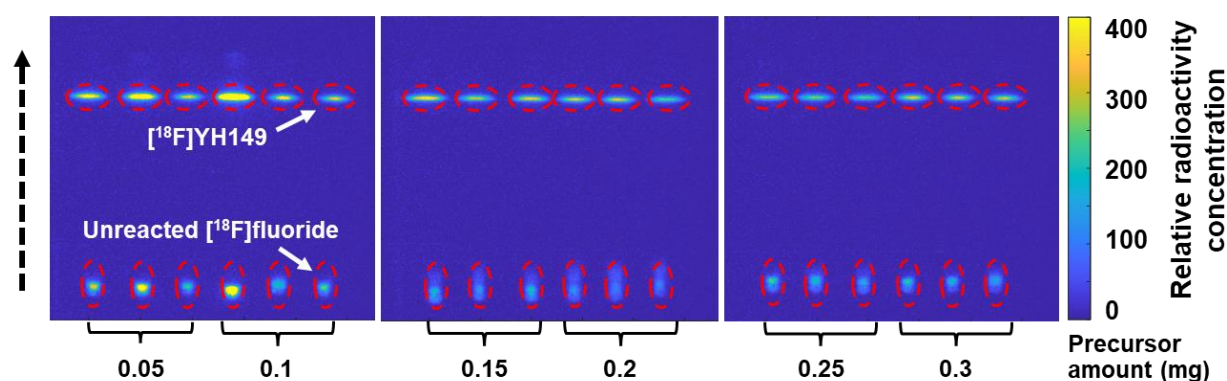


Figure 8-4 Example of high-throughput analysis of crude fluorination products (from study of precursor amount) using multi-lane TLC with Cerenkov luminescence imaging (CLI) readout.

### 8.3.1.8 Additional tests

Inspired by a separate study, in which we saw significantly improved production of  $[^{18}\text{F}]\text{FBnTP}$  achieved by using DMI as a solvent instead of DMA(94), we conducted additional tests for the synthesis of  $[^{18}\text{F}]\text{YH149}$ . When replacing DMA with DMI under the fixed conditions derived from previous optimization stages (Table 8-10 and Figure 8-13), the synthesis showed

higher fluorination conversion ( $71 \pm 5\%$ ,  $n = 3$  for DMI vs.  $62 \pm 2\%$ ,  $n = 3$  for DMA,  $n = 3$ ), however collection efficiency was lower ( $57 \pm 1\%$ ,  $n = 3$  for DMI vs.  $68 \pm 4\%$ ,  $n = 3$  for DMA), resulting in an overall lower crude RCY of  $40 \pm 4\%$  ( $n = 3$ ) compared to  $42 \pm 4\%$  for DMA. Therefore, we retained DMA/nBuOH/Py as the optimal solvent combination. Additionally, given the superior performance of  $\text{Cs}_2\text{CO}_3$  compared to  $\text{K}_2\text{CO}_3$  in the same  $[^{18}\text{F}]\text{FBnTP}$  study (94), we were curious to compare these bases again for the preparation of  $[^{18}\text{F}]\text{YH149}$  (Table 8-10 and Figure 8-13). To our surprise, the use of  $\text{Cs}_2\text{CO}_3$  exhibited a significant increase in both fluorination conversion ( $80 \pm 2\%$ ,  $n = 4$ ) compared to  $\text{K}_2\text{CO}_3$  ( $62 \pm 2\%$ ,  $n = 3$ ) and collection efficiency ( $71 \pm 3\%$ ,  $n = 4$ ) compared to  $\text{K}_2\text{CO}_3$  ( $68 \pm 4\%$ ,  $n = 3$ ). Consequently, this configuration yielded the highest crude RCY of  $56 \pm 3\%$  ( $n = 4$ ) compared to  $\text{K}_2\text{CO}_3$  ( $42 \pm 4\%$ ,  $n = 3$ ). As a result, we selected  $\text{Cs}_2\text{CO}_3$  as the optimal base type.

### 8.3.1.9 Overall synthesis including purification

**Table 8-1 Summary of optimization experiments and findings. At each stage, the best performing condition was selected and held constant in later experiments.**

Day	Optimization study	Selected optimal condition
1	Initial attempts at droplet reaction	Use Condition B (in Table S1)
	Optimize solvent type	← Solvent must contain pyridine ← DMA/nBuOH/pyridine (64:32:4, v/v)
2	Optimize PTC/base type	← TEAOTf/ $\text{Cs}_2\text{CO}_3$
3	Optimize temperature and base type	← $140^\circ\text{C}$ ← TEAOTf/ $\text{K}_2\text{CO}_3$
4	Optimize reaction time	← 3 min
	Optimize base amount	← 10 nmol
5	Optimize precursor amount	← 0.15 mg
	Additional solvent test	No change
	Additional base type test	← TEAOTf/ $\text{Cs}_2\text{CO}_3$

Overall, as summarized in Table 8-1, 36 distinct conditions (totaling 117 experiments when replicates are included) were explored over a span of 5 days, consuming a total of <15 mg

of precursor. In order to account for potential interfering factors (e.g. variations in [<sup>18</sup>F]fluoride quality from day to day, batch-to-batch inconsistencies in stock solution preparation, etc.), each optimization experiment included conditions that repeated data points from the previous day as a control. We found such replicated measurements to be remarkably consistent, suggesting little impact of fluoride quality and batches of reagents. Each experimental reaction was performed with starting activity ranging from 22-170 MBq. The optimal process involved drying [<sup>18</sup>F]fluoride with TEAOTf (0.3 μmol) and Cs<sub>2</sub>CO<sub>3</sub> (0.01 μmol) at 105 °C for 1 min. No azeotropic drying steps were necessary. Subsequently, the fluorination reaction was performed at 140 °C for 3 min using 0.15 mg (0.28 μmol) of precursor and 0.68 μmol of Cu(OTf)<sub>2</sub>(Py)<sub>4</sub> in a 10 μL solvent mixture of DMA/BuOH/pyridine (64:32:4, v/v). This optimized method achieved fluorination conversion (80 ± 2%, n = 3) and collection efficiency (71 ± 3%, n = 3) at the end of the reaction, resulting in a crude RCY of 56 ± 3% (n = 3). The optimized synthesis was then scaled to higher activities (0.2 to 1.45 GBq) and combined with purification. Taking advantage of the microscale radiosynthesis, the collected crude product volume (~80 μL) and reagent mass were sufficiently low that purification was possible using an analytical radio-HPLC system under isocratic conditions. Purified product could be collected in ~20 min. The radio-HPLC chromatogram of the crude [<sup>18</sup>F]YH149 injection showed excellent separation resolution (**Figure 8-5A**). The isolated RCY (52 ± 8%, n=4) closely matched the calculated crude RCY (56 ± 3%, n = 3; based on radio-TLC measurement), suggesting minimal residual losses during the HPLC injection and purification process. The radiochemical purity of the purified [<sup>18</sup>F]YH149 was 100%, determined by radio-HPLC (using the analytical mobile phase). **Figure 8-5B** shows an HPLC chromatogram of a blank injection of the purification mobile phase (20 μL), and **Figure 8-5C** shows a chromatogram of the injected purified product (20 μL). Co-injection of the purified [<sup>18</sup>F]YH149 and the reference standard confirmed the product identity (**Figure 8-5D**). Note that the analytical mobile phase had higher organic content (30% vs 26% MeCN), thus the retention time is lower (8.5 min vs 18.6

min). The molar activity at the end of synthesis was determined to be 77-854 GBq/ $\mu$ mol. The overall synthesis time was 26 min, comprising 6 min for radiolabeling and 20 min for purification.

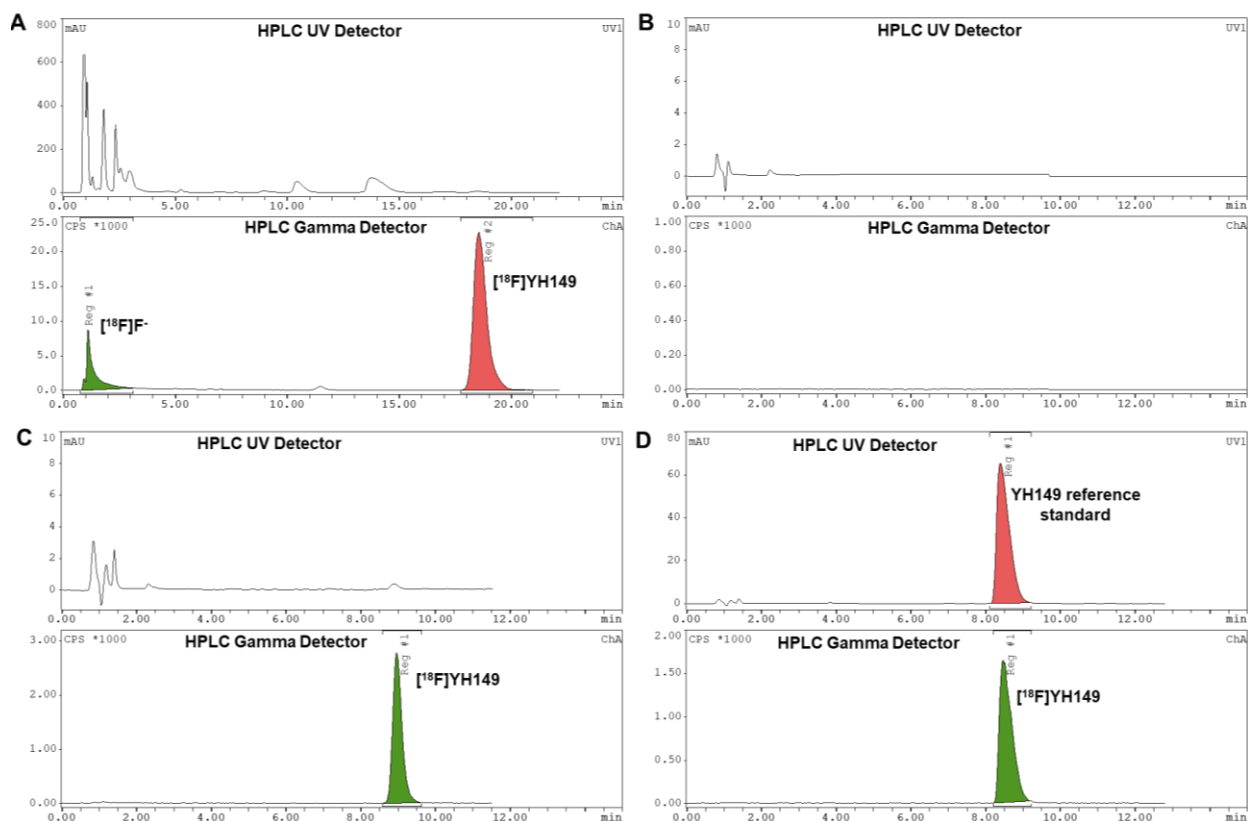


**Figure 8-5 Example radio-HPLC chromatograms via droplet-based radiosynthesis.** (A) crude  $[^{18}\text{F}]$ YH149, (B) blank injection of purification mobile phase, (C) purified  $[^{18}\text{F}]$ YH149, and (D) co-injection of  $[^{18}\text{F}]$ YH149 and YH149 reference standard. Note that retention times are different because panel A uses the purification mobile phase while other panels use a different analytical mobile phase.

The performance is summarized in **Table 8-2** and compared to the results of the originally-reported macroscale synthesis,<sup>(326)</sup> highlighting notable improvements in synthesis time and RCY. One reason for the improved RCY at the microscale could be the increased precursor concentration (28 mM vs 12.3-18.3 mM). Despite this increased concentration, we achieved a 13-20x reduction in precursor consumption by using a significantly smaller reaction volume (10 vs. 300  $\mu$ L). The concentration of the copper reagent was similar (68 mM for the microscale reaction vs. 68.7 mM in He *et al.* (326)), but the total amount was  $\sim$ 30x lower due to the reduced reaction volume. The reduced reagent usage significantly reduced the formation of side products, resulting

in simplified purification. The elevated temperature (140 °C in this work vs. 110 °C in (326)) likely also played a role in improving performance. Only two major radio-peaks, corresponding to unreacted [<sup>18</sup>F]fluoride and [<sup>18</sup>F]YH149, were seen in the HPLC chromatogram from the crude droplet reaction (**Figure 8-5A**). Furthermore, the UV chromatogram showed only a few impurities in very low quantities, well separated from the product peak. Notably, purification could be streamlined on an analytical-scale HPLC with an isocratic mobile phase, while the conventional radiosynthesis method required a gradient protocol, leading to the need for a more complex HPLC setup. Overall, the droplet synthesis exhibited a ~12-fold increase in RCY (52 ± 8%, n = 4) compared to the previous macroscale approach (4.4 ± 0.5%, n = 4). Moreover, despite commencing with significantly lower initial activity compared to the conventional macroscale approach (0.2-1.45 GBq vs. 50-60 GBq), the droplet method achieved high molar activity ranging from 77 to 854 GBq/μmol at the end of synthesis. Furthermore, despite using ~41x lower starting activity, the droplet reaction could still produce enough product amount for preclinical and clinical studies. This high-performing microscale synthesis paves the way for efficient production of small tracer batches through Cu-mediated radiofluorination, delivering the high molar activity needed for preclinical imaging scenarios. Sufficient product amount of [<sup>18</sup>F]YH149 (80-623 MBq) was also obtained for multiple preclinical imaging studies or a single patient scan for a clinical study. Finally, the total preparation time using the droplet method was merely one-third of that required by the conventional method, resulting in significant time savings.

**Table 8-2 Comparison of performance prior macroscale synthesis method, optimized droplet-based synthesis, and translated vial-based (macroscale) preparation.**

	mL-scale synthesis	Optimized droplet synthesis	Translated vial-based synthesis
	He et al.	This work	This work
Number of repeats (n)	5	4	4
Starting <sup>18</sup> F-activity (GBq)	50-60	0.2-1.45	0.2-1.44
Amount of PTC/base (μmol)	K <sub>2</sub> CO <sub>3</sub> (0.7) K <sub>2</sub> C <sub>2</sub> O <sub>4</sub> (6) K <sub>222</sub> (16.7)	Cs <sub>2</sub> CO <sub>3</sub> (0.01) TEAOTf (0.3)	Cs <sub>2</sub> CO <sub>3</sub> (0.1) TEAOTf (3)
Amount of precursor (μmol)	3.7-5.5	0.28	2.8
Precursor concentration (mM)	12.3-18.3	28	9.3
Amount of Cu(Py) <sub>4</sub> (OTf) <sub>2</sub> (μmol)	20.6	0.68	6.8
Reaction volume (μL)	300	10	300
Temperature (°C)	110	140	140
Reaction time (min)	10	3	10
Radiochemical yield (RCY, %) <sup>a</sup>	4.4 ± 0.5	52 ± 8	50 ± 10
Radiochemical purity (RCP, %) <sup>b</sup>	>99	100	100
Product activity at EOS (GBq)	1.8-3.02	0.080-0.623	0.058-0.410
Molar activity (GBq/μmol) at EOS	100-308	77-854	20-46
Total preparation time (min)	75	26 <sup>c</sup>	58 <sup>c</sup>

<sup>a</sup>RCY was obtained by radio-HPLC isolation and is calculated by dividing activity of collected pure product by initial activity and correcting for decay. <sup>b</sup>RCP was determined by radio-HPLC. <sup>c</sup>Product formulation was not included. EOS = End of synthesis.

### 8.3.2 Translation of microscale conditions to vial-based reaction

Though we have previously shown the possibility of performing relatively large scale (multiple patient doses) in individual droplet reactions (83,99), we understand that droplet reactor systems are not currently widely available, preventing others from taking advantage of the improved synthesis process. Therefore, we decided to explore the potential of directly scaling the optimized droplet conditions to a vial-based (macroscale) reaction.



To continue to leverage the benefits of isolating the crude product via an analytical radio-HPLC system (i.e. excellent separation capabilities and shorter purification time), we minimized the reagent use in the macroscale reaction by employing only a 10X scale-up of all reagents (i.e. 3  $\mu\text{mol}$  of TEAOTf, 0.1  $\mu\text{mol}$  of  $\text{Cs}_2\text{CO}_3$ , 2.8  $\mu\text{mol}$  of precursor, 6.8  $\mu\text{mol}$  of  $\text{Cu}(\text{Py})_4(\text{OTf})_2$ ), while increasing the reaction volume 30x from a 10  $\mu\text{L}$  droplet to a 300  $\mu\text{L}$  vial-based reaction. In order to ensure a sufficiently small volume for injection into analytical HPLC, we needed to add a solvent-exchange step after the fluorination step (from reaction solvent to MeCN) and then an evaporative concentration step to reduce the volume. The overall process flow of the macroscale reactor synthesis is depicted in **Figure 8-14**.

The performance and duration of each step in the macroscale synthesis are summarized in **Table 8-11**. To enable comparisons to the droplet reaction, the synthesis used a comparable activity level (0.2-1.44 GBq) and same volume of aqueous [ $^{18}\text{F}$ ]fluoride. The aliquot was mixed with 5  $\mu\text{L}$  of PTC/base (10x more concentrated), added to the vial, and heated at 105  $^\circ\text{C}$  for evaporation. It took  $\sim 5$  min to evaporate most of the initial 25  $\mu\text{L}$  solution. Since a tiny amount of liquid remained on the bottom of the vial even after the extra heating time, azeotropic drying was conducted with 30  $\mu\text{L}$  of MeCN (repeated 3X), taking an additional  $\sim 6$  min. It took  $\sim 1$  min to cool down the vial to room temperature with water bath after each evaporation. Due to the macroscale reaction solution being more dilute than the microscale reaction (3x less due to 30x volume increase but only 10x reagent increase), we anticipated a potential decrease in reaction rate, as well as slower mixing and heating in the macroscale reactor, and a potential need to increase the reaction time. To monitor the progress of the macroscale reaction, 0.5  $\mu\text{L}$  samples were taken at different time points (3, 6, and 10 min) to measure the fluorination conversion (**Figure 8-15**). The reaction exhibited a high fluorination conversion of  $69 \pm 1\%$  ( $n = 4$ ) within the first 3 min, which increased to  $76 \pm 1\%$  ( $n = 4$ ) at 6 min. Beyond 10 min, the fluorination conversion only exhibited a slight increase, reaching  $77 \pm 2\%$  ( $n = 4$ ), prompting the reaction to be stopped after 10 min.

Following the 10 min reaction,  $81 \pm 5\%$  ( $n = 4$ ) of the starting activity (corrected for decay) was successfully extracted into a collection vial.  $17 \pm 4\%$  ( $n = 4$ ) of the starting activity remained in the reactor and the reactor cap, despite attempts to extract it using additional water (1 mL) or MeCN (1 mL). The collected activity was further diluted with DI water and loaded onto a light C18 cartridge, followed by washing with an additional 6 mL of DI water to remove unreacted [ $^{18}\text{F}$ ]fluoride. Around  $52 \pm 10\%$  ( $n = 4$ ) of the starting activity was trapped on the cartridge, and the waste activity resulting from the trapping and washing procedure was  $27 \pm 11\%$  ( $n = 4$ ) of the starting activity. Using 0.5 mL of MeCN, most of the activity was eluted off of the cartridge, i.e.,  $51 \pm 10\%$  of the starting activity was recovered with minimal residual activity on the cartridge ( $1 \pm 0\%$ ,  $n = 4$ ). The eluted activity was then concentrated to less than 0.1 mL by heating at  $60\text{ }^\circ\text{C}$ . The concentrated reaction mixture was purified using analytical-scale radio-HPLC in  $\sim 13$  min, resulting in an isolated RCY of  $50 \pm 10\%$  ( $n = 4$ , Table 2), suggesting negligible losses during the purification step. An example HPLC chromatogram during the purification process is shown in **Figure 8-17**. According to radio-HPLC measurements, the purified [ $^{18}\text{F}$ ]YH149 exhibited a radiochemical purity of 100% (**Figure 8-18**), and the molar activity at the end of synthesis was determined to be 20-46 GBq/ $\mu\text{mol}$ . The co-injection of purified [ $^{18}\text{F}$ ]YH149 and the reference standard confirm the chemical identity from this macroscale synthesis (**Figure 8-19**). The overall preparation time was  $\sim 58$  min, including 15 min for [ $^{18}\text{F}$ ]fluoride drying, 15 min for radiofluorination, 15 min for crude product concentration, and 13 min for purification.

To ensure a fair and direct comparison between the optimized droplet method and the translated vial-based method, both were conducted on the same day, employing identical amounts of [ $^{18}\text{F}$ ]fluoride loaded manually to eliminate any possible interference (like [ $^{18}\text{F}$ ]fluoride losses within fluidic pathways from a QMA process), and using the aliquots of the same batch of radioisotope, precursor and copper reagent. (The stock solutions for the precursor and  $\text{Cu}(\text{Py})_4(\text{OTf})_2$  had to be diluted to the appropriate concentration for the macroscale reaction.) The translated macroscale synthesis yielded a high RCY of  $50 \pm 10\%$  ( $n = 4$ ), nearly identical to

that achieved by the droplet method ( $52 \pm 8\%$ ,  $n = 4$ ). One notable difference is that the molar activity obtained from the translated macroscale synthesis was 4-18x lower than that achieved with the droplet method (20-46 GBq/ $\mu\text{mol}$  vs. 77-854 GBq/ $\mu\text{mol}$ ), despite starting with the same initial activity. This discrepancy suggests the presence of non-radioactive fluoride contamination, likely from the vial materials and/or reagents and solvents, and likely be overcome by starting with higher activity scale.<sup>(134)</sup> Another difference is that the translated macroscale synthesis needed double the preparation time due to additional required processes, such as azeotropic drying and crude product concentration. Interestingly, the purification time was shortened to 13 min (**Figure S9**) (compared to 20 min for the droplet method in **Figure 8-5**) since the product peak emerged earlier upon injection of the crude product when dissolved in 100% MeCN, versus when it is dissolved in the collection solution as was the case for the droplet reactions. This suggests that the purification time for the droplet reaction could in fact be further reduced by an optimized collection solution or HPLC mobile phase, shrinking the overall preparation time.

If we compare our droplet-to-vial translated protocol with the previously reported macroscale conditions of He *et al.* (326), interesting findings emerge. Though both approaches used the same reaction volume (300  $\mu\text{L}$ ), this approach required lower concentrations of precursor (9.3 mM vs. 12.3 mM) and  $\text{Cu}(\text{Py})_4(\text{OTf})_2$  (22.7 mM vs. 68.7 mM), yet it delivered an impressive 11-fold increase in RCY. We should point out that the amount of PTC (3  $\mu\text{mol}$ ) and base (0.1  $\mu\text{mol}$ ) used in the translated vial-based method was slightly lower than the quantities of PTC/base typically utilized to achieve efficient [ $^{18}\text{F}$ ]fluoride elution from QMA cartridges for Cu-mediated synthesis in the same co-solvent system, e.g. as reported by Zlatopolskiy *et al.* (using  $\sim 14$   $\mu\text{mol}$  of  $\text{TEAHCO}_3$ )(328) and Hoffmann *et al.* (using 4  $\mu\text{mol}$  of  $\text{TEAOTf}$ ).(318) Since a lower amount of PTC and base can adversely impact the efficiency of eluting [ $^{18}\text{F}$ ]fluoride from a QMA cartridge, we performed an additional study of different elution conditions (in MeOH:water solvent mixture) and found that >99% elution efficiency could be achieved with an increased amount (12  $\mu\text{mol}$ ) of  $\text{TEAOTf}$  and no change in the amount of  $\text{Cs}_2\text{CO}_3$  (0.1  $\mu\text{mol}$ ). We tested in droplet

reactions the effect of the larger TEAOTf amount and found comparable performance as using the 3  $\mu\text{mol}$  optimized condition. Thus, these reports suggest that the current translated vial-based recipe would be compatible with conventional synthesizers using QMA-cartridge processing, without significant need for further adjustments other than the drying process for the [ $^{18}\text{F}$ ]fluoride / PTC / base complex.

Additionally, these results represent a successful demonstration of using droplet-based methods for optimization (which can be performed with high throughput and very low reagent consumption), and then adapting those optimal reaction conditions to a macroscale process with minimal modification. This shows the current utility of using high-throughput droplet-based reaction optimization, even when the vast majority of installed radiotracer production systems currently rely on vial-based reactions. The 300  $\mu\text{L}$  reaction volume (selected to match previously reported vial-based conditions), though at the low end of the volume capability of modern radiosynthesizers (300-500  $\mu\text{L}$ ) (310,315,326,329,330), suggests that this protocol could be automated using widely-available radiosynthesis systems easily.

Building upon the successful macroscale translation experience presented in this study, further investigations could be conducted to explore the versatility of micro-to-macroscale translation for other tracers synthesized through Cu-mediated routes, such as [ $^{18}\text{F}$ ]FDOPA and [ $^{18}\text{F}$ ]FBnTP, as well as different radiolabeling mechanisms like [ $^{18}\text{F}$ ]FET, [ $^{18}\text{F}$ ]Flumazenil, and [ $^{18}\text{F}$ ]PBR06. This would contribute to expanding our understanding of the translation process and its applicability to various radiotracers. Moreover, the scaling up of radiosynthesis using the droplet-based optimized condition on a conventional automated system to achieve multiple clinical doses would be of great interest to the radiochemistry community. Currently, the field has extremely limited approaches for increasing optimization throughput that are applicable to macroscale radiosynthesis, and thus this droplet-to-vial based approach demonstrated here could fill a much-needed gap to streamline the development and production of novel tracers from initial synthesis through clinical studies.

## 8.4 Conclusions

In this work, we used a novel droplet-based high-throughput technique to perform a rapid optimization of the Cu-mediated radiosynthesis for the recently-reported monoacylglycerol lipase PET tracer [ $^{18}\text{F}$ ]YH149. A total of 117 experiments were performed across 5 days to explore 36 distinct conditions, while consuming <15 mg total amount of precursor. The optimized synthesis exhibited high radiochemical yield up to  $52 \pm 8\%$  ( $n = 4$ ) in a 26 min process, with excellent radiochemical purity (100%) and high molar activity (77-854 GBq/ $\mu\text{mol}$ ), providing significant improvement upon the originally reported conditions based on a 300  $\mu\text{L}$  vial-based reaction (with RCY of  $4.4 \pm 0.5\%$ ,  $n = 5$ ). In conjunction with prior results of droplet-based optimization for [ $^{18}\text{F}$ ]FDOPA(291) and [ $^{18}\text{F}$ ]FBnTP(94), the results suggest that the droplet-based technique is well-suited to Cu-mediated radiosyntheses of  $^{18}\text{F}$ -labeled tracers.

In addition, we demonstrated for the first time the successful translation of the optimized droplet conditions to a vial-based (macroscale) reaction. By simply scaling reagent amounts by 10x and extending reaction time to an optimal value based on a single time-course study, we observed that a 300  $\mu\text{L}$  vial-based reaction had similar RCY to the microscale method i.e.,  $50 \pm 10\%$  ( $n = 4$ ), excellent radiochemical purity (100%), and acceptable molar activity (20-46 GBq/ $\mu\text{mol}$ ). It is likely that molar activity would be increased by starting with higher initial activity. While macroscale studies were limited by availability of precursor, this work establishes a connection between microscale and macroscale reactions, and suggests the possibility of a rapid and economical approach for novel tracer development, i.e., optimizing radiochemistry on a high-throughput microdroplet platform and then performing straightforward translation to vial-based systems to enable wider applicability to the existing install base of radiosynthesizer technology.

## 8.5 Appendix

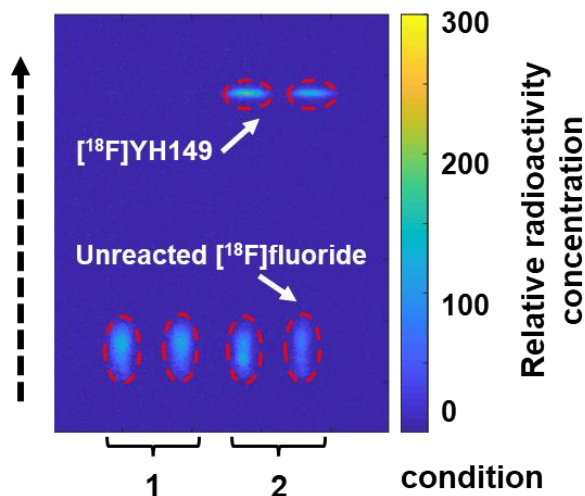
### 8.5.1 Optimization of [ $^{18}\text{F}$ ]YH149 synthesis on droplet reactors

#### 8.5.1.1 Initial conditions

**Table 8-3 Results of initial experiments.**

**Condition 1** was adapted from the macroscale conditions reported by He et al. for the Cu-mediated radiosynthesis of [<sup>18</sup>F]YH149(331) by reducing reagent amounts by 10x (30x for Cu(OTf)<sub>2</sub>(Py)<sub>4</sub>) and volume by 30x. **Condition 2** was taken from a previous study where we optimized the Cu-mediated radiofluorination step for [<sup>18</sup>F]FDOPA, and we simply changed the precursor to that for [<sup>18</sup>F]YH149(291). Abbreviations: PTC = phase transfer catalyst.

Adapted reference condition	1	2
PTC (amount (μmol))	K <sub>222</sub> (1.7), K <sub>2</sub> C <sub>2</sub> O <sub>4</sub> (0.6)	TEAOTf (0.3)
Base (amount (μmol))	K <sub>2</sub> CO <sub>3</sub> (0.07)	Cs <sub>2</sub> CO <sub>3</sub> (0.01)
Amount of precursor (μmol) [mg]	0.45 [0.24]	0.45 [0.24]
Amount of Cu(OTf) <sub>2</sub> (Py) <sub>4</sub> (μmol)	0.68	0.68
10 μL of solvent	DMA/nBuOH (2:1, v/v)	DMA/Py (96:4, v/v)
Temperature (°C)	110	110
Reaction time (min)	5	5
<b>Radiosynthesis performance (n = 2)</b>		
Starting activity (MBq)	45 ± 1	46 ± 1
Fluorination conversion (%)	0	44 ± 1
Collection efficiency (%), decay-corrected	84 ± 1	81 ± 2
Crude RCY (%), decay-corrected	0	36 ± 2

**Figure 8-6 Analysis of crude fluorination products from initial experiments using multi-lane TLC with Cerenkov luminescence imaging (CLI) readout.**

### 8.5.1.2 Influence of solvent type

**Table 8-4 Impact of fluorination solvent on the performance of the droplet radiosynthesis of [<sup>18</sup>F]YH149.**

Solvent <sup>a</sup>	Fluorination conversion (%)	Collection efficiency (%)	Crude RCY (%)
DMF	11 ± 2	64 ± 4	7 ± 1
DMA	43 ± 3	69 ± 3	29 ± 3
DMSO	3 ± 0	70 ± 2	2 ± 0
NMP	36 ± 1	75 ± 6	27 ± 2
DMA/nBuOH (v/v, 2:1)	49 ± 2	75 ± 1	35 ± 0
DMA/nBuOH (v/v, 2:1) <sup>b</sup>	0	84 ± 1	0

<sup>a</sup>All reactions were performed with 0.3 μmol of TEAOTf, 0.01 μmol of Cs<sub>2</sub>CO<sub>3</sub>, 0.18 μmol of precursor and 0.68 μmol of Cu(OTf)<sub>2</sub>(Py)<sub>4</sub> in 10 μL of solvent/pyridine (96:4, v/v) at 110°C for 5 min (n = 3 replicates each condition). <sup>b</sup>The reaction was performed in the absence of pyridine (n = 2 replicates).

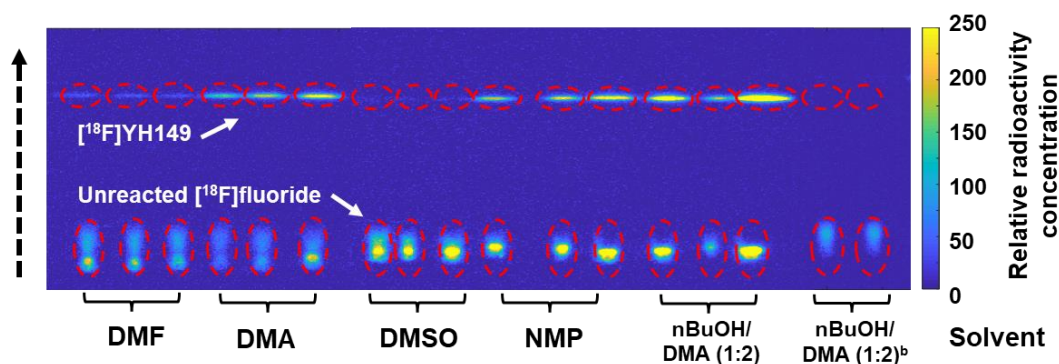


**Figure 8-7 High-throughput analysis of crude fluorination products (from study of solvent) using multi-lane TLC with CLI readout.**

### 8.5.1.3 Influence of type of phase transfer catalyst (PTC)/base

**Table 8-5 Impact of type of PTC/base on the performance of the droplet radiosynthesis of [<sup>18</sup>F]YH149.**

PTC/base <sup>a</sup>	Fluorination conversion (%)	Collection efficiency (%)	Crude RCY (%)
TEAOTf/Cs <sub>2</sub> CO <sub>3</sub>	44 ± 3	71 ± 3	31 ± 3
TBAOTf/Cs <sub>2</sub> CO <sub>3</sub>	36 ± 2	73 ± 8	26 ± 4
TEAOTf	36 ± 1	70 ± 1	25 ± 1
TBAOTf	28 ± 7	66 ± 6	19 ± 6
TBAHCO <sub>3</sub>	18 ± 1	77 ± 2	14 ± 1

<sup>a</sup>All reaction was performed with 0.3 μmol of PTC, 0.01 μmol of Cs<sub>2</sub>CO<sub>3</sub> (if applied), 0.18 μmol of precursor and 0.68 μmol of Cu(OTf)<sub>2</sub>(Py)<sub>4</sub> in 10 μL of DMA/nBuOH/pyridine (64:32:4, v/v) at 110°C for 5 min (n = 3 replicates each condition).

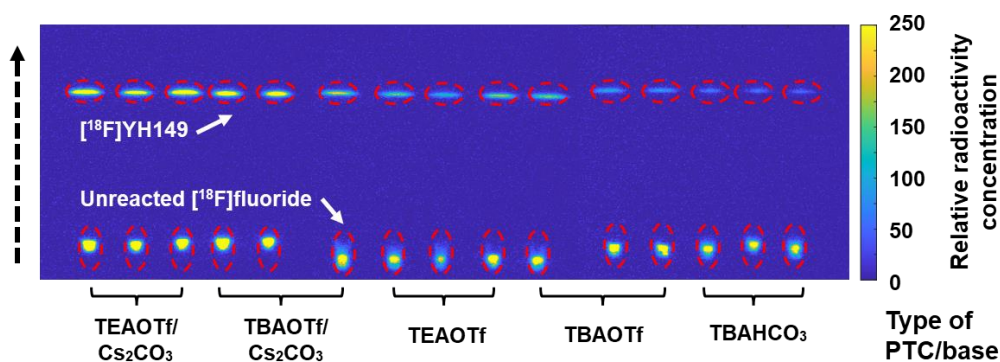


Figure 8-8 High-throughput analysis of crude fluorination products (from study of PTC/base type) using multi-lane TLC with CLI readout.

#### 8.5.1.4 Impact of fluorination temperature and base type

Table 8-6 Impact of fluorination temperature (when using TEAOTf/Cs<sub>2</sub>CO<sub>3</sub>) on the performance of the droplet radiosynthesis of [<sup>18</sup>F]YH149.

Fluorination temperature (°C) <sup>a</sup>	Fluorination conversion (%)	Collection efficiency (%)	Crude RCY (%)
100	29 ± 1	70 ± 0	21 ± 1
110	49 ± 1	68 ± 1	33 ± 1
115	58 ± 1	65 ± 2	38 ± 2
120	64 ± 4	63 ± 2	40 ± 2
130	70 ± 4	59 ± 4	41 ± 5
140	78 ± 1	55 ± 1	43 ± 1

<sup>a</sup>All reaction was performed with 0.3 μmol of PTC, 0.01 μmol of Cs<sub>2</sub>CO<sub>3</sub>, 0.18 μmol of precursor and 0.68 μmol of Cu(OTf)<sub>2</sub>(Py)<sub>4</sub> in 10 μL of DMA/nBuOH/pyridine (64:32:4, v/v) at investigating temperature for 5 min (n = 3 replicates each condition).



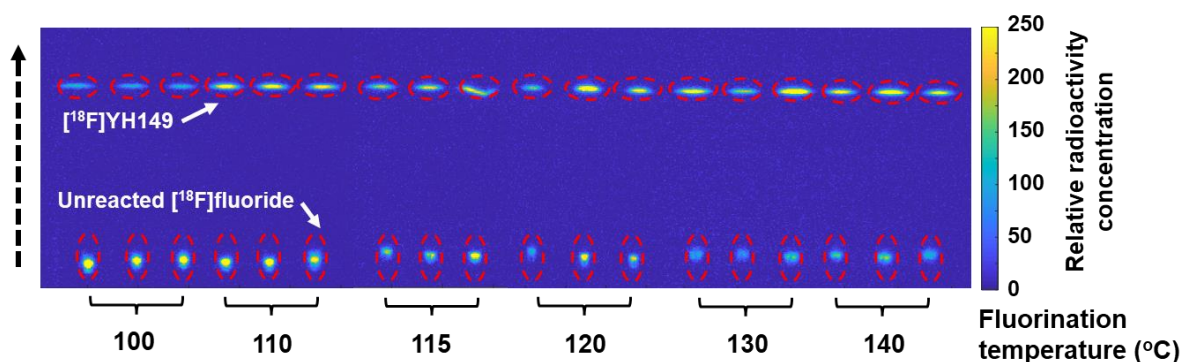


Figure 8-9 High-throughput analysis of crude fluorination products (from study of reaction temperature with TEAOTf/Cs<sub>2</sub>CO<sub>3</sub>) using multi-lane TLC with CLI readout.

Table 8-7 Impact of fluorination temperature (when using TEAOTf/K<sub>2</sub>CO<sub>3</sub>) on the performance of the droplet radiosynthesis of [<sup>18</sup>F]YH149.

Fluorination temperature (°C) <sup>a</sup>	Fluorination conversion (%)	Collection efficiency (%)	Crude RCY (%)
120	66 ± 3	59 ± 2	39 ± 3
140	67 ± 1	57 ± 3	38 ± 2
150	68 ± 1	52 ± 2	35 ± 1
160	58 ± 4	46 ± 4	26 ± 2

<sup>a</sup>All reaction was performed with 0.3 μmol of PTC, 0.01 μmol of K<sub>2</sub>CO<sub>3</sub>, 0.18 μmol of precursor and 0.68 μmol of Cu(OTf)<sub>2</sub>(Py)<sub>4</sub> in 10 μL of DMA/nBuOH/pyridine (64:32:4, v/v) at investigating temperature for 5 min (n = 3 replicates each condition).

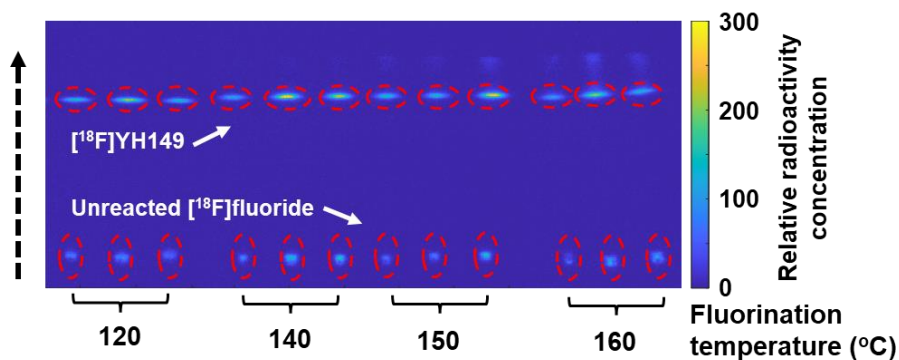


Figure 8-10 High-throughput analysis of crude fluorination products (from study of reaction temperature with TEAOTf/K<sub>2</sub>CO<sub>3</sub>) using multi-lane TLC with CLI readout.

#### 8.5.1.5 Impact of reaction time

**Table 8-8 Impact of reaction time on the performance of the droplet radiosynthesis of [<sup>18</sup>F]YH149.**

Reaction time (min) <sup>a</sup>	Fluorination conversion (%)	Collection efficiency (%)	Crude RCY (%)
0.5	35 ± 1	74 ± 0	26 ± 1
1	41 ± 2	63 ± 0	26 ± 2
2	61 ± 1	63 ± 3	39 ± 2
3	66 ± 3	64 ± 0	42 ± 2
5	68 ± 1	52 ± 2	36 ± 2
7	73 ± 6	49 ± 3	36 ± 5

<sup>a</sup>All reaction was performed with 0.3 μmol of PTC, 0.01 μmol of K<sub>2</sub>CO<sub>3</sub>, 0.18 μmol of precursor and 0.68 μmol of Cu(OTf)<sub>2</sub>(Py)<sub>4</sub> in 10 μL of DMA/nBuOH/pyridine (64:32:4, v/v) at 140°C for investigating reaction time (n = 3 replicates each condition).

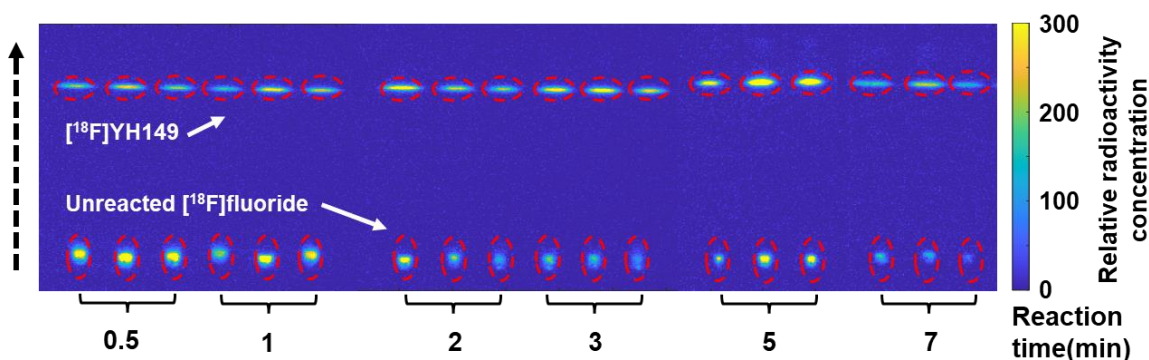


**Figure 8-11 High-throughput analysis of crude fluorination products (from study of reaction time) using multi-lane TLC with CLI readout.**

### 8.5.1.6 Influence of amount of base

**Table 8-9 Impact of amount of base on the performance of the droplet radiosynthesis of [<sup>18</sup>F]YH149.**

Base amount (nmol) <sup>a</sup>	Fluorination conversion (%)	Collection efficiency (%)	Crude RCY (%)
10	73 ± 6	49 ± 3	36 ± 5
20 <sup>b</sup>	68 ± 7	47 ± 1	32 ± 4
30 <sup>b</sup>	61 ± 2	50 ± 2	30 ± 2

<sup>a</sup>All reaction was performed with 0.3 μmol of PTC, investigating amount of K<sub>2</sub>CO<sub>3</sub>, 0.18 μmol of precursor and 0.68 μmol of Cu(OTf)<sub>2</sub>(Py)<sub>4</sub> in 10 μL of DMA/nBuOH/pyridine (64:32:4, v/v) at 140°C for 7 min (n = 3 replicates each condition). <sup>b</sup>n = 2 replicates each condition.

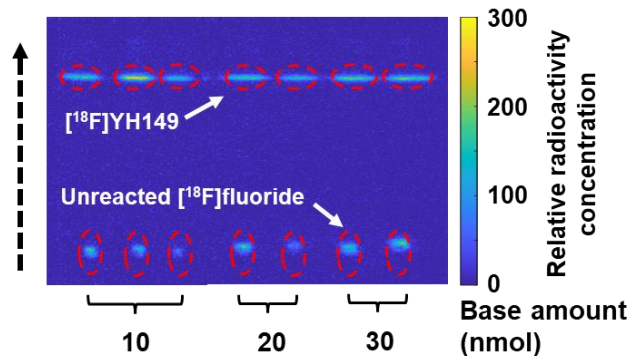


Figure 8-12 High-throughput analysis of crude fluorination products (from study of base amount with  $K_2CO_3$ ) using multi-lane TLC with CLI readout.

### 8.5.1.7 Influence of amount of precursor

Table 8-10 Influence of amount of precursor on the performance of the droplet radiosynthesis of  $[^{18}F]YH149$ .

Amount of precursor (mg) <sup>a</sup>	Fluorination conversion (%)	Collection efficiency (%)	Crude RCY (%)
0.05	66 ± 0	53 ± 4	35 ± 2
0.1	64 ± 5	60 ± 6	38 ± 1
0.15	62 ± 2	68 ± 4	42 ± 4
0.15 <sup>b</sup>	80 ± 2	71 ± 3	56 ± 3
0.15 <sup>c</sup>	71 ± 5	57 ± 1	40 ± 4
0.2	60 ± 1	61 ± 2	36 ± 1
0.25	59 ± 2	61 ± 1	36 ± 1
0.3	64 ± 3	62 ± 2	39 ± 3

<sup>a</sup>All reaction was performed with 0.3 μmol of PTC, 0.01 μmol of  $K_2CO_3$ , investigating amount of precursor and 0.68 μmol of  $Cu(OTf)_2(Py)_4$  in 10 μL of DMA/nBuOH (v/v, 2:1) along with 4% of pyridine (v/v) at 140°C for 3 min (n=3 replicates each condition). <sup>b</sup>The reaction was performed with  $Cs_2CO_3$  instead of  $K_2CO_3$ , and was repeated n = 4 times. <sup>c</sup>The reaction was performed in presence of DMA/nBuOH/pyridine (64:32:4, v/v), and was repeated n = 4 times.

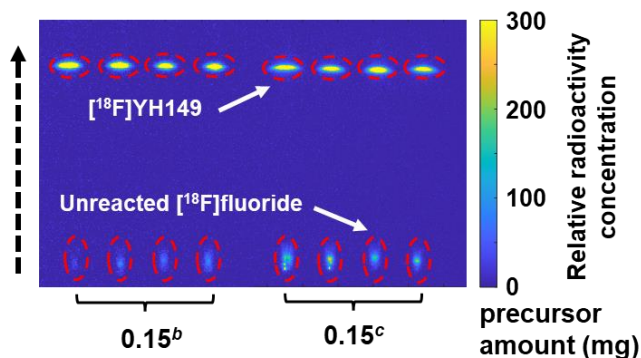


Figure 8-13 High-throughput analysis of crude fluorination products (from additional tested conditions) using multi-lane TLC with CLI readout.

## 8.5.2 Macroscale synthesis performance

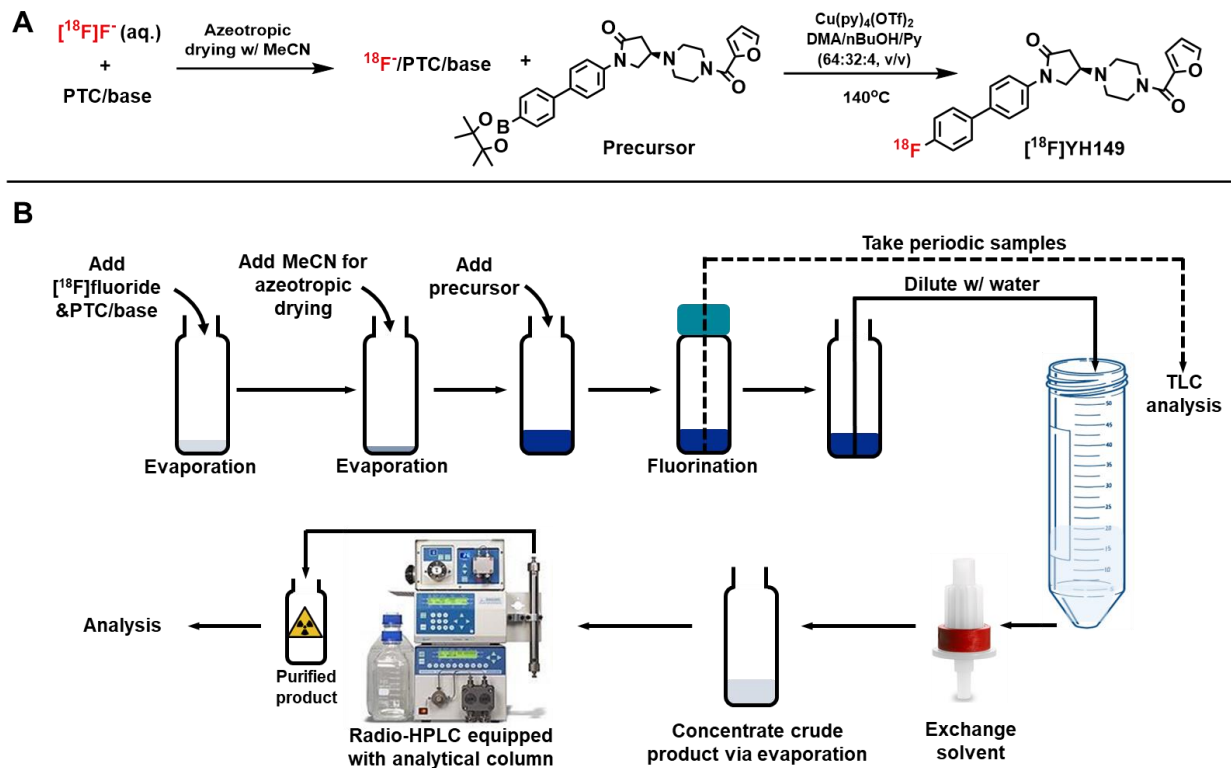


Figure 8-14 Implementation of radiosynthesis in a vial-based (macroscale) reaction.

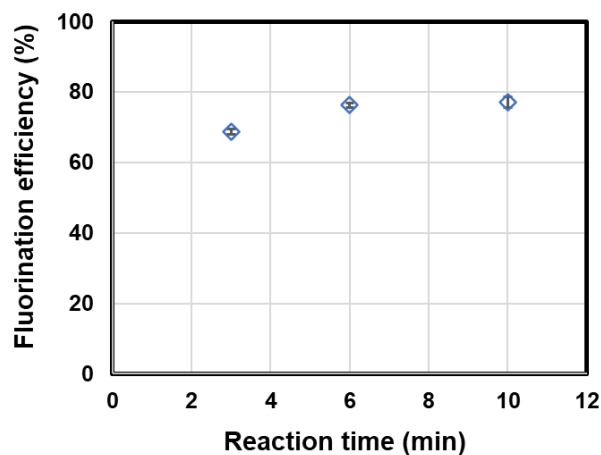


Figure 8-15 Impact on fluorination efficiency of different reaction times ( $n = 4$ ) in the macroscale synthesis.

**Table 8-11 Performance of translated (droplet to vial) radiosynthesis of [<sup>18</sup>F]YH149. Activity measurements are expressed as fractions of starting activity (corrected for decay).**

Process	Measurement	Result
<b>[<sup>18</sup>F]F<sup>-</sup> drying</b>	Starting activity (GBq)	0.2-1.4
	Duration for evaporating initial 25 µL [ <sup>18</sup> F]F <sup>-</sup> /PTC/base (min)	5
	Duration for cooling down (min)	1
	3 X Duration for additional MeCN (30 µL) azeotropic evaporation (min)	6
	3 X Duration for cooling down (min)	3
	Duration of the whole drying process (min)	15
<b>Radio-fluorination</b>	Activity of 3-min sample (%)	0.3 ± 0.2
	Activity of 6-min sample (%)	0.4 ± 0.2
	Activity of 10-min sample (%)	0.3 ± 0.2
	Collected activity from reactor (%)	81 ± 5
	Residual activity in reactors after extraction (%)	17 ± 4
	Duration (min)	15
<b>Exchange solvent to MeCN and concentrate to &lt;0.1 mL</b>	Activity before loading on cartridge (%)	81 ± 5
	Activity trapped on light C18 (%)	52 ± 10
	Waste from trapping and washing process (%)	27 ± 11
	Eluted activity with 0.5 mL of MeCN (%)	51 ± 10
	Residue activity on cartridge (%)	1 ± 0
	Duration of the solvent-exchange process (min)	10
	Duration of MeCN evaporation	5
<b>Purification</b>	Isolated [ <sup>18</sup> F]YH149 from radio-HPLC (%)	50 ± 10
	Duration (min)	13
	Total preparation time (min)	58

### 8.5.3 Calibration curve to determine molar activity

The same analytical scale radio-HPLC system was used to determine the molar activity of the purified [<sup>18</sup>F]YH149. The area under the curve for the UV absorbance peak was determined for a range of mole amounts of YH149 reference standard (0.06-0.98 nmol) to generate a linear

calibration curve (**Figure S11**). This curve was then used to determine the mass of YH149 in the unknown sample, and subsequently compute the molar activity, following standard procedures.

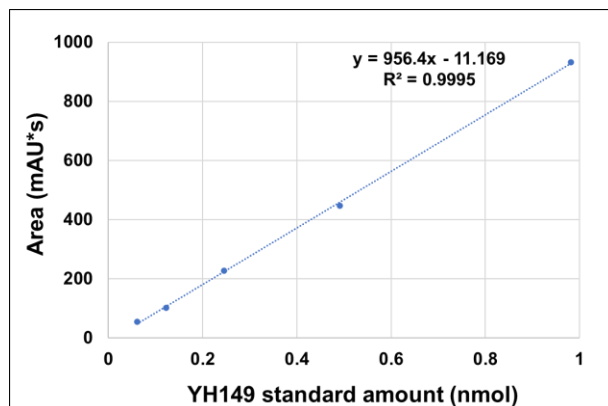


**Figure 8-16** Calibration curve of YH149 reference standard (254 nm wavelength).

#### 8.5.4 Example HPLC chromatograms from translated synthesis

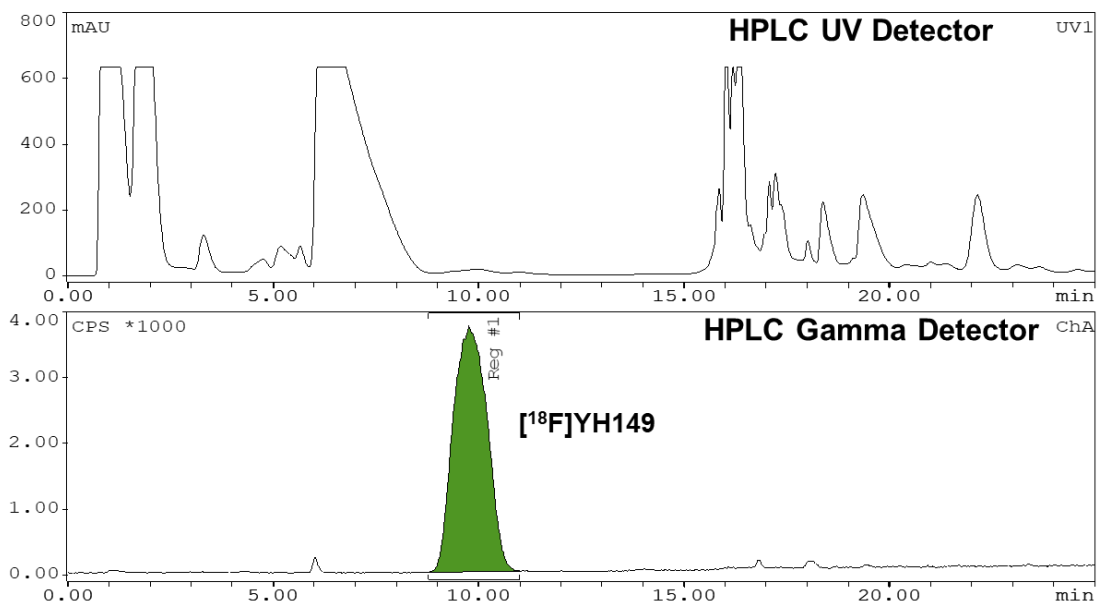


**Figure 8-17** Example radio-HPLC chromatogram of crude [<sup>18</sup>F]YH149 from macroscale radiosynthesis.

The retention time was 10.0 min, earlier than that with microscale purification ( $t_R=18.6$  min) because the crude sample was injected in 100  $\mu$ L MeCN (versus 80  $\mu$ L of the HPLC mobile phase for the microscale synthesis).

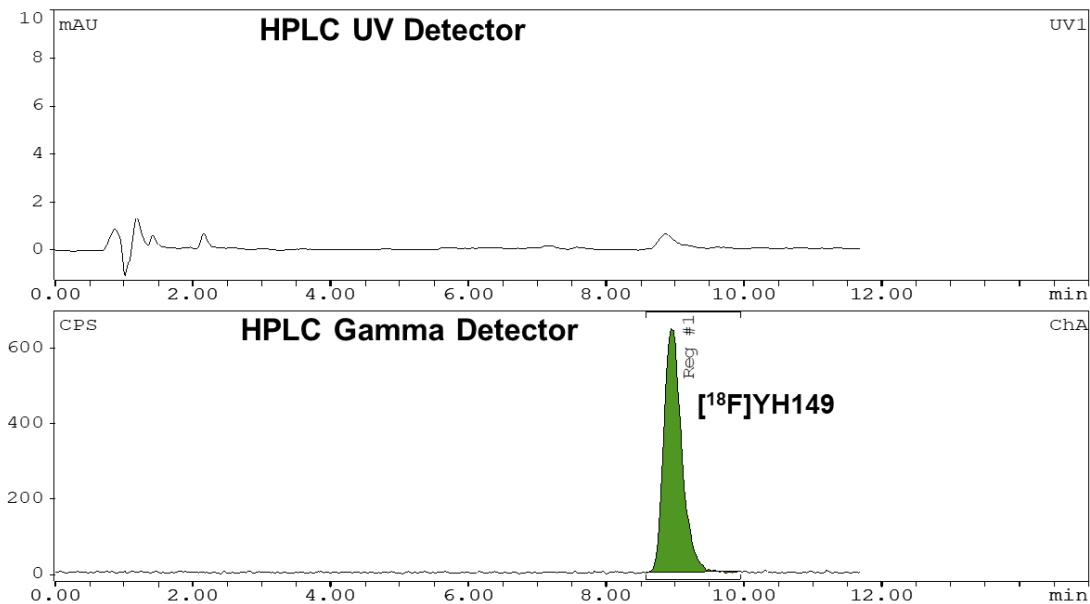


**Figure 8-18** Example radio-HPLC chromatogram of purified [<sup>18</sup>F]YH149 from macroscale radiosynthesis.

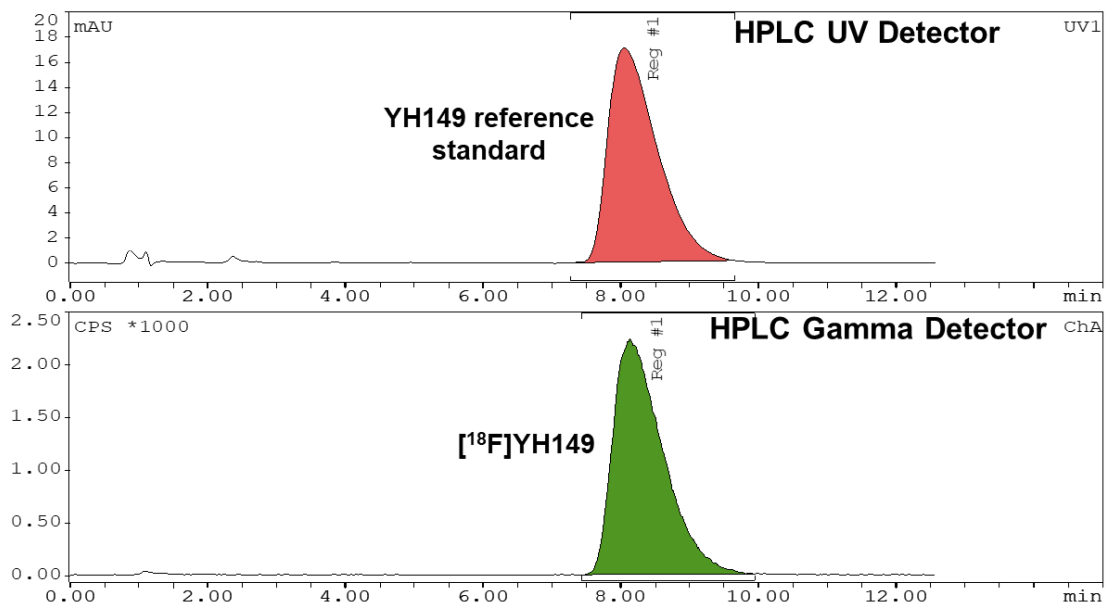


**Figure 8-19** Example radio-HPLC chromatogram of co-injection of purified [<sup>18</sup>F]YH149 (from macroscale radiosynthesis) and reference standard.

## Chapter 9: A rapid and systematic approach for the optimization of radio-TLC resolutions

### 9.1 Introduction

The analysis of radiolabelled species is vital in applications encompassing the development of novel radiopharmaceuticals (e.g., synthesis optimization)(95,332–335), quality control analysis of formulated radiopharmaceuticals(266,336), and the analysis of radiometabolites(261,337). Separation can be challenging as impurities or metabolites may be numerous, and many may have structural similarities to the radiopharmaceutical.

Radiopharmaceutical analysis is traditionally performed using chromatographic methods such as radio high-performance liquid chromatography (radio-HPLC) and radio thin-layer chromatography (radio-TLC). Though it exhibits high resolution, radio-HPLC has been criticized because species such as [<sup>18</sup>F]fluoride can be trapped in the column. Thus, based on detectors at the column output, the chromatogram may not accurately reflect the actual radiochemical composition(338). Traditional radioactivity scanning readouts used in radio-TLC circumvent this issue by assessing the entire distribution of analytes along the whole plate. However, radio-TLC can suffer from lower resolution than radio-HPLC. Imaging-based TLC readout methods can improve readout resolution compared to scanning detectors(96,339). Still, they may not offer improvement if the underlying chromatographic resolution of the separation process on the TLC plate is poor.

Though factors such as separation length can improve resolution, short plate lengths are usually used because of the need for rapid separations when using short-lived radioisotopes. In principle, other factors like stationary phase could be varied. Still, the radiochemistry field has predominantly used silica (normal-phase) plates(340–344) and, occasionally, C<sub>18</sub> (reverse-phase) plates(345), instead relying on adjustment of mobile phase to improve resolution.



Due to the limited knowledge of analytes (e.g., synthesis impurities or metabolites), it is often difficult to determine which mobile phases are most appropriate for crude radiopharmaceutical mixtures. Traditionally, mobile phases for radio-TLC are selected from the literature for a radiopharmaceutical structurally similar to the one of interest. Many reports use an organic solvent mixed with water (i.e., with the water added to increase migration for highly polar species)(346–349). However, we recently showed that water could lead to the complex behavior of species on the plate(350), including migration of multiple bands corresponding to [<sup>18</sup>F]fluoride (normally sequestered at the origin), and purely organic mobile phases would be preferable.

A systematic approach called PRISMA was developed to facilitate optimal mobile phase selection without needing prior knowledge about the structures and properties of analytes(351). Herein, we describe, for the first time in radiochemistry, the use of the PRISMA method for the rapid selection of mobile phase conditions to achieve baseline separation of the desired radiopharmaceutical from both radioactive impurities (e.g., free radionuclide and other radioactive species) and UV-active non-radioactive impurities (e.g., precursor or precursor-derived impurities). Multiple radiopharmaceuticals with various chemical characteristics, prepared from crude radiosyntheses (which contain many impurities with high structural and chemical similarity to the desired product), are examined to illustrate this approach.

## 9.2 Experimental

### 9.2.1 Materials

All reagents and solvents were obtained from commercial suppliers. 2,3-dimethyl-2-butanol (thexyl alcohol; anhydrous, 98%), 4,7,13,16,21,24-hexaoxa-1,10-diazabicyclo[8.8.8]hexacosane (K<sub>222</sub>; 98%), acetic acid (AcOH; glacial, >99.9%), acetone (suitable for HPLC, >99.9%), acetonitrile (MeCN; anhydrous, 99.8%), ammonium molybdate (99.98% trace metal basis), cerium sulfate, cesium carbonate (Cs<sub>2</sub>CO<sub>3</sub>; 99.995%), chloroform (>99.5%, contains 100-200 ppm amylenes as stabilizer), dichloromethane (DCM; anhydrous,

>99.8% contains 40-150 ppm amylene as stabilizer), diethyl ether (Et<sub>2</sub>O; >99.9% inhibitor free), N,N-dimethylacetamide (DMA; extra dry, 99.8%), dimethylsulfoxide (DMSO; anhydrous, >99.9%), hydrochloric acid (HCl; 36.5-38%), methanol (MeOH; anhydrous, 99.8%), n-butanol (n-BuOH; anhydrous, 99.8%), n-hexanes (98%), ninhydrin (suitable for amino acid detection), n-methyl-2-pyrrolidone (NMP; anhydrous, 99.5%), pyridine (anhydrous, 99.8%), sulfuric acid (99.9%), tetrahydrofuran (THF; anhydrous, >99.9% inhibitor free), tetrakispyridine copper(II) trifluoromethanesulfonate (Cu(py)<sub>4</sub>(OTf)<sub>2</sub>; 95%), toluene (anhydrous, 99.8%), and water (H<sub>2</sub>O; suitable for ion chromatography) were purchased from Sigma-Aldrich (St. Louis, MO, USA).

(S)-2,3-dimethoxy-5-[3-[[4-methylphenyl]-sulfonyl]oxy]-propyl]-N-[[1-(2-propenyl)-2-pyrrolidinyl]methyl]-benzamide ([<sup>18</sup>F]Fallypride precursor, >95%), 5-(3-fluoropropyl)-2,3-dimethoxy-N-(((2S)-1-(2-propenyl)-2-pyrrolidinyl)methyl)benzamide (Fallypride reference standard, >95%), 2-((2,5-dimethoxybenzyl)(2-phenoxyphenyl)amino)-2-oxoethyl 4-methylbenzenesulfonate ([<sup>18</sup>F]PBR06 precursor, >95%), 2-fluoro-N-(2-methoxy-5-methoxybenzyl)-N-(2-phenoxyphenyl)acetamide (PBR06 reference standard, >95%), acetamide, N-[2-[2-[[4-methylphenyl]sulfonyl]oxy]ethoxy]phenyl]methyl]-N-(4-phenoxy-3-pyridinyl) ([<sup>18</sup>F]FEPPA precursor, >90%), N-acetyl-N-(2-fluoroethoxybenzyl)-2-phenoxy-5-pyridinamine (FEPPA reference standard, >95%), 3-nitro-5-[2-(2-pyridinyl)ethynyl]benzonitrile ([<sup>18</sup>F]FPEB precursor, >95%), 3-fluoro-5-[(pyridin-2-yl)ethynyl]benzonitrile ([<sup>18</sup>F]FPEB reference standard, >95%), ethyl-(2S)-3-[4,5-bis[(2-methylpropan-2-yl)oxycarbonyloxy]-2-trimethylstannylphenyl]-2-formamidopropanoate ([<sup>18</sup>F]FDOPA precursor, >95%), (2S)-2-amino-3-(2-fluoro-4,5-dihydroxyphenyl)propanoic acid ([<sup>18</sup>F]FDOPA reference standard, >95%), and tetrabutylammonium bicarbonate (TBAHCO<sub>3</sub>; 75 mM in ethanol), were purchased from ABX Advanced Biochemical Compounds (Radeberg, Germany). Silica gel 60 F<sub>254</sub> sheets (aluminum backing, 5 cm x 20 cm) were purchased from Merck KGaA (Darmstadt, Germany). Silica with concentration zone (Silica 60 with diatomaceous earth zone), TLC plates, channeled F<sub>254</sub>, were purchased from Sorbtech (Norcross, GA, USA). Glass microscope slides (76.2 mm x 50.8 mm, 1

mm thick) were obtained from C&A Scientific (Manassas, VA, USA). UV-C lightbulbs (25W, 254 nm with socket) and pendant lamp sockets (light cord with on/off switch) were purchased from Amazon (Seattle, WA, USA).

No-carrier-added [ $^{18}\text{F}$ ]fluoride was produced by the (p, n) reaction of [ $^{18}\text{O}$ ]H<sub>2</sub>O (98% isotopic purity, Huayi Isotopes Co., Changshu, Jiangsu, China) in an RDS-111 cyclotron (Siemens, Knoxville, TN, USA) at 11 MeV, using a 1.2-mL silver target with havar foil.

### 9.2.2 Preparation of radiopharmaceuticals and standard mixtures

A series of radiopharmaceuticals were prepared using droplet radiochemistry methods on Teflon-coated silicon surface tension trap chips(80,83(p),352) to illustrate PRISMA's ability to optimize mobile phases for radiopharmaceutical analysis. Detailed protocols for the preparation of [ $^{18}\text{F}$ ]FEPPA, [ $^{18}\text{F}$ ]PBR-06, [ $^{18}\text{F}$ ]Fallypride, and [ $^{18}\text{F}$ ]FDOPA have been previously reported(93,291).

Crude [ $^{18}\text{F}$ ]FPEB was prepared by adding an 8  $\mu\text{L}$  droplet of [ $^{18}\text{F}$ ]fluoride/[ $^{18}\text{O}$ ]H<sub>2</sub>O (37-55 MBq [1-1.5 mCi]; mixed with 120 nmol of Cs<sub>2</sub>CO<sub>3</sub> and 360 nmol of K<sub>222</sub>) and drying at 105 °C for 1 min. Then, the fluorination step was performed by adding a 10  $\mu\text{L}$  droplet containing 200 nmol of FPEB precursor dissolved in DMSO to the dried [ $^{18}\text{F}$ ]fluoride residue and reacting at 120 °C for 5 min. The crude product was collected by dispensing 10  $\mu\text{L}$  of 9:1 (v/v) MeOH:H<sub>2</sub>O to the reaction site and aspirating the volume. This process was repeated 6x for 60  $\mu\text{L}$  of collected crude product.

Stock solutions of reference standards were prepared at 20 mM concentrations. 5 mg of Fallypride was added to 685  $\mu\text{L}$  of MeOH. 5 mg of PBR-06 was added to 632  $\mu\text{L}$  MeOH. 5 mg of FEPPA was added to 657  $\mu\text{L}$  of MeOH. 5 mg of FPEB was added to 1130  $\mu\text{L}$  of MeOH. 5 mg of FDOPA was added to 1167  $\mu\text{L}$  of MeOH.

### 9.2.3 TLC spotting, developing, and readout

TLC plates were cut (L x W, 6 cm x 3 cm), then marked with a pencil at 1 cm (origin line) and 5 cm (development line) from the bottom edge. 1  $\mu\text{L}$  of the relevant crude radiopharmaceutical sample was applied to the plate via a micro-pipette. Standard and precursor

samples were spotted in adjacent individual lanes. The spots were then dried under a gentle stream of nitrogen for 1 min. After development using a PRISMA-determined mobile phase (see below), the plates were dried under a gentle stream of nitrogen for 3 min and then visualized via Cerenkov luminescence imaging (CLI)(96,130) with 1 min exposure and UV imaging for 7 ms exposure, as previously reported(350).

Following CLI and UV imaging, some cases used TLC stains by dipping the developed TLC plates in the stain of interest (Hanessian stain or ninhydrin). Gentle heating of the TLC plate at 80 °C by a hot plate was used to stain the TLC plates. Hanessian stain was prepared according to the literature(353).

#### **9.2.4 Radio-HPLC analysis of [<sup>18</sup>F]Fallypride**

As a performance comparison, some crude [<sup>18</sup>F]Fallypride microscale reactions were analyzed with radio-TLC and radio-HPLC. The radio-HPLC system setup comprised a Smartline HPLC system (Knauer, Berlin, Germany) equipped with a degasser (Model 5050), pump (Model 1000), UV detector (254 nm; Eckert & Ziegler, Berlin, Germany), gamma-radiation detector (BFC-4100, Bioscan, Inc., Poway, CA, USA), and counter (BFC-1000; Bioscan, Inc., Poway, CA, USA). A C<sub>18</sub> Gemini column was used for separations (Kinetex, 250 × 4.6 mm, 5 μm, Phenomenex, Torrance, CA, USA). Samples were separated with a mobile phase of 60% MeCN in 25 mM HN<sub>4</sub>HCO<sub>2</sub> with 1% TEA (v/v) and a flow rate of 1.5 mL/min resulting in a retention time for [<sup>18</sup>F]Fallypride of 5.8 min.

### **9.3 Theory**

#### **9.3.1 Analysis of TLC plates**

To determine the chromatographic resolution for the crude radiopharmaceutical lane on each plate, a MATLAB program with a graphical user interface (GUI) was developed (**Figure 9-5**). Initially, the user is asked to select a CLI image file. The program performs background corrections as previously described(96,130), the user can scale the image by selecting an upper-intensity

value. In the next step, the user selects the corresponding UV image file and is instructed to adjust the brightness and contrast through programmed slider controls. The adjusted CLI and UV images are combined into a composite black and white image (after inverting the pixel intensities of the UV image), which is used to define the lane for the automatic generation of CLI and UV line profiles (chromatograms). To select the lane's width, the user draws a line across the broadest chromatographic band in the composite image. Following this, the user is prompted to draw a line along the center of the lane.

To generate the CLI chromatogram, the program automatically creates a series of adjacent line profiles (image brightness versus distance along lane) at 1-pixel increments within the defined lane width and, from these, calculates an average line profile and then normalizes it to the highest intensity analyte. This user-defined line profile is then displayed, enabling the user to set a threshold height for automated peak identification to ignore background noise. The MATLAB program performs automatic peak detection on the resultant chromatogram, then fits Gaussian curves to each peak and sums these to create a single multi-Gaussian fit.

A similar process is carried out to generate the UV chromatogram, except that an additional correction is made at the end to account for uneven UV illumination along the length of the lane. In the UV image, immediately adjacent to the user-selected lane, the program captures an additional 20 'background' line profiles just adjacent to each side of the selected lane and averages them together into a single 'background' line profile, which is subtracted from the initial UV chromatogram to give the final corrected UV chromatogram.

After fitting, the MATLAB program computes the centroid and full width half maximum (FWHM) for each peak in the CLI and UV chromatograms, enabling the user to calculate the chromatographic resolution between the radiopharmaceutical and the nearest impurity.

### **9.3.2 Analysis of TLC plates**

The originally reported PRISMA method<sup>(351)</sup> was applied with minor modifications. The entire optimization process could be carried out with a single batch of crude radiopharmaceutical

using twenty identically-prepared TLC plates in a few hours. Each plate was spotted with three lanes: the crude radiopharmaceutical, the precursor, and the reference standard.

#### Step 1: solvent selection

A total of eight plates were developed with pure solvents selected from Snyder selectivity groups(354) to compare separation resolution. The pure solvents were miscible with n-hexanes (Table 9-4). Based on a visual assessment of their ability to separate impurities (radioactive and non-radioactive) from the target radiopharmaceutical, three solvents (A, B, and C) exhibiting the highest degree of separation were chosen, where A, B, and C are listed in order of increasing solvent polarity.

#### Step 2: solvent polarity optimization

To account for the intrinsic differences in solvent polarity, solvents are all 'normalized' to the same polarity before optimizing the solvent mixture. The polarity of a mixture is simply the volumetric average of polarities of its constituents ( $S_t = x \cdot S_x + y \cdot S_y$ , where x and y are the volume fraction of each solvent, and  $S_x$  and  $S_y$  are the polarities of each solvent). N-hexanes (solvent polarity = 0) was used to reduce all solvent polarities to equal  $S_A$  (the lowest pure solvent polarity) - 0.5, and also two more strength values,  $S_A - 1.0$  and  $S_A - 1.5$ . For each of the three resulting strength values, the diluted solvents were mixed in a 1:1:1 ratio, designated as 333 in selectivity point ( $P_s$ ) notation, where the three digits represent the volume fraction of each of the diluted solvents (i.e., volume fraction X 10 and then rounded to an integer value). 3 TLC plates were developed with these equal volume polarity-adjusted solvent mixtures. The optimal polarity was selected, so the desired radiopharmaceutical band was in the range  $0.2 < R_f < 0.8$ . If multiple solvent polarities mobilized the radiopharmaceutical into this range, the polarity with the greatest separation of the nearest impurity to the radiopharmaceutical was chosen for further optimization. Should none of the solvents mobilize the radiopharmaceutical to the desired range, the solvents that moved UV active impurities to the greatest degree were selected for further optimization.

#### Step 3: additive selection

Adding ionic pairing reagents (e.g., TEA and AcOH) can sometimes further improve separation resolution. This process was typically performed with only a few additional TLC plates. Due to the low concentration of these additives in the mobile phases, their polarities were treated as negligible (e.g., 0) and were included in the solvent mixture by simultaneously removing an equal volume of n-hexanes from the mixture recipe. Initially, the addition of each additive was tested at concentrations of 0.1%. Should the resolution or band shapes be improved (i.e., reduced tailing or fronting), proportions of 0.5% are additionally surveyed. Should additives in these low concentrations lead to no observable differences, additional concentrations at 5% are surveyed. Further optimization of the additive concentrations was dynamically determined if they led to heightened resolution of the radiopharmaceutical.

#### Step 4: composition optimization

Nine additional TLC plates were separated using different solvent compositions to optimize the mobile phase composition ( $P_s$  values of 100, 010, 001, 622, 262, 226, 406, 460, and 055, all at the previously selected optimal solvent strength and additive amount). The resolution was quantified for each lane. In addition to these selectivity points, we also included resolution data for the other selectivity points surveyed. We picked the mobile phase composition from this data set that gave the highest resolution, performing linear interpolation if needed (**Appendix 7.6.1**).

## **9.4 Results and Discussion**

The PRISMA method optimized radio-TLC mobile phases for several clinically-relevant radiopharmaceuticals with varying chemical properties (**Table 9-1**).

**Table 9-1. Selected radiopharmaceuticals and their calculated properties.**

<b>Radiopharmaceutical</b>	<b>cLogP</b>	<b>TPSA</b>	<b>H-Bond Donor Count</b>	<b>H-Bond Acceptor Count</b>
[ <sup>18</sup> F]PBR-06	4.6	48.0	0	5
[ <sup>18</sup> F]FEPPA	3.6	51.7	0	5
[ <sup>18</sup> F]Fallypride	3.3	50.8	1	5
[ <sup>18</sup> F]FPEB	2.7	36.7	0	3
[ <sup>18</sup> F]FDOPA	-2.0	104.0	4	6



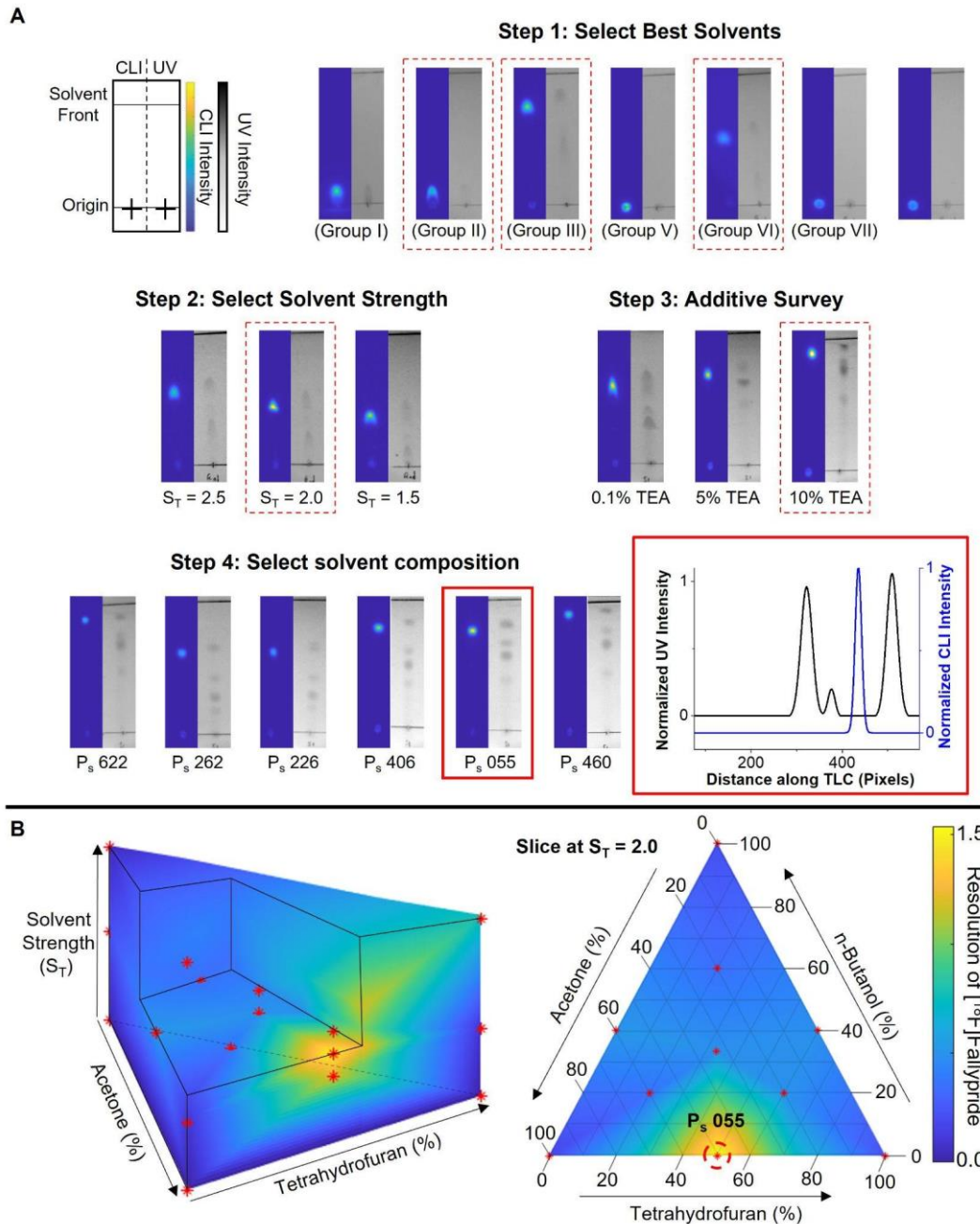


**Figure 9-1. PRISMA optimization of [<sup>18</sup>F]Fallypride.**

(A) The PRISMA method comprises several stages of mobile phase optimization to determine conditions that provide the best resolution. TLC plates prepared with mixtures of [<sup>18</sup>F]Fallypride and impurities are separated under different conditions and visualized via CLI and UV imaging. A custom software program computes the resolution between the radiopharmaceutical and the nearest impurity (radioactive or non-radioactive). Dashed red lines denote the optimal selection from each stage of the process, and the inset shows a chromatogram from the final optimized conditions. (B) The resolution is mapped as a function of mobile phase composition and solvent strength (left), and a slice of this prism taken at the optimal solvent strength (2.0) shows how resolution varies as a function of composition (right).

#### 9.4.1 Optimization of separation of [<sup>18</sup>F]Fallypride samples

Due to its moderate polarity and polar surface area, [<sup>18</sup>F]Fallypride was selected as an initial model compound to undergo the PRISMA process (**Figure 9-1A**). The solvent-screening step revealed that n-BuOH (solvent A), THF (solvent B), and acetone (solvent C) provided the best separation of [<sup>18</sup>F]Fallypride from impurities. Based on the minimum solvent strength of n-BuOH (3.9), the solvent polarities of 3.5, 3.0, and 2.5 were chosen for the survey at the equivolume mixture of strength-adjusted solvents (i.e.,  $P_s = 333$ ). While all the surveyed polarities led to the mobilization of [<sup>18</sup>F]Fallypride in the  $R_f$  range of 0.2-0.8,  $S_t = 2.5$  led to the greatest separation of [<sup>18</sup>F]Fallypride from other analytes. Tailing of [<sup>18</sup>F]Fallypride was observable with all mobile phases tested to this point. A possible explanation for this tailing could be ion pairing induced by interactions between the amide functional group of [<sup>18</sup>F]Fallypride and surface silanol groups on the TLC plate. Different concentrations of TEA(355) were added in percentages of 0.1, 5, and 10% (v/v) to reduce ionic pairing across the plate during development. Using 10% (v/v) TEA led to well-defined bands and was used for further optimization. After surveying nine additional solvent mixtures ( $P_s$ ), the optimal chromatographic resolution for [<sup>18</sup>F]Fallypride from nearest impurity ( $R = 1.54$ ) was found to be  $P_s = 055$ ,  $S_t = 2.5$  (**Figure 9-1B**). This selectivity point corresponds to a mobile phase composition of 31.3:24.5:34.3:10.0 (v/v) THF:acetone:n-hexanes:TEA.

#### 9.4.2 Comparison of optimized radio-TLC to radio-HPLC

We next compared the chromatographic resolution of the optimized TLC method with an isocratic HPLC method. A crude sample of [<sup>18</sup>F]Fallypride was produced under droplet-radiochemistry conditions(93) modified to result in a low yield and high prevalence of side products. Briefly, increased TBAHCO<sub>3</sub> (300 vs. 240 nmol) was used in the [<sup>18</sup>F]fluoride drying step, and the radiofluorination was performed with 100 nmol instead of 234 nmol of precursor and reacted at 140 °C for 10 min instead of 110 °C for 1 min. Interestingly, the radio-TLC optimized method separated the same number of radioactive analytes as radio-HPLC (**Figure 9-2**).

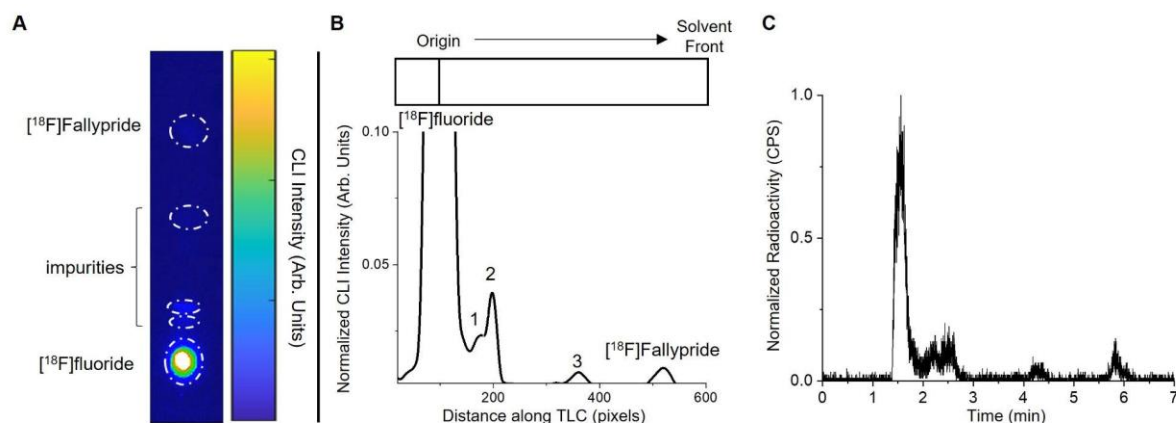


**Figure 9-2. Chromatographic resolution comparison of optimized TLC against conventional isocratic HPLC.**

(A) Cerenkov luminescence image of a TLC plate after spotting with a crude  $[^{18}\text{F}]$ Fallypride sample and separation via the PRISMA-optimized mobile phase. (B) TLC chromatogram was generated by taking a line profile of the Cerenkov luminescence image along the lane. The chromatogram is truncated to better show the smaller peaks. (C) Isocratic radio-HPLC chromatogram of the same sample.

We can see evidence, however, of the well-known underestimation of  $[^{18}\text{F}]$ fluoride in the radio-HPLC analysis(338): the abundance of  $[^{18}\text{F}]$ fluoride computed from the radio-HPLC chromatogram is 71%, but, in comparison, was 95% when computed from the radio-TLC. Even more alarming, the apparent formation of  $[^{18}\text{F}]$ Fallypride calculated from the radio-HPLC chromatogram was nearly 7%, while it was <1% using radio-TLC (**Table 9-2**), suggesting more than a 7-fold error by radio-HPLC. If the discrepancy in the size of the  $[^{18}\text{F}]$ fluoride peaks is removed by ignoring this peak in both the radio-HPLC and radio-TLC chromatograms, the proportions of all other species are found to be similar, indicating excellent quantitative agreement between radio-HPLC and radio-TLC (with the PRISMA-optimized mobile phase).

**Table 9-2. Comparison of the radiochemical composition of a crude [<sup>18</sup>F]Fallypride sample as determined by radio-TLC and Radio-HPLC.**

Peak	Integration (%)			
	HPLC <sup>A</sup>	HPLC <sup>B</sup>	TLC <sup>A</sup>	TLC <sup>B</sup>
[ <sup>18</sup> F]fluoride	70.5	-	94.7	-
1	8.7	29.9	1.6	30.7
2	11.0	37.2	2.4	36.3
3	3.3	11.0	0.6	11.6
[ <sup>18</sup> F]Fallypride	6.5	22.0	0.8	21.3

<sup>A</sup>Estimation accounts for all peaks, including [<sup>18</sup>F]fluoride; <sup>B</sup>Estimation ignores [<sup>18</sup>F]fluoride and is calculated solely based on other peaks

Because of the excellent agreement, it is possible to consider using an imaging-based readout of TLC plates separated according to the PRISMA-optimized mobile phase as a simpler and more rapid alternative to radio-HPLC for radiopharmaceutical analysis. If multiple samples need to be analyzed, then the advantage of radio-TLC is further magnified as multiple samples can be spotted on the same plate and separated and read out in parallel(96). In contrast, analyzing multiple samples via radio-HPLC requires ample time for cleaning and re-equilibration between samples.

#### **9.4.3 Comparison of literature mobile phases to PRISMA-optimized mobile phase**

The separation achieved with the PRISMA-optimized mobile phase was compared to mobile phases reported in the literature for the analysis of [<sup>18</sup>F]Fallypride. We produced [<sup>18</sup>F]Fallypride under previously-reported droplet radiochemistry conditions(93) modified to give a moderate yield and many side products. Specifically, the amount of TBAHCO<sub>3</sub> used in the [<sup>18</sup>F]fluoride drying step was increased (from 240 to 800 nmol), and the fluorination was performed with 200 nmol instead of 234 nmol of precursor and reacted at 140 °C for 10 min instead of 110

°C for 1 min. Analysis was performed using TLC plates with pre-concentration zones, and the separation distance was extended from 4 to 5 cm to ensure the highest possible separation resolution in all cases. All lanes were spotted with 1  $\mu$ L of the same crude reaction mixture. **Figure 9-3** details the mobile phases surveyed, along with the obtained CLI images and generated chromatograms. For each mobile phase, we also performed separations using only [ $^{18}$ F]TBAF (**Figure 9-7**) or [ $^{19}$ F]Fallypride (**Figure 9-8**) to confirm the  $R_f$  values of these species.

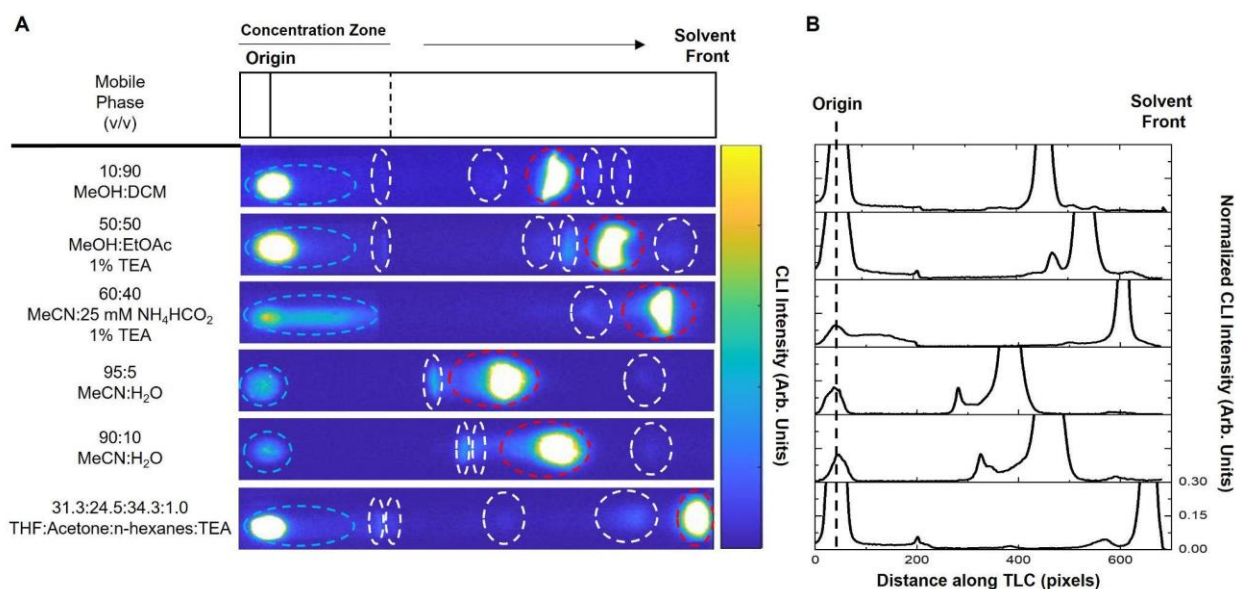


**Figure 9-3. Mobile phases comparisons for the analysis of crude [ $^{18}$ F]Fallypride conversion.**

(A) CLI images of TLC plates spotted with crude [ $^{18}$ F]Fallypride and developed with different mobile phases from literature (first five entries) and the PRISMA-derived mobile phase (last entry). [ $^{18}$ F]fluoride is denoted with dashed blue ellipses, side-products denoted with dashed white ellipses, and [ $^{18}$ F]Fallypride denoted with dashed red ellipses. (B) TLC chromatograms were generated by taking a line profile of the Cerenkov luminescence images. Chromatograms are truncated to better show the smaller peaks.

Abundances of species, computed from areas under peaks in the chromatograms, are summarized in **Table 9-3**. A significant disparity in the estimated abundance of [ $^{18}$ F]Fallypride and other species between different mobile phases is evident. Mobile phases with aqueous compositions (rows 3, 4, and 5) led to the greatest apparent abundance of [ $^{18}$ F]Fallypride (i.e., 66.1%, 82.7%, and 84.7%), while purely organic mobile phases (rows 1, 2, and 6) led to a similar abundance of [ $^{18}$ F]Fallypride compared to the PRISMA optimized mobile phase (i.e., 46.5%,

47.4%, and 41.4%). The discrepancy in results obtained from the aqueous mobile phases is difficult to explain, but due to the high degree of band overlap (with a low number of resolved bands), there are likely species co-eluting with [<sup>18</sup>F]Fallypride. The moderate discrepancy between the organic mobile phases suggests that the initial two literature mobile phases may result in incomplete separation of analytes, and an overlapping band may be counted with the [<sup>18</sup>F]Fallypride band. Using the same crude [<sup>18</sup>F]Fallypride sample, we performed a radio-HPLC separation, collected the [<sup>18</sup>F]Fallypride fraction, and compared the activity to the injected activity. In addition to the high similarity between the radio-TLC and radio-HPLC chromatograms (**Figure 9-9**), the abundance of collected [<sup>18</sup>F]Fallypride was 40.2%, in excellent agreement with the abundance obtained from radio-TLC using the PRISMA-optimized mobile phase.

**Table 9-3. Integration of analytes detected by radio-TLC in the analysis of [<sup>18</sup>F]Fallypride.**

Mobile Phase (v/v)	Number of Observable Peaks	Abundance (%)						Fallypride R <sub>f</sub>
		[ <sup>18</sup> F]fluoride	[ <sup>18</sup> F]Fallypride	Impurities				
				1	2	3	4	
10:90 MeOH:DCM <sup>16</sup>	6	46.7	46.5	1.7	2.0	1.3	1.8	0.65
50:50 MeOH:EtOAc 1% TEA <sup>17</sup>	6	43.9	47.4	0.7	1.7	4.7	1.7	0.76
60:40 MeCN:25 mM NH <sub>4</sub> HCO <sub>2</sub> 1% TEA <sup>11,34</sup>	3	30.4	66.1	3.6	-	-	-	0.87
95:5 MeCN:H <sub>2</sub> O <sup>19</sup>	4	9.6	82.7	6.6	1.1	-	-	0.55
90:10 MeCN:H <sub>2</sub> O <sup>35</sup>	4	6.9	84.7	4.3	2.3	-	-	0.66
31.3:24.5:34.3:1.0 THF:Acetone:n-hexanes:TEA	6	49.8	41.4	2.3	1.0	1.5	4.0	0.91

These results further underscore the problems of [<sup>18</sup>F]fluoride retention on HPLC columns, which can lead to significant over-estimation errors of radiochemical species, especially low-abundance ones. Furthermore, the discrepancy when using different radio-TLC mobile phases,

even for the identical sample, raises questions about the accuracy of reported results using certain mobile phases and underscores the importance of ensuring high chromatographic resolution of the analysis method.

#### 9.4.4 Optimization of separation of [<sup>18</sup>F]PBR-06 samples

For crude samples of [<sup>18</sup>F]PBR-06 (**Figure 9-10**), the solvent screening step revealed that diethyl ether (solvent A), dichloromethane (solvent B), and chloroform (solvent C) exhibited the greatest separation of impurities from [<sup>18</sup>F]PBR-06. Solvent polarities were normalized to 2.5, 2.0, and 1.5. With the solvents mixed in equal proportions ( $P_s = 333$ ), the greatest separation of [<sup>18</sup>F]PBR-06 from impurities was obtained with  $S_t = 2.5$ . Low amounts of AcOH and TEA (0.5%) were tested as chromatographic additives. The use of AcOH resulted in more observable UV-active impurities and a slightly higher chromatographic resolution for [<sup>18</sup>F]PBR-06 than the use of TEA. After evaluating the impact of other mixtures of the solvents (tested at  $S_t = 2.5$  using 0.5% AcOH (v/v)), the greatest resolution of [<sup>18</sup>F]PBR-06 from nearest impurity ( $R = 1.84$ ) was obtained at  $P_s = 333$ ,  $S_t = 2.5$  (**Figure 9-10**). This selectivity point corresponds to a mobile phase composition of 29.8:26.9:20.4:22.85:0.05 (v/v) diethyl ether:dichloromethane:chloroform:n-hexanes:AcOH.

#### 9.4.5 Optimization of separation of [<sup>18</sup>F]FEPPA samples

For samples of [<sup>18</sup>F]FEPPA (**Figure 9-11**), the solvent screening test revealed that n-BuOH (solvent A), THF (solvent B), and acetone (solvent C) provided the best separation of [<sup>18</sup>F]FEPPA from impurities. These solvents were normalized to have polarities of 3.5, 3.0, and 2.5. In equivolume mixtures ( $P_s = 333$ ),  $S_t = 2.5$  showed the greatest separation of impurities from [<sup>18</sup>F]FEPPA. A screening of additives revealed heightened resolution of [<sup>18</sup>F]FEPPA from impurities using 1% TEA. Further solvent mixtures were tested (at  $S_t = 2.5$  and with the addition of 1% TEA), and  $P_s = 262$ ,  $S_t = 2.5$  showed the greatest chromatographic resolution of [<sup>18</sup>F]FEPPA from its nearest impurity ( $R = 2.07$ ). This selectivity point corresponds to a mobile phase composition of 12.8:37.5:9.8:38.8:1 n-BuOH:THF:Acetone:n-hexanes:TEA (v/v).

#### 9.4.6 Optimization of separation of [<sup>18</sup>F]FDOPA samples

We next considered the two-step radiofluorination of [<sup>18</sup>F]FDOPA (**Figure 9-12**), in which the crude product contains a relatively nonpolar radioactive intermediate and the highly polar [<sup>18</sup>F]FDOPA product. It is notoriously difficult to separate extremely polar compounds on normal phase silica TLC plates. For this reason, it is notable that the literature for [<sup>18</sup>F]FDOPA analysis cites the use of reverse phase chromatography for radio-TLC analyses(356–358). In the solvent-screening step, [<sup>18</sup>F]FDOPA could not be mobilized, but using the criteria of the furthest migration of UV impurity bands from one another, we selected n-butanol (solvent A), THF (solvent B), and acetone (solvent C). The polarity of each pure solvent was normalized to 3.5, 3.0, and 2.5. When comparing solvent strengths (at  $P_s = 333$ ),  $S_t = 3.5$  led to the greatest degree of movement for UV impurities, but  $S_t = 3.0$  led to more distinguishable peaks and was chosen for further optimization. High percentages of chromatographic additives were tested to address the tailing across the TLC plate. The best separation was found with AcOH in 30% abundance. After comparing different solvent mixtures,  $P_s = 333$ , (at  $S_t = 3.0$  at 30% AcOH) exhibited the greatest chromatographic resolution of [<sup>18</sup>F]FDOPA from its nearest impurity ( $R = 1.18$ ). This selectivity point corresponds to a mobile phase composition of 22.6:21.7:19.6:61:30 (v/v) n-butanol:THF:acetone:n-hexanes:AcOH. While baseline resolution was not achieved, the resolution achieved may be sufficient for synthesis optimization or may be improved by adapting the PRISMA method to other types of TLC plates.

#### 9.4.7 Optimization of separation of [<sup>18</sup>F]FPEB samples

Simple leaving groups in aromatic substitutions, such as NO<sub>2</sub> groups, are commonly used to radiofluorinate radiopharmaceuticals. It is noteworthy that the separation of these radiopharmaceuticals and precursor structures is relatively difficult using HPLC. Thus the application of the PRISMA method to [<sup>18</sup>F]FPEB (**Figure 9-13**), which is produced via SNAR of a NO<sub>2</sub> leaving group, serves as a good illustration of the high-resolution capabilities of PRISMA. The solvent screening step revealed that diethyl ether (solvent A), n-BuOH (solvent B), and



acetone (solvent C) yielded the greatest separation of impurities from [ $^{18}\text{F}$ ]FPEB. Normalizing the polarities of the solvents to 2.5, 2.0, and 1.5, a comparison of equivolume mixtures ( $P_s = 333$ ) showed that the best separation could be achieved with  $S_t = 1.5$ . Evaluation of chromatographic additives showed a minor improvement when using 1% TEA. After comparing additional solvent mixtures, the  $P_s = 406$  mixture (with  $S_t = 1.5$ , 1% TEA) exhibited the best resolution of [ $^{18}\text{F}$ ]FPEB from the nearest impurity ( $R = 1.71$ ). This selectivity point corresponds to a mobile phase composition of 21.4:17.6:60.0:1.0 diethyl ether:acetone:n-hexanes:TEA (v/v).

#### 9.4.8 Optimization of [ $^{18}\text{F}$ ]FPEB radiosynthesis with high-resolution TLC analysis

As an example of how the PRISMA method can be used, we performed a high-throughput synthesis optimization of [ $^{18}\text{F}$ ]FPEB using multi-reaction droplet-radiochemistry methods(93) and performed radio-TLC analysis of reactions in a multi-lane fashion(96) (8 samples per TLC plate) using the PRISMA-derived mobile phase. In the literature, harsh reaction conditions, like high temperature and base concentrations, lead to the formation of hydrolyzed impurities similar to the [ $^{18}\text{F}$ ]FPEB(359,360), and HPLC analysis of crude microscale reactions (via flow-based reactor) of [ $^{18}\text{F}$ ]FPEB shows closely eluting radioactive impurities(359), that may be difficult to resolve via TLC without careful optimization.

Initial microscale conditions were adapted by scaling down conditions reported in literature(361). [ $^{18}\text{F}$ ]fluoride (20-30 MBq) mixed with 500 nmol of the base was first dried at 105 °C for 1 min, and then a 10  $\mu\text{L}$  droplet of precursor solution (containing 250 nmol) was added and reacted for 5 min at 140 °C. We first compared the use of different bases ( $\text{K}_2\text{C}_2\text{O}_4$ ,  $\text{K}_2\text{CO}_3$ ,  $\text{KHCO}_3$ , and  $\text{Cs}_2\text{CO}_3$ ) and two different reaction solvents (DMSO and NMP), with  $n=2$  replicates per condition (Figure 9-4A).  $\text{Cs}_2\text{CO}_3$ , in combination with DMSO, was selected for further optimization based on good RCY and low volatile loss (high collection efficiency). In optimization of the base amount (Figure 9-4B), 290 nmol was selected as the best compromise of good RCY and low volatile losses. From a comparison of the impact of precursor amount (Figure 9-4C), a high amount of precursor is needed to improve RCY. By replotting the results as a function of the

base to precursor ratio (**Figure 9-4D**), we noticed we achieved a similar yield with only 120 nmol of the precursor by lowering the amount of  $\text{Cs}_2\text{CO}_3$  to 200 nmol. The reaction temperature was further optimized, revealing an optimal temperature of 140 °C (**Figure 9-4E**).

Under the optimized conditions,  $^{18}\text{F}$ FPEB could be produced in a crude RCY of ~16%, greater than other reported literature conditions (4-10%)(252,359,361–363). Sixty-four reactions could be performed per day, and by employing multi-lane TLC using the optimized mobile phase, all samples each day could be analyzed within 60 min. In contrast, using radio-HPLC analysis would likely have significantly overestimated the product yield (due to loss of  $^{18}\text{F}$ fluoride in the column), and test reactions would have taken approximately 30-40 min each to analyze. Due to the limited half-life of F-18, only 12-16 samples could be practically analyzed each day if HPLC was used. Thus the study would have taken many more days, more batches of radioisotope (potentially adding other variables for which additional replicates are needed), and more labor hours.

#### 9.4.9 Additional readout channels via staining

In addition to radiation readout (via Cerenkov imaging) and readout via UV imaging, additional chemical information can be gleaned from the TLC plate. Staining is a widely used method in TLC analysis that is inexpensive, can be used to detect low abundance analytes (via water-based stains like Hanessian), stain for specific functional groups (e.g., ninhydrin for the detection of amines), and detect analytes that are not UV-active. To demonstrate this principle, we employed TLC stains in the analysis of  $^{18}\text{F}$ PBR-06 and  $^{18}\text{F}$ Fallypride crude samples. In the samples of  $^{18}\text{F}$ PBR-06, few analytes can be visualized by UV analysis by TLC (**Figure 9-14**). Hanessian staining reveals faint traces of additional impurities near the product band. Ninhydrin staining did not reveal additional bands (**Figure 9-14**), but because it stains amine groups, this can help determine the potential identities of the bands. For  $^{18}\text{F}$ Fallypride, Hanessian staining revealed no additional impurities (**Figure 9-15**). Ninhydrin staining revealed a previously unseen impurity (**Figure 9-15**).

Staining methods pose an interesting method to visualize low-abundance species and to glean additional chemical information about specific bands that could help to identify bands and improve understanding of competing reaction pathways. It is striking that the additional impurities detected via staining were well separated from the radiopharmaceutical, even though they were not visible during the PRISMA procedure to optimize the mobile phase.

## 9.5 Conclusions

In this study, a systematic mobile phase selection process, PRISMA, was applied to optimize TLC mobile phases to separate crude samples of radiopharmaceuticals. The PRISMA method provided a systematic framework to rapidly (<4 h) and efficiently (with only 1 batch of the crude radiopharmaceutical) reach a set of development conditions resulting in high-resolution separation without prior knowledge of impurity identities or properties. The method was successfully applied to multiple examples of diverse radiopharmaceuticals, achieving baseline separation of the radiopharmaceutical from radioactive and non-radioactive impurities. In the case of [<sup>18</sup>F]Fallypride, the optimized radio-TLC method rivaled the resolution of isocratic radio-HPLC while resulting in a more accurate analysis as the method does not suffer from the issue of loss of [<sup>18</sup>F]fluoride to the column of radio-HPLC. Notably, the optimized TLC conditions can be applied for synthesis optimization and potentially to portions of QC testing (e.g., radiochemical purity) or radio-metabolite studies(364–372). UV imaging and TLC staining can reveal additional species that are not visible with the traditional use of radio-TLC. This streamlined methodology can be easily employed by radiochemistry labs, using ubiquitous materials, and enabling anyone to develop high-resolution TLC separation methods for accurate radiopharmaceutical analysis.

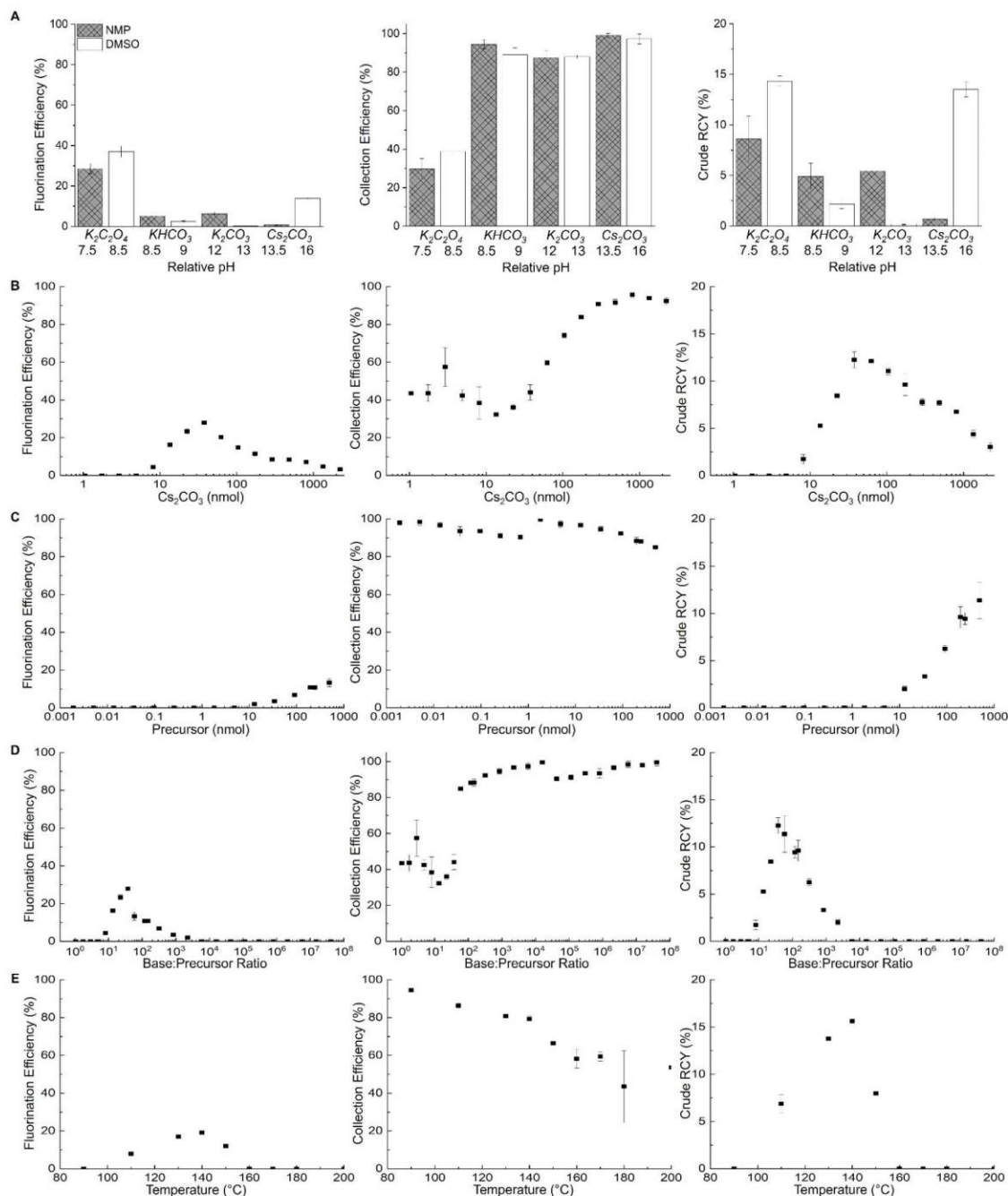


**Figure 9-4. Optimization of the synthesis of <sup>18</sup>F]FPFB (n = 2), leveraging high-throughput analyses enabled by multi-lane radio-TLC using the PRISMA-optimized mobile phase. Reaction volume is 10  $\mu$ L and reaction time is 5 min in all cases.**

(A) Impact of different bases and two different reaction solvents. Relative pH is shown below each data point.<sup>53</sup> Precursor amount: 250 nmol, base amount: 500 nmol, reaction temperature: 140 °C. (B) Effect of the amount of Cs<sub>2</sub>CO<sub>3</sub>. Precursor amount: 250 nmol, reaction temperature: 140 °C. (C) Effect of precursor amount. Cs<sub>2</sub>CO<sub>3</sub> amount: 290 nmol, reaction temperature: 140 °C. (D) Data from B and C were replotted to show the effect of the base:precursor ratio. (E) Effect of reaction temperature. Precursor amount: 200 nmol, Cs<sub>2</sub>CO<sub>3</sub> amount: 120 nmol.

## 9.6 Appendix

**Table 9-4. Solvents in Snyder selectivity groups that are miscible with n-hexanes and used for the PRISMA optimizations performed in this work.**

Snyder Group Number <sup>A</sup>	Solvent Name	Polarity
1	diethyl ether (Et <sub>2</sub> O)	2.8
2	n-butanol (n-BuOH)	3.9
3	tetrahydrofuran (THF)	4.0
5	dichloromethane (DCM)	3.1
6	acetone	5.1
7	toluene (PhMe)	2.4
8	chloroform (CHCl <sub>3</sub> )	4.1

<sup>A</sup>Group 4 (Formamide) was omitted due to incompatibility with silica-based TLC, and its ability to visibly etch silica from the TLC plate. A list of all group solvents is detailed in the literature. (354)

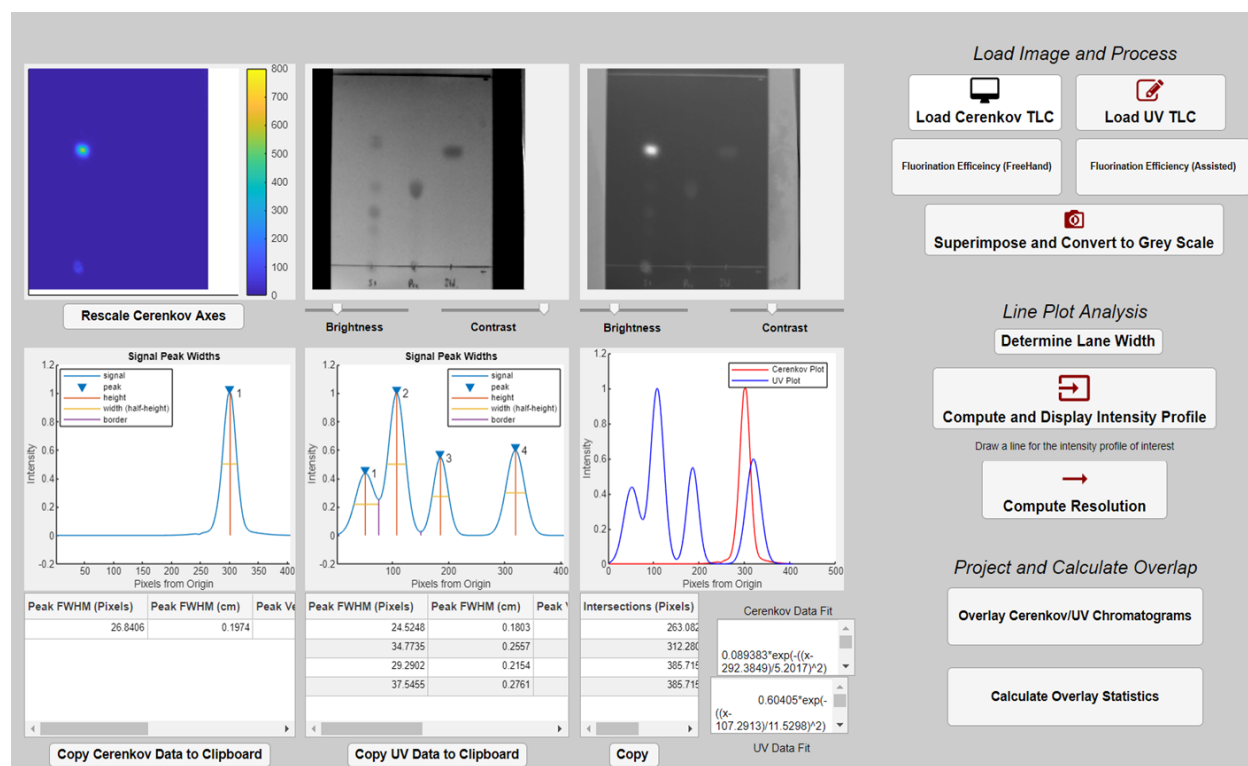


**Figure 9-5. The graphical user interface of software used for analyzing TLC images.**

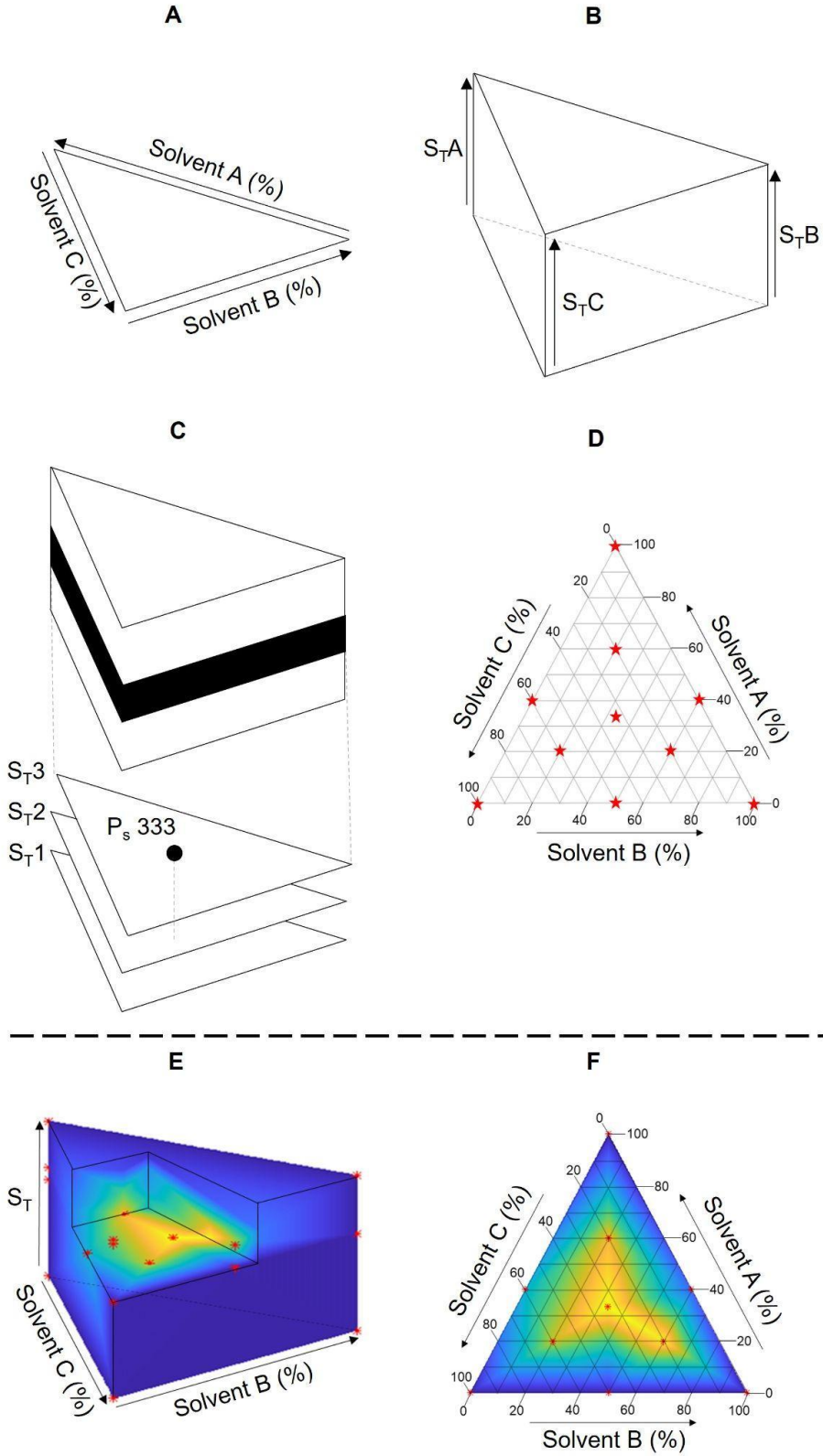
### 9.6.1 PRISMA “Prism” Construction

The data resulting from the PRISMA process (described in Methods) can be visualized in a 3D representation (**Figure 9-6**). First, we draw a triangle (**Figure 9-6A**) where each side represents the volume fraction of the three pure solvents (A, B, and C) selected in Step 1. By convention, the ordering of the solvents is chosen in ascending order of solvent polarity strength. A mixture of solvents can be represented as a point within the triangle. According to the PRISMA method, selectivity point notation can be used to describe the proportion of each solvent (e.g.,  $P_s = 622$  comprises 60% solvent A, 20% solvent B, and 20% solvent C). Solvent strength is plotted on the vertical axis. Since each solvent can be diluted down to a strength of zero via n-hexanes, the available parameter space is a prism-shaped volume with the three vertical edges having lengths equal to the strength of the corresponding solvents. In our optimization process, we limit ourselves to a maximum strength corresponding to the minimum of all the solvent strengths (i.e.,  $\min(S_A, S_B, S_C)$ ) (**Figure 9-6B**).

By normalizing all 3 solvents to the same strength value, we ensure that we are working on a horizontal slice of the parameter space when varying the solvent mixture. Equivolume mixtures ( $P_s = 333$ ) of solvents at three different solvents strengths are compared in Step 2 (**Figure 9-6C**). The  $P_s = 333$  point is at the center of each triangular slice (corresponding to the three different strengths). In Step 3, chromatographic additives are considered and used in later optimization stages. The amounts of the additives are small, and they are not reflected in the 3D construction. Finally, in Step 4, we work in the triangular slice corresponding to the best strength and additives from Steps 2 and 3, and the volumetric ratio of the strength-adjusted solvents is varied. Different mixtures (i.e., selectivity points,  $P_s$ ) are explored and denoted as red asterisks in **Figure 9-6D**.

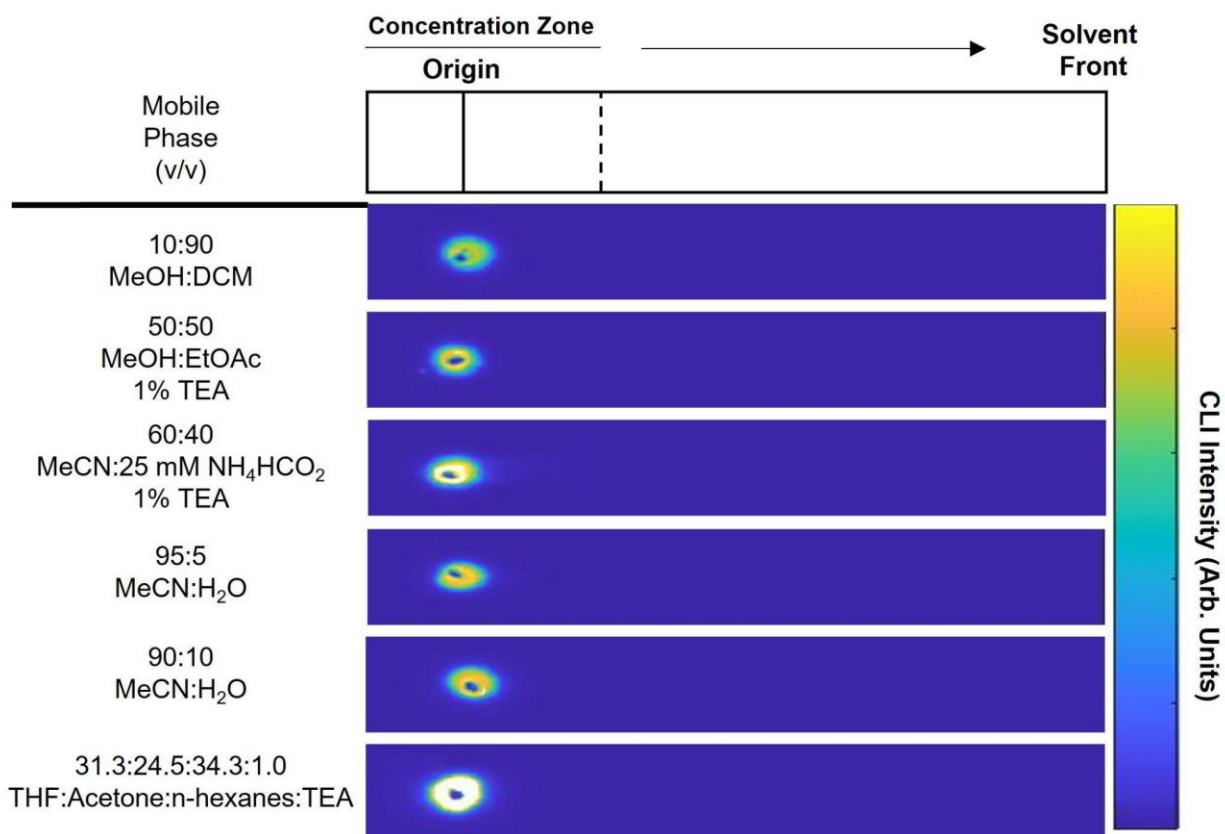
For each point examined (i.e., solvent strength and composition), we compute a resolution value (between the radiopharmaceutical and its nearest impurity) and plot this as a color.

Using the resolution values from the tested points, the space's color in between points was determined by linear interpolation, and data was plotted on a triangular mesh grid with step size 0.05 (**Figure 9-6E**). The slice on which the highest resolution value occurred is shown in **Figure 9-6F**.

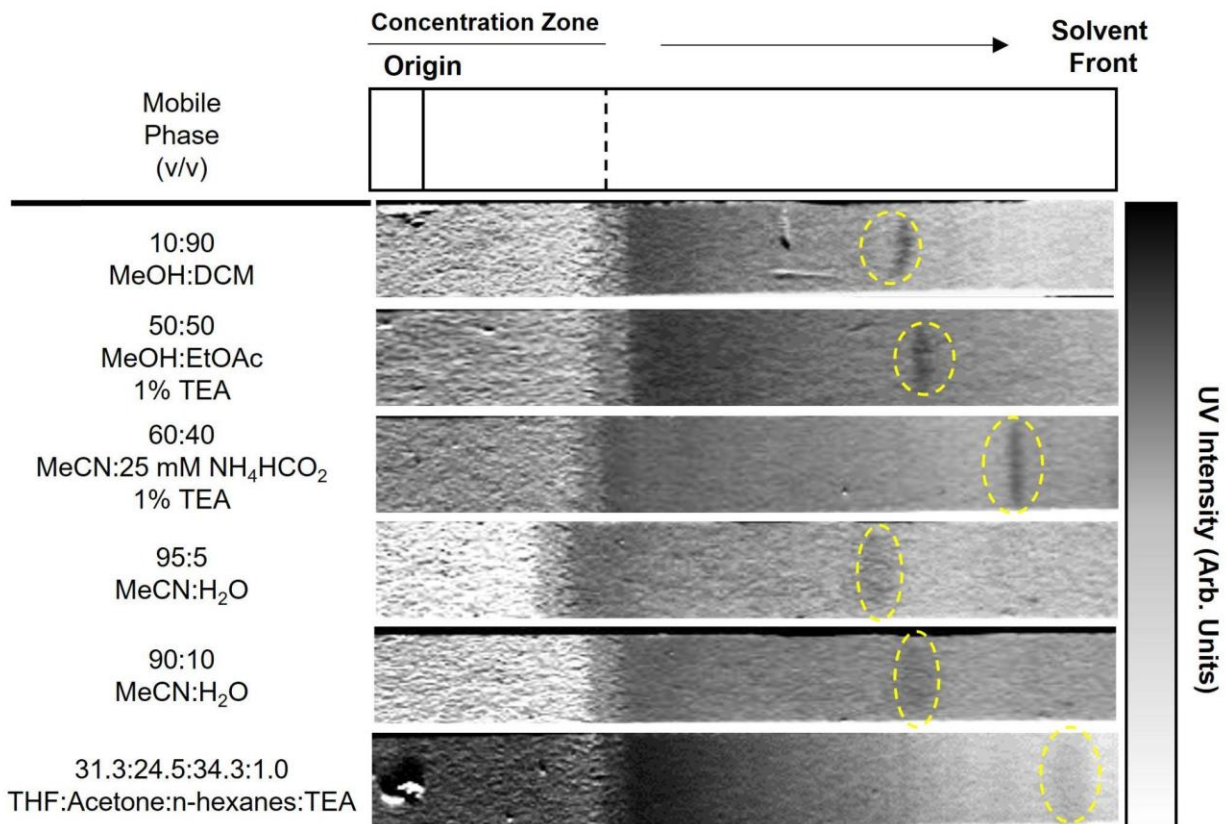


**Figure 9-6. Procedure for the 3D visualization of resolution as a function of mobile phase composition.**

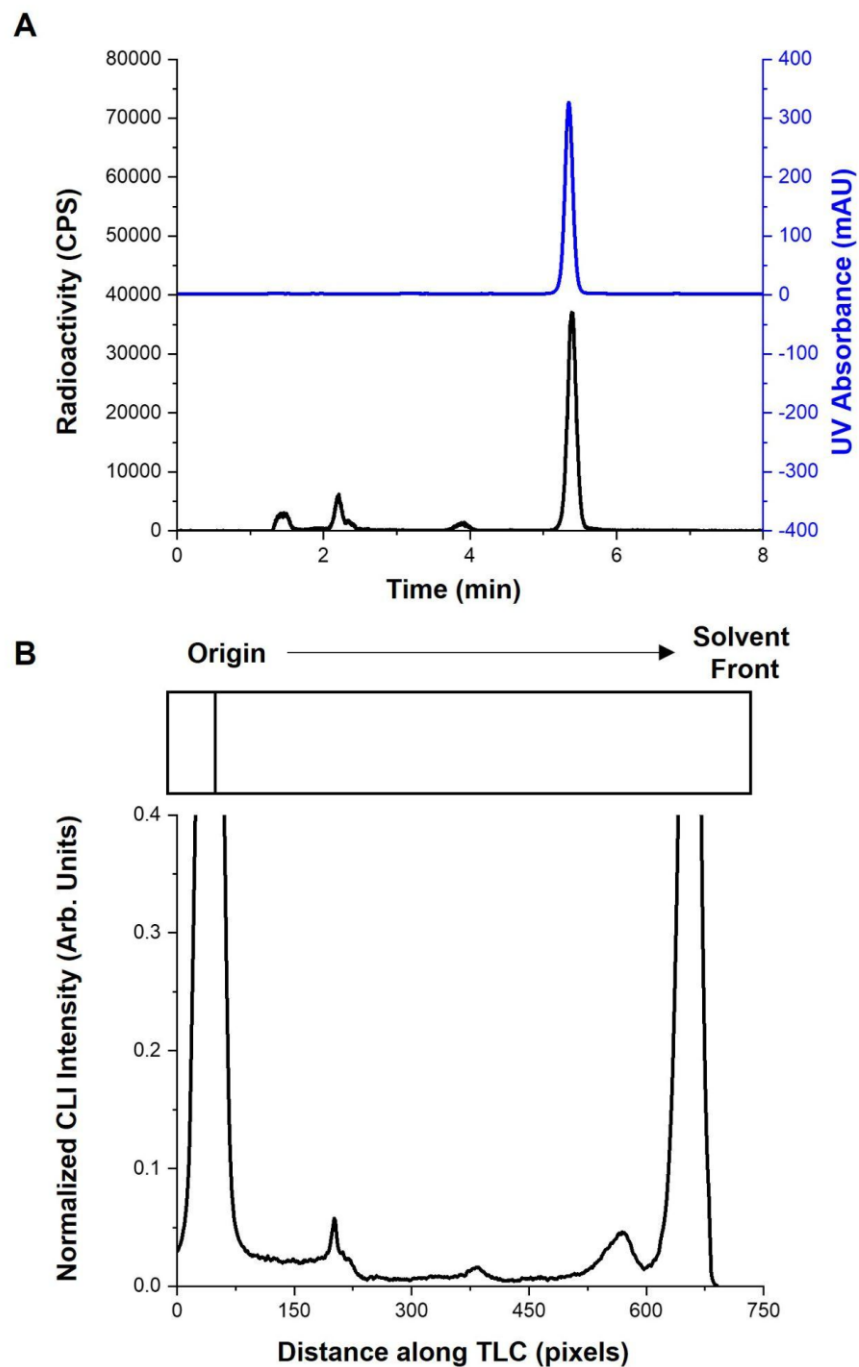




**Figure 9-7. CLI images of TLC plates spotted with 1  $\mu\text{L}$  crude  $[^{18}\text{F}]\text{TBAF}$  (30-50 MBq  $[^{18}\text{F}]\text{fluoride}$ , 800 nmol  $\text{TBAHCO}_3$ , diluted to 60  $\mu\text{L}$ ) developed with different  $[^{18}\text{F}]\text{Fallypride}$  mobile phases from literature (first 5 entries) and the PRISMA-derived mobile phase (last entry).**

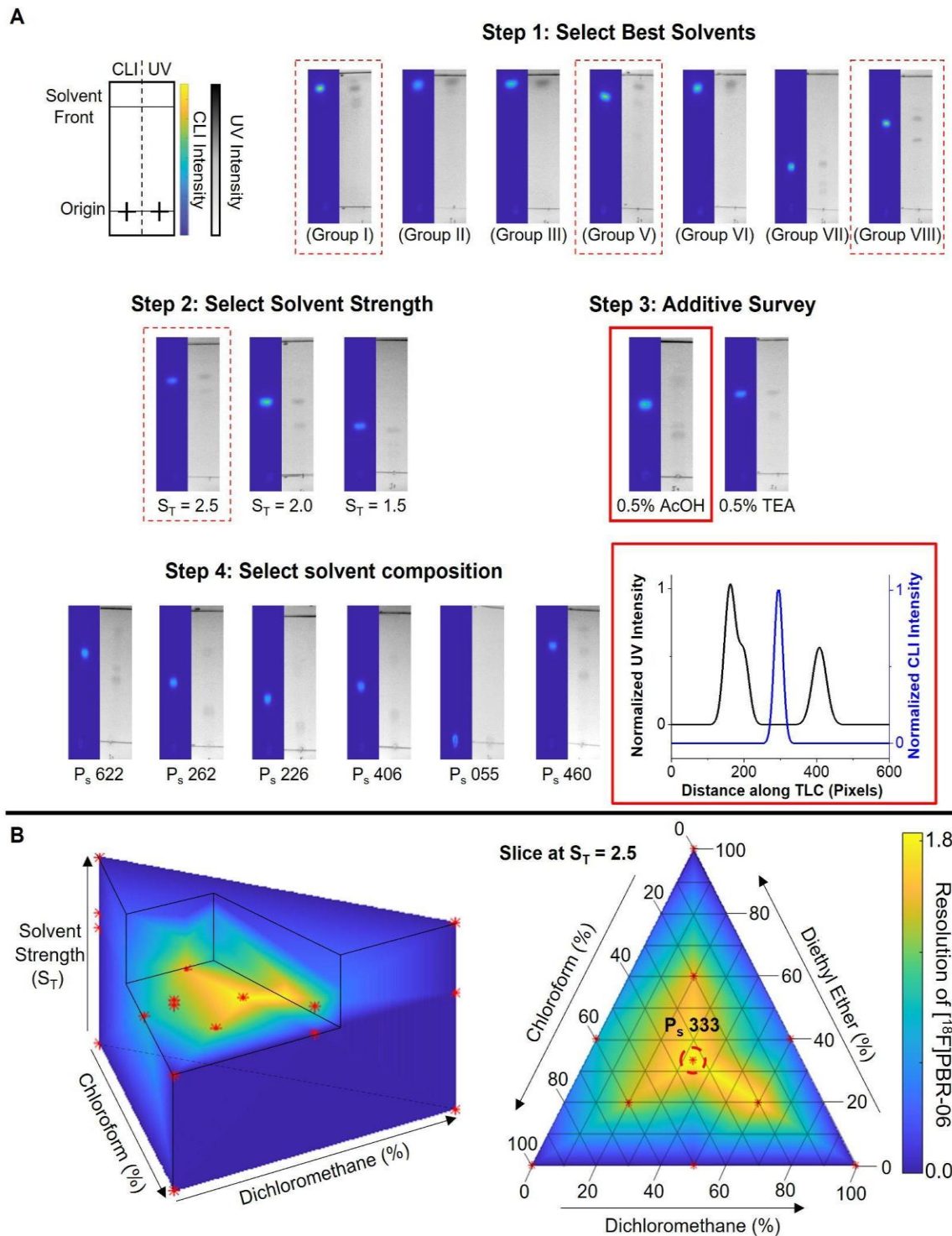


**Figure 9-8. UV images of TLC plates spotted with Fallypride reference standard and developed with different mobile phases from literature (first 5 entries) and the PRISMA-derived mobile phase (last entry).**



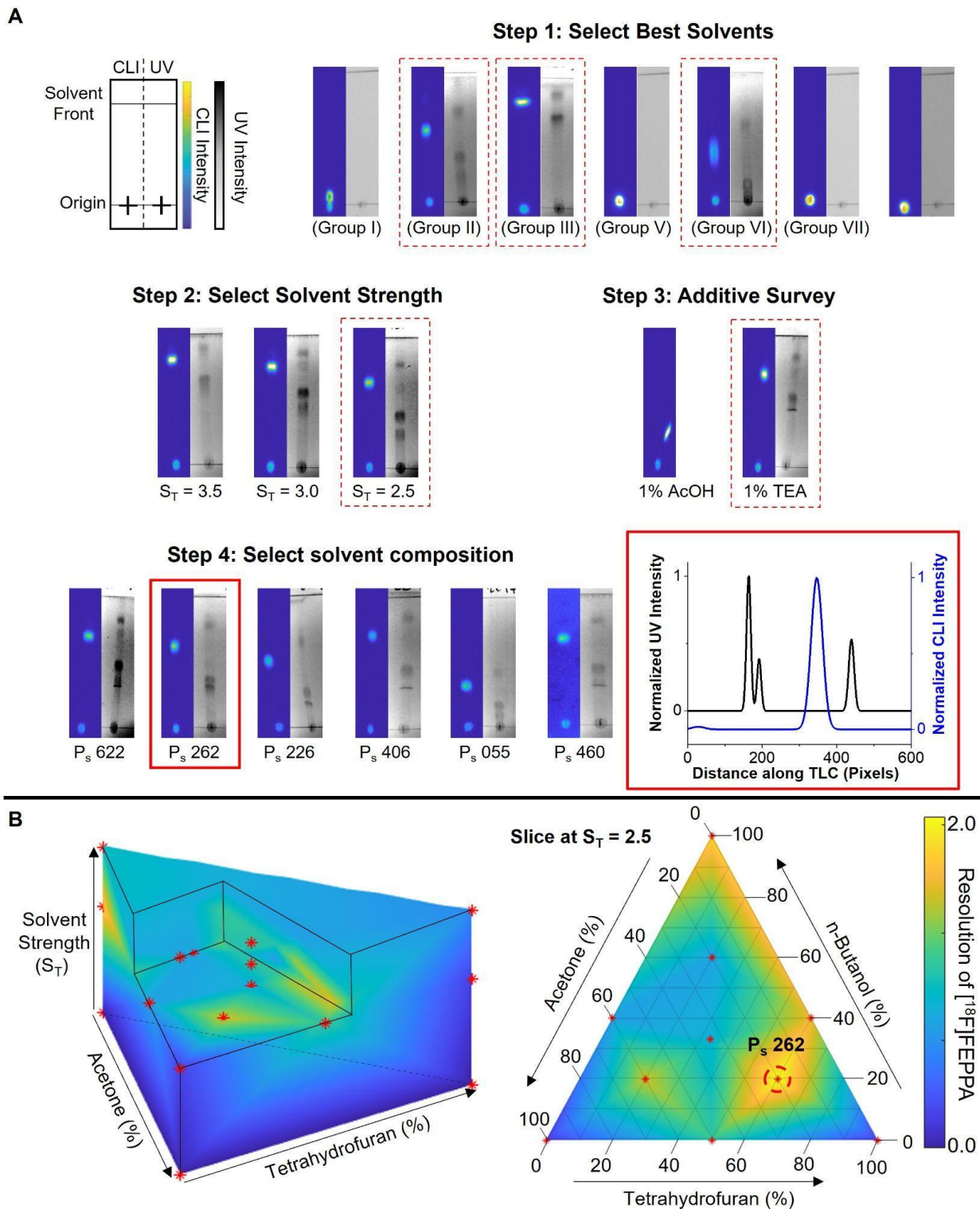
**Figure 9-9. Isocratic HPLC compared to the PRISMA optimized mobile phase of a crude  $[^{18}\text{F}]$ Fallypride sample.**

(A) Radio-HPLC chromatograms (Top) Standard trace of  $[^{19}\text{F}]$ Fallypride (Bottom) Crude  $[^{18}\text{F}]$ Fallypride. (B) Radio-TLC chromatograms of crude  $[^{18}\text{F}]$ Fallypride.



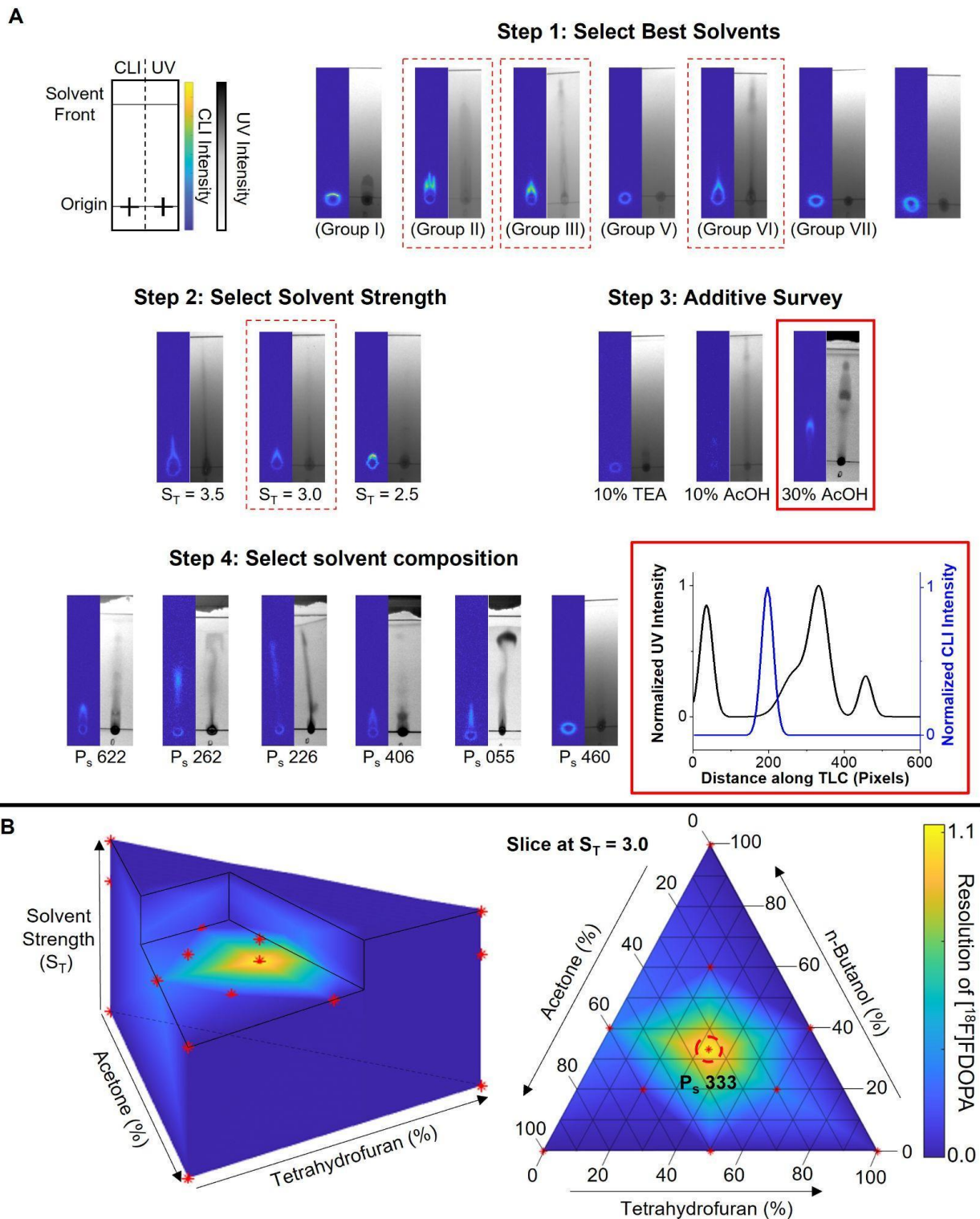
**Figure 9-10. PRISMA optimization of  $[^{18}\text{F}]\text{PBR-06}$ .**

(A) Results of PRISMA optimization applied to samples of  $[^{18}\text{F}]\text{PBR-06}$ . The condition(s) giving the best resolution at each step is outlined in dashed boxes. The optimal condition is outlined in solid red. (B) 3D visualization of resolution as a function of mobile phase composition.



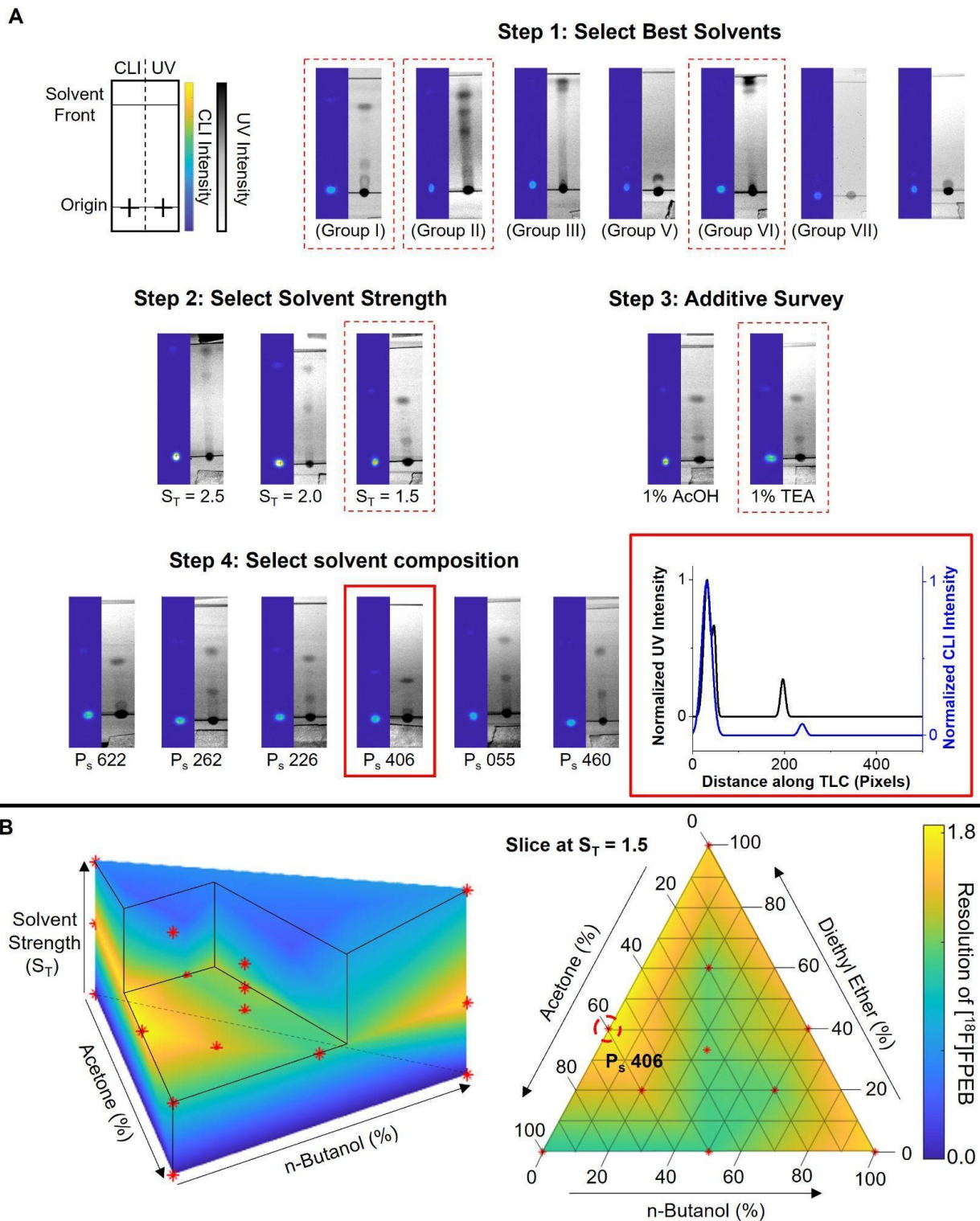
**Figure 9-11. PRISMA optimization of [ $^{18}$ F]FEPPA.**

(A) Results of PRISMA optimization applied to samples of [ $^{18}$ F]FEPPA. The condition(s) giving the best resolution at each step is outlined in dashed boxes. The optimal condition is outlined in solid red. (B) 3D visualization of resolution as a function of mobile phase composition.



**Figure 9-12. PRISMA optimization of  $[^{18}\text{F}]\text{FDOPA}$ .**

(A) Results of PRISMA optimization applied to samples of  $[^{18}\text{F}]\text{FDOPA}$ . The condition(s) giving the best resolution at each step is outlined in dashed boxes. The optimal condition is outlined in solid red. (B) 3D visualization of resolution as a function of mobile phase composition.



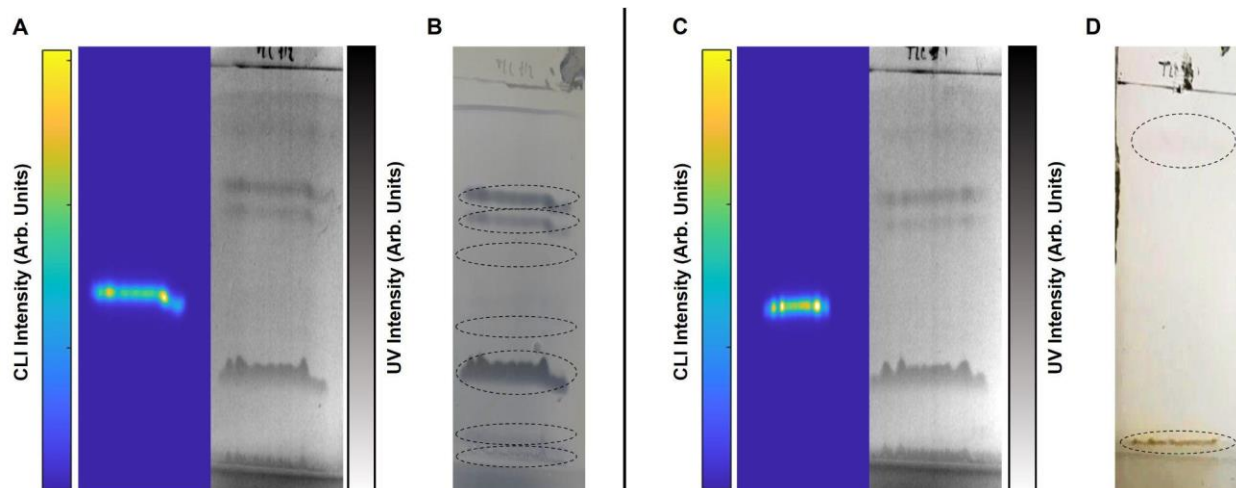


**Figure 9-14. Examples of Hanessian staining possible with TLC readout.**

(A) CLI and UV images of crude  $[^{18}\text{F}]$ PBR-06 reaction separated under the PRISMA-optimized TLC conditions. (B) Hanessian stain of the same TLC plate. (C) CLI and UV images of a different crude  $[^{18}\text{F}]$ PBR-06 reaction separated under the PRISMA-optimized TLC conditions. (D) Ninhydrin stain of the same TLC plate. Black dashed lines are used to denote the observable bands on the stained plates in B and D.

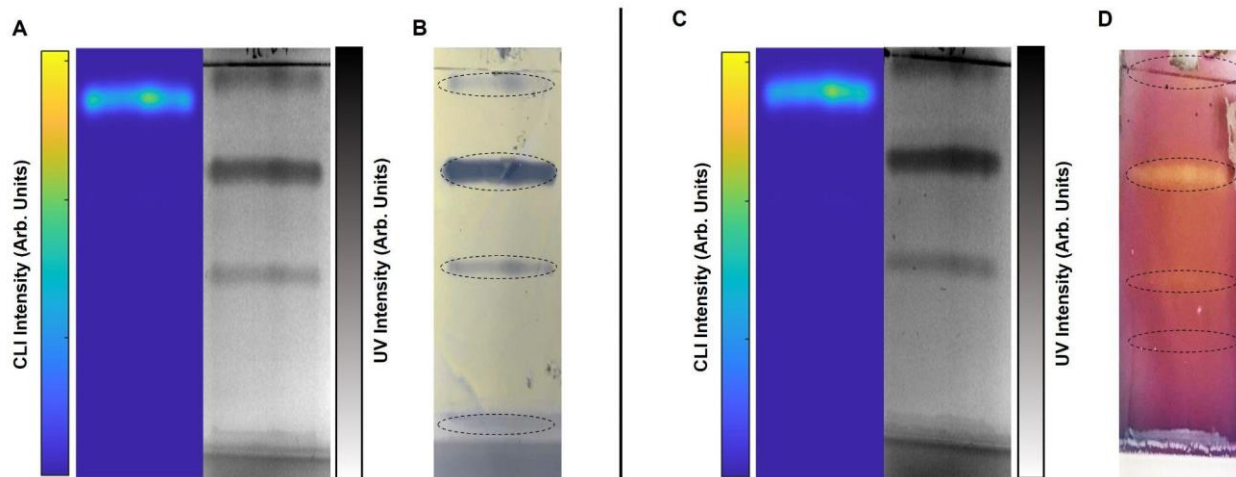


**Figure 9-15. Examples of Ninhydrin staining possible with TLC readout.**

(A) CLI and UV images of crude  $[^{18}\text{F}]$ Fallypride reaction separated under the PRISMA-optimized TLC conditions. (B) Hanessian stain of the same TLC plate. (C) CLI and UV images of a different crude  $[^{18}\text{F}]$ Fallypride reaction separated under the PRISMA-optimized TLC conditions. (D) Ninhydrin stain of the same TLC plate. (The pink cast across the plate may be due to incomplete drying of the TLC plate after separation, leaving residual TEA from the mobile phase.) Black dashed lines are used to denote the observable bands on the stained plate.



## Chapter 10: PHENYX – A flexible pipetting-based platform for automated microvolume radiochemistry

### 10.1 Introduction

The rapid pace of developments in the fields of molecular imaging, theranostics, and radiochemistry is leading to a wealth of new radiopharmaceuticals, including tracers for single-photon emission computed tomography (SPECT) and positron-emission tomography (PET) as well as targeted agents for radioligand therapy (RLT) (373–375). Due to the short half-lives of these compounds, they must be manufactured repeatedly and frequently to make them available throughout the whole radiopharmaceutical development lifecycle, including *in vitro* studies, preclinical *in vivo* imaging, clinical research, etc. Compounds that prove useful may require ongoing production for preclinical or clinical use to study disease or develop new drugs, or for clinical use in diagnosing disease, predicting or monitoring response to therapy, or, in the case of theranostics, treating disease.

Throughout most of this lifecycle, these compounds are currently manufactured using commercial radiosynthesizers that are designed and optimized for production of large, multi-dose batches (376). Reactions are performed in milliliter scale volumes, despite the miniscule amounts of these compounds needed (e.g. nmol amounts for imaging). To ensure reactions proceed at reasonable rates, large amounts of radioisotope are used, and other species in the reaction (i.e. precursor molecule) are used in high concentrations. Excess precursor leads to significant waste and to difficulties in downstream purification to remove excess precursor and side products. The use of large amounts of radioisotope ensures high molar activity but is very wasteful when only a small batch is needed, e.g. for an *in vitro* study, preclinical scan, or a single clinical scan; most of the radiopharmaceutical is discarded in these cases. These inefficiencies combined with the high cost of radiochemistry equipment and facilities make radiopharmaceuticals quite expensive and difficult to integrate into routine research.

As the number of new radiopharmaceutical compounds rapidly grows there are increasing pressures to innovate more efficient, compact, and low-cost methods for their production. During at least the last 15 years, investigators have recognized the potential for microfluidic devices to provide a more optimal platform for production of radiopharmaceuticals, and have developed a wide range of microfluidic tools for radiochemistry. A comprehensive accounting of these approaches can be found in numerous recent reviews in the field (36,38,44,377,378). These can roughly be classified into flow chemistry systems and batch systems. Though flow chemistry systems have exhibited high synthesis performance for a wide range of radiopharmaceuticals, they rely on macroscale components to perform some synthesis steps and have similar size and volume requirements as conventional radiosynthesizers. On the other hand, recent batch systems have exhibited a high degree of integration (e.g. including both [<sup>18</sup>F]fluoride isotope processing and subsequent reactions) into simple and compact devices. The Iwata group has developed a microvial-based system for performing reactions as low as ~5  $\mu$ L using principles similar to conventional systems (62,63), though no automation has yet been reported. Our group has developed several generations of semi-automated and fully-automated droplet-based reaction chips including EWOD (320,321,379), passive transport chips (380), and new surface-tension trap chips (381). These devices exhibit yields comparable to conventional approaches, up to ~100x reduced precursor consumption (162,325,382,383), much shorter synthesis times in part due to the use of analytical-scale high performance liquid chromatography (HPLC), rather than semi-preparative scale, for purification. Reaction products also exhibit high molar activity, even starting with low amounts of activity, which is not possible in conventional systems (and thus they are not capable of making small batches that have high molar activity) (134). Recently we have shown that droplet reactions can be scaled to large clinically-relevant amounts by starting with more radioactivity (83,99). However, the [<sup>18</sup>F]fluoride concentrator (83) that enabled shrinking the radioisotope volume so that a larger amount could fit on the chip (i.e. reducing volume from ~1

mL to ~28  $\mu$ L) involves a complex and relatively bulky fluidic system. Furthermore, the open nature of these chips (droplet sitting on the chip surface), while critical to achieve fast evaporation times, can result in unwanted evaporation, making it challenging to maintain solvent during reactions, or to work with reactions involving volatile reagents, intermediates, or product. A number of other batch microfluidic approaches have successfully synthesized numerous radiopharmaceuticals (57,250,384–386), though most are much larger in size, use significantly larger volumes or have a fixed fluid path (e.g. with specific number of inlets connected to a microreactor), which requires different chip designs to perform different syntheses.

To provide more flexibility, an approach that has been used successfully for macroscale reactions in the ELIXYS radiosynthesizer (SOFIE, Inc.) was to employ a robotic system to move the reaction vial to different fluidic interfaces and load different reagents (33,346). This robotic mechanism replaced most of the tubing and valves used in conventional (fixed plumbing) systems, enabling a high degree of dynamic reconfigurability *via* programming (225). This strategy avoids problems due to valve failures, and by avoiding the need for manually reconfiguring connections, eliminated the lengthy system switchover process and the associated chance for errors and leaks. Our preclinical imaging facility has implemented >30 different syntheses on the ELIXYS system (212), all of which can be implemented without any reconfiguration of the fluidic system. Similarly, a macroscale system has been developed by GeSIM mbH and ABX Advanced Biochemical Compounds GmbH, which used a robotic mechanism to transfer liquids among conventional reagent vessels, reaction vessels and solid-phase cartridges to implement different radiosyntheses (387).

To bring the flexibility of robotic pipetting systems to microscale reactions, while also addressing the issues of open droplet reactions, we developed here a novel flexible robotic-based radiosynthesis system (“PHENYX”). It is designed to perform radioisotope concentration in addition to the subsequent multi-step microscale radiosynthesis in 5-50  $\mu$ L volumes on a

disposable cassette. The robotic system moves a high-precision pipettor among a disposable tip rack and various components on a disposable cassette, including a [ $^{18}\text{F}$ ]fluoride source reservoir, a QMA-based fluoride concentration system, reagent reservoirs, a reaction vessel, and an outlet reservoir (connected to downstream purification and formulation system). Notably, the system contains no fluidic valves: all operations are performed by pipetting (i.e. liquid transfers) or with special attachments for the pipetting head (i.e. radioisotope concentration, sealing of the reaction vessel with a heated lid, pressurization of reservoir for transfer to purification system). We describe here the design and characterization of this system, and demonstrate the high-yield synthesis of [ $^{18}\text{F}$ ]Fallypride as an example radiopharmaceutical.

## 10.2 Materials and methods

### 10.2.1 System design

#### 10.2.1.1 Robotic system and cassette stage

The PHENYX system consists of a fixed instrument and an interchangeable single-use cassette (**Figure 10-1A**). The main part of the system is the robotic pipettor (Cavro Air-Displacement Pipettor; ADP, Tecan Group Ltd., Männedorf, Switzerland), mounted to the Z-axis of an XYZ gantry (Cavro Omni Robot, Tecan). The baseplate holds a pipette tip carrier (DiTi carrier, Tecan) with capacity of 2 racks of disposable tips, a waste container for discarded tips, and a “stage” (**Figure 10-1B**) to hold the disposable cassette. The stage also provides temperature control of the Reactor in the cassette via an aluminum reactor heating block with conical cavity (**Figure 10-2A**) mounted to a 200W ceramic heater (Ultramic CER-1-01-00097, Watlow, St. Louis, MO, USA), heatsink, and cooling fans (**Figure 10-2A,B**). This Reactor heater assembly is spring-loaded to ensure good thermal contact between the heater and Reactor, and to avoid contact directly with the cassette stage (**Figure 10-2C**).

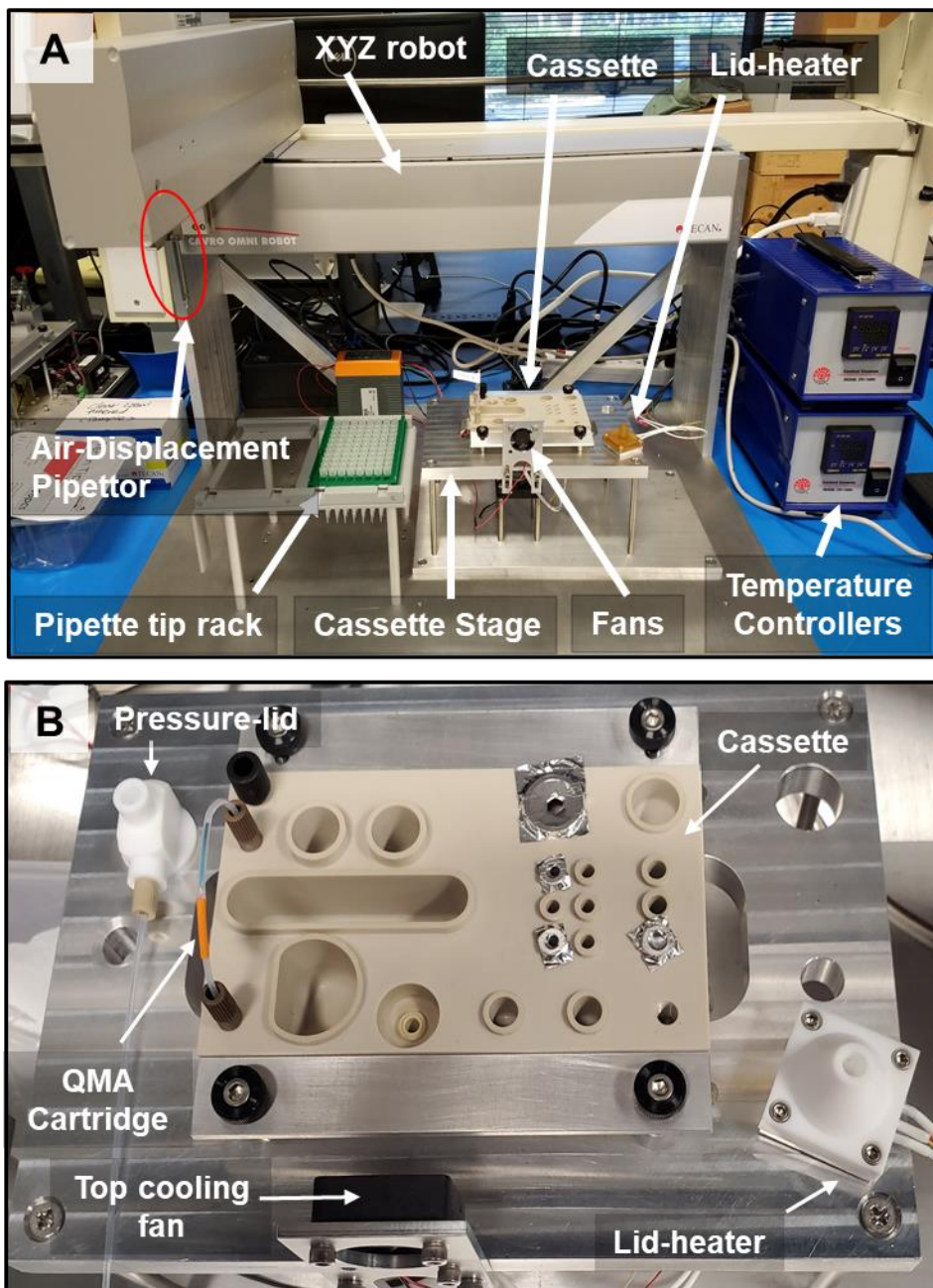


**Figure 10-1 The PHENYX system.**

**A.** The PHENYX prototype system includes a working bed containing the Cassette Stage and racks for disposable pipette tips. Control electronics are located outside the footprint of the main system. **B.** The cassette stage holds the disposable PEEK cassette atop a Reactor heater, as well as storage sites for the Lid-heater and Pressure-lid.

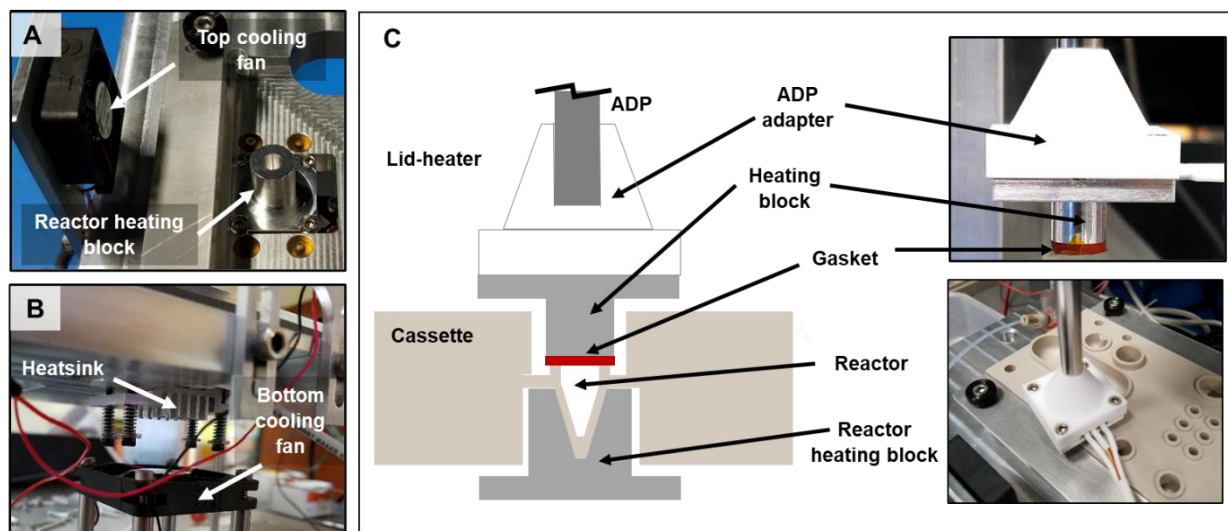


**Figure 10-2 The stage of PHENYX.**

**A.** The top side of the Reactor heater consists of a heat block with conical cavity that mates to the bottom of the Reactor reservoir on the cassette. There is also a top cooling fan. **B.** The bottom side of the Reactor heater includes a heatsink and a bottom cooling fan. **C.** The Lid-heater consists of a custom Teflon adapter designed to mate with the ADP, attached to a heat block with a silicone elastomer layer on the bottom, which seals onto the top rim of the Reactor reservoir (inset). ADP = air displacement pipettor.

### 10.2.1.2 Disposable cassette

The 127 mm x 80 mm x 22 mm cassette (**Figure 10-3**) was fabricated from polyether ether ketone (PEEK) due to this material's high temperature stability and chemical inertness. Prototype cassettes were made by computer numerical controlled (CNC) machining but could be injection molded in the future. In addition to the reservoirs in the top surface, there are several millifluidic channels (joining a few ports and reservoirs) machined into the bottom side of the cassette (**Figure 10-3B**), and closed off with a layer of silicone pressure-sensitive adhesive film (9795R, 3M, Saint Paul, MN, USA). The cassette features three sections: (i) a radioisotope concentrator, (ii) a reactor reservoir and associated reagent reservoirs, and (iii) a dilution reservoir and connection for transfer of product to a downstream purification and formulation module.

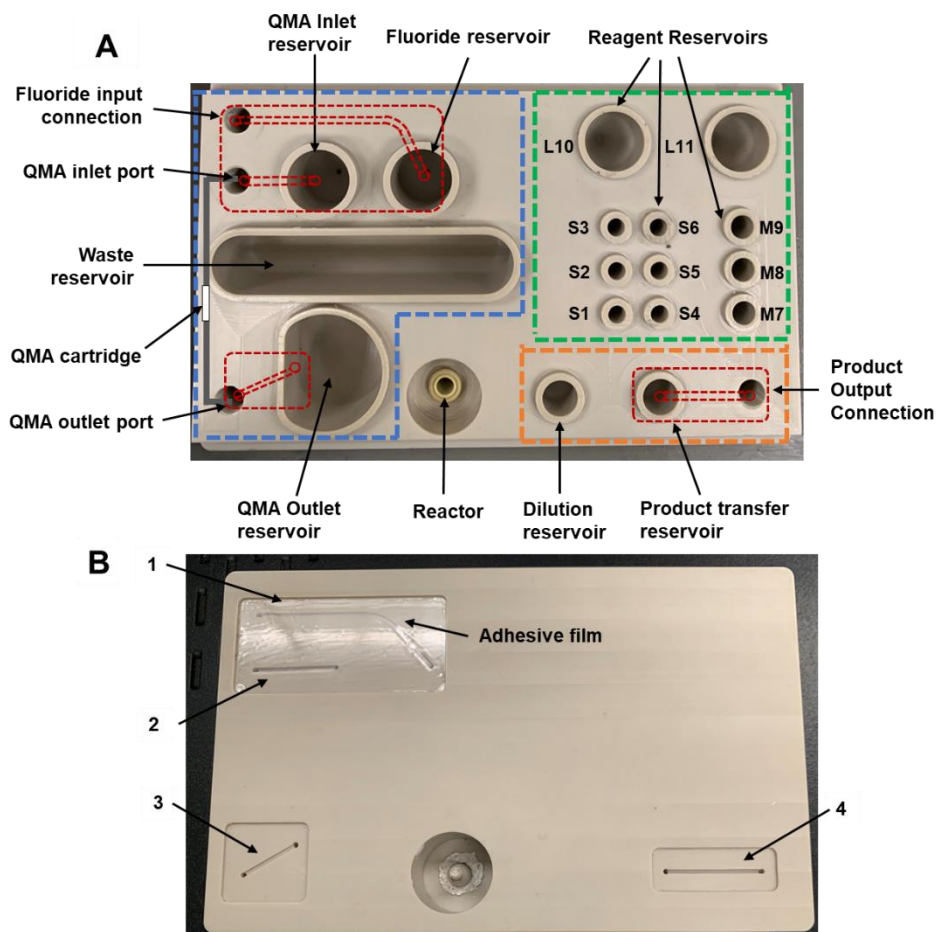


**Figure 10-3 PHENYX cassette.**

**A.** Overhead photograph of cassette. The cassette includes a section for receiving and concentrating [ $^{18}\text{F}$ ]fluoride (blue), a Reactor and reagent storage reservoirs section (green), and a product dilution and transfer section (orange). The cassette contains a number of reservoirs: QMA inlet reservoir (2 mL capacity), QMA outlet reservoir (6 mL capacity), Waste reservoir (7 mL capacity), Reagent reservoirs (small: 50  $\mu\text{L}$  for S1-S6; medium: 200  $\mu\text{L}$  for M7-M9; large: 2 mL for L10-L11), Reactor (50  $\mu\text{L}$ ), Dilution reservoir (200  $\mu\text{L}$ ). A micro-QMA cartridge is connected to the two points joined by the blue arrow. The red dashed areas show locations of fluidic channels on the bottom of cassette. **B.** Photograph of the bottom of the cassette showing the machined fluidic channels, some open and some sealed with adhesive films. The fluidic channels connect: (1) fluoride-input connection to Fluoride reservoir, (2) QMA inlet reservoir to QMA inlet connection, (3) QMA outlet connection to QMA Outlet Reservoir, and (4) Product transfer reservoir to Product Output connection. The image is mirrored to match locations with the overhead view. The cassette measures 12.7 cm x 8 cm x 2.2 cm. QMA = quaternary methylammonium (cartridge).

The concentrator section has a [ $^{18}\text{F}$ ]fluoride input connection port to introduce the radioisotope from an external source through a millifluidic channel into the [ $^{18}\text{F}$ ]fluoride reservoir.

The pipettor is used to transfer the desired amount of radioisotope into the QMA inlet reservoir,

which is connected to the QMA inlet fitting by a millifluidic channel. The QMA outlet fitting is connected via a millifluidic channel to the QMA Outlet reservoir. A custom miniature QMA cartridge (see **Materials**) is connected between the two ports. To move liquid through the cartridge, the Pressure-lid (see below) is positioned at the QMA Inlet reservoir by the pipettor to push the contents through the QMA cartridge and into the QMA Outlet reservoir. A large waste reservoir is used to store [<sup>18</sup>O]water pipetted out of the QMA Outlet reservoir after trapping. The trapped [<sup>18</sup>F]fluoride is eluted by pipetting a small volume of eluent solution into the QMA inlet reservoir and repeating the above process. In this way, [<sup>18</sup>F]fluoride volumes of 1-2 mL can be concentrated into 20-40 µL at the QMA outlet reservoir, which can then be transferred to the Reactor reservoir by the pipettor.

The radiosynthesis section of the cassette consists of a 50 µL Reactor reservoir as well as an array of Reagent Reservoirs. The Reactor reservoir was designed to hold a maximum of 50 µL of fluid and has thin walls to ensure rapid heat transfer between the reactor heating block beneath and the reactor reservoir contents. The array of Reagent Reservoirs includes two large (1 mL) reservoirs, six small (50 µL) reservoirs, and three medium (200 µL) reservoirs. The user can fill these with any reagents necessary for the fluoride concentration and radiosynthesis steps. A sealing foil can be applied after filling to limit evaporation or atmospheric exposure of reagents. The Reactor is located sufficiently far from the Reagent reservoirs such that unwanted heating of the reagents is avoided.

The crude reaction product is transferred by the pipettor to the dilution reservoir (if dilution is desired), and then to the Product transfer reservoir. Upon pressurization using the Pressure-lid, the contents are driven through a millifluidic channel to the product output connection and into the downstream purification and formulation system.

### **10.2.1.3 Pipettor attachments**



The stage also provides storage locations for special attachments (“Pressure-lid” and “Lid-heater”) that are designed to be picked up and moved by the pipettor for use on-demand at any desired location on the cassette.

The Pressure-lid (**Figure 10-4**) provides air pressure to drive fluids through the cassette, i.e. during the radioisotope concentration step (to push solutions through the trapping cartridge), and to transfer the final diluted product after synthesis out of the cassette and into a downstream purification/formulation system. The Pressure-lid has a Teflon body with a silicone elastomer gasket on the bottom (**Figure 10-4A**). The top of the Pressure-lid mates to the pipettor (**Figure 10-4B**), thus allowing the Pressure-lid to be picked up and pressed down on top of the desired cassette reservoir (with 0.5 mm of compression), and pressure is provided to the reservoir through a hole in the gasket from a regulated inert gas source connected to the Pressure-lid body. Additionally, by adjusting the vertical position so the lid is not sealed, the Pressure-lid can also be used to provide convective air flow above the Reactor reservoir to accelerate evaporation steps.

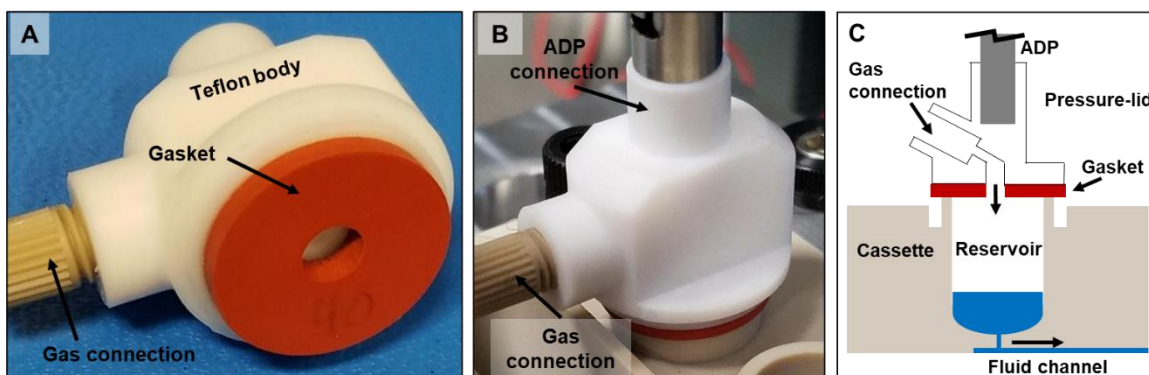


**Figure 10-4 Pressure-lid.**

**A.** Photograph showing the silicone gasket at the bottom of the Pressure-lid. A hole in the middle connects to pressurized air via a fitting on the side of the Pressure-lid. **B.** The Pressure-lid mounted on the ADP robot and interfaced to the top rim of a reservoir on the cassette. **C.** Cross-section showing the operation of the Pressure-lid. ADP = air displacement pipettor.

The Lid-heater (**Figure 10-2C**) is designed to seal the reactor, but is heated to prevent reaction solvent condensation remaining on the gasket surface. This is imperative for small volume reactions where solvent redistribution (due to evaporation and condensation elsewhere)

could otherwise drastically affect the synthesis yield. It comprises a 200W ceramic heater (Ultramic CER-1-01-00097, Watlow, St. Louis, MO, USA) sandwiched between a Teflon adapter (to interface with the pipettor), and a cylindrical aluminum heater transfer block with a thin 1/16” silicone elastomer layer affixed to the bottom surface. This assembly can be moved by the pipettor and pushed down (with 1 mm of gasket compression) on top of the Reactor to form a tight seal when performing reaction steps. A second cooling fan is mounted to the stage and can be activated as needed to cool the lid heater before unsealing the Reactor (**Figure 10-2A**). An illustration of how both the bottom and top heaters interface with the Reactor reservoir is shown in **Figure 10-2C**. Typically, evaporation steps were performed using only the bottom heater, but reaction steps were performed using both heaters.

#### 10.2.1.4 Control system

Heaters were controlled with the aid of their built-in K-type thermocouples *via* standalone controllers (TPC-1000, Tempco Electric Heater Corp., Wood Dale, IL, USA). Actuation of the Omni Robot robotic system was controlled *via* a series of custom scripts implementing several “unit operations” of the synthesis process.

#### 10.2.2 Characterization of subsystems

Evaluation of sealing performance of the Pressure-lid is described in the **Appendix 10.5.1.1**. Calibration of the internal Reactor reservoir temperature and Lid-heater gasket surface temperature to heater setpoints, and measurement of heating and cooling rates are described in the **Appendix 10.5.1.2**. A series of experiments was conducted to compare the quality of sealing (i.e. ability to prevent loss of solvent) of the Lid-heater to different Reactor rim designs (**Figure 4**), and using different durometers of the gasket material (see **Appendix 10.5.1.4**). The pipettor was calibrated for the different liquids used in the synthesis (see **Appendix 10.5.1.5**). To minimize the losses of eluent solution from [<sup>18</sup>F]fluoride concentration process, optimization of the QMA Outlet reservoir geometry was performed (see **Appendix 10.5.1.6**).

### 10.2.3 [<sup>18</sup>F]Fallypride synthesis

#### 10.2.3.1 Materials

TBAHCO<sub>3</sub> (75 mM in ethanol), tosyl fallypride (fallypride precursor, >95%), and fallypride (reference standard for [<sup>18</sup>F]fallypride, >95%) were purchased from ABX Advanced Biochemical Compounds (Radeberg, Germany). Anhydrous MeCN (99.8%), 2,3-dimethyl-2-butanol (98%), anhydrous methanol MeOH (99.8%), anhydrous ethanol (EtOH, 99.5%), ammonium formate (NH<sub>4</sub>HCO<sub>2</sub>, 97%) and triethylamine (TEA, 99.5%) were purchased from Sigma-Aldrich (St. Louis, MO, USA). DI water was obtained from a Milli-Q water purification system (EMD Millipore Corporation, Berlin, Germany). No-carrier-added aqueous [<sup>18</sup>F]fluoride was obtained from the UCLA Ahmanson Biomedical Cyclotron Facility. Micro-cartridges were prepared by loading 3 mg of quaternary methylammonium (QMA) resin (Waters Corporation, Milford, USA) into an ethylene tetrafluoroethylene (ETFE) tube (1/16" OD x 0.040" ID, 1517L; IDEX Health and Sciences, Wallingford, USA) with polyethylene frits as previously described (83). These cartridges were preconditioned with 0.5 mL of 1M KHCO<sub>3</sub> and 10 mL of DI water sequentially prior to the radiosynthesis process. An eluent stock solution of TBAHCO<sub>3</sub> was prepared by diluting the 75 mM TBAHCO<sub>3</sub> solution (in EtOH) with DI water to provide 25 mM TBAHCO<sub>3</sub> in the mixed solvent of EtOH and DI water (1:2, v/v). Precursor stock solution (77 mM) was prepared by dissolving 4 mg of tosyl fallypride (7.75 μmol) in 100 μL of the mixed solvent MeCN and 2,3-dimethyl-2-butanol (1:1, v/v). Collection solution was prepared by mixing MeOH and DI water (9:1, v/v). In some experiments, HPLC mobile phase (described below) was used for collecting the crude product.

#### 10.2.3.2 Synthesizer setup

Prior to performing a synthesis, the cassette was loaded with the following reagents. 30 μL of eluent stock solution (25 mM TBAHCO<sub>3</sub>), 40 μL of DI water and 20 μL of precursor stock solution were pre-loaded into small-volume reservoirs (S1-S3, respectively). 120 μL of collection solution was loaded into a medium-volume reservoir (M7). Microwell sealing tape (Nunc™ 276014, Thermo Scientific, Waltham, USA) was cut into squares (~0.8 x 0.8 cm) and used to seal

the small-volume and medium-volume reservoirs to minimize evaporation and moisture contamination prior to use. Disposable pipette tip racks 50  $\mu\text{L}$  (Part No. 30126097, Tecan, Männedorf, Zürich, Switzerland) and 200  $\mu\text{L}$  (Part No. 30126093, Tecan) with filter were installed in the system. As a final setup step, 500  $\mu\text{L}$  of aqueous [ $^{18}\text{F}$ ]fluoride was introduced into the QMA inlet reservoir *via* pipette.

### 10.2.3.3 Analytical equipment and methods

Radioactivity measurements were performed with a calibrated dose calibrator (CRC-25R, Capintec, Florham Park, NJ, USA). The crude reaction product collected from reactor was analyzed by radio-thin layer chromatography (radio-TLC). A small sample ( $\sim 1$   $\mu\text{L}$ ) was spotted onto a TLC plate (silica gel 60  $\text{F}_{254}$  TLC plastic plate, Merck KGaA, Darmstadt, Germany) and the plate was developed with 60% MeCN in 25 mM  $\text{NH}_4\text{HCO}_2$  with 1% TEA (v/v). After drying, the TLC plate was scanned using a radio-TLC scanner (miniGITA, Elysia-Raytest GmbH, Straubenhardt, Germany) for 3 min. The proportion of each species was computed using GINA-STAR software (Elysia-Raytest) by computing areas under the peaks in the chromatogram corresponding to the product ( $R_f = 0.9$ ), side-product ( $R_f = 0.5$ ) and unreacted [ $^{18}\text{F}$ ]fluoride ( $R_f = 0.0$ ), and dividing the individual peak area by the sum of all peak areas. Fluorination efficiency was computed as the proportion of the product peak area. Collection efficiency was calculated as the activity of the crude product collected from the cassette divided by the starting activity (corrected for decay). Crude radiochemical yield (RCY) was computed as collection efficiency multiplied by the fluorination conversion. The isolated RCY was determined by performing radio-HPLC purification on an analytical C18 column (Kinetex, 250 x 4.6 mm, 5  $\mu\text{m}$ , Phenomenex, Torrance, CA, USA) using mobile phase of 60% MeCN in 25 mM  $\text{NH}_4\text{HCO}_2$  with 1% TEA (v/v) and flow rate of 1.5 mL/min with UV absorbance (254 nm) and radiation detectors, as previously reported (83). The retention time of [ $^{18}\text{F}$ ]fluoride and [ $^{18}\text{F}$ ]Fallypride were 1.5 and 4.5 min, respectively. To determine the residual activity left behind in reservoirs (QMA inlet, QMA outlet,

Dilution), the reactor, and the Lid-heater, the wetted surfaces were carefully wiped with Kimwipes (Kimberly-Clark, Irving, Texas, U.S.A.) pre-wetted with a solution of EtOH and DI water (7:3, v/v), repeated a total of 2 times, and measured via dose calibrator. The values were expressed as a proportion of the starting activity (corrected for decay). After wiping the reservoirs and reactor, the residual activity in the cassette was visualized via PET/CT. The cassette was scanned in a HiPET scanner (388) for 60 min first and then in a CT scanner (CrumpCAT (389)) for 10 min. The PET/CT image registration was carried out with AMIDE version 1.0.5 software.

#### 10.2.3.4 Radiosynthesis of [ $^{18}\text{F}$ ]Fallypride

The synthesis was developed in a step-wise fashion, beginning with the radioisotope concentration step and then adding the remaining steps, with intermediate measurements and samples taken to quantify performance and losses. Afterward, the synthesis was carried out without the intermediate measurements in order to determine a more accurate estimate of the duration of the automated synthesis.

To perform the radioisotope concentration step, [ $^{18}\text{F}$ ]fluoride was manually added into the QMA inlet reservoir, and the starting activity was determined (i.e., difference in source activity before and after transfer). Trapping was performed by applying 20 psi for 90 s *via* the Pressure-lid, and the [ $^{18}\text{O}$ ]H<sub>2</sub>O was transferred by the pipettor from the QMA Outlet reservoir to waste. Later this liquid was collected to compute the trapping efficiency by dividing the activity in the waste by the starting activity (corrected for decay) and subtracting from 100%. Next, several elution protocols were compared. First, eluent stock solution (7  $\mu\text{L}$ ) was transferred from the reservoir S1 to the QMA inlet reservoir, and was pushed through the cartridge *via* the Pressure-lid with by gradually ramping the pressure from 0 to 5 psi over 40 s, then switching to 10 psi for 20 s. This process was then repeated for another portion of elution solution (7  $\mu\text{L}$ ). After that, a similar procedure was carried out to rinse the fluid pathways. DI water (7 or 15  $\mu\text{L}$ ) was transferred from reservoir S2 to the QMA inlet reservoir and then, after

installing the Pressure-lid, was passed through the micro-QMA cartridge to wash out the residual activity. This was repeated multiple times, depending on the details of the elution protocol being tested. The elution efficiency was calculated by dividing total eluted activity (collected manually *via* pipette from the QMA outlet reservoir) by the starting activity (corrected for decay). The residual activity on the cartridge after elution was also measured using a dose calibrator, and this value was expressed as a fraction of the starting activity (corrected for decay).

The eluted [ $^{18}\text{F}$ ]fluoride /TBAHCO<sub>3</sub> mixture was then transferred *via* the pipettor from the QMA Outlet reservoir into the Reactor. The Pressure-lid was picked up and moved to a position ~1 mm above the reactor to provide convective nitrogen flow at 5 psi to accelerate evaporation. Evaporation was performed at 100 °C (using calibration data) for 8 or 10 min, with heat supplied by the bottom heater. After drying, the reactor was cooled down to 25 °C (~2 min) by turning on both the top and bottom cooling fans. To perform the fluorination reaction, 8  $\mu\text{L}$  of precursor stock solution (77 mM), which contains 0.62  $\mu\text{mol}$  of precursor, was transferred from reservoir S3 into the Reactor. After closing the reactor using the Lid heater, the mixture was heated for 7 min by setting both bottom and lid heaters to 110 °C. The crude product was then cooled down to 25 °C (~2 min) by turning on the bottom and top cooling fans. Next, 30  $\mu\text{L}$  of collection solution was transferred *via* pipette from the reservoir M7 to the Reactor and then mixed *via* aspirating and dispensing with the same pipette tip 10x in a row. The mixed collection solution was then transferred to the Dilution Reservoir. This process was repeated a total of 3x resulting in a final volume of ~90  $\mu\text{L}$ , which was transferred to a vial (0.5 mL) from the Dilution Reservoir. The collected crude product was analyzed by radio-TLC and its activity measured. Afterward, the crude product can be further diluted (e.g. for downstream cartridge purification) or injected for HPLC purification.

## 10.3 Results and discussion

### 10.3.1 System characterization

#### 10.3.1.1 Pressure-lid function

The Pressure-lid was tested for its ability to seal onto cassette reservoirs and for the ability to push fluid through the cassette. With 0.5 mm of gasket compression, pressures up to 20 psi could be maintained (i.e. pressure decay < 0.1 psi in 2 min). Fluid in the QMA Inlet reservoir could be pushed through the millifluidic channel and QMA cartridge into the QMA Outlet reservoir using 15-20 psi. 500  $\mu$ L of water could be transferred at 15 psi within  $\sim$ 75 s. The same volume of MeCN could be flushed through this same path at 10 psi in  $\sim$ 30 s.

#### 10.3.1.2 Heater calibration and performance

Calibrations for the internal Reactor temperature and Lid-heater gasket surface temperature versus the built-in thermocouple of the ceramic heaters are summarized in **Figure 10-8**. Heating was relatively fast. For example, as in **Figure 10-9** an internal temperature of 150  $^{\circ}$ C can be reached in  $\sim$ 60-75 s, with reactor heater and lid heater setpoints at 170  $^{\circ}$ C and 220  $^{\circ}$ C, respectively. A temperature of 110  $^{\circ}$ C (as needed for [ $^{18}$ F]Fallypride fluorination) could be reached in <20 s by setting the reactor heater and lid heater at 117  $^{\circ}$ C and 147  $^{\circ}$ C, respectively.

#### 10.3.1.3 Reactor sealing by the Lid-heater

Multiple reactor rim designs were tested for the ability to seal under pressure (**Figure 10-5**). The flat rim was unable to seal, resulting in substantial loss of MeCN via evaporation when heated to 150 $^{\circ}$ C for 5 min, and thus further experiments focused on the other designs (double-rim and beveled-rim). MeCN was used for these tests as it is commonly used in  $^{18}$ F-radiosyntheses and has a relatively low boiling point and high vapor pressure. For various durometers of the gasket, the double-rim Reactor design exhibited consistently less fluid loss ( $3.0 \pm 2.2\%$ , n=9) than the beveled-rim design ( $5.4 \pm 2.4\%$ , n = 9), but there was not a significant difference among different gasket durometers (see **Figure 10-11A**). To further explore potential

differences among durometers, sealing repeatability was compared (3 successive trials) for each durometer using the double-rim Reactor design. No significant difference was observed (see **Figure 10-11B**). Ultimately, the 50A durometer was chosen based on the qualitative assessment that the mean fluid loss tended to be lower across all tests.

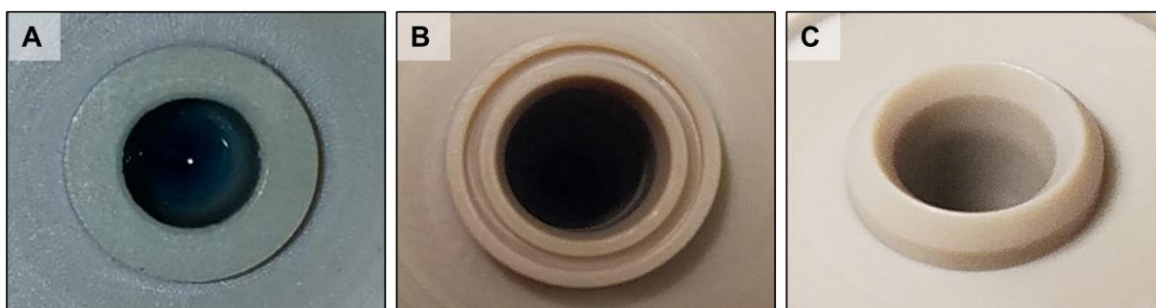


**Figure 10-5 Reactor rim designs tested for sealing.**

**A.** Flat rim design consisting of a 1.4 mm wide flat sealing surface. **B.** Double-rim design consisting of two 0.5 mm wide, concentric flat sealing rims with a 0.38 mm wide recessed gap between them. **C.** Beveled rim design consisting of a single beveled rim.

#### 10.3.1.4 Pipettor calibration

Calibration plots of actual volume dispensed versus programmed volume are shown in **Figure 10-12** for different liquids: DI water, MeCN, 9:1 (v/v) MeOH:DI water (collection solution), 30 mM TBAHCO<sub>3</sub> in 7.5% (v/v) EtOH:water (eluent solution), and 1:1 (v/v) thexyl alcohol : MeCN (fluorination solvent). As expected, the relative error was larger at lower target volumes. These calibration curves can be programmed directly into the software, creating a library for various reagent types. The pipettor has additional parameters (aspirate/dispense speed, and aspirate/dispense delay) that can also impact accuracy and precision, but these were not optimized in this work.

### 10.3.2 Microvolume radiosynthesis of [<sup>18</sup>F]Fallypride

#### 10.3.2.1 [<sup>18</sup>F]fluoride concentration

First the trapping/release performance using the micro-QMA cartridge was evaluated. Initially, (**Table 10-1, entry 1**) elution was carried out using two 7 µL volumes of elution solution (25 mM TBAHCO<sub>3</sub>), followed by 15 µL of DI water to rinse any residual activity out of the fluid



path. High trapping efficiency (100%) was observed, but there was only a moderate elution efficiency (75%), with significant residual activity in the cartridge (14%) and other parts of the fluid path. The addition of a second 15  $\mu$ L DI water rinse (**Table 10-1, entry 2**) did not significantly change the performance (trapping: 95%, elution: 70%, residual activity on the cartridge: 18%).

In our previous work performing concentration of [ $^{18}$ F]fluoride using a micro-QMA cartridge [36], we observed that splitting the eluent or rinse solution into multiple smaller volumes can improve the elution efficiency. Therefore, we attempted the rinse step with four 7  $\mu$ L portions of DI water (**Table 10-4, entries 3-4**), resulting in a modest improvement of elution efficiency to 82-83%.

We attempted to repeat these measurements with cassettes that had been thoroughly cleaned, but where the adhesive layer on the bottom of the cassette had not been replaced (**Table 10-4, entries 5-10**). However, the elution efficiency ( $42 \pm 35\%$ ,  $n = 6$ , **Table 10-1, entry 3**) showed a large fluctuation, and also low trapping efficiency in some cases. We hypothesized that organic solvents and basic reagents used in the cassette caused damage to the adhesive layer, possibly creating small voids and dead volumes where the fluid can flow outside of the intended channel and become trapped under the adhesive layer. Indeed, after performing similar experiments, but with adhesive layers replaced each time, the elution efficiency was significantly increased and consistent, i.e. up to  $88 \pm 5\%$  ( $n = 10$ ) with excellent trapping efficiency of  $100 \pm 1\%$  ( $n = 10$ ) (**Table 10-1, entry 4**), comparable to our previous report with a more complicated automated micro-concentrator design ( $100 \pm 0\%$ ,  $n=6$  trapping efficiency and  $91 \pm 7\%$ ,  $n = 6$  elution efficiency) (83).

**Table 10-1 Performance of [<sup>18</sup>F]fluoride trap and release on the integrated QMA cartridge. The starting activity was 3-10 MBq [0.08-0.3 mCi]. All percentages are decay-corrected.**

Entry	1 <sup>a</sup>	2 <sup>b</sup>	3 <sup>c</sup>	4 <sup>c</sup>
Number of repeats (n)	1	1	6	10
Elution with TBAHCO <sub>3</sub> (μL x repeats)	7 x 2	7 x 2	7 x 2	7 x 2
Rinse with DI water (μL x repeats)	15 x 1	15 x 2	7 x 4	7 x 4
Cassette adhesive layer (new or reused)	new	new	reused	new
Trapping efficiency (%)	100	95	95 ± 8	100 ± 1
Elution efficiency (%)	75	70	42 ± 35	88 ± 5
Residual activity on cartridge (%)	14	18	N.M.	N.M.

<sup>a</sup>Elution condition: gradually ramping from 0 to 3 psi over 30 s and holding pressure for an additional 10 s. <sup>b</sup>Elution condition: gradually ramping from 0 to 2 psi over 100 s and holding pressure for another 20 s. <sup>c</sup>Elution condition: gradually ramping from 0 to 5 psi over 40 s, then switching to 10 psi for 20 s. N.M. = Not measured.

### 10.3.2.2 [<sup>18</sup>F]fallypride synthesis

After optimizing the [<sup>18</sup>F]fluoride concentration process, we proceeded to perform the full synthesis of [<sup>18</sup>F]Fallypride on the platform at ~10 MBq scale (**Table 10-2**). The reaction conditions were selected based on a previous optimization study we performed in open droplet-based reactions (83). Under these conditions (0.62 μmol precursor; 0.35 μmol of TBAHCO<sub>3</sub>; 8 μL reaction; mixed solvent of MeCN and 2,3-dimethyl-2-butanol (1:1 v/v)), the fluorination reaction in the PHENYX system exhibited a high conversion of 79 ± 1% (n = 3), just slightly lower than previously observed for droplet-based reactions (89 ± 5%, n = 6). Prior to the fluorination reaction, 99.8 ± 0.1% (n = 3) of starting activity was trapped on the micro-cartridge and was eluted with high efficiency (90 ± 4%, n = 3), consistent with previous trapping/release performance (**Table 10-1, entry 4**). Wipe measurements of residual activity showed that only a small amount of removable activity was left behind in the QMA outlet reservoir (3 ± 1%, n = 3) and surface of the Lid-heater (3 ± 1%, n = 3), and a similar amount of removable activity (3 ± 1%, n=3) remained in the Reactor after collection of the crude product. Afterward, [<sup>18</sup>F]Fallypride production was carried out without the intermediate measurements (**Table 10-2**) to determine the overall automated

synthesis time. The total time was ~48 min (i.e. ~25 min for concentration, 8 min for drying, 7 min for fluorination, 2x2 min for cooling down after heating and 4 min for product collection). Fluorination efficiency remained the same (79%), but there was a slight increase in collection efficiency (i.e. 73% vs.  $71 \pm 5\%$ ,  $n=3$ ) because losses associated with intermediate measurements were reduced.

There was ~15% of activity unaccounted for in our measurements (“Other loss” in **Table 10-2**). We hypothesized this may be due to residual, non-removable activity on the cassette. Though the cassette was too large for activity to be measured with the dose calibrator, a PET/CT scan was performed to explore the distribution of residual activity on the cassette after product collection (**Figure 10-6**). It showed that the residual activity was mainly located in the vicinity of the reactor, with an additional small amount of activity deposited around the exit hole in the QMA outlet reservoir and in the Dilution Reservoir. Because the activity was not removed using the Kimwipe, the residue may be more strongly adhered to the PEEK surface (or even absorbed slightly into the polymer), suggesting it may be worthwhile to optimize the composition of the collection solution.

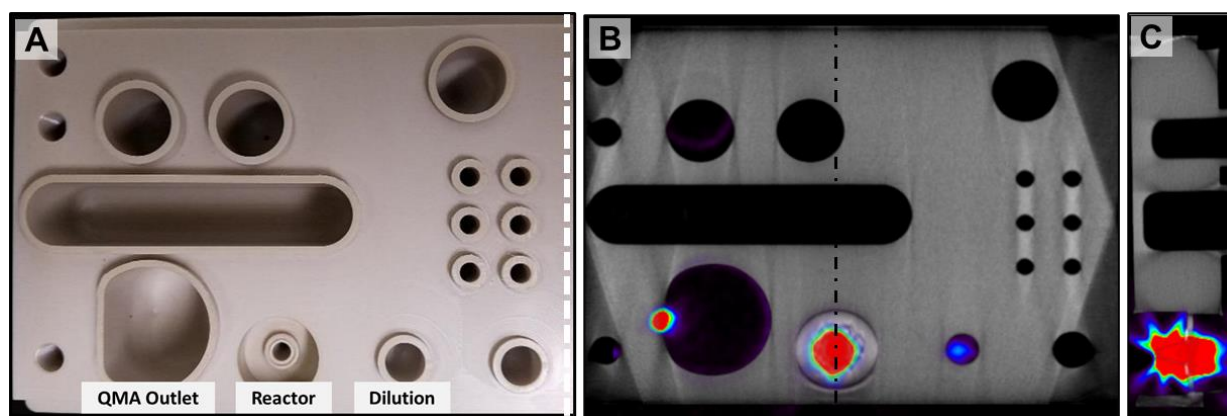


**Figure 10-6 Residual radioactivity in the cassette.**

**A.** Overview of cassette. **B.** PET/CT scan of cassette after synthesis of [ $^{18}\text{F}$ ]Fallypride showing areas where residual activity is concentrated. **C.** Cross section through the cassette along the dashed line.

### 10.3.2.3 [ $^{18}\text{F}$ ]Fallypride synthesis on simplified (reactor-only) cassette

We performed further experiments using a smaller, reactor-only cassette that could fit inside a dose calibrator (**Figure 10-10B**) to allow accurate measurement of residual activity on the cassette. Furthermore, to minimize confounding variables, instead of using a micro-QMA cartridge for activity concentration, we mixed 5  $\mu\text{L}$  of aqueous [ $^{18}\text{F}$ ]fluoride ( $\sim 9$  MBq), 14  $\mu\text{L}$  of  $\text{TBAHCO}_3$  stock solution and 15  $\mu\text{L}$  of DI water and directly added this mixture into the reactor.

Because the fluorination efficiency was somewhat lower than we had observed for droplet-based reactions, we explored variations of the [ $^{18}\text{F}$ ]fluoride drying protocol. As typically is done in conventional macroscale syntheses, we added an azeotropic distillation step. After performing drying at 100  $^\circ\text{C}$  for 8 min, 34  $\mu\text{L}$  of MeCN was added, and heated to 100  $^\circ\text{C}$  for another 8 min. While results were comparable to the reaction without azeotropic distillation, the fluorination yield was much less consistent ( $75 \pm 13\%$ ,  $n = 3$  vs.  $79 \pm 1\%$ ,  $n = 3$ ) as was the collection efficiency ( $73 \pm 18\%$ ,  $n = 3$  vs.  $79 \pm 5\%$ ). Residual activity in the reactor (via Kimwipe) was found to be  $11 \pm 8\%$ ,  $n = 3$ , and negligible activity was found on the lid heater. When the cassette was measured in the dose calibrator, an additional  $13 \pm 10\%$  ( $n = 3$ ) of the starting activity was found. We hypothesized that the inconsistencies may be caused by boiling and splashing of the MeCN within the reactor.

As an alternative enhanced drying protocol, we increased the initial evaporation time to 10 min (and did not use the MeCN drying step). The fluorination yield was improved ( $86 \pm 1\%$ ,  $n = 3$ ) as was the collection efficiency ( $92 \pm 1\%$ ,  $n = 3$ ). Residual activity extracted out of the Reactor using a Kimwipe was very small ( $1 \pm 1\%$ ,  $n = 3$ ), activity on the Lid-heater was negligible, and residual activity measured by inserting the cassette in a dose calibrator was  $5 \pm 2\%$  ( $n = 3$ ).

#### 10.3.2.4 Higher-activity [ $^{18}\text{F}$ ]Fallypride synthesis

Using this optimized protocol, the synthesis was scaled to higher starting activity (0.3 to 0.5 GBq), using the full cassette to enable automated operation with results summarized in **Table 10-2**. The fluorination efficiency was high ( $92 \pm 1\%$ ,  $n = 3$ ). Since we intended to perform HPLC purification, we attempted to collect the product using the HPLC mobile phase (60% MeCN in 25

mM  $\text{NH}_4\text{HCO}_2$  with 1% TEA (v/v)), instead of the MeOH and DI water mixture (9:1 v/v). The collection efficiency with the former was  $86 \pm 7\%$  ( $n = 3$ ), which is comparable to the previously measured collection efficiency ( $92 \pm 1\%$ ,  $n = 3$ ; simplified cassette). Very little residual activity was found in the pipette tips, as shown in the table. Though the full cassette residual activity could not be directly measured, the amount of unaccounted activity in this experiment (likely stuck to the cassette) was lower than the unoptimized protocol ( $7 \pm 4\%$ ,  $n = 3$  vs.  $15 \pm 2\%$ ,  $n = 3$ ). Overall, the crude RCY was  $79 \pm 7\%$  ( $n = 3$ ). The  $\sim 90 \mu\text{L}$  of collected crude product was separated by analytical-scale radio-HPLC in 5 min, giving an isolated RCY of  $71 \pm 6\%$  ( $n = 3$ ). Radiochemical purity was  $>99\%$  based on radio-HPLC and molar activity at the end of purification was 270-670 GBq/ $\mu\text{mol}$  [7.7-18 Ci/ $\mu\text{mol}$ ]. The synthesis time was  $55 \pm 3$  min ( $n = 3$ ), corresponding to 50 min synthesis and 5 min purification.

**Table 10-2 [<sup>18</sup>F]Fallypride synthesis performance. All activity percentages are made relative to the starting activity (and corrected for decay) unless otherwise indicated.**

	Automated synthesis; full cassette		Manual synthesis; simplified cassette		Higher-activity automated synthesis; full cassette
	With intermediate measurements	Skip intermediate measurements	With azeotropic drying	With extended drying	
Starting activity (MBq)	10 ± 3	3	10 ± 2	9 ± 3	430 ± 105
Number of repeats (n)	3	1	3	3	3
Activity in Waste reservoir (%)	0.2 ± 0.1	0.2	N.A.	N.A.	0 ± 0
Trapping efficiency (%)	99.8 ± 0.1	99.8	N.A.	N.A.	100 ± 0
Elution efficiency (%)	90 ± 4	N.M.	N.A.	N.A.	N.M.
Residual activity on micro-QMA (%)	5 ± 3	5	N.A.	N.A.	4 ± 4
Drying conditions (at 100 °C)	8 min	8 min	8 min + 8 min azeotropic drying	10 min	10 min
Activity of cassette (Reactor) after drying (%)	N.A.	N.A.	92 ± 6	96 ± 1	N.A.
Collected crude product (%) <sup>a</sup>	71 ± 5	73	73 ± 18	92 ± 1	86 ± 7 <sup>b</sup>
Residual activity (wipe) on QMA outlet reservoir (%)	3 ± 1	2	N.A.	N.A.	2 ± 0
Residual activity (wipe) on Reactor (%)	3 ± 1	3	11 ± 8	1 ± 1	1 ± 1
Residual activity (wipe) on Lid Heater (%)	3 ± 1	2	0.1 ± 0.2	0 ± 0.1	0 ± 0
Residual activity of cassette (Reactor) after wiping	N.A.	N.A.	13 ± 10	4 ± 1	N.A.
Residual activity on pipette tip for QMA outlet reservoir to waste transfer (%)	N.A.	N.A.	N.A.	N.A.	0 ± 0
Residual activity of pipette tip for QMA outlet reservoir to reactor transfer (%)	N.A.	N.A.	N.A.	N.A.	1 ± 1
Residual activity of pipette tip for precursor to Reactor transfer (%)	N.A.	N.A.	N.A.	N.A.	0 ± 0
Residual activity of pipette tip for collection from reactor (%)	N.A.	N.A.	N.A.	N.A.	0.1 ± 0.1
Other loss (%) <sup>c</sup>	15 ± 2	14	3 ± 1	3 ± 1	7 ± 4
Fluorination conversion (%) <sup>d</sup>	79 ± 1	79	75 ± 13	86 ± 1	92 ± 1
Crude RCY (%)	56 ± 4	58	55 ± 17	79 ± 1	79 ± 7
Synthesis time (min)	N.M.	48	N.M.	N.M.	50

<sup>a</sup>The crude product was collected with MeOH / water (9:1 v/v). <sup>b</sup>The crude product was collected with mobile phase for HPLC purification (60% MeCN in 25 mM NH<sub>4</sub>HCO<sub>2</sub> with 1% TEA (v/v)). <sup>c</sup>Other loss was computed by subtracting from 100% the residual activity on the micro-QMA (%), collected crude product (%), and residual activities (wipe) of the QMA

outlet reservoir (%), Reactor (%) and Lid Heater (%).<sup>d</sup>Fluorination conversion (%) was determined by radio-TLC. N.A. = Not applicable. N.M. = Not measured. RCY = Radiochemical yield.

### 10.3.3 Comparison to other approaches

**Table 10-3** compares this work to macroscale and microscale methods for producing [<sup>18</sup>F]Fallypride using the same precursor and phase transfer catalyst (TBAHCO<sub>3</sub>).

Compared to macroscale methods, the microscale method on PHENYX platform allows >10x higher precursor concentration (77 mM for PHENYX, 7.7 mM for ELIXYS (212) and 3.9 mM for TracerLab FX<sub>FN</sub> (390)) but with a net 7-13x reduction of precursor consumption due to the much smaller reaction volume. The high concentration may contribute to the high conversion and yield. The analytical-scale HPLC purification was faster (5 min) than semi-preparative methods used in conventional systems (>12 min, e.g. with ELIXYS (212) and TracerLab FX<sub>FN</sub> (390)). Consistent with previous reports of microvolume synthesis (134), high molar activity was observed without requiring high starting activity that is needed in conventional macroscale reactions. This provides opportunities to efficiently make small batches of tracers (e.g. for preclinical imaging or a single clinical dose) that have sufficient molar activity (378).

[<sup>18</sup>F]Fallypride synthesis on an open-droplet-based microvolume synthesizer at low radioactivity level was reported by Wang *et al.* with a high crude RCY (96 ± 3%, n = 9) and isolated RCY (78%, n = 1), based on high fluorination conversion (94.6 ± 0.4%, n = 9) and excellent collection efficiency (101 ± 3%, n = 9) (381). However, this synthesis was only conducted with a small amount of activity. In another report, Wang *et al.* integrated a micro-cartridge-based radioisotope concentrator with a droplet synthesizer (83). Compared to that configuration, the PHENYX method provided slightly higher fluorination conversion (92 ± 1%, n = 3 vs. 89 ± 5%, n = 6) and collection efficiency (86 ± 7%, n = 3 vs. 81 ± 9%, n = 6), resulting in higher crude RCY of 79 ± 1% (n = 3) (vs. 72 ± 8%, n = 6), when compared at similar activity levels (0.3-0.5 GBq in this work and 0.01-0.2 GBq in (83)). However, the overall crude synthesis time was 15 min longer (50 vs.

35 min (83)) due to a larger number of QMA elution steps, a longer [<sup>18</sup>F]fluoride drying time (due to the reduced surface area for evaporation in the PHENYX cassette reactor versus an open droplet), and some additional processing (e.g. transferring [<sup>18</sup>O]H<sub>2</sub>O from QMA outlet reservoir to the waste reservoir after the trapping step). A detailed breakdown of the timing for each setup is summarized in **Table 10-5**. The overall synthesis time on the PHENYX system could likely be further reduced by automated inert gas control when using the Pressure-lid, perhaps increasing the drying temperature, and by selecting faster motion actuators (or shortening actuation distances by shrinking the platform).

**Table 10-3 Comparison of automated [<sup>18</sup>F]fallypride synthesis performance on PHENYX (at higher activity level tested) with other methods. All activity percentages are made relative to the starting activity (and corrected for decay) unless otherwise indicated.**

	This work (PHENYX)	Wang <i>et al.</i> (microdroplet synthesizer)	Wang <i>et al.</i> (Integrated concentrator and microdroplet synthesizer)	Collins <i>et al.</i> (conventional synthesizer : ELIXYS)	Moon <i>et al.</i> (conventional synthesizer : TracerLab FX <sub>FN</sub> )
Number of repeats (n)	3	9	6	6	42
Starting activity (GBq)	0.3-0.5	0.01	0.01-0.2	1.3-1.9	8.1-52
Activity volume before concentration/drying (μL)	500	8	500-1000	800	1200
TBAHCO <sub>3</sub> (μmol)	0.35	0.24	0.31	N.R.	1.54
Precursor amount (μmol [mg])	0.6 [0.3]	0.2 [0.1]	0.6 [0.3]	7.7 [4]	3.9 [2]
Reaction volume (μL)	8	6	8	1000	1000
Synthesis duration (min)	55 ± 3 <sup>a</sup>	22 <sup>b</sup>	50	56 <sup>a</sup>	51 ± 1
Fluorination conversion (%) <sup>c</sup>	92 ± 1	94.6 ± 0.4	89 ± 5	N.R.	N.R.
Collection efficiency (%)	86 ± 7	101 ± 3	81 ± 9	N.R.	N.R.
Crude RCY (%)	79 ± 7	96 ± 3	72 ± 8	N.R.	N.R.
Isolated RCY (%) <sup>d</sup>	71 ± 6	78 <sup>e</sup>	N.R.	66 ± 8	68 ± 2
Radiochemical purity (%) <sup>d</sup>	>99	>99 <sup>e</sup>	>98	>95	>97
Molar activity (GBq μmol <sup>-1</sup> )	286-668 <sup>a</sup>	N.R.	81-270	15-78 <sup>a</sup>	140-192

<sup>a</sup>The value does not include formulation step. <sup>b</sup>This method did not include [<sup>18</sup>F]fluoride concentration and product formulation step. <sup>c</sup>Fluorination conversion (%) was determined by radio-TLC. <sup>d</sup>Isolated RCYs and radiochemical purity were determined by radio-HPLC. <sup>e</sup>Purification was only performed for one batch (i.e. n=1). N.R. = Not reported.



The system presented here combines both the intrinsic benefits of performing radiochemistry at 10s of  $\mu\text{L}$  volume scale, while also offering the advantage of integrated [ $^{18}\text{F}$ ]fluoride metering (i.e. selecting the amount of activity to be used in a synthesis and loading it into the QMA Inlet reservoir) and [ $^{18}\text{F}$ ]fluoride concentration (shrinking the radioisotope volume down to 10s of  $\mu\text{L}$ ). Inclusion of these features into the same disposable cassette as the reaction (and same system) greatly simplifies setup and operation.

To perform pipetting, the design leverages existing robotic fluidic handling systems commonly used in high-throughput laboratories, which have well-established reliability and accuracy in handling microscale reagent volumes. Unlike conventional or microchannel-based radiosynthesizer systems where there are pre-established fluidic connections between components, the pipetting system allows any reagent to be added to any other part of the system, providing greater flexibility in terms of reactions (e.g. number of reagents, volume of each reagent, number of reaction steps), without requiring any replumbing of fluidics in the system. The feature also allows significant customization and optimization of the radioisotope concentration process if needed, without the complexity of using bulky components like HPLC injection valves to meter the small 'plugs' of elution solution (255).

Beyond the proven fluid handling capabilities of the liquid handling robot, we leveraged the pipettor (ADP) by designing custom "attachments" to provide additional functions. Both the Pressure-lid and the Lid-heater were designed to mount to the ADP much like a pipette tip, so that the ADP robot could be used to pick them up and move them into any desired position on the cassette. For example, the Pressure-lid was used at three cassette positions: (i) to provide air pressure to drive fluid flow through the QMA cartridge, (ii) to provide convective airflow during evaporation steps (e.g. drying of [ $^{18}\text{F}$ ]fluoride), and (iii) to provide air pressure to drive the product fluid out of the cassette to downstream purification and formulation. These components could be reused and when not in use, the components were simply parked onto the instrument cassette stage. By adapting these components directly to the XYZ robot, we eliminated the need for

additional actuators or valves to control the application of pressure or to seal the reactor reservoir. Combined with the pipette-based liquid transfers, this completely avoided the need for dedicated fluid connections (e.g. inert gas pressure, vacuum, fluid sources) directly to the cassette, thus simplifying installation and removal of the cassette and eliminating issues due to incorrect cassette installation. In fact, the cassette-instrument interface is reduced to only a single heater interface.

The use of the liquid handling robot also completely eliminated the need for on-cassette valves. Many current radiosynthesizer systems have complex disposable cassettes comprised of numerous fluidic tubes, multiple valves, and numerous connection points for syringes, reagent vials, or pressure sources, all of which can be complex to fabricate and can introduce risks of failures. In contrast, the PHENYX systems requires only a simple, small disposable cassette that can be easily manufactured by standard molding methods. Cassette assembly would also be simple: only the QMA cartridge would need to be attached to the cassette. Since we observed some limitations of the adhesive films to the millifluidic channels, it may be preferable to use a PEEK film attached via standard laser welding or thermal bonding systems. The on-cassette reservoirs could also be pre-filled with select reagents for a particular PET probe synthesis and the reservoirs sealed for long term storage using metalized films, to prepare ready-to-use “kits”. While the cassette was fabricated from PEEK for these studies, a more cost-effective material such as cyclic olefin copolymer (COC), which provides similar temperature compatibility and chemical compatibility but is more amenable to mass production, could be explored. This material has been used for disposable components in other microfluidic radiochemistry systems (384–386).

This system leveraging the pipettor and attachments to mediate fluid transfers and other operations shares many of the concepts of dynamically reconfigured fluid paths found in the ELIXYS radiosynthesizer (SOFIE, Inc.), enabling high synthetic flexibility with only software changes (and no need for reconfiguration of the fluidics) (33,212,346). Another shared feature is

the use of an applied actuation force to seal the reaction vessel. Testing showed the Lid-heater to be able to withstand at least 150 °C for 5 min in the presence of 25 µL of MeCN (Bp: 81-82 °C) suggesting the possibility to perform microvolume reactions under relatively high pressure (and thus high temperature conditions), much like the ELIXYS system (218).

Currently, the prototype system measures 69 cm (L) x 59 cm (W) x 75 cm (H) and can fit into many different lead-shielded hot cells. However, it is unable to fit into the smaller production hot cells used in many radiopharmacy sites. Future efforts on the platform will focus on miniaturization to enable integration into a wider range of hot cell sizes. For example, the X, Y and Z movement axes have far more travel distance needed for the relatively small work area, and could be replaced with a much smaller custom XYZ gantry to make the system more user friendly, increased integration of controllers and development of an improved software interface to automate all aspects of the system could be developed. An example of a flexible software approach that could be used here was reported for the ELIXYS system, in which low-level operation steps were grouped into useful chemistry “unit operations” (macros) that can more intuitively and quickly sequenced together into synthesis protocols (225).

## 10.4 Conclusions

We developed a novel cassette-based radiosynthesizer where all operations are carried out with a small pipetting robot, including concentration of [<sup>18</sup>F]fluoride via a miniature QMA cartridge, reagent addition, closing and opening the reaction vessel, and transferring crude product out of the reactor to a downstream purification system. The system combines the advantages of performing radiochemistry in microscale volumes (<10s of µL), but addresses some limitations in other systems (e.g. ability to seal the reaction, unlike EWOD and open-droplet systems), and integrates radioisotope concentration into the same cassette as the reaction steps. After characterization of the system, we have successfully demonstrated the synthesis of [<sup>18</sup>F]Fallypride, a clinical PET probe for neuropsychiatric diseases (391,392). The method here

provided the highest radiochemical yield of  $71 \pm 6\%$  ( $n = 3$ ) among current reports of microvolume syntheses with scalable synthesis (i.e. using [ $^{18}\text{F}$ ]fluoride concentrator), as well as excellent radiochemical purity ( $>99\%$ ) and molar activity ( $290\text{-}670 \text{ GBq}/\mu\text{mol}$  [ $7.7\text{-}18 \text{ Ci}/\mu\text{mol}$ ]). This platform could readily be programmed to make a wide range of other  $^{18}\text{F}$ -labeled radiopharmaceuticals and likely compounds labeled with many other radionuclides.

## 10.5 Appendix

### 10.5.1 PHENYX system design and characterization

#### 10.5.1.1 Pressure-lid characterization

The sealing of the Pressure-lid to the cassette was verified using the setup shown in **Figure 10-7A**. A  $\frac{1}{4}$ "-28 plug fitting was used to block the port where the QMA cartridge inlet would normally be connected. Targeting an elastomer compression of about 20%, the Pressure-lid was driven vertically an extra 0.5 mm after contacting the top of the QMA Inlet reservoir. After supplying an input pressure and allowing time for equilibration, the inline valve was closed and the pressure decay monitored using the pressure gauge for 2 min (**Figure 10-7B**). The stability of pressure over time confirms adequate sealing of the pressure lid to the QMA inlet reservoir.

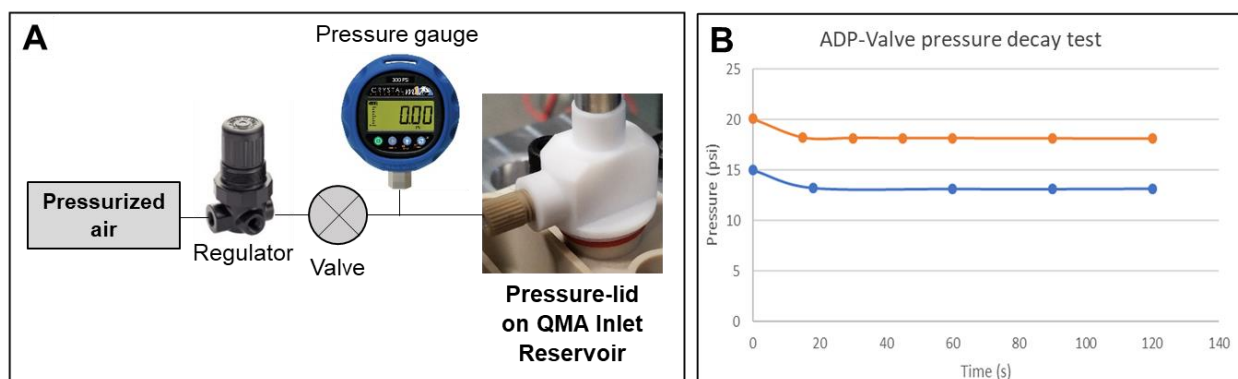


**Figure 10-7 A. Pressure-lid testing setup. B. Pressure monitoring after isolating pressure-lid from the pressure source.**

To test the ability to drive fluid through the quaternary methylammonium (QMA) cartridge and the cassette channels, deionized (DI) water or MeCN was loaded into the QMA Inlet reservoir

(i.e. mimicking the expected solutions during trap and elute workflow), and the amount of time it took to transfer fluid under different driving pressures was measured. Time varied as a function of reagent type, volume, and pressure.

A final pressure was selected for each reagent type with a target of being able to transfer 500  $\mu\text{L}$  of fluid in  $\sim 60$  s. Operating at 15 psi, 500  $\mu\text{L}$  of water could be pushed from the QMA Inlet reservoir through the QMA cartridge and into the QMA Outlet reservoir in  $\sim 75$  s. 500  $\mu\text{L}$  of MeCN could be flushed through this same path at in  $\sim 30$  s using 10 psi driving pressure. For the elution step, which used small volumes of  $\sim 10$ - $20$   $\mu\text{L}$ , a target flush time of 15-20 s was appropriate to ensure there was sufficient residence time of the elution solution in the QMA cartridge to effectively elute off the [ $^{18}\text{F}$ ]fluoride. Ramping of pressure was necessary to ensure the small volume remained as a single 'slug' of liquid as it moved.

Note that we observed during these experiments that the acetonitrile was degrading the adhesive layer on the film used to seal the cassette channels, leading to the possibility of leaks. The problem was solved by replacement of the film for each experiment. (With single-use cassettes, this would not be an issue.)

#### **10.5.1.2 Heater calibration and characterization**

To calibrate the internal Reactor temperature as a function of heater setpoint, 40  $\mu\text{L}$  of mineral oil (CAS# 8042-47-5, MP Biomedicals, Santa Ana, USA) was added to the Reactor reservoir and a small thermocouple inserted into the oil. The mineral oil provides a medium that can heat up to high temperatures (150  $^{\circ}\text{C}$ ) without evaporating and surrounds the thermocouple to provide an accurate temperature reading. The Reactor heater was then set to various temperature setpoints (as measured by the built-in thermocouple) and the temperature in the Reactor measured over time using a temperature meter (HH802U, Omega Engineering, Norwalk, USA) until a steady state was reached (**Figure 10-8A**). As expected, the internal temperature is somewhat lower than the setpoint.

To characterize the Lid-heater, the Lid-heater was placed onto the ADP robot and brought down to just contact a flat portion of the cassette body. A thin thermocouple (Part No. 88309K, Omega Engineering, Norwalk, USA) was placed between the gasket on the bottom of the Lid-heater and the top surface of the cassette. The Lid-heater was then compressed down 0.1 mm to ensure good contact, and was then heated to various setpoints and the temperature of the thermocouple measured over time using the Fluke temperature meter (**Figure 10-8B**). As expected, the gasket temperature is significantly lower than the setpoint.

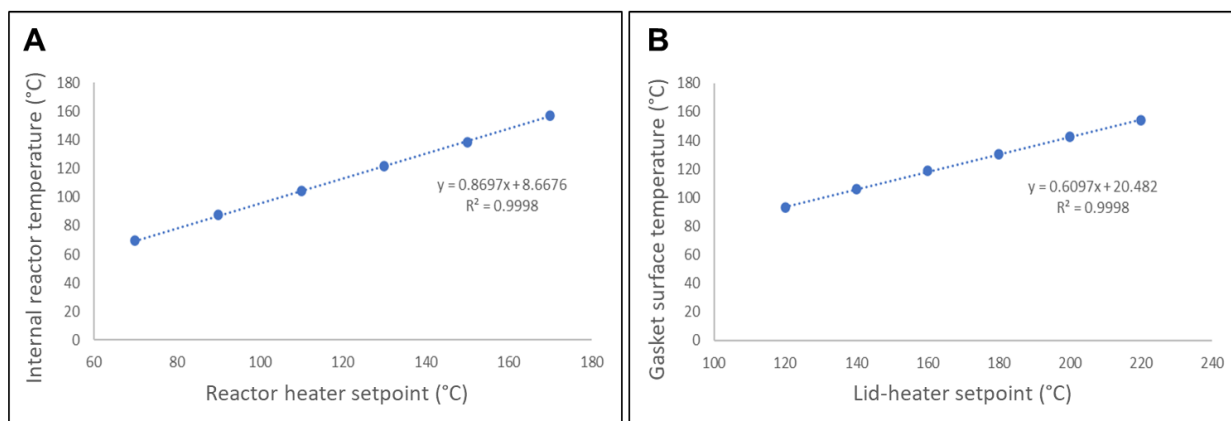


**Figure 10-8 Temperature calibrations.**

**A.** Temperature of liquid inside the reactor as a function of setpoint, measured 2 min after reaching the setpoint. **B.** Temperature at bottom of gasket on Lid-heater as a function of heater setpoint, measured 2 min after reaching the setpoint.

An example of the dynamic temperature profile is shown in **Figure 10-9**, giving a sense of the heating and cooling rates. As expected, the heater temperatures change quite rapidly and more time is needed for the internal reactor temperature or gasket surface temperature to stabilize.

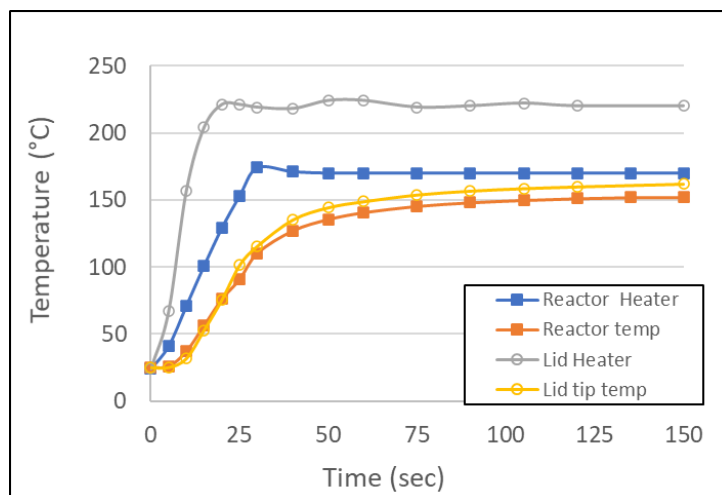


**Figure 10-9 Dynamic heater temperature characterization.**

The plot shows the thermal ramp of the heaters (Reactor and Lid-heater) along with the measured temperature within the Reactor and at the lid-tip. In this case, the internal target temperature is 150 °C, for which the Reactor heater must be set to 170 °C and the Lid-heater to 220 °C.

### 10.5.1.3 Simplified cassette with a single reactor

To better understand the performance of the synthesis, some experiments were performed with a specialized PEEK cassette containing only a reactor. The full cassette and reactor-only cassette are shown in **Figure 10-10**. This cassette was small enough to fit in a dose calibrator to quantify the residual activity. The Reactor well in the simplified cassette has the identical shape as the Reactor in full PHENYX cassette and mates with the same reactor heating block on the cassette stage. It also has the same double-rim style for sealing of the Lid-heater.

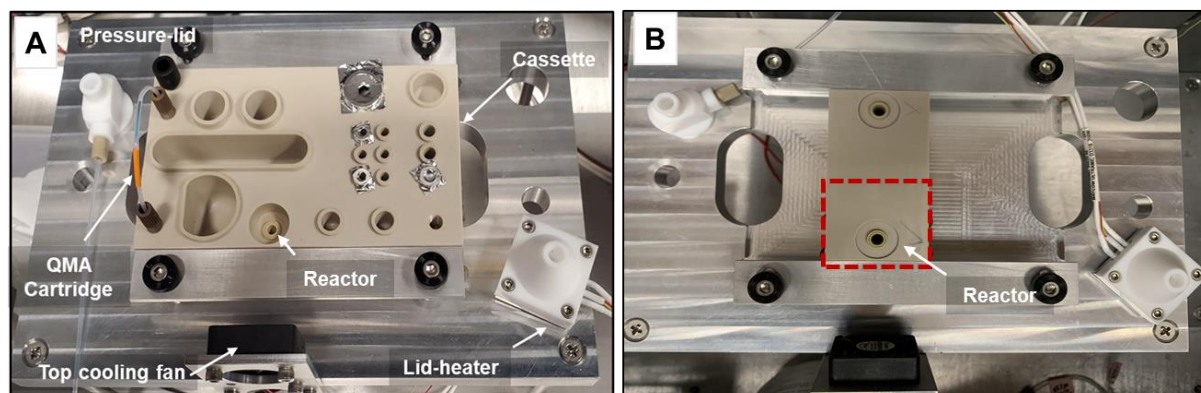


**Figure 10-10 A. Full cassette. B. Simplified cassette with only a reactor.**

### 10.5.1.4 Characterization of reactor sealing

Several designs of the top of the reactor were explored to ensure a robust vapor-tight seal between the reactor and the gasket layer of the Lid-heater. Three reactor sealing rim designs (**Figure 10-5(A-C)** in main paper) were prototyped as reactor-only miniature cassettes and sealing with the Lid-heater was evaluated. Tests were conducted by first weighing the empty Reactor prototypes on a balance (XP205, Mettler-Toledo International Inc., Greifensee, Switzerland), then adding 25  $\mu\text{L}$  of MeCN and weighing again. The Lid-heater was then sealed down onto the Reactor by first making contact, then actuating further to compress the gasket by 1.0 mm. Using the temperature calibration, the reactor was heated to 150  $^{\circ}\text{C}$  (bottom and top heaters) and then held for 5 min, after which both heaters were turned off and cooled back to room temperature. The Lid-heater was then removed from the Reactor and the Reactor prototype weighed a final time. The change in mass before and after heating was used to determine the amount of solvent mass that escaped.

Parameters tested included the Reactor designs (flat-rim, double-rim, beveled-rim) as well as the durometer of the silicone elastomer gasket (50A, 60A, 70A) on the bottom of the Lid-heater. **Figure 10-11A** shows the resulting two-factor interaction plot of mean fluid loss (%) for the combinations of Reactor type and silicone durometer. Results were analyzed using a two-way ANOVA, indicating a significant difference between the Reactor types ( $p = 0.034$ ), but no significant difference between the durometers ( $p = 0.564$ ) and no significant interaction between the Reactor type and the durometer ( $p = 0.107$ ). From this result, the double-rim Reactor was selected as the final design incorporated into the disposable cassette.

Moreover, because some radiosynthesis reactions require more than one high-temperature heating step, the elastomer gaskets were tested multiple times in succession to determine any effects of reusing the material. The results of this testing for each the 3 durometers are plotted in **Figure 10-11B**. A two-factor ANOVA resulted in no significant p-values for the durometer, the test number, nor the interaction of the two parameters. This indicates that from



the data collected, all three durometers performed equally well at sealing across a succession of three consecutive tests.

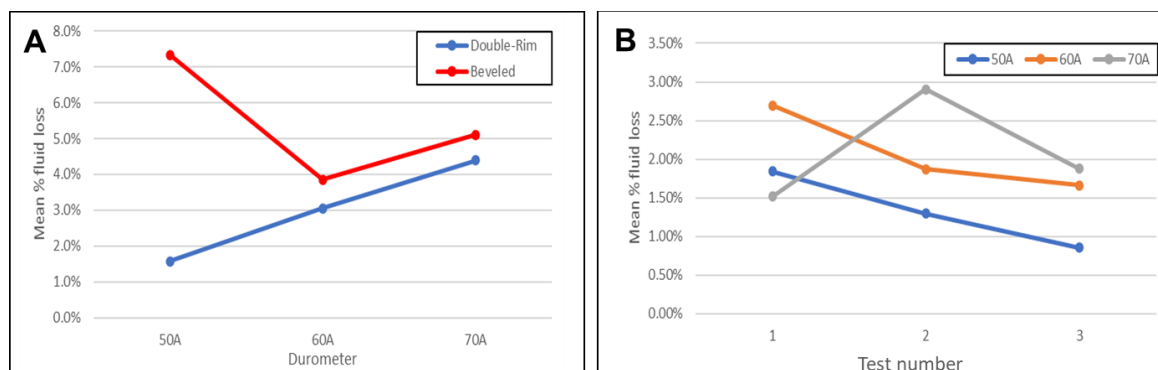


**Figure 10-11 Parameters tested included the Reactor designs (flat-rim, double-rim, beveled-rim) and the durometer of the silicone elastomer gasket (50A, 60A, 70A) on the bottom of the Lid-heater.**

Interaction plot showing the mean % fluid loss for the two parameters: (i) Reactor design (double-rim vs. beveled), and (ii) silicone elastomer durometer (50A, 60A, and 70A). **B.** Interaction plot showing the mean % fluid loss for the two parameters: (i) Test number (1, 2, or 3) and (ii) silicone elastomer durometer (50A, 60A, and 70A). All tests were performed using the double-rim Reactor design. Each experiment was repeated 3 times.

### 10.5.1.5 Pipettor calibration

Because the ADP uses air displacement to meter the fluid volumes, it must be calibrated for various reagent types and pipette tip sizes to account for the compressibility of the air in the tip along with the differing fluid properties. Key solvents/reagents relevant to the radiosynthesis were evaluated, including acetonitrile (MeCN), methanol (MeOH), water, tetrabutylammonium bicarbonate (TBAHCO<sub>3</sub>), etc. The ADP was programmed to dispense a specified volume, ranging from 10% to 100% of the pipette tip capacity (using 50  $\mu$ L and 200  $\mu$ L sized tips), and the actual volume dispensed was then measured gravimetrically. A calibration curve was created for each given reagent type and pipette tip size to enable dispensing of the desired volume at each step of the synthesis.

Moreover, to ensure the full volume was available for transfer via pipette, we measured the dead volumes of the small and medium reagent reservoirs, QMA Outlet reservoir and the Reactor which were used in the proof-of-concept radiosynthesis. For each test, we loaded the

following solutions: 7  $\mu\text{L}$  of 30 mM  $\text{TBAHCO}_3$  into the small reagent reservoir, 30  $\mu\text{L}$  of mixture of MeOH and DI water (v/v, 9:1) into the medium reagent reservoir, 30  $\mu\text{L}$  of DI water into the QMA outlet reservoir and 8, 15 and 40  $\mu\text{L}$  of DI water into the Reactor. The ADP (using calibrations) was then used to pick up the nominal volume from each source. The residual liquid was then estimated by manually collecting with a fine pipette tip and gravimetrically determining the recovered liquid. The volume loss (i.e. residual volume) for the small and medium reservoirs was found to be  $1.5 \pm 0.2 \mu\text{L}$  ( $n = 3$ ) and  $1.4 \pm 0.9 \mu\text{L}$  ( $n = 3$ ), respectively. Residual volume left in the QMA Outlet reservoir and Reactor was negligible.

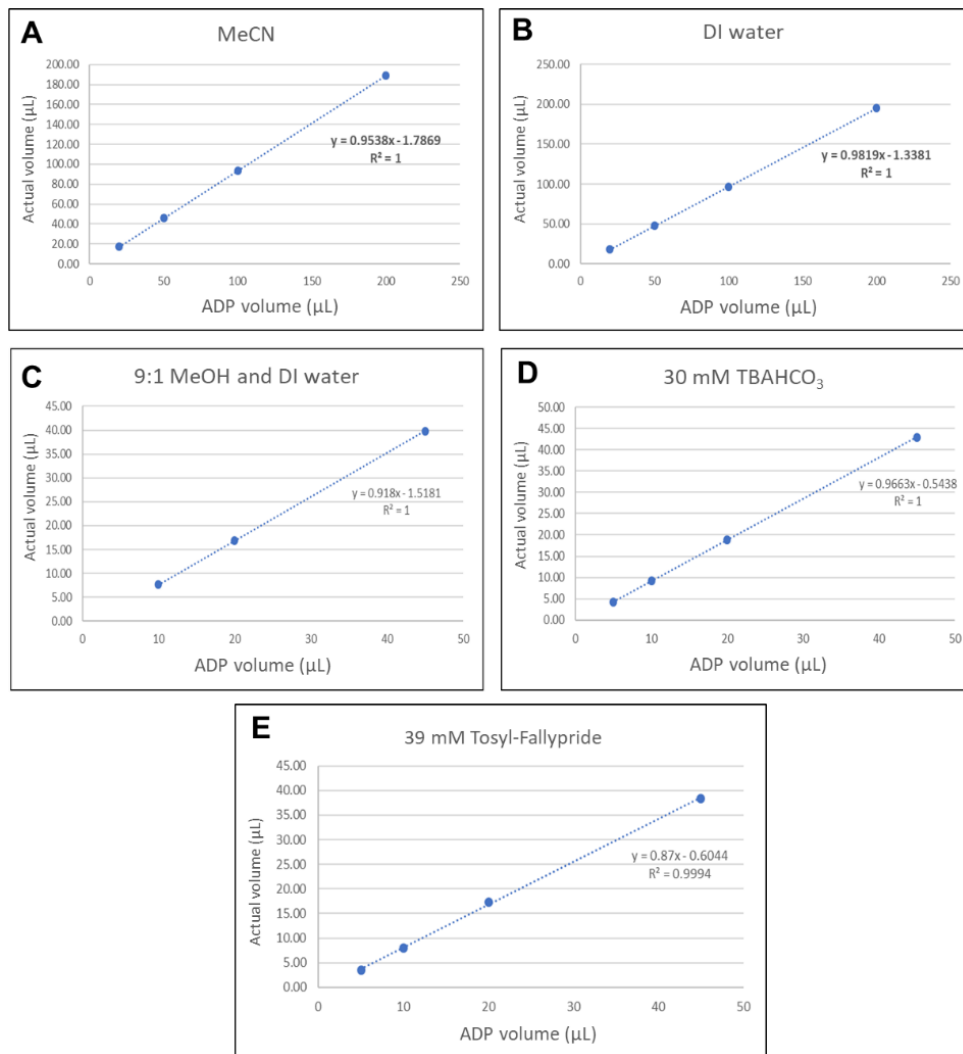


**Figure 10-12 Volume calibration curves for ADP dispensing of reagents.**

**A.** MeCN (dispensed with 200 μL tip). **B.** Deionized (DI) water (dispensed with 200 μL pipette tip). **C.** Mixed solution of MeOH and DI water (9:1, v/v), dispensed with 50 μL tip. **D.** 30 mM of TBAHCO<sub>3</sub> in 7.5% (v/v) EtOH:water, dispensed with 50 μL tip. **E.** 39 mM of tosyl-Fallypride in mixed solvent of MeCN and hexyl alcohol (1:1, v/v), dispensed with 50 μL pipette tip.

#### 10.5.1.6 Optimization of QMA Outlet reservoir design

Recovery of the small volume of eluent solution used to recover [<sup>18</sup>F]fluoride from the miniature QMA cartridge into the QMA Outlet reservoir is a critical step of the [<sup>18</sup>F]fluoride concentration process. To ensure minimal losses when using elution volumes in the range of 10-40 μL, it was important to design the QMA Outlet reservoir to allow efficient recovery (*via* pipette tip) with minimal residual fluid left behind. At the same time, the reservoir must be able to handle

multiple mL volumes of [ $^{18}\text{O}$ ]H<sub>2</sub>O that are collected during the trapping step (and subsequently transferred to the Waste reservoir).

A total of six configurations were designed, fabricated using 3D printing, and tested, two of which are shown in **Figure 10-13**. The QMA outlet fitting port is connected *via* a millifluidic channel on the underside of the cassette and liquid rises up to the QMA outlet reservoir *via* a vertical hole. Design parameters of the reservoir included the location of the vertical inlet hole into the QMA Outlet reservoir, the geometry of the inlet hole region, and the shape and slope of the reservoir walls. Testing was conducted by mimicking the [ $^{18}\text{F}$ ]fluoride trap and elute workflow. First, 500  $\mu\text{L}$  of fluid was flushed through a test QMA cartridge and into the prototype QMA Outlet reservoir. Then, 500  $\mu\text{L}$  of acetonitrile rinse was flushed through. Finally, 15  $\mu\text{L}$  of blue dyed eluent solution was flushed through the QMA cartridge and into the QMA Outlet reservoir prototype. This was repeated one more time for a total volume of 30  $\mu\text{L}$  of eluent solution. The fluid was collected from the bottom of the QMA Outlet reservoir using a pipette (simulating a transfer to the Reactor using the ADP) and weighed to determine the volume of eluent recovered. The QMA Outlet reservoir was also qualitatively assessed by visualizing residual blue-dyed eluent solution near the inlet hole or on the walls of the reservoir. The best QMA Outlet reservoir design was then used in the final disposable cassette prototype.

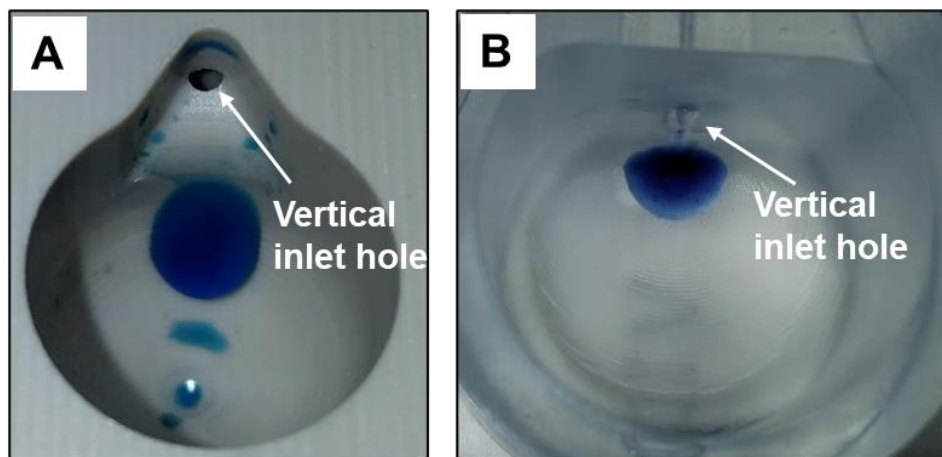


**Figure 10-13 Example QMA Outlet reservoir prototypes.**

A. The cylindrical design featured the inlet channel at the top of the reservoir with a V-shaped slope leading into the main body of the reservoir. B. The asymmetric reservoir design placed the inlet channel very near the bottom of the reservoir. Both images show elution of two 15  $\mu\text{L}$  eluent plugs (30  $\mu\text{L}$  total) in each reservoir prototype.

The design shown in **Figure 10-13B**, had the highest eluent recovery, losing only  $3.4 \pm 1.0 \mu\text{L}$  ( $n=3$ ) from a total of 30  $\mu\text{L}$  of eluent, and was selected to be incorporated into the final cassette design. This design shown in more detail in **Figure 10-14**, has an asymmetric reservoir shape with a steep wall where the fluid enters *via* a vertical inlet channel. Unlike other designs where residual fluid was stuck to the walls after elution (e.g. **Figure 10-13A**), the positioning of the inlet channel hole directly in the steep reservoir wall and located very close to the deepest point in the reservoir addressed this problem.

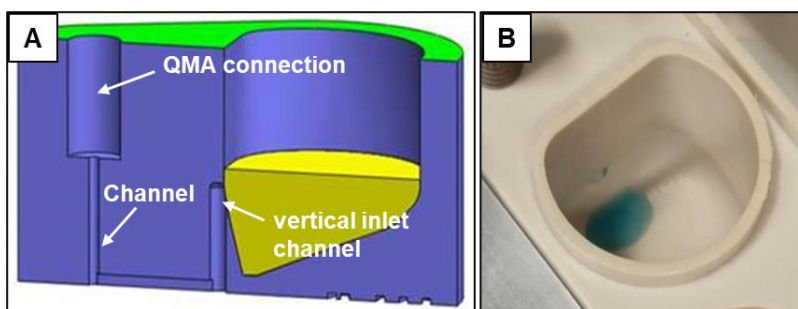


**Figure 10-14 Final QMA Outlet Reservoir design.**

A. Cross-section CAD model of the final QMA Outlet reservoir design showing the fluidic channel leading from the port connected to the outlet of the QMA cartridge to the inlet hole of the QMA Outlet reservoir. The yellow fluid represents 2 mL volume within the 6 mL reservoir as would be

present after completing the trapping step. **B.** Photograph of 30  $\mu\text{L}$  of blue-dyed eluent solution collected in the QMA Outlet reservoir after the elution step.

### 10.5.2 Cassette cleaning

Though the PHENYX cassette is envisioned to be used in a disposable manner, the initial prototype cassettes were cleaned and re-used. After completion of radiosynthesis, the cassette was stored at least overnight to allow residual radioactivity to decay to background levels. The adhesive layer was removed and the used reservoirs and reactor on the cassette were washed with DI water (2x) and then with MeCN (2x). The cleaned cassette was dried in the oven ( $\sim 65^\circ\text{C}$ ) for at least 4 h. After cooling, fresh pieces of adhesive film were affixed to the bottom of the cassette to close the channels.

### 10.5.3 QMA trapping and release performance

**Table 10-4 QMA trapping and release performance.**

Trapping was performed using [ $^{18}\text{F}$ ]fluoride (1.7-15 MBq) in DI water (total of 500  $\mu\text{L}$ ). Each elution step is performed using pressure ramping from 0 to 5 psi (over 40 s) and then switching to 10 psi for another 20 s, unless otherwise indicated. All percentages are corrected for decay.

Entry <sup>a</sup>	Base elution ( $\mu\text{L}$ )	DI water elution ( $\mu\text{L}$ )	Adhesive layer (New or reused)	Trapping efficiency (%) <sup>d</sup>	Elution efficiency (%) <sup>e</sup>	Residual activity on cartridge (%) <sup>f</sup>
1 <sup>b</sup>	7 x 2	15 x 1	New	99.6	75.0	13.7
2 <sup>c</sup>	7 x 2	15 x 2	New	94.9	70.2	18.3
3	7 x 2	7 x 4	New	99.8	83.0	6.5
4	7 x 2	7 x 4	New	97.9	82.2	14.1
5	7 x 2	7 x 4	Reused	82.7	74.8	0.2
6	7 x 2	7 x 4	Reused	87.9	78.9	3.3
7	7 x 2	7 x 4	Reused	99.8	65.5	N.A.
8	7 x 2	7 x 4	Reused	99.9	0.9	N.A.
9	7 x 2	7 x 4	Reused	99.9	18.9	N.A.
10	7 x 2	7 x 4	Reused	100.0	11.6	N.A.
11	7 x 2	7 x 4	New	99.9	89.3	N.A.
12	7 x 2	7 x 4	New	100.0	94.0	N.A.
13	7 x 2	7 x 4	New	99.7	83.8	8.1
14	7 x 2	7 x 4	New	99.7	90.5	7.6
15	7 x 2	7 x 4	New	99.4	83.8	10.4
16	7 x 2	7 x 4	New	99.9	95.4	3.3
17	7 x 2	7 x 4	New	99.7	86.7	8.0
18	7 x 2	7 x 4	New	99.7	88.6	4.6

<sup>a</sup>Elution is achieved by gradual ramping to 5 psi over 40 s and then switching to 10 psi and holding for another 20 s.

<sup>b</sup>Used a variation in pressure ramping, i.e. gradually ramping to 3 psi over 30 s and holding at 3 psi for another 10 s.

<sup>c</sup>Used a variation in pressure ramping, i.e. gradually ramping to 2 psi over 100 s and holding at 2 psi for another 20 s. N.A. = not applicable.

## 10.5.4 Timing of synthesis steps

**Table 10-5 Duration of steps involved in [<sup>18</sup>F]fallypride synthesis.**

Comparison for implementation on PHENYX (this work) and previously-reported integrated radioisotope concentrator and microdroplet synthesizer (83).

Synthesis stage	PHENYX system (this work)		Integrated radioisotope concentrator and microdroplet synthesizer	
	Detailed steps	Time (min)	Detailed steps	Time (min)
[ <sup>18</sup> F]fluoride concentration via QMA cartridge	Trap [ <sup>18</sup> F]fluoride on QMA cartridge and pipette waste to the waste reservoir	3	Trap [ <sup>18</sup> F]Fluoride, release with 25 mM TBAHCO <sub>3</sub> (6.2 μL x 2), rinse DI water (6.2 μL x 2)	10
	Elute with 25 mM TBAHCO <sub>3</sub> (7 μL x 2)	3.5 (x 2)		
	Rinse with DI water (7 μL x 4)	3.5 (x 4)		
Loading and drying concentrated [ <sup>18</sup> F]fluoride	Transfer the eluted [ <sup>18</sup> F]fluoride to the Reactor	0.5	Transfer concentrated [ <sup>18</sup> F]fluoride to chip as a series of tiny droplets and dry continuously	6
	Dry [ <sup>18</sup> F]fluoride at 100 °C	10		
	Cool to 25 °C	2		
Fluorination	Fluorinate at 110 °C	7	Fluorinate at 110 °C	7
	Cool to 25 °C	2	Cool to 25 °C	2
Collection	Collect crude product	4	Collect crude product	8
	<b>Total</b>	<b>49.5</b>	<b>Total</b>	<b>35</b>

## 10.5.5 HPLC purification of [<sup>18</sup>F]fallypride

After the synthesis in the PHENYX cassette, the crude product was transferred to the Dilution Reservoir, and then was manually transferred to an analytical-scale HPLC system for purification. **Figures S10, S11, and S12**, show chromatograms of the crude product, purified product, and purified product co-injected with fallypride reference standard, respectively.

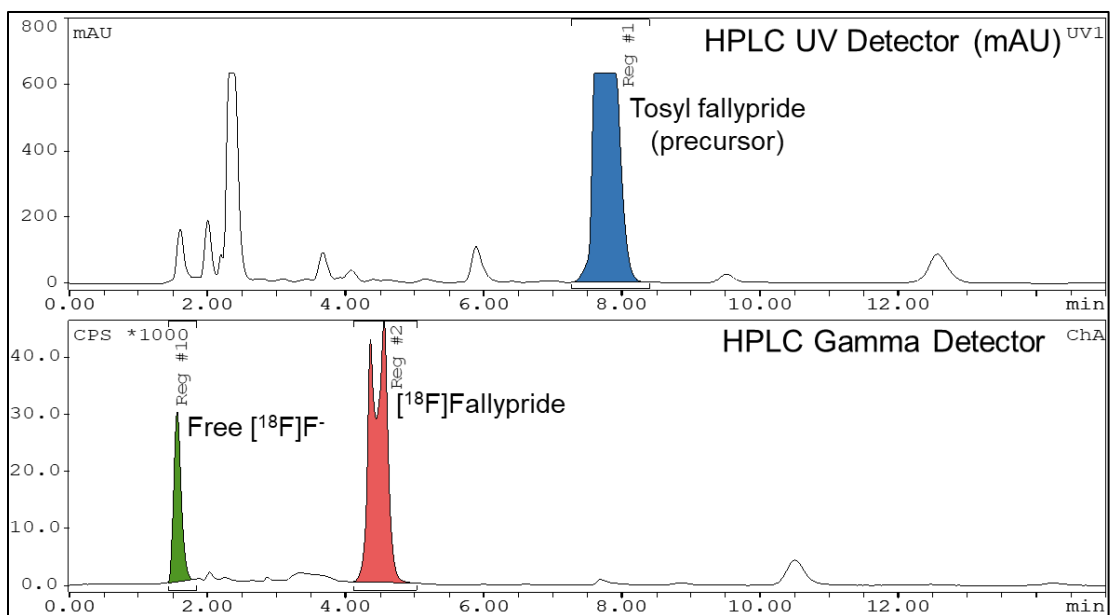


**Figure 10-15** Radio-HPLC chromatogram of crude  $[^{18}\text{F}]$ Fallypride (upper: UV-254 nm and bottom:  $\gamma$ -ray).

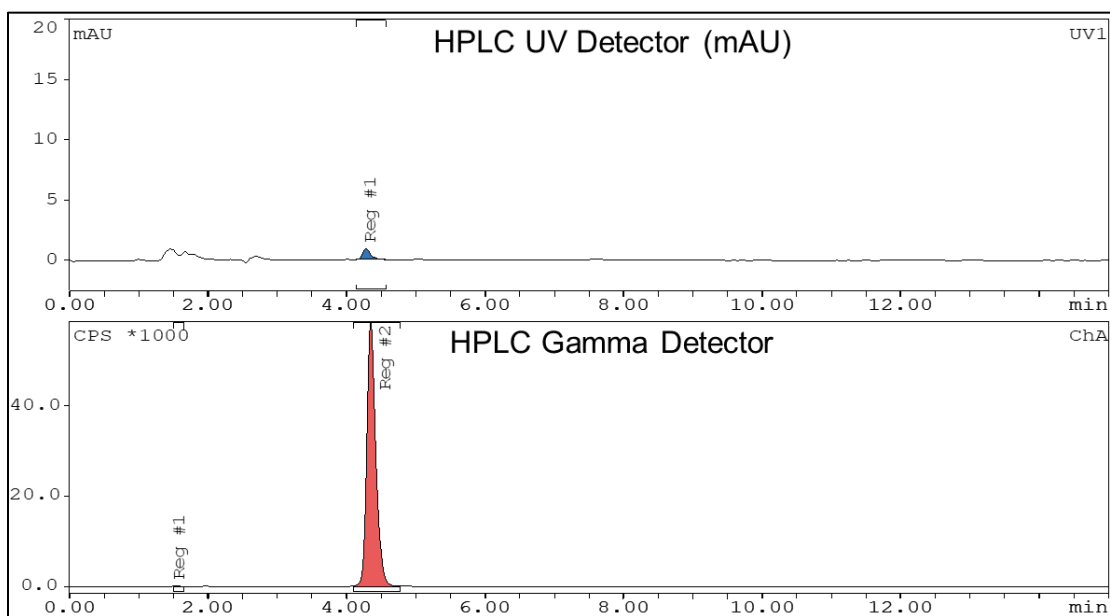


**Figure 10-16** Radio-HPLC chromatogram of purified  $[^{18}\text{F}]$ Fallypride (upper: UV-254 nm and bottom:  $\gamma$ -ray). Radiochemical purity was >99%.



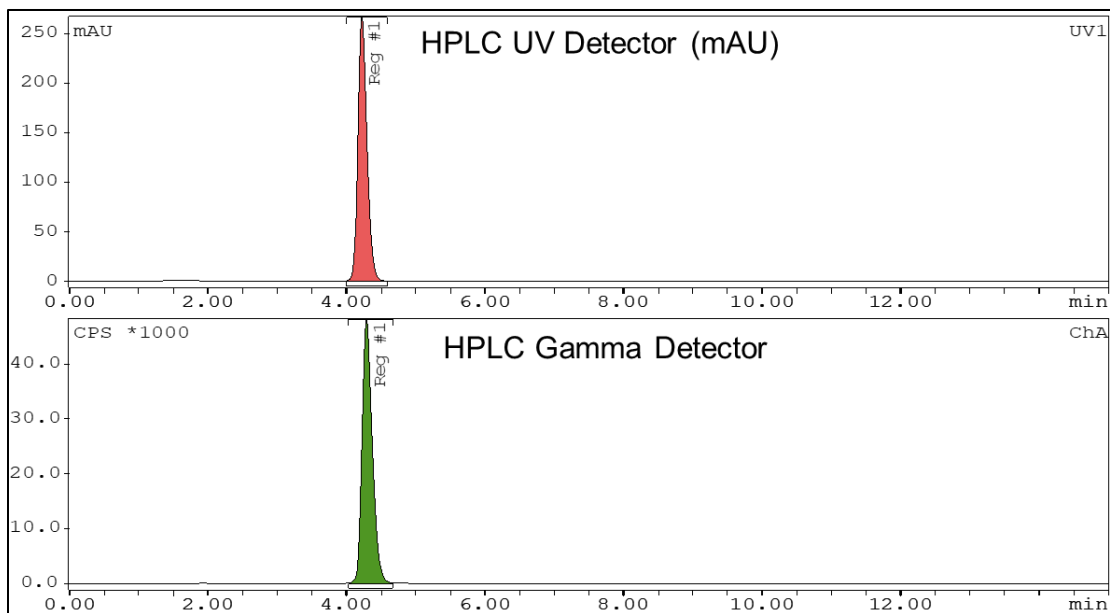


**Figure 10-17** Radio-HPLC chromatogram of purified [<sup>18</sup>F]Fallypride co-injected with fallypride reference standard for identity verification. (upper: UV-254 nm and bottom:  $\gamma$ -ray).

### 10.5.6 Calibration curve to determine molar activity

The same analytical scale radio-HPLC system was also used to determine the molar activity of the purified [<sup>18</sup>F]Fallypride. The area under the curve for the UV absorbance peak was determined for a range of masses of fallypride reference standard (0.3-13 nmol) to generate a linear calibration curve (**Figure S13**). This curve was then used to determine the mass of fallypride in the unknown sample and in turn to compute the molar activity following standard procedures.

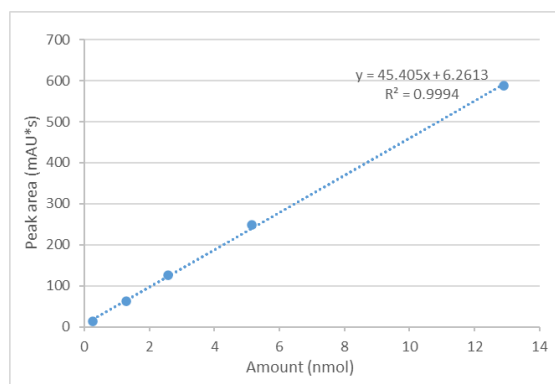


**Figure 10-18** Calibration curve of fallypride reference standard (254 nm wavelength).

# Chapter 11: Electrochemical Radiofluorination of Methyl (Methylthio)acetate Using a Split-Bipolar Electrode

## 11.1 Introduction

Many fluorine-containing compounds have found use as pharmaceuticals and bioactive materials (393–395). In addition, fluorine-18 ( $^{18}\text{F}$ ), a radioisotope of fluorine, has been widely used for molecular imaging through positron emission tomography (PET) because of its ideal nuclear properties, such as low positron energy and moderate half-life ( $t_{1/2} = 109.8$  min). (396–398) Encouraged by the attractive features of fluorine-containing organic compounds, various synthetic methodologies to synthesize them have been developed (393,394,399–401). Electrophilic fluorinating reagents, including  $\text{F}_2$  gas and  $\text{F}_2$  gas derived reagents such as NFSI and Selectfluor<sup>TM</sup>, are often used for the fluorination of the electron-rich position on molecules (396,397,402). However, the use of these reagents in radiofluorination leads to a drop of molar activity ( $A_m$ ; amount of radioactivity per mole of total radioactive and non-radioactive product) because of the intrinsic low  $A_m$  of the  $^{18}\text{F}[\text{F}_2]$  production process (396,397). On the other hand, nucleophilic fluorination using  $^{18}\text{F}$ -fluoride ( $^{18}\text{F}[\text{F}^-]$ ) ions as a fluorine-18 source is preferable to achieve higher  $A_m$  (396,397,402).  $^{18}\text{F}[\text{F}^-]$  is easily accessible via a  $^{18}\text{O}(\text{p},\text{n})^{18}\text{F}$  nuclear reaction in a cyclotron. Various  $^{18}\text{F}[\text{F}^-]$  ion-derived nucleophilic fluorinating reagents, such as HF, KF/kryptofix ( $\text{K}_{222}$ ), and tetrabutylammonium fluoride (TBAF), are available for nucleophilic radiofluorination (396,397,402). In general, nucleophilic radiofluorination is efficient for introducing  $^{18}\text{F}$  into electro-deficient moieties (403); however, its application to electron-rich positions remains challenging (404–406).

Electrochemical (radio)fluorination (ECF) might be a promising approach to carry out nucleophilic fluorination of electron-rich moieties on molecules. ECF generally proceeds through the generation of cationic intermediates from anodic oxidation of substrates followed by nucleophilic substitution with fluoride ( $\text{F}^-$ ) ions (407,408). ECF has great potential to be applied in

radiofluorination of PET tracers because  $^{18}\text{F}^-$  ion obtained by  $^{18}\text{O}(p,n)^{18}\text{F}$  reaction in a cyclotron can be directly used for the ECF (409–413). A major limitation of ECF is to require large amounts of supporting salts and carrier  $^{19}\text{F}^-$  to drive the reaction, usually more than 0.1 M of salts is used. The high concentration of supporting salts ensure sufficient electrical conductivity of the electrolytic solution where the presence of carrier  $^{19}\text{F}^-$  ions mainly serve as a nucleophile to stabilize the cationic intermediates. In most reported ECF reactions,  $\text{F}^-$  ion-contained salts, such as HF salts (407,408), alkali-metal fluorides (414,415), and alkylammonium salts (416,417), are often used. The presence of carrier  $^{19}\text{F}^-$  ions produces a mixture of  $^{18}\text{F}$  and  $^{19}\text{F}$ -radiofluorinated products, which significantly decrease the  $A_m$  (409). To improve the  $A_m$ , no-carrier-added ECF has been developed, where  $^{18}\text{F}^-$  ions are obtained from the ion-exchange cartridge capturing  $^{18}\text{F}^-$  ions by using other salts different from  $^{19}\text{F}^-$  ions (418). However, impurities of  $^{19}\text{F}^-$  ions often arise from the target, tubing, or reagents used in experimental procedures (419). Despite the no-carrier-added ECF, using the large amount of supporting salt to elute  $^{18}\text{F}^-$  ions from the ion exchange cartridge would result in contamination of more amount of  $^{19}\text{F}^-$  ions as impurities into electrolyte used in ECF. Besides, large amounts of supporting salts are difficult to remove through downstream purification which largely lengthens the production procedure and decreases the activity yield (AY) due to time decay of radioactive products. Therefore, ECF carried out under the low concentration of supporting salts is promising to achieve good  $A_m$ .

A plausible alternative to achieve ECF at low concentration of supporting salts and  $^{19}\text{F}^-$  is to focus on bipolar electrochemistry. A bipolar electrode (BPE) is a conductive material immersed in an electrolytic cell containing a low concentration of supporting electrolyte and equipped with driving electrodes connected to a power supply. When voltage is applied to the driving electrodes, an electrical field is generated to simultaneously cause anodic and cathodic reactions on the surface of BPE (420–422). The common BPE system has both anodic and cathodic poles on the same surface of a BPE. We have developed a split bipolar electrode (s-BPE) system which is composed of two conductive materials with electrical connection and can

perform anodic and cathodic reactions at different surfaces of the conductive materials. Recently, we have demonstrated ECF with moderate yields under low concentration of  $[^{19}\text{F}]\text{F}^-$  salts using a U-shaped cell with the s-BPE system (423,424). Encouraged by these results, we envisage that no-carrier-added ECF using s-BPE system could achieve high  $A_m$ . To highlight the first application of BPE to electrochemical radiofluorination, we have carefully investigated the effects of various reaction conditions on the radiochemical yield (RCY), AY, and  $A_m$  of the final products. As a proof-of-concept, we performed ECF of methyl (methylthio)acetate (MMTA) in a U-shaped cell equipped with a s-BPE using  $[^{18}\text{F}]\text{TBAF}$  as a  $^{18}\text{F}$ -fluorine source. Although carrier-added and no-carrier-added electrochemical radiofluorination of some thioether derivatives have already been achieved (413,425,426), large amounts of supporting salts and fluorine sources are required in the previous reports; therefore, the  $A_m$  of the obtained radiofluorinated thioethers from the ECF remains insufficient for clinical uses (i.e.  $>18.5 \text{ GBq}/\mu\text{mol}$ ) because of the contamination of the impurities of  $[^{19}\text{F}]\text{F}^-$  ions. In addition, nucleophilic fluorination of the specific  $\alpha$ -position to the sulfur atom is still difficult and largely under explored because of electron-donating characteristics of the sulfur atom (427,428). Therefore, ECF of MMTA with picomole or nanomole of  $[^{18}\text{F}]\text{fluoride}$  using the BPE approach is challenging and would also be of great interest to the radiochemistry community (409).

## 11.2 Result and discussion

The ECF of thioether derivatives is known to proceed based on the Pummerer-type mechanism (**Figure 11-1**) (407,408). Firstly, anodic oxidation of the sulfur atom of thioether moieties occurs, followed by a nucleophilic attack with fluoride ion to the oxidized sulfur atom, which results in the generation of the fluorosulfonium intermediate via second oxidation of the sulfur atom. A final product is obtained from the fluorination of the  $\alpha$ -position to the sulfur atom accompanying dehydrofluorination of the fluorosulfonium intermediate. In ECF of thioether derivatives, fluoroalcohols, such as 2,2,2-trifluoroethanol (TFE), and 1,1,1,3,3,3-hexafluoro-2-

propanol (HFIP), are suitable solvents because they can stabilize cationic species generated from anodic oxidation (429,430). We optimized ECF conditions of MMTA based on non-decay corrected radiochemical yield (RCY) determined by radio-TLC measurement for aliquots from the reaction mixture.

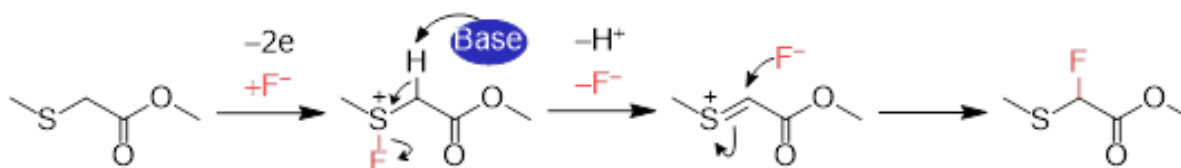


**Figure 11-1 Electrochemical (radio)fluorination of MMTA following a Pummerer-type mechanism via generation of the fluorosulfonium intermediate.**

First, we investigated the effects of the reaction temperature on ECF of MMTA (**Figure 11-2**). Optimization was performed in TFE containing 5 mM MMTA, tetrabutylammonium perchlorate (TBAP), and [<sup>18</sup>F]TBAF (approximate 5 mCi) using platinum wire (length = 20 cm, diameter = 0.33 mm) as both driving electrodes and s-BPEs. The applied voltage to the driving electrodes was set at 50 V. The detailed procedures are described in the supplementary information. **Figure 11-2** shows the trace of RCY of the reaction mixture collected at different reaction times (5, 10, 20, 30, 40, 50, and 60 min). The highest RCY was obtained at 40 °C after 30 min. The changes in the RCY with the reaction time were found to be also dependent on the reaction temperature. Elevating the reaction temperature from 10 °C improved the RCC with the extension of the reaction time, presumably because of the facilitation of the diffusion of MMTA and [<sup>18</sup>F]F<sup>-</sup> ions in the solution. On the other hand, setting reaction temperature at 60 °C resulted in lower RCY than that obtained at 40 °C. Extending reaction times beyond 30 min at both 40 °C and 60 °C also impaired the RCY. These results suggested that side reactions, such as decomposition or overoxidation of products, occurred during the reaction. Particularly, when the reaction temperature was set at 60 °C, such side reactions presumably tended to take place. Therefore, we concluded that 40 °C was the optimal reaction temperature in the present reaction system and used for further optimization.

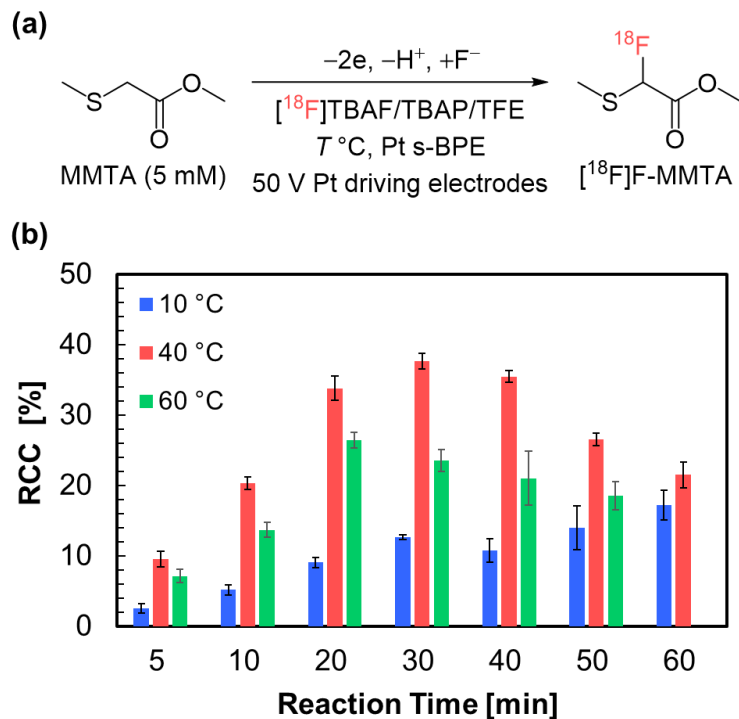


**Figure 11-2 (a) Scheme of ECF of MMTA under different temperature ( $T$  [ $^{\circ}C$ ] = 10, 40, 60). (b) The trace of RCY (non-decay corrected) of the reaction mixture collected at different reaction times. RCY was determined by radio-TLC of the reaction mixture ( $n = 3$ ).**

Applied voltage to the driving electrode affects the potential difference between the s-BPE, which influences the yield of electrochemical fluorinated products (423,424). Next, we optimized the applied voltage to the driving electrodes at 40 °C. **Figure 11-3** exhibits the relationship between the applied voltage to the driving electrodes and non-decay corrected RCY of the crude collected at 30 and 60 min, respectively. RCY gradually increased with the applied voltage up to 37.5 V, and RCY at 60 min was larger than that at 30 min. On the other hand, as described above, when the applied voltage was set at 50 V, the RCY at 60 min was lower than that at 30 min. Through these optimization, application of 37.5 V to the driving electrodes was found to result in the highest RCY at 60 min. Therefore, 37.5 V was determined to be the optimum applied voltage and used for further investigation in this work.

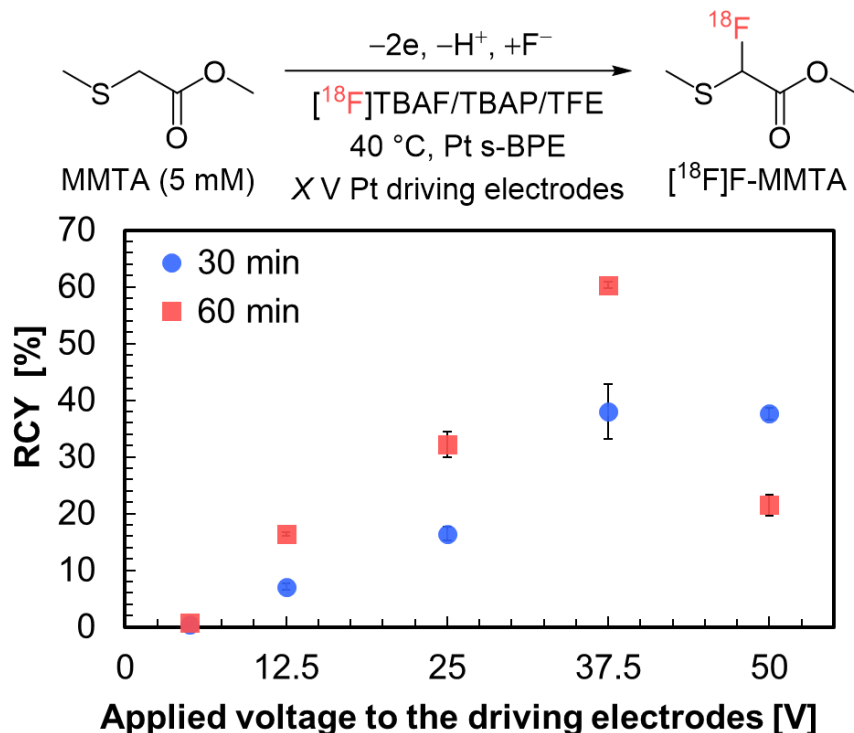


**Figure 11-3** Influence of driving electrode potential and reaction time on RCY. RCY was determined by radio-TLC of the crude samples (n = 3 or 15 (37.5 V at 30 min)).

Generally, the choice of supporting salts and solvents generally plays an important role in the electrochemistry including ECF due to their impact on the stability and reactivity of intermediates generated from the working electrode. Therefore, we also investigated the effects of supporting salts and solvents on our ECF system. Electrolysis was performed using different tetrabutylammonium salts (TBAX; X<sup>-</sup> = TsO<sup>-</sup>, TfO<sup>-</sup>, ClO<sub>4</sub><sup>-</sup>, BF<sub>4</sub><sup>-</sup>, and PF<sub>6</sub><sup>-</sup> in the descending order of reported donating abilities) (431). A [<sup>18</sup>F]TBAF solution in TFE was prepared by passing 1 mL of 25 mM TBAX/TFE through the cartridge with [<sup>18</sup>F]F<sup>-</sup> ion-loaded anion exchange resin. **Figure 11-4** shows the effects of TBAX salts on both the elution efficiencies and RCC. The elution efficiency of [<sup>18</sup>F]F<sup>-</sup> gradually decreased with the increase in the donating nature of anions of TBAX. ECF using more donating anions (i.e., TsO<sup>-</sup> and TfO<sup>-</sup>) than ClO<sub>4</sub><sup>-</sup> gave lower RCY than that using less donating anions than ClO<sub>4</sub><sup>-</sup> because donating anions have potential to behave as a nucleophile, which would lead to the decrease of the stability of the reaction intermediates (432).

On the other hand, using less donating anions (i.e.,  $\text{BF}_4^-$  and  $\text{PF}_6^-$ ) than  $\text{ClO}_4^-$  also decreased RCY. In the ECF of MMTA using the s-BPE system, these anions (i.e.,  $\text{BF}_4^-$  and  $\text{PF}_6^-$ ) were considered to serve not only as supporting salts but also base for generating the sulfonium intermediate in the Pummerer-type mechanism (Scheme 1); however, the basicity of these anions was lower than  $\text{ClO}_4^-$ , which seemed to result in lower RCY. The trend was similar to our previous work.<sup>(425)</sup> To investigate the effects of solvents on RCY of the ECF of MMTA, we attempted to use HFIP, acetonitrile (MeCN), and 1,2-dimethoxyethane (DME) as a solvent (**Table 11-2**). However, these solvents were found not to be suitable for the reaction. During the ECF performed in HFIP solution, the U-typed cell made of ULTEM<sup>TM</sup> was partially dissolved. Using both MeCN solution and DME solution for the extraction of [<sup>18</sup>F]TBAF from the cartridge resulted in very low elution efficiency. From these results, we concluded that using TBAP as a supporting salt and TFE as a solvent was the most suitable combination for our electrolysis system.



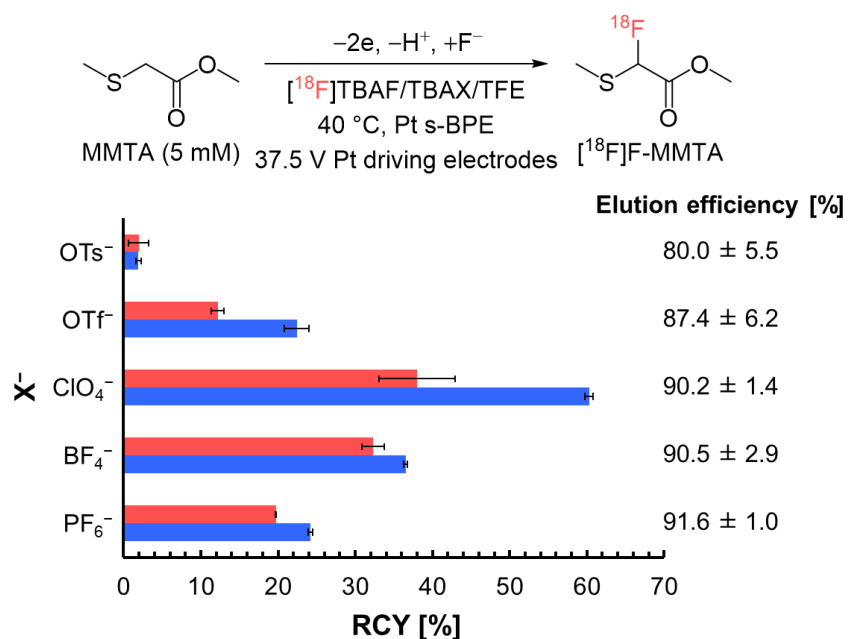


**Figure 11-4 Influence of different anions (X<sup>-</sup> of TBAX) on the elution efficiencies (n = 3) and RCC at 30 (blue bar) and 60 min (red bar).**

ECF was performed in [<sup>18</sup>F]TBAF/TBAX/TFE solutions containing 5 mM MMTA with the application of 37.5 V to driving electrodes at 40 °C. RCC was determined by radio-TLC of the crude samples (n = 3 or 15 (X<sup>-</sup> = ClO<sub>4</sub><sup>-</sup> at 30 min)).

We also investigated the effects of the concentration of MMTA on RCY (**Table 11-1**). RCY increased together with the concentration of MMTA up to 5 mM, suggesting that at low concentration of MMTA (below 5mM) the formed sulfonium cation intermediate could not react with [<sup>18</sup>F]F<sup>-</sup> ions. In contrast, for concentrations of MMTA higher than 5 mM, the RCY of the crude collected at 60 min remains about constant at 60% suggesting the nucleophilic attack of [<sup>18</sup>F]F<sup>-</sup> limits the reaction. Surprisingly, when 25 mM of MMTA was used, the RCY of the crude collected at 30 min was up to approximately 70% with high reproducibility; however, this reason is not clear in this work. Considering PET trace synthesis, the higher RCY with less reaction time is preferential because of the decay of the activity. Therefore, from the series of the optimization process, the optimal reaction conditions were determined as shown in Entry 7 in **Table 11-1**, where ECF of MMTA (25 mM) was performed in [<sup>18</sup>F]TBAF/TBAP/TFE with the application of 37.5 V to the driving electrodes at 40 °C for 30 min.

**Table 11-1 Effects of the concentration of MMTA on RCC.**

Entry	[MMTA] [mM]	RCY (n = 3) [%] <sup>a</sup>	
		30 min	60 min
1	0.1	5.8 ± 0.9	7.2 ± 1.3
2	1.0	4.6 ± 0.5	4.1 ± 0.1
3	2.5	18.2 ± 1.0	11.9 ± 2.0
4	5.0	38.0 ± 4.9 <sup>b</sup>	60.3 ± 0.5
5	7.5	31.9 ± 2.5	58.3 ± 1.1
6	10.0	33.8 ± 1.0	56.3 ± 1.9
7	25.0	71.1 ± 2.9 <sup>c</sup>	62.0 ± 6.5
8	50.0	34.9 ± 1.1	67.2 ± 0.4

<sup>a</sup>Determined by radio-TLC of the crude. <sup>b</sup>n = 15 <sup>c</sup>n = 9.

The optimized ECF conditions were applied to MMTA and the RCY and  $A_m$  of [ $^{18}\text{F}$ ]F-MMTA were determined by radio-HPLC analysis. The purification protocol of the crude [ $^{18}\text{F}$ ]F-MMTA is described in the **Appendix 11.4.5**. The overall preparation time for [ $^{18}\text{F}$ ]F-MMTA including the radiosynthesis and isolation process was about 80 minutes. The isolated RCY of [ $^{18}\text{F}$ ]F-MMTA was  $46.3 \pm 4.2\%$  (n = 3), and the radiochemical purity (RCP) was approximate 100%.  $A_m$  was 28–43 GBq/ $\mu\text{mol}$  (0.74–1.1 Ci/ $\mu\text{mol}$ ) (n = 3) with starting activity of 2.5–3.3 GBq (67–89 mCi). Although the RCY was lower on a s-BPE system compared to the previous report using a conventional ECF platform ( $46.3 \pm 4.2\%$ , n = 3 for BPEs vs.  $88 \pm 3\%$ , n = 3(418)), the  $A_m$  obtained in this work was five times higher (28–43 GBq/ $\mu\text{mol}$  vs. 4.7–5.3 GBq/ $\mu\text{mol}$ (418)), and had satisfied the quality-control requirement for clinical use (i.e. >18.5 GBq/ $\mu\text{mol}$ ) which was impossible to be achieved by previous ECF approaches. The present study fills the gap in the literature by applying

BPE systems to ECF to provide clinically-relevant  $A_m$  for radiofluorinated compounds,(419) and eases the pain for radiofluorination of thioether derivatives with acceptable  $A_m$ .

## 11.3 Conclusions

In conclusion, this report successfully demonstrated the first application of wireless electrodes (i.e., BPE) to radiochemistry. ECF of MMTA was achieved under low concentration of supporting salts using a s-BPE system. Through the optimization of reaction conditions such as temperature, applied voltage to driving electrodes, electrolytic solution, and concentration of MMTA, we achieved comparable RCY of  $46.3 \pm 4.2\%$  ( $n = 3$ ) with clinical use (i.e.,  $>18.5$  GBq/ $\mu\text{mol}$ ) and high  $A_m$  of 28–43 GBq/ $\mu\text{mol}$  (0.74–1.1 Ci/ $\mu\text{mol}$ ) ( $n = 3$ ) by using starting activity of 2.5–3.3 GBq (67–89 mCi). The obtained  $A_m$  in this work was five times higher than that reported in the previous report.(418) The s-BPE system can be potentially integrated with other efficient synthetic platforms, such as flow electrosynthesis(433) and automated ECF systems.(426) Further research is underway to construct a novel ECF platform based on such systems for realizing efficient nucleophilic radiofluorination systems.

## 11.4 Appendix

### 11.4.1 Materials

All reagents and solvents were purchased from commercial suppliers and used without further purification. Distilled water or deionized (DI) water was used for all experiments requiring the use of water. Platinum wire (99.9%) were purchased from Sigma-Aldrich (St. Louis, MO, USA) or Thermo Fisher Scientific (Waltham, MA, USA). Silver wire was obtained from MiliporeSigma (Burlington, MA, USA). The light quaternary methylammonium (QMA) cartridge with  $\text{CO}_3^{2-}$  as counter ions (130 mg, Part No. K-920) was purchased from ABX Advanced Biochemical Compounds (Radeberg, Germany) and used for trapping/releasing F-18 for radiosynthesis. The short tC18 cartridges (WAT036810, 400 mg) used for purifying crude product before HPLC separation were obtained from Waters Corporation (Milford, MA, USA). [ $^{18}\text{F}$ ]fluoride was produced

using [ $^{18}\text{O}$ ]H<sub>2</sub>O (84% isotopic purity, Medical Isotopes) in a RDS-112 cyclotron (Siemens) from a 11 MeV bombardment with a 1 mL tantalum target with havar foil. Methyl 2-[ $^{19}\text{F}$ ]fluoro-2-(methylthio)acetate ([ $^{19}\text{F}$ ]F-MMTA) was synthesized by performing electrochemical fluorination of methyl 2-(methylthio)acetate (MMTA) according to the literature.(418)

#### 11.4.2 General

##### *Nuclear magnetic resonance (NMR)*

All  $^1\text{H}$  and  $^{19}\text{F}$  NMR spectra were recorded on a Bruker AV600 MHz spectrometer (600.13 MHz for  $^1\text{H}$ , and 564.68 MHz for  $^{19}\text{F}$ ) using CD<sub>3</sub>CN as a solvent at room temperature.

##### *Gas chromatography mass spectrometer (GC-MS)*

GC-MS spectra were recorded on Agilent Analytics System (HP 6890 GC with 5973 Mass Selective Detector; Santa Clara, CA, USA) using electron ionization (EI) method.

##### *High-performance liquid chromatography (HPLC)*

HPLC characterization for [ $^{19}\text{F}$ ]F-MMTA was performed on a Waters Binary HPLC System (Model 1525; Milford, MA, USA) equipped with a UV detector (Model 2489, Waters) under UV absorbance detection of 254 nm and 241 nm, and a gamma-radiation detector and counter (Model 106, Bioscan Inc., Poway, CA, USA). Spectra were analyzed on Empower 3 software (Waters).

#### 11.4.3 Preparation of BPE cell

Electrochemical radiofluorination (ECF) was carried out using a U-shaped cell with a split bipolar electrode (s-BPE) system. The U-shaped cell was made of ULTEM™ (Polyetherimide) (Figure S1). The U-shaped cell was designed by following our previous report (423).

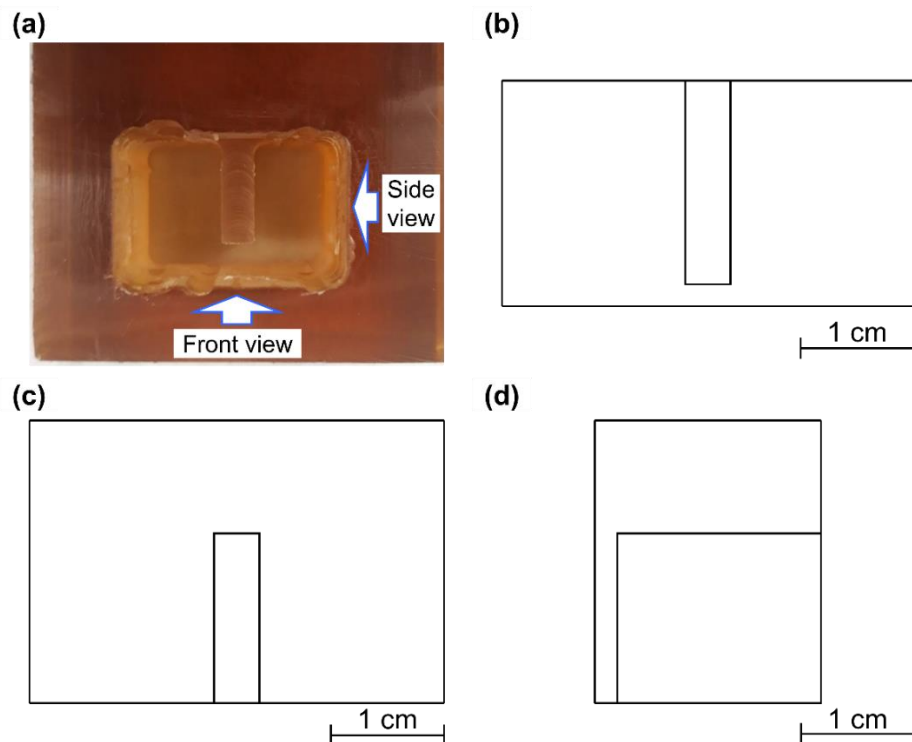


**Figure 11-5** (a) A photograph of the top view of a U-shaped cell. (b–d) Detail designs of the U-shaped cell, including (b) top view, (c) front view, and (d) side view.

#### 11.4.4 Synthesis and purification of [<sup>19</sup>F]F-MMTA

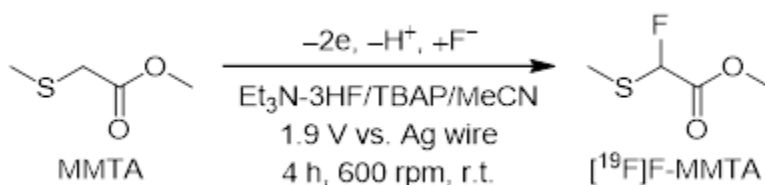


**Figure 11-6** Electrochemical synthesis of [<sup>19</sup>F]F-MMTA condition.

[<sup>19</sup>F]F-MMTA was synthesized according to the literature (418). Autolab 128 (Metrohm, Herisau, Switzerland) was used as a power supply. An electrochemical cell (E-cell) equipped with a three-electrode system was used for electrochemical fluorination of MMTA (**Figure 11-7(a)**). A platinum wire with 10 cm length and 0.25 mm diameter was used as both a working electrode and a counter electrode, and a silver wire was used as a reference electrode. A 10 mL of solution containing 50 mM MMTA, tetrabutylammonium perchlorate (TBAP) (50 mM) and triethylamine

trihydrofluoride ( $\text{Et}_3\text{N}\cdot 3\text{HF}$ ) (500 mM) in acetonitrile (MeCN) was prepared. Electrochemical fluorination of MMTA was performed in the prepared MeCN solutions using a single chamber E-cell under constant-potential conditions (1.9 V vs. Ag wire) at room temperature for 4 hours with stirring at 600 rpm as shown in **Figure 11-7(b)**. To reduce the passivation of the electrodes, multiple cycles of 60 seconds oxidation at 1.9 V (vs. Ag wire) followed by 6 seconds reduction at  $-0.6$  V (vs. Ag wire) were performed.

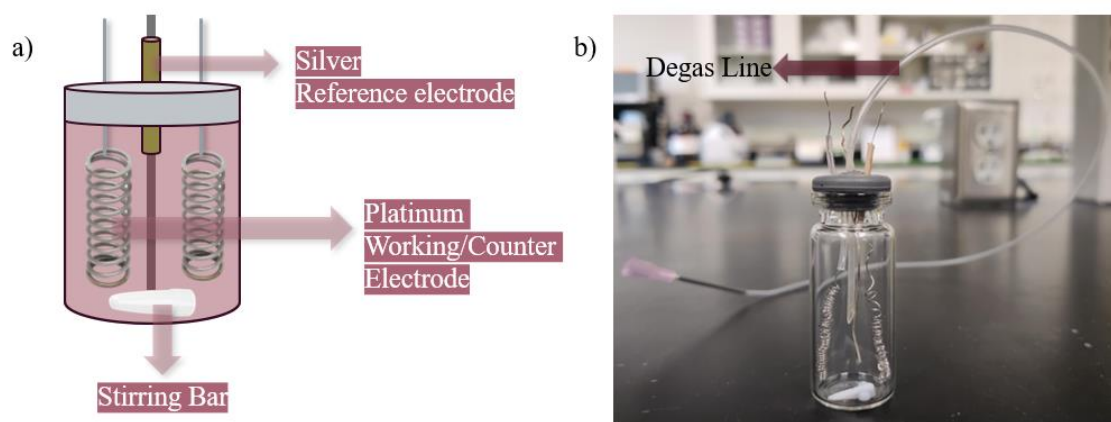


**Figure 11-7 (a) Schematic representation of an E-cell setup with three electrodes, including two platinum electrodes, a silver reference electrode and a stirring bar. (b) Photograph of an E-cell used for the preparation of  $[^{19}\text{F}]\text{F-MMTA}$ .**

After the electrolysis, the crude product solution was purified as follows. The crude product (10 mL) was diluted with 30 mL of dichloromethane (DCM) and loaded into a pre-conditioned Sep-Pak Plus Long Silica cartridge to remove salts. 2–5 mL of DCM was used to wash the cartridge. The organic solution containing the product in MeCN/DCM mixture was concentrated to 1–2 mL with air flow. (Rotary evaporation and performing high vacuum lyophilization were not suitable to concentrate the mixture because of the high volatility of  $[^{19}\text{F}]\text{F-MMTA}$ .) The concentrated crude was diluted with 10–20 mL of water and loaded onto a preconditioned Sep-Pak C18 Short cartridge. Afterwards, the cartridge was washed with 3 mL of water and then the crude product was eluted with 1.5 mL of ethanol/ $\text{H}_2\text{O}$  (v/v = 70/30). The resultant mixture was purified with

semipreparative HPLC. Column: Gemini 5  $\mu\text{m}$  NX-C18 110  $\text{\AA}$  column (250  $\times$  10.0 mm). Gradient: A =  $\text{H}_2\text{O}$  with 0.1% formic acid (v/v); B = MeCN with 0.1% formic acid (v/v); flow rate = 4 mL/min; 0–13 min 80% to 40% A, 12–13 min 40% to 5% A, 13–15 min 5% A, 15–18 min 5% to 60% A, 18–22min 60% to 80% A. UV wavelength: 254 nm and 241 nm. The product was collected around 8.5 min. The purity of the collected product was assessed by an analytical HPLC. Column: Gemini 5  $\mu\text{m}$  NX-C18 110  $\text{\AA}$  column (250  $\times$  4.6 mm). Gradient: A =  $\text{H}_2\text{O}$  with 0.1% formic acid (v/v); B = MeCN with 0.1% formic acid (v/v); flow rate = 1.5 mL/min; 0–13 min 80% to 40% A, 12–13 min 40% to 5% A, 13–15 min 5% A, 15–18min 5% to 60% A, 18–20 min 60% to 80% A. The obtained product was also analyzed using GC-MS, and  $^1\text{H}$  and  $^{19}\text{F}$  NMR to confirm the identity.

#### 11.4.5 Electrochemical radiofluorination (ECF) of MMTA using a s-BPE

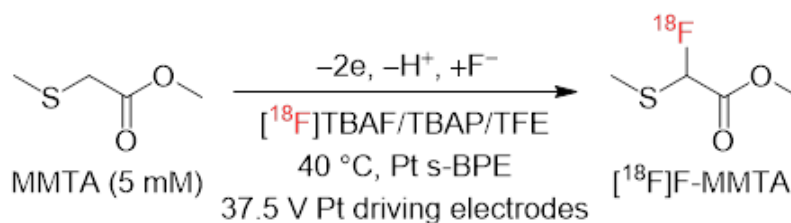


**Figure 11-8 Electrochemical radiofluorination (ECF) of MMTA using a s-BPE**

ECF was performed using a U-shaped cell equipped with Pt wires (length = 20 cm, diameter = 0.33 mm, **Figure 11-9(a)**) as both driving electrodes and a s-BPE. The two Pt wires were connected with an Ag wire, and the tied Pt wire was used as a s-BPE (**Figure 11-9 (b)**). The reaction setup for ECF is shown in **Figure 11-9(c)**. GPS-4303 (GW-INSTEK, Taiwan) was used as a power supply for ECF.

Typical experimental procedures of ECF of MMTA are described as follows. 0.19–3.3 GBq (5–89 mCi) of  $[\text{}^{18}\text{F}]\text{F}^-$  was trapped on a preconditioned cartridge by passing 1 mL of diluted aqueous  $[\text{}^{18}\text{F}]\text{fluoride}$  with water through the resin. To remove all water residue from the cartridge, nitrogen was flowed through the cartridge for 10 min, then 1 mL of anhydrous MeCN (2

times), nitrogen flow for 10 min, and then 1 mL of 2,2,2-trifluoroethanol (TFE).  $[^{18}\text{F}]\text{F}^-$  was subsequently eluted out from the cartridge with 1 mL of 25 mM TBAP in TFE. The MMTA stock solution (0.025 mmol in 4 mL of TFE) and the eluted  $[^{18}\text{F}]\text{TBAF}$  (1 mL) solution, (i.e. total 5 mL of reaction mixture), were added to the U-shaped cell. ECF of MMTA was performed in the U-shaped cell at 40°C by using a water bath, with application of 37.5 V to the driving electrode. To suppress the evaporation of solution during the ECF, the U-shaped cell was covered with a parafilm as shown in Figure 11-9(c).

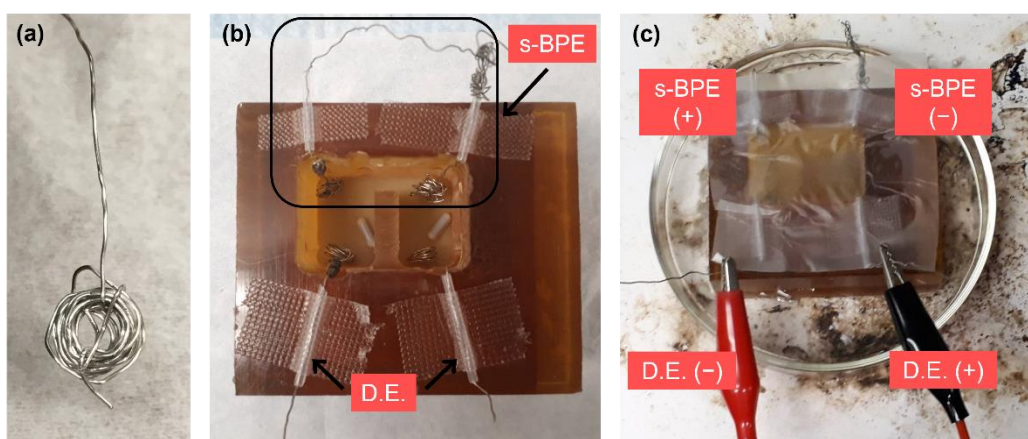


**Figure 11-9 Photographs of (a) a Pt electrode, (b) the U-shaped cell equipped with the driving electrode (D.E.) and a s-BPE, and (c) electrolysis setup for ECF.**

After reaction, the radiochemical yield (RCY) of the crude mixture was analyzed by radio-thin layer chromatography (radio-TLC) to determine the reaction efficiency. A small sample ( $\sim 1$   $\mu\text{L}$ ) was spotted onto a TLC plate (silica gel 60 F<sub>254</sub> TLC plastic plate, Merck KGaA, Darmstadt, Germany) by pipetting, and the plate was developed with 100% MeCN. After drying, the TLC plate was scanned by a radio-TLC scanner (miniGITA, Elysia-Raytest GmbH, Straubenhardt, Germany) for 3 min. The percentage of each species was obtained with GINA-STAR software (Elysia-Raytest) by computing areas under the peaks in the chromatogram corresponding to the product ( $R_f = 0.9$ ) and unreacted  $[^{18}\text{F}]\text{fluoride}$  ( $R_f = 0.0$ ), and dividing each individual peak area by



the sum of all peak areas. RCC was computed as the percentage of product. 0.5 mL of the crude product was diluted with 10 mL of water, and then the diluted mixture was loaded onto a tC18 cartridge, which was pre-conditioned with 3 mL of ethanol followed by 30 mL of water. The crude product was eluted out with 1.5 mL of water and MeCN (v/v, 1:1). 0.2 mL of the eluted crude product was injected into an analytical C18 column (Luna, 250 × 4.6 mm, 5 μm, Phenomenex, Torrance, CA, USA), and purified by using isocratic mobile phase of MeCN and water (v/v, 1:1) with 0.1% TFA (v/v) at a flow rate of 1.5 mL/min, under UV absorbance of 241 nm with radiation detectors (**Figure 11-10**). Radiochemical yield (RCY) and radiochemical purity (RCP) were determined by radio-HPLC.

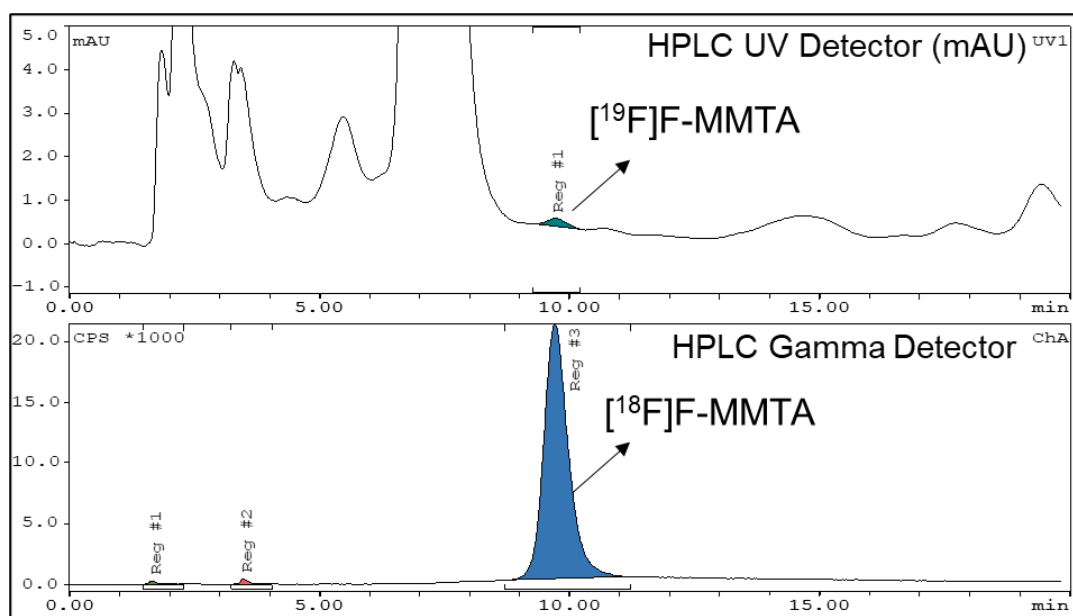


**Figure 11-10** Enlarged radio-HPLC chromatogram of crude [<sup>18</sup>F]F-MMTA (upper: UV-241 nm and bottom: γ-ray).

#### 11.4.6 Molar activity ( $A_m$ ) calculation

Analytical HPLC was used to determine the molar activity ( $A_m$ ) of purified [ $^{18}\text{F}$ ]F-MMTA. A calibration curve was generated by injecting known amounts of [ $^{19}\text{F}$ ]F-MMTA reference standard (0.04–0.1  $\mu\text{mol}$ ) and determining area under the peak under same conditions (at 241 nm) (Figure S5). This curve was then used to determine the amount of [ $^{19}\text{F}$ ]F-MMTA in the unknown sample and  $A_m$  was computed following standard procedures.

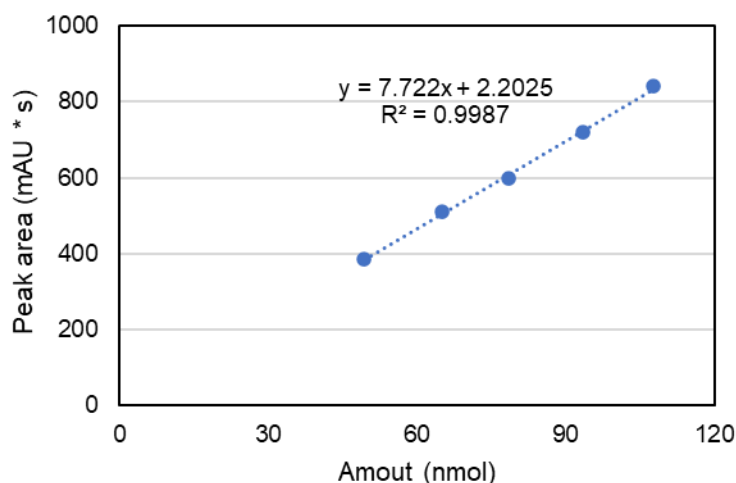


**Figure 11-11 Calibration curve of [ $^{19}\text{F}$ ]F-MMTA reference standard (241 nm wavelength).**

#### 11.4.7 Effects of solvents on both elution efficiencies of [ $^{18}\text{F}$ ]F $^-$ and RCC in ECF

To investigate the effects of solvents on our proposed ECF system, we performed ECF by using various solvents, such as 1,1,1,3,3,3-hexafluoro-2-propanol (HFIP), MeCN, and 1,2-dimethoxyethane (DME), instead of TFE. The same experimental protocols described in the section 5 were used. Table S1 summarizes the effects of solvents on both elution efficiencies of [ $^{18}\text{F}$ ]F $^-$  and RCC.

**Table 11-2 Effects of solvents on elution efficiencies and RCC**

Entry	Solvent	Elution efficiency (n = 2) [%]	RCY [%] <sup>a</sup>	
			30 min	60 min
1	TFE	90.2 ± 1.4 <sup>b</sup>	38.0 ± 4.9 <sup>c</sup>	60.3 ± 0.5 <sup>d</sup>
2	HFIP	70.6 ± 4.4	-	-
3	MeCN	~ 0	-	-
4	DME	~ 0	-	-

<sup>a</sup>Determined by radio-TLC of the crude samples. <sup>b</sup>n = 3. <sup>c</sup>n = 15. <sup>d</sup>n = 3.

## Chapter 12: Outlook

As discussed in **Chapter 1**, the production of radiopharmaceuticals for PET diagnostics faces numerous challenges, including its expensive and intricate nature. The miniaturization of different aspects of PET tracer production holds the potential to address some of these challenges by creating more compact, cost-effective, and efficient devices. Microfluidics, through the reduction of shielding, physical footprint, and reagent consumption, offers the prospect of low-cost decentralized production of PET tracers. This entails producing tracers on demand within imaging centers, diverging from the traditional centralized large-batch production and distribution model. Despite the existence of microfluidic analogues for conventional radiosynthesizers, their widespread adoption is currently hindered, partly due to high costs, dependence on specialized parts, and limitations in the macro-to-micro interface. Additional challenges arise when production practices must be validated and approved in compliance with various clinical use regulations. Notably, our lab, among other research groups, has developed several microfluidic instruments with the aim of replacing various components of PET tracer production.

This dissertation centers on the microscale radiosynthesis of PET tracers, aiming to showcase the versatility and advantages inherent in droplet-based synthesis methods. In **Chapter 2**, droplet synthesis methods were initially applied to the copper-mediated radiofluorination approach—a highly promising and primary method for introducing aromatic C-<sup>18</sup>F bonds into both novel and established PET tracers. The well-known clinical PET agent [<sup>18</sup>F]FDOPA served as an illustrative example. This successful study revealed a significantly more economical manufacturing strategy for [<sup>18</sup>F]FDOPA, requiring much less precursor and a substantially shorter preparation time compared to the conventional approach. Encouraged by the markedly improved production performance of [<sup>18</sup>F]FDOPA in a microreactor, further endeavors in **Chapter 5 and 8** focused on the translation of microdroplet synthesis for both established ([<sup>18</sup>F]FBnTP) and novel ([<sup>18</sup>F]YH149) tracers via a similar copper-mediated synthesis route. In addition to the pivotal

copper-mediated radiosynthesis, this dissertation delves into the successful application of another metal-based radiochemistry, [ $^{18}\text{F}$ ]AIF, in droplet reactions, as detailed in **Chapter 3**. Building upon this, **Chapter 4** leverages my extensive past experience to explore the feasibility of executing a one-pot three-step radiosynthesis of [ $^{18}\text{F}$ ]FMAU on a microdroplet reactor. The optimization process involved optimizing fluorination, coupling, and deprotection conditions on microfluidic chips. This was achieved through a comprehensive series of experiments conducted on a novel high-throughput radiochemistry platform, where I investigated the impact of diverse PTCs/bases, solvents, varying amounts of precursor and coupling reagents, reaction temperatures and times, and purification methods. It is worth noting that this work represents the most complex radiosynthesis to date performed in any microscale reaction. These chapters demonstrated that the high versatility of droplet-based radiolabeling, extending applications to new chemistries, including Cu-mediated radiosyntheses of  $^{18}\text{F}$ -labeled tracers, and [ $^{18}\text{F}$ ]AIF radiolabeling, and also extending to the extremely complex preparation process for [ $^{18}\text{F}$ ]FMAU, offering advantages of simplicity, speed, and versatility compared to conventional approaches.

**Chapters 6 and 7** provide evidence that droplet synthesis can be easily scaled up to produce a few human doses of tracers. While ongoing research explores further scale-up possibilities, the current production level proves sufficient for scenarios with moderate tracer demand, such as the early stages of novel radiopharmaceutical development, clinical or research studies, and the use of approved radiotracers for specialized diseases. In **Chapter 6**, the produced [ $^{18}\text{F}$ ]FET and [ $^{18}\text{F}$ ]FBB successfully met all necessary quality control (QC) requirements, affirming the viability and robustness of the droplet synthesis approach on a larger scale. Additionally, **Chapter 7** introduces a successful demonstration of the numbering up scale-up method, providing an alternative and viable approach for producing clinically-relevant batches. The proof-of-concept example, [ $^{18}\text{F}$ ]FBnTP, highlights the potential of this new method to significantly reduce the time from droplet optimization to clinical scale-up, offering increasing dose-on-demand flexibility.

The limited availability of droplet reactor systems currently poses a substantial barrier to adoption, preventing wider access to the enhanced droplet-based synthesis process. Researchers have long been curious about the performance of droplet-based optimized conditions when scaled up to macroscale reactors. In a groundbreaking development, **Chapter 8** presents the first demonstration of successfully translating the optimized droplet conditions to a vial-based macroscale reaction. This not only addresses the current scarcity of droplet reactor systems but also opens the door for broader utilization of the improved synthesis process on a larger scale. This approach provides a temporary stopgap measure to enable researchers to be comfortable with the benefits of droplet technology, until droplet reactors become commercially available for preclinical and clinical production in the future. Eventually, we believe droplet reactors will be used for production as well. To seamlessly integrate the droplet reaction technique into routine clinical practice, it is imperative to automate the droplet-based synthesis process. This involves developing a fully-integrated prototype equipped with a multi-reaction-site chip, HPLC purification, and cartridge formulation. This effort is currently underway.

In addition to advancing droplet-based radiosynthesis techniques, this dissertation emphasizes efforts to develop supporting technologies for efficiently conducting numerous droplet reactions, facilitated by robotic automation in **Chapter 5**. The high-resolution and high-throughput analysis of these reactions is detailed in **Chapter 9** through the implementation of the PRISMA method, coupled with multi-lane TLC separation and readout. This innovative analysis technique provides a comprehensive solution for high-throughput optimization, enabling the execution of hundreds of reactions within a few days and seamlessly transitioning to production in a droplet-based automated radiosynthesizer. To date the high-throughput technique has been employed for synthesis optimization, but it could also be extended to study substrate scope of new labeling methods, or potentially to label libraries of related compounds (e.g. peptides), to enable rapid initial evaluation and screen via *in vitro* and *in vivo* measurements.

The ideal end goal in PET tracer miniaturization is a fully automated, integrated device that demands minimal user intervention, seamlessly managing the entire production process from radioisotope dispensing to quality control. We firmly believe that the straightforward yet versatile droplet techniques presented in this dissertation will not only inspire but also drive further advancements in radiochemistry miniaturization—ultimately influencing its application in both research and clinical settings. Our vision encompasses the transformative impact of such low-footprint, low reagent consumption, and low waste devices, offering substantial benefits to the field of radiochemistry. These advancements have the potential to simplify, reduce costs, enhance safety, and increase accessibility in PET tracer production. Paired with ongoing progress in PET imaging technology, we anticipate a global promotion of powerful PET diagnostics, extending their reach to diverse settings, including those with limited resources.

## References

1. Cherry SR. Fundamentals of Positron Emission Tomography and Applications in Preclinical Drug Development. *J Clin Pharmacol*. 2001;41:482-491.
2. Hargreaves R. The Role of Molecular Imaging in Drug Discovery and Development. *Clin Pharmacol Ther*. 2008;83:349-353.
3. Dendl K, Koerber SA, Kratochwil C, et al. FAP and FAPI-PET/CT in Malignant and Non-Malignant Diseases: A Perfect Symbiosis? *Cancers*. 2021;13:4946.
4. Berti V, Osorio RS, Mosconi L, Li Y, Santi SD, Leon MJ de. Early Detection of Alzheimer's Disease with PET Imaging. *NDD*. 2010;7:131-135.
5. Deleye S, Waldron A-M, Verhaeghe J, et al. Evaluation of Small-Animal PET Outcome Measures to Detect Disease Modification Induced by BACE Inhibition in a Transgenic Mouse Model of Alzheimer Disease. *J Nucl Med*. 2017;58:1977-1983.
6. Shukla AK, Kumar U. Positron emission tomography: An overview. *J Med Phys*. 2006;31:13-21.
7. Eckelman WC. The Use of Positron Emission Tomography in Drug Discovery and Development. In: Bailey DL, Townsend DW, Valk PE, Maisey MN, eds. *Positron Emission Tomography: Basic Sciences*. London: Springer; 2005:327-341.
8. Knowles SM, Tavaré R, Zettlitz KA, et al. Applications of immunoPET: using <sup>124</sup>I-anti-PSCA A11 minibody for imaging disease progression and response to therapy in mouse xenograft models of prostate cancer. *Clin Cancer Res*. October 2014:clincanres.1452.2014.
9. Bailey DL, Karp JS, Surti S. Physics and Instrumentation in PET. In: Bailey DL, Townsend DW, Valk PE, Maisey MN, eds. *Positron Emission Tomography: Basic Sciences*. London: Springer; 2005:13-39.
10. Vandenberghe S, Mikhaylova E, D'Hoe E, Mollet P, Karp JS. Recent developments in time-of-flight PET. *EJNMMI Physics*. 2016;3:3.
11. Papathanassiou D, Bruna-Muraille C, Liehn J-C, Nguyen TD, Curé H. Positron Emission Tomography in oncology: Present and future of PET and PET/CT. *Crit Rev Oncol Hematol*. 2009;72:239-254.
12. Kapoor V, McCook BM, Torok FS. An Introduction to PET-CT Imaging1. *RadioGraphics*. March 2004.
13. Townsend DW, Carney JPJ, Yap JT, Hall NC. PET/CT Today and Tomorrow. *J Nucl Med*. 2004;45:4S-14S.
14. Judenhofer MS, Wehrl HF, Newport DF, et al. Simultaneous PET-MRI: a new approach for functional and morphological imaging. *Nat Med*. 2008;14:459-465.



15. Delso G, Ziegler S. PET/MRI system design. *Eur J Nucl Med Mol Imaging*. 2009;36:86-92.
16. Catana C, Drzezga A, Heiss W-D, Rosen BR. PET/MRI for Neurologic Applications. *J Nucl Med*. 2012;53:1916-1925.
17. Ehman EC, Johnson GB, Villanueva-Meyer JE, et al. PET/MRI: Where might it replace PET/CT? *J Magn Reson Imaging*. 2017;46:1247-1262.
18. Ametamey SM, Honer M, Schubiger PA. Molecular Imaging with PET. *Chem Rev*. 2008;108:1501-1516.
19. Banister S, Roeda D, Dolle F, Kassiou M. Fluorine-18 Chemistry for PET: A Concise Introduction. *Curr Radiopharm*. 2010;3:68-80.
20. Jacobson O, Kiesewetter DO, Chen X. Fluorine-18 Radiochemistry, Labeling Strategies and Synthetic Routes. *Bioconjug Chem*. 2015;26:1-18.
21. Brooks AF, Makaravage KJ, Wright J, Sanford MS, Scott PJH. Fluorine-18 Radiochemistry. In: *Handbook of Radiopharmaceuticals*. John Wiley & Sons, Ltd; 2020:251-289.
22. Huang X, Liu W, Ren H, Neelamegam R, Hooker JM, Groves JT. Late Stage Benzylic C-H Fluorination with [18F]Fluoride for PET Imaging. *J Am Chem Soc*. 2014;136:6842-6845.
23. Richard M, Specklin S, Roche M, Hinnen F, Kuhnast B. Original synthesis of radiolabeling precursors for batch and on resin one-step/late-stage radiofluorination of peptides. *Chem comm*. 2020;56:2507-2510.
24. Babin V, Taran F, Audisio D. Late-Stage Carbon-14 Labeling and Isotope Exchange: Emerging Opportunities and Future Challenges. *JACS Au*. 2022;2:1234-1251.
25. Chyng-Yann Shiue, Joanna S. Fowler, Alfred P. Wolf, Masazumi Watanabe, Carroll D. Arnett. Synthesis and Specific Activity Determinations of No-Carrier-Added Fluorine-18-Labeled Neuroleptic Drugs. *J Nucl Med*. 1985;26:181-186.
26. Kilbourn MR, Rodnick ME, Clark M. Production of Short Half-Life PET Radionuclides. In: *Handbook of Radiopharmaceuticals*. John Wiley & Sons, Ltd; 2020:45-69.
27. GE Healthcare. FASTlab 2 Multi-Tracer Platform. [http://www3.gehealthcare.com/en/products/categories/molecular\\_imaging/pet-radiopharmacy/tracer\\_center\\_equipment/fastlab](http://www3.gehealthcare.com/en/products/categories/molecular_imaging/pet-radiopharmacy/tracer_center_equipment/fastlab).
28. Siemens Healthcare. Explora GN - Overview. <http://usa.healthcare.siemens.com/molecular-imaging/cyclotron-chemistry-solution/explora-gn>.
29. IBA. Synthera: Small dimensions. Huge potential.

30. GE Healthcare. TRACERlab.  
[http://www.gehealthcare.com/euen/fun\\_img/products/radiopharmacy/products/tracerlabfxc.html](http://www.gehealthcare.com/euen/fun_img/products/radiopharmacy/products/tracerlabfxc.html).
31. Synthra GmbH Home Page. <http://synthra.com/>.
32. Eckert & Ziegler Eurotope GmbH. Modular-Lab PharmTracer.  
<http://www.ezag.com/home/products/radiopharma/radiosynthesis-technology/modular-lab-pharmtracer.html>.
33. Lazari M, Quinn KM, Claggett SB, et al. ELIXYS - a fully automated, three-reactor high-pressure radiosynthesizer for development and routine production of diverse PET tracers. *EJNMMI Res.* 2013;3:52.
34. SOFIE. ELIXYS FLEX/CHEM. <http://sofiebio.com/products/chemistry/elixys/>.
35. Wang J, van Dam RM. Economical Production of Radiopharmaceuticals for Preclinical Imaging Using Microdroplet Radiochemistry. In: Ossandon MR, Baker H, Rasooly A, eds. *Biomedical Engineering Technologies: Volume 1. Methods in Molecular Biology*. New York, NY: Springer US; 2022:813-828.
36. Rensch C, Jackson A, Lindner S, et al. Microfluidics: A Groundbreaking Technology for PET Tracer Production? *Mol.* 2013;18:7930-7956.
37. Kuge Y, Shiga T, Tamaki N. *Perspectives on Nuclear Medicine for Molecular Diagnosis and Integrated Therapy*. Springer; 2016.
38. Knapp K-A, Nickels ML, Manning HC. The Current Role of Microfluidics in Radiofluorination Chemistry. *Mol Imaging Biol.* 2020;22:463-475.
39. Wang J, van Dam RM. High-Efficiency Production of Radiopharmaceuticals via Droplet Radiochemistry: A Review of Recent Progress. *Mol Imaging.* 2020;19:1536012120973099.
40. Elkawad H, Xu Y, Tian M, et al. Recent advances in microfluidic devices for radiosynthesis of PET-imaging probes. *Chemistry – An Asian Journal.* 2022.
41. Razzaq T, Kappe CO. Continuous Flow Organic Synthesis under High-Temperature/Pressure Conditions. *Chem Asian J.* 2010;5:1274-1289.
42. Wiles C, Watts P. Continuous Flow Reactors, a Tool for the Modern Synthetic Chemist. *Eur J Org Chem.* 2008:1655-1671.
43. Arima V, Watts P, Pascali G. Microfluidics in Planar Microchannels: Synthesis of Chemical Compounds On-Chip. In: Castillo-León J, Svendsen WE, eds. *Lab-on-a-Chip Devices and Micro-Total Analysis Systems*. Springer International Publishing; 2015:197-239.
44. Pascali G, Watts P, Salvadori PA. Microfluidics in radiopharmaceutical chemistry. *Nucl Med Biol.* 2013;40:776-787.

45. Zeng D, Desai AV, Ranganathan D, Wheeler TD, Kenis PJA, Reichert DE. Microfluidic radiolabeling of biomolecules with PET radiometals. *Nuclear Medicine and Biology*. 2013;40:42-51.
46. Wright BD, Whittenberg J, Desai A, et al. Microfluidic Preparation of a <sup>89</sup>Zr-Labeled Trastuzumab Single-Patient Dose. *J Nucl Med*. 2016;57:747-752.
47. Pfaff S, Philippe C, Pichler V, Hacker M, Mitterhauser M, Wadsak W. Microfluidic <sup>68</sup>Ga-labeling: a proof of principle study. *Dalton Trans*. 2018;47:5997-6004.
48. Liu Z, Schaap KS, Ballemans L, et al. Measurement of reaction kinetics of [<sup>177</sup>Lu]Lu-DOTA-TATE using a microfluidic system. *Dalton Trans*. 2017;46:14669-14676.
49. Saiki H, Iwata R, Nakanishi H, et al. Electrochemical concentration of no-carrier-added [<sup>18</sup>F]fluoride from [<sup>18</sup>O]water in a disposable microfluidic cell for radiosynthesis of <sup>18</sup>F-labeled radiopharmaceuticals. *Appl Radiat Isot*. 2010;68:1703-1708.
50. Wong R, Iwata R, Saiki H, Furumoto S, Ishikawa Y, Ozeki E. Reactivity of electrochemically concentrated anhydrous [<sup>18</sup>F]fluoride for microfluidic radiosynthesis of <sup>18</sup>F-labeled compounds. *Appl Radiat Isot*. 2012;70:193-199.
51. Sergeev M, Lazari M, Morgia F, et al. Performing radiosynthesis in microvolumes to maximize molar activity of tracers for positron emission tomography. *Commun Chem*. 2018;1:10.
52. Keng PY, Sergeev M, van Dam RM. Advantages of Radiochemistry in Microliter Volumes. In: Kuge Y, Shiga T, Tamaki N, eds. *Perspectives on Nuclear Medicine for Molecular Diagnosis and Integrated Therapy*. Springer Japan; 2016:93-111.
53. Keng PY, van Dam RM. Digital Microfluidics: A New Paradigm for Radiochemistry. *Mol Imag*. 2015;14:579-594.
54. Iwata R, Pascali C, Terasaki K, Ishikawa Y, Furumoto S, Yanai K. Practical microscale one-pot radiosynthesis of <sup>18</sup>F-labeled probes. *J Label Compd Radiopharm*. 2018;61:540-549.
55. Iwata R, Terasaki K, Ishikawa Y, et al. A concentration-based microscale method for <sup>18</sup>F-nucleophilic substitutions and its testing on the one-pot radiosynthesis of [<sup>18</sup>F]FET and [<sup>18</sup>F]fallypride. *Appl Radiat Isot*. August 2020:109361.
56. Lu Y, Wang J, van Dam RM, Hsiao A. PHENYX – A flexible pipetting-based platform for automated microvolume radiochemistry. *Chem Eng J*. 2022;435:134983.
57. Zhang X, Liu F, Knapp K-A, Nickels ML, Manning HC, Bellan LM. A simple microfluidic platform for rapid and efficient production of the radiotracer [<sup>18</sup>F]fallypride. *Lab Chip*. 2018;18:1369-1377.
58. Zhang X, Liu F, Payne AC, Nickels ML, Bellan LM, Manning HC. High-Yielding Radiosynthesis of [<sup>68</sup>Ga]Ga-PSMA-11 Using a Low-Cost Microfluidic Device. *Mol Imaging Biol*. 2020;22:1370-1379.

59. Hume SP, Gunn RN, Jones T. Pharmacological constraints associated with positron emission tomographic scanning of small laboratory animals. *EJNMMI*. 1998;25:173-176.
60. Jagoda EM, Vaquero JJ, Seidel J, Green MV, Eckelman WC. Experiment assessment of mass effects in the rat: implications for small animal PET imaging. *Nucl Med*. 2004;31:771-779.
61. Knapp K-A, Nickels ML, Manning HC. The Current Role of Microfluidics in Radiofluorination Chemistry. *Mol Imaging Biol*. 2020;22:463-475.
62. Iwata R, Pascali C, Terasaki K, Ishikawa Y, Furumoto S, Yanai K. Practical microscale one-pot radiosynthesis of <sup>18</sup>F-labeled probes. *J Label Compd Radiopharm*. 2018;61:540-549.
63. Iwata R, Terasaki K, Ishikawa Y, et al. A concentration-based microscale method for <sup>18</sup>F-nucleophilic substitutions and its testing on the one-pot radiosynthesis of [<sup>18</sup>F]FET and [<sup>18</sup>F]fallypride. *Appl Radiat Isot*. 2020;166:109361.
64. Seok Moon B, Hyung Park J, Jin Lee H, et al. Highly efficient production of [<sup>18</sup>F]fallypride using small amounts of base concentration. *Appl Radiat Isot*. 2010;68:2279-2284.
65. Hamacher K, Coenen HH. Efficient routine production of the <sup>18</sup>F-labelled amino acid O-(2-[<sup>18</sup>F]fluoroethyl)-L-tyrosine. *Appl Radiat Isot*. 2002;57:853-856.
66. Ovdichuk O, Mallapura H, Pineda F, et al. Implementation of iMiDEV™, a new fully automated microfluidic platform for radiopharmaceutical production. *Lab Chip*. 2021;21:2272-2282.
67. Mallapura H, Tanguy L, Långström B, Meunier LL, Halldin C, Nag S. Production of [<sup>11</sup>C]Carbon Labelled Flumazenil and L-Deprenyl Using the iMiDEV™ Automated Microfluidic Radiosynthesizer. *Mol*. 2022;27:8843.
68. Ovdichuk O, Béen Q, Tanguy L, Collet C. Synthesis of [<sup>68</sup>Ga]Ga-PSMA-11 using the iMiDEV™ microfluidic platform. *React Chem Eng*. 2023;8:1476-1492.
69. Keng PY, Chen S, Ding H, et al. Micro-chemical synthesis of molecular probes on an electronic microfluidic device. *PNAS*. 2012;109:690-695.
70. Chen S, Javed MR, Kim H-K, et al. Radiolabelling diverse positron emission tomography (PET) tracers using a single digital microfluidic reactor chip. *Lab Chip*. 2014;14:902-910.
71. Javed MR, Chen S, Lei J, et al. High yield and high specific activity synthesis of [<sup>18</sup>F]fallypride in a batch microfluidic reactor for micro-PET imaging. *Chem Commun*. 2014;50:1192-1194.
72. Javed MR, Chen S, Kim H-K, et al. Efficient Radiosynthesis of 3'-Deoxy-3'-<sup>18</sup>F-Fluorothymidine Using Electrowetting-on-Dielectric Digital Microfluidic Chip. *J Nucl Med*. 2014;55:321-328.
73. Koag MC, Kim H-K, Kim AS. Efficient microscale synthesis of [<sup>18</sup>F]-2-fluoro-2-deoxy-d-glucose. *J Chem Eng*. 2014;258:62-68.

74. Koag MC, Kim H-K, Kim AS. Fast and efficient microscale radiosynthesis of 3'-deoxy-3'-[18F]fluorothymidine. *J Fluor Chem.* 2014;166:104-109.
75. Mogi K, Kimura H, Kondo Y, Inoue T, Adachi S, Natsume T. Automatic radioisotope manipulation for small amount of nuclear medicine using an EWOD device with a dimple structure. *R Soc open sci.* 2021;8:201809.
76. Ahmadi F, Simchi M, Perry JM, et al. Integrating machine learning and digital microfluidics for screening experimental conditions. *Lab Chip.* 2023;23:81-91.
77. Mogi K, Kimura H, Kondo Y, Inoue T, Adachi S, Natsume T. Automatic radioisotope manipulation for small amount of nuclear medicine using an EWOD device with a dimple structure. *R Soc Open Sci.* 8:201809.
78. Wang J, Chao PH, Hanet S, Dam RM van. Performing multi-step chemical reactions in microliter-sized droplets by leveraging a simple passive transport mechanism. *Lab Chip.* 2017;17:4342-4355.
79. Lisova K, Sergeev M, Evans-Axelsson S, et al. Microscale radiosynthesis, preclinical imaging and dosimetry study of [18F]AMBF3-TATE: A potential PET tracer for clinical imaging of somatostatin receptors. *Nucl Med Biol.* 2018;61:36-44.
80. Wang J, Chao PH, van Dam RM. Ultra-compact, automated microdroplet radiosynthesizer. *Lab Chip.* 2019:2415-2424.
81. Ghosh A, Ganguly R, Schutzius TM, Megaridis CM. Wettability patterning for high-rate, pumpless fluid transport on open, non-planar microfluidic platforms. *Lab Chip.* 2014;14:1538-1550.
82. Lisova K, Chen BY, Wang J, Fong KM-M, Clark PM, van Dam RM. Rapid, efficient, and economical synthesis of PET tracers in a droplet microreactor: application to O-(2-[18F]fluoroethyl)-L-tyrosine ([18F]FET). *EJNMMI radiopharm chem.* 2019;5:1.
83. Wang J, Chao PH, Slavik R, van Dam RM. Multi-GBq production of the radiotracer [18F]fallypride in a droplet microreactor. *RSC Adv.* 2020;10:7828-7838.
84. Wang J, van Dam RM. High-Efficiency Production of Radiopharmaceuticals via Droplet Radiochemistry: A Review of Recent Progress. *Mol Imaging.* 2020;19:1-21.
85. Lisova K, Wang J, Chao PH, van Dam RM. A simple and efficient automated microvolume radiosynthesis of [18F]Florbetaben. *EJNMMI radiopharm chem.* 2020;5:30.
86. Wang J, Holloway T, Lisova K, van Dam RM. Green and efficient synthesis of the radiopharmaceutical [18F]FDOPA using a microdroplet reactor. *React Chem Eng.* 2020;5:320-329.
87. Pascali G, Matesic L, Collier TL, et al. Optimization of nucleophilic 18F radiofluorinations using a microfluidic reaction approach. *Nat Protocols.* 2014;9:2017-2029.

88. Pascali G, Mazzone G, Saccomanni G, Manera C, Salvadori PA. Microfluidic approach for fast labeling optimization and dose-on-demand implementation. *Nucl Med Biol.* 2010;37:547-555.
89. Matesic L, Kallinen A, Greguric I, Pascali G. Dose-on-demand production of diverse <sup>18</sup>F-radiotracers for preclinical applications using a continuous flow microfluidic system. *Nucl Med Biol.* 2017;52:24-31.
90. Chen Y-C, Liu K, Shen CK-F, van Dam RM. On-demand generation and mixing of liquid-in-gas slugs with digitally programmable composition and size. *J Micromech Microeng.* 2015;25:084006.
91. Laube M, Wodtke R, Kopka K, Kniess T, Pietzsch J. <sup>18</sup>F-Chemistry in HPLC vials - a microliter scale radiofluorination approach. *Nucl Med Biol.* 2021;96-97:S61.
92. Verhoog S. 25th International Symposium on Radiopharmaceutical Sciences. <https://www.xcdsystem.com/srsweb/program/gbn28OI/index.cfm?pgid=2860&SearchTerm=Stefan+Verhoog+>.
93. Rios A, Holloway TS, Chao PH, De Caro C, Okoro CC, van Dam RM. Microliter-scale reaction arrays for economical high-throughput experimentation in radiochemistry. *Sci Rep.* 2022;12:10263.
94. Jones J, Do V, Lu Y, van Dam RM. Accelerating radiochemistry development: Automated robotic platform for performing up to 64 droplet radiochemical reactions in a morning. *J Chem Eng.* 2023;468:143524.
95. Rios A, Wang J, Chao PH, Dam RM van. A novel multi-reaction microdroplet platform for rapid radiochemistry optimization. *RSC Adv.* 2019;9:20370-20374.
96. Wang J, Rios A, Lisova K, Slavik R, Chatziioannou AF, van Dam RM. High-throughput radio-TLC analysis. *Nucl Med Biol.* 2020;82-83:41-48.
97. Lisova K, Wang J, Hajagos TJ, et al. Economical droplet-based microfluidic production of [<sup>18</sup>F]FET and [<sup>18</sup>F]Florbetaben suitable for human use. *Sci Rep.* 2021;11:20636.
98. Wang J, Chao PH, Slavik R, van Dam RM. Multi-GBq production of the radiotracer [<sup>18</sup>F]fallypride in a droplet microreactor. *RSC Adv.* 2020;10:7828-7838.
99. Lisova K, Wang J, Hajagos TJ, et al. Economical droplet-based microfluidic production of [<sup>18</sup>F]FET and [<sup>18</sup>F]Florbetaben suitable for human use. *Sci Rep.* 2021;11:20636.
100. Zhang X, Basuli F, Shi Z-D, et al. Automated synthesis of [<sup>18</sup>F](2S,4R)-4-fluoroglutamine on a GE TRACERlab™ FX-N Pro module. *Appl Radiat Isot.* 2016;112:110-114.
101. Fischman AJ. Role of [<sup>18</sup>F]-dopa-PET imaging in assessing movement disorders. *Radiol Clin North Am.* 2005;43:93-106.
102. Darcourt J, Schiazza A, Sapin N, et al. <sup>18</sup>F-FDOPA PET for the diagnosis of parkinsonian syndromes. *Q J Nucl Med Mol Imaging.* 2014;58:355-365.

103. Schiepers C, Chen W, Cloughesy T, Dahlbom M, Huang S-C. 18F-FDOPA Kinetics in Brain Tumors. *J Nucl Med.* 2007;48:1651-1661.
104. Chen W, Silverman DHS, Delaloye S, et al. 18F-FDOPA PET Imaging of Brain Tumors: Comparison Study with 18F-FDG PET and Evaluation of Diagnostic Accuracy. *J Nucl Med.* 2006;47:904-911.
105. Calabria F, Cascini GL. Current status of 18F-DOPA PET imaging in the detection of brain tumor recurrence. *Hell J Nucl Med.* 2015;18:152-156.
106. Shah P, Demirbilek H, Hussain K. Persistent hyperinsulinaemic hypoglycaemia in infancy. *Semin Pediatr Surg.* 2014;23:76-82.
107. Kapoor RR, James C, Hussain K. Advances in the diagnosis and management of hyperinsulinemic hypoglycemia. *Nat Rev Endocrinol.* 2009;5:101-112.
108. Kauhanen S, Seppänen M, Ovaska J, et al. The clinical value of [18F]fluoro-dihydroxyphenylalanine positron emission tomography in primary diagnosis, staging, and restaging of neuroendocrine tumors. *Endocr Relat Cancer.* 2009;16:255-265.
109. Beheshti M, Pöcher S, Vali R, et al. The value of 18F-DOPA PET-CT in patients with medullary thyroid carcinoma: comparison with 18F-FDG PET-CT. *Eur Radiol.* 2009;19:1425-1434.
110. Koopmans KP, Groot JWB de, Plukker JTM, et al. 18F-Dihydroxyphenylalanine PET in Patients with Biochemical Evidence of Medullary Thyroid Cancer: Relation to Tumor Differentiation. *J Nucl Med.* 2008;49:524-531.
111. Becherer A, Szabó M, Karanikas G, et al. Imaging of Advanced Neuroendocrine Tumors with 18F-FDOPA PET. *J Nucl Med.* 2004;45:1161-1167.
112. Minn H, Kauhanen S, Seppänen M, Nuutila P. 18F-FDOPA: A Multiple-Target Molecule. *J Nucl Med.* 2009;50:1915-1918.
113. Pretze M, Wängler C, Wängler B. 6-[18F]Fluoro-L-DOPA: A Well-Established Neurotracer with Expanding Application Spectrum and Strongly Improved Radiosyntheses. *Biomed Res Int.* 2014;2014.
114. Taïeb D, Imperiale A, Pacak K. 18F-DOPA: the versatile radiopharmaceutical. *Eur J Nucl Med Mol Imaging.* 2016;43:1187-1189.
115. Tredwell M, Gouverneur V. 18F Labeling of Arenes. *Angew Chem Int Ed.* 2012;51:11426-11437.
116. de Vries EFJ, Luurtsema G, Brüssermann M, Elsinga PH, Vaalburg W. Fully automated synthesis module for the high yield one-pot preparation of 6-[18F]fluoro-L-DOPA. *Appl Radiat Isot.* 1999;51:389-394.
117. Adam M, Ruth T, Grierson J, Abeysekera B, Pate B. Routine synthesis of L-[18F]6-fluorodopa with fluorine-18 acetyl hypofluorite. *J Nucl Med.* 1986;27:1462-6.

118. Libert LC, Franci X, Plenevaux AR, et al. Production at the Curie Level of No-Carrier-Added 6-<sup>18</sup>F-Fluoro-L-Dopa. *J Nucl Med*. 2013;54:1154-1161.
119. Mossine AV, Tanzey SS, Brooks AF, et al. One-pot synthesis of high molar activity 6-[<sup>18</sup>F]fluoro-L-DOPA by Cu-mediated fluorination of a BPin precursor. *Org Biomol Chem*. 2019;17:8701-8705.
120. Krasikova RN. Nucleophilic Synthesis of 6-I-[<sup>18</sup>F]FDOPA. Is Copper-Mediated Radiofluorination the Answer? *Mol*. 2020;25.
121. Jiang H, Jain MK, Cai H. HPLC-free and cassette-based nucleophilic production of [<sup>18</sup>F]FDOPA for clinical use. *Am J Nucl Med Mol Imaging*. 2021;11:290-299.
122. Tredwell M, Preshlock SM, Taylor NJ, et al. A General Copper-Mediated Nucleophilic <sup>18</sup>F Fluorination of Arenes. *Angew Chem Int Ed*. 2014;126:1-6.
123. Edwards R. Synthesis of [<sup>18</sup>F]F-DOPA using hypervalent iodine compounds. 2015.
124. Lee E, Hooker JM, Ritter T. Nickel-Mediated Oxidative Fluorination for PET with Aqueous [<sup>18</sup>F] Fluoride. *J Am Chem Soc*. 2012;134:17456-17458.
125. Zischler J, Kolks N, Modemann D, Neumaier B, Zlatopolskiy BD. Alcohol-Enhanced Cu-Mediated Radiofluorination. *Chem Eur J*. 2017;23:3251-3256.
126. Mossine AV, Tanzey SS, Brooks AF, et al. Synthesis of high-molar-activity [<sup>18</sup>F]6-fluoro-L-DOPA suitable for human use via Cu-mediated fluorination of a BPin precursor. *Nat Protoc*. April 2020:1-18.
127. Gillies JM, Prenant C, Chimon GN, et al. Microfluidic reactor for the radiosynthesis of PET radiotracers. *Appl Radiat Isot*. 2006;64:325-332.
128. Audrain H. Positron Emission Tomography (PET) and Microfluidic Devices: A Breakthrough on the Microscale? *Angew Chem Int Ed*. 2007;46:1772-1775.
129. Keng PY, Esterby M, van Dam RM. Emerging Technologies for Decentralized Production of PET Tracers. In: Hsieh C-H, ed. Positron Emission Tomography - Current Clinical and Research Aspects. Rijeka, Croatia: InTech; 2012:153-182.
130. Dooraghi AA, Keng PY, Chen S, et al. Optimization of microfluidic PET tracer synthesis with Cerenkov imaging. *Analyst*. 2013;138:5654-5664.
131. Lisova K, Chen BY, Wang J, Fong KM-M, Clark PM, van Dam RM. Rapid, efficient, and economical synthesis of PET tracers in a droplet microreactor: application to O-(2-[<sup>18</sup>F]fluoroethyl)-L-tyrosine ([<sup>18</sup>F]FET). *EJNMMI radiopharm chem*. 2020;5:1.
132. Kim H-K, Rashed Javed M, Chen S, et al. On-demand radiosynthesis of N-succinimidyl-4-[<sup>18</sup>F]fluorobenzoate ([<sup>18</sup>F]SFB) on an electrowetting-on-dielectric microfluidic chip for <sup>18</sup>F-labeling of protein. *RSC Adv*. 2019;9:32175-32183.
133. Wang J, Chao PH, van Dam RM. Ultra-compact, automated microdroplet radiosynthesizer. *Lab Chip*. 2019;19:2415-2424.



134. Sergeev M, Lazari M, Morgia F, et al. Performing radiosynthesis in microvolumes to maximize molar activity of tracers for positron emission tomography. *Commun Chem*. 2018;1:10.
135. Laferriere-Holloway TS, Rios A, Lu Y, Okoro CC, Van Dam RM. A rapid and systematic approach for the optimization of radio thin-layer chromatography resolution. *J Chromatogr A*. 2023;1687:463656.
136. Lu Y, He Y, Schibli R, Mu L, Dam RM van. Proof-of-concept optimization of a copper-mediated <sup>18</sup>F-radiosynthesis of a novel MAGL PET tracer on a high-throughput microdroplet platform and its macroscale translation. *Lab Chip*. 2023;23:4652-4663.
137. Hoffmann C, Kolks N, Smets D, et al. Next Generation Copper Mediators for the Efficient Production of <sup>18</sup>F-Labeled Aromatics. *Chem Eur J*. 2023;29:e202202965.
138. Archibald SJ, Allott L. The aluminium-[<sup>18</sup>F]fluoride revolution: simple radiochemistry with a big impact for radiolabelled biomolecules. *EJNMMI radiopharm chem*. 2021;6:30.
139. McBride WJ, D'Souza CA, Sharkey RM, Goldenberg DM. The radiolabeling of proteins by the [<sup>18</sup>F]AIF method. *Appl Radiat Isot*. 2012;70:200-204.
140. McBride WJ, D'Souza CA, Sharkey RM, et al. Improved <sup>18</sup>F Labeling of Peptides with a Fluoride-Aluminum-Chelate Complex. *Bioconjugate Chem*. 2010;21:1331-1340.
141. Miller PW, Long NJ, Vilar R, Gee AD. Synthesis of <sup>11</sup>C, <sup>18</sup>F, <sup>15</sup>O, and <sup>13</sup>N Radiolabels for Positron Emission Tomography. *Angew Chem Int Ed*. 2008;47:8998-9033.
142. Bruce Martin R. Ternary hydroxide complexes in neutral solutions of A<sup>13+</sup> and F<sup>-</sup>. *BBRC*. 1988;155:1194-1200.
143. McBride WJ, Sharkey RM, Goldenberg DM. Radiofluorination using aluminum-fluoride (Al<sup>18</sup>F). *EJNMMI Research*. 2013;3:36.
144. Dubash SR, Keat N, Mapelli P, et al. Clinical Translation of a Click-Labeled <sup>18</sup>F-Octreotate Radioligand for Imaging Neuroendocrine Tumors. *J Nucl Med*. 2016;57:1207-1213.
145. Allott L, Dubash S, Aboagye EO. [<sup>18</sup>F]FET-βAG-TOCA: The Design, Evaluation and Clinical Translation of a Fluorinated Octreotide. *Cancers*. 2020;12:865.
146. Strosberg J, El-Haddad G, Wolin E, et al. Phase 3 Trial of <sup>177</sup>Lu-Dotatate for Midgut Neuroendocrine Tumors. *NEJM*. 2017;376:125-135.
147. Haeger A, Soza-Ried C, Kramer V, et al. Al[<sup>18</sup>F]F-NOTA-Octreotide Is Comparable to [<sup>68</sup>Ga]Ga-DOTA-TATE for PET/CT Imaging of Neuroendocrine Tumours in the Latin-American Population. *Cancers*. 2023;15:439.
148. Pauwels E, Cleeren F, Tshibangu T, et al. <sup>18</sup>F-AIF-NOTA-Octreotide Outperforms <sup>68</sup>Ga-DOTATATE/NOC PET in Neuroendocrine Tumor Patients: Results from a Prospective, Multicenter Study. *J Nucl Med*. 2023;64:632-638.

149. Piron S, Verhoeven J, Vanhove C, De Vos F. Recent advancements in <sup>18</sup>F-labeled PSMA targeting PET radiopharmaceuticals. *Nucl Med Biol.* 2022;106-107:29-51.
150. Lütje S, Franssen GM, Herrmann K, et al. In Vitro and In Vivo Characterization of an <sup>18</sup>F-AIF-Labeled PSMA Ligand for Imaging of PSMA-Expressing Xenografts. *J Nucl Med.* 2019;60:1017-1022.
151. Sandgren K, Johansson L, Axelsson J, et al. Radiation dosimetry of [<sup>68</sup>Ga]PSMA-11 in low-risk prostate cancer patients. *EJNMMI Physics.* 2019;6:2.
152. Piron S, Man KD, Laeken NV, et al. Radiation Dosimetry and Biodistribution of <sup>18</sup>F-PSMA-11 for PET Imaging of Prostate Cancer. *J Nucl Med.* 2019;60:1736-1742.
153. Yang T, Peng L, Qiu J, et al. A radiohybrid theranostics ligand labeled with fluorine-18 and lutetium-177 for fibroblast activation protein-targeted imaging and radionuclide therapy. *Eur J Nucl Med Mol Imaging.* 2023;50:2331-2341.
154. Lepage ML, Kuo H-T, Roxin Á, et al. Toward <sup>18</sup>F-Labeled Theranostics: A Single Agent that Can Be Labeled with <sup>18</sup>F, <sup>64</sup>Cu, or <sup>177</sup>Lu. *ChemBioChem.* 2020;21:943-947.
155. Hall AJ, Haskali MB. Radiolabelled Peptides: Optimal Candidates for Theranostic Application in Oncology. *Aust J Chem.* 2021;75:34-54.
156. McBride WJ, D'Souza CA, Karacay H, Sharkey RM, Goldenberg DM. New Lyophilized Kit for Rapid Radiofluorination of Peptides. *Bioconjug Chem.* 2012;23:538-547.
157. Allott L, Pieve CD, Turton DR, Smith G. A general [<sup>18</sup>F]AIF radiochemistry procedure on two automated synthesis platforms. *React Chem Eng.* 2017;2:68-74.
158. Tshibangu T, Cawthorne C, Serdons K, et al. Automated GMP compliant production of [<sup>18</sup>F]AIF-NOTA-octreotide. *EJNMMI radiopharm chem.* 2020;5:4.
159. Fu Z, Yu L, Gai Y, et al. Custom-built automated radiosynthesis platform for Al[<sup>18</sup>F]F radiochemistry and its application for clinical production. *J Chem Eng.* 2023;456:141080.
160. Rios A, Wang J, Chao PH, van Dam RM. A novel multi-reaction microdroplet platform for rapid radiochemistry optimization. *RSC Adv.* 2019;9:20370-20374.
161. Lisova K, Chen BY, Wang J, Fong KM-M, Clark PM, van Dam RM. Rapid, efficient, and economical synthesis of PET tracers in a droplet microreactor: application to O-(2-[<sup>18</sup>F]fluoroethyl)-L-tyrosine ([<sup>18</sup>F]FET). *EJNMMI radiopharm chem.* 2019;5:1.
162. Wang J, Holloway T, Lisova K, van Dam RM. Green and efficient synthesis of the radiopharmaceutical [<sup>18</sup>F]FDOPA using a microdroplet reactor. *React Chem Eng.* 2020;5:320-329.
163. Lisova K, Gras E, van Dam RM. SP-055 - Improved droplet-based method for isotopic exchange labeling of trifluoroborate precursors. *Nucl Med Biol.* 2021;96-97:S64-S65.

164. Naka S, Watabe T, Lindner T, et al. One-pot and one-step automated radio-synthesis of [<sup>18</sup>F]AIF-FAPI-74 using a multi purpose synthesizer: a proof-of-concept experiment. *EJNMMI radiopharm chem.* 2021;6:28.
165. Kuhajda FP. Fatty-acid synthase and human cancer: new perspectives on its role in tumor biology. *Nutr.* 2000;16:202-208.
166. Malone ER, Oliva M, Sabatini PJB, Stockley TL, Siu LL. Molecular profiling for precision cancer therapies. *Genome Med.* 2020;12:8.
167. Waldman AD, Fritz JM, Lenardo MJ. A guide to cancer immunotherapy: from T cell basic science to clinical practice. *Nat Rev Immunol.* 2020;20:651-668.
168. Wallace TA, Martin DN, Ambbs S. Interactions among genes, tumor biology and the environment in cancer health disparities: examining the evidence on a national and global scale. *Carcinog.* 2011;32:1107-1121.
169. Wagner Jr HN, Conti PS. Advances in medical imaging for cancer diagnosis and treatment. *Cancer.* 1991;67:1121-1128.
170. Pauwels EKJ, Ribeiro MJ, Stoot JHMB, McCready VR, Bourguignon M, Mazière B. FDG Accumulation and Tumor Biology. *Nuclear Medicine and Biology.* 1998;25:317-322.
171. Neves AA, Brindle KM. Assessing responses to cancer therapy using molecular imaging. *Biochim Biophys Acta Rev Cancer.* 2006;1766:242-261.
172. Pysz MA, Gambhir SS, Willmann JK. Molecular imaging: current status and emerging strategies. *Clin Radiol.* 2010;65:500-516.
173. Hussain T, Nguyen QT. Molecular imaging for cancer diagnosis and surgery. *Adv Drug Deliv Rev.* 2014;66:90-100.
174. Bai J-W, Qiu S-Q, Zhang G-J. Molecular and functional imaging in cancer-targeted therapy: current applications and future directions. *Sig Transduct Target Ther.* 2023;8:1-32.
175. Phelps ME. PET: The Merging of Biology and Imaging into Molecular Imaging. *J Nucl Med.* 2000;41:661-681.
176. Hanahan D, Weinberg RA. Hallmarks of Cancer: The Next Generation. *Cell.* 2011;144:646-674.
177. Bading JR, Shields AF. Imaging of Cell Proliferation: Status and Prospects. *J Nucl Med.* 2008;49:64S-80S.
178. Evan GI, Vousden KH. Proliferation, cell cycle and apoptosis in cancer. *Nature.* 2001;411:342-348.
179. Chung J-K, Lee YJ, Kim SK, Jeong JM, Lee DS, Lee MC. Comparison of [<sup>18</sup>F]fluorodeoxyglucose uptake with glucose transporter-1 expression and proliferation rate in human glioma and non-small-cell lung cancer: *Nucl Med Commun.* 2004;25:11-17.

180. Buck AK, Halter G, Schirrmeister H, et al. Imaging Proliferation in Lung Tumors with PET: 18F-FLT Versus 18F-FDG.
181. Schiepers C, Haustermans K, Geboes K, Filez L, Bormans G, Penninckx F. The effect of preoperative radiation therapy on glucose utilization and cell kinetics in patients with primary rectal carcinoma. *Cancer*. 1999;85:803-811.
182. Haberkorn U, Bellemann ME, Altmann A, et al. PET 2-Fluoro-2-Deoxyglucose Uptake in Rat Prostate Adenocarcinoma During Chemotherapy with Gemcitabine.
183. Waarde A van, Been LB, Ishiwata K, Dierckx RA, Elsinga PH. Early Response of  $\sigma$ -Receptor Ligands and Metabolic PET Tracers to 3 Forms of Chemotherapy: An In Vitro Study in Glioma Cells. *J Nucl Med*. 2006;47:1538-1545.
184. Willmann JK, van Bruggen N, Dinkelborg LM, Gambhir SS. Molecular imaging in drug development. *Nat Rev Drug Discov*. 2008;7:591-607.
185. Weissleder R, Pittet MJ. Imaging in the era of molecular oncology. *Nat*. 2008;452:580-589.
186. Conti PS, Alauddin MM, Fissekis JR, Schmall B, Watanabe KA. Synthesis of 2'-fluoro-5-[11C]-methyl-1- $\beta$ -d-arabinofuranosyluracil ([11C]-FMAU): A potential nucleoside analog for in vivo study of cellular proliferation with PET. *Nucl Med Biol*. 1995;22:783-789.
187. Grierson JR, Shields AF, Courter JH. Radiosynthesis of 2'-deoxy-1-[C-11]methyl-pseudouridine, an isostere of labeled thymidine, as an agent for the measurement of DNA synthesis in vivo. *J Label Compd Radiopharm*. 1994;35.
188. Chou TC, Kong XB, Fanucchi MP, et al. Synthesis and biological effects of 2'-fluoro-5-ethyl-1-beta-D-arabinofuranosyluracil. *Antimicrob Agents Chemother*. 1987;31:1355-1358.
189. Eriksson S, Kierdaszuk B, Munch-Petersen B, Oberg B, Gunnar Johansson N. Comparison of the substrate specificities of human thymidine kinase 1 and 2 and deoxycytidine kinase toward antiviral and cytostatic nucleoside analogs. *Biochemical and Biophysical Research Communications*. 1991;176:586-592.
190. Sun H, Mangner TJ, Collins JM, Muzik O, Douglas K, Shields AF. Imaging DNA Synthesis In Vivo with 18F-FMAU and PET. :5.
191. Sun H, Sloan A, Mangner TJ, et al. Imaging DNA synthesis with [18F]FMAU and positron emission tomography in patients with cancer. *Eur J Nucl Med Mol Imaging*. 2005;32:15-22.
192. Conti P, Chen K, Tripathy D, Jadvar H. [18F]FMAU for PET imaging in breast cancer patients. *JCO*. 2015;33:11056-11056.
193. Jadvar H, Ju Y, Eng C, et al. Multi-compartment pharmacokinetic modeling of dynamic 18F-FMAU PET/CT in patients with brain lesions. *J Nucl Med*. 2023;64:P747-P747.

194. Vaishampayan UN, Tehrani OS, Lawhorn-Crews JM, et al. A Pilot Trial Evaluating Zoledronic Acid Induced Changes in [18F]FMAU-Positron Emission Tomography Imaging of Bone Metastases in Prostate Cancer. *Mol Imaging Biol.* 2017;19:810-816.
195. Reichman U, Watanabe KA, Fox JJ. A practical synthesis of 2-deoxy-2-fluoro-d-arabinofuranose derivatives. *Carbohydr Res.* 1975;42:233-240.
196. Pankiewicz KW, Watanabe KA. Nucleosides. CXLIII. Synthesis of 5'-Deoxy-5'-substituted-2, 2'-anhydrol- ( $\beta$ -D-arabinofuranosyl) uracils. A New 2, 5'-to 2, 2'-Anhydronucleoside Transformation. Studies Directed toward the Synthesis of 2'-Deoxy-2'-substituted arabino- Nucleosides. (4). *Chem Pharm Bull.* 1987;35:4494-4497.
197. Alauddin MM, Conti PS, Fissekis JD. Synthesis of [18F]-labeled 2'-deoxy-2'-fluoro-5-methyl-1- $\beta$ -D-arabinofuranosyluracil ([18F]-FMAU). *J Labelled Cpd Radiopharm.* 2002;45:583-590.
198. Mangner TJ, Klecker RW, Anderson L, Shields AF. Synthesis of 2'-deoxy-2'-[18F]fluoro- $\beta$ -D-arabinofuranosyl nucleosides, [18F]FAU, [18F]FMAU, [18F]FBAU and [18F]FIAU, as potential PET agents for imaging cellular proliferation: synthesis of [18F]labelled FAU, FMAU, FBAU, FIAU. *Nuc Med Biol.* 2003;30:215-224.
199. Li Z, Cai H, S. Conti P. Improved Synthesis of 2-deoxy-2-[18F]fluoro-5-Methyl-1- $\beta$ -D-Arabinofuranosyluracil ([18F]FMAU). *Curr Radiopharm.* 2011;4:24-30.
200. Li Z, Cai H, Conti PS. Automated synthesis of 2'-deoxy-2'-[18F]fluoro-5-methyl-1- $\beta$ -d-arabinofuranosyluracil ([18F]-FMAU) using a one reactor radiosynthesis module. *Nucl Med Biol.* 2011;38:201-206.
201. Chen K, Li Z, Conti PS. Microwave-assisted one-pot radiosynthesis of 2'-deoxy-2'-[18F]fluoro-5-methyl-1- $\beta$ -d-arabinofuranosyluracil ([18F]-FMAU). *Nuclear Medicine and Biology.* 2012;39:1019-1025.
202. Li J, Van Valkenburgh J, Conti PS, Chen K. Exploring Solvent Effects in the Radiosynthesis of 18F-Labeled Thymidine Analogues toward Clinical Translation for Positron Emission Tomography Imaging. *ACS Pharmacol Transl Sci.* 2021;4:266-275.
203. Lisova K, Wang J, Chao PH, van Dam RM. A simple and efficient automated microvolume radiosynthesis of [18F]Florbetaben. *EJNMMI radiopharm chem.* 2020;5:30.
204. Javed MR, Chen S, Kim H-K, et al. Efficient Radiosynthesis of 3'-Deoxy-3'-18F-Fluorothymidine Using Electrowetting-on-Dielectric Digital Microfluidic Chip. *J Nucl Med.* 2014;55:321-328.
205. Lu Y, van Dam RM. SSP-04 - First microvolume metal-mediated synthesis of [18F]FDOPA in a microreactor. *Nucl Med Biol.* 2021;96-97:S15-S16.
206. Rios A, Wang J, Chao PH, van Dam RM. A novel multi-reaction microdroplet platform for rapid radiochemistry optimization. *RSC Adv.* 2019;9:20370-20374.

207. Rios A, Holloway TS, Chao PH, De Caro C, Okoro CC, van Dam RM. Microliter-scale reaction arrays for economical high-throughput experimentation in radiochemistry. *Sci Rep.* 2022;12:10263.
208. Jones J, Do V, Lu Y, van Dam RM. Accelerating radiochemistry development: Automated robotic platform for performing up to 64 droplet radiochemical reactions in a morning. *J Chem Eng.* 2023;468:143524.
209. Phelps ME. PET: Molecular Imaging and Its Biological Applications. 1st ed. Berlin, Germany: Springer Science & Business Media; 2004.
210. Radiosynthesis Database of PET Probes (RaDaP). <http://www.nirs.qst.go.jp/research/division/mic/db2/>.
211. Molecular Imaging and Contrast Agent Database (MICAD). Bethesda (MD): National Center for Biotechnology Information (US); 2004.
212. Collins J, Waldmann CM, Drake C, et al. Production of diverse PET probes with limited resources: 24 <sup>18</sup>F-labeled compounds prepared with a single radiosynthesizer. *PNAS.* 2017;114:11309-11314.
213. Bruton L, Scott PJH. Automated Synthesis Modules for PET Radiochemistry. In: Handbook of Radiopharmaceuticals. John Wiley & Sons, Ltd; 2020:437-456.
214. Bowden GD, Pichler BJ, Maurer A. A Design of Experiments (DoE) Approach Accelerates the Optimization of Copper-Mediated 18 F-Fluorination Reactions of Arylstannanes. *Sci Rep.* 2019;9:11370.
215. Webb EW, Scott PJH. Potential Applications of Artificial Intelligence and Machine Learning in Radiochemistry and Radiochemical Engineering. *PET Clinics.* 2021;16:525-532.
216. Ahmadi F, Simchi M, Perry JM, et al. Integrating machine learning and digital microfluidics for screening experimental conditions. *Lab Chip.* November 2022.
217. Zhang X, Dunlow R, Blackman BN, Swenson RE. Optimization of 18F-syntheses using 19F-reagents at tracer-level concentrations and liquid chromatography/tandem mass spectrometry analysis: Improved synthesis of [18F]MDL100907. *J Label Compd Radiopharm.* 2018;61:427-437.
218. Lazari M, Iribarren J, Zhang S, van Dam RM. Understanding temperatures and pressures during short radiochemical reactions. *Appl Radiat Isot.* 2016;108:82-91.
219. Liu K, Lepin EJ, Wang M-W, et al. Microfluidic-Based 18F-Labeling of Biomolecules for Immuno-Positron Emission Tomography. *Mol Imaging.* 2011;10:168-176.
220. Laferriere-Holloway TS, Rios A, Lu Y, Okoro CC, van Dam RM. A rapid and systematic approach for the optimization of radio thin-layer chromatography resolution. *J Chromatogr A.* 2023;1687:463656.

221. Kim D-Y, Kim H-J, Yu K-H, Min J-J. Synthesis of [18F]-labeled (2-(2-fluoroethoxy)ethyl)tris(4-methoxyphenyl)phosphonium cation as a potential agent for positron emission tomography myocardial imaging. *Nucl Med Biol.* 2012;39:1093-1098.
222. Zhang Z, Zhang C, Lau J, Colpo N, Bénard F, Lin K-S. One-step synthesis of 4-[18F]fluorobenzyltriphenylphosphonium cation for imaging with positron emission tomography. *J Label Compd Radiopharm.* 2016;59:467-471.
223. Franck D, Nann H, Davi P, Schubiger PA, Ametamey SM. Faster analysis of radiopharmaceuticals using ultra performance liquid chromatography (UPLC®) in combination with low volume radio flow cell. *Appl Radiat Isot.* 2009;67:1068-1070.
224. Gagnon MKJ, Hausner SH, Marik J, Abbey CK, Marshall JF, Sutcliffe JL. High-throughput in vivo screening of targeted molecular imaging agents. *Proc Natl Acad Sci U S A.* 2009;106:17904-17909.
225. Claggett SB, Quinn KM, Lazari M, Moore MD, Dam RM van. Simplified programming and control of automated radiosynthesizers through unit operations. *EJNMMI Res.* 2013;3:53.
226. Zeng M, Hu C-Z, Hu P-F. Control Algorithm of Acceleration Curve for Stepper Motor. *JCSE.* 2016;4:32-39.
227. Nguyen K-D, Ng T, Chen I-M. On Algorithms for Planning S-curve Motion Profiles. *Int J Adv Robot Syst.* 2008;5.
228. Dunet V, Pomoni A, Hottinger A, Nicod-Lalonde M, Prior JO. Performance of 18F-FET versus 18F-FDG-PET for the diagnosis and grading of brain tumors: systematic review and meta-analysis. *Neuro-oncology.* 2016;18:426-434.
229. Marcu LG, Moghaddasi L, Bezak E. Imaging of Tumor Characteristics and Molecular Pathways With PET: Developments Over the Last Decade Toward Personalized Cancer Therapy. *IJROBP.* 2018;102:1165-1182.
230. Phelps ME. Molecular Imaging with Positron Emission Tomography. *Annual Review of Nuclear and Particle Science.* 2002;52:303-338.
231. Antonios JP, Soto H, Everson RG, et al. Detection of immune responses after immunotherapy in glioblastoma using PET and MRI. *PNAS.* 2017;114:10220-10225.
232. Raccagni I, Belloli S, Valtorta S, et al. [18F]FDG and [18F]FLT PET for the evaluation of response to neo-adjuvant chemotherapy in a model of triple negative breast cancer. *PLOS ONE.* 2018;13:e0197754.
233. Cerami C, Iaccarino L, Perani D. Molecular Imaging of Neuroinflammation in Neurodegenerative Dementias: The Role of In Vivo PET Imaging. *Int J Mol Sci.* 2017;18:993.
234. Walker Z, Gandolfo F, Orini S, et al. Clinical utility of FDG PET in Parkinson's disease and atypical parkinsonism associated with dementia. *Eur J Nucl Med Mol Imaging.* 2018;45:1534-1545.

235. Chiaravalloti A, Danieli R, Lacanfora A, Palumbo B, Caltagirone C, Schillaci O. Usefulness of <sup>18</sup>F Florbetaben in Diagnosis of Alzheimer's Disease and Other Types of Dementia. *Curr Alzheimer Res.* 2017;14:154-160.
236. Juneau Daniel, Golfam Mohammad, Hazra Samir, et al. Positron Emission Tomography and Single-Photon Emission Computed Tomography Imaging in the Diagnosis of Cardiac Implantable Electronic Device Infection. *Circ Cardiovasc.* 2017;10:e005772.
237. Granados U, Fuster D, Pericas JM, et al. Diagnostic Accuracy of <sup>18</sup>F-FDG PET/CT in Infective Endocarditis and Implantable Cardiac Electronic Device Infection: A Cross-Sectional Study. *J Nucl Med.* 2016;57:1726-1732.
238. Colombo I, Overchuk M, Chen J, Reilly RM, Zheng G, Lheureux S. Molecular imaging in drug development: Update and challenges for radiolabeled antibodies and nanotechnology. *Methods.* 2017;130:23-35.
239. Naganawa M, Gallezot J-D, Rossano S, Carson RE. Quantitative PET Imaging in Drug Development: Estimation of Target Occupancy. *Bull Math Biol.* 2019;81:3508-3541.
240. Waaijer SJH, Kok IC, Eisses B, et al. Molecular Imaging in Cancer Drug Development. *J Nucl Med.* 2018;59:726-732.
241. Yaghoubi SS, Campbell DO, Radu CG, Czernin J. Positron Emission Tomography Reporter Genes and Reporter Probes: Gene and Cell Therapy Applications. *Theranostics.* 2012;2:374-391.
242. Challapalli A, Aboagye EO. Positron Emission Tomography Imaging of Tumor Cell Metabolism and Application to Therapy Response Monitoring. *Front Oncol.* 2016;6:44.
243. Martinez O, Sosabowski J, Maher J, Papa S. New Developments in Imaging Cell-Based Therapy. *J Nucl Med.* 2019;60:730-735.
244. Elizarov AM. Microreactors for radiopharmaceutical synthesis. *Lab Chip.* 2009;9:1326-1333.
245. Rensch C, Jackson A, Lindner S, et al. Microfluidics: A Groundbreaking Technology for PET Tracer Production? *Mol.* 2013;18:7930-7956.
246. Pascali G, Matesic L. How Far Are We from Dose On Demand of Short-Lived Radiopharmaceuticals? In: Kuge Y, Shiga T, Tamaki N, eds. *Perspectives on Nuclear Medicine for Molecular Diagnosis and Integrated Therapy.* Springer Japan; 2016:79-92.
247. Frank C, Winter G, Rensei F, et al. Development and implementation of ISAR, a new synthesis platform for radiopharmaceutical production. *EJNMMI radiopharm chem.* 2019;4:24.
248. Frank C, Winter G, Rensei F, et al. Enhancing radiotracer development: Channel routing on ISAR without single fluid bus constraint. *J Nucl Med.* 2018;59:671-671.



249. Awasthi V, Watson J, Gali H, et al. A “dose on demand” Biomarker Generator for automated production of [18F]F- and [18F]FDG. *Applied Radiation and Isotopes*. 2014;89:167-175.
250. Lebedev A, Miraghaie R, Kotta K, et al. Batch-reactor microfluidic device: first human use of a microfluidically produced PET radiotracer. *Lab Chip*. 2012;13:136-145.
251. Liang SH, Yokell DL, Normandin MD, et al. First Human Use of a Radiopharmaceutical Prepared by Continuous-Flow Microfluidic Radiofluorination: Proof of Concept with the Tau Imaging Agent [18F]T807. *Mol Imaging*. 2014;13:1-5.
252. Liang SH, Yokell DL, Jackson RN, et al. Microfluidic continuous-flow radiosynthesis of [18F]FPEB suitable for human PET imaging. *Med Chem Commun*. 2014;5:432-435.
253. Akula MR, Collier TL, Blevins DW, Kabalka GW, Osborne D. Sequential Preparation of [18F]FLT and [18F]FMISO Employing Advion NanoTek® Microfluidic Synthesis System. *Advances in Molecular Imaging*. 2019;9:53-59.
254. Zheng M-Q, Collier L, Bois F, et al. Synthesis of [18F]FMISO in a flow-through microfluidic reactor: Development and clinical application. *Nucl Med Biol*. 2015;42:578-584.
255. Chao PH, Lazari M, Hanet S, Narayanam MK, Murphy JM, van Dam RM. Automated concentration of [18F]fluoride into microliter volumes. *Appl Radiat Isot*. 2018;141:138-148.
256. Langen K-J, Stoffels G, Filss C, et al. Imaging of amino acid transport in brain tumours: Positron emission tomography with O-(2-[18F]fluoroethyl)-L-tyrosine (FET). *Methods*. 2017;130:124-134.
257. Bourdier T, Greguric I, Roselt P, Jackson T, Faragalla J, Katsifis A. Fully automated one-pot radiosynthesis of O-(2-[18F]fluoroethyl)-l-tyrosine on the TracerLab FXFN module. *Nucl Med Biol*. 2011;38:645-651.
258. Zhang W, Oya S, Kung M-P, Hou C, Maier DL, Kung HF. F-18 Polyethyleneglycol stilbenes as PET imaging agents targeting A $\beta$  aggregates in the brain. *Nucl Med Biol*. 2005;32:799-809.
259. Elizarov AM. Automation of PET Radiopharmaceutical Quality Control. In: Handbook of Radiopharmaceuticals. John Wiley & Sons, Ltd; 2020:457-489.
260. Lakshminarayanan N, Kumar A, Roy S, Pawar Y, Chaudhari PR, Rajan MGR. Fully automated synthesis of O-(2'-[18F]fluoroethyl)-l-tyrosine ([18F]FET) using solid phase extraction (SPE) purification with neutral alumina. *J Radioanal Nucl Chem*. June 2016:1-9.
261. Patt M, Schildan A, Barthel H, et al. Metabolite analysis of [18F]Florbetaben (BAY 94-9172) in human subjects: a substudy within a proof of mechanism clinical trial. *J Radioanal Nucl Chem*. 2010;284:557-562.

262. Rominger A, Brendel M, Burgold S, et al. Longitudinal Assessment of Cerebral  $\beta$ -Amyloid Deposition in Mice Overexpressing Swedish Mutant  $\beta$ -Amyloid Precursor Protein Using  $^{18}\text{F}$ -Florbetaben PET. *J Nucl Med*. 2013;54:1127-1134.
263. Wang H, Shi H, Yu H, Jiang S, Tang G. Facile and rapid one-step radiosynthesis of [ $^{18}\text{F}$ ]BAY94-9172 with a new precursor. *Nucl Med Biol*. 2011;38:121-127.
264. Brendel M, Jaworska A, Griebinger E, et al. Cross-Sectional Comparison of Small Animal [ $^{18}\text{F}$ ]-Florbetaben Amyloid-PET between Transgenic AD Mouse Models. *PLOS ONE*. 2015;10:e0116678.
265. Badawi RD, Shi H, Hu P, et al. First Human Imaging Studies with the Explorer Total-Body Pet Scanner. *J Nucl Med*. February 2019;jnumed.119.226498.
266. Fermi E. Quality Control of PET Radiopharmaceuticals. In: *Molecular Imaging: Radiopharmaceuticals for PET and SPECT*. Springer Berlin Heidelberg; 2009:197-204.
267. Scott PJH, Hockley BG. *Radiochemical Syntheses, Radiopharmaceuticals for Positron Emission Tomography*. Hoboken, NJ, USA: John Wiley & Sons; 2011.
268. U.S. Pharmacopeia (USP). General Chapter <823>: Positron Emission Tomography Drugs for Compounding, Investigation, and Research Uses. November 2011.
269. CFR - Code of Federal Regulations Title 21. <http://www.accessdata.fda.gov/scripts/cdrh/cfdocs/cfcfr/CFRSearch.cfm>.
270. European directorate for the quality of medicines & healthcare. "Unfair" regulatory stance on radiotracers poses threat to PET's future. AuntMinnie.com. <http://www.auntminnie.com/index.aspx?sec=ser&sub=def&pag=dis&itemid=102799>.
271. Lodi F, Boschi S. Quality Control of PET Radiopharmaceuticals. In: *Basic Science of PET Imaging*. Springer, Cham; 2017:105-126.
272. Ha NS, Sadeghi S, van Dam RM. Recent Progress toward Microfluidic Quality Control Testing of Radiopharmaceuticals. *Micromachines*. 2017;8:337.
273. Ferguson D, McGrath S, O'Hara G, Marshall C. Investigation of staff finger doses during quality control of FDG production. *Health Physics*. 2011;100:523-529.
274. Kuntzsch M, Lamparter D, Bruggener N, Muller M, Kienzle GJ, Reischl G. Development and Successful Validation of Simple and Fast TLC Spot Tests for Determination of Kryptofix® 2.2.2 and Tetrabutylammonium in  $^{18}\text{F}$ -Labeled Radiopharmaceuticals. *Pharmaceuticals (Basel)*. 2014;7:621-633.
275. Halvorsen NE, Kvernenes OH. A Fast and Simple Method for the Determination of TBA in  $^{18}\text{F}$ -Labeled Radiopharmaceuticals. *Pharmaceuticals*. 2020;13:27.
276. The top 10 causes of death. <https://www.who.int/news-room/fact-sheets/detail/the-top-10-causes-of-death>.

277. Camici PG, Rimoldi OE. The Clinical Value of Myocardial Blood Flow Measurement. *J Nucl Med*. 2009;50:1076-1087.
278. Manabe O, Kikuchi T, Scholte AJHA, et al. Radiopharmaceutical tracers for cardiac imaging. *J Nucl Cardiol*. 2018;25:1204-1236.
279. Werner RA, Chen X, Rowe SP, Lapa C, Javadi MS, Higuchi T. Moving into the next era of PET myocardial perfusion imaging: introduction of novel 18F-labeled tracers. *Int J Cardiovasc Imaging*. 2019;35:569-577.
280. Driessen RS, Raijmakers PG, Stuijzand WJ, Knaapen P. Myocardial perfusion imaging with PET. *Int J Cardiovasc Imaging*. 2017;33:1021-1031.
281. Alam L, Omar AMS, Patel KK. Improved Performance of PET Myocardial Perfusion Imaging Compared to SPECT in the Evaluation of Suspected CAD. *Curr Cardiol Rep*. 2023;25:281-293.
282. Rischpler C, Park M-J, Fung GSK, Javadi M, Tsui BMW, Higuchi T. Advances in PET myocardial perfusion imaging: F-18 labeled tracers. *Ann Nucl Med*. 2012;26:1-6.
283. Ravert HT, Madar I, Dannals RF. Radiosynthesis of 3-[18F]fluoropropyl and 4-[18F]fluorobenzyl triarylphosphonium ions. *J Label Compd Radiopharm*. 2004;47:469-476.
284. Tominaga T, Ito H, Ishikawa Y, Iwata R, Ishiwata K, Furumoto S. Radiosynthesis and preliminary biological evaluation of a new 18F-labeled triethylene glycol derivative of triphenylphosphonium. *Journal of Labelled Compounds and Radiopharmaceuticals*. 2016;59:117-123.
285. Madar I, Ravert HT, Du Y, et al. Characterization of Uptake of the New PET Imaging Compound 18F-Fluorobenzyl Triphenyl Phosphonium in Dog Myocardium. *J Nucl Med*. 2006;47:1359-1366.
286. Madar I, Ravert H, DiPaula A, Du Y, Dannals RF, Becker L. Assessment of Severity of Coronary Artery Stenosis in a Canine Model Using the PET Agent 18F-Fluorobenzyl Triphenyl Phosphonium: Comparison with 99mTc-Tetrofosmin. *J Nucl Med*. 2007;48:1021-1030.
287. Higuchi T, Fukushima K, Rischpler C, et al. Stable Delineation of the Ischemic Area by the PET Perfusion Tracer <sup>18</sup>F-Fluorobenzyl Triphenyl Phosphonium After Transient Coronary Occlusion. *J Nucl Med*. 2011;52:965-969.
288. Ravert HT, Holt DP, Dannals RF. A microwave radiosynthesis of the 4-[18F]-fluorobenzyltriphenylphosphonium ion. *J Label Compd Radiopharm*. 2014;57:695-698.
289. Waldmann CM, Gomez A, Marchis P, et al. An Automated Multidose Synthesis of the Potentiometric PET Probe 4-[18F]Fluorobenzyl-Triphenylphosphonium ([18F]FBnTP). *Mol Imaging Biol*. 2018;20:205-212.

290. Zhang Z, Zhang C, Lau J, Colpo N, Bénard F, Lin K-S. One-step synthesis of 4-[<sup>18</sup>F]fluorobenzyltriphenylphosphonium cation for imaging with positron emission tomography. *J Label Compd Radiopharm.* 2016;59:467-471.
291. Lu Y, van Dam RM. First microvolume metal-mediated synthesis of [<sup>18</sup>F]FDOPA in a microreactor [ABSTRACT]. *Nucl Med Biol.* 2021;96-97:S15-S16.
292. Rios A, Holloway TS, Chao PH, De Caro C, Okoro CC, van Dam RM. Microliter-scale reaction arrays for economical high-throughput experimentation in radiochemistry. *Sci Rep.* 2022;12:10263.
293. Packard RRS, Lazewatsky JL, Orlandi C, Maddahi J. Diagnostic Performance of PET Versus SPECT Myocardial Perfusion Imaging in Patients with Smaller Left Ventricles: A Substudy of the <sup>18</sup>F-Flurpiridaz Phase III Clinical Trial. *J Nucl Med.* 2021;62:849-854.
294. Tominaga T, Ito H, Ishikawa Y, Iwata R, Ishiwata K, Furumoto S. Radiosynthesis and preliminary biological evaluation of a new <sup>18</sup>F-labeled triethylene glycol derivative of triphenylphosphonium. *J Label Compd Radiopharm.* 2016;59:117-123.
295. Momcilovic M, Jones A, Bailey ST, et al. In vivo imaging of mitochondrial membrane potential in non-small-cell lung cancer. *Nat.* 2019;575:380-384.
296. Han M, Bushong EA, Segawa M, et al. Spatial mapping of mitochondrial networks and bioenergetics in lung cancer. *Nat.* 2023;615:712-719.
297. Zhang X, Basuli F, Swenson RE. An azeotropic drying-free approach for copper-mediated radiofluorination without addition of base. *J Label Compd Radiopharm.* 2019;62:139-145.
298. Fowler JS, Wolf AP. Working against Time: Rapid Radiotracer Synthesis and Imaging the Human Brain. *Acc Chem Res.* 1997;30:181-188.
299. Edem PE, Steen EJJ, Kjær A, Herth MM. Chapter 2 - Fluorine-18 Radiolabeling Strategies—Advantages and Disadvantages of Currently Applied Labeling Methods. In: Postigo A, ed. Late-Stage Fluorination of Bioactive Molecules and Biologically-Relevant Substrates. Elsevier; 2019:29-103.
300. Kuchar M, Mamat C. Methods to Increase the Metabolic Stability of <sup>18</sup>F-Radiotracers. *Molecules.* 2015;20:16186-16220.
301. Le Bars D. Fluorine-18 and medical imaging: Radiopharmaceuticals for positron emission tomography. *J Fluor Chem.* 2006;127:1488-1493.
302. Cai L, Lu S, Pike VW. Chemistry with [<sup>18</sup>F]Fluoride Ion. *EurJOC.* 2008;2008:2853-2873.
303. Jacobson O, Kiesewetter DO, Chen X. Fluorine-18 Radiochemistry, Labeling Strategies and Synthetic Routes. *Bioconjug Chem.* 2015;26:1-18.
304. Ajenjo J, Destro G, Cornelissen B, Gouverneur V. Closing the gap between <sup>19</sup>F and <sup>18</sup>F chemistry. *EJNMMI radiopharm chem.* 2021;6:33.

305. Pike VW, Aigbirhio FI. Reactions of cyclotron-produced [ $^{18}\text{F}$ ]fluoride with diaryliodonium salts—a novel single-step route to no-carrier-added [ $^{18}\text{F}$ ]fluoroarenes. *J Chem Soc, Chem Commun.* 1995;2215-2216.
306. Satyamurthy N, Barrio JR. No-carrier-added nucleophilic [ $^{18}\text{F}$ ] fluorination of aromatic compounds. March 2011.
307. Hull KL, Anani WQ, Sanford MS. Palladium-Catalyzed Fluorination of Carbon–Hydrogen Bonds. *J Am Chem Soc.* 2006;128:7134-7135.
308. Watson DA, Su M, Teverovskiy G, et al. Formation of ArF from LPdAr(F): Catalytic Conversion of Aryl Triflates to Aryl Fluorides. *Science.* 2009;325:1661-1664.
309. Lee E, Kamlet AS, Powers DC, et al. A Fluoride-Derived Electrophilic Late-Stage Fluorination Reagent for PET Imaging. *Science.* 2011;334:639-642.
310. Tredwell M, Preshlock SM, Taylor NJ, et al. A General Copper-Mediated Nucleophilic  $^{18}\text{F}$  Fluorination of Arenes. *Angew Chem Int Ed.* 2014;53:7751-7755.
311. Mossine AV, Brooks AF, Makaravage KJ, et al. Synthesis of [ $^{18}\text{F}$ ]Arenes via the Copper-Mediated [ $^{18}\text{F}$ ]Fluorination of Boronic Acids. *Org Lett.* 2015;17:5780-5783.
312. Chen W, Huang Z, Tay NES, et al. Direct arene C–H fluorination with  $^{18}\text{F}^-$  via organic photoredox catalysis. *Science.* 2019;364:1170-1174.
313. Makaravage KJ, Brooks AF, Mossine AV, Sanford MS, Scott PJH. Copper-Mediated Radiofluorination of Arylstannanes with [ $^{18}\text{F}$ ]KF. *Org Lett.* 2016;18:5440-5443.
314. Taylor NJ, Emer E, Preshlock S, et al. Derisking the Cu-Mediated  $^{18}\text{F}$ -Fluorination of Heterocyclic Positron Emission Tomography Radioligands. *J Am Chem Soc.* 2017;139:8267-8276.
315. Preshlock S, Calderwood S, Verhoog S, et al. Enhanced copper-mediated  $^{18}\text{F}$ -fluorination of aryl boronic esters provides eight radiotracers for PET applications. *Chem Commun.* 2016;52:8361-8364.
316. Mossine AV, Tanzey SS, Brooks AF, et al. One-pot synthesis of high molar activity 6- $^{18}\text{F}$ fluoro-L-DOPA by Cu-mediated fluorination of a BPin precursor. *Org Biomol Chem.* 2019;17:8701-8705.
317. Zlatopolskiy BD, Zischler J, Krapf P, et al. Copper-Mediated Aromatic Radiofluorination Revisited: Efficient Production of PET Tracers on a Preparative Scale. *Chem - Eur J.* 2015;21:5972-5979.
318. Hoffmann C, Kolks N, Smets D, et al. Next Generation Copper Mediators for the Efficient Production of  $^{18}\text{F}$ -Labeled Aromatics. *Chem Eur J.* 2023;29:e202202965.
319. Mossine AV, Brooks AF, Bernard-Gauthier V, et al. Automated synthesis of PET radiotracers by copper-mediated  $^{18}\text{F}$ -fluorination of organoborons: Importance of the order of addition and competing protodeborylation. *J Label Compd Radiopharm.* 2018;61:228-236.

320. Keng PY, Chen S, Ding H, et al. Micro-chemical synthesis of molecular probes on an electronic microfluidic device. *PNAS*. 2012;109:690-695.
321. Keng PY, van Dam RM. Digital Microfluidics: A New Paradigm for Radiochemistry. *Mol Imaging*. 2015;14:7290.2015.00030.
322. Ghosh A, Ganguly R, M. Schutzius T, M. Megaridis C. Wettability patterning for high-rate, pumpless fluid transport on open, non-planar microfluidic platforms. *Lab Chip*. 2014;14:1538-1550.
323. Wang J, Chao PH, Hanet S, van Dam RM. Performing multi-step chemical reactions in microliter-sized droplets by leveraging a simple passive transport mechanism. *Lab Chip*. 2017;17:4342-4355.
324. Wang J, Chao PH, van Dam RM. Ultra-compact, automated microdroplet radiosynthesizer. *Lab Chip*. 2019;19:2415-2424.
325. Lisova K, Chen BY, Wang J, Fong KM-M, Clark PM, van Dam RM. Rapid, efficient, and economical synthesis of PET tracers in a droplet microreactor: application to O-(2-[<sup>18</sup>F]fluoroethyl)-L-tyrosine ([<sup>18</sup>F]FET). *EJNMMI radiopharm chem*. 2020;5:1.
326. He Y, Schild M, Grether U, et al. Development of High Brain-Penetrant and Reversible Monoacylglycerol Lipase PET Tracers for Neuroimaging. *J Med Chem*. 2022;65:2191-2207.
327. 4.pdf.
328. Zischler J, Kolks N, Modemann D, Neumaier B, Zlatopolskiy BD. Alcohol-Enhanced Cu-Mediated Radiofluorination. *Chem - Eur J*. 2017;23:3251-3256.
329. Tian J, He Y, Deuther-Conrad W, et al. Synthesis and evaluation of new 1-oxa-8-azaspiro[4.5]decane derivatives as candidate radioligands for sigma-1 receptors. *Bioorg Med Chem Lett*. 2020;28:115560.
330. Jia H, Cai Z, Holden D, et al. Positron Emission Tomography Imaging Evaluation of a Novel <sup>18</sup>F-Labeled Sigma-1 Receptor Radioligand in Cynomolgus Monkeys. *ACS Chem Neurosci*. 2020;11:1673-1681.
331. He Y, Schild M, Grether U, et al. Development of High Brain-Penetrant and Reversible Monoacylglycerol Lipase PET Tracers for Neuroimaging. *J Med Chem*. 2022;65:2191-2207.
332. Wang M, Gao M, Miller KD, Zheng Q-H. Synthesis of [<sup>11</sup>C]PBR06 and [<sup>18</sup>F]PBR06 as agents for positron emission tomographic (PET) imaging of the translocator protein (TSPO). *Steroids*. 2011;76:1331-1340.
333. Chang C-W, Chiu C-H, Lin M-H, et al. GMP-compliant fully automated radiosynthesis of [<sup>18</sup>F]FEPPA for PET/MRI imaging of regional brain TSPO expression. *EJNMMI Res*. 2021;11:26.

334. Laat B de, Leurquin-Sterk G, Celen S, et al. Preclinical evaluation and quantification of <sup>18</sup>F-FPEB as a radioligand for PET imaging of the metabotropic glutamate receptor 5. *J Nucl Med*. September 2015;jnumed.115.162636.
335. Shen B, Ehrlichmann W, Uebele M, Machulla H-J, Reischl G. Automated synthesis of n.c.a. [<sup>18</sup>F]FDOPA via nucleophilic aromatic substitution with [<sup>18</sup>F]fluoride. *Appl Radiat Isot*. 2009;67:1650-1653.
336. Dahlbom M. PET Calibration, Acceptance Testing, and Quality Control. In: *Basic Science of PET Imaging*. Springer, Cham; 2017:229-255.
337. Peyronneau M-A, Saba W, Goutal S, et al. [<sup>18</sup>F]Fallypride: Metabolism studies and quantification of the radiotracer and its radiometabolites in plasma using a simple and rapid solid-phase extraction method. *Nucl Med Biol*. 2013;40:887-895.
338. Ory D, Van den Brande J, de Groot T, et al. Retention of [<sup>18</sup>F]fluoride on reversed phase HPLC columns. *J Pharm Biomed Anal*. 2015;111:209-214.
339. Ha YS, Lee W, Jung J-M, et al. Visualization and quantification of radiochemical purity by Cerenkov luminescence imaging. *Anal Chem*. 2018;90:8927-8935.
340. Ryzhikov NN, Seneca N, Krasikova RN, et al. Preparation of highly specific radioactivity [<sup>18</sup>F]flumazenil and its evaluation in cynomolgus monkey by positron emission tomography. *Nucl Med Biol*. 2005;32:109-116.
341. Vaulina D, Nasirzadeh M, Gomzina N. Automated radiosynthesis and purification of [<sup>18</sup>F]flumazenil with solid phase extraction. *Appl Radiat Isot*. 2018;135:110-114.
342. Nasirzadeh M, Vaulina DD, Kuznetsova OF, Gomzina NA. A novel approach to the synthesis of [<sup>18</sup>F]flumazenil, a radioligand for PET imaging of central benzodiazepine receptors. *Russ Chem Bull*. 2016;65:794-800.
343. Inkster J a. H, Akurathi V, Sromek AW, Chen Y, Neumeyer JL, Packard AB. A non-anhydrous, minimally basic protocol for the simplification of nucleophilic <sup>18</sup>F-fluorination chemistry. *Sci Rep*. 2020;10:6818 (9 pages).
344. Ismail R, Irribarren J, Javed MR, Machness A, van Dam M, Keng PY. Cationic imidazolium polymer monoliths for efficient solvent exchange, activation and fluorination on a continuous flow system. *RSC Advances*. 2014;4:25348-25356.
345. Mandap KS, Ido T, Kiyono Y, et al. Development of microwave-based automated nucleophilic [<sup>18</sup>F]fluorination system and its application to the production of [<sup>18</sup>F]flumazenil. *Nucl Med Biol*. 2009;36:403-409.
346. Lazari M, Collins J, Shen B, et al. Fully Automated Production of Diverse <sup>18</sup>F-Labeled PET Tracers on the ELIXYS Multireactor Radiosynthesizer Without Hardware Modification. *J Nucl Med Technol*. 2014;42:203-210.
347. Ungersboeck J, Philippe C, Haeusler D, et al. Optimization of [<sup>11</sup>C]DASB-synthesis: Vessel-based and flow-through microreactor methods. *Appl Radiat Isot*. 2012;70:2615-2620.

348. Koivula T, Laine J, Lipponen T, et al. Assessment of labelled products with different radioanalytical methods: study on 18F-fluorination reaction of 4-[18F]fluoro-N-[2-[1-(2-methoxyphenyl)-1-piperazinyl]ethyl-N-2-pyridinyl-benzamide (p-[18F]MPPF). *J Radioanal Nucl Chem.* 2010;286:841-846.
349. Yu H-M, Chan C-H, Yang C-H, Hsia H-T, Wang M-H. Hexavalent lactoside labeled with [18F]AIF for PET imaging of asialoglycoprotein receptor. *Appl Radiat Isot.* 2020;162:109199.
350. Laferriere-Holloway TS, Rios A, Dam RM van. Detrimental impact of aqueous mobile phases on 18F-labelled radiopharmaceutical analysis via radio-TLC. *Anal Methods.* 2023;15:377-387.
351. Nyiredy S. Planar Chromatographic Method Development Using the PRISMA Optimization System and Flow Charts. *J Chromatogr Sci.* 2002;40:553-563.
352. Wang J, Holloway T, Lisova K, Dam RM van. Green and efficient synthesis of the radiopharmaceutical [18F]FDOPA using a microdroplet reactor. *React Chem Eng.* December 2019.
353. Cai L. Thin Layer Chromatography. *Curr Protoc Essent Lab.* 2014;8:6.3.1-6.3.18.
354. Snyder L. Solvent selectivity in normal-phase TLC. *JPC - J Planar Chromat.* 2008;21:315-323.
355. Fried B, Sherma B. Thin-Layer Chromatography, Revised And Expanded. Boca Raton: CRC Press; 1999.
356. Huang Y-Y, Tzen K-Y, Liu Y-L, et al. Impact of residual 18F-fluoride in 18F-FDOPA for the diagnosis of neuroblastoma. *Ann Nucl Med.* 2015;29:489-498.
357. Huang Y-Y, Poniger S, Tsai C-L, Tochon-Danguy HJ, Ackermann U, Yen R-F. Three-step two-pot automated production of NCA [18F]FDOPA with FlexLab module. *Appl Radiat Isot.* 2020;158:108871.
358. Nanabala R, Pillai MRA, Gopal B. Experience of 6-I-[18F]FDOPA Production Using Commercial Disposable Cassettes and an Automated Module. *Nucl Med Mol Imaging.* 2022;56:127-136.
359. Varlow C, Murrell E, Holland JP, et al. Revisiting the Radiosynthesis of [18F]FPEB and Preliminary PET Imaging in a Mouse Model of Alzheimer's Disease. *Mol.* 2020;25:982.
360. Stephenson NA, Holland JP, Kassenbrock A, et al. Iodonium Ylide Mediated Radiofluorination of 18F-FPEB and Validation for Human Use. *J Nucl Med.* 2015;56:489-492.
361. Wang J-Q, Tueckmantel W, Zhu A, Pellegrino D, Brownell A-L. Synthesis and preliminary biological evaluation of 3-[18F]fluoro-5-(2-pyridinylethynyl)benzotrile as a PET radiotracer for imaging metabotropic glutamate receptor subtype 5. *Synapse.* 2007;61:951-961.



362. Sullivan JM, Lim K, Labaree D, et al. Kinetic Analysis of the Metabotropic Glutamate Subtype 5 Tracer [18F]FPPEB in Bolus and Bolus-Plus-Constant-Infusion Studies in Humans. *J Cereb Blood Flow Metab.* 2013;33:532-541.
363. Lim K, Labaree D, Li S, Huang Y. Preparation of the metabotropic glutamate receptor 5 (mGluR5) PET tracer [18F]FPPEB for human use: An automated radiosynthesis and a novel one-pot synthesis of its radiolabeling precursor. *Appl Radiat Isot.* 2014;94:349-354.
364. Li F, Hicks JW, Yu L, et al. Plasma radio-metabolite analysis of PET tracers for dynamic PET imaging: TLC and autoradiography. *EJNMMI Research.* 2020;10:141 (12 pages).
365. Jin Z-H, Furukawa T, Sogawa C, et al. PET imaging and biodistribution analysis of the effects of succinylated gelatin combined with l-lysine on renal uptake and retention of 64Cu-cyclam-RAFT-c(-RGDfK-)4 in vivo. *Eur J Pharm Biopharm.* 2014;86:478-486.
366. Kokic M, Honer M, Kessler LJ, Grauert M, Schubiger PA, Ametamey SM. Synthesis and in Vitro and in Vivo Evaluation of [11c]methyl-Biii277cl for Imaging the Pcp-Binding Site of the Nmda Receptor by Pet. *J Recept Signal Transduct Res.* 2002;22:123-139.
367. Kuang Y, Salem N, Corn DJ, et al. Transport and Metabolism of Radiolabeled Choline in Hepatocellular Carcinoma. *Mol Pharmaceutics.* 2010;7:2077-2092.
368. Kuang Y, Wang F, Corn DJ, Tian H, Lee Z. Metabolism of Radiolabeled Methionine in Hepatocellular Carcinoma. *Mol Imaging Biol.* 2014;16:44-52.
369. Matusch A, Meyer PT, Bier D, et al. Metabolism of the A1 adenosine receptor PET ligand [18F]CPFPX by CYP1A2: implications for bolus/infusion PET studies. *Nucl Med Biol.* 2006;33:891-898.
370. Roivainen A, Nägren K, Hirvonen J, et al. Whole-body distribution and metabolism of [N-methyl-11C](R)-1-(2-chlorophenyl)-N-(1-methylpropyl)-3-isoquinolinecarboxamide in humans; an imaging agent for in vivo assessment of peripheral benzodiazepine receptor activity with positron emission tomography. *Eur J Nucl Med Mol Imaging.* 2009;36:671-682.
371. Tang D, Li J, Buck JR, et al. Evaluation of TSPO PET Ligands [18F]VUIIS1009A and [18F]VUIIS1009B: Tracers for Cancer Imaging. *Mol Imaging Biol.* 2017;19:578-588.
372. Steinmetz A. The Broad Scope of Cesium Salts in Organic Chemistry. *Catalysts Cesium from Acros Organics.* 2011:3-11.
373. Khalil MM, Tremoleda JL, Bayomy TB, Gsell W. Molecular SPECT Imaging: An Overview. *International Journal of Molecular Imaging.* 2011;2011:1-15.
374. Schwaiger M, Wester H-J. How Many PET Tracers Do We Need? *J Nucl Med.* 2011;52:36S-41S.
375. L. Pimlott S, Sutherland A. Molecular tracers for the PET and SPECT imaging of disease. *Chem Soc Rev.* 2011;40:149-162.

376. Krasikova R. PET Radiochemistry Automation: State of the Art and Future Trends in  $^{18}\text{F}$ -nucleophilic Fluorination. *COC*. 2013;17:2097-2107.
377. Liu K, Wang M-W, Lin W-Y, et al. Molecular Imaging Probe Development Using Microfluidics. *COS*. 2011;8:473-487.
378. Wang J, van Dam RM. High-Efficiency Production of Radiopharmaceuticals via Droplet Radiochemistry: A Review of Recent Progress. *Mol Imaging*. 2020;19:1536012120973099.
379. Ding H, Sadeghi S, Shah GJ, et al. Accurate dispensing of volatile reagents on demand for chemical reactions in EWOD chips. *Lab Chip*. 2012;12:3331-3340.
380. Wang J, Chao PH, Hanet S, van Dam RM. Performing multi-step chemical reactions in microliter-sized droplets by leveraging a simple passive transport mechanism. *Lab Chip*. 2017;17:4342-4355.
381. Wang J, Chao PH, van Dam RM. Ultra-compact, automated microdroplet radiosynthesizer. *Lab Chip*. 2019;19:2415-2424.
382. Lisova K, Sergeev M, Evans-Axelsson S, et al. Microscale radiosynthesis, preclinical imaging and dosimetry study of  $^{18}\text{F}$ AMBF3-TATE: A potential PET tracer for clinical imaging of somatostatin receptors. *Nucl Med Biol*. 2018;61:36-44.
383. Rios A, Wang J, Chao PH, van Dam RM. A novel multi-reaction microdroplet platform for rapid radiochemistry optimization. *RSC Adv*. 2019;9:20370-20374.
384. Frank C, Winter G, Rensei F, et al. Development and implementation of ISAR, a new synthesis platform for radiopharmaceutical production. *EJNMMI radiopharm chem*. 2019;4:24.
385. Ovdichuk O, Mallapura H, Pineda F, et al. Implementation of iMiDEV<sup>TM</sup>, a new fully automated microfluidic platform for radiopharmaceutical production. *Lab Chip*. 2021;21:2272-2282.
386. Rensch C, Lindner S, Salvamoser R, et al. A solvent resistant lab-on-chip platform for radiochemistry applications. *Lab Chip*. 2014;14:2556-2564.
387. Mueller M, Howitz S. Device and method for the production of radiochemical compounds. January 2017.
388. Gu Z, Taschereau R, Vu NT, Prout DL, Lee J, Chatziioannou AF. Performance evaluation of HiPET, a high sensitivity and high resolution preclinical PET tomograph. *Phys Med Biol*. 2020;65:045009.
389. Taschereau R, Vu NT, Chatziioannou AF. Calibration and data standardization of a prototype bench-top preclinical CT. In: 2014 IEEE Nuclear Science Symposium and Medical Imaging Conference (NSS/MIC). ; 2014:1-2.
390. Seok Moon B, Hyung Park J, Jin Lee H, et al. Highly efficient production of  $^{18}\text{F}$ fallypride using small amounts of base concentration. *Appl Radiat Isot*. 2010;68:2279-2284.

391. Siessmeier T, Zhou Y, Buchholz H-G, et al. Parametric Mapping of Binding in Human Brain of D2 Receptor Ligands of Different Affinities. *J Nucl Med.* 2005;46:964-972.
392. Vandehey NT, Moirano JM, Converse AK, et al. High-Affinity Dopamine D2/D3 PET Radioligands 18F-Fallypride and 11C-FLB457: A Comparison of Kinetics in Extrastriatal Regions Using a Multiple-Injection Protocol. *J Cereb Blood Flow Metab.* 2010;30:994-1007.
393. Cresswell AJ, Davies SG, Roberts PM, Thomson JE. Beyond the Balz–Schiemann Reaction: The Utility of Tetrafluoroborates and Boron Trifluoride as Nucleophilic Fluoride Sources. *Chem Rev.* 2015;115:566-611.
394. Zhou Y, Wang J, Gu Z, et al. Next Generation of Fluorine-Containing Pharmaceuticals, Compounds Currently in Phase II–III Clinical Trials of Major Pharmaceutical Companies: New Structural Trends and Therapeutic Areas. *Chem Rev.* 2016;116:422-518.
395. Meyer F. Fluorinated conjugated polymers in organic bulk heterojunction photovoltaic solar cells. *Progress in Polymer Science.* 2015;47:70-91.
396. Ametamey SM, Honer M, Schubiger PA. Molecular Imaging with PET. *Chem Rev.* 2008;108:1501-1516.
397. Preshlock S, Tredwell M, Gouverneur V. 18F-Labeling of Arenes and Heteroarenes for Applications in Positron Emission Tomography. *Chem Rev.* 2016;116:719-766.
398. Halder R, Ritter T. 18F-Fluorination: Challenge and Opportunity for Organic Chemists. *J Org Chem.* 2021;86:13873-13884.
399. Campbell MG, Ritter T. Modern Carbon–Fluorine Bond Forming Reactions for Aryl Fluoride Synthesis. *Chem Rev.* 2015;115:612-633.
400. Champagne PA, Desroches J, Hamel J-D, Vandamme M, Paquin J-F. Monofluorination of Organic Compounds: 10 Years of Innovation. *Chem Rev.* 2015;115:9073-9174.
401. Liang T, Neumann CN, Ritter T. Introduction of Fluorine and Fluorine-Containing Functional Groups. *Angewandte Chemie International Edition.* 2013;52:8214-8264.
402. van der Born D, Pees A, Poot AJ, Orru RVA, Windhorst AD, Vugts DJ. Fluorine-18 labelled building blocks for PET tracer synthesis. *Chem Soc Rev.* 2017;46:4709-4773.
403. See YY, Morales-Colón MT, Bland DC, Sanford MS. Development of SNAr Nucleophilic Fluorination: A Fruitful Academia-Industry Collaboration. *Acc Chem Res.* 2020;53:2372-2383.
404. Sander K, Gendron T, Yiannaki E, et al. Sulfonium Salts as Leaving Groups for Aromatic Labelling of Drug-like Small Molecules with Fluorine-18. *Scientific Reports.* 2015;5:9941.
405. Rotstein BH, Stephenson NA, Vasdev N, Liang SH. Spirocyclic hypervalent iodine(III)-mediated radiofluorination of non-activated and hindered aromatics. *Nature Communications.* 2014;5:4365.

406. Cardinale J, Ermert J, Humpert S, Coenen HH. Iodonium ylides for one-step, no-carrier-added radiofluorination of electron rich arenes, exemplified with 4-([<sup>18</sup>F]fluorophenoxy)-phenylmethyl)piperidine NET and SERT ligands. *RSC Adv.* 2014;4:17293-17299.
407. Fuchigami T, Inagi S. Selective electrochemical fluorination of organic molecules and macromolecules in ionic liquids. *Chem Commun.* 2011;47:10211.
408. Fuchigami T, Inagi S. Recent Advances in Electrochemical Systems for Selective Fluorination of Organic Compounds. *Acc Chem Res.* 2020;53:322-334.
409. Hernández-Valdés D, Sadeghi S. Electrochemical Radiofluorination of Small Molecules: New Advances. *The Chemical Record.* 2021;21:2397-2410.
410. Reischl G, Kienzle GJ, Machulla H-J. Electrochemical radiofluorination. Part 211 For part 1 see Reischl et al. (2002).. Anodic monofluorination of substituted benzenes using [<sup>18</sup>F]fluoride. *Applied Radiation and Isotopes.* 2003;58:679-683.
411. He Q, Wang Y, Alfeazi I, Sadeghi S. Electrochemical nucleophilic synthesis of di-tert-butyl-(4-[<sup>18</sup>F]fluoro-1,2-phenylene)-dicarbonate. *Applied Radiation and Isotopes.* 2014;92:52-57.
412. Lebedev A, Jiao J, Lee J, et al. Radiochemistry on electrodes: Synthesis of an <sup>18</sup>F-labelled and in vivo stable COX-2 inhibitor. Garg P, ed. *PLoS ONE.* 2017;12:e0176606.
413. Balandeh M, Waldmann C, Shirazi D, et al. Electrochemical Fluorination and Radiofluorination of Methyl(phenylthio)acetate Using Tetrabutylammonium Fluoride (TBAF). *J Electrochem Soc.* 2017;164:G99-G103.
414. Sawamura T, Takahashi K, Inagi S, Fuchigami T. Electrochemical Fluorination Using Alkali-Metal Fluorides. *Angew Chem Int Ed.* 2012;51:4413-4416.
415. Shida N, Takenaka H, Gotou A, et al. Alkali Metal Fluorides in Fluorinated Alcohols: Fundamental Properties and Applications to Electrochemical Fluorination. *J Org Chem.* 2021;86:16128-16133.
416. Fujie S, Matsumoto K, Suga S, Yoshida J. Thiofluorination of Carbon–Carbon Multiple Bonds Using Electrochemically Generated ArS(ArSSAr)+BF<sub>4</sub><sup>-</sup>. *Chem Lett.* 2009;38:1186-1187.
417. Yoshida J, Ishichi Y, Ise S. Intramolecular carbon-carbon bond formation by the anodic oxidation of unsaturated .alpha.-stannyl heteroatom compounds. Synthesis of fluorine containing heterocyclic compounds. *J Am Chem Soc.* 1992;114:7594-7595.
418. Allison N, Balandeh M, Holloway T, et al. Electrochemical no-carrier-added radiofluorination of thioethers. *Journal of Fluorine Chemistry.* 2022;257-258:109988.
419. Sergeev M, Lazari M, Morgia F, et al. Performing radiosynthesis in microvolumes to maximize molar activity of tracers for positron emission tomography. *Commun Chem.* 2018;1:1-10.

420. Shida N, Zhou Y, Inagi S. Bipolar Electrochemistry: A Powerful Tool for Electrifying Functional Material Synthesis. *Acc Chem Res.* 2019;52:2598-2608.
421. Fosdick SE, Knust KN, Scida K, Crooks RM. Bipolar Electrochemistry. *Angewandte Chemie International Edition.* 2013;52:10438-10456.
422. Loget G, Zigah D, Bouffier L, Sojic N, Kuhn A. Bipolar Electrochemistry: From Materials Science to Motion and Beyond. *Acc Chem Res.* 2013;46:2513-2523.
423. Miyamoto K, Nishiyama H, Tomita I, Inagi S. Development of a Split Bipolar Electrode System for Electrochemical Fluorination of Triphenylmethane. *ChemElectroChem.* 2019;6:97-100.
424. Shida N, Villani E, Sanuki M, et al. Bipolar Electrochemical Fluorination of Triphenylmethane and Bis(phenylthio)diphenylmethane Derivatives in a U-shaped Cell. *Electrochemistry.* 2021;89:476-479.
425. Balandeh M, Rios A, Allison N, et al. Electrochemical Flash Fluorination and Radiofluorination. *ChemElectroChem.* 2018;5:3353-3356.
426. Waldmann CM, Lebedev A, Allison N, Sadeghi S. An automated synthesizer for electrochemical <sup>18</sup>F-fluorination of organic compounds. *Applied Radiation and Isotopes.* 2017;127:245-252.
427. Fuchigami T, Konno A, Nakagawa K, Shimojo M. Electrolytic Partial Fluorination of Organic Compounds. 12. Selective Anodic Monofluorination of Fluoroalkyl and Alkyl Sulfides. *J Org Chem.* 1994;59:5937-5941.
428. Konno A, Nakagawa K, Fuchigami T. New mechanistic aspects of anodic monofluorination of halogenoalkyl and alkyl phenyl sulphides. *J Chem Soc, Chem Commun.* 1991:1027-1029.
429. An X-D, Xiao J. Fluorinated Alcohols: Magic Reaction Medium and Promoters for Organic Synthesis. *The Chemical Record.* 2020;20:142-161.
430. Wencel-Delord J, Colobert F. A remarkable solvent effect of fluorinated alcohols on transition metal catalysed C–H functionalizations. *Org Chem Front.* 2016;3:394-400.
431. Schmeisser M, Illner P, Puchta R, Zahl A, van Eldik R. Gutmann Donor and Acceptor Numbers for Ionic Liquids. *Chemistry – A European Journal.* 2012;18:10969-10982.
432. Shida N, Imada Y, Nagahara S, Okada Y, Chiba K. Interplay of arene radical cations with anions and fluorinated alcohols in hole catalysis. *Commun Chem.* 2019;2:24.
433. Sakagami H, Takenaka H, Iwai S, et al. A Flow Electrochemical Cell with Split Bipolar Electrode for Anodic Oxidation of Organic Compounds. *ChemElectroChem.* 2022;9:e202200084.